

# Magnetic Resonance Elastography of Prostate Cancer

by

**Ramin Sebastian Sahebjavaheer**

B.A.Sc., University of British Columbia, 2006

M.A.Sc., University of British Columbia, 2008

A THESIS SUBMITTED IN PARTIAL FULFILLMENT OF  
THE REQUIREMENTS FOR THE DEGREE OF

**Doctor of Philosophy**

in

The Faculty of Graduate and Postdoctoral Studies  
(Biomedical Engineering)

The University of British Columbia

(Vancouver)

September 2013

© Ramin Sebastian Sahebjavaheer, 2013

# Abstract

This work presents new approaches to *in-vivo* and *ex-vivo* human prostate cancer imaging using magnetic resonance elastography (MRE) – a method to non-invasively image tissue elasticity using magnetic resonance imaging (MRI). From a clinical perspective, stiffness correlates with underlying tissue disease processes and has been traditionally probed with palpation. Thus, diagnosis based on mechanical properties may have great implications in terms of staging of prostate cancer, monitoring disease progression, treatment planning and post treatment follow up. In MRE, mechanical shear waves generated by an external transducer are imaged using an MRI scanner. From the acquired wave field it is possible to reconstruct mechanical properties such as the elastic modulus based on the wave equation.

In this work two MR compatible trans-perineal transducers are developed for imaging of the human prostate on a 3T MR scanner. A new MRI pulse sequence is also developed to acquire the three dimensional wave field induced by these transducers. The methods are validated in quality assurance phantoms and volunteer repeatability studies. The system is used for a patient study and the results are compared to the gold standard (whole-mount histopathology marked with Gleason score). Similarly, a transducer is developed for *ex-vivo* prostate studies on a 7T MR scanner. After validation, prostate specimens of patients are examined and the results are compared to the Gleason score.

The overall conclusion are: (i) trans-perineal excitation is well tolerated by the subjects, (ii) the transducers do not interfere with the MR acquisition, (iii) the three dimensional wave field are successfully captured using the new pulse sequence, (iv) phantom validation studies prove that the methods are in fact repeatable and that the stiffness values match with the manufacturer's specifications, (v) patient motion and the standing wave pattern degrade the repeatability of the reconstructed images, (vi) the prostate gland stands out in the stiffness and shear strain images, (vii) the central gland and in particular the transition zone are stiffer than the peripheral zone, (viii) cancer could indeed be detected with MRE with an area under the receiver-operator-curve of approximately 0.7, and finally (ix) the chemical fixation process degrades the stiffness contrast.

# Preface

This study was approved by the University of British Columbia (UBC) Research Ethics Board. The UBC CREB number of this study is H09-03163 with Dr. Septimiu Salcudean as the principle investigator and the author as a co-investigator. Refer to Appendix B for the consent form used for this study.

This thesis is primarily based on four manuscripts, resulting from collaboration of multiple researchers. All publications have been modified to make the thesis coherent. The contributions from this thesis has led to the following publications, submissions and presentations:

## **First author journal papers**

1. Sahebjavaher RS, Baghani A, Honarvar M, Sinkus R, Salcudean SE, Trans-perineal Prostate MR Elastography: initial *in-vivo* results, *Magnetic Resonance in Medicine*, vol. 69, no. 2, pp. 411–20, 2013. (published, Part of Chapter 1 and 2)
2. Sahebjavaher RS, Frew S, Bylinskii A, terBeek L, Garteiser P, Sinkus R, Salcudean S, Rapid 3D MR Elastography of the Prostate with a Shielded Electromagnetic Transducer and Multi-slice Steady-state Gradient Echo Sequence: design and characterization results, *Journal of Magnetic Resonance Imaging*. (submitted, Part of Chapter 3)
3. Sahebjavaher RS, ...Kozlowski, Sinkus R, Salcudean S, *in-vivo* prostate cancer MRE: quantitative comparison to histopathology, *Magnetic Resonance in Medicine*. (manuscript ready to be submitted, Part of Chapter 4)
4. Sahebjavaher RS, ...Kozlowski, Sinkus R, Salcudean S, *ex-vivo* prostate cancer MRE and diffusion-weighted imaging: quantitative comparison to histopathology, *Magnetic Resonance in Medicine*. (manuscript ready to be submitted, Part of Chapter 5)

## **Secondary author journal papers**

5. Baghani A, Salcudean SE, Honarvar M, Sahebjavaher RS, Rohling R, Sinkus R, Travelling Wave Expansion: a model fitting approach to the inverse problem of elasticity reconstruction, *Medical Imaging, IEEE Transactions on* 30, no. 8 (2011): 1555-1565. (Part of Chapter 2)
6. Honarvar M, Sahebjavaher RS, Salcudean SE, Rohling R, Sparsity Regularization in Dynamic Elastography, *Physics in Medicine and Biology* 57, no. 19 (2012): 5909. (Part of Chapter 3)
7. Garteiser P, Sahebjavaher RS, terBeek LC, Salcudean SE, Vilgrain V, vanBeers B, Sinkus R, Rapid acquisition of multifrequency, multislice and multidirectional MR elastography data with a fractionally encoded gradient echo sequence, *NMR in Biomedicine* 2013. (in press, Part of Chapter 3)

8. Honarvar M, Sahebjavaher RS, Sinkus R, Rohling R, Salcudean SE, Curl-based Finite Element Reconstruction of the Shear Modulus Without Assuming Local Homogeneity: Time Harmonic Case, Transactions in Medical Imaging, 2013. (submitted, Part of Chapter 3)
9. Nir G, Sahebjavaher RS, Kozlowski P, Chang SD, Sinkus R, Goldenberg L, Salcudean SE, Model-Based Registration of *Ex-vivo* and *In-vivo* MRI of the Prostate Using Elastography, Transactions in Medical Imaging, 2012. (in press, Part of Chapter 4 and 5).
10. Nir G, Sahebjavaher R, ... Chang SD, Jones EC, Goldenberg SL, Salcudean SE, A Framework for Registration of Whole mount Histology and Volumetric Imaging of the Prostate Using Particle Filtering. (manuscript to be submitted, Part of Chapter 4 and 5)

### **Refereed conferences**

1. Sahebjavaher RS, Sinkus R, and Salcudean SE, Trans-perineal Prostate MRE at 3T, in Proceedings of the International Tissue Elasticity Conference, Snowbird, USA, 2010, p. 33. (Part of Chapter 2)
2. Sahebjavaher RS, Baghani A, Sinkus R, and Salcudean SE, Prostate MRE at 3T: Trans-perineal wave propagation, Int. Society for Magnetic Resonance in Medicine, Montreal, Canada, May 2011 p. 1477. (Part of Chapter 2)
3. Sahebjavaher RS, Garteiser P, Van Beers B, Salcudean SE, and Sinkus R, *In-vivo* MR Rheology of liver at multiple frequencies in 3D: effect of displacement data dimensionality on shear modulus, in Proceedings International Tissue Elasticity Conference, Arlington, Texas, USA, 2011, p. 102. (Part of Chapter 3)
4. Sahebjavaher RS, Garteiser P, Van Beers B, Salcudean SE, and Sinkus R, Rapid 3D motion-encoding using spoiled FFE: application towards multi-frequency MR rheology in liver, European Society for Magnetic Resonance in Medicine and Biology, Leipzig, Germany, May 2011, p. 124. (Part of Chapter 3)
5. Sahebjavaher RS, Garteiser P, Sinkus R, Gagnon LO, Baghani A, Chang S, Chatelin S, Jones EC, Nguan C, Goldenberg L, Moradi M, Kozlowski P, and Salcudean SE, 3D MR Elastography of *in-vivo* Prostate Cancer and Correlation with Histology: Preliminary results, Int. Society for Magnetic Resonance in Medicine, Melbourne, Australia, May 2012, p. 2514. (Part of Chapter 4)
6. Sahebjavaher RS, Nir G, Mohareri O, Gagnon LO, Jones EC, Goldenberg L, Garteiser P, Sinkus R, Kozlowski P, Salcudean S, MR Elastography of *in-vivo* and *ex-vivo* Prostate Cancer and Correlation with Histology, in Proceedings International Tissue Elasticity Conference, Deauville, France, 2012, p. 81. (Part of Chapter 4 and 5)
7. Sahebjavaher RS, Nir G, Honarvar M, Yung A, Kozlowski P, Gagnon LO, Jones EC, Garteiser P, Sinkus R, Chang S, Goldenberg L, Salcudean SE, MR Elastography of *ex-vivo* Prostate Cancer at Multiple Frequencies at 7T, Int. Society for Magnetic Resonance in Medicine, 2013. (Part of Chapter 5)

## Patent

1. Salcudean SE, Sahebjavaher RS, Sinkus R, Trans-perineal Prostate MRE U.S. Patent United States Patent Application 2012/0053450, A101-Mar-2012 (2012), Pending Patent. (Part of Chapter 2)

## Book chapter

1. Salcudean SE, Sahebjavaher RS, Goksel O, Baghani A, Mahdavi SS, Nir G, Sinkus R, and Moradi M, Biomechanical Modeling of the Prostate for Procedure Guidance and Simulation, Soft Tissue Biomechanical Modeling for Computer Assisted Surgery (2012): 169-198. (Part of Chapter 2).

All of the chapters of this thesis are written by the author with the assistance of Prof. Salcudean. The author spearheaded the majority of the work of this project including: design and simulation of the transducers, construction of the final designs, performance evaluation of the system, image analysis and interpretation. All work related to phantom, *in-vivo* and *ex-vivo* validation work was also performed by the author. That being said, this work would have been impossible without contributions from collaborators mentioned below.

This project is the brainchild of Prof. Septimiu Salcudean who, from the very beginning, had the vision for this project, and supported it with numerous grants, supported me financially and provided invaluable guidance as my primary supervisor. He assisted with the design phase of the transducers, and provided valuable insight in the image processing, and development of reconstruction algorithms. Additionally, Dr. Salcudean provided assistance in setting up the patient studies and helped with the interpretation and analysis of the results.

Dr. Ralph Sinkus provided indispensable know-how in MRE methods. In a research visit to UBC, he provided the first pulse sequence for MRE, assisted with acquisition of the first successful cases, and provided the curl-based direct inversion algorithm that this work heavily relies on. The eXpresso pulse sequence was developed by the author, Dr. Philippe Garteiser, and Prof Sinkus during a six-month research visit by the author at Prof Sinku's group in Paris, France. Dr. Garteiser performed some of the comparative studies between the eXpresso and SE-EPI pulse sequence re-visited in this work.

Prof Robert Rohling provided guidance for the direction and scope of this work.

Dr. Piotr Kozlowski provided significant assistance, grant support and guidance of this project for the protocol of the *in-vivo* patient study as well as the setup of the *ex-vivo* study. The device used for cutting of the prostate glands was kindly provided by his group. Dr. Kozlowski's group especially Andrew Yung, Barry Bohnet and Shirin Sabouri also contributed with imaging of some of the *ex-vivo* MRE cases.

Dr. Mehdi Moradi assisted with the development of the image processing algorithm used for calculating the receiver-operating-characteristic curves.

Dr. Ali Baghani developed the 3D LFE and TWE code based on the phantom data acquired by the author. The LFE code is also used for some of the image processing in this work. Dr. Baghani assisted with interpretation and analysis of some of the data.

Mr. Guy Nir developed the registration algorithm that was instrumental to this work for *in-vivo* and *ex-vivo* prostate images. He also provided assistance with segmentation and image analysis of the data from the patient studies.

Mr. Mohammad Honarvar developed the mixed FEM code as well as the curl-FEM algorithm based on data acquired by the author. He also designed and constructed the spatially heterogeneous phantom used in this work.

Mr. Omid Mohareri assisted with conducting some of the patient study cases, as well as comparison of the MRE and Ultrasound elastography images. Guy Nir and Hamid Moradi also assisted with some of the patient data collection.

Dr. Sheldon L Goldenberg is a world-renowned urology surgeon and researcher at Vancouver General Hospital (VGH). He supported this project through his two amazing fellows Dr. Louis O. Gagnon and Dr. Joseph Ischia who recruited patients for the patient studies conducted in this work.

Dr. Edward Jones is an experienced pathologists at Vancouver General Hospital (VGH) who allocated significant time out of his busy schedule for this project. He contributed by cutting the prostate glands using a custom made device and patiently delineated the tumors (marked the outline using a pen under a microscope and indicated the Gleason score) on the histology slides.

Dr. Ladan Fazli is an experienced pathologist at Vancouver General Hospital (VGH) and helped with the understanding of the results from the patient study based on underlying tissue changes.

Dr. Silvia Chang is an experienced radiologist at UBC who assisted with the protocol of the patient study. She also helped with the segmentations of the images used for registration and analysis.

Mr. Samuel Frew assisted with the design and construction of the final version of the transducer including the electronics.

Mr. Artem Bylinskii assisted with the design and construction of the final version of the electromagnetic trans-perineal transducer as a Co-op student.

The thesis is heavily based on articles resulting from this research. Chapters 1 to 6 are modified versions of these articles.

# Table of Contents

|  |             |
|--|-------------|
| <b>Abstract</b> .....  | <b>ii</b>   |
| <b>Preface</b> .....   | <b>iii</b>  |
| <b>Table of Contents</b> .....   | <b>vii</b>  |
| <b>List of Tables</b> .....  | <b>x</b>    |
| <b>List of Figures</b> .....   | <b>xi</b>   |
| <b>Glossary</b> .....  | <b>xx</b>   |
| <b>Acknowledgements</b> .....  | <b>xxii</b> |
| <b>Dedication</b> .....  | <b>xxiv</b> |
| <b>Chapter 1 - Introduction</b> .....  | <b>1</b>    |
| 1.1 CLINICAL MOTIVATION .....  | 1           |
| 1.2 BACKGROUND .....   | 2           |
| 1.2.1 Magnetic resonance elastography (MRE).....   | 2           |
| 1.2.2 MRE in prostate cancer.....  | 3           |
| 1.2.3 Mechanical transducer .....  | 4           |
| 1.2.4 Acquisition of the displacement field .....  | 6           |
| 1.2.5 Reconstruction of viscoelastic parameters.....   | 13          |
| 1.2.6 Literature review: elasticity of prostate.....   | 14          |
| 1.3 THESIS OBJECTIVES .....  | 15          |
| 1.4 THESIS OUTLINE .....   | 17          |
| <b>Chapter 2 - <i>In-vivo</i> prostate MRE with hydraulic transducer and harmonic acquisition method</b> ..... | <b>18</b>   |
| 2.1 INTRODUCTION.....  | 18          |
| 2.2 METHODS .....  | 18          |
| 2.2.1 Trans-perineal excitation with hydraulic transducer.....   | 18          |
| 2.2.2 Acquisition of the 3D wave field using harmonic method.....  | 22          |
| 2.2.3 Reconstruction and repeatability.....  | 24          |
| 2.3 RESULTS .....  | 25          |
| 2.3.1 Phantom experiments.....   | 25          |
| 2.3.2 <i>In-vivo</i> prostate examinations .....   | 28          |
| 2.4 DISCUSSION.....  | 34          |

|   |           |
|---|-----------|
| 2.5 CASE STUDIES.....   | 35        |
| 2.5.1 Phantom: TWE algorithm.....   | 35        |
| 2.6 CONCLUSION .....  | 35        |
| <b>Chapter 3 - <i>In-vivo</i> prostate MRE with trans-perineal electromagnetic actuation and a fast fractionally encoded steady-state gradient echo sequence.....</b> | <b>37</b> |
| 3.1 INTRODUCTION.....   | 37        |
| 3.2 METHODS .....   | 39        |
| 3.2.1 Design of a shielded electromagnetic transducer.....  | 39        |
| 3.2.2 Transducer characterization .....   | 43        |
| 3.2.3 Acquisition of the 3D wave field ( <i>eXpresso</i> pulse sequence).....   | 44        |
| 3.2.4 Phantom experiments.....  | 48        |
| 3.2.5 <i>In-vivo</i> human studies .....  | 49        |
| 3.2.6 Image processing.....   | 49        |
| 3.3 RESULTS .....   | 49        |
| 3.3.1 Transducer characterization .....   | 49        |
| 3.3.2 Phantom experiments.....  | 51        |
| 3.3.3 <i>In-vivo</i> human study.....   | 53        |
| 3.4 DISCUSSION.....   | 55        |
| 3.5 CASE STUDIES.....   | 57        |
| 3.5.1 Comparison studies between SE-EPI and <i>eXpresso</i> pulse sequences.....  | 57        |
| 3.5.2 Phantom: sparsity regularized FEM.....  | 61        |
| 3.5.3 Phantom: curl-based FEM .....   | 62        |
| 3.6 CONCLUSION .....  | 62        |
| <b>Chapter 4 - <i>In-vivo</i> prostate cancer MRE: quantitative comparison to histopathology.....</b>   | <b>63</b> |
| 4.1 INTRODUCTION.....   | 63        |
| 4.2 METHODS .....   | 63        |
| 4.2.1 Volunteer and patient studies.....  | 63        |
| 4.2.2 Setup and acquisition .....   | 66        |
| 4.2.3 Quality metrics for 3D wave field.....  | 66        |
| 4.2.4 Reconstruction of mechanical parameters and image processing.....   | 68        |
| 4.2.5 Histology.....  | 68        |
| 4.2.6 Registration.....   | 68        |
| 4.2.7 Receiver operator curve (ROC) analysis.....   | 69        |
| 4.3 RESULTS .....   | 69        |
| 4.3.1 Repeatability study.....  | 69        |

|   |            |
|---|------------|
| 4.3.2 Patient study .....   | 71         |
| 4.4 DISCUSSION .....  | 80         |
| 4.5 CASE STUDIES .....  | 81         |
| 4.5.1 Repeatability in phantom (200±6 Hz frequency shift) .....   | 81         |
| 4.5.2 Reputability in Volunteers .....  | 84         |
| 4.6 CONCLUSION .....  | 90         |
| <b>Chapter 5 - <i>Ex-vivo</i> prostate cancer MRE and diffusion-weighted imaging: quantitative comparison to histopathology .....</b> | <b>91</b>  |
| 5.1 INTRODUCTION .....  | 91         |
| 5.2 METHODS .....   | 91         |
| 5.2.1 Patient study .....   | 91         |
| 5.2.2 Mechanical transcoder and experimental setup .....  | 93         |
| 5.2.3 Acquisition .....   | 95         |
| 5.2.4 Image processing .....  | 96         |
| 5.2.5 Quality metrics for 3D wave field .....   | 96         |
| 5.2.6 Histology, registration and data analysis .....   | 97         |
| 5.2.7 Phantom validation .....  | 98         |
| 5.3 RESULTS .....   | 98         |
| 5.3.1 Transducer and phantom study .....  | 98         |
| 5.3.2 Patient study .....   | 100        |
| 5.4 DISCUSSION .....  | 112        |
| 5.5 COMPARISON BETWEEN IN-VIVO AND EX-VIVO MRE .....  | 116        |
| 5.6 CONCLUSION .....  | 118        |
| <b>Chapter 6 - Conclusion .....</b>   | <b>119</b> |
| 6.1 SUMMARY .....   | 119        |
| 6.2 CONTRIBUTIONS .....   | 120        |
| 6.3 FUTURE WORK .....   | 120        |
| <b>Bibliography .....</b>   | <b>122</b> |
| <b>Appendix A – Modeling of the Hydraulic Transducer .....</b>  | <b>131</b> |
| <b>Appendix B – Consent form .....</b>  | <b>140</b> |
| <b>Appendix C – Additional images from <i>in-vivo</i> patient studies .....</b>   | <b>147</b> |
| <b>Appendix D – Additional images from <i>ex-vivo</i> patient studies .....</b>   | <b>175</b> |

# List of Tables

|   |     |
|---|-----|
| Table 1-1. Comparison between MR elastography (MRE) sequence parameters in the literature. diff. = difference; NA = not available; var. = variable. (Adapted from [83] with permission) .....   | 12  |
| Table 2-1. Elasticity of the prostate for six healthy volunteers.....   | 30  |
| Table 2-2. Elasticity of the prostate for healthy volunteers (F, B and D) was repeated at various times. The table shows that the results from trans-perineal MRE are repeatable within the experimental error. Same colour highlight denotes that the experiment was taken the same day. The first protocol with 1.5 mm resolution is indicated as (P1) and the second protocol with 3 mm resolution is indicated as (P2). ..... | 33  |
| Table 3-1. The geometry and measured properties of the coils. ....  | 41  |
| Table 3-2. Elasticity values (in kPa) for inclusion of different stiffness in a quality assurance as reported by the manufacturer (in brackets) and measured using methods discussed in this thesis.....  | 53  |
| Table 4-1. Clinical data for patients with biopsy confirmed cancer. (NPH=Nodular prostatic hyperplasia, PIN=Prostatic Intraepithelial neoplasia, PNI= Perineural invasion, SV= seminal vesicles, PUE=Prostatic Urethral Ectasia, BPU=Benign prostatic urothelium).....  | 65  |
| Table 4-2. Quality metrics for the volunteer (mean only) and patient study. ....  | 68  |
| Table 5-1. Clinical data for patients with biopsy confirmed cancer. (NPH=Nodular prostatic hyperplasia, PIN=Prostatic Intraepithelial neoplasia, PNI= Perineural invasion, SV= seminal vesicles, PUE=Prostatic Urethral Ectasia, BPU=Benign prostatic urothelium).....  | 92  |
| Table 5-2. Quality metrics for the patient study at 800 Hz.....   | 96  |
| Table 5-3. Average values for Gd, Gl and ADC in the PZ and CG zone for normal tissue and cancer. (p-value: <0.005 ***; <0.05 **; <0.1 *) .....  | 105 |
| Table 5-4. The results from the receiver-operator-characteristic analysis are summarized (Sens=Sensitivity, Spec=Specificity, AUC= area under curve).....   | 106 |
| Table A-1. Required power (or loss of power) and pressure drop for various cases in the hydraulic transmission pipe.....  | 134 |

# List of Figures

|   |    |
|---|----|
| Figure 1-1. The displacements are encoded in the phase of the signal using motion encoding gradients (MEG) superimposed on MRI pulse sequences such as the (a) spin echo pulse sequence with echo planar readout and (b) gradient echo pulse sequence. The mechanical excitation is synchronized with the pulse sequence. ....  | 7  |
| Figure 1-2. Phase shift of the MR signal as a function of motion and applied gradient field in four cases.....  | 8  |
| Figure 1-3. Top: time sampling of the mechanical wave for four phase offsets. Bottom: the motion encoding gradients are consecutively superimposed on the all gradient axes to acquire the full 3D displacement field. ....   | 9  |
| Figure 1-4. a) Conventional spin-echo based pulse sequence for MRE, (b) corresponding encoding efficiency at various mechanical excitation frequencies.....   | 10 |
| Figure 1-5. Elasticity of human prostate as reported in literature.....   | 16 |
| Figure 2-1. The transducer is applied to the perineum of the subject as illustrated in (a). A photo of the actual setup is shown in b).....   | 19 |
| Figure 2-2. The subject-end (a-b) and the active end (b-c) of the hydraulic transducer and its component are shown. e) The overall schematic of the transducer system: the electromechanical exciter (c-d) is in the console room and the hydraulic transmission line passes through the waveguide and connects to the subject-end. f) The mobile MRE system that is positioned in the console room.....  | 21 |
| Figure 2-3. a) The SE-EPI based harmonic sequence is shown where the frequency of the MEGs (e.g., 100Hz) is twice that of the mechanical excitation (e.g., 50Hz). The motion-encoding efficiency is shown as a function of frequency in (b). The sensitivity loss of the harmonic approach compared to conventional MRE sequence is offset by the SNR gain due to a shorter echo time. ....   | 23 |
| Figure 2-4. a) Trans-perineal excitation is applied to a prostate elasticity phantom. b) The stiffer lesions (10mm in diameter) are visible in the T2-weighted anatomical MRI image. The waves at 50 Hz (c) and 250 Hz (d) are observed along the z-direction (in-plane). The elasticity maps in (e) at 50 Hz and (f) at 250 Hz show that the stiffer lesions stand out, even though the wavelength is significantly longer than the lesion size at 50Hz..... | 26 |
| Figure 2-5. The elasticity reconstruction at 50 Hz across several slices in the prostate elastography phantom is depicted. Inclusions of 10mm in diameter (0.5 cc) are readily observable in the elasticity maps. ....  | 27 |
| Figure 2-6. a) Standard T2-weighted anatomical MRI image of sagittal human prostate showing bladder (bl), pubic bone (pb) and transducer (blue “T” shape) (b) amplitude of wave: transducer at perineum position 1 and (c) position 2. Thus wave penetration depends on position and angle of the transducer. ....  | 28 |
| Figure 2-7. a) Transverse view of T2-weighted anatomical MRI of human pelvis b) measured total wave amplitude c) in-plane shear waves d) elasticity and e) damping of the prostate. Refer to Figure 8a for the gray scale image of (d).....   | 29 |
| Figure 2-8. Elasticity images of the human Prostate using the trans-perineal approach. The prostate clearly stands out in all the elasticity images (in color and gray scales) and shows reasonable correlation with anatomy (T2-weighted images). ....   | 31 |
| Figure 2-9. Elasticity images of the human Prostate using the trans-perineal approach across several slices. ....   | 32 |
| Figure 2-10. Sample 3D displacement field and elasticity image reconstructed using the Traveling Wave Algorithm (TWE). Adapted from [109] with permission .....   | 35 |

Figure 3-1. In the trans-perineal prostate MRE approach the transducer (a) rests between the legs of the subject and the vibration is applied to the perineal region as illustrated in (b). c) The point and angle of contact as well as the pre-compression applied by the transducer can be adjusted using three positioning screws. The custom made electromechanical transducer is quickly installed on the rails of the MR patient table, integrates well with the abdominal coil due its low profile (d), and is comfortable for the patient.....38

Figure 3-2. a) The counter-wound coils (a) generate a torque in a magnetic field. The outer coil is fixed and acts as a compensation coil to reduce the fringe field in generated by the inner moving coil the region of the expected FOV. Temperature fuses mounted on the inner coil, and a current fuse on the electronics side, protect the transducer and subject in the event of overheating. The equivalent circuit of the transducer is shown in (b), where  $V_{emf}$  is the voltage generated by the vibrating coil in the magnetic field  $B_0$ . The coils are driven by the electronics system (c) placed outside the scanner room. ....40

Figure 3-3. Simulations were performed to obtain the optimal number-of-turns ratio of the outer to inner coil to minimize the magnetic fringe fields. The cross-sectional geometry of half of the coils and the symmetry point is shown in (a). Three cases each are shown for aligned coils (a-c) and for tilted coils (d-f). The cases are: (i) coil 2 is off (no fringe field compensation), (ii) number-of-turns ratio of 0.5 (optimum shielding based on Biot-Savart equation) and (iii) number-of-turns ratio of 0.75 (optimum shielding based on simulations). The magnetic field in the region of interest as a function of number-of-turns ratio is shown in (g).....43

Figure 3-4. a) Bipolar trapezoidal motion-encoding gradients (MEG) are overlaid on a low-flip angle steady-state gradient echo shot. Only a fraction of the mechanical excitation is encoded, as  $q = T_{MEG}/T_{MECH} < 1$ . b) corresponding encoding efficiency at various mechanical excitation frequencies .....45

Figure 3-5. Over all looping structure of the *eXpresso* sequence. B) if several shot are fit within a vibration cycle then each slices acquires a phase shift that is compensated for in image post processing step.....47

Figure 3-6. The electromagnetic transducer was placed in the magnetic field of the MR scanner and its mechanical performance was characterized. a) shows the time domain response to a 70 Hz, 10 V sinusoidal excitation, where the output displacement of the transducer closely follows the sinusoidal pattern of the current in the coils. b) shows the frequency response of the transducer where the first resonant peak occurs at ~100 Hz. The displacement amplitude of the transducer can reach beyond 100  $\mu\text{m}$  at 300 Hz for a current less than 3 A.....50

Figure 3-7. The effectiveness of the shielding to suppress magnetic fringe fields of the transducer was assessed using a phantom. The phase images acquired for the three cases are shown: a) transducer not present, b) transducer active without active shielding and c) transducer active with active shielding enabled (same as a) when uncorrected). These images show that the shielding is effective. ....51

Figure 3-8. A T2-weighted image of a phantom with inclusions of different elasticities that was tested with the new sequence and transducer. The resulting mechanical waves (200 Hz) are shown in the projections in the three orthogonal planes. The inclusions can be visualized in the reconstruction elastogram verifying the functionality of the transducer and pulse sequence.....52

Figure 3-9. The *in-vivo* results from the testing of the improved sequence together with the new electromagnetic transducer. The images show the prostate of a healthy subject in transverse (center), sagittal (left) and coronal (bottom) planes. The T2-weighted image, magnitude of the MRE image (in-phase gradient echo) and waves in  $x$ ,  $y$  and  $z$ -direction (70 Hz) are shown. The total wave amplitude,  $U_{tot}$ , shows that the waves illuminate the entire region of the prostate and are present in all three encoding directions. This verifies the functionality of the transducer and pulse sequence. The bottom row shows a close up T2-weighted image of the prostate and the corresponding reconstructed elasticity image.....54

Figure 3-10. The total wave amplitude across the prostate (dotted line) in the coronal plane is shown for one case.....55

|  |    |
|--|----|
| Figure 3-11. a) Comparison between MRE of the liver using <i>eXpresso</i> and spin-echo echo planar imaging (SE-EPI). Noticeable signal loss in SE-EPI images is due to fat suppression. b) The phase to noise ratio is significantly higher for the <i>eXpresso</i> methods compared to the SE-EPI method. ....   | 58 |
| Figure 3-12. Comparison between mono- and multi-frequency experiments in a homogeneous phantom using the <i>eXpresso</i> pulse sequence. Top row: mono-frequency experiments at 28 Hz, 56 Hz and 84 Hz performed separately. Middle row: a single multi-frequency experiment using simultaneous mechanical excitation at 28+56+84Hz (equal amplitude weighting). Bottom row: difference image between the mono-frequency and multi-frequency images.....   | 59 |
| Figure 3-13. a) Comparison between the magnitude image and the y-component of the curl of the wave field for the <i>eXpresso</i> and conventional SE-EPI scan. b) Comparison of the waves between individual mono frequency experiments and single multi-frequency experiment. ....  | 60 |
| Figure 3-14. Sample 3D displacement field and elasticity image reconstructed using the mixed FEM approach. Adapted from [120] with permission .....  | 61 |
| Figure 3-15. Sample elasticity image reconstructed using the curl-based FEM approach. ....   | 62 |
| Figure 4-1. The trans-perineal prostate MRE setup. The rotary movement of the counter-wound coils is converted to linear motion that vibrates the perineum. The outer coil acts as a compensation coil to reduce the fringe field from the moving coil. The point and angle of contact as well as the pre-compression applied by the transducer can be adjusted positioning screws at the back of the scanner. ....  | 66 |
| Figure 4-2. Sample repeat volunteer studies. A1 and A2 are repeat cases of the same subject (similarly B1 and B2) Images shown in axial and coronal projections from left to right: T2-weighted, magnitude image of MRE, 3D waves, reconstructed shear modulus $ G $ , max shear strain $\tau_{max}$ , and their Bland-Altman plots. ....  | 70 |
| Figure 4-3. Sample images for the patient study. Images shown in axial and coronal projections from left to right: T2-weighted, magnitude image of MRE, 3D waves, reconstructed shear modulus $ G $ , max shear strain $\tau_{max}$ , and ADC (where available).....   | 72 |
| Figure 4-4. Average shear modulus $G_s= G $ and loss modulus $G_l$ in various zones of the prostate for volunteers and patients. (PC=prostate capsule, PZ=peripheral zone, CG=central gland, TZ=transition zone). ....   | 73 |
| Figure 4-5. Sample results of shear moduli ( $ G $ and $G_l$ ) and maximum shear strain ( $\tau_{max}$ ) as registered to histopathology slides.....   | 75 |
| Figure 4-6. Normal versus cancer stiffness for each case in PZ and CG.....   | 76 |
| Figure 4-7. The receiver-operator-characteristic curve and the corresponding AUC is shown for each case for parameters $G_s= G $ and $G_l$ in two dominant zones of the prostate PZ and CG. ....   | 77 |
| Figure 4-8. The histogram of tumor and normal tissue where the horizontal axis is the shear modulus $G_d$ (kPa) and vertical axis is the number of bins.....   | 78 |
| Figure 4-9. Phantom repeat studies at 194 Hz, 200 Hz and 206 Hz. The T2-weighted, 3D waves, reconstructed shear modulus $ G $ are shown for each case.....   | 82 |
| Figure 4-10. The top row shows the pair-wise comparison for the three experiments. In each case the reconstructed shear modulus is shown, and on the right the voxel-by-voxel percentage difference is shown. The percentage difference was an average of 7% for all cases. The bottom row shows the Bland-Altman plots for these experiments where the coefficient of repeatability and Intra-class coefficient are marked on each plot. The results show that the methods are very repeatable for small changes in the mechanical excitation frequency (and wave pattern effects) in phantoms..... | 83 |
| Figure 4-11. The top row shows the pair-wise comparison for the three experiments at 70 Hz in a volunteer using a faster scan. In each case the reconstructed shear modulus is shown, and on the right the voxel-by-   |    |

voxel percentage difference is shown. The bottom row shows the Bland-Altman plots for these experiments where the coefficient of repeatability and Intra-class coefficient are marked on each plot. .85

Figure 4-12. The top row shows the pair-wise comparison for the three experiments at 70 Hz in three volunteers using a the original. In each case the reconstructed shear modulus is shown, and on the right the voxel-by-voxel percentage difference is shown. The bottom row shows the Bland-Altman plots for these experiments where the coefficient of repeatability and Intra-class coefficient are marked on each plot. .86

Figure 4-13. The top row shows the pair-wise comparison for the three experiments (68Hz, 70 Hz and 72 Hz) in a volunteer using a faster scan. In each case the reconstructed shear modulus is shown, and on the right the voxel-by-voxel percentage difference is shown. The bottom row shows the Bland-Altman plots for these experiments where the coefficient of repeatability and Intra-class coefficient are marked on each plot .....88

Figure 4-14. The top row shows the pair-wise comparison for the three experiments (68Hz, 70 Hz and 72 Hz) in volunteers using the original scan. In each case the reconstructed shear modulus is shown, and on the right the voxel-by-voxel percentage difference is shown. The bottom row shows the Bland-Altman plots for these experiments where the coefficient of repeatability and Intra-class coefficient are marked on each plot .....89

Figure 5-1. a) The custom made mechanical transducer consists of a swiveling current-carrying coil that generates linear vibrations when the transducer is placed in the fringe field of the MR scanner. b) shows a photo of manufactured transducer as attached to the scanner outside the bore. c) The prostate specimen (with a rod inserted in the urethra) is placed on a cradle that is inserted into the RF coil. d) The transducer rod is a carbon-fiber tube that on one side is pressing on the apex of the prostate and on the other side is fastened to the transducer.....94

Figure 5-2. A T2-weighted anatomical image of a phantom with spatially heterogeneous inclusions of different elasticity values was tested with the transducer. The resulting mechanical waves (350Hz) and the projection in the three orthogonal planes are as shown. The inclusions can be easily visualized in the reconstruction elastogram .....99

Figure 5-3. Typical images acquired for an *ex-vivo* prostate: T2-weighted, magnitude image of MRE, waves, reconstructed shear modulus  $G_d$  and the power-law exponent  $\Gamma$ . The axial, sagittal and coronal projections of the displacement field in the three dimensions are shown. The experiment was repeated for different excitation frequencies (600, 800 and 1000Hz). The wave propagation is complex and present in all three axes. ....101

Figure 5-4. Sample results of shear moduli ( $G_d$  and  $G_l$ ) and ADC as registered to histopathology. The tumors are visible in the viscoelastic maps and in some cases in the ADC maps.....103

Figure 5-5. The receiver-operator-characteristic curve and the corresponding AUC is shown for each case for parameters  $G_d$ ,  $G_l$ , ADC and combined (CA). .....107

Figure 5-6. The histogram of tumor and normal tissue where the horizontal axis is the shear modulus  $G_d$  (kPa) and vertical axis is the number of bins.....108

Figure 5-7. Sample results of multi-frequency shear moduli ( $G_d$  and  $G_l$ ) and power-law exponent  $\Gamma$  as registered to histopathology. Even though the tumors are not particularly visible in the viscoelastic maps or the ADC image, the  $\Gamma$  map seems to highlight the small Gleason 3+3 tumor. ....110

Figure 5-8. Result for  $\Gamma$  for all six patients with multi-frequency MRE data.....111

Figure 5-9. A plot of shear moduli  $G_d$  and ADC in the normal and cancer tissue in the peripheral zone as a function of the time the *ex-vivo* prostate gland was immersed in fixation solution.....112

Figure 5-10. A modest differentiation was observed in the shear moduli values between the peripheral zone (PZ) and central gland (CG) but the differentiation was not significant ( $p < 0.065$  for  $G_d$  and  $< 0.058$  for  $G_l$ ). .....113

|  |     |
|--|-----|
| Figure 5-11. The differentiation (expressed as percentage) between cancer and normal tissue for Gd versus ADC.<br>.....  | 114 |
| Figure 5-12. Sample images comparison <i>in-vivo</i> and <i>ex-vivo</i> MRE of the same patients. ....   | 117 |
| Figure A-1. Effective bulk modulus of the hydraulic system as a function of volume of entrapped air bubbles<br>in 1L of fluid. Any air bubbles less than 1mL are difficult to remove in practice. The working pressure is<br>between 0.5 and 2 atm. ....   | 132 |
| Figure A-2. Static characterization of hydraulic transducer (HSv2.0 and HSv2.1): bulk modulus (a) and spring<br>constant (b) of pipe. The spring constants of input(c) and output (d) springs as determined from $V$ vs. $P$<br>and position vs. $P$ measurements. ....  | 133 |
| Figure A-3. Required power for each case is shown in as a function on excitation frequency (a), pipe diameter<br>(b) and amplitude of output (c). The red dotted line represents the theoretical power limit of the commercial<br>exciter (180W). The calculated pressure drop along the hydraulic exciter is shown in (d). .... | 135 |
| Figure A-4. The multi-degrees of freedom model (a) and its schematic (b) used in approximating the dynamic<br>response of the hydraulic transducer.....  | 136 |
| Figure A-5. The results from dynamic response simulation as a function of pipe diameter (a), input spring (b)<br>and output spring (c). The model was fitted to the measured dynamic response to identify the parameters<br>(d).....   | 139 |
| Figure C-1. Raw data for patient P01. ....   | 148 |
| Figure C-2. Raw data for patient P04. ....   | 149 |
| Figure C-3. Raw data for patient P05. ....   | 150 |
| Figure C-4. Raw data for patient P08. ....   | 151 |
| Figure C-5. Raw data for patient P10. ....   | 152 |
| Figure C-6. Raw data for patient P12. ....   | 153 |
| Figure C-7. Raw data for patient P13. ....   | 154 |
| Figure C-8. Raw data for patient P15. ....   | 155 |
| Figure C-9. Raw data for patient P17. ....   | 156 |
| Figure C-10. Raw data for patient P18. ....  | 157 |
| Figure C-11. Raw data for patient P19. ....  | 158 |
| Figure C-12. Raw data for patient P20. ....  | 159 |
| Figure C-13. Waves, maximum shear strain and absolute value of shear modulus for patients P01, P04 and P05.<br>.....   | 160 |
| Figure C-14. Waves, maximum shear strain and absolute value of shear modulus for patients P06, P08 and P10.<br>.....   | 161 |
| Figure C-15. Waves, maximum shear strain and absolute value of shear modulus for patients P12, P15 and P17.<br>.....   | 162 |
| Figure C-16. Waves, maximum shear strain and absolute value of shear modulus for patients P18, P19 and P20.<br>.....   | 163 |
| Figure C-17. Results for P01. Shear moduli ( $ G $ and $G_I$ ) and maximum shear strain ( $\tau_{\max}$ ) as registered to<br>histopathology slides. The total wave amplitude and THD are also shown. ....   | 164 |
| Figure C-18. Results for P04. Shear moduli ( $ G $ and $G_I$ ) and maximum shear strain ( $\tau_{\max}$ ) as registered to<br>histopathology slides. The total wave amplitude and THD are also shown. ....   | 165 |

|   |     |
|---|-----|
| Figure C-19. Results for P05. Shear moduli ( $ G $ and $G_I$ ) and maximum shear strain ( $\tau_{\max}$ ) as registered to histopathology slides. The total wave amplitude and THD are also shown. .... | 166 |
| Figure C-20. Results for P06. Shear moduli ( $ G $ and $G_I$ ) and maximum shear strain ( $\tau_{\max}$ ) as registered to histopathology slides. The total wave amplitude and THD are also shown. .... | 167 |
| Figure C-21. Results for P08. Shear moduli ( $ G $ and $G_I$ ) and maximum shear strain ( $\tau_{\max}$ ) as registered to histopathology slides. The total wave amplitude and THD are also shown. .... | 168 |
| Figure C-22. Results for P10. Shear moduli ( $ G $ and $G_I$ ) and maximum shear strain ( $\tau_{\max}$ ) as registered to histopathology slides. The total wave amplitude and THD are also shown. .... | 169 |
| Figure C-23. Results for P15. Shear moduli ( $ G $ and $G_I$ ) and maximum shear strain ( $\tau_{\max}$ ) as registered to histopathology slides. The total wave amplitude and THD are also shown. .... | 170 |
| Figure C-24. Results for P17. Shear moduli ( $ G $ and $G_I$ ) and maximum shear strain ( $\tau_{\max}$ ) as registered to histopathology slides. The total wave amplitude and THD are also shown. .... | 171 |
| Figure C-25. Results for P18. Shear moduli ( $ G $ and $G_I$ ) and maximum shear strain ( $\tau_{\max}$ ) as registered to histopathology slides. The total wave amplitude and THD are also shown. .... | 172 |
| Figure C-26. Results for P19. Shear moduli ( $ G $ and $G_I$ ) and maximum shear strain ( $\tau_{\max}$ ) as registered to histopathology slides. The total wave amplitude and THD are also shown. .... | 173 |
| Figure C-27. Results for P20. Shear moduli ( $ G $ and $G_I$ ) and maximum shear strain ( $\tau_{\max}$ ) as registered to histopathology slides. The total wave amplitude and THD are also shown. .... | 174 |
| Figure D-1. Raw data for patient P01 600 Hz.....  | 176 |
| Figure D-2. Raw data for patient P04 600 Hz.....  | 177 |
| Figure D-3. Raw data for patient P08 600 Hz.....  | 178 |
| Figure D-4. Raw data for patient P09 600 Hz.....  | 179 |
| Figure D-5. Raw data for patient P17 600 Hz.....  | 180 |
| Figure D-6. Raw data for patient P18 600 Hz.....  | 181 |
| Figure D-7. Raw data for patient P19 600 Hz.....  | 182 |
| Figure D-8. Raw data for patient P20 600 Hz.....  | 183 |
| Figure D-9. Raw data for patient P01 800 Hz.....  | 184 |
| Figure D-10. Raw data for patient P04 800 Hz.....   | 185 |
| Figure D-11. Raw data for patient P05 800 Hz.....   | 186 |
| Figure D-12. Raw data for patient P06 800 Hz.....   | 187 |
| Figure D-13. Raw data for patient P08 800 Hz.....   | 188 |
| Figure D-14. Raw data for patient P09 800 Hz.....   | 189 |
| Figure D-15. Raw data for patient P10 800 Hz.....   | 190 |
| Figure D-16. Raw data for patient P11 800 Hz.....   | 191 |
| Figure D-17. Raw data for patient P13 800 Hz.....   | 192 |
| Figure D-18. Raw data for patient P16 800 Hz.....   | 193 |
| Figure D-19. Raw data for patient P17 800 Hz.....   | 194 |
| Figure D-20. Raw data for patient P18 800 Hz.....   | 195 |
| Figure D-21. Raw data for patient P19 800 Hz.....   | 196 |

|   |     |
|---|-----|
| Figure D-22. Raw data for patient P20 800 Hz.....   | 197 |
| Figure D-23. Raw data for patient P01 1000 Hz.....  | 198 |
| Figure D-24. Raw data for patient P06 1000 Hz.....  | 199 |
| Figure D-25. Raw data for patient P08 1000 Hz.....  | 200 |
| Figure D-26. Raw data for patient P09 1000 Hz.....  | 201 |
| Figure D-27. Raw data for patient P11 1000 Hz.....  | 202 |
| Figure D-28. Raw data for patient P13 1000 Hz.....  | 203 |
| Figure D-29. Raw data for patient P16 1000 Hz.....  | 204 |
| Figure D-30. Raw data for patient P17 1000 Hz.....  | 205 |
| Figure D-31. Raw data for patient P18 1000 Hz.....  | 206 |
| Figure D-32. Raw data for patient P19 1000 Hz.....  | 207 |
| Figure D-33. Raw data for patient P20 1000 Hz.....  | 208 |
| Figure D-34. Results for P01 600 Hz. Shear moduli ( $ G $ and $G_I$ ) as registered to histopathology slides. The total wave amplitude and THD are also shown. .... | 209 |
| Figure D-35. Results for P06 600 Hz. Shear moduli ( $ G $ and $G_I$ ) as registered to histopathology slides. The total wave amplitude and THD are also shown. .... | 210 |
| Figure D-36. Results for P08 600 Hz. Shear moduli ( $ G $ and $G_I$ ) as registered to histopathology slides. The total wave amplitude and THD are also shown. .... | 211 |
| Figure D-37. Results for P09 600 Hz. Shear moduli ( $ G $ and $G_I$ ) as registered to histopathology slides. The total wave amplitude and THD are also shown. .... | 212 |
| Figure D-38. Results for P17 600 Hz. Shear moduli ( $ G $ and $G_I$ ) as registered to histopathology slides. The total wave amplitude and THD are also shown. .... | 213 |
| Figure D-39. Results for P18 600 Hz. Shear moduli ( $ G $ and $G_I$ ) as registered to histopathology slides. The total wave amplitude and THD are also shown. .... | 214 |
| Figure D-40. Results for P19 600 Hz. Shear moduli ( $ G $ and $G_I$ ) as registered to histopathology slides. The total wave amplitude and THD are also shown. .... | 215 |
| Figure D-41. Results for P20 600 Hz. Shear moduli ( $ G $ and $G_I$ ) as registered to histopathology slides. The total wave amplitude and THD are also shown. .... | 216 |
| Figure D-42. Results for P01 800 Hz. Shear moduli ( $ G $ and $G_I$ ) as registered to histopathology slides. The total wave amplitude and THD are also shown. .... | 217 |
| Figure D-43. Results for P04 800 Hz. Shear moduli ( $ G $ and $G_I$ ) as registered to histopathology slides. The total wave amplitude and THD are also shown. .... | 218 |
| Figure D-44. Results for P05 800 Hz. Shear moduli ( $ G $ and $G_I$ ) as registered to histopathology slides. The total wave amplitude and THD are also shown. .... | 219 |
| Figure D-45. Results for P06 800 Hz. Shear moduli ( $ G $ and $G_I$ ) as registered to histopathology slides. The total wave amplitude and THD are also shown. .... | 220 |
| Figure D-46. Results for P08 800 Hz. Shear moduli ( $ G $ and $G_I$ ) as registered to histopathology slides. The total wave amplitude and THD are also shown. .... | 221 |
| Figure D-47. Results for P10 800 Hz. Shear moduli ( $ G $ and $G_I$ ) as registered to histopathology slides. The total wave amplitude and THD are also shown. .... | 222 |

|  |     |
|--|-----|
| Figure D-48. Results for P11 800 Hz. Shear moduli ( $ G $ and $G_I$ ) as registered to histopathology slides. The total wave amplitude and THD are also shown. ....  | 223 |
| Figure D-49. Results for P13 800 Hz. Shear moduli ( $ G $ and $G_I$ ) as registered to histopathology slides. The total wave amplitude and THD are also shown. ....  | 224 |
| Figure D-50. Results for P16 800 Hz. Shear moduli ( $ G $ and $G_I$ ) as registered to histopathology slides. The total wave amplitude and THD are also shown. ....  | 225 |
| Figure D-51. Results for P17 800 Hz. Shear moduli ( $ G $ and $G_I$ ) as registered to histopathology slides. The total wave amplitude and THD are also shown. ....  | 226 |
| Figure D-52. Results for P18 800 Hz. Shear moduli ( $ G $ and $G_I$ ) as registered to histopathology slides. The total wave amplitude and THD are also shown. ....  | 227 |
| Figure D-53. Results for P19 800 Hz. Shear moduli ( $ G $ and $G_I$ ) as registered to histopathology slides. The total wave amplitude and THD are also shown. ....  | 228 |
| Figure D-54. Results for P20 800 Hz. Shear moduli ( $ G $ and $G_I$ ) as registered to histopathology slides. The total wave amplitude and THD are also shown. ....  | 229 |
| Figure D-55. Results for P01 1000 Hz. Shear moduli ( $ G $ and $G_I$ ) as registered to histopathology slides. The total wave amplitude and THD are also shown. .... | 230 |
| Figure D-56. Results for P06 1000 Hz. Shear moduli ( $ G $ and $G_I$ ) as registered to histopathology slides. The total wave amplitude and THD are also shown. .... | 231 |
| Figure D-57. Results for P08 1000 Hz. Shear moduli ( $ G $ and $G_I$ ) as registered to histopathology slides. The total wave amplitude and THD are also shown. .... | 232 |
| Figure D-58. Results for P09 1000 Hz. Shear moduli ( $ G $ and $G_I$ ) as registered to histopathology slides. The total wave amplitude and THD are also shown. .... | 233 |
| Figure D-59. Results for P10 1000 Hz. Shear moduli ( $ G $ and $G_I$ ) as registered to histopathology slides. The total wave amplitude and THD are also shown. .... | 234 |
| Figure D-60. Results for P11 1000 Hz. Shear moduli ( $ G $ and $G_I$ ) as registered to histopathology slides. The total wave amplitude and THD are also shown. .... | 235 |
| Figure D-61. Results for P16 1000 Hz. Shear moduli ( $ G $ and $G_I$ ) as registered to histopathology slides. The total wave amplitude and THD are also shown. .... | 236 |
| Figure D-62. Results for P17 1000 Hz. Shear moduli ( $ G $ and $G_I$ ) as registered to histopathology slides. The total wave amplitude and THD are also shown. .... | 237 |
| Figure D-63. Results for P18 1000 Hz. Shear moduli ( $ G $ and $G_I$ ) as registered to histopathology slides. The total wave amplitude and THD are also shown. .... | 238 |
| Figure D-64. Results for P19 1000 Hz. Shear moduli ( $ G $ and $G_I$ ) as registered to histopathology slides. The total wave amplitude and THD are also shown. .... | 239 |
| Figure D-65. Results for P20 1000 Hz. Shear moduli ( $ G $ and $G_I$ ) as registered to histopathology slides. The total wave amplitude and THD are also shown. .... | 240 |
| Figure D-66. Results for P06 gamma. The power law for $G_d$ and $G_I$ as registered to histopathology slides. The total wave amplitude and THD are also shown. ....  | 241 |
| Figure D-67. Results for P08 gamma. The power law for $G_d$ and $G_I$ as registered to histopathology slides. The total wave amplitude and THD are also shown. ....  | 242 |
| Figure D-68. Results for P09 gamma. The power law for $G_d$ and $G_I$ as registered to histopathology slides. The total wave amplitude and THD are also shown. ....  | 243 |

Figure D-69. Results for P18 gamma. The power law for Gd and Gl as registered to histopathology slides. The total wave amplitude and THD are also shown. ....244

Figure D-70. Results for P19 gamma. The power law for Gd and Gl as registered to histopathology slides. The total wave amplitude and THD are also shown. ....245

Figure D-71. Results for P20 gamma. The power law for Gd and Gl as registered to histopathology slides. The total wave amplitude and THD are also shown. ....246

Figure D-72. Summary of multi-frequency results. ....247

# Glossary

|                 |  |
|-----------------|--|
| <b>1D/2D/3D</b> | one/two/three dimensional                    |
| <b>ADC</b>      | apparent diffusion coefficient               |
| <b>ANOVA</b>    | analysis of variance                         |
| <b>AUC</b>      | area under the curve                         |
| <b>BH</b>       | breath hold                                  |
| <b>bSSFP</b>    | balanced steady-state free precession        |
| <b>cDI</b>      | curl-based direct inversion                  |
| <b>CG</b>       | central gland                                |
| <b>DCE</b>      | dynamic contrast enhanced imaging            |
| <b>DENSE</b>    | displacement encoding with stimulated echoes |
| <b>DI</b>       | direct inversion                             |
| <b>DTI</b>      | diffusion tensor imaging                     |
| <b>DWI</b>      | diffusion weighted imaging                   |
| <b>EPI</b>      | echo planar imaging                          |
| <b>FEM</b>      | finite element modeling                      |
| <b>FOV</b>      | field of view                                |
| <b>GRE</b>      | gradient recalled echo                       |
| <b>ICC</b>      | intraclass correlation coefficient           |
| <b>LFE</b>      | local frequency estimation                   |
| <b>MEG</b>      | motion encoding gradients                    |
| <b>mpMRI</b>    | multi-parametric magnetic resonance imaging  |
| <b>MRE</b>      | magnetic resonance elastography              |
| <b>MRI</b>      | magnetic resonance imaging                   |
| <b>MRSI</b>     | magnetic resonance spectroscopy imaging      |

|              |   |
|--------------|---|
| <b>MSG</b>   | motion sensitizing gradients                  |
| <b>NMR</b>   | nuclear magnetic resonance                    |
| <b>PC</b>    | prostate capsule                              |
| <b>PNR</b>   | phase to noise ratio                          |
| <b>PZ</b>    | peripheral Zone                               |
| <b>RARE</b>  | rapid acquisition with relaxation enhancement |
| <b>RF</b>    | radio frequency                               |
| <b>ROC</b>   | receiver operating characteristic curve       |
| <b>ROI</b>   | region of interest                            |
| <b>SE</b>    | spin echo                                     |
| <b>SENSE</b> | acceleration based on sensitivity encoding    |
| <b>SNR</b>   | signal to noise ratio                         |
| <b>SV</b>    | seminal vesicles                              |
| <b>TE</b>    | echo time                                     |
| <b>TR</b>    | repetition time                               |
| <b>TWE</b>   | traveling wave expansion                      |
| <b>TZ</b>    | transition zone                               |

# Acknowledgements

First and foremost, I would like to express my deepest gratitude to Prof. Septimiu Salcudean who has provided fantastic technical guidance and research direction, and has created numerous fruitful opportunities for me and this research. It is still a mystery to me how he manages to supervise more than 20 graduate students and engineers and yet know their work to the last detail. All this while attending to his other responsibilities and starting a company! He has always guided and pushed me to perform at my limit in this fast-paced research. He is one of my top role models in life and academic work.

They say stand on the shoulder of giants! Certainly Prof. Ralph Sinkus would be one of them. He tirelessly worked with me from the trenches of engineering and science and provided instrumental support for this project. I'd also like to thank both my supervisors for creating the opportunity for me to go to Paris France as a visiting researcher, and especially Prof Sinkus for arranging the hardcore research trip to Philips Headquarters in Best, Netherlands.

My sincere gratitude also goes to Dr. Piotr Kozlowski and Dr. Robert Rohling for their continually helpful advice. In particular, Dr. Kozlowski has dedicated significant effort to get the patient study going and helped with the patient protocol on both the 3T and 7T scanners.

The rapid progress of this project hinged on many key inspiring and hardworking people - in particular Dr. Ali Baghani, Philippe Garteiser, Guy Nir, Mohammad Honarvar, Artem Bylinskii, Sam Frew and Andrew Yung. I also would like to thank: the staff at 3T (Trudy, Paul, Linda J, Linda Z, Tracey, Alex M), and 7T UBC MRI center (Andrew, Barry, Shirin), the machinist/staff at the Mechanical (Markus Fengler and Glenn Jolly) and Electrical Engineering (Neil, Mark, Donald, and Ken Madore), Alex MacKay, Jing Zhang, Dan Gelbart, Edward Jones, Margaret Luk, Silvia Chang, Chris Nguan, Larry Goldenberg, Joseph Ischia, Louis Gagnon, Dr. Alex Rauscher, and Dr. Stefan Reinsberg for their help and valuable feedback. Also, the support from Jonathan Chia and Leon terBeek at Philips Medical is much appreciated.

My thanks goes to members of the UBC Robotics and Control Lab (RCL) at UBC in Vancouver, Canada (Ali B, Diego, Reza, Jing, Hedyeh, Jeff, Caitlin, Mehdi, Troy, Orcun, Tricia, Sam, Omid, Julio, Philip, Abtin, Hussam, Weiqi, Saman, Samira, Alex, Ali K, Mohammad H), and IRM Physiologique et Moléculaire de l'Abdomen (IPMA) in Paris, France (Philippe, Sabrina, Lauriane, Eric, Jean-Luc, Simon C, Simon L).

I would like to acknowledge the financial support I received from Natural Sciences and Engineering Research Council (NSERC) of Canada, Prostate Cancer Foundation of British Columbia, the UBC FYF Graduate scholarship, the UBC Faculty of Applied Science Graduate award, UBC Biomedical Engineering award, and research assistantship received from Prof Salcudean and Prof Sinkus.

Many thanks to my friends for your support - in particular Pirooz, Ben and Iman. Of most honorable mention is my beautiful Aylin who always supports me at every step and brings out the best in me. A special thanks to my brother who encouraged me throughout my work and made life on campus enjoyable (looking forward to implementing some of our many crazy ideas together). And finally, and most importantly, my deepest gratitude to my parents for their unconditional and infinite support throughout my life.

# Dedication

To my mother who taught me discipline and determination.

To my father who gave me motivation and vision.

# Chapter 1 - Introduction

## 1.1 Clinical motivation

Problem: Prostate cancer is one of the leading causes of cancer related deaths in men [1].

Treatment: Over 90% of prostate cancer cases are curable. The challenge is to detect this ‘silent’ disease at the most curable stage when it has no apparent symptoms. Different prostate cancer treatment methods exist and are used depending on disease condition and age of patient. The most common treatments available today (such as brachytherapy where radioactive seeds are permanently implanted into the prostate) affect the entire prostate gland and often lead to complications, including incontinence and impotence [2]. Alternatively, if the exact location and grade of the cancer is known, treatment could be applied locally through less proven solutions such as thermal ablation, cryotherapy, injection therapies or high intensity focused ultrasound [3]. These methods are collectively referred to as focal treatment and aim at reducing treatment complications. Regardless of the treatment method used, accurate identification of cancerous locations may provide physicians with important information for treatment decisions that may improve outcome. For thermal ablation for example, the accurate information regarding the boundary of the prostate and location and grade of the cancer is key in guiding the treatment (i.e., where to apply heat and how much). Brachytherapy can also greatly benefit from this supplementary knowledge for planning the location of the radioactive seeds, possibly reducing treatment side effects even further.

Diagnosis: To date, the standard screening and diagnosis methods for prostate cancer includes palpation (i.e., digital rectal exam or DRE) performed by the physician, checking for PSA (Prostate-Specific Antigen) levels in blood, and TRUS (trans-rectal ultrasound) guided biopsies which are evaluated based on the Gleason score. TRUS guided biopsies are indicated if an elevated PSA is detected and DRE suggests presence of abnormal tissue [4]. Biopsy procedures are fairly invasive with complication rates in excess of 12% [5]. TRUS biopsy procedures still fail to detect 10-30% of prostate cancers due to sampling errors [6]–[8]. Unfortunately, in as many as 39% of cases, the prostate biopsy is under-graded as compared to the final pathology (upon removal of the entire prostate) [9]. Therefore, there has been a trend towards increased number of core samples, resulting in higher chances of complications, in an effort to improve the accuracy of staging of prostate cancer. Researchers are trying to develop new diagnostic techniques in a non-invasive manner that will differentiate normal prostate from benign prostatic hyperplasia (BPH) and cancer; and predict biologic behaviour more accurately than currently available methods.

mpMRI: The first step to improve the diagnosis and treatment outcome of prostate cancer is to improve the quality of the obtained images of the prostate. MRI has also been widely used for staging of prostate cancer with varying success [10] for over a decade [11]. Sensitivity values ranging from 51% to 89% have been

reported [12] for detecting prostate cancer and the accuracy of staging of prostate cancer has been fairly low. It has been shown that current MRI techniques are not efficient in determining the extra-capsular extension with sensitivities in range of 23%-75% [13], [14]. Several MRI-based techniques have been investigated recently [15] with the aim to improve tumor delineation and thus provide more reliable staging and the ability to predict the grade of tumor. For high sensitivity and specificity of prostate cancer staging, it is widely believed that the way forward is multi-parametric (mpMRI) imaging [16], [17]. mpMRI utilizes the collective information provided by several MRI techniques – that rely on different contrast mechanisms – to significantly improve the accuracy of diagnosis imaging.

The reported results of recent mpMRI studies vary widely. For example, for just localization of prostate cancer Futterer *et al.* [18] reported an area under the curve (AUC) of 0.90 when T2, DCE-MRI, and MRSI were combined. Also maximum sensitivities and specificities of 80%–88% and 96%–100%, respectively [19], [20] have been reported. Other studies, however, report more conservative values. For example, recent prospective studies [21], [22] found improved localization of prostate cancer with AUC of 0.66-0.79 when T2 was combined with DWI. Other studies [10], [18], [23], [24] found that the localization accuracy with T2 and DCE was 72-91%. Also, the combination of T2 and DW imaging improved the sensitivity to 81%, whereas specificity was slightly lower for T2-weighted MR imaging combined with DWI (84%) than for T2-weighted MR imaging alone (91%) in this prospective prostatectomy-referenced study [25]. In contrast, in a recent retrospective with whole mount specimen as gold standard, DWI did not improve MR imaging for prostate cancer localization compared to T2 images [26] where AUC values were 0.78–0.79. At this time, it appears that due to a lack of consensus and standardization of methods, and lack of multi-center clinical trials, the debate how far mpMRI can truly improve diagnosis remains unanswered.

MRE: In this thesis, a method called Magnetic Resonance Elastography (MRE) is developed for *in-vivo* and *ex-vivo* prostate imaging. The contrast mechanism in MRE is based on mechanical properties such as stiffness. The development and evaluation of these methods is the subject of this work.

## **1.2 Background**

### **1.2.1 Magnetic resonance elastography (MRE)**

Magnetic Resonance Elastography (MRE) is a non-invasive medical imaging modality that aims to depict the mechanical properties of tissue [27]–[29]. The aim of MRE is to obtain images of intrinsic mechanical properties of tissue such as shear modulus and viscosity. If changes in intrinsic mechanical properties correlate well with tissue abnormalities, such as cancer or liver fibrosis, then MRE images can be used in diagnosis and management of disease. The mechanical properties of tissues vary widely among different physiological and pathological states [30], as demonstrated by the common use of palpation to differentiate abnormal and normal tissues by physicians. The use of tissue elasticity as a contrast mechanism to detect cancer has been suggested in many previous studies, in an area of medical imaging called elastography.

The stiffness of prostatic tissue has been measured using various techniques in both *ex-vivo* and *in-vivo* studies as summarized in the literature survey section in this chapter. Previous initial clinical results have been quite encouraging and show a good correlation between change in mechanical properties such as elasticity of benign and malignant tissue. Therefore, new efforts have been made to add the measurement of visco-elastic properties to more established techniques such as dynamic contrast enhanced (DCE), diffusion tensor imaging (DTI) and magnetic resonance spectroscopy imaging (MRSI).

Applications: Elastography techniques were first demonstrated in the field of ultrasound [31]. In case of ultrasound elastography of the prostate [32], recent studies have shown that this technique provides a significantly higher contrast in visualization of prostate compared to B-scan ultrasound (an SNR of  $36.2 \pm 2.06$  in VE vs.  $11.5 \pm 1.05$  in B-scan). Furthermore, it has been reported that ultrasound elastography can provide a sensitivity of 80% in detection of prostate cancer [33]. Shortly thereafter, elastography was introduced in the field of MRI [28], where the shear waves generated by a harmonically driven mechanical exciter were imaged and used to compute shear modulus. In the following years elastography was shown to be of clinical value for detecting and staging of hepatic fibrosis [34]–[36], detecting abnormalities in breast [27], [37], [38], brain [39]–[42] and more recently lung [43], [44] and the heart [45], [46]. In breast cancer, for example, analysis of 39 malignant and 29 benign lesions with MRE showed a significant diagnostic gain with an increase of about 20% in specificity at 100% sensitivity compared to conventional BIRADs staging techniques [47]. In MRE of hepatic fibrosis, receiver operating curve (ROC) analysis of 50 patients and 35 volunteers demonstrated that the predicted sensitivity and specificity for detecting all grades of liver fibrosis is 98% and 99%. ROC analysis also provided evidence that MR Elastography can discriminate between patients with moderate and severe fibrosis (grades 2–4) and those with mild fibrosis (sensitivity 86%, specificity 85%) [36].

How it works: In MRE, an external mechanical excitation is applied to the tissue of interest to induce harmonic vibrations. The induced wave fields are imaged using a motion-sensitized MRI pulse sequence. The resulting displacement field is post-processed to extract viscoelastic information. This work is based on dynamic MRE where the displacements caused by the steady state harmonic excitation (resulting in a standing wave) are measured, as opposed to transient and static elastography.

### **1.2.2 MRE in prostate cancer**

From a clinical point of view, there has been great interest in applying MRE techniques for *in-vivo* imaging of prostate cancer because of their potential to detect and stage cancer, monitor disease progression for patients in active surveillance, and monitor treatment of patients after radiation or focal therapy. With MR elastography of the prostate at its infancy, the application of MRE to prostate cancer has been mostly limited to *ex-vivo* studies [48]–[51], feasibility studies in canine [52], and initial human studies [53]–[57]. For the *in-vivo* prostate MRE, the main technical challenges are (i) inducing shear waves of sufficient amplitude into the prostate reliably such that it is well tolerated by the subject, and (ii) acquiring high quality displacement field in a clinically acceptable time. The other main issue for elastography in general is the reconstruction algorithm. At the moment, a number

of reconstruction algorithms exist, however the search for the ultimate algorithm, that is robust to noisy data, is insensitive to reconstruction parameters and immune to patient motion, is not over.

The focus of his work has been on developing MRE systems consisting of mechanical transducers and advanced pulse sequences. The MRE systems developed are also used to acquire high quality data sets which are used to develop several new reconstruction algorithms with the author as a secondary contributor. A brief background into each of the aforementioned issues along with a literature review is discussed in the following section. Also, in an effort to establish a baseline for the elasticity of the prostate and to validate the results, a comprehensive literature survey is presented in this chapter.

### **1.2.3 Mechanical transducer**

Several transducers used in MRE studies have been reported in the literature [58]. In general, transducers consist of two components: the actuation source and the transmission system. The following actuation sources have been reported: electromechanical [59]–[61], piezoelectric [62]–[64], pneumatic [65], and hydraulic [66]. Transmission systems that have been employed include a mechanical rod or tube [59], a belt or a cam [62], [67], a bite-bar [60], and mechanisms that change direction of movement or mechanical impedance [61], [68], [69]. The transmission system can also be acoustic [70]–[72] or hydraulic [55], [69]. Positioning is typically achieved by applying the end-effector (the vibrating element of the transducer at the subject-end) as close as possible to the tissue to be imaged. The end-effector may be the bellows of a drum, or an appropriately sized ball or plate [61], [73]. While most end-effectors are non-invasive and are positioned against the skin, there are instances in which invasive methods using needles [63], [74], [75], trans-urethral transducers [55] or endo-rectal transducers [56], [76] have been used. For *in-vivo* prostate MRE, there have been three main approaches. Kemper *et al.* [53] used a electromechanical source to apply vibrations directly to the pubic bone while the subject lies in a prone position pressing on the transducer. The advantage of this method is that it is non-intrusive compared to endo-cavity approaches. Arani *et al.* [55], [56], used a piezoelectric source to apply the vibrations via a standard endorectal RF coil. The advantage of this method is that higher frequency mechanical vibrations can be induced in the prostate. In our study [66] used an electromechanical actuation source placed outside the scanner room and a hydraulic transmission system to apply the vibrations to the perineum. The advantage of the trans-perineal method is that it is non-intrusive (compared to the endo-rectal approach) and well tolerated even for extended examination (compared to trans-pubic approach). An electromagnetic transducer was designed for this study because such a transducer can produce higher displacements compared to piezoelectric transducers, has superior frequency spectrum characteristics compared to acoustic and hydraulic methods, and can be easily set up by MRI technicians. Depending on the application, such transducers can interfere with the MRI and cause artifacts if not properly shielded or placed far away from the imaging area. A shielded transducer design for trans-perineal prostate MRE has not been published in the literature. The transducer setup time has not been reported by the previous studies.

For this work, two main transducer concepts were explored. The first design included a hydraulic transmission with permanent-magnet based electromagnetic source placed outside the scanner room. The second design consisted of a shielded electromagnetic transducer utilizing the magnetic field of the MRI scanner itself.

### 1.2.3.1 Design considerations

MRI issues: The main magnetic field  $B_0$  of the MRI scanner can exert large forces and torques on ferromagnetic materials. Small amounts of ferromagnetic material close to the field of view would distort the homogeneity of the scanner resulting in artefacts. The gradient coils and radiofrequency (RF) transmit coils of the scanner introduce rapidly switching magnetic fields that will induce eddy currents in conductive materials. The low frequency eddy currents induced by the gradient fields may cause image artefacts by distorting the magnetic field close to the field of view. The high frequency eddy currents induced by the RF fields are dissipated as heat and can generate undesired heating of the material in proximity of the subject being scanned. Thus, the use of ferromagnetic and conductive materials must be avoided as much as possible. Another issue is that the MRI room is enclosed by an RF shield to reduce noise near the RF receiver coil; therefore, any external conductor introduced to the scanner room must be electrically filtered or must pass through a wave guide.

Mechanical issues: In MRE, excitation amplitudes can be as large as 2 mm at the surface of the object for successful excitation. The amplitude should preferably be independent of the pre-compression force or the type of tissue. The typical excitation frequency is between 30 Hz to 90 Hz for *in-vivo* tissue, however depending on the application this range can extend from 1 to 5000 Hz. A linear dynamic response is preferred so that it can be used for various applications such as applying multiple excitations at once. The time stability of the synchronization between the exciter and the MRE pulse sequences is important, otherwise the data acquired during the displacement encoding process will be corrupt. MRI examinations are typically long (approx. 30-90 min); a typical MRE exam may add 5-45 min. Therefore, for successful imaging it is important that the MRE excitation be comfortable and not cause the subject to move during the examination. The exciter needs to be positioned quickly for the desired application. The static force exerted on the tissue of interest has to be controlled, since the *in-vivo* tissue is non-linear and becomes stiffer as the pre-compression load is increased. Safety can become a concern if the frequency of excitation is high with large amplitudes; however, in a typical situations where the amplitude is less than 2 mm and the frequency is less than 100 Hz this should not pose a problem [77]. To save MRI time and for the convenience of the operators, the entire transducer system needs to be easy to use, quick to set up and easy to transport.

Choice of excitation frequency: At a lower excitation frequency the attenuation and dispersion are typically lower [47], resulting in better wave penetration [78]. However, for the same imaging field-of-view and matrix size, the resolution of the elasticity map will be degraded at a lower mechanical frequency [79].

## 1.2.4 Acquisition of the displacement field

A short introduction of mechanism of MRE acquisition is covered in this section. For an excellent primer on MRI physics on signal generation, encoding and acquisition refer to [80]. In MRI, the precession frequency  $\omega$  of spins that are perturbed from the axis of the magnetic field  $\mathbf{B}$  is given by the Larmor equation

$$\omega = \gamma \cdot \mathbf{B} \quad (1-1)$$

where  $\gamma$  is the gyromagnetic ratio (= 42.58 MHz/T for hydrogen). The magnetic field  $\mathbf{B}$  is given by

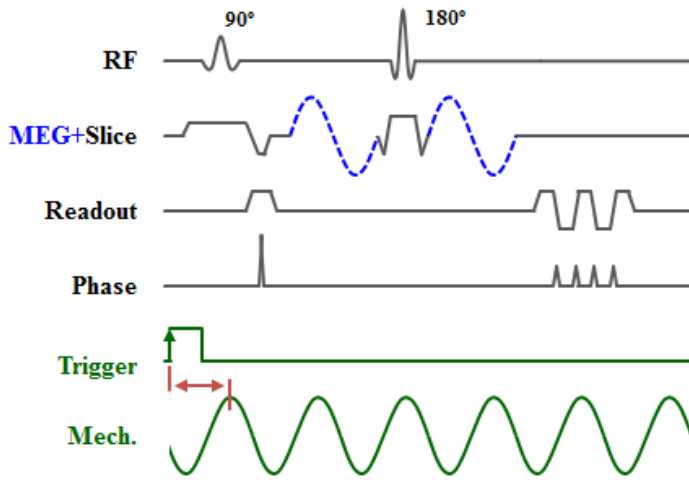
$$\mathbf{B} = B_{z,0} + \mathbf{G}(t) \cdot \mathbf{r} = B_{z,0} + \left( \frac{dB_z}{dx} + \frac{dB_z}{dy} + \frac{dB_z}{dz} \right) \cdot \mathbf{r} \quad (1-2)$$

and consists of the polarizing magnetic field  $B_{z,0}$  and the time-varying gradient field  $\mathbf{G}(t)$ . The spatial information of the spins is encoded using these gradients. The gradient fields modify the polarizing magnetic field such that it becomes linearly dependent on location  $\mathbf{r}$ .

Traditionally two paradigms have been used for generation of NMR echo signals: spin echo (SE) and gradient echo (GRE). In spin echo, a RF pulse perturbs the spins away from the axis of the polarizing magnetic field by  $90^\circ$ . This generates the free induction decay (FID) signal that decays according to  $T2^*$  relaxation. After a short delay  $\tau$ , a  $180^\circ$  degree inversion RF pulse is applied which results in an echo signal at  $2\tau$ . Because the self-aligning nature of the inversion pulse, the de-phasing of spins due to the magnetic field inhomogeneity is re-focused. Thus the signal decays according to the  $T2$  relaxation. In a gradient echo method, the FID signal generated by a smaller flip angle (typically between  $10^\circ$  and  $35^\circ$  to reduce the repetition time) and is de-phased by the application of a gradient, and is subsequently re-phased with the frequency encoding gradient. This results in an echo signal that has decays according to  $T2^*$  relaxation.

For MRE, in addition to the gradients used for encoding spatial information of the sample, oscillating motion encoding gradients (MEG) are selectively superimposed on the gradient axes to encode displacements in the phase images. For SE, the MEGs are typically inserted before and after the  $180^\circ$  pulse but before the frequency encoding gradients; for GRE, the MEGs are inserted anywhere between the excitation pulse and before the frequency encoding gradients. This is illustrated in Figure 1-1.

a) Spin echo with MEG



b) Gradient echo with MEG

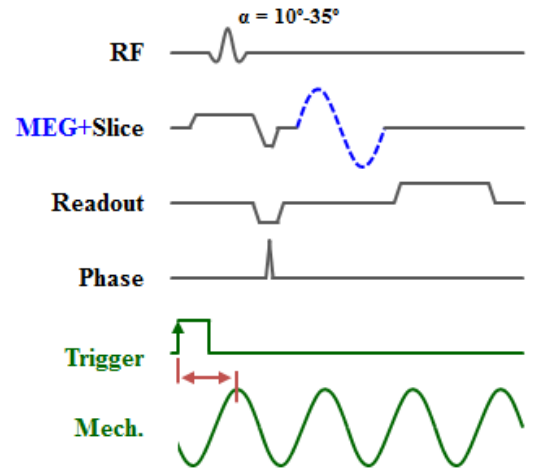


Figure 1-1. The displacements are encoded in the phase of the signal using motion encoding gradients (MEG) superimposed on MRI pulse sequences such as the (a) spin echo pulse sequence with echo planar readout and (b) gradient echo pulse sequence. The mechanical excitation is synchronized with the pulse sequence.

In dynamic MRE, the signal is encoded in the phase of the NMR signal [81], [82]. The phase of the NMR signal  $\varphi$  in the rotating frame of reference (removing effects of  $B_{z,0}$ ) is found from equation (1-1) and (1-2) and is given by

$$\varphi = \gamma \int_0^{TE} \mathbf{G}(t) \cdot \mathbf{r} dt . \quad (1-3)$$

Assuming sinusoidal motion in MRE, the displacement is given by

$$\mathbf{r} = \mathbf{r}_0 + A_m \cdot \sin(\omega_m \cdot t + \varphi_m) \quad (1-4)$$

where  $\mathbf{r}_0$  is the voxel position,  $A_m$  is the amplitude of the mechanical wave,  $\omega_m$  is the frequency of the mechanical oscillation, and  $\varphi_m$  is the phase of the mechanical wave. The phase shift due to motion in the one direction is illustrated in Figure 1-2.

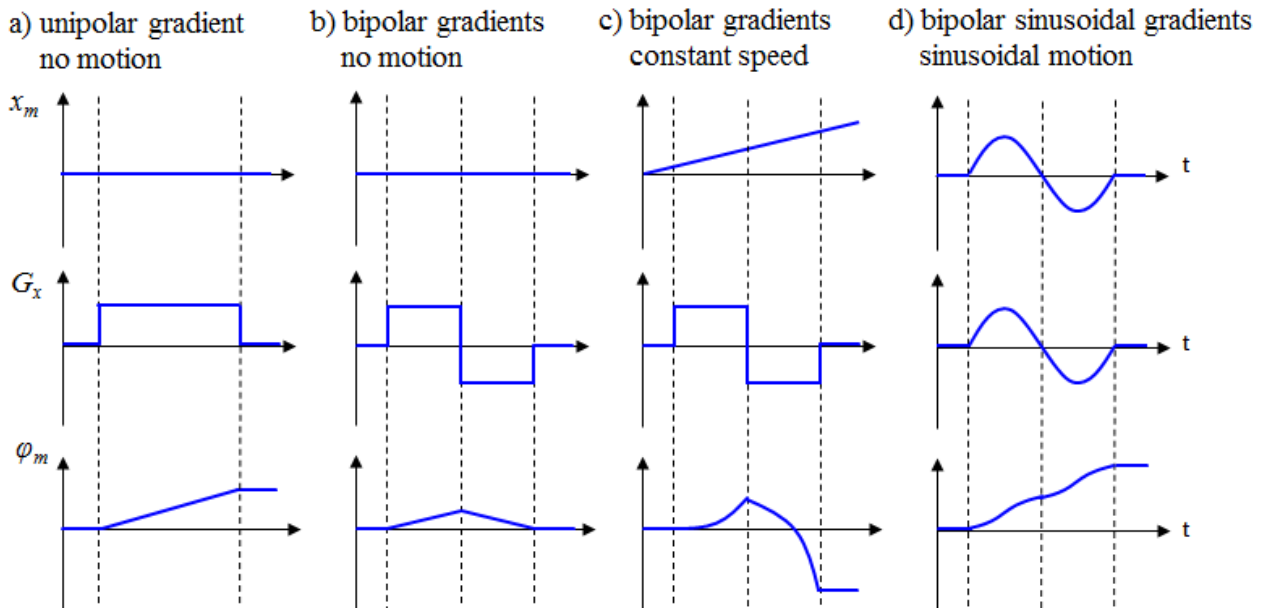


Figure 1-2. Phase shift of the MR signal as a function of motion and applied gradient field in four cases.

A trigger pulse generated by the MR console electronics is used to synchronise the mechanical excitations with the pulse sequence. This allows the steady-state motion of the standing waves to be “frozen” in time in order to acquire all the information in repeated experiments. The motion is encoded in the axis the MEGs are superimposed. For a 1D displacement field data set for example, MEG is applied on one axis for a certain time delay between MEG and the mechanical excitation. The k-space is acquired for each slice. The delay is increased, for instance, by a quarter of the mechanical period if four sampling points in time are desired. This is illustrated in Figure 1-3. The procedure is repeated until the four sampling point are acquired. This constitutes a 1D displacement field data set. For a full 3D data set, the procedure is repeat to acquire the other dimensions by superimposing the MEG on the remaining gradient axes. The 3D motion encoding at four phase offsets is illustrated in Figure 1-3.

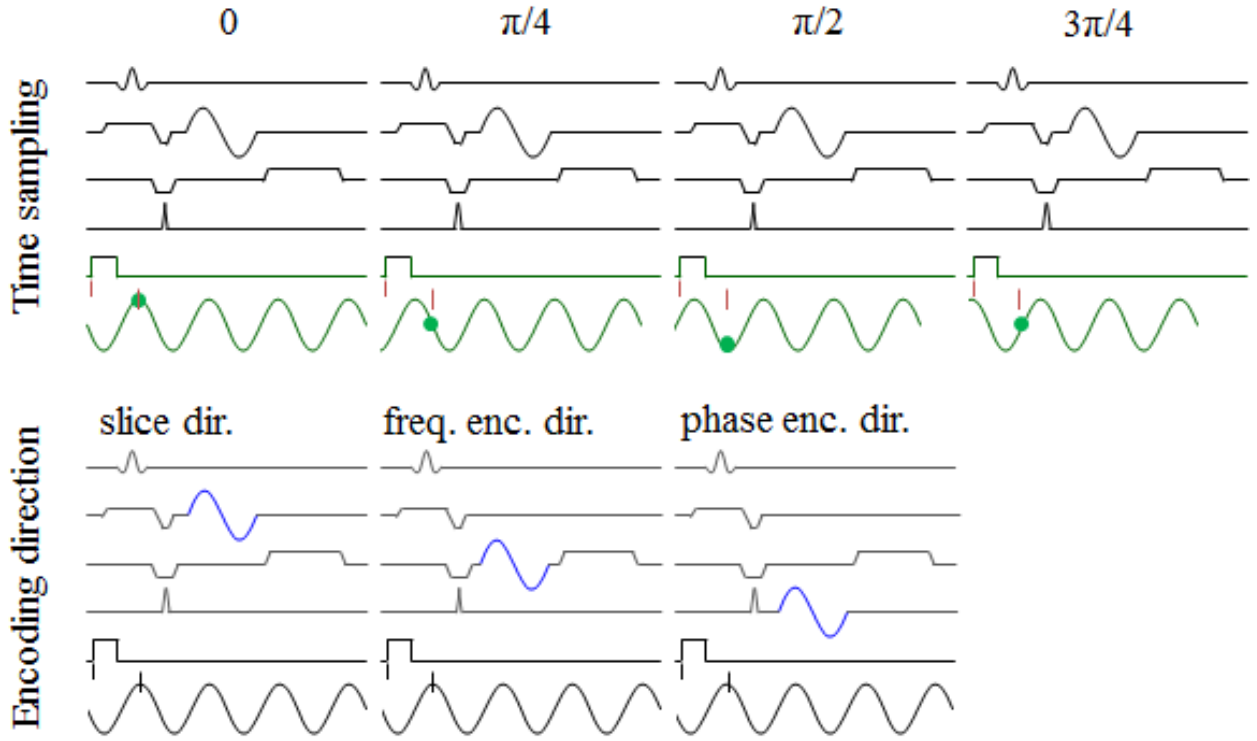


Figure 1-3. Top: time sampling of the mechanical wave for four phase offsets. Bottom: the motion encoding gradients are consecutively superimposed on the all gradient axes to acquire the full 3D displacement field.

An example pulse sequence is shown in Figure 1-4 where the MEGs are superimposed on the slice direction before and after the  $180^\circ$  pulse.

The motion is encoded in the phase of the MR signal is given by

$$\varphi = \gamma \int_0^{TE} G_0 \cdot \sin(\omega_{mge} \cdot t + \varphi_{meg}) \cdot A_m \cdot \sin(\omega_m \cdot t + \varphi_m) dt \quad (1-5)$$

where  $G_0$  is the maximum amplitude of the oscillating motion encoding gradient at frequency  $\omega_{meg}$  and phase  $\varphi_{meg}$ . Assuming the frequency of mechanical excitation  $\omega_m$  to be the same as that of the MEG,  $\omega_{meg}$ , then the motion encoding efficiency  $\eta$  [rad/m] (a measure of phase shift per unit displacement) becomes:

$$\eta = \frac{n \cdot \gamma \cdot G_0}{2\pi\omega_m} \quad (1-6)$$

The motion encoding sensitivity can be increased by increasing the number of MEGs  $n$  at the expense of longer echo time and thus lower SNR. Spectrum of the motion encoding efficiency is shown in Figure 1-4b. In this example, the gap between the two lobes of the MEG is set to  $2T_m$  and the frequency of MEG is 100 Hz, where  $T_m = 1/(4 \cdot \pi \cdot \omega_m)$  is half the period of the mechanical excitation. For conventional MRE imaging the mechanical excitation is the same frequency as the MEG (e.g., 100 Hz). In this case for example, the sign of the two MEG lobes needs to be opposite of each other in order to encode motion (red).

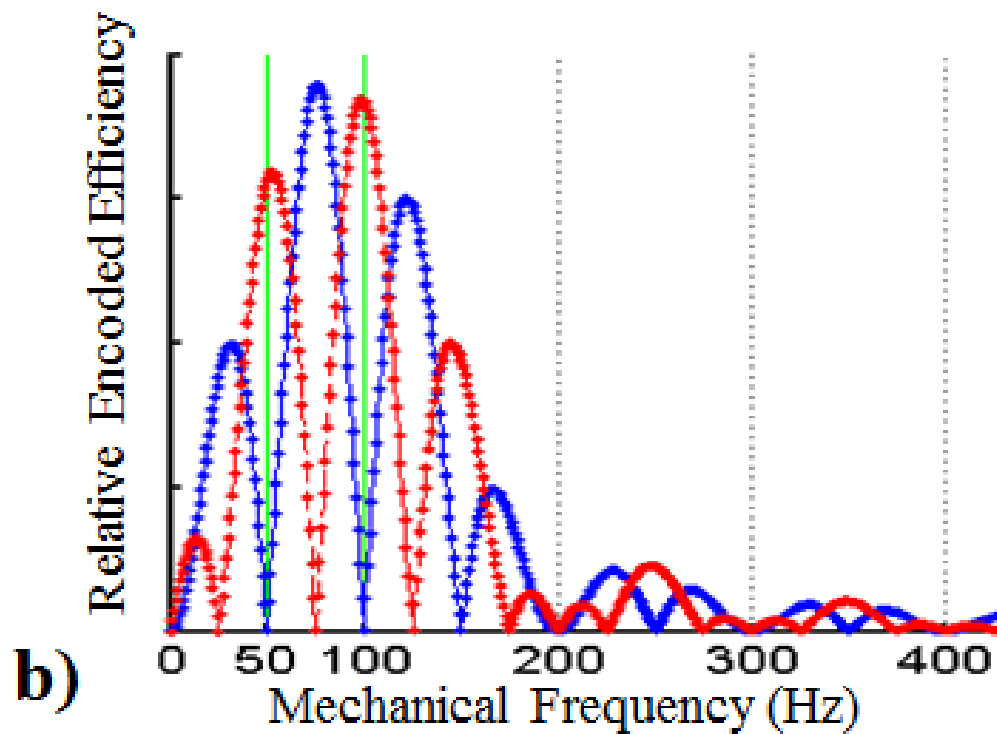
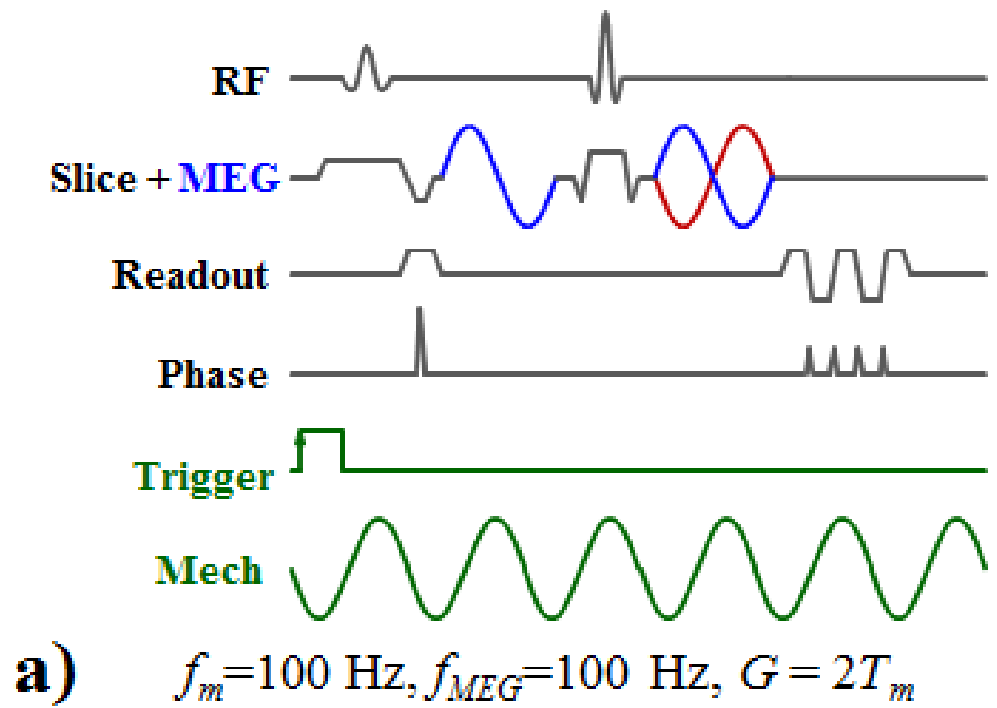


Figure 1-4. a) Conventional spin-echo based pulse sequence for MRE, (b) corresponding encoding efficiency at various mechanical excitation frequencies.

Several pulse sequences for MRE experiments have been reported in literature. Table 1-1 summarizes the MRE pulse sequences used in this work and reported in the literature as found in [83]. The original table focuses mostly on pulse sequences for liver MRE and was prepared by my colleague Dr. Garteiser where I contributed to the initial research of the literature. Several additional entries relating to pulse sequences used for prostate MRE are included in Table 1-1. Relatively few works exist for *in-vivo* prostate MRE. Kemper *et al.* [53] used a standard SE method on the human prostate and reported an imaging time of 24 min for 3D wave encoding in seven slices with an in-plane resolution of 2.2 mm and 3 mm slice thickness. Chopra [55] used a standard fast GRE method for canine and phantom prostates and reported an imaging time between 8 and 40 sec for 1D wave encoding in 5 slices with an in-plane resolution of 0.78 mm and 3 mm slice thickness. Arani *et al.* [56], [57] used a standard fast GRE method for a prostate phantom and reported an imaging time of 15 min for 1D wave encoding in 27 slices with an in-plane resolution of 1.25 mm and 2 mm slice thickness. Most recently, the same group also used a standard fast GRE method for in-vivo human prostate imaging and reported an imaging time of 2-8 min for volunteers for 1-3D wave encoding in single slices with an in-plane resolution of 1.1 mm and 6 mm slice thickness. For patients they reported an imaging time of 9 min for 3D wave encoding in 10 slices with an in-plane resolution of 1.1 mm and 3 mm slice thickness. Thoermer *et al.* [76] used a single-shot, SE-EPI sequence in a porcine model and reported an imaging time of 34 sec for 1D wave encoding in single a slice with an in-plane resolution of 1.4 mm and 5 mm slice thickness. Li *et al.* [54] used a standard SE method on patients and reported an imaging time of 5 min, 17 sec for 3D wave encoding in five slices and an isotropic voxel size of 3.9 mm.

For this study, two main approaches were used on phantoms, volunteers and patients that will be explained in detail in relevant chapters. First, the harmonic imaging concept based on echo-planar (EPI) spin-echo pulse sequence was explored (implemented by Dr. Sinkus [84]). This pulse sequence was modified for imaging of the prostate and provided an important starting point for this project. For in-vivo human prostate (volunteers), the imaging time was 12 min for 3D wave encoding in seven slices and the isotropic voxel size was 1.5 mm. This pulse sequence was modified to allow the entire prostate to be imaged where the imaging time was 13 min for 3D wave encoding in 20 slices and the isotropic voxel size was 3 mm. The second approach was the fractionally encoded GRE method which enabled much faster imaging [66]. This pulse sequence was first implemented for both liver and prostate imaging. For in-vivo human prostate MRE (volunteers and patients), the imaging time between 8 and 10 min for 3D wave encoding in 24 slices with an isotropic voxel size of 2 mm. Further details are tabulated in Table 1-1.

**Table 1-1. Comparison between MR elastography (MRE) sequence parameters in the literature. diff. = difference; NA = not available; var. = variable. (Adapted from [83] with permission)**

| Study                  | Object of study (organ)          | Imaging method (EPI factor) | Encoding method   | TR/TE (ms)       | Matrix        | Resolution (mm)  | Mechanical / encoding frequencies (Hz) | Fractional encoding ratio | No. of phase offsets | Total acquisition time |
|------------------------|----------------------------------|-----------------------------|-------------------|------------------|---------------|------------------|--|---------------------------|----------------------|------------------------|
| Sahebjavaher 2013      | patient (prostate)               | GRE                         | 3D, direct + ref  | 9.2 / 344        | 128×128×24    | 2×2×2            | 70 / 119                               | 0.59                      | 8                    | 8-10 min               |
| Sahebjavaher 2013 [66] | volunteer (prostate)             | SE-EPI (5)                  | 3D, direct        | 44 / 2700        | 64×64×20      | 3×3×3            | 45 / 90                                | 0.5                       | 4                    | 13 min                 |
| Sahebjavaher 2013 [66] | volunteer (prostate)             | SE-EPI (5)                  | 3D, direct        | 44 / 2700        | 64×64×7       | 1.5×1.5×1.5      | 45 / 90                                | 0.5                       | 4                    | 12 min                 |
| Kemper 2004 [53]       | volunteer (prostate)             | SE                          | 3D, direct        | 45 / 500         | 64×64×7       | 2.2×2.2×3.0      | 65 / 65                                | 1                         | 4                    | 24 min                 |
| Chopra 2009 [55]       | phantom, canine (prostate)       | GRE                         | 1D, phase diff.   | 20-35 / 100      | 256×256× ×1-5 | 0.78×0.78×3      | 100-400 / 100-400                      | 1                         | 8                    | 8-40 s                 |
| Arani 2009 [56]        | phantom (prostate)               | GRE                         | 1D, phase diff.   | 10 / 375         | 128×128×27    | 1.25×1.25×2      | 400 / 400                              | 1                         | 4                    | 15 min                 |
| Arani 2013 [57]        | volunteer (prostate)             | GRE                         | 1-3D, phase diff. | 13 / 18          | 128×128×1     | 1.1×1.1×6        | 100-400 / 100-400                      | 1                         | 4                    | 2-8 min                |
| Arani 2013 [57]        | patient (prostate)               | GRE                         | 3D, phase diff.   | 12-14 / 125-250  | 128×128×10    | 1.1×1.1×3        | 100-200 / 100-200                      | 1                         | 4                    | 9 min                  |
| Thoermer 2012 [76]     | porcine (prostate)               | SE-EPI (NA)                 | 1D, phase diff.   | 150 / 3000       | 128×128×1     | 1.4×1.4×5        | 50-150 / 50-150                        | 1                         | 10                   | 34 s                   |
| Li 2011 [54]           | patient (prostate)               | SE                          | 3D, direct        | 100 / 615        | NA × NA ×5    | 3.9×3.9×3.9      | 100/100                                | 1                         | 8                    | 5 min 17s              |
| Garteiser 2013 [83]    | volunteer (liver)                | GRE                         | 3D, direct        | var. / 9.21      | 80×80×9       | 4×4.6×4          | 28,56,84 / 120                         | 0.23,0.47,0.7             | 8                    | 4×16 s B.H.            |
| Venkatesh 2008 [85]    | patient (liver)                  | GRE                         | 1D, direct        | 100 / 25.6       | 256×96×4-8    | 1.25×3.33×(6-10) | 60 / 60                                | 1                         | 4                    | 4×16 s B.H.            |
| Hines 2010 [86]        | patient (liver)                  | GRE                         | n.s., phase diff. | 100 / 24.2       | 256×128×4     | 1.33×1.99×10     | 60 / 60                                | 1                         | 4                    | 2×4×22 s B.H.          |
| Rouviere 2006 [87]     | patient (liver)                  | GRE                         | 2D, phase diff.   | 33.3 / 17.8      | 256×64×1      | 1.33×5.3×10      | 90 / 90                                | 1                         | 4                    | 8×10 s B.H.            |
| Maderwald 2006 [88]    | volunteer (biceps)               | GRE                         | 1D, phase diff.   | 196 / 24.9       | 256×256×1     | 0.78×0.78×NA     | 142 / 142                              | 1                         | 8                    | 2×20 s B.H.            |
| Asbach 2008 [89]       | volunteer, patient (liver)       | SE-EPI (1)                  | 1D, phase diff.   | 500 / 64         | 64×128×1      | 2.34×4.69×10     | 25,37.5,50,62.5 / 50                   | 0.5,0.75,1,1.25           | 40                   | 2×20 s B.H.            |
| Asbach 2010 [90]       | patient (liver)                  | SE                          | 1D, phase diff.   | 500 / 64         | 64×128×1      | 2.34×4.71×10     | 25,37.5,50,62.5 / 50                   | 0.5,0.75,1,1.25           | 40                   | 2×20 s B.H.            |
| Klatt 2007 [39]        | volunteer (brain, liver)         | SE                          | 1D, phase diff.   | 500 / 64         | 64×128×1      | 2.34×4.73×10     | 25,37.5,50,62.5 / 50                   | 0.5,0.75,1,1.25           | 40                   | 2×20 s B.H.            |
| Huwart 2008 [35]       | patient (liver)                  | SE-EPI (3)                  | 3D, direct        | 462 / 54         | 64×64×5       | 3.9×3.9×4        | 65 / 65                                | 1                         | 4                    | 12×10 s B.H.           |
| Huwart 2008 [91]       | patient (liver)                  | SE                          | 3D, direct        | 431 / 61         | 64×64×5       | 3.9×3.9×4        | 65 / 65                                | 1                         | 4                    | 20 min navigated       |
| Nedredal 2011 [92]     | canine (spleen, liver)           | SE                          | 3D, direct        | 1634 / 48        | NA×40         | 3×3×3            | 60 / 80                                | 0.75                      | 4                    | 8×15 s B.H.            |
| Robert 2009 [46]       | volunteer (heart)                | DENSE-EPI (3)               | 2D, direct        | var. / 4.4       | 64×64×1       | 2×2×8            | 50 / 500                               | 0.1                       | 4                    | 8×25 s B.H.            |
| Rump 2007 [93]         | volunteer (liver, biceps, heart) | bSSFP                       | 1D, phase diff.   | 9.8 - 13 / n. s. | 128×104×1     | 2.34×2.34×10     | 51 or 76 / 150 or 100                  | 0.34 or 0.76              | 10                   | 4×17 s B.H.            |
| Kolipaka 2009 [94]     | phantom (heart)                  | GRE                         | 2D, direct        | 3333 / 10.9      | 256×64×1      | 0.55×2.19×10     | 200 / 200                              | 1                         | 8                    | NA                     |
| Kolipaka 2009 [95]     | phantom (heart)                  | GRE                         | 2D, direct        | 1000 / 15.9      | 256×64×1      | 0.55×2.19×10     | 200 / 200                              | 1                         | 4                    | NA                     |
| Sack 2009 [45]         | phantom (heart)                  | SE-EPI                      | 3D, phase diff.   | NA               | NA            | NA               | 32.35 / 32.35                          | 1                         | 10                   | NA                     |
| Sack 2009 [45]         | volunteer (heart)                | GRE                         | 3D, phase diff.   | 5,16 / NA        | 128×128×2     | 2.5×2.66×5       | 24.3 / 500                             | 0.05                      | 8                    | 10 min                 |
| Elgeti 2012 [96]       | volunteer (heart)                | bSSFP                       | 1D, phase diff.   | 3.65 / 1.51      | 256×192×1     | 1.56×1.56×5      | 22.83 / 274                            | 0.08                      | 12                   | NA                     |

### 1.2.4.1 Design considerations

Encoding efficiency: to encode the micron level displacements, a large motion encoding efficiency at the desired frequency is required. As seen in (1-6), the encoding efficiency is directly proportional to the maximum gradient amplitude. The performance of the gradient system can be amplitude and heat limited. Increasing the number of the MEG periods can also increase the encoding efficiency but at the expense of SNR due to longer echo times.

Trade-offs: besides the well know trade-off between image resolution, signal-to-noise-ratio (SNR) and acquisition time, there is an addition constraint set by MRE. That constraint is that the wavelength of the mechanical shear wave needs to be on the order of the detectable lesion size. In other words, the wavelength must be sampled at enough points for the reconstruction algorithm to work. For example, the Local Frequency Estimation (LFE) algorithm works best when the object to be detected is at half the wave-length of the mechanical shear waves.

Imaging parameters: A clinical accepted setup and imaging time for a MRE examination is considered to be approximately 5-15 min which is similar to a dynamic contrast enhanced (DCE) imaging and diffusion tensor imaging (DTI), and spectroscopy examination. The field of view (FOV) must cover the entire prostate. The resolution must be sufficient to detect lesions of interest.

### 1.2.5 Reconstruction of viscoelastic parameters

The acquired raw phase images must be phase unwrapped, subtracted from the reference scan, and corrected for phase offsets. A voxel is marked as invalid if its magnitude in the image was below a certain threshold of the average magnitude; or the total wave amplitude  $U_{tot}$  falls below a threshold. Typically a Gaussian filter is applied to the displacement field prior to reconstruction.

Development of reconstruction algorithms is not the focus of this work. A brief summary of some of the most prominent reconstruction algorithms is given in this section for completeness. The algorithms used are the local frequency estimate (LFE) developed at the Mayo Clinic [97] and curl-based direct inversion (cDI) developed by Dr. Sinkus' group [47]. These algorithms are based on a simplified version of the wave equation and assume locally homogeneous, isotropic, nearly incompressible and viscoelastic (except LFE that assumes purely elastic) mechanical properties. For such assumptions the wave equation for harmonic excitation becomes

$$-\rho\omega^2\vec{u} = \mu\nabla^2\vec{u} + (\lambda + \mu)\nabla\nabla\cdot\vec{u}, \quad (1-7)$$

where  $\rho$  is density,  $u$  is the displacement phasor,  $\lambda$  is the dilatational modulus and  $\mu$  is the shear modulus (Lamé parameters). The second term on the right hand side of (1-7) can be removed by applying the curl operator to both sides of the equation. The Young's modulus of elasticity is found as  $E=3\mu$ , typically reported in kPa. The local frequency estimate (LFE) method [97] uses wavelet-based filter banks at specific frequencies to estimate the wave number. The wavelength was estimated using

$$\lambda = \frac{1}{f} \sqrt{\frac{\mu}{\rho}} = \frac{1}{f} \sqrt{\frac{E}{3\rho}}, \quad (1-8)$$

where  $E$  was calculated from the direct inversion methods described previously. The final stiffness results were also filtered using the same filter.

### 1.2.6 Literature review: elasticity of prostate

In the literature the elasticity of the human prostate is typically reported as the Young's modulus in units of Pascals (Pa). Only articles reporting absolute values of  $E$  are included in this survey. The motivation for this literature survey was to establish a baseline for the elasticity of the human prostate. However, as it becomes evident, the reported elasticity values vary over two orders of magnitude. Mechanical properties strongly depend on the tissue condition (*in-vivo*, *ex-vivo* tissue and whether it was fixed in formalin), frequency of excitation, type of pathology (healthy or malignant), measurement method (mechanical probing methods, ultrasound or MRI) and experimental conditions (e.g. pre-compression loading, sample temperature for *ex-vivo* cases). Krouskop *et al.* [98] used a mechanical indenter to estimate the elasticity of various *ex-vivo* prostate samples under various pre-compression levels (2-4%) and excitation frequencies (0.1-4 Hz). They found elasticity values between 55-71 kPa for healthy prostate tissue, 36-41 kPa for BPH (benign prostatic hyperplasia) and 96-241 kPa for cancerous prostate tissue. Parker *et al.* [99] used ultrasound imaging methods (sonoelasticity) to estimate linear (2.15-3.96 kPa) and non-linear (17.3-39 kPa) elasticity properties of healthy prostate tissue for pre-compressions between 1-10%. Zhang *et al.* [6] characterized the frequency-dependent complex Young's modulus of normal and cancerous prostate tissues *in-vitro* by using stress relaxation testing and viscoelastic tissue modeling methods. They compared their results to histology. A viscoelastic Kelvin-Voigt fractional derivative (KVFD) model was used to obtain the parameters. For 8 normal and 9 cancerous prostate samples, the average magnitudes of the complex Young's moduli  $|E^*|$  were  $15.9 \pm 5.9$  kPa and  $40.4 \pm 15.7$  kPa at 150 Hz, respectively, giving an elastic contrast of 2.6:1. For sinusoidal excitation,  $|E^*|$  is defined as the amplitude of the displacement phasor divided by the excitation force phasor and  $\tan \delta$  is their phase difference. Yang *et al.* [100] report  $|E^*|$  values of *in-vitro* prostate tissue using dynamic micro probing performed at 3% and 5% pre-compression of epithelial tissue (360-510 kPa) and stromal tissue (190-245 kPa) for frequencies between 5 and 30 Hz. Phipps *et al.* [101] collected fresh tissue specimens from patients undergoing transurethral resection of the prostate (TURP) for benign or malignant prostatic enlargement. Individual TURP chippings underwent immediate mechanical testing for excitation frequencies 5-50 Hz. The  $|E^*|$  elasticity value for untreated cancer tissue was 110 kPa and for treated prostate cancer tissue it was 118 kPa, and the phase difference between force and displacement was 0.17 rad. Hoyt *et al.* [102] used the KVFD viscoelastic model to characterize mechanical stress relaxation data measured from human prostate tissue samples *in-vivo* using sonoelasticity and mechanical testing for a frequency range of 0.1-250 Hz. The values for healthy tissue ranged between 3.8-25 kPa and for cancerous tissue between 7.8-40.6 kPa. They also concluded that tissue elasticity was a promising biomarker for prostate cancer. Murayama *et al.* [103] used a

resonant dynamic micro probing setup (100 kHz) and mapped elastic modulus of histology samples containing healthy and cancerous tissue that were measured to be 10 kPa on average. Ahn *et al.* [104] used a custom motorized indentation device and analyzed the elasticity of 46 *ex-vivo* prostate specimens from radical prostatectomy. They found an elasticity of  $17.0 \pm 9.0$  kPa for healthy and  $24.1 \pm 14.5$  for cancerous tissue. Sarvazyan *et al.* [105] developed phantom models for the healthy prostate with values 1-5 kPa (static) which they adopted from [106]. Using MRE, the first *ex-vivo* results of 17 healthy tissue specimens were reported by Dresner *et al.* [48] where the excitation frequency was varied between 100-500 Hz. They reported elasticity values between 3-47 kPa. Later, Dresner *et al.* [49] also compared elasticity measurements of *ex-vivo* specimens to histological reports. Estimates of healthy tissue and cancerous tissue were of 11.9 kPa and 21.5 kPa, respectively. McGrath *et al.* [50], [51] studied *ex-vivo* samples using quasi-static MR methods at 7T. They concluded that the fixation in formalin increased the stiffness of the prostate nine-fold. They report elasticity of 53 kPa for healthy and 172 kPa for tumors and 457 kPa for tissue after fixation. The first *in-vivo* elasticity value of the prostate of a healthy subject using MRE was reported by Sinkus *et al.* [107] using a 1.5 T scanner, for an excitation frequency of 65 Hz. The reported values ranged from 9 to 15 kPa (dynamic shear modulus of 3 to 5 kPa). Kemper *et al.* [53] reported the elasticity of healthy tissue to be between 6.6-9.9 kPa (dynamic shear Modulus of 2.2-3.3 kPa) and of the adjacent fat tissue to be 3.3 kPa using *in-vivo* MRE techniques at 65 Hz. Li *et al.* [54] used *in-vivo* MRE and report elasticity of  $1.99 \pm 0.66$  kPa for prostatitis and  $6.55 \pm 0.47$  kPa for prostate lesions. They also report viscosity of  $2.13 \pm 0.21$  Pa·s for prostatitis and  $6.56 \pm 0.99$  Pa·s for lesions. The reported values of elasticity of the human prostate are summarized in Figure 1-5, where the cases with malignant tissue are marked by a cross.

As a comparison to a study reporting only strain [108], 15 radical prostatectomy prostate glands were embedded in gel and indentation test were performed. This study reported that the transition zone has less strain than the peripheral zone and is thus stiffer. Also, they reported that prostate cancer and benign hyperplasia (BPH) tissue to be stiffer.

The prostate elastography literature survey shows that there is a wide variability in the reported elasticity values. Therefore, there is no consensus value for the elasticity of the prostate, regardless of whether the data is acquired at static excitation or at frequencies typical for MRE such as 40-100Hz. Furthermore, other mechanical properties such as viscosity and anisotropy have not been studied in detail. Mechanical properties strongly depend on the tissue condition, frequency of excitation, type of pathology, measurement method and experimental conditions. Therefore, it is challenging to find a baseline of elasticity of the *in-vivo* human prostate.

### 1.3 Thesis objectives

This work is focused on (i) the development of *in-vivo* MRE system for prostate cancer imaging at 3T, (ii) development of *ex-vivo* MRE system for prostate cancer imaging at 7T, and (iii) evaluation of MRE for prostate

cancer diagnosis based on whole mount histopathology, and (iv) acquisition of high-quality data for development of new reconstruction algorithms by others.

For the *in-vivo* system the objectives were:

1. To develop a transducer that induces sufficient mechanical waves in a patient friendly manner.
2. To develop an acquisition method that enables rapid imaging in a clinically acceptable time.
3. To develop a protocol for a patient study for multi-parametric imaging of prostate cancer with MRE, DWI and DCE.
4. To test the repeatability of the MRE system in volunteers.
5. To assess the diagnostic power of detecting prostate cancer using MRE. Whole mount histology marked with Gleason score was used as the gold standard.

For the *ex-vivo* system the objectives were:

6. To develop a transducer prostate MRE.

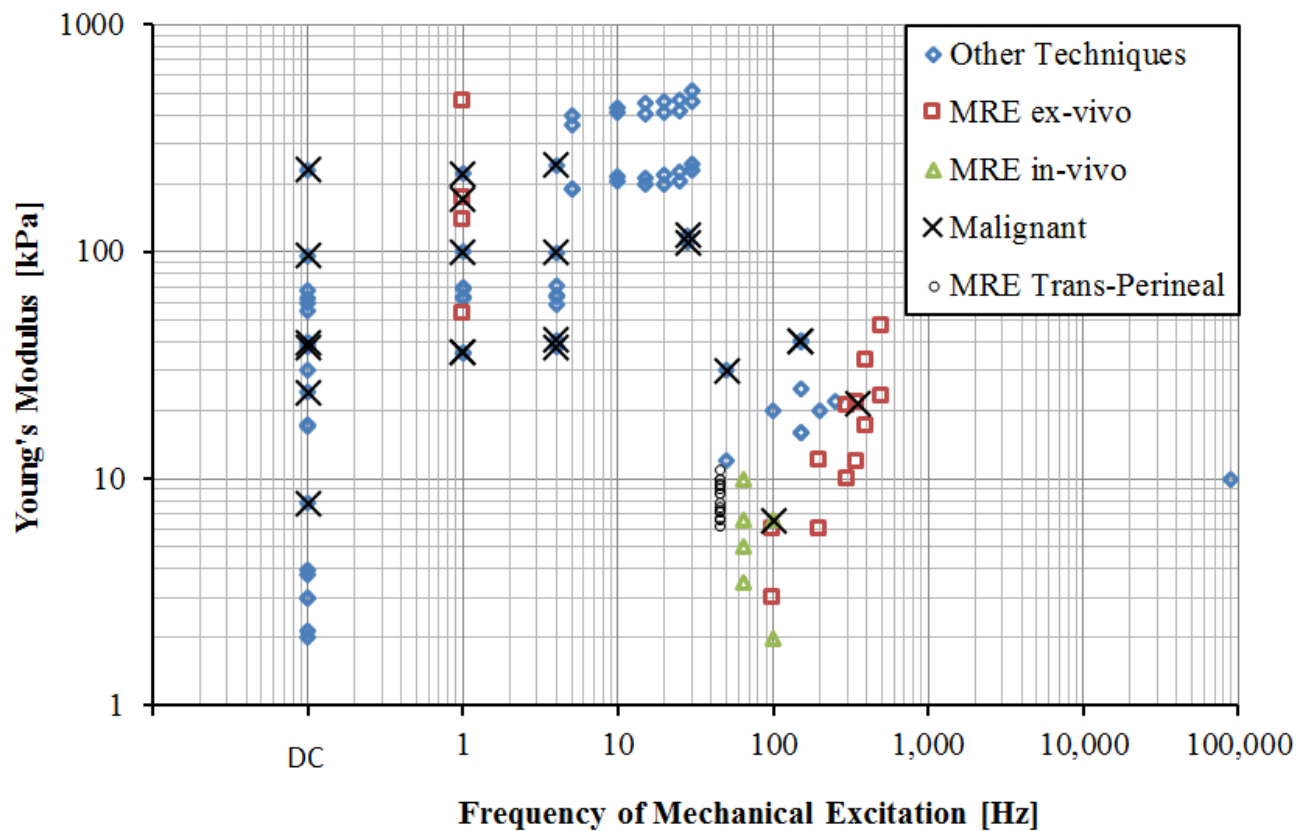


Figure 1-5. Elasticity of human prostate as reported in literature.

7. To develop a protocol for a patient study for multi-parametric imaging of prostate cancer with MRE and DWI.
8. To assess the diagnostic power of detecting prostate cancer using MRE alone and in combination with DWI.

For the development of the reconstruction algorithms the objectives were:

9. To acquire high quality 3D displacement data of phantoms and volunteers at multiple frequencies.

## 1.4 Thesis outline

Chapter 2 describes the first MRE system developed for *in-vivo* prostate imaging at UBC. The concept of trans-perineal prostate MRE using a hydraulic based transducer is introduced. The application of harmonic acquisition method for 3D displacement imaging using the prostate is described. The methods are validated in phantoms and human repeatability studies. This system is used to acquire data for validation of the Traveling Wave Expansion (TWE) algorithm developed by Baghani *et al.* [109].

Chapter 3 describes a new MRE system for trans-perineal prostate MRE. The design and validation of the new shielded electro-magnetic transducer are discussed. A new acquisition pulse sequence is developed for rapid imaging of the prostate. The methods are validated in phantom and volunteers studies. Data acquired using this system is then used for validation of the mixed displacement–pressure finite element method (FEM) [110] and the curl-based finite element (FEM) reconstruction algorithm developed by Honarvar *et al.* [111].

In Chapter 4, a clinical protocol is developed for a patient study based on the system described in Chapter 3. The repeatability of the system is evaluated in a volunteer study. The results from the patient study are presented and compared to whole mount histology slides marked with the Gleason score.

Chapter 5 describes an *ex-vivo* prostate MRE system. The design and validation of the new shielded electro-magnetic transducer are discussed. A standard spin-echo based pulse sequence is used. The methods are validated in phantom. A clinical protocol is developed for a patient study based on the system described in this chapter. Multi-frequency MRE and DWI was performed for a subset of the cases. The results from the patient study are presented and compared to whole mount histology slides marked with the Gleason score.

Finally, Chapter 6 describes the conclusions and contributions of this thesis as well as the future research directions.

# Chapter 2 - *In-vivo* prostate MRE with hydraulic transducer and harmonic acquisition method

## 2.1 Introduction

The reconstruction of viscoelastic parameters relies on propagating shear waves in tissue. The prostate is naturally well protected within the pelvis by the surrounding ligaments and muscles. Even though Sinkus *et al.* [23] reported the first successful *in-vivo* MRE image of the human prostate by applying vibrations of 65 Hz to the pubic bone, the pelvis is a massive structure that is difficult to move with large amplitudes without significant discomfort to the patient [77]. This method of tissue excitation is not repeatable across subjects of different size and age groups. Furthermore, this method of excitation can become uncomfortable after an extended examination time. See discussion section for more detail. Other more invasive approaches for mechanical excitation such as endo-rectal [56] and trans-urethral [52] have also been proposed and their success remains to be seen in *in-vivo* studies. Therefore, to ensure good shear wave penetration into the prostate in a non-invasive manner, a new approach is proposed where the excitation is applied via the perineum (trans-perineal). Such excitation can be applied over the patient's undergarment, and can be used with either an endo-rectal or pelvic coil.

## 2.2 Methods

### 2.2.1 Trans-perineal excitation with hydraulic transducer

A custom hydraulic excitation system [112] was developed to provide trans-perineal excitation. This system does not induce any distortions in the MR images and is compatible with the RF coils. The subject lies in the supine position during MRE imaging, with the vibrations being applied in the superior-anterior direction via a transducer that is positioned between the legs of the patient, as shown in Figure 2-1.

The transducer (shown in Figure 2-2) can be adjusted in height and angle to comfortably fit the anatomy of the patient while still exerting a small compression ( $< 50$  N) on the perineum over an area of 20 mm $\times$ 30 mm. The transducer is fastened to the MR table and is covered by cushions for the comfort of the patient. The vibrations originate from an active external commercial electro-mechanical vibration source (Bruel & Kjaer Inc., Model 4808, USA) located in the console room. The vibrations (45 Hz) from the vibration source are transferred to the patient via a passive low-pressure ( $< 100$  kPa) hydraulic system via a semi-rigid hose. The transducer on the patient end is shown in Figure 2-2. The applied pressure variations from the inlet are transferred to the

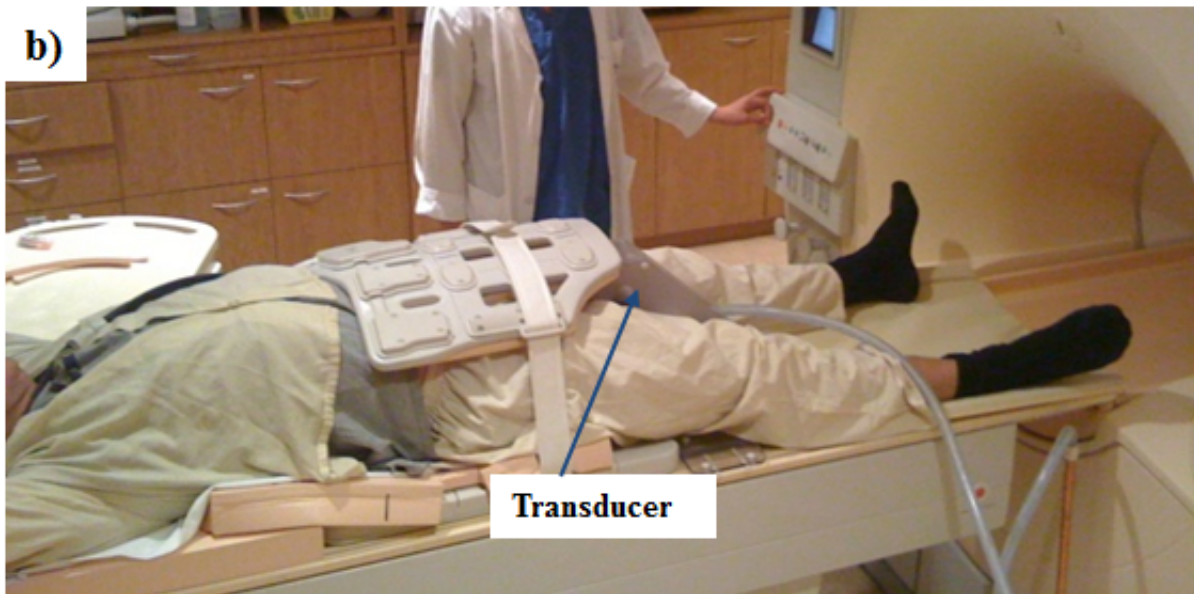
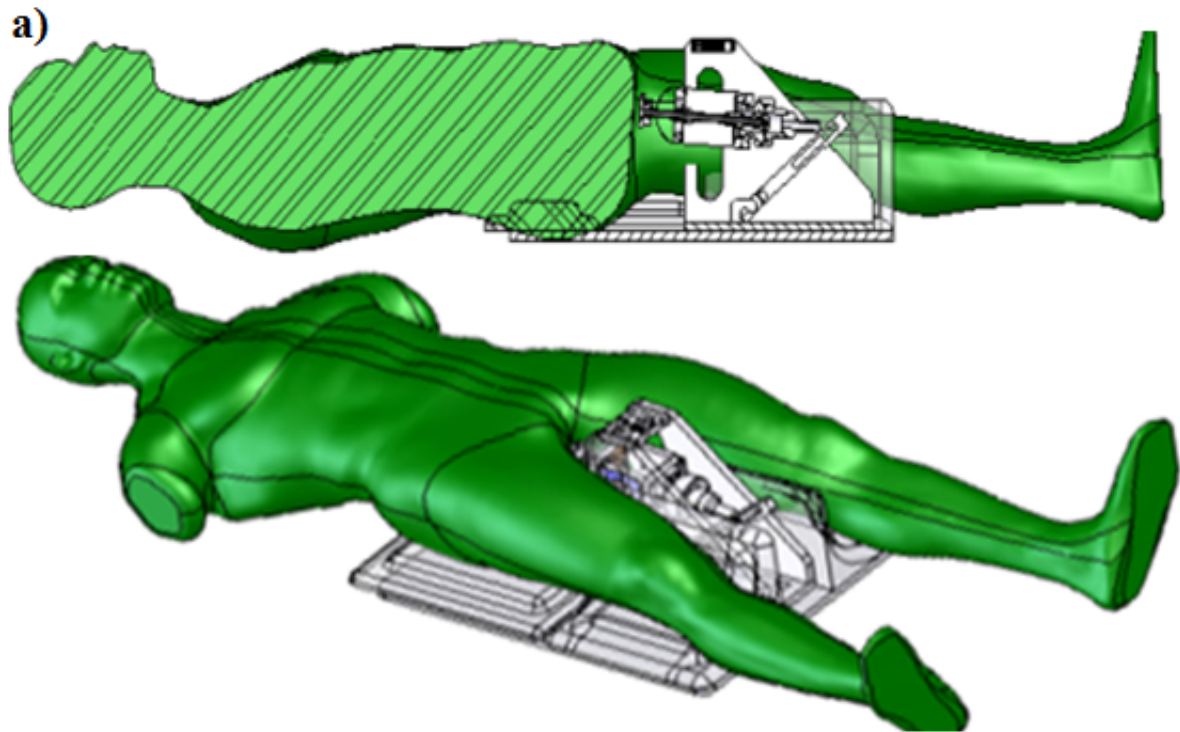


Figure 2-1. The transducer is applied to the perineum of the subject as illustrated in (a). A photo of the actual setup is shown in b).

diaphragm that moves the carbon fiber tube and the transducer head. The flexural springs hold the carbon-fiber and constrain the motion to a single direction (Head-feet). The modeling of the hydraulic transducer is detailed in Appendix A. Several intrinsic safety features have been incorporated in the transducer, including limited travel. Also, the transducer is passively coupled to the patient and the subject may easily pull away from the transducer at any time. Furthermore, the hydraulic system is designed to operate at low pressures with water as the hydraulic medium. This ensures that even in an event of a failure of the hydraulic system, only 60 mL of

water would slowly leak out and the transducer head will retract with no chance of causing harm to the patient. This system was approved by the local clinical ethics review board for patient studies. Given the significant level of vibrations experienced by men when riding a bicycle over moderately rough roads, it was not expected that the trans-perineal excitation to cause subject discomfort. Nevertheless, at the start of each trans-perineal MRE study, the vibration amplitude applied was gradually increased from a very low value, while repeatedly confirming with the subject that the vibration does not cause any discomfort. A call bell was given to the subjects to indicate if they felt uncomfortable or pain at any time so that the experiment would be stopped immediately. No discomfort or pain was reported by the subjects during or after the examination when asked.

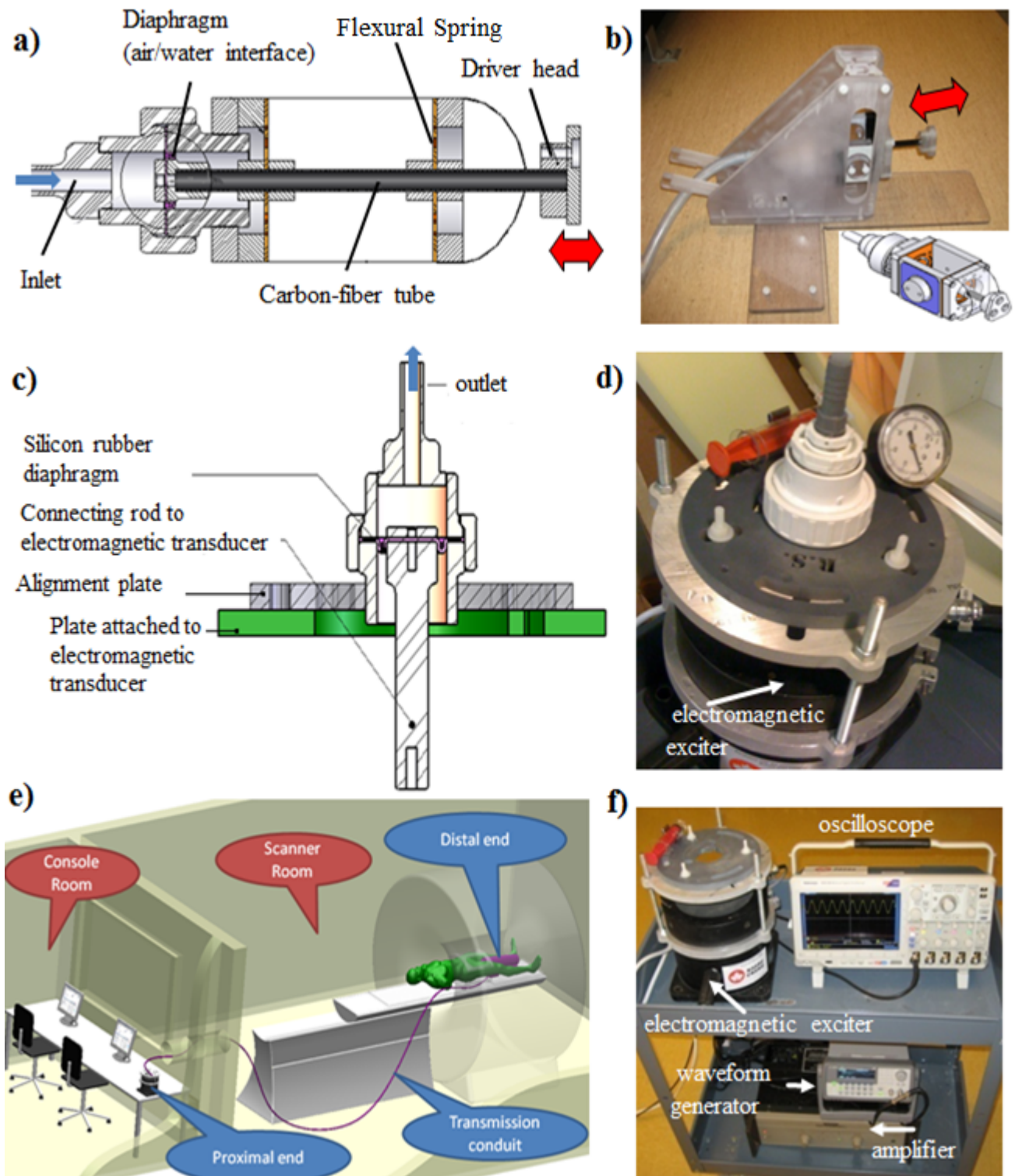


Figure 2-2. The subject-end (a-b) and the active end (b-c) of the hydraulic transducer and its component are shown. e) The overall schematic of the transducer system: the electromechanical exciter (c-d) is in the console room and the hydraulic transmission line passes through the waveguide and connects to the subject-end. f) The mobile MRE system that is positioned in the console room.

### **2.2.2 Acquisition of the 3D wave field using harmonic method**

The experiments were carried out on a 3T Achieva (Philips Inc., Netherlands) scanner. A standard 6-channel cardiac coil with acceleration factor (SENSE) 2 was used. A sagittal scout image was performed to ensure that the trans-perineal transducer is properly positioned at the beginning of each examination. For the anatomical image a standard axial T2-weighted FSE sequence (TE/TR = 86/2500 ms, FOV 320 mm×320 mm×70 mm with 0.5 mm in-plane resolution and 4 mm slice thickness) was acquired. The MRE images were acquired using a multi-slice multi-shot SE-EPI method [84]. For the first series of subjects the wave images were acquired on a 64×64×7 matrix with 1.5 mm isotropic voxel size. For subsequent subjects the matrix size was increased to 64×64×20 with 3 mm isotropic voxels to cover the entire prostate. The signal was averaged twice and an EPI factor (number of gradient echoes in per shot in a multi-shot experiment) of 5 was used. A single sinusoidal cycle was used as the motion encoding gradient with strength of 60 mT/m.

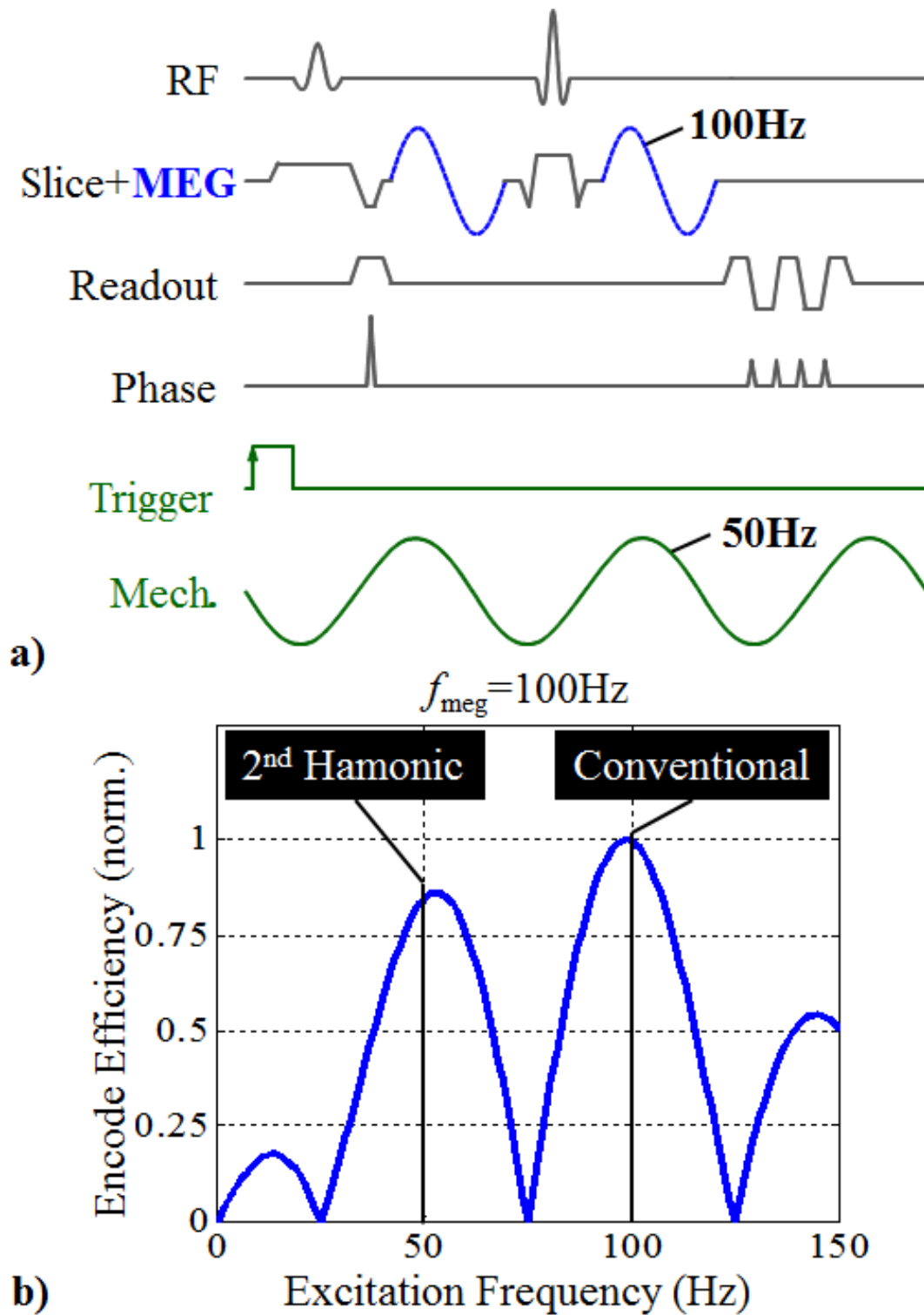


Figure 2-3. a) The SE-EPI based harmonic sequence is shown where the frequency of the MEGs (e.g., 100Hz) is twice that of the mechanical excitation (e.g., 50Hz). The motion-encoding efficiency is shown as a function of frequency in (b). The sensitivity loss of the harmonic approach compared to conventional MRE sequence is offset by the SNR gain due to a shorter echo time.

At a lower excitation frequency the attenuation and dispersion are typically lower [47], resulting in better wave penetration [78]. However, for the same imaging field-of-view and matrix size, the resolution of the elasticity

map will be degraded at a lower mechanical frequency [79]. The timing of the imaging sequence is coupled to the echo time. Thus, a lower excitation frequency results in an extended echo time and therefore a lower SNR. For *in-vivo* examinations, to reduce the image acquisition time for clinical feasibility, the harmonic acquisition methods was used. In this method the frequency of the motion sensitizing gradients was twice the frequency of the mechanical excitation ( $f_{\text{meg}} = 2f_{\text{mech}}$ ) [84]. Figure 2-3a shows an example case of a harmonic pulse sequence used for this study where motion encoding gradients (MEG) were at 100 Hz while the mechanical excitation was at 50 Hz. Echo planar imaging (EPI) was used to accelerate the imaging time. The normalized motion encoding efficiency is shown in Figure 2-3b as calculated from the theoretical phase accumulation [28]. The sensitivity loss of the harmonic approach ( $f_{\text{meg}} = 100$  Hz and  $f_{\text{mech}} = 50$  Hz) compared to the conventional approach ( $f_{\text{meg}} = 100$  Hz and  $f_{\text{mech}} = 100$  Hz) is offset by the shorter echo time (TE/TR = 44/2700 ms) thus enabling acquisition of high SNR data especially at higher magnetic fields, as described in [84]. In addition, undesired motion components at higher frequencies (90 Hz) are suppressed by choosing the correct sign for the motion encoding gradients (MEG) after the  $\pi$  pulse. The MEGs were superimposed to encode motion in all three spatial directions. Hadamard-style encoding schemes may be applied to improve the encoding efficiency and shorten the echo time [113]. The total imaging time for the MRE examinations was approximately 13 min, or approximately 4 min per encoding direction. Saturation slabs were applied in the AP direction to suppress signal outside the FOV. The signal from fat was suppressed using a SPIR (Spectral Presaturation with Inversion Recovery) sequence. Phantom studies were also performed with the same protocol except that the excitation frequency was 50 Hz in one case and 250 Hz in another case.

### 2.2.3 Reconstruction and repeatability

Six healthy volunteers were scanned with an age range 28-51 and a mean of 34 years. None of the volunteers reported any prostate relevant symptoms. The study was approved by the ethics review committee of our institution. The displacement ( $u$ ) images were reconstructed using established 3D reconstruction algorithms: LFE, curl-based direct inversion, and TWE. The wavelength was estimated using

$$\lambda = \frac{1}{f} \sqrt{\frac{\mu}{\rho}} = \frac{1}{f} \sqrt{\frac{E}{3\rho}} \quad (2-1)$$

where  $E$  was calculated from the direct inversion methods described previously. The results were comparable to manual ‘ruler’ measurements. A thorough study of the aforementioned reconstruction algorithms that are compared to other reconstruction methods has been reported by Baghani *et al.* [109] where MRE experiments were performed at 210 Hz and 300 Hz on an elasticity controlled phantom with various inclusions (CIRS Model 049, USA). In order to verify the reconstruction results at lower frequencies and smaller inclusions, further performed MRE tests were performed on a Prostate Elastography Phantom (CIRS Model 066, USA) which has three 10 mm-diameter inclusions and a more realistic anatomy where the trans-perineal protocol can be verified.

To validate the repeatability of our approach the MRE scans were repeated on three subjects (F, B and D) at least three times, and reconstructed the elastograms using the LFE algorithm. The analysis is applied to a region enclosing the entire prostate. For subject F, three experiments were performed: experiment two was performed three months after experiment one, and the third experiment was performed four months after that. For subject B, four experiments were performed. The last three experiments were performed on the same day, approximately a year after experiment number one. Experiment two and three were performed sequentially with the same transducer position. For experiment four, subject B was taken out of the scanner and the transducer was repositioned with a subsequent repetition of the scan on the same day. For subject D, in total six experiments were performed. Experiment two and three were performed on the same day, one day after experiment one. After each examination the subject D was removed from the scanner and the transducer position was changed. The last three scans (experiments four to six) were acquired on the same day approximately 12 months after the initial scan. The transducer position was changed slightly from one scan to the next.

## **2.3 Results**

### **2.3.1 Phantom experiments**

The elasticity reconstruction results for one slice are shown in Figure 2-4.

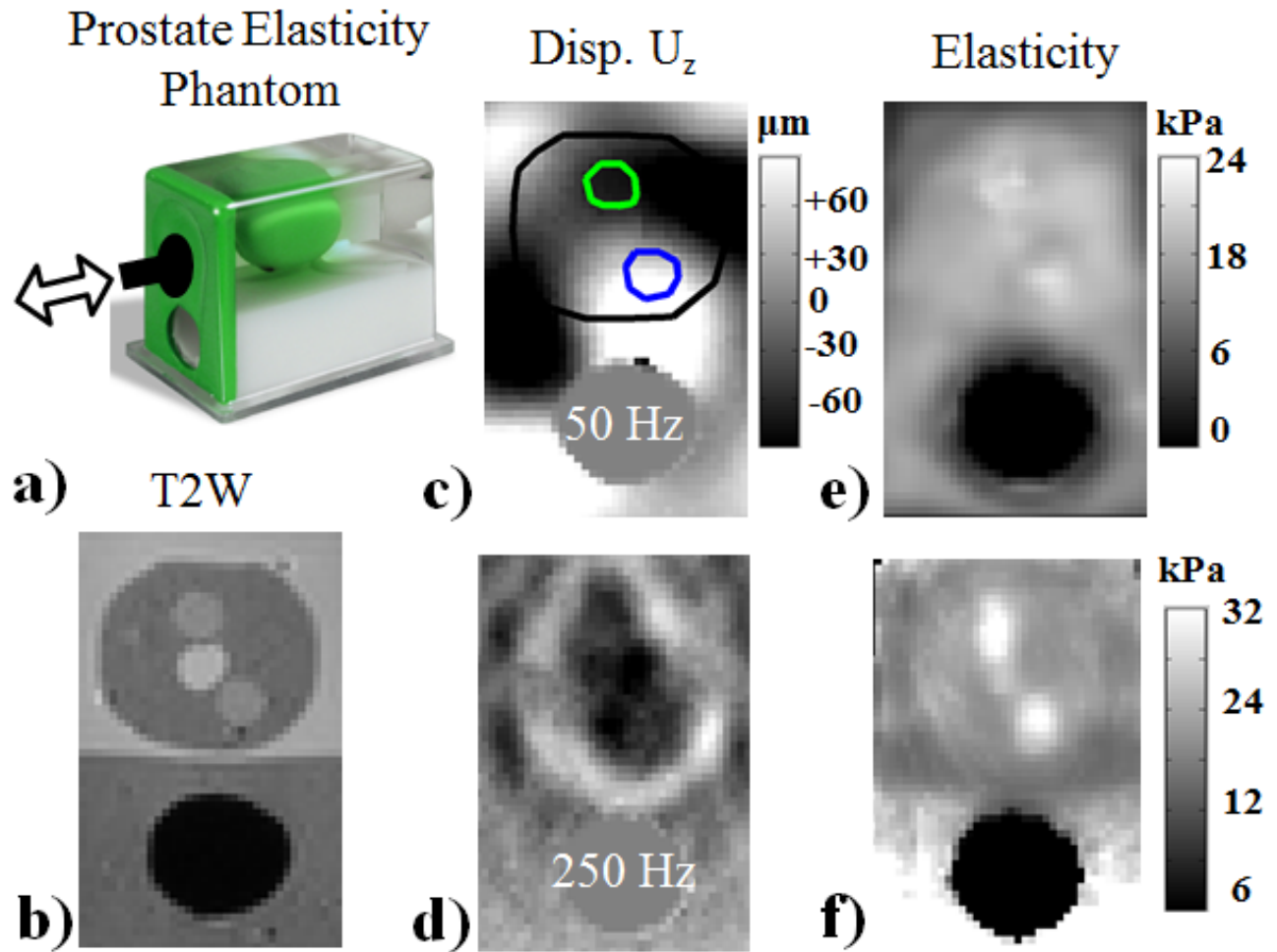


Figure 2-4. a) Trans-perineal excitation is applied to a prostate elasticity phantom. b) The stiffer lesions (10mm in diameter) are visible in the T2-weighted anatomical MRI image. The waves at 50 Hz (c) and 250 Hz (d) are observed along the z-direction (in-plane). The elasticity maps in (e) at 50 Hz and (f) at 250 Hz show that the stiffer lesions stand out, even though the wavelength is significantly longer than the lesion size at 50Hz.

A photo of the phantom is shown in (a) where the excitation is applied via the perineum, as proposed for the *in-vivo* studies. The T2W MRI image is shown in (b) where the inclusion can be visualized and the wave image (displacement in z-direction) is depicted in (c) and (d). Finally, the reconstructed elasticity map is shown in (e) and (f) for 50 Hz and 250 Hz, respectively. The mean elasticity of the background and of the lesion was 12.9 (min 11.9) kPa and 19.6 (max 21) kPa, respectively, yielding to a ratio of 1.5 (max 1.8). The reconstruction results using the LFE approach are shown in Figure 2-5 for several slices. The first few slices from either end are not shown.

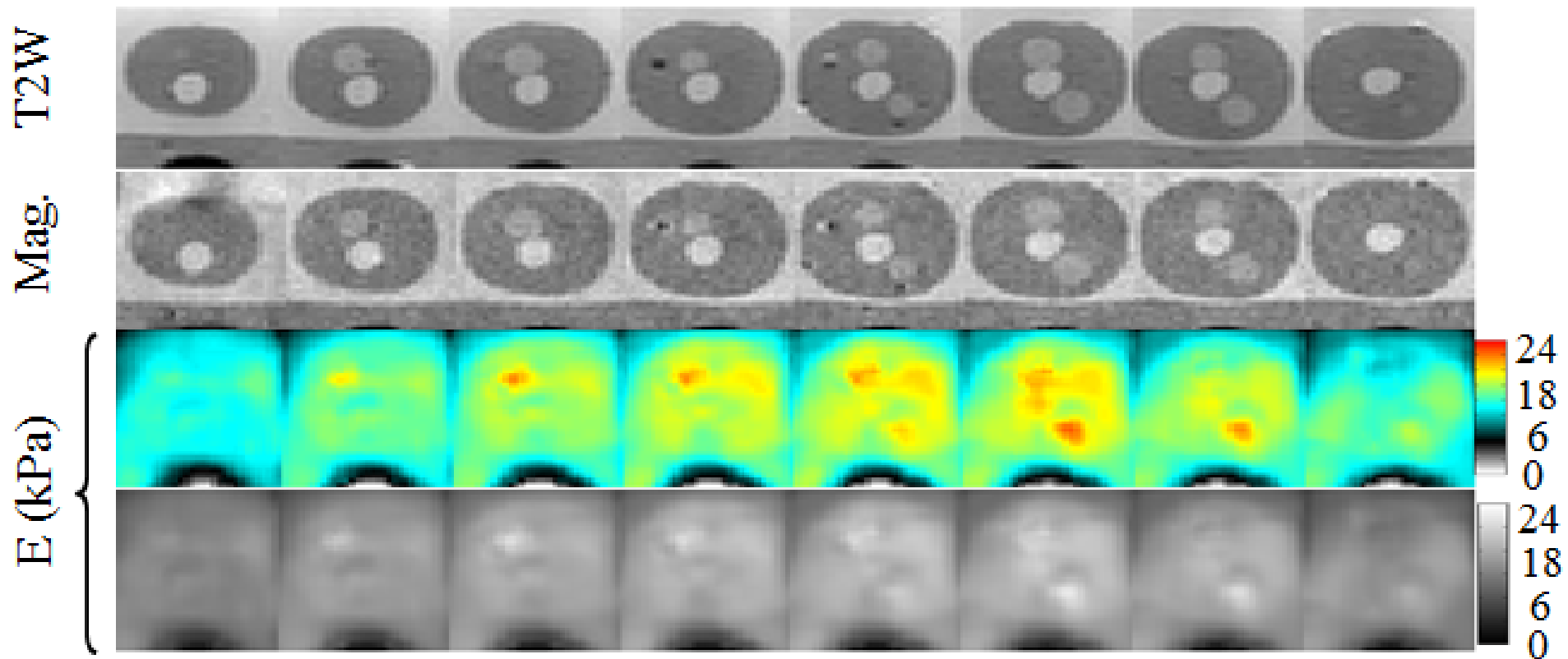


Figure 2-5. The elasticity reconstruction at 50 Hz across several slices in the prostate elastography phantom is depicted. Inclusions of 10mm in diameter (0.5 cc) are readily observable in the elasticity maps.

### 2.3.2 *In-vivo* prostate examinations

The transducer produced sufficient amplitude (up to 2 mm maximum at the surface) for the generation of waves. The displacement of the transducer was verified using accelerometer and laser vibrometer measurements. Image artifacts due to the hydraulic transducer were not present. Mechanical waves were transmitted effectively from the perineum to the prostate as shown in Figure 2-6(c).

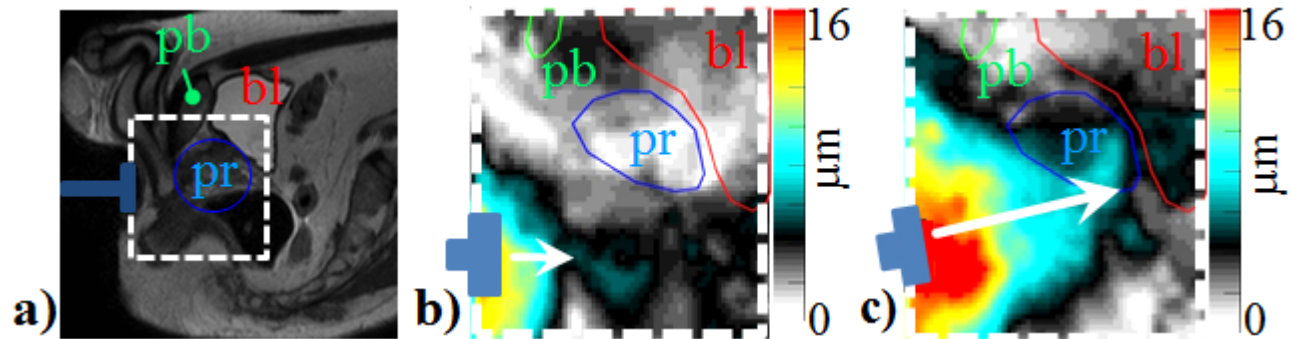


Figure 2-6. a) Standard T2-weighted anatomical MRI image of sagittal human prostate showing bladder (bl), pubic bone (pb) and transducer (blue “T” shape) (b) amplitude of wave: transducer at perineum position 1 and (c) position 2. Thus wave penetration depends on position and angle of the transducer.

It was observed that the proper mechanical coupling and angle at the perineum is a key factor to the efficient transmission of waves into the prostate. For example, if the transducer is positioned horizontally, the mechanical waves are significantly attenuated before they reach the prostate (b). However, if the transducer is positioned at the correct height (just below the pubic bone) and angle ( $\sim 25^\circ$ ) the waves enter the prostate as seen in (c). A sagittal scout image is performed at the start of each examination to ensure proper positioning of the transducer.

Selected *in-vivo* images in transverse orientation acquired for a healthy subject are shown in Figure 2-7.

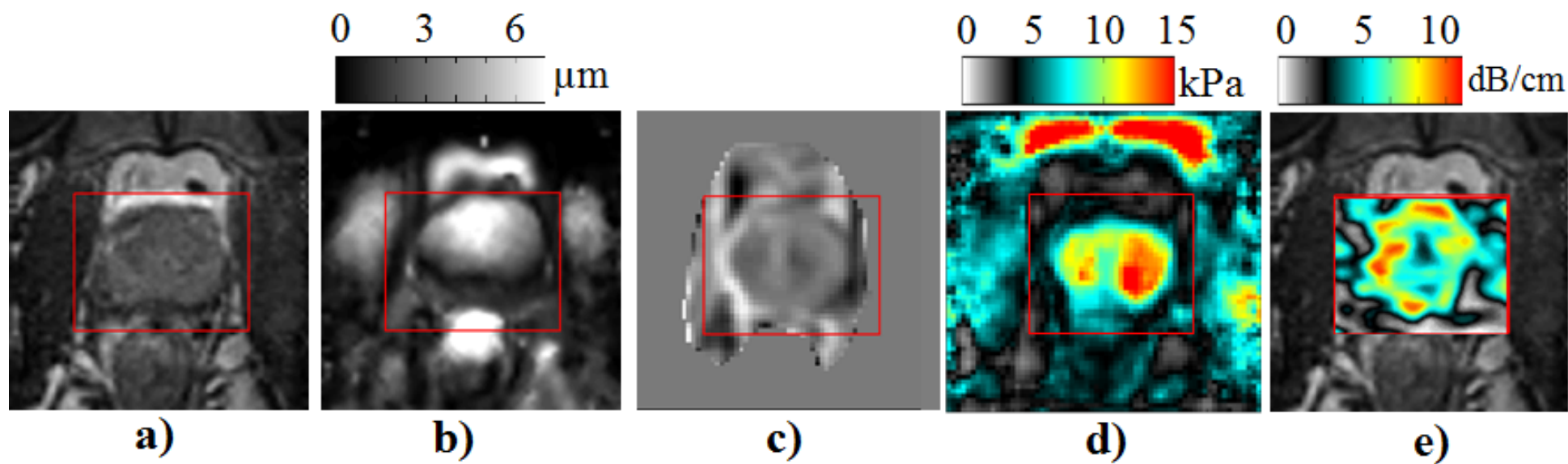


Figure 2-7. a) Transverse view of T2-weighted anatomical MRI of human pelvis b) measured total wave amplitude c) in-plane shear waves d) elasticity and e) damping of the prostate. Refer to Figure 8a for the gray scale image of (d).

The maximum wave amplitude in the prostate in (b) was  $7.5 \mu\text{m}$  in this case and ranged between 6 and  $30 \mu\text{m}$  in subsequent MRE examinations. The wave amplitude is the envelope of the different phases of the motion that were captured. Shear wavelengths of  $38 \pm 6 \text{ mm}$  were observed in (c) where the components of the compressional wave had been removed using the curl operator. The elasticity map reconstructed using LFE is shown in (d). Compared to the background, the prostate gland stands out in the elastogram with a global elasticity of  $8.6 \pm 3.1 \text{ kPa}$ . Because LFE does not calculate attenuation, the TWE reconstruction [109] was used to estimate it. The attenuation of the mechanical wave on this dataset as shown in (e) where the damping was  $6.5 \pm 2 \text{ dB/cm}$ .

**Table 2-1. Elasticity of the prostate for six healthy volunteers.**

| Case (age) | Mean Elasticity (kPa) |
|------------|-----------------------|
| A (44)     | $8.6 \pm 3.1$         |
| B (28)     | $6.7 \pm 2.4$         |
| C (30)     | $9.6 \pm 3.1$         |
| D (51)     | $9.4 \pm 2.4$         |
| E (30)     | $7.3 \pm 2.9$         |
| F (30)     | $7.8 \pm 3.3$         |
| mean (36)  | $8.2 \pm 2.9$         |

The results from six subjects reconstructed using LFE are shown in Figure 2-8

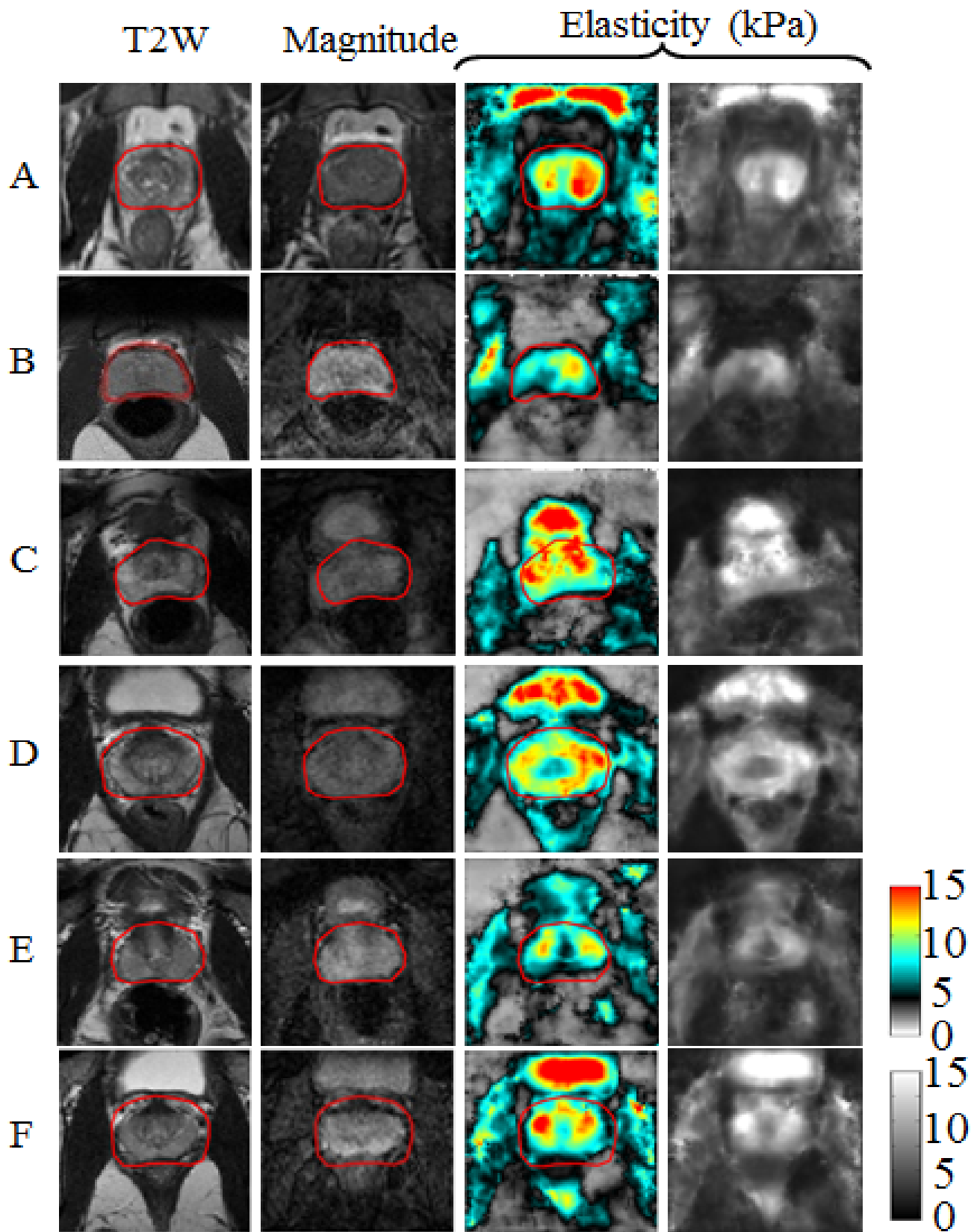


Figure 2-8. Elasticity images of the human Prostate using the trans-perineal approach. The prostate clearly stands out in all the elasticity images (in color and gray scales) and shows reasonable correlation with anatomy (T2-weighted images).

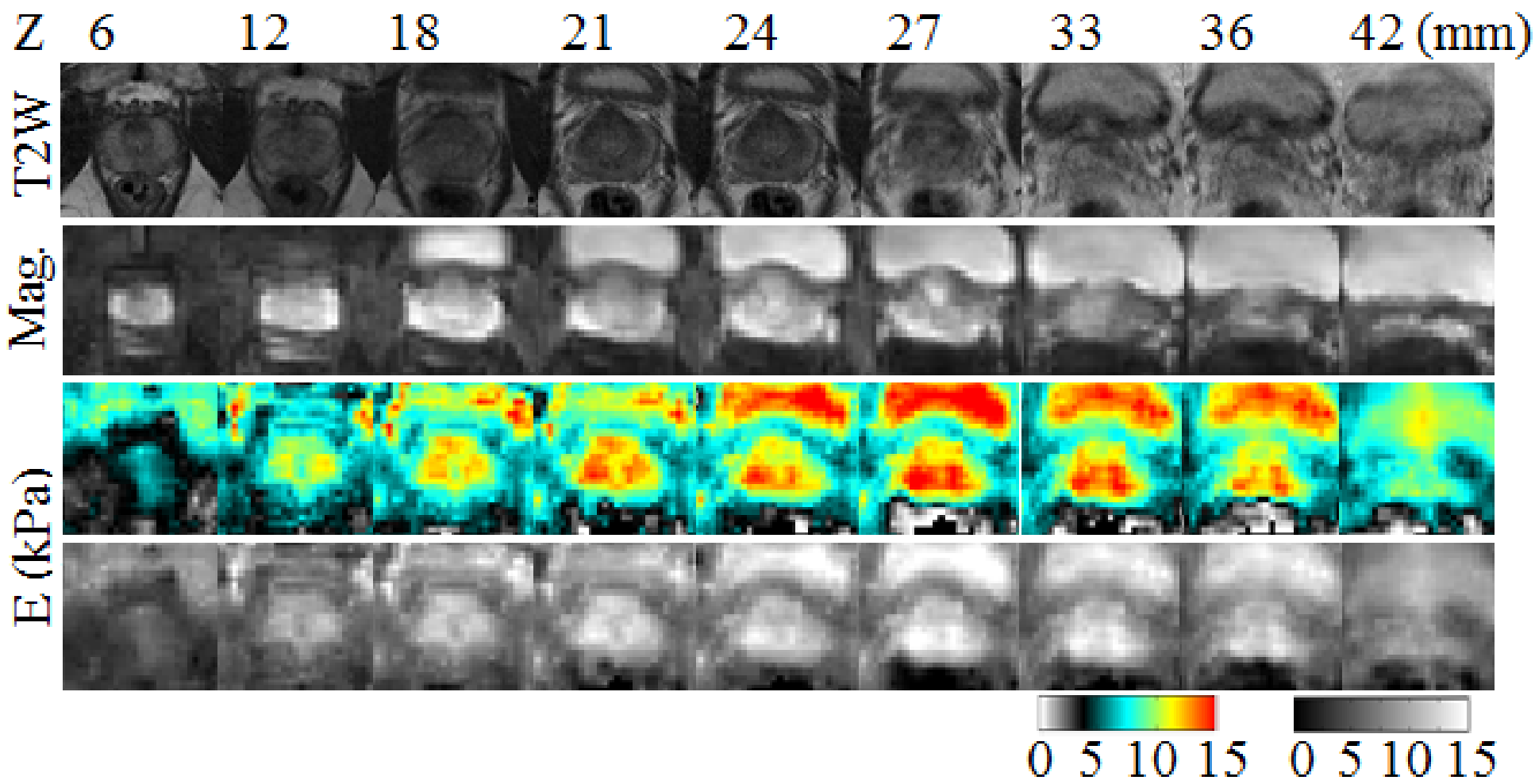


Figure 2-9. Elasticity images of the human Prostate using the trans-perineal approach across several slices.

**Table 2-2. Elasticity of the prostate for healthy volunteers (F, B and D) was repeated at various times. The table shows that the results from trans-perineal MRE are repeatable within the experimental error. Same colour highlight denotes that the experiment was taken the same day. The first protocol with 1.5 mm resolution is indicated as (P1) and the second protocol with 3 mm resolution is indicated as (P2).**

| Experiment #                           | E (kPa) [subject age]   |              |               |
|--|---|--------------|---------------|
|  | F [30]  | B [28]       | D [51]        |
| 1                                      | 8.6±2.9 (P1)  | 7.1±2.6 (P1) | 7.5±1.7 (P1)  |
| 2                                      | 7.8±3.3 (P1)  | 6.6±2.0 (P1) | 10.9±3.1 (P1) |
| 3                                      | 9.2±2.0 (P2)  | 6.2±1.5 (P1) | 9.4±3.1 (P1)  |
| 4                                      | -   | 6.7±2.4 (P1) | 9.0±1.2 (P2)  |
| 5                                      | -   | -            | 9.9±1.8 (P2)  |
| 6                                      | -   | -            | 9.9±1.4 (P2)  |
| Mean (SD of the mean)                  | 8.6±0.7   | 6.7±0.4      | 9.4±1.2       |
| ANOVA (p-value)                        | 0.80 (all data)<br>0.89 (latest 3 experiments)                            |              |               |
| ICC value                              | 0.77 (worst case)<br>0.97 (latest 3 experiments)                          |              |               |
| Bland-Altman<br>95% limit of agreement | -27.4% and 12.2% for last three experiments of case B and D. CR = 1.37kPa |              |               |

The elastograms are shown in both gray and colored scales for better visualization. The results for the mid-gland are shown where the prostate appears to be the largest. Care was taken to ensure the same anatomy was selected for each case, although some variability is inevitable without imaging the entire prostate volume. Figure 2-9 shows the elasticity image for volunteer D for several slices covering the entire prostate.

The mean elasticity results for the six volunteers (A to F) are summarized in Table 2-1 and have been included in Figure 1-5 for visual comparison with elasticity values from the literature. The elasticity results for the repeatability experiments are summarized in Table 2-2. Statistical results are also provided in this table. In this table, elasticity values with the same colour highlight denote that the experiment was taken the same day. The variances of the data from repeated measurements were analyzed using the one-way ANOVA method. No significant statistical difference between repeated measurements from each subject was detected ( $p = 0.80$  for all data,  $p = 0.89$  for the 3 most recent experiments). The intra-class correlation coefficient (ICC) was calculated for two scenarios: (i) where the three most recent set of experiments (our best-case scenario) were used, and (ii) where data with the highest variability for each subject was chosen (our worst-case scenario). For the first case the ICC coefficient was 0.97 with a 95% confidence interval of 0.75 kPa to 1.0 kPa, and for the latter case an ICC coefficient of 0.77 was calculated with a 95% confidence interval of -2.82 kPa to 0.99 kPa. Also, a Bland-Altman [114] analysis of the 3 most recent scans for subject B and D revealed that the 95% limits of agreement are between -27.4% and 12.2%. The coefficient of repeatability (CR) was 1.37 kPa.

## 2.4 Discussion

In the prostate phantom, the 10 mm inclusion can be readily distinguished from the background in the elasticity image. Note that the wavelength is between 35 to 50 mm, which is significantly longer than the 10 mm lesions. This demonstrates that features smaller than the mechanical wavelength can be resolved. This resolution corresponds to resolving lesions of 0.5 cc in volume which is of clinical significance for treatment planning. Note that the phantom specifications indicate an elasticity ratio between lesion and background of approximately 3 however a elasticity ratio of 1.5-1.8 was observed. Experiments at frequencies up to 250 Hz resulted in ratios between 1.5 and 2. The manufacturer used ultrasound strain measurement techniques in static loading conditions, therefore discrepancies in reported elasticity values are to be expected. Also, such phantoms do dehydrate over time which may affect their elasticity. The total amplitude maps of shear waves showed very good penetration throughout the entire phantom. As seen in these images, the lesions can be clearly distinguished from the background for the entire volume of the prostate.

For the *in-vivo* prostate case, sufficient shear wave amplitudes were present in all cases. Reproducible stiffness maps could be produced, and the measurements of stiffness seem to be stable within 10-30%. In the authors' experience, displacement amplitudes above half a micron with displacement SNR of 6 dB are considered sufficient for valid reconstruction of viscoelastic maps. Factors such as displacement SNR and high attenuation may bias the elasticity results. Some of these effects have been studied in [43], [115], however, they need to be studied in more detail in the future. Regions such as the urethra and the stiffer and more viscous zones surrounding it (peripheral zone) can be visually identified in Figure 2-8 (d) and (e). Some of the inter-subject and intra-subject variation may be associated with the centering of the slice in the mid-gland. In the initial protocol very few slices were available for MRE which limited our ability to image the same anatomy. The improved protocol capable of imaging the entire prostate (Figure 2-9) solved this problem and enabled us to view any location of interest in the prostate. As can be seen in both Figure 2-8 and Figure 2-9, the elasticity maps are consistent and the prostate boundary is clear in all images. The urine falsely appearing as a stiff object within the bladder is an artifact of the LFE algorithm. Fluids cannot sustain shear waves, so shear wave amplitude drops to the noise level in fluid pockets. The LFE algorithm falsely assigns a long spatial wavelength in this region. A reasonable anatomical correspondence between the elasticity map and the T2-weighted image can be appreciated. These elasticity values are consistent with the reported values by other groups, especially groups using dynamic MRE. The elasticity images typically resulted in images which have two stiffer lobes or rotated C-shaped features in the prostate. This observation is consistent with what Kemper *et al.* [53] have reported. For the repeatability study, the statistical results confirm that the trans-perineal approach is repeatable within error. Some of the variability in the repeat measurements may be associated with bladder and colon filling which could affect the pre-compression on the prostate and thereby affecting the elasticity results. The range of the color scale for the elasticity images was arbitrarily chosen (15 kPa) to depict the variations in the elasticity due to anatomy alone across all the subjects.

## 2.5 Case studies

### 2.5.1 Phantom: TWE algorithm

Dr. Ali Baghani developed the Traveling Wave Expansion (TWE) reconstruction algorithm based on the phantom data acquired as outlined in this section [109]. Data was collected from a standard elasticity quality assurance phantom CIRS Model 049 (CIRS Inc., Norfolk, VA) which has eight spherical inclusions (four with diameter of 20 mm and four with diameter of 10 mm). A conventional spin-echo based MRE sequence [84] ( $TE/TR=33/433$  ms with EPI factor 5) was used to capture the 3D displacement field. The MEG was a sinusoid with frequency of 210 Hz and amplitude 60 mT/m amplitude. The excitation was applied to the open face of the phantom using the trans-perineal hydraulic transducer. The voxel resolution was 1.5 mm isotropic on seven slice. The mechanical wave was sampled at four points.

In TWE, the solution of the wave equation is expanded as a sum of waves travelling in different directions. The solution is then fitted as a model to the measured displacements to locally calculate the elasticity. The main advantage of this method over other inversion methods is that the derivatives are applied on the analytical model rather than original noisy data.

Sample image of the displacement field and the reconstructed elasticity are shown in Figure 2-10. For details of the algorithm and comparison to other methods refer to [109].

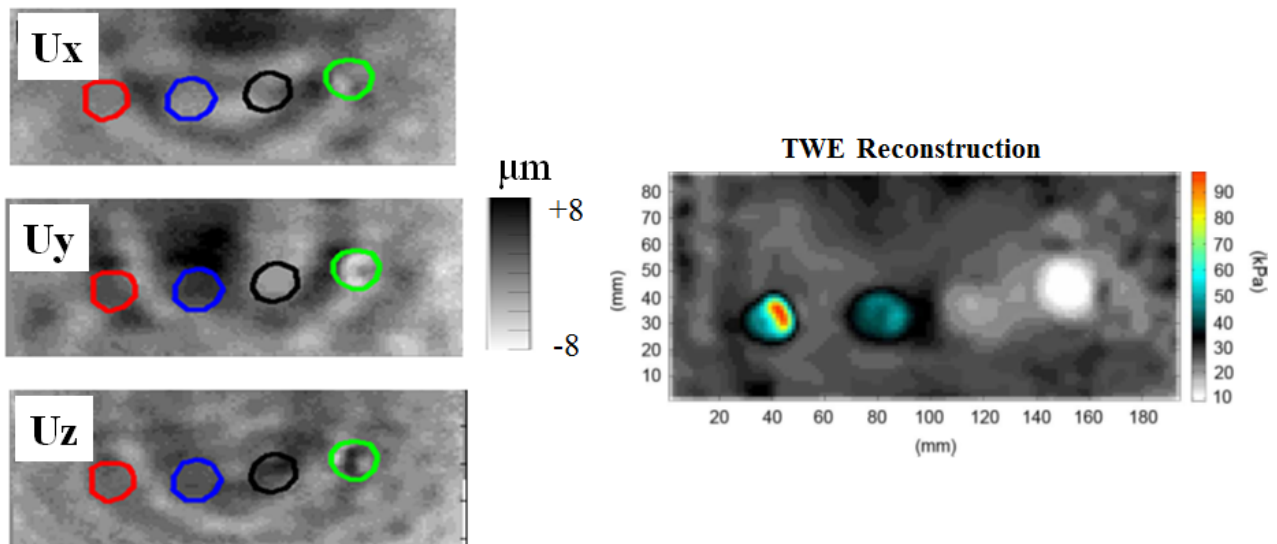


Figure 2-10. Sample 3D displacement field and elasticity image reconstructed using the Traveling Wave Algorithm (TWE). Adapted from [109] with permission

## 2.6 Conclusion

MR elastography of the prostate using a hydraulic transducer applied to the perineum is feasible. The transducer does not interfere with the acquisition process of the MRI images due to its inherent non-magnetic design. The

harmonic approach allows for reasonable scan times at 3T [84]. Unlike other proposed methods, the trans-perineal approach is non-invasive and can be readily used with a pelvic coil and - if needed - with an endo-rectal coil. Compared to this excitation technique, the trans-perineal approach does not cause any discomfort to subjects and would be suitable even for long patient examinations. In the trans-pubic method, the larger mass of the subject did not only make the positioning of the transducer more difficult but also required larger vibration amplitude to vibrate the larger mass. In our experience, this combination of increased pressure on the transducer and the increased transducer amplitude rendered the trans-pelvic method unbearable for the patient. This problem would be exacerbated when the exam time is extended to perform multi-parametric type of studies. In the trans-perineal method proposed here however, gravity plays no role in the 'patient friendliness' of the method. While a larger subject required larger vibration amplitude, this did not cause discomfort.

Other techniques to induce vibrations into the prostate, such as endo-rectal [56] and trans-urethral [52], have also been proposed that promise higher frequency excitation as they are applying vibrations closer to the prostate. However, their success in clinical setting remains to be shown. The MR elastography results have been analyzed using LFE and validated using a prostate elasticity phantom. The prostatic gland consistently stands out in the elastograms. A reasonable correspondence has been observed between the mechanical properties and the anatomical features inside the prostate gland, but further studies are needed to correlate our images to pathology. A preliminary repeatability study was performed which confirms that the elasticity results produced using the trans-perineal approach are reasonably repeatable. Further work will validate the elasticity dependence on subject state (bladder filling, colon filling, and leg position).

# Chapter 3 - *In-vivo* prostate MRE with trans-perineal electromagnetic actuation and a fast fractionally encoded steady-state gradient echo sequence

## 3.1 Introduction

In the previous chapter, an initial feasibility study of trans-perineal prostate MRE for *in-vivo* imaging of human prostate was introduced [66]. While that study did show the feasibility of the trans-perineal approach using a hydraulic transmission system, the imaging method was limited to relatively low excitation frequencies of 45 Hz and required an extended setup and acquisition time. The purpose of the work in this chapter was to develop and evaluate a new trans-perineal MRE system that can provide higher excitation frequencies and that has a shorter set-up and acquisition time to make it viable in mpMRI studies that can last as long as 1 hour even without the MRE component. In chapter the following are presented: (i) the design of a new actively shielded electromechanical transducer that is quick to set up and easy to use in a clinical setting (see Figure 3-1), and (ii) the adaptation of a new pulse sequence for the prostate that can acquire the 3D displacement field of the entire prostate gland in a much shorter time than previously reported.

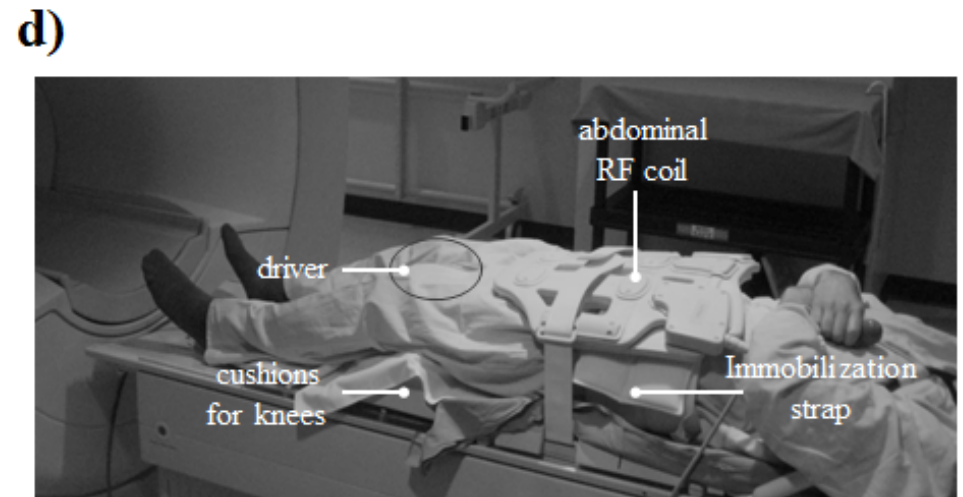
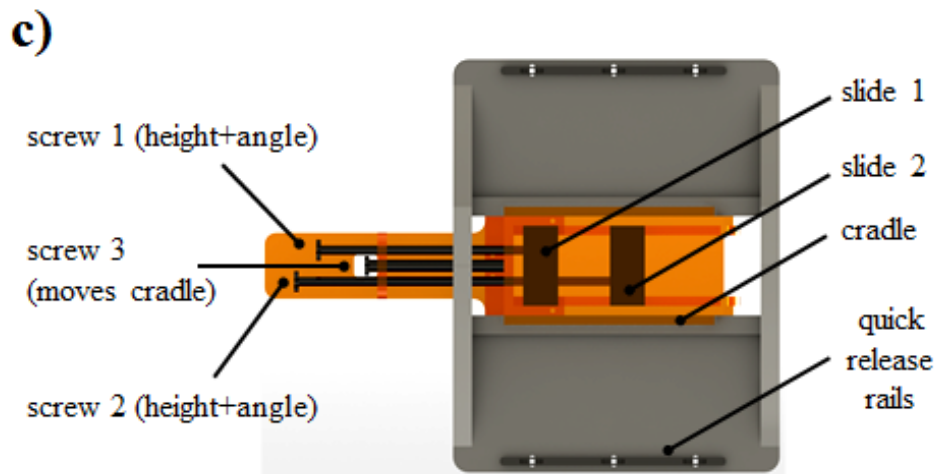
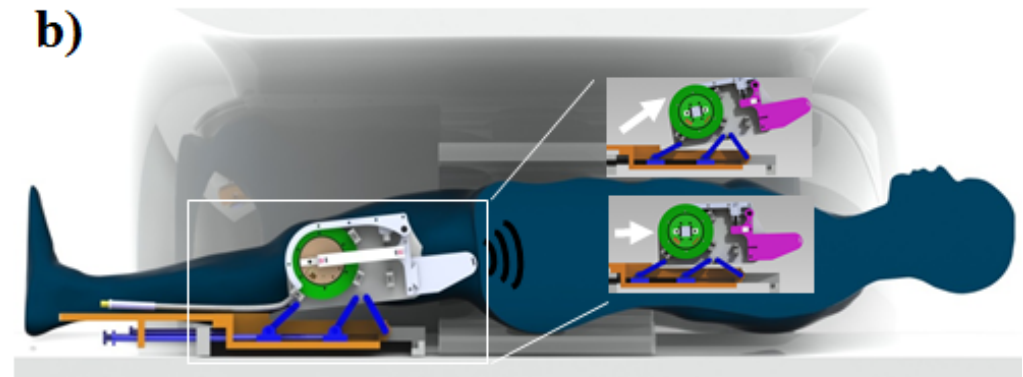
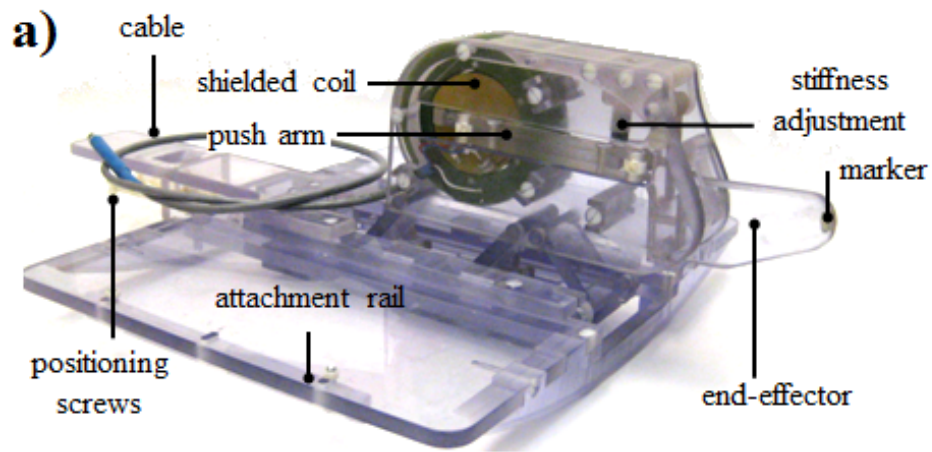


Figure 3-1. In the trans-perineal prostate MRE approach the transducer (a) rests between the legs of the subject and the vibration is applied to the perineal region as illustrated in (b). c) The point and angle of contact as well as the pre-compression applied by the transducer can be adjusted using three positioning screws. The custom made electromechanical transducer is quickly installed on the rails of the MR patient table, integrates well with the abdominal coil due its low profile (d), and is comfortable for the patient.

Additional improvements included a higher excitation frequency and a larger excitation amplitude. A mechanical excitation frequency of 70 Hz was used in this study to enable detection of smaller lesions. In a previous prostate phantom study [66], an excitation frequency of 45 Hz was sufficient to detect 10 mm diameter lesions (0.5 cc) that were approximately 2 times stiffer than the surrounding tissue. The wavelength of the shear waves encountered in the human studies was in the range of  $25 \pm 10$  mm, which may be sufficient to resolve features even smaller than 0.5 cc. Since trans-perineal excitation was well tolerated by the volunteers in the previous study the amplitude was increased to increase the signal-to-noise-ratio (SNR) of the waves beyond the 6 dB that is considered by the author to be the limit SNR needed for reliable reconstruction of elastograms. The transducer methods were validated in two phantoms, six volunteers and two patients with confirmed prostate cancer.

In this chapter, first the design of the transducer is discussed, followed by a description of the pulse sequence. Then, the methods are validated in phantoms and human studies. This represents the first evaluation of the trans-perineal transducer and sequence in an *in-vivo* study including two prostate cancer patients.

## **3.2 Methods**

### **3.2.1 Design of a shielded electromagnetic transducer**

The transducer has two counter-wound concentric coils. When placed in the magnetic field of the MRI scanner, the inner coil moves and exerts a torque proportional to its current, producing the desired mechanical motion. The outer coil is stationary and fixed to the housing. Its purpose is to oppose the magnetic field generated by the inner coil, thereby reducing the total magnetic field generated by the transducer within the field of view of the prostate, which could induce artefacts in the MRI images.

The overall design and components of the transducer for trans-perineal prostate MRE are illustrated in Figure 1-4a. The vibration is applied to the perineum of the subject as shown in Figure 1-4b and d. The transducer rests between the subject's legs and the vibration is applied over the undergarments. Cushions are placed underneath the subject's knees for comfort. A restraining Velcro strap is wrapped around the abdomen of the subject to encourage chest breathing, and thus reduce motion artefacts. Figure 1-4c shows the bottom view of the supporting base of the transducer that contains quick release rails that rest on the rails of the MR table (Philips Inc., Netherlands) and a manual adjustment mechanism for quick positioning of the transducer in three degrees of freedom. The adjustment mechanisms allows for height (anterior-posterior direction), angle and depth (superior-inferior direction) adjustments while the subject lies in the scanner.

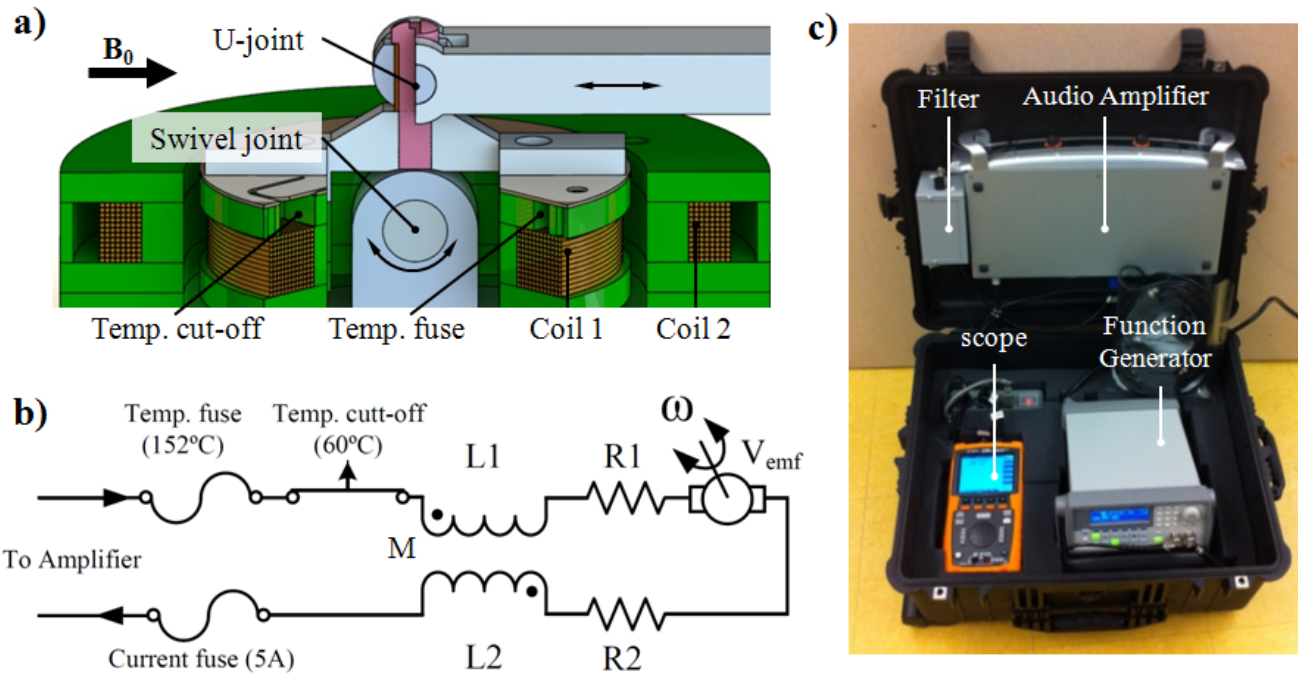


Figure 3-2. a) The counter-wound coils (a) generate a torque in a magnetic field. The outer coil is fixed and acts as a compensation coil to reduce the fringe field in generated by the inner moving coil the region of the expected FOV. Temperature fuses mounted on the inner coil, and a current fuse on the electronics side, protect the transducer and subject in the event of overheating. The equivalent circuit of the transducer is shown in (b), where  $V_{emf}$  is the voltage generated by the vibrating coil in the magnetic field  $B_0$ . The coils are driven by the electronics system (c) placed outside the scanner room.

Figure 3-2a shows the geometry of the coils. The magnetic flux density of the main MRI magnet,  $B_0$ , is in the horizontal direction, as shown. The rotating inner coil (coil 1) is attached to a push arm by a U-joint. The push arm is connected by another U-joint to the end-effector (thickness 12.7 mm), which rests on the perineum. The stationary outer coil (coil 2) is attached to the housing of the transducer. As a safety feature, two thermal components are incorporated into coil 1 to protect the subject and the transducer in the event of potential overheating. A thermal cut-off switch opens the circuit if the temperature exceeds 60 °C. This switch is slow acting and resets the circuit if the temperature drops below the cut-off. The second sensor is a fast-acting thermal fuse that permanently disconnects the circuit if the temperature reaches 152 °C.

The transducer is made of non-ferromagnetic and non-conductive materials except for the copper coils (AWG 19). The spool is made of a Granolite® G10 Material, which is known for its mechanical stability even at elevated temperatures. The U-joints are made of Acetal (Delrin®) plastic, and the rest of the transducer parts are made of waterjet cut polycarbonate (Lexan) sheets held together by nylon fasteners.

The electrical schematic is shown in Figure 3-2b. Current is supplied by the amplifier of the electronics system and passes through both thermal components, coil 1 (with resistance  $R_1$  and inductance  $L_1$ ), coil 2 (reverse winding, with resistance  $R_2$  and inductance  $L_2$ ), and the current fuse. The mutual inductance is  $M$ . The moving coil generates an electromotive voltage,  $V_{emf}$ , which depends on the excitation frequency,  $\omega$ , and amplitude of the excitation,  $A$  (see equation (3-5)). The geometry and the measured electrical properties are tabulated in Table 3-1.

**Table 3-1. The geometry and measured properties of the coils.**

|        | Number of turns | Radius (mm) | Width/Height (mm) | R ( $\Omega$ ) | L (mH) | M (mH) |
|--------|-----------------|-------------|-------------------|----------------|--------|--------|
| Coil 1 | 182             | 34.5        | 14/12.5           | 1.6            | 2.6    |        |
| Coil 2 | 128             | 58.5        | 10/12.5           | 1.8            | 2.9    | 1.0    |

As shown in Figure 3-2c, the electronics consists of an arbitrary waveform generator (Agilent 33220A, USA), which is triggered by the MR scanner; a  $2 \times 440\text{W}$  ( $8\Omega$ ) switching audio amplifier (Behringer NU3000, Germany); a passive low-pass filter with a cut-off at 2.8 kHz, designed to remove switching noise from the amplifier output; and a handheld oscilloscope (Agilent U1602B, USA), used to monitor signal levels and fine-tune the synchronisation between the MR scanner and the driving frequency. The current fuse (5 A) is incorporated into the filter module.

### 3.2.1.1 Optimization of the number-of-turns ratio

It is important that the magnetic fringe field due to coils be minimized. This can be achieved by applying the correct current density on the stationary coil to reduce the residual field due to the first coil. Since the cross-sectional area of the wire is constant, the current density for each coil can be modeled as the current  $I$  time the number of turns  $N$ . The coil current is given by

$$I = \frac{V_{in} - V_{emf}}{j\omega(L_1 + L_2 + 2M) + (R_1 + R_2)}, \quad (3-1)$$

where  $V_{in}$  is the output voltage of the amplifier.

For concentric aligned coils the magnetic flux density on the center axis can be approximated by the Biot-Savart equation

$$B_z = \frac{\mu_0 NI r^2}{2(z^2 + r^2)^{3/2}}, \quad (3-2)$$

where  $B_z$  is the magnetic flux density perpendicular to the plane of the coil,  $\mu_0$  is the permeability of free space,  $I$  is the current,  $N$  is the number of turns,  $r$  is the radius of the coil, and  $z$  is distance along the center axis of the coil. If we set the magnetic flux density as  $B_{z1} = -B_{z2}$  to cancel out the on-axis field for two concentric coils of different radii, the number-of-turns ratio becomes

$$n = \frac{N_2}{N_1} = \frac{1}{k^2} \left( \frac{z^2 + (kr_1)^2}{z^2 + r_1^2} \right)^{3/2}, \quad (3-3)$$

where  $k = r_2/r_1$  and is 1.7 in this design. Therefore, in this simplified model the ideal number-of-turns ratio to minimize fringe fields due to the coils is  $n = 1.7$  at  $z = 0$  (the center of the coils) and  $n = 0.5$  at  $z = 100\text{mm}$ .

For a coil current  $I$ , the force on the push arm is given by

$$F = \tau \cdot L \cos(\theta) = \frac{\pi}{4} d^2 N B_0 I, \quad (3-4)$$

where  $L$  is the length of the lever connecting the coil to the push arm, and  $\tau$  is the torque generated by coil 1.

For a mechanical excitation with a frequency of  $\omega_m$ , the rotation of coil 1 is  $\theta = A_0 \sin(\omega_m t)$ , with amplitude  $A_0$ . The coil motion induced by the force induces a back-emf voltage,  $V_{emf}$ , given by

$$\begin{aligned} V_{emf} &= \frac{d\Phi}{dt} = \frac{d}{dt} \left( \frac{\pi}{4} d^2 N B_0 \cos(\theta) \right) \\ &= \frac{\pi}{8} d^2 N B_0 A_0^2 \omega_m \sin(2\omega_m t) \end{aligned} \quad (3-5)$$

where  $\Phi$  is the magnetic flux linkage,  $d$  is the diameter of coil 1, and  $N$  is the number of turns of the moving coil.

In fact, while equation (3-3) above does provide a first approximation that could be used in a design, the minimization of the magnetic field along the center-line of the coils is not the most appropriate for use in MRE. Indeed, as the spring-loaded actuator is pressed against the patient, the moving coil will be rarely aligned with the stationary one. Hence it is important to check whether the ratio of the number of turns for the two coils provides a reasonable cancellation of the two fields not only along the stationary coil axis, but also for a range of coil angles. For the case of non-aligned coils and off-axis regions of interest (ROI), finite element simulations were performed in 2D (COMSOL MultiPhysics, USA). The region of interest ROI2 is approximately where the prostate would be imaged. Simulations at different number of turns ratios  $n=N_2/N_1$  were carried out and the average flux density in ROI1 and ROI2 was computed for each  $n$ . Two coil configurations were considered: (i) aligned coils and (ii) coil 1 is tilted by  $10^\circ$  with respect to coil 2. The value of  $n$  that provides the smallest ROI2 average flux density for the coil in the tilted configuration ( $n=0.75$ ) was selected as an optimal design. The results of the calculated magnetic flux density are shown in Figure 3-3. Figure 3-3a shows the cross-sections of half of coil 1 and coil 2, with the symmetry point as marked. While the number-of-turns ratio was increased, three cases were considered: (i) the secondary shielding coil is disabled, so that  $I_2 = 0$ ; (ii) the number-of-turns ratio is  $n = 0.5$  (as calculated from the Biot-Savart equation); and (iii) the number-of-turns ratio is  $n = 0.75$  (lower fringe fields in the relevant ROI, thus optimum shielding).

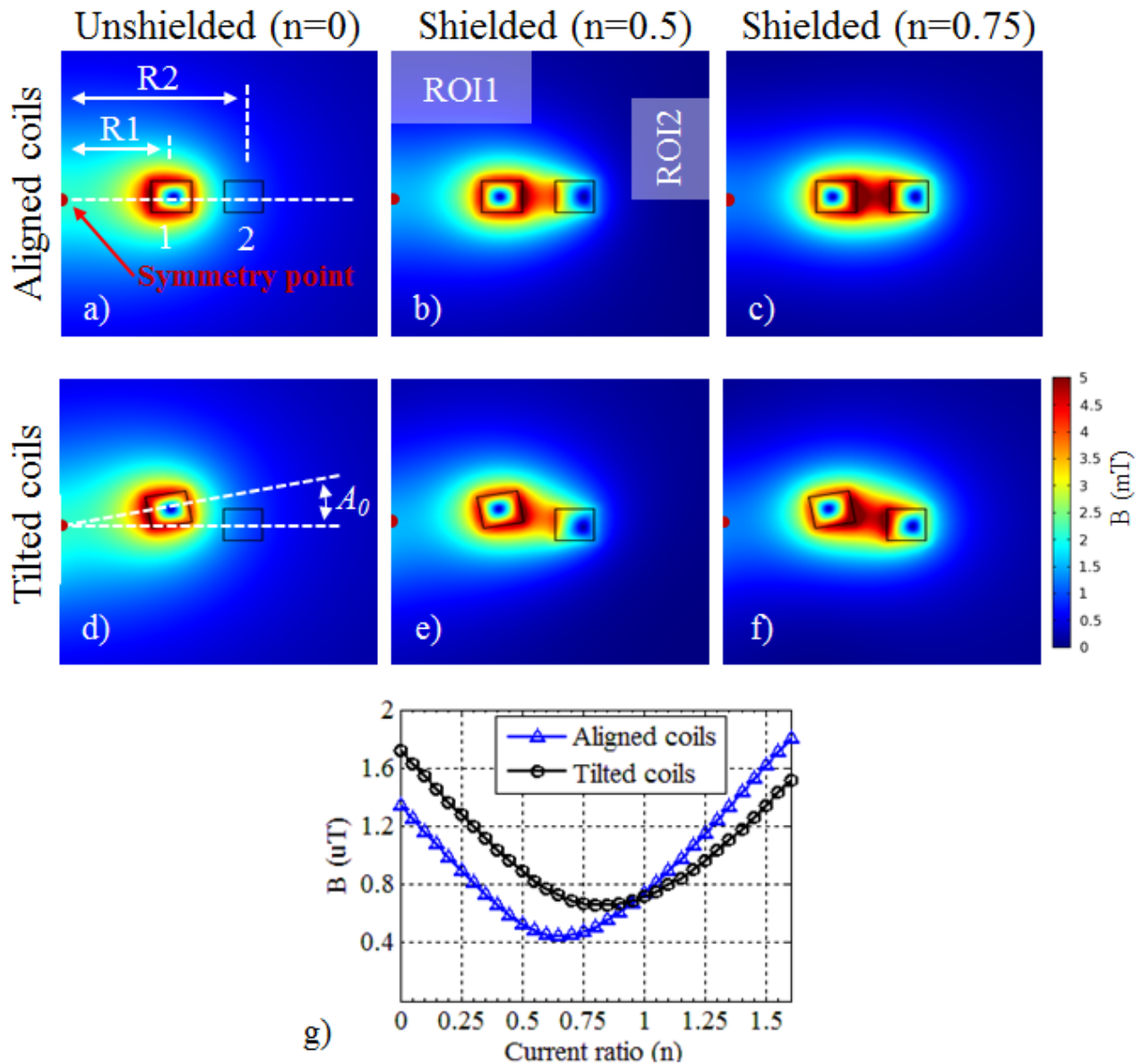


Figure 3-3. Simulations were performed to obtain the optimal number-of-turns ratio of the outer to inner coil to minimize the magnetic fringe fields. The cross-sectional geometry of half of the coils and the symmetry point is shown in (a). Three cases each are shown for aligned coils (a-c) and for tilted coils (d-f). The cases are: (i) coil 2 is off (no fringe field compensation), (ii) number-of-turns ratio of 0.5 (optimum shielding based on Biot-Savart equation) and (iii) number-of-turns ratio of 0.75 (optimum shielding based on simulations). The magnetic field in the region of interest as a function of number-of-turns ratio is shown in (g).

### 3.2.2 Transducer characterization

Figure 3-3g shows the simulated average magnetic fields in the region of interest ROI2 (see Figure 3-3b). A device was constructed with  $n = 0.75$ . The device was tested and the magnetic field was measured with a Hall-effect magnetometer (Model 5180, F.W. Bell, USA) at the end-effector of the transducer and in the ROIs considered in the simulation.

The frequency response and time domain signal were measured using a non-magnetic accelerometer (PCB Piezotronics Inc., USA) placed on the transducer while the end-effector was placed against a phantom with similar loads present in the *in-vivo* studies. The excitation amplitude and resonance frequency were recorded. To evaluate the effectiveness of the active shielding, a phantom study was performed where SNR and change in the phase of the MR signal were recorded.

### 3.2.3 Acquisition of the 3D wave field (*eXpresso* pulse sequence)

All experiments were performed on a 3T Achieva (Philips Inc., Best, Netherlands) scanner with a standard 6-element cardiac coil. To acquire the displacement field, this pulse sequence utilizes (i) *fractional wave encoding*, enabling a short echo time to increase SNR [116]; (ii) *low flip angles* ( $\alpha=25^\circ$ ) in a steady-state gradient echo sequence, allowing for short echo times,  $TE$ , that boost SNR, especially for echo times for which the signal from water and fat are in phase; and (iii) *a reference scan* to compensate for erroneous phase accumulation due to the imaging gradients, and due to the residual field from the electromagnetic transducer.

Bipolar trapezoidal motion encoding gradients (MEG) were superimposed on a RF spoiled steady-state gradient echo pulse sequence, as shown in Figure 3-4a. The duration of each imaging shot (comprising excitation, encoding, and read-out) was adjusted so that an integer number of shots were fitted within a vibration cycle,  $T_{MECH} = 1/f_{MECH}$ . Consequently, the duration of the MEG,  $T_{MEG}$ , was only a fraction of  $T_{MECH}$  ( $q = T_{MEG} / T_{MECH}$ ), thereby only encoding a fraction of the vibration period. This enabled a short TE and a very short shot duration, which translated into a shorter acquisition time, achieved at the expense of reduced encoding efficiency. The encoding efficiency for sinusoidal gradient waveform (a crude approximation to the trapezoidal waveform) as derived by [116] is given by:

$$\eta = \frac{n \cdot \gamma \cdot G_0}{2\pi\omega_{meg}} \cdot \frac{\sin(\pi \cdot \gamma \cdot q)}{\pi(1 - q^2)} \quad (3-6)$$

where  $G_0$  is the maximum amplitude of the oscillating motion encoding gradient at frequency  $\omega_{meg}$ ,  $n$  is the number of periods of the oscillating gradient,  $q = \omega_{mech} / \omega_{meg}$ , and  $\omega_{mech}$  is the frequency of the mechanical excitation. The spectrum of the motion encoding efficiency for trapezoidal gradients is shown in Figure 3-4b. The TE of the sequence was chosen to match with the second or third in-phase condition between water and fat signal.

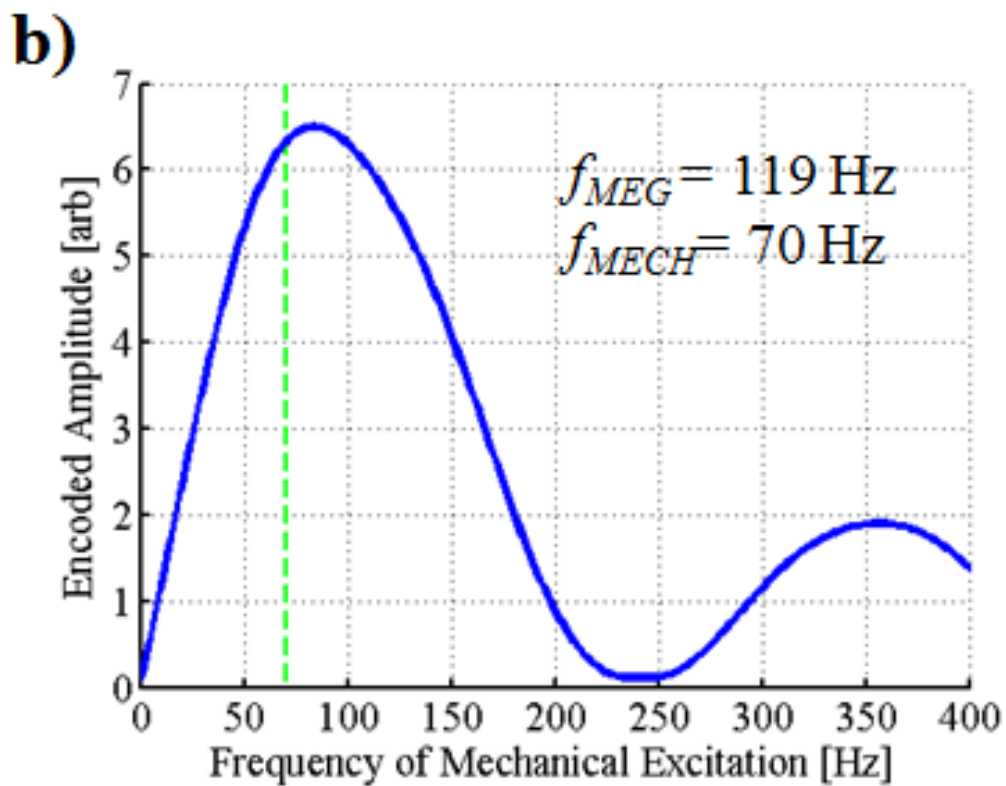
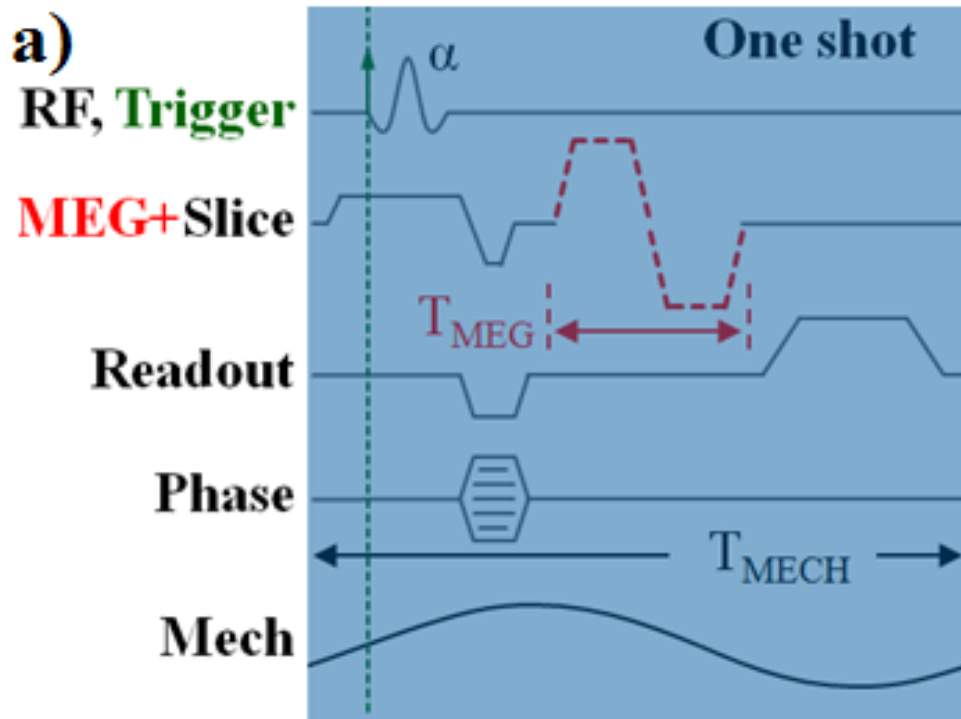


Figure 3-4. a) Bipolar trapezoidal motion-encoding gradients (MEG) are overlaid on a low-flip angle steady-state gradient echo shot. Only a fraction of the mechanical excitation is encoded, as  $q = T_{MEG}/T_{MECH} < 1$ . b) corresponding encoding efficiency at various mechanical excitation frequencies

The timing of the entire sequence is shown in Figure 3-5a. The acquisition was first repeated over all slices (and then k-lines) in order to maximize the repetition time, TR, and thereby increase the SNR. Phase coherence between the mechanical excitation and acquisition was maintained by extending the duration of each shot by  $\delta_{extn}$ . The delay is calculated such that an integer number of shots  $N_{shotsPerVib}$  with shot length  $T_{SHOT}$  fit within the vibration cycle  $T_{MECH}$ :

$$\delta_{extn} = \frac{T_{MECH} - N_{shotsPerVib} \cdot T_{SHOT}}{N_{shotsPerVib}} \quad (3-7)$$

Thus, in a multi-slice acquisition, each slice acquired different mechanical phase depending on the number of shots per vibration cycle. This is illustrated in Figure 3-5b. This phase offset was compensated by applying the predetermined phase shift ( $2\pi/T_{MECH}/N$ ) according to acquisition order of the slices. Another constraint to maintain synchronization across several vibration phases was that the number of slices had to be a multiple of the shots per mechanical excitation period  $N_{shotsPerVib}$ .

Once all shots are repeated over all slices (i.e., for each vibration phase), a delay  $\Delta=1/N_{samples}$  is added between the mechanical excitation and gradients to sample the mechanical vibration at several time points per period. Next, this process is repeated to acquire all k-space lines. The direction of the motion encoding axis was modified by superimposing the MEGs on different gradient axes. For the reference scan, the MEG was set to zero while the mechanical excitation was applied during the acquisition process. The signal generator was triggered at every TR by the MR console.

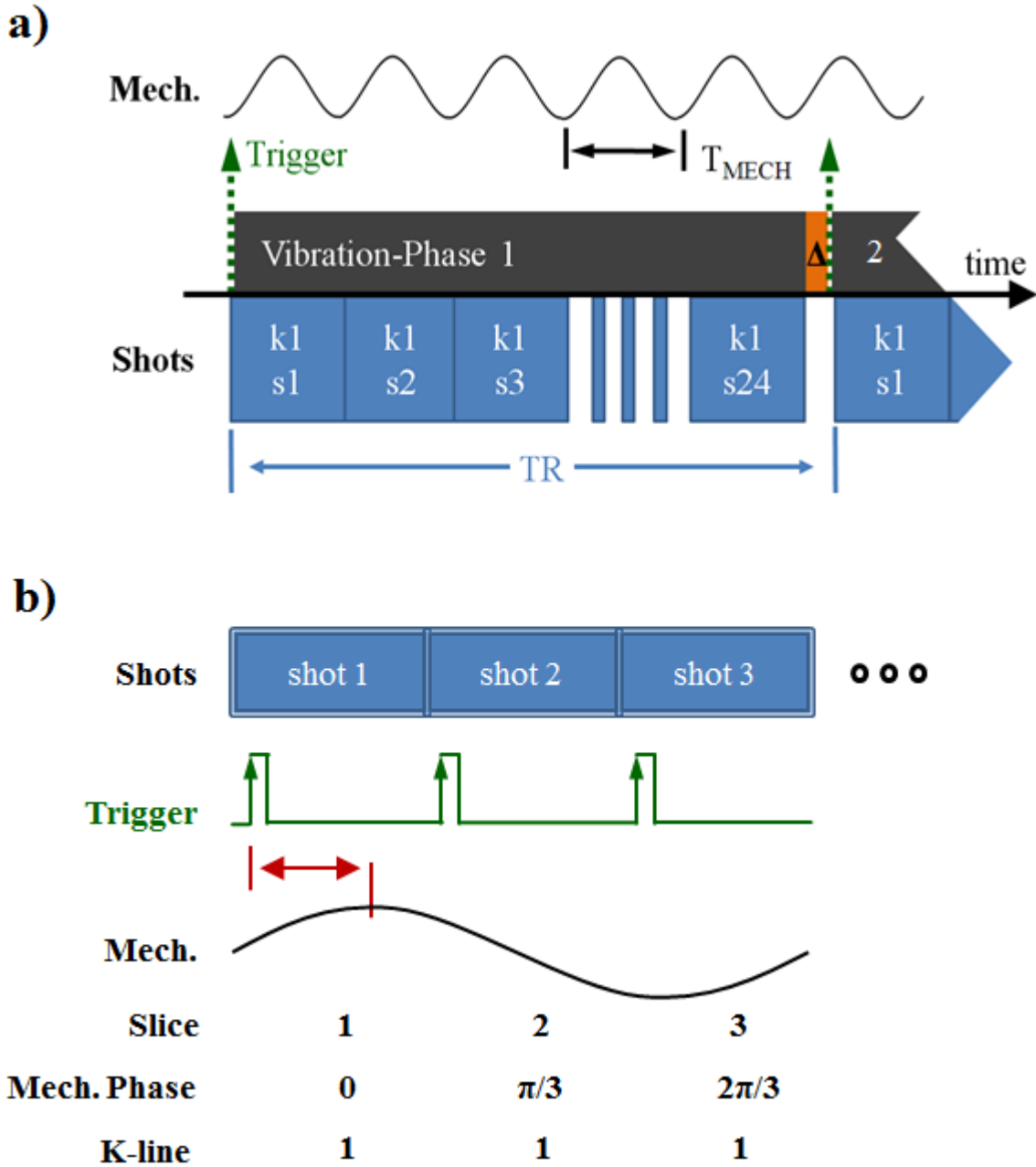


Figure 3-5. Over all looping structure of the *eXpresso* sequence. B) if several shot are fit within a vibration cycle then each slices acquires a phase shift that is compensated for in image post processing step.

Due to the broadband motion sensitivity of the sequence (Figure 3-4b), it is possible to acquire multiple harmonics of the mechanical excitation if sufficient time points according to the Nyquist criterion are acquired. For example, with 8 time point it is possible to encode three frequencies (the fundamental, twice the fundamental and three times the fundamental mechanical excitation). This feature was utilized to acquire multi-frequency wave-field data in the liver (see section 3.5.1) but not explored for the case of prostate in this thesis.

The sequence presented here was co-developed in parallel for liver and prostate MR elastography, and first reported in single-page abstracts in reference [117], [118]. For comparison studies between SE-EPI and

*eXpresso* pulse sequence in phantoms and in-vivo liver studies in volunteers refer to section 3.5.1. For completeness, the details of imaging the prostate have been provided here. The following trade-offs should be noted between the two applications. In the liver, a short echo time is needed because of its short T2\* signal decay. The duration of the MEGs are in turn reduced to accommodate for this fact. Also, because the shorter TE (and thus shorter shot duration) and lower excitation frequency it was possible to fit up to 4 shots per vibration cycle ( $N_{\text{shotsPerVib}} = 4$ ) in the liver but for prostate only one shot per vibration was possible ( $N_{\text{shotsPerVib}} = 1$ ). Considering the large size of the liver compared to the prostate, and the relative ease of exciting the liver at lower frequencies (56 Hz, as reported in [117], [118]), it was sufficient to image the entire liver with eight slices and 4 mm isotropic resolution in four 15-second breathholds. In the prostate however, the smaller size of the organ (typical prostate glands bounded by an ellipsoid with major axis < 60 mm, minor axes < 40 mm) and higher stiffness require that smaller voxels size (2 mm isotropic) and higher excitation frequency (70 Hz) be used. The larger attenuation at this frequency required a longer duration of the MEGs to encode the motion at increased sensitivity.

### 3.2.4 Phantom experiments

The transducer was placed in the bore of the MR scanner and connected to the aforementioned electronics system, which was placed outside of the scanner room. The experiments were carried out on a phantom (model CIRS066, Computer Imaging Reference Systems Inc., USA).

For the first phantom experiment for testing the shielding during the acquisition was carried out with TE = 9.2 ms (water and fat in-phase at 3T) and TR = 344 ms. The image reconstruction matrix was  $128 \times 128 \times 24$ , which is large enough to cover the entire prostate of most subjects with an isotropic resolution of 2 mm. The water-fat pixel shift was set to 0.4 pixels (bandwidth 141 kHz), acceleration (SENSE) to 2, and k-space filling to 80%. The mechanical excitation frequency was  $f_{\text{MECH}} = 70$  Hz, and eight vibration phases,  $N_{\text{samples}} = 8$ , were used. The period of the motion encoding gradient was  $T_{\text{MEG}} = 8.4$  ms, and the maximum amplitude of the gradients fields was 48 mT/m, which resulted in an encoding efficiency of  $\eta = 14.5 \mu\text{m/rad}$ . The acquisition time per encode direction was 2 min, 32 sec, with a total acquisition time of 10 min, 8 sec for the 3D displacements and the reference scan. For this experiment the end-effector of the transducer was mechanically detached from the phantom to avoid generating waves. Three successive experiments were carried out: (i) transducer off, (ii) transducer active without shielding (shielding coil was shorted) and (iii) transducer active with shielding enabled. A sinusoidal current signal with a frequency of 70 Hz and amplitude of 0.7 A was used.

For the second phantom experiments the acquisition was carried out with TE = 4.6 ms (water and fat in-phase at 3T) and TR =  $(N_{\text{slices}} + 1/N_{\text{samples}}) \cdot T_{\text{MECH}} = 321.2$ ms. The image reconstruction matrix was  $128 \times 128 \times 32$  with isotropic voxels with a resolution of  $1.5 \text{ mm}^3$ . The water-fat pixel shift was set to 0.4 pixels (Bandwidth 141 kHz), and an acceleration (SENSE) of 2 was used. The mechanical excitation frequency was  $f_{\text{MECH}} = 200$  Hz, and eight vibration phases,  $N_{\text{samples}} = 8$ , were used. The period of the motion encoding gradient was  $T_{\text{MEG}} = 3.3$  ms, and the maximum amplitude of the gradients fields was 48 mT/m, which resulted in an encoding

efficiency of  $\eta = 51.3 \mu\text{m}/\text{rad}$ . The acquisition time per encode direction was 2 min, 34 sec, with a total acquisition time of 10 min, 19 sec for the 3D displacements and the reference scan. The transducer was mechanically attached to the phantom in order to generate waves. A sinusoidal voltage signal with a frequency of 70 Hz and amplitude of 10 V was applied to the transducer, resulting in a current amplitude of  $I \approx 0.5 \text{ A}$ .

### **3.2.5 *In-vivo* human studies**

The study was approved by the University Clinical Research Ethics Board and signed informed consent was provided by all subjects. The experiments were performed on six volunteers (mean age 34) and two prostate cancer patients (mean age 66). For the human experiments, the acquisition of the 3D wave field used the same parameters as used in the first phantom experiment. The transducer set-up time was consistently under two minutes. A ten-second sagittal scout scan (3D T1-weighted Turbo Field Echo, TE/TR = 1.78/3.46 ms, FOV  $400 \times 280 \times 140 \text{ mm}$  with 1.5 mm in-plane resolution and 2 mm slice thickness) was performed to ensure that the trans-perineal transducer was properly positioned at the beginning of each examination. With feedback from the scout scan, the position of the transducer was modified using the three positioning screws previously described (see Figure 3-1c) until the MR marker on the end-effector of the transducer (see Figure 3-1a) appeared approximately 20 mm posterior to the pubic bone, as observed in the scout image, and the perineal tissue was pressed superiorly 5-20 mm. This is approximately equivalent to a pre-compression pressure of 40 kPa and corresponds to a compression force of approximately 10 N. Following transducer placement and preload, the amplitude of vibration was adjusted from an initial low value, to a higher but still comfortable level, while communicating with the subject. The input current amplitude to the transducer was typically around  $I = 0.5 \text{ A}$ . A standard axial T2-weighted Fast Spin Echo sequence (TE/TR = 80/1850 ms, FOV  $140 \times 140 \times 72 \text{ mm}$  with 0.5 mm in-plane resolution and 4 mm slice thickness) was acquired prior to the MRE scan. Subsequently the MRE scan was performed with the sequence discussed above.

### **3.2.6 Image processing**

The raw phase images were phase unwrapped, subtracted from the reference scan, and corrected for phase offsets. A voxel was marked invalid if (i) its magnitude in the image was below a threshold of 30% of the average magnitude; or (ii) the total wave amplitude  $U_{tot}$  was less than  $0.5 \mu\text{m}$ . The elasticity was reconstructed using the curl based direct inversion with physical boundary conditions [38], [115]. A Gaussian filter with a 2 mm window size was applied to the displacement field prior to reconstruction. The final stiffness results were also filtered using the same filter.

## **3.3 Results**

### **3.3.1 Transducer characterization**

Figure 3-3 shows the simulated average magnetic fields. The optimum shielding occurs when the number-of-turns ratio was between 0.5 and 0.8. It is worth noting that the number-of-turns ratio for optimum shielding was

slightly different between the cases of aligned and misaligned coils. The design of the constructed transducer was based on the geometry found in the simulations. Due to anticipated geometrical construction errors, the number-of-turns ratio was adjusted based on measurements of the magnetic field close to the imaging area using a Hall-effect magnetometer. The measured residual magnetic field was minimized by removing between one and two turns on the secondary shielding coil. The final number-of-turns ratio chosen was  $n = 0.7$ , which matches within 2% of the results from the simulations. With a sinusoidal peak-to-peak input current of  $I = 1.0$  A at 70 Hz, the amplitude of the magnetic field was less than 5 mT near the center of the coils, while the magnetic field was too small ( $< 0.1$  mT) to measure at the end-effector.

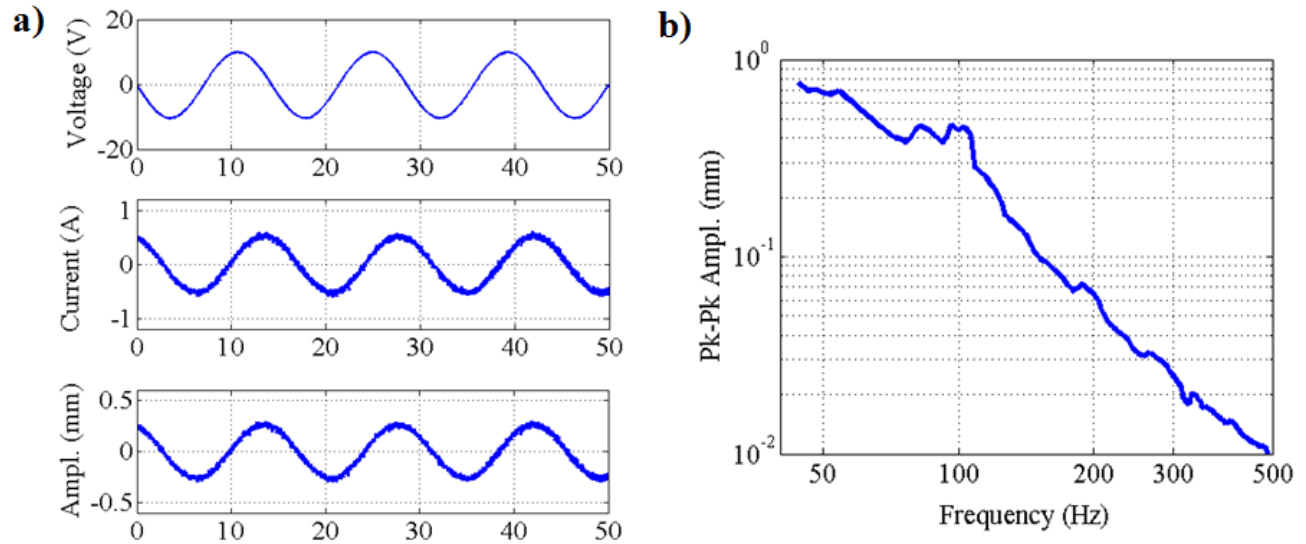


**Figure 3-6.** The electromagnetic transducer was placed in the magnetic field of the MR scanner and its mechanical performance was characterized. a) shows the time domain response to a 70 Hz, 10 V sinusoidal excitation, where the output displacement of the transducer closely follows the sinusoidal pattern of the current in the coils. b) shows the frequency response of the transducer where the first resonant peak occurs at  $\sim 100$  Hz. The displacement amplitude of the transducer can reach beyond  $100 \mu\text{m}$  at 300 Hz for a current less than 3 A.

Figure 3-6a shows the output displacement of the transducer. The time-domain response shows that the transducer closely follows the input current in a sinusoidal manner. The frequency response is shown in Figure 3-6b as a Bode plot. The output displacement of the transducer can exceed  $400 \mu\text{m}$  at 70 Hz for  $I \approx 0.5$  A, depending on the applied load. The first resonance peak is at 100 Hz, and the transducer can output  $70 \mu\text{m}$  at 200 Hz (depending on the applied load) for  $I \approx 0.5$  A. Current amplitudes up to  $I \approx 3$  A have been used with no heating issues, effectively extending the frequency range beyond 300 Hz, for an amplitude of  $100 \mu\text{m}$ . The phantom load was a reasonable approximation to the *in-vivo* case and therefore similar amplitudes were expected for patients.

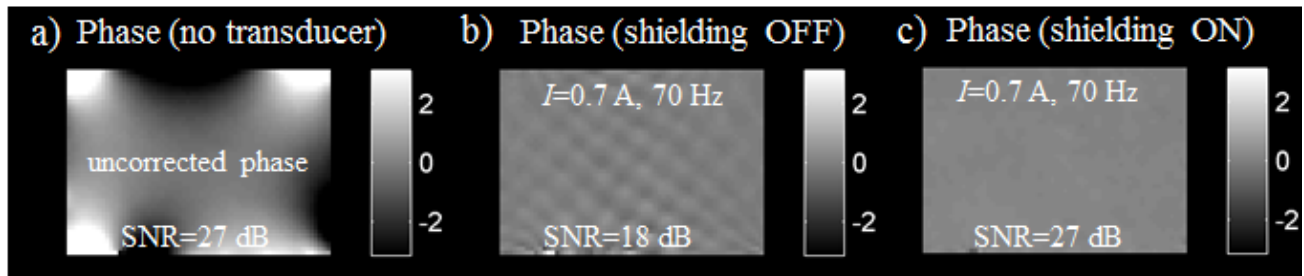


Figure 3-7. The effectiveness of the shielding to suppress magnetic fringe fields of the transducer was assessed using a phantom. The phase images acquired for the three cases are shown: a) transducer not present, b) transducer active without active shielding and c) transducer active with active shielding enabled (same as a) when uncorrected). These images show that the shielding is effective.

### 3.3.2 Phantom experiments

Figure 3-7 shows the effectiveness of the active shielding of the transducer. The raw uncorrected phase is shown in (a) where the SNR was 27 dB in the magnitude images. When the transducer is activated in unshielded mode (coil 2 shorted out), artefacts are present in the phase images and the SNR drops to 18 dB in the magnitude images. These artefacts are removed once the shielding is activated as seen in Figure 3-7c and the SNR is restored to its original value. These images show that the shielding is effective.

The T2-weighted MRI image of the inclusions (each of different stiffness) is shown in Figure 3-8 along with images of all its orthogonal projections. The waves in the  $x$ ,  $y$  and  $z$  directions and the reconstructed elasticity are also shown. The projected displacement images clearly show the waves, while the inclusions are visible in the elastogram. This further illustrates that the transducer does not interfere with the images in the MRE experiments.

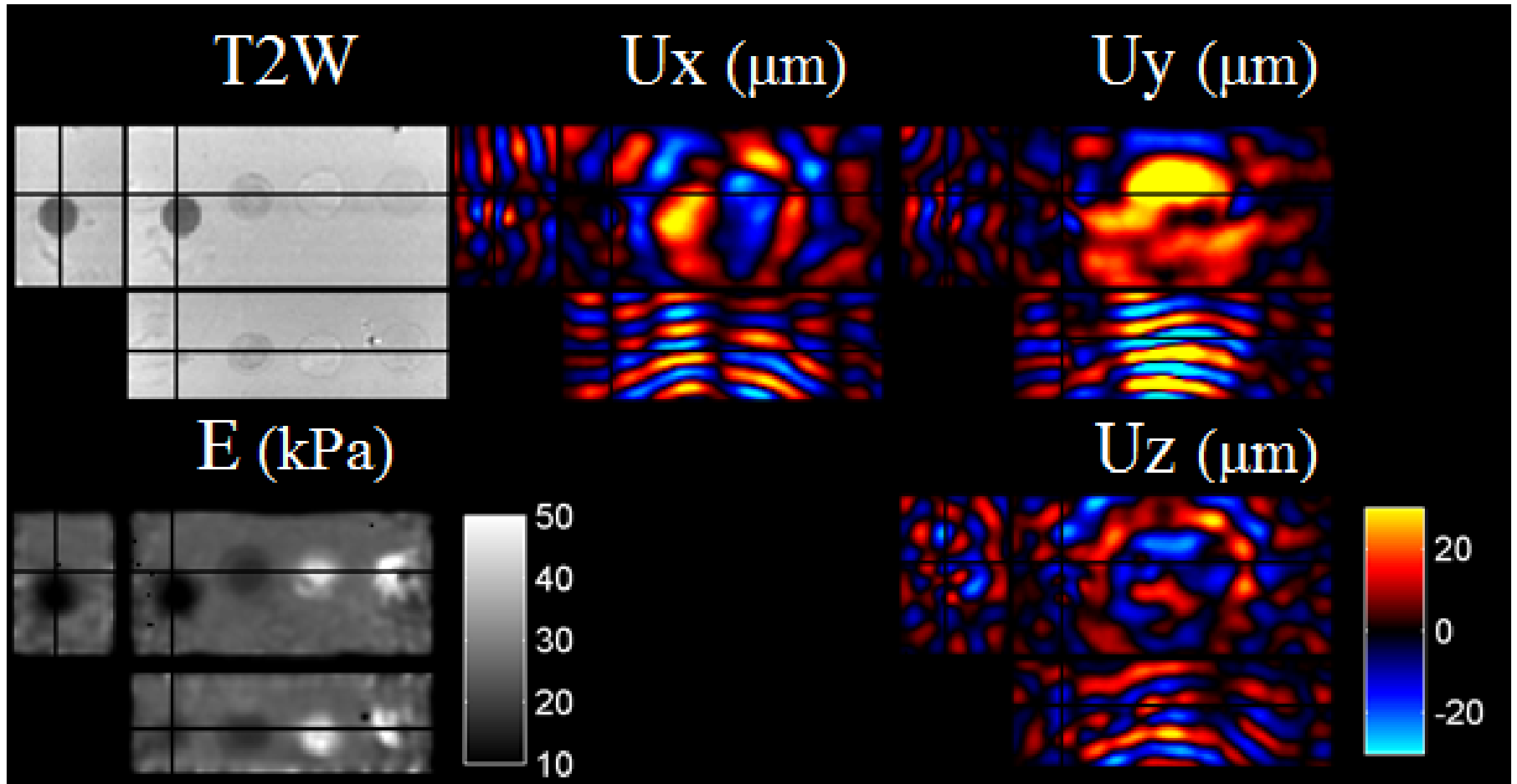


Figure 3-8. A T2-weighted image of a phantom with inclusions of different elasticities that was tested with the new sequence and transducer. The resulting mechanical waves (200 Hz) are shown in the projections in the three orthogonal planes. The inclusions can be visualized in the reconstruction elastogram verifying the functionality of the transducer and pulse sequence.

The measured elasticity values of the inclusion as well as the manufacturer reported values are tabulated in Table 3-2.

**Table 3-2. Elasticity values (in kPa) for inclusion of different stiffness in a quality assurance as reported by the manufacturer (in brackets) and measured using methods discussed in this thesis.**

| <b>inclusion 1 [left]</b> | <b>inclusion 2</b> | <b>inclusion 3</b> | <b>inclusion 4 [right]</b> | <b>Background</b>  |
|---------------------------|--------------------|--------------------|----------------------------|--------------------|
| 11.5 ± 2.1<br>(6)         | 18.7 ± 1.3<br>(17) | 30.5 ± 5.6<br>(54) | 40.1 ± 11.4<br>(62)        | 24.3 ± 1.1<br>(29) |

### **3.3.3 *In-vivo* human study**

This transducer system was approved by the local clinical ethics review board and the biomedical engineering department at the Vancouver General Hospital for human studies. For the human study, the transducer did not overheat at an average power of 45 W r.m.s. For all cases, waves were observed in the images, and an example result is shown in Figure 3-9.

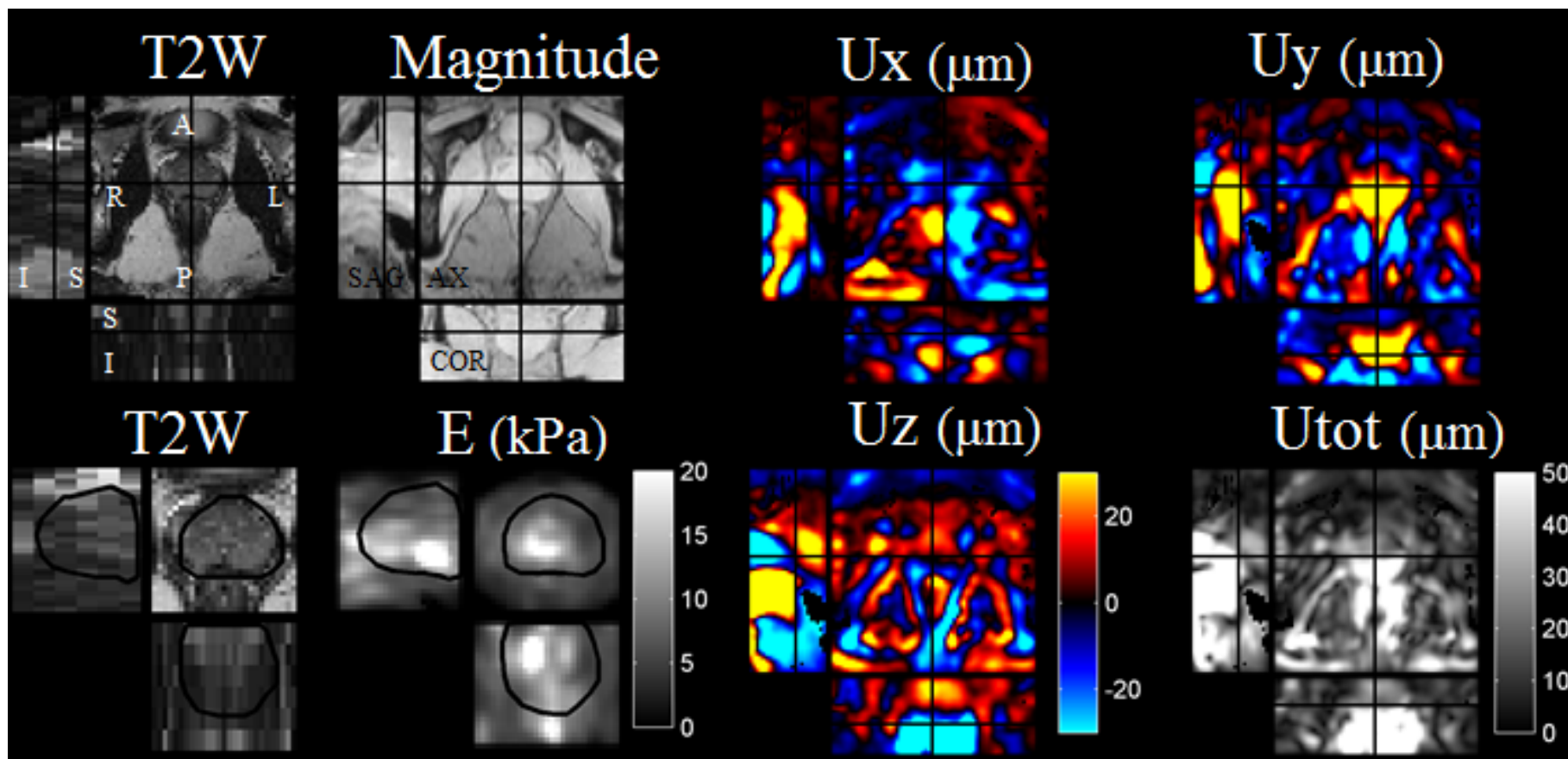


Figure 3-9. The *in-vivo* results from the testing of the improved sequence together with the new electromagnetic transducer. The images show the prostate of a healthy subject in transverse (center), sagittal (left) and coronal (bottom) planes. The T2-weighted image, magnitude of the MRE image (in-phase gradient echo) and waves in  $x$ ,  $y$  and  $z$ -direction (70 Hz) are shown. The total wave amplitude,  $U_{tot}$ , shows that the waves illuminate the entire region of the prostate and are present in all three encoding directions. This verifies the functionality of the transducer and pulse sequence. The bottom row shows a close up T2-weighted image of the prostate and the corresponding reconstructed elasticity image.

The images are shown as axial (center), sagittal (left), and coronal (bottom) planes. The figure shows the T2-weighted image and the corresponding magnitude image from the MRE experiment (in-phase gradient echo), the waves in all three dimensions, total wave amplitude, and the reconstructed elastogram. Invalid voxels are marked as mentioned previously. As can be seen, the waves are easily visualized in all three directions and are present in the entire prostate. The total wave amplitude,  $U_{tot}$ , in the coronal plane is shown in Figure 3-10. The average wave amplitude was  $29 \pm 23 \mu\text{m}$  (apex:  $46 \pm 23 \mu\text{m}$  and base:  $12 \pm 7\mu\text{m}$ ) in the prostate. In the elastogram, the prostate stands out compared to the surrounding tissue, as expected. The average elasticity (Young's modulus) of the entire prostate gland was  $7.4 \pm 3.2 \text{ kPa}$  (apex:  $5.6 \pm 1.3 \text{ kPa}$ , base:  $9.1 \pm 3.9 \text{ kPa}$ ) and agrees with our previous results. Figure 3-10 shows the wave attenuation from apex to base which is approximately  $\alpha = 0.38 \text{ dB/cm}$ . When asked "is the shaking comfortable?" and "would this level of shaking be ok for 10 min?" the subjects responded positively. Also, when the subjects asked at the end of the session "was the examination tolerable" and "could the shaking be increased by 50%?" they responded "yes". In terms of speed, the MRE image acquisition takes 10 min, while the total scan, including positioning and setup, can be performed in  $20 \pm 5 \text{ min}$ .

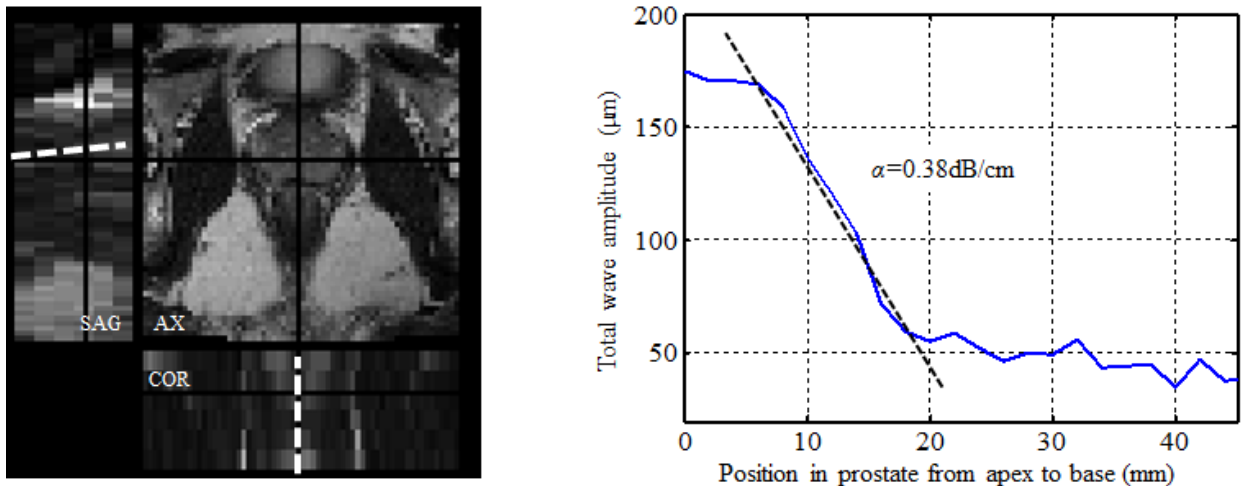


Figure 3-10. The total wave amplitude across the prostate (dotted line) in the coronal plane is shown for one case.

### 3.4 Discussion

The results of this study verify that (i) the sequence is capable of encoding waves in 3D in an *in-vivo* human prostate, and (ii) the transducer is usable for trans-perineal MRE and does not interfere with the MRE experiments. The transducer did not overheat and was well tolerated by the subjects. No MR image artefacts due to the transducer were present, showing the effectiveness of shielding as optimized using simulations, and further fined tuned using magnetometer measurements.

In terms of the pulse sequence, accumulation of erroneous phase due to (i) imaging gradients that are synchronous to the mechanical excitation (exploited in bSSFP MRE [119]), and (ii) residual fringe field from the electromagnetic transducer, were eliminated by subtracting each wave-encoded image from the reference image during the post-processing step. Even with the additional reference scan, the speed advantage of this method is substantial. The effect of patient motion on the quality of displacement data remains to be studied in future.

In terms of the design of the transducer, there are certain disadvantages to electromagnetic designs placed within the bore of the scanner. For example, the gradient fields of the MR scanner that are used for imaging and wave encoding can induce eddy currents in the transducer coils that generate undesired mechanical excitations at the MRE imaging frequency. However, the induced currents were typically less than 10% of the currents used for mechanical excitation, even for MRE experiments where large gradients are used. In this design, due to the orientation of the inner coils and the axis of rotation, the undesired excitation is more prominent when the horizontal gradient  $G_x$  is active. While MRE data is not acquired, the coils can be electrically disconnected. Another solution to this is to introduce a circuitry such as crossed diodes to the transducer to suppress low voltages induced by the gradient coil; therefore, only large voltages (greater than the forward bias voltage of diodes) of the desired excitation signal activate the coils. Yet another method would be to increase the effective output impedance of the amplifier. While less efficient, this design would decrease the current due to the back-emf from equation (3-5).

The coils were specifically oriented in the sagittal plane in order to (i) reduce the width of the transducer for the comfort of the subject, and (ii) produce position independent vibration amplitude, because the magnetic field is essentially perpendicular to the coil normal. A precaution for designs that utilize the magnetic field of the scanner is that if a voltage amplifier is used, the current may increase in the coils as the transducer is removed from the magnetic field. During actuation, the  $V_{emf}$  of coil 1 can be as high as 18 V at 70 Hz. As the vibrating coils are removed from the magnetic field, the voltage induced in the coils will vanish, thereby increasing the current if a constant voltage source is used. This may result in overheating and potentially damage the transducer. The problem can be alleviated by using a current amplifier, or simply turning off the transducer whenever it is outside the bore.

In experiments with the quality assurance phantom, the elasticity differences between the inclusions are clearly visible. However, an underestimation for hard inclusions and an overestimation of soft inclusions was observed. The elasticity values are similar to those reported by [109], [120], and the discrepancy is associated with the aging of the phantom material, limitations related to the inversion algorithm (ratio of the wave-length to inclusion size, sudden change in wave amplitude, etc.) and any temperature difference relative to the conditions in which the phantom was characterized by the manufacturer.

In the *in-vivo* experiments, the transducer amplitude must be adjusted for each subject undergoing trans-perineal MRE. The required excitation amplitude is a function of the positioning of the transducer, size and weight of the subject. The subjects did not report any discomfort or pain during the examination.

In terms of speed, the MRE image acquisition takes 10 min for acquiring the 3D displacement field in a volume covering the prostate. This is substantially shorter than previously reported in the literature (based on extrapolated acquisition parameters settings). The new actively shielded electromagnetic transducer allows for a two-minute installation, similar to that of an RF coil. Previously, in the trans-perineal approach, the subject had to be removed from the scanner if the transducer was improperly positioned. With the added remote positioning system, it is possible to re-position the transducer while the patient is in the scanner, thereby saving valuable time. Also, the relatively narrow width and low profile of the new transducer design ensure the subject is comfortable during the examination. They are therefore less inclined to move, even during extended examinations, as in multi-parametric imaging, for example. The remote positioning concept would be of benefit for MRE of other organs as well.

## **3.5 Case studies**

### **3.5.1 Comparison studies between SE-EPI and *eXpresso* pulse sequences**

The new MRE pulse sequence (code named *eXpresso*) was co-developed during a six-month research visit in Paris, France. Initially, the pulse sequence was developed for liver imaging. This work was published in ref [83], [117].

#### **3.5.1.1 Phase to noise ratio (PNR) in phantom in *in-vivo* liver of volunteers**

A phantom test was performed by my colleague Philippe Garteiser to compare the Phase-to-noise-ratio (PNR) and the resulting average shear modulus between the *eXpresso* sequence introduced here and the conventional SE-EPI sequence. The phantom was a homogeneous paraffin wax (Sentosphere, Paris, France) with dimensions 120×120×230 mm. The average storage modulus at 56 Hz was 7.16±0.25 kPa for *eXpresso* MRE versus 7.12±0.33 kPa for spin-echo EPI. This showed that the methods produce equivalent stiffness values in phantoms for exactly the same experimental conditions independent of which acquisition method is used. In fact the spatial variation of the shear modulus was less with *eXpresso* compared to SE-EPI.

A sample volunteer test comparing the two methods is shown in Figure 3-11 where the magnitude image for *eXpresso* sequence was 16 dB and for SE-EPI it was 8 dB. The PNR for the *eXpresso* sequence were 59.6±11.9, 60.2±8.2 and 58.2±10.4 and for SE-EPI they were 27.9±3.8, 24.8±2.5 and 23.5±2.9 for  $U_x$ ,  $U_y$  and  $U_z$  respectively. The PNRs were always significantly higher ( $p < 0.01$ ) for *eXpresso* than for spin-echo when using unpaired, two-tailed Mann–Whitney statistical testing.

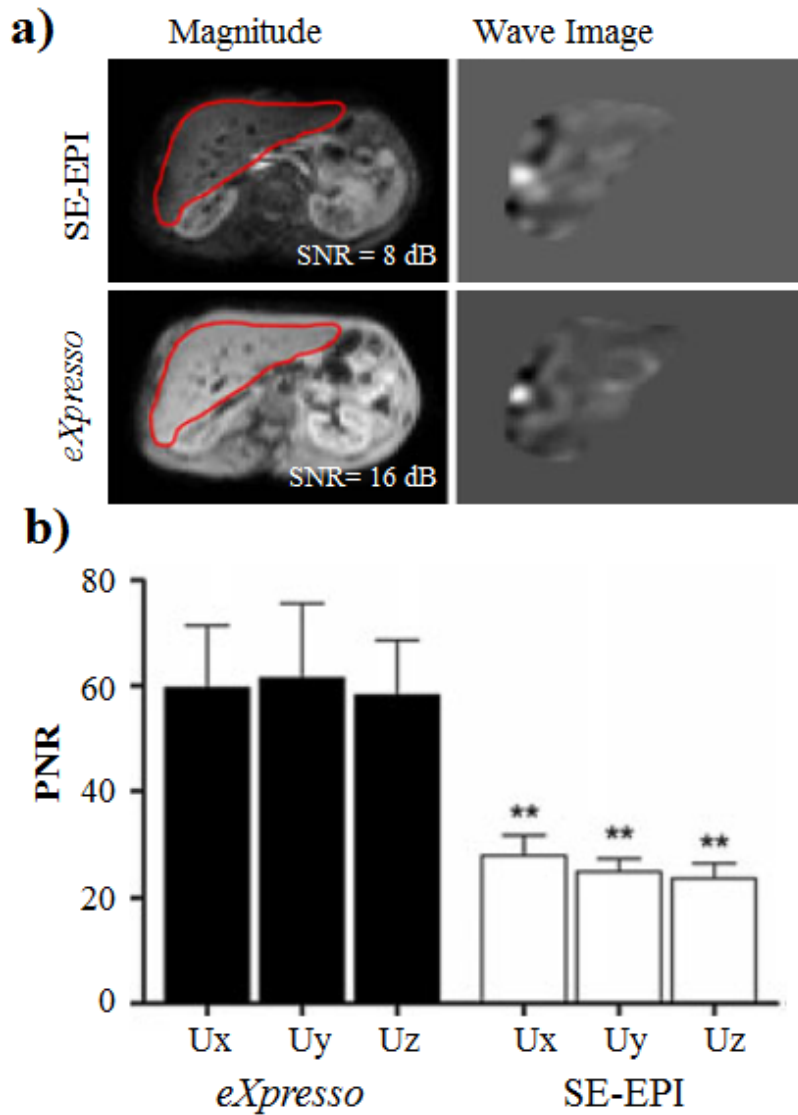


Figure 3-11. a) Comparison between MRE of the liver using *eXpresso* and spin-echo echo planar imaging (SE-EPI). Noticeable signal loss in SE-EPI images is due to fat suppression. b) The phase to noise ratio is significantly higher for the *eXpresso* methods compared to the SE-EPI method.

### 3.5.1.2 Multi-frequency experiments in phantom and in-vivo liver of volunteers

Results comparing mono and multi-frequency experiments in phantoms are shown in Figure 3-12. In the mono frequency experiment (top row), the examination was repeated three times. Each examination only a single mono-frequency excitation was applied. In the multi-frequency experiment (middle row), only one experiment was performed and three simultaneous excitations (28+56+84Hz) were applied to the phantom. The amplitude weighting was the same for each excitation frequency in the multi-frequency exam. Due to the encoding efficiency spectrum of *eXpresso* pulse sequence (see Figure 3-4) higher frequency excitations are encoded more efficiently, thus alleviating the need to increase the excitation amplitude to overcome wave attenuation effects. As seen in Figure 3-12, the mono- and multi- frequency examinations produce almost identical wave patterns and the difference images are small.

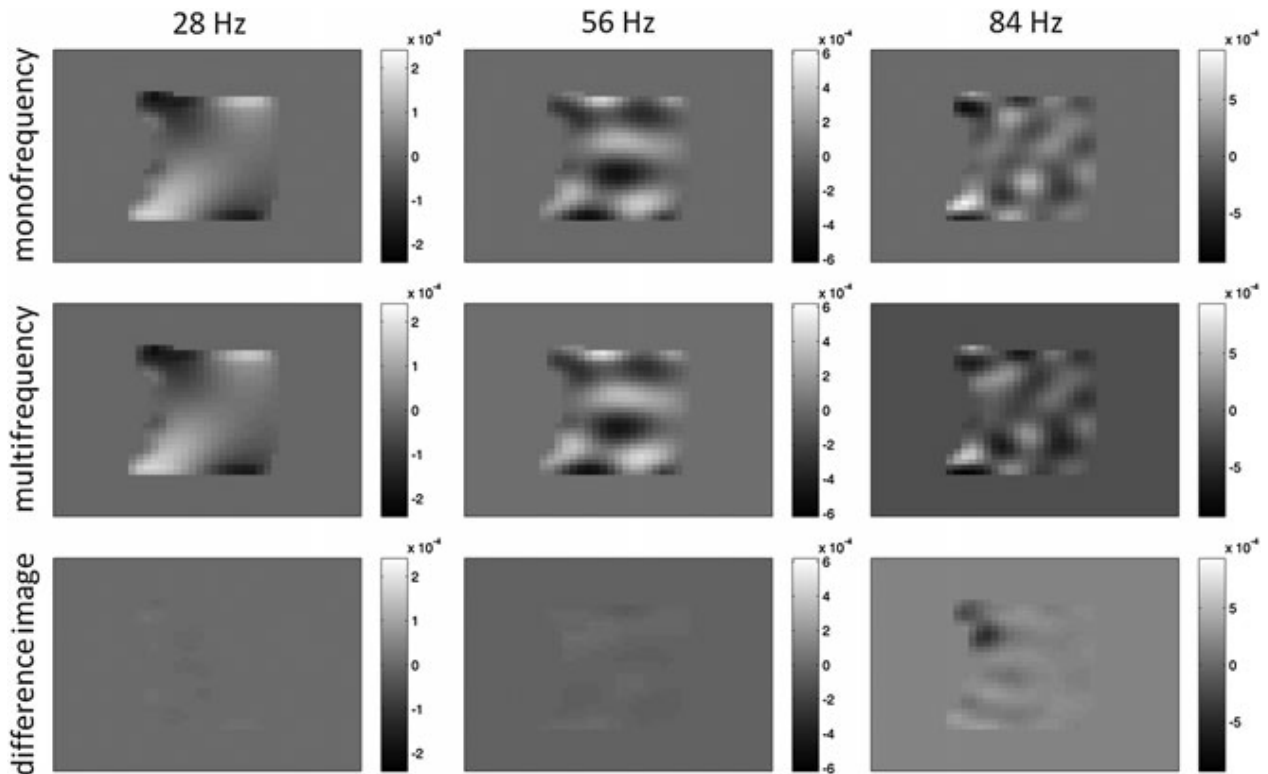


Figure 3-12. Comparison between mono- and multi-frequency experiments in a homogeneous phantom using the *eXpresso* pulse sequence. Top row: mono-frequency experiments at 28 Hz, 56 Hz and 84 Hz performed separately. Middle row: a single multi-frequency experiment using simultaneous mechanical excitation at 28+56+84Hz (equal amplitude weighting). Bottom row: difference image between the mono-frequency and multi-frequency images.

*In-vivo* liver experiments were carried out at TE=6.8 ms (water and fat in-phase at 3T) and TR=147 ms. The number of slices (eight) was a multiple of the number of shots per vibration period ( $N_{\text{shotsPerVib}}=4$ ) for synchronization purposes. Eight vibration phases encoded excitations at 28, 56, and 84 Hz that were applied simultaneously. The acquisition ( $80 \times 80 \times 8$ , 4 mm isotropic, SENSE factor 2) was performed within four breath holds (~15 s each). The entire acquisition lasted 59s. Sample images are shown in Figure 3-13. Figure 3-13a) shows that the SNR is greatly improved with the *eXpresso* sequence compared to the conventional SE-EPI MRE sequence, and that the waves are almost identical in both cases away from the liver blood vessel on the right lobe of the liver. The small differences arise due to small patient motion between the examinations and also the amplitude weighting of each excitation frequency for the multi-frequency experiment. Figure 3-13b) shows the y-component of the curl of the wave field at three different frequencies. The images obtained on the left side are three individual acquisitions, whereas the images on the right are obtained in a single multi-frequency experiment. This demonstrated the feasibility of frequency multiplexing using the *eXpresso* pulse sequence, which essentially triples the acquisition speed in this case.

A multi center trial of liver MRE is currently being carried out using this pulse sequence with site in France, South Korea, and Spain.

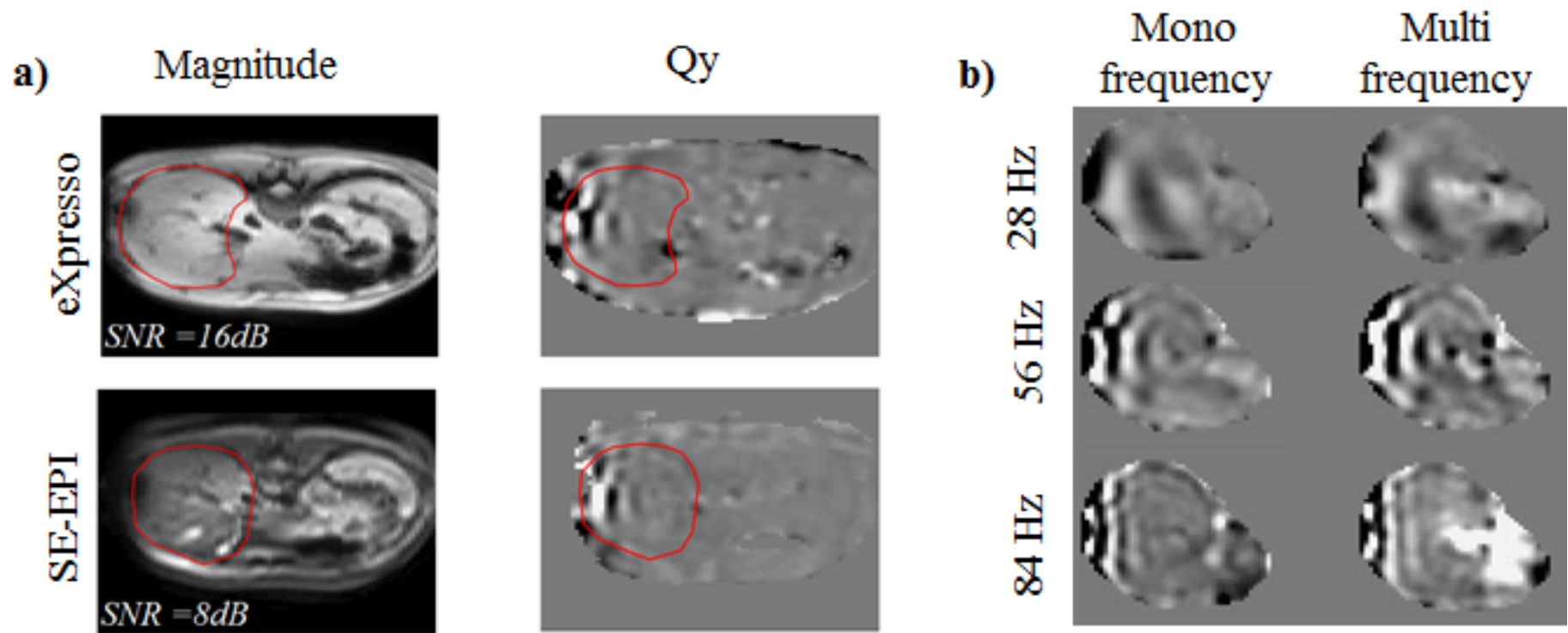


Figure 3-13. a) Comparison between the magnitude image and the y-component of the curl of the wave field for the eXpresso and conventional SE-EPI scan. b) Comparison of the waves between individual mono frequency experiments and single multi-frequency experiment.

### 3.5.2 Phantom: sparsity regularized FEM

Mr. Mohammad Honarvar developed the sparsity regularized mixed FEM algorithm based on the phantom data acquired using the electromagnetic driver outlined in this section [110]. Data was collected from a standard elasticity quality assurance phantom CIRS Model 049 (CIRS Inc., Norfolk, VA) which has eight spherical inclusions (four with diameter of 20 mm and four with diameter of 10 mm). The MRE images were acquired using a 2D multi-slice multi-shot SE-EPI method with turbo factor 11 [84]. A single sinusoidal cycle MEG was used as the motion encoding gradient with a strength of 60 mT/m, which captured eight states of the mechanical motion. All three components of displacement were acquired on a  $224 \times 112 \times 48$  matrix with 1.5 mm isotropic voxel size. The excitation was applied using the new electromagnetic transducer to the open face of the phantom.

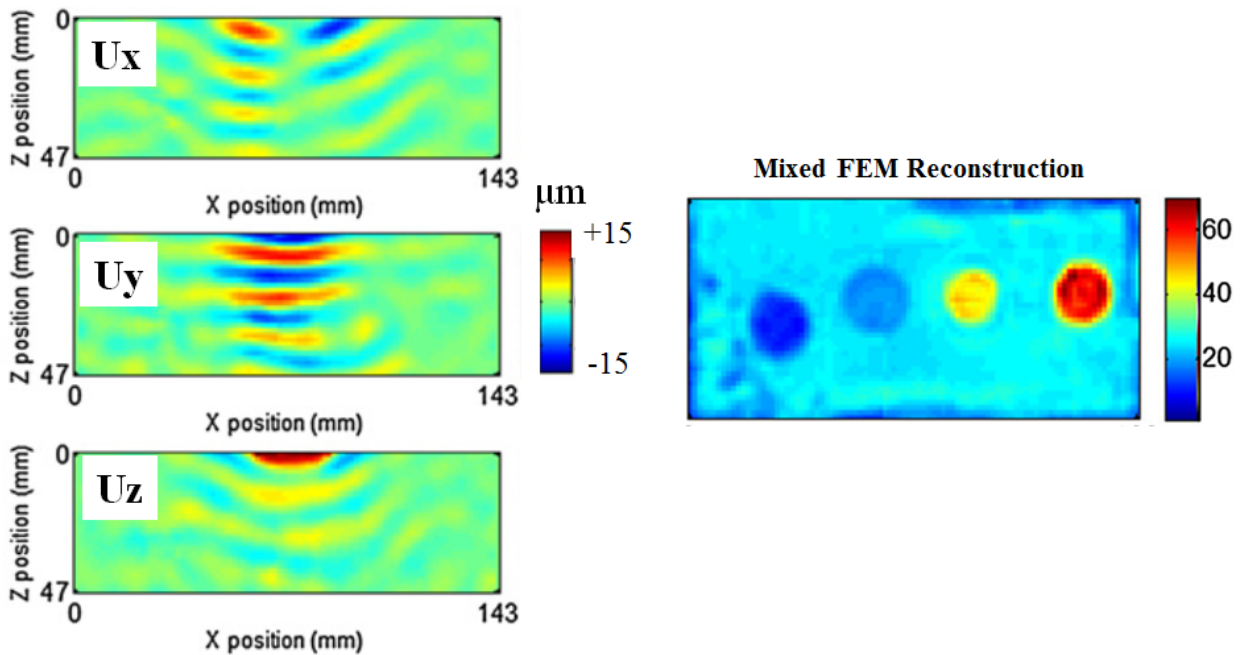


Figure 3-14. Sample 3D displacement field and elasticity image reconstructed using the mixed FEM approach. Adapted from [120] with permission

The mixed FEM reconstruction as formulated in [121] allows for the simultaneous reconstruction of shear modulus and pressure term. The main challenge in the inversion is poor numerical condition due to the ratio of the pressure term to the shear modulus being several orders of magnitude, which makes regularization necessary for meaningful reconstruction. A sparsity regularization is proposed by Honarvar *et al.* [110] that is based on discrete cosine transform to transform the elasticity and pressure fields to a sparse domain in which a smaller number of unknowns is required to represent the original field. The main advantage of this method is that with sparsity regularisation the reconstruction becomes less dependent on boundary conditions, less influenced by noise, requires no parameter tuning and is computationally faster.

Sample images of the displacement field and the reconstructed elasticity are shown in Figure 3-14. For details of the algorithm and comparison to other methods refer to [110].

### 3.5.3 Phantom: curl-based FEM

Similarly, Mr. Mohammad Honarvar developed the curl-based FEM algorithm based on the same phantom data acquired as outlined in this section. Additional multi-frequency phantom data was also acquired for this case study. The novelty in this approach is that this method does not rely on the simplifying assumption of local homogeneity. The curl operator is directly applied to the original equation of motion (rather than the displacement field). This allows the derivatives of the shear modulus to be calculated resulting in improved reconstruction. This method was evaluated in simulations and on phantom MRE data. A sample result is shown in Figure 3-15. It is shown that the reconstruction results are superior to those obtained using previous curl-based methods with homogeneity assumption [111].

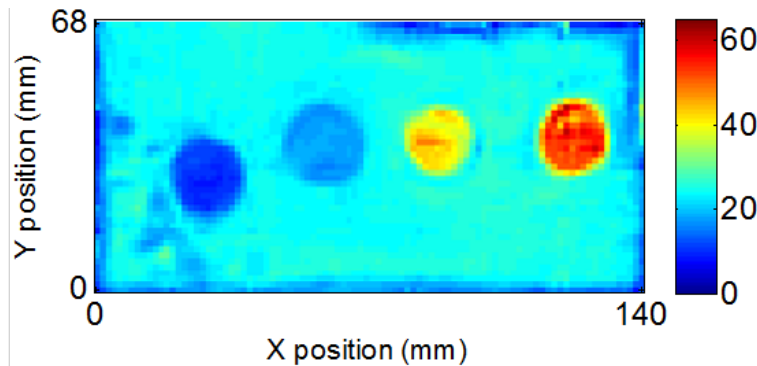


Figure 3-15. Sample elasticity image reconstructed using the curl-based FEM approach.

## 3.6 Conclusion

In conclusion, the contributions of the research in this chapter include the design of a new actively shielded electromechanical transducer that can be set up quickly and positioned remotely while the subject is in the scanner, the implementation of a pulse sequence for acquiring a 3D displacement field that enables fast imaging of the entire prostate gland in just 10 min, and the integration and testing of these methods and equipment in phantoms and human subjects including prostate cancer patients. The developed system is functional and can be integrated in a clinical study for multi-parametric imaging.

# Chapter 4 - *In-vivo* prostate cancer MRE: quantitative comparison to histopathology

## 4.1 Introduction

The previous two chapters described the development of two *in-vivo* prostate MR elastography systems. The latter system is a much improved version in terms of excitation device and acquisition pulse sequence. This chapter discusses the results of a patient study performed using the latter MRE system. Previously in the literature, MRE of human *in-vivo* prostate cancer has been demonstrated only by two groups [54], [56]. However, a patient study with quantitative analysis with whole mount pathology has not been reported before.

In this chapter, first the repeatability and sensitivity of the reconstructed shear modulus in repeated imaging studies in six volunteers is discussed. Then, the shear stiffness results of a prostate patient study using transperineal MRE is compared with whole mount pathology marked by the Gleason score. Finally, the limitations of this study are discussed in the discussion section. To our knowledge, this presents the first prostate MRE study that compares the results to whole mount pathology.

## 4.2 Methods

### 4.2.1 Volunteer and patient studies

The studies were approved by the university clinical research ethics board and signed informed consent (see Appendix B) was provided by all subjects.

Volunteer repeatability study: The experiments were performed on six volunteers (mean age 34). For the repeatability study, the exact same acquisition was performed at least twice while the subject was asked not to move. In two cases, the excitation frequency was shifted by  $\pm 2$  Hz, and the experiments were repeated. For repeatability analysis, the difference-versus-mean plot (Bland-Altman), the correlation coefficient [114] and the intraclass correlation coefficient (ICC), were calculated.

Patient study: The experiments were performed on prostate cancer patients (mean age 64) scheduled for radical prostatectomy recruited between December 2011 and March 2013. From the original 18 patients recruited, MRE experiments could not be performed or analyzed in the following cases: P02 (prohibitive patient size), P03 (transducer mechanical failure), P09 (scanner malfunction). The ROC analysis could not be analyzed in the following cases: P13 (unwrapping failed due to waves) and P20 (poor waves due to patient motion). In one patient (P13) Gleason score was not assigned by the pathologist due to previous androgen therapy, and thus was not included in the analysis. The analysis in this paper was performed on the remaining 11 patients. Clinical

data including age, patient weight (kg), gland size (gr), prostatectomy Gleason scores, and clinical stage, the number and size of tumors, and notes from Pathology for patients who had biopsy confirmed cancer are summarized in Table 4-1.

**Table 4-1. Clinical data for patients with biopsy confirmed cancer. (NPH=Nodular prostatic hyperplasia, PIN=Prostatic Intraepithelial neoplasia, PNI= Perineural invasion, SV= seminal vesicles, PUE=Prostatic Urethral Ectasia, BPU=Benign prostatic urothelium).**

| Case | Age (yr) | Patient Weight (kg) | Gland Weight (gr) | Gleason Score | Clinical Stage | # Tumors (size range mm) | Pathology  |
|------|----------|---------------------|-------------------|---------------|----------------|--------------------------|--|
| P01  | 61       | 74                  | 48                | 4+3<br>PZ     | pT2c           | 20<br>(19×11 - 2.5×1.6)  | NPH, PIN   |
| P04  | 71       | 72                  | 61                | 3+4<br>PZ     | pT2c           | 21<br>(13×8.5 - 2.4×1.7) | PNI, PIN, NPH, irregular nodule 10mm in left PZ  |
| P05  | 59       | 109                 | 32<br>(no SV)     | 3+3<br>CG     | -              | 7<br>(17×8 - 3.4×2.5)    | PIN, NPH, cyst (15mm) with calcification in TZ   |
| P06  | 63       | 74                  | 65                | 4+3<br>PZ     | pT3b           | 12<br>(17×11 - 1.9×1.6)  | PNI, PIN,NPH   |
| P08  | 66       | 81                  | 64                | 3+4<br>PZ)    | pT2c           | 4<br>(9×7.2 - 2×1.6)     | PNI, PIN, NPH, irregular nodule 5mm right PZ base  |
| P10  | 72       | 84                  | 34                | 3+4<br>PZ     | pT2c           | 5<br>(21×8.8 - 2.8×1.8)  | prominent PIN, PIN, NPH,   |
| P12  | 60       | 98                  | 50                | 3+4<br>CG,PZ  | pT2c           | 25<br>(19×13 - 2.1×1.2)  | PIN, NPH, BPU  |
| P13  | 76       | 94                  | 74                | NA            | pT2a           | 6<br>(22×7.8 - 5.3×2.6)  | Pre-op androgen therapy, 8-month withdrawal  |
| P15  | 66       | 63                  | 47                | 4+4<br>PZ     | pT3a           | 4<br>(15×4.7 - 3.7×1.9)  | prostatic lithiasis (calcification), PNI, NPH, BPU, foci of chronic active prostatitis with atrophic gland |
| P17  | 70       | 80                  | 53                | 4+3<br>PZ     | pT2a           | 4<br>(13×11 - 7.4×3.6)   | PIN, PUE, scars from biopsy, NPH, cystic atrophy, Transurethral Curettage                                  |
| P18  | 53       | 79                  | 39                | 4+3<br>PZ     | pT2c           | 6<br>(7.1×6 - 1.7×1.2)   | PIN,NPH, BPU, 1-cm cyst  |
| P19  | 53       | 77                  | 53                | 4+4<br>PZ     | pT3c           | 13<br>(24×16 - 2.2×1.2)  | PNI, PIN, BPU, 1cm utricular cyst  |
| P20  | 60       | 79                  | 111               | 3+4<br>(PZ)   | pT2c           | 18<br>(10×7.1 - 1.5×0.9) | PIN, NPH, BPU, scars from biopsy, benign cyst, compression of PZ by hyperplastic nodules of TZ             |

### 4.2.2 Setup and acquisition

All experiments were performed on a 3T Achieva (Philips Inc., Best, Netherlands) scanner using a standard 6-element cardiac coil. A shielded electromagnetic transducer was placed against the perineum of the subject in supine position [118] as shown in Figure 4-1. After the patient was centered in the scanner, the position of the contact point and pre-compression was adjusted with feedback from a 30 second sagittal scout scan. This procedure took approximately 5 min. The 3D displacement field of the prostate was obtained using a fractionally encoded steady-state gradient echo sequence described in the previous chapter.

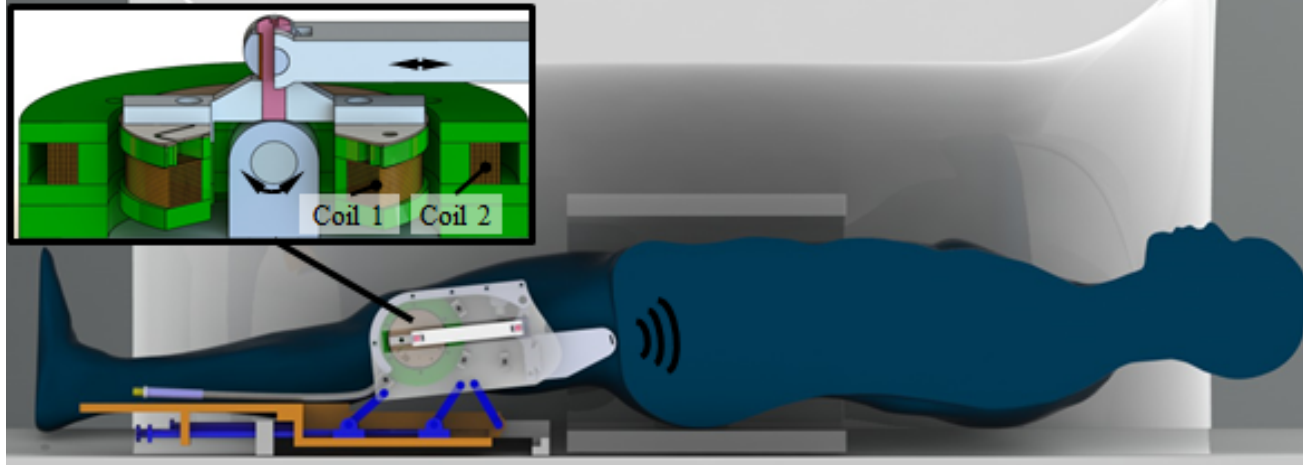


Figure 4-1. The trans-perineal prostate MRE setup. The rotary movement of the counter-wound coils is converted to linear motion that vibrates the perineum. The outer coil acts as a compensation coil to reduce the fringe field from the moving coil. The point and angle of contact as well as the pre-compression applied by the transducer can be adjusted positioning screws at the back of the scanner.

The MRE acquisition settings are as follows: matrix size =  $128 \times 128 \times 24$ , voxel size = 2 mm isotropic, echo-time (TE) = 9.2 ms (water and fat in-phase at 3T), repetition-time (TR) = 344 ms, water-fat shift = 0.4 pixels (bandwidth 141 kHz), acceleration (SENSE) = 2, and k-space filling = 80%. The period of the motion encoding gradient was 8.4 ms, and the maximum amplitude of the gradients fields was 48 mT/m, which resulted in an encoding efficiency of 14.5  $\mu\text{m}/\text{rad}$ . The sinusoidal mechanical excitation frequency was 70 Hz and was sampled at eight phase offsets. The acquisition time per encode direction was 2 min, 32 sec, with a total acquisition time of 10 min, 8 sec for the 3D displacements and the reference scan. A standard axial T2-weighted fast spin echo sequence (TE/TR = 80/1850 ms, FOV  $140 \times 140 \times 72$  mm with 0.5 mm in-plane resolution and 4 mm slice thickness) was acquired prior to the MRE scan.

### 4.2.3 Quality metrics for 3D wave field

To evaluate the quality of the acquired wave field several parameters were calculated from each data set. The total absolute wave amplitude ( $\mu\text{m}$ ) was the Cartesian sum of each displacement component  $U_{total} = (U_x^2 + U_y^2 + U_z^2)^{0.5}$  (derived from MRE phase images at excitation frequency) in the mid-gland of the prostate. The phase-to-noise-ratio (PNR) in decibels was calculated based on the signal to noise ratio of the

MRE magnitude images in the mid-gland of the prostate. The harmonic distortion is the ratio of the sum of the powers of all harmonic components to the power of the fundamental frequency, and is given by:

$$THD = \frac{\sum_{k=2}^{\infty} U_k}{U_1} \quad (4-1)$$

where  $U$  is the wave amplitude at harmonic frequency  $k$ . This is a measured of non-linearity of the system (transducer, tissue, etc). The linear misalignment between each motion component was calculated taking the cross-correlation of the magnitude MRE images. This information reveals patient motion during the examination. The quality metrics are tabulated in Table 4-2 for the patient study. For comparison, the mean quality metrics for the volunteer study are also shown at the bottom of this table. For more images of the raw waves in the patients refer to Appendix C.

Table 4-2. Quality metrics for the volunteer (mean only) and patient study.

| Case           | PNR (dB) | Wave Ampl. ( $\mu\text{m}$ ) | Total Harmonic Distortion (%) | Displacement Misalignment error (mm) |     |     |         |     |     |         |     |      |
|----------------|----------|------------------------------|-------------------------------|--------------------------------------|-----|-----|---------|-----|-----|---------|-----|------|
|                |          |                              |                               | Ux - Uy                              |     |     | Ux - Uz |     |     | Uy - Uz |     |      |
|                |          |                              |                               | x                                    | y   | z   | x       | y   | z   | x       | y   | z    |
| P01            | 13.1     | 103                          | 29                            | 0.2                                  | 1.0 | 0.1 | 0.1     | 0.2 | 0.0 | 0.2     | 0.9 | 0.2  |
| P04            | 8.2      | 44                           | 53                            | 1.1                                  | 0.9 | 0.1 | 0.6     | 1.0 | 0.5 | 0.7     | 3.0 | 0.2  |
| P05            | 10.3     | 44                           | 49                            | 0.3                                  | 1.0 | 0.4 | 0.9     | 1.0 | 0.4 | 0.8     | 0.2 | 0.0  |
| P06            | 8.9      | 45                           | 62                            | 0.1                                  | 1.0 | 0.2 | 0.4     | 1.2 | 0.1 | 0.5     | 0.3 | 0.6  |
| P08            | 10.5     | 46                           | 68                            | 0.1                                  | 0.7 | 0.2 | 0.3     | 0.2 | 0.6 | 0.3     | 0.6 | 1.0  |
| P10            | 13.0     | 82                           | 30                            | 0.3                                  | 0.0 | 0.1 | 0.2     | 0.3 | 0.1 | 0.2     | 0.5 | 0.2  |
| P12            | 8.1      | 23                           | 85                            | 0.2                                  | 0.6 | 0.8 | 0.2     | 2.4 | 2.2 | 0.0     | 1.5 | 0.6  |
| P13            | 13.6     | -                            | 43                            | 0.1                                  | 0.0 | 0.2 | 0.2     | 0.2 | 0.1 | 0.2     | 0.2 | 0.1  |
| P15            | 9.6      | 55                           | 43                            | 0.2                                  | 0.7 | 0.1 | 0.2     | 0.3 | 0.6 | 0.0     | 0.6 | 0.4  |
| P17            | 9.8      | 41                           | 48                            | 0.2                                  | 0.4 | 0.4 | 0.3     | 0.1 | 0.5 | 0.1     | 0.6 | 0.1  |
| P18            | 9.4      | 56                           | 44                            | 0.0                                  | 0.4 | 0.2 | 0.5     | 0.6 | 0.4 | 0.3     | 0.5 | 10.2 |
| P19            | 9.0      | 44                           | 47                            | 0.2                                  | 0.6 | 0.0 | 0.2     | 2.1 | 0.7 | 0.4     | 6.6 | 1.2  |
| P20            | 6.9      | 24                           | 109                           | 0.0                                  | 0.7 | 0.5 | 0.5     | 2.1 | 1.7 | 0.2     | 1.5 | 2.0  |
| Mean patients  | 10.0     | 51 $\pm$ 22                  | 55 $\pm$ 21                   | 0.2                                  | 0.6 | 0.3 | 0.3     | 0.9 | 0.6 | 0.3     | 1.3 | 1.3  |
| Mean volunteer | 17.7     | 47 $\pm$ 18                  | 47 $\pm$ 30                   | 0.1                                  | 0.4 | 0.1 | 0.1     | 0.2 | 0.1 | 0.1     | 0.3 | 0.2  |

#### 4.2.4 Reconstruction of mechanical parameters and image processing

The absolute shear modulus  $|G|$  and loss modulus  $G_l$ , were determined using the curl-based direct inversion of the wave equation assuming local incompressibility and homogeneity [122]. For comparison, an image of the maximum shear strain  $\tau_{\max}$  is also provided. The maximum shear strain  $\tau_{\max}$  is given by  $\tau_{\max} = 1/2 \cdot (\varepsilon_{11} - \varepsilon_{33})$  where  $\varepsilon_{11}$  and  $\varepsilon_{33}$  are the principle normal strain components as calculated from the Cauchy's strain tensor  $\varepsilon_{ij} = 1/2 \cdot (\nabla \mathbf{u} + (\nabla \mathbf{u})^T)$  where  $\mathbf{u}$  is the displacement field.

A voxel was marked invalid if (i) its magnitude in the image was below a threshold of 10% of the average magnitude; or (ii) the total wave amplitude was less than 0.5  $\mu\text{m}$ .

#### 4.2.5 Histology

Following surgery, the prostate gland is immersed in formalin solution (70 hrs on average). The specimens were sliced in 4 mm intervals similar to methods discussed by [123] using a custom cutting device, in attempt to align the histology slides with the transverse images. The slices were then sent for whole mount histology procedure where an experienced pathologist marked the outline of the tumours, along with the Gleason score, on the histology slides.

#### 4.2.6 Registration

The outline of the prostate was segmented on the histology slides and the T2-weighted images. An experienced radiologist verified the segmentations. The 2D segmented contours of the histopathology were then registered

to the surface of prostate that was extracted from the segmented T2-weighted volume [124]. The method uses particle filtering to minimize the Euclidean distance between the contours and the surface with respect to in-plane translation and rotation of each histology slice alone, and out-of-plane translation and rotation of all the slices together.

#### **4.2.7 Receiver operator curve (ROC) analysis**

The analysis was performed using MATLAB<sup>®</sup> (Mathworks Inc., USA) software. For each case, the tumors marked with the Gleason score were outlined in Stradwin (Medical Imaging Group, Cambridge University, UK) to generate binary masks. The prostate capsule (PC), peripheral zone (PZ), central gland (CG) and transition zone (TZ) were identified in the T2-weighted images by the author (some cases were verified by an experienced radiologist) for zonal analysis. After the registration process, the calculated transformation was applied to the images (T2-weighted,  $|G|$ , GI, shear strain) as well as masks to transform them to the histology slide coordinates. For tumors less than 4 mm the mask was dilated by 1-2 mm while for tumors larger than 8 mm the mask was eroded by 1-2 mm. This was done to account for errors such as registration misalignments, and enable analysis of smaller tumors. Depending on the zonal masks (PC, PZ and CG), the mask for normal tissue was calculated by removing all the tumors marked in the histology slides and eroding the masks by 3-4 mm. Analysis for each case was performed by dividing the data in windows (size between 5-6 mm) with 10% overlap between subsequence windows. A window was labeled as cancer if more than half of the window intersected with a Gleason 3+3=6 or larger tumor, otherwise it was marked as normal. Similarly for the zones, if more than half of the window intersected with for example PZ the zones was labeled as PZ. We refer to this method as the voxel-to-voxel approach. The data was then used to calculate the receiver-operating characteristic curve (ROC), and find the sensitivity, specificity and area-under-curve (AUC) values. A Wilcoxon rank sum test was performed to test the differentiation between normal and cancerous tissue.

### **4.3 Results**

#### **4.3.1 Repeatability study**

Sample images from the volunteer studies are shown in Figure 4-2 (axial and coronal). The figure shows the T2-weighted image, displacement field in three directions  $U_x$ ,  $U_y$  and  $U_z$ , as well as the absolute part of the shear modulus  $|G|$ , maximum shear strain  $\tau_{max}$  and their corresponding Bland-Altman plot. The displacement field reveals that the wave propagation is complex and the waves are present in all spatial components. The elasticity image in particular the shear strain corresponds to the T2-weighted image. The average intraclass correlation coefficient (ICC) was 77% for the magnitude image, 73% for  $|G|$  (4.2% worse than magnitude image), and 75% for  $\tau_{max}$  (2.3% worse than magnitude image). The absolute shear modulus had a coefficient of repeatability (CR) of 1.12 kPa. As shown in repeat cases A1-A2 and B1-B2, the wave patterns and the reconstructed parameters are almost identical in these cases demonstrating that the system is fairly repeatable.

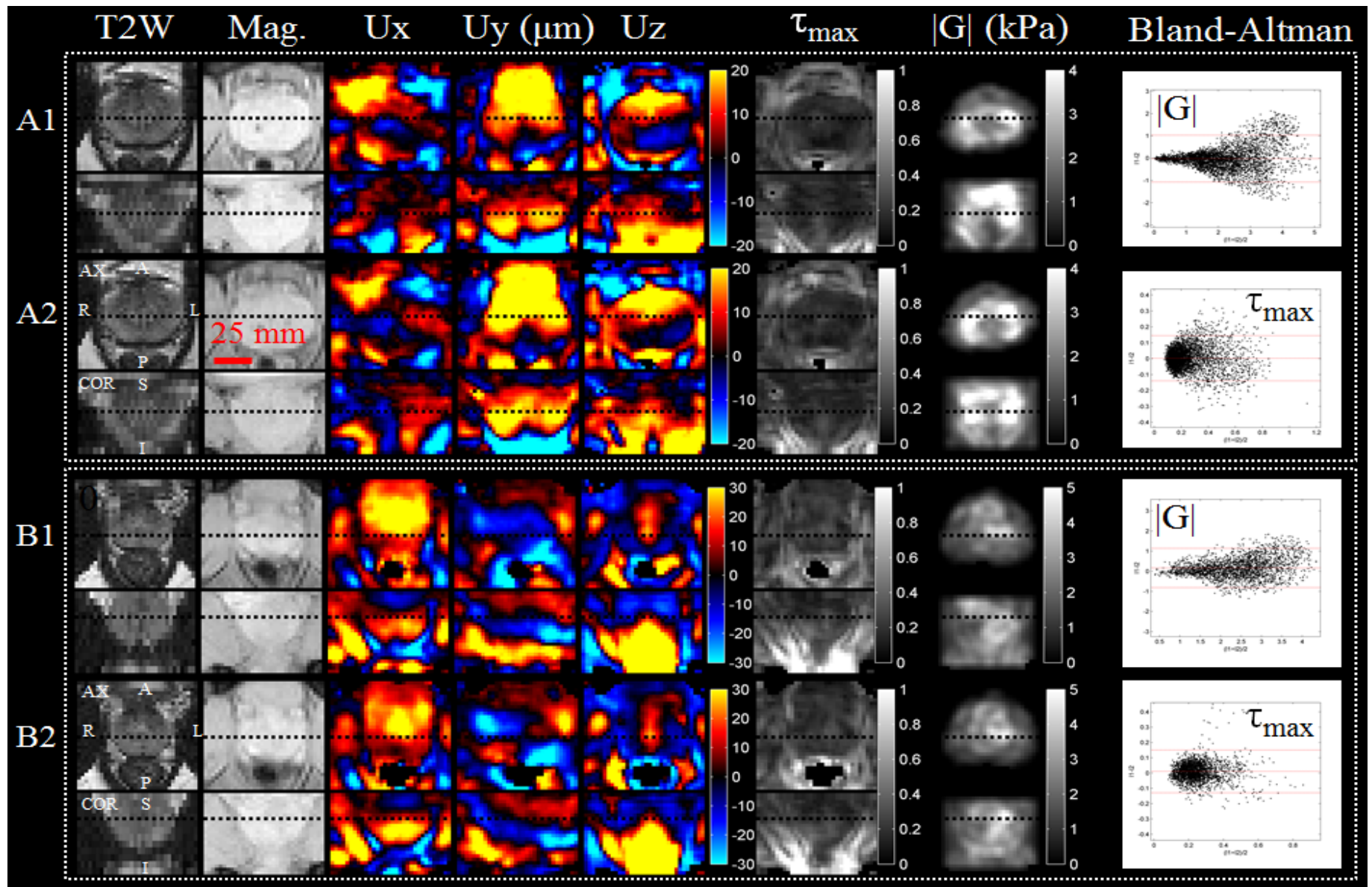


Figure 4-2. Sample repeat volunteer studies. A1 and A2 are repeat cases of the same subject (similarly B1 and B2) Images shown in axial and coronal projections from left to right: T2-weighted, magnitude image of MRE, 3D waves, reconstructed shear modulus  $|G|$ , max shear strain  $\tau_{max}$  and their Bland-Altman plots.

### 4.3.2 Patient study

The MRE setup and imaging time was between 15 and 20 min depending on the initial positioning of the transducer. The total MR examination was between 30 and 70 min. The transducer did not overheat and was well tolerated by the subjects. For the patient study, waves were clearly visible in all directions in the prostate glands with an amplitude of  $47 \pm 18 \mu\text{m}$  at 70 Hz.

Sample images of the patients study before registration are shown in Figure 4-3 (axial and coronal). The figure shows the T2-weighted image, displacement field in three directions  $U_x$ ,  $U_y$  and  $U_z$ , as well as the absolute part of the shear modulus  $|G|$ , maximum shear strain  $\tau_{max}$  and ADC map (where available). The complex wave patters are present in the patients as shown. The shear strain shows the outline of the prostate. P20 is a case where the wave quality is low due to patient motion and poor mechanical contact with the transducer. For more images refer to Appendix C.

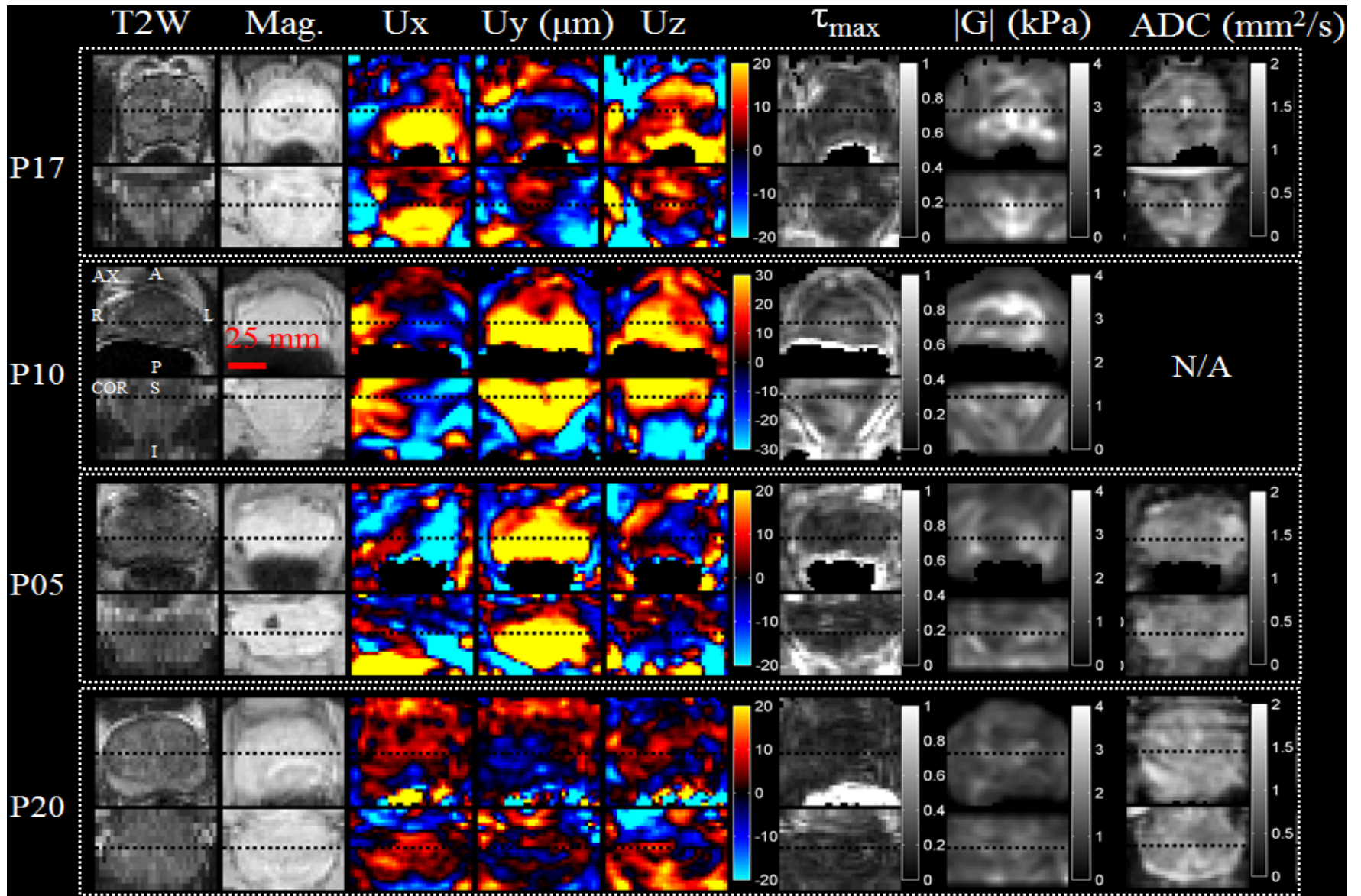


Figure 4-3. Sample images for the patient study. Images shown in axial and coronal projections from left to right: T2-weighted, magnitude image of MRE, 3D waves, reconstructed shear modulus  $|G|$ , max shear strain  $\tau_{\text{max}}$ , and ADC (where available).

Figure 4-4 shows the average shear modulus (black) and loss modulus (white) in various zones of the prostate for both volunteers and patients. For volunteers, the average value of  $|G|$  (and  $G_l$ ) were  $1.9 \pm 0.4$  ( $1.0 \pm 0.2$ ) kPa in the prostate capsule (PC),  $1.9 \pm 0.5$  ( $0.9 \pm 0.3$ ) kPa in PZ,  $2.1 \pm 0.3$  ( $1.2 \pm 0.2$ ) kPa in CG and  $1.9 \pm 0.5$  ( $1.1 \pm 0.3$ ) kPa in the transition zone (TZ). For patients, the average value of  $|G|$  (and  $G_l$ ) were  $1.7 \pm 0.2$  ( $0.9 \pm 0.1$ ) kPa in the prostate capsule (PC),  $1.7 \pm 0.2$  ( $0.9 \pm 0.1$ ) kPa in PZ,  $1.8 \pm 0.4$  ( $1.0 \pm 0.2$ ) kPa in CG and  $2.0 \pm 0.7$  ( $1.1 \pm 0.4$ ) kPa in the transition zone (TZ). The differentiation between PZ and CG was most significant for  $G_l$  in volunteers ( $p < 0.002$ ) and modest for patients ( $p < 0.062$ ).

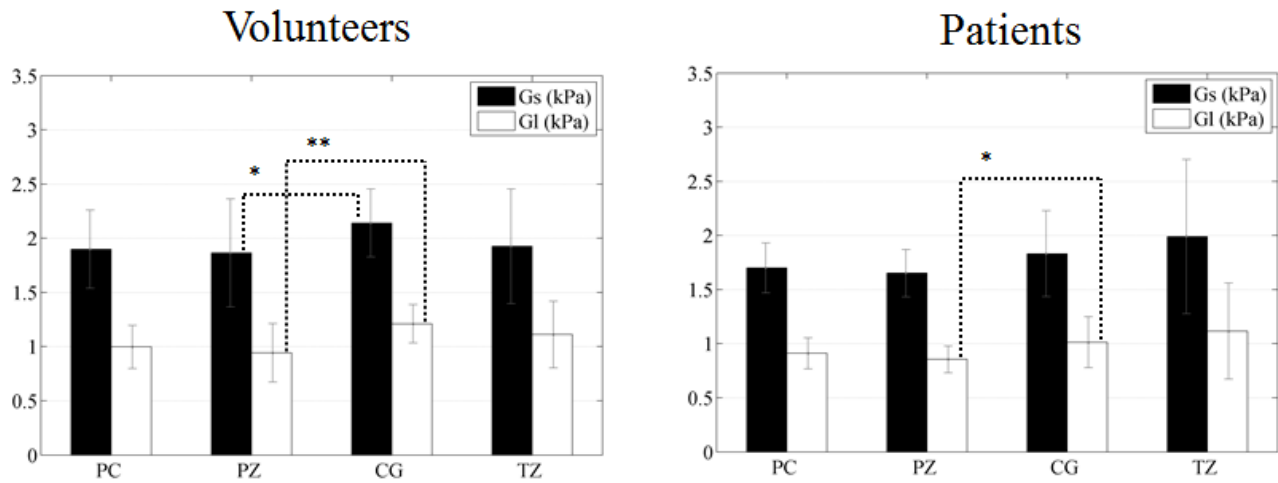
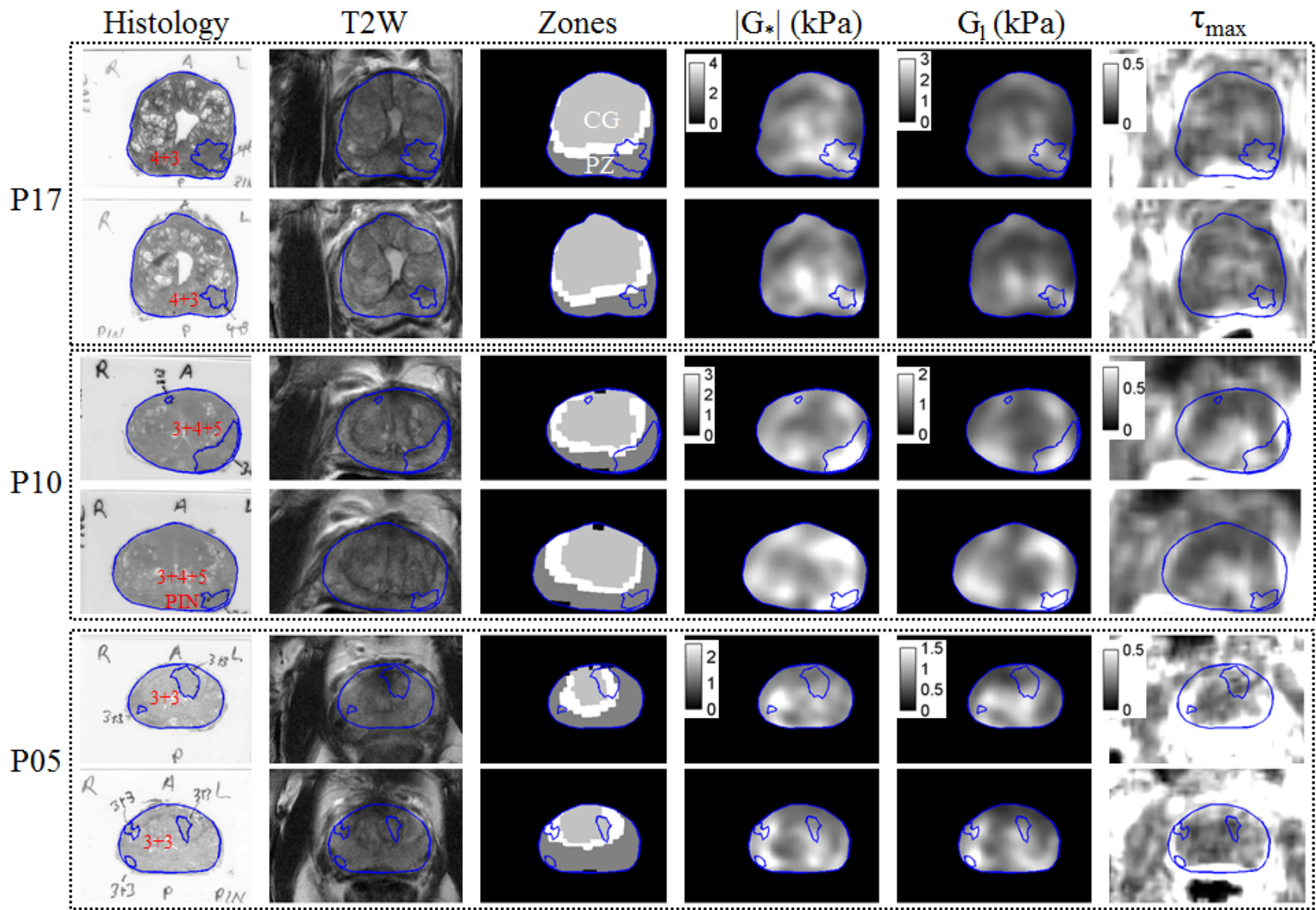


Figure 4-4. Average shear modulus  $G_s=|G|$  and loss modulus  $G_l$  in various zones of the prostate for volunteers and patients. (PC=prostate capsule, PZ=peripheral zone, CG=central gland, TZ=transition zone).

In terms of the quantitative study and comparison to whole mount, a hundred-and-forty-five tumors with a size between  $24 \text{ mm} \times 16 \text{ mm}$  and  $1.5 \text{ mm} \times 0.9 \text{ mm}$  (mean of  $9.4 \text{ mm} \times 5.5 \text{ mm}$ ) and Gleason score of at least 3+3 were analyzed. Figure 4-5 shows sample MRE results as registered to the pathology slides (two consecutive slides per case). The following images are shown: histology slides with marked tumors, registered T2-weighted anatomy, registered masks of the zones (PZ and CG), and registered  $|G|$ ,  $G_l$ , and  $\tau_{\max}$ . In terms of registration performance, area overlap between the segmented histology and registered segmented MR slices was  $95 \pm 5\%$ , and the error between landmarks on histology and the corresponding registered MR was  $2.0 \pm 1.5 \text{ mm}$ . As seen in the figure, the tumors can be visualized in the elasticity images in many cases even though in some cases they are not visible in the T2-weighted images. However, many false positives exist for many cases. For example in P17 (Gleason 4+3) and P10 (Gleason 3+4+5), the tumor on the patient left PZ can be appreciated in the shear moduli images (but not seen in T2 in P10). In P05 (Gleason 3+3) for example, the anterior CG tumor appears softer compared to the background, while the smaller tumors on patient right in PZ appear stiffer. In P04 (Gleason 3+3 and 3+4) for example, the tumors of on patient right PZ do no stand out while the left side appears much stiffer compared to the background. In P12 (Gleason 3+3) for example, the anterior tumors appear softer than the background. For more images refer to Appendix C.



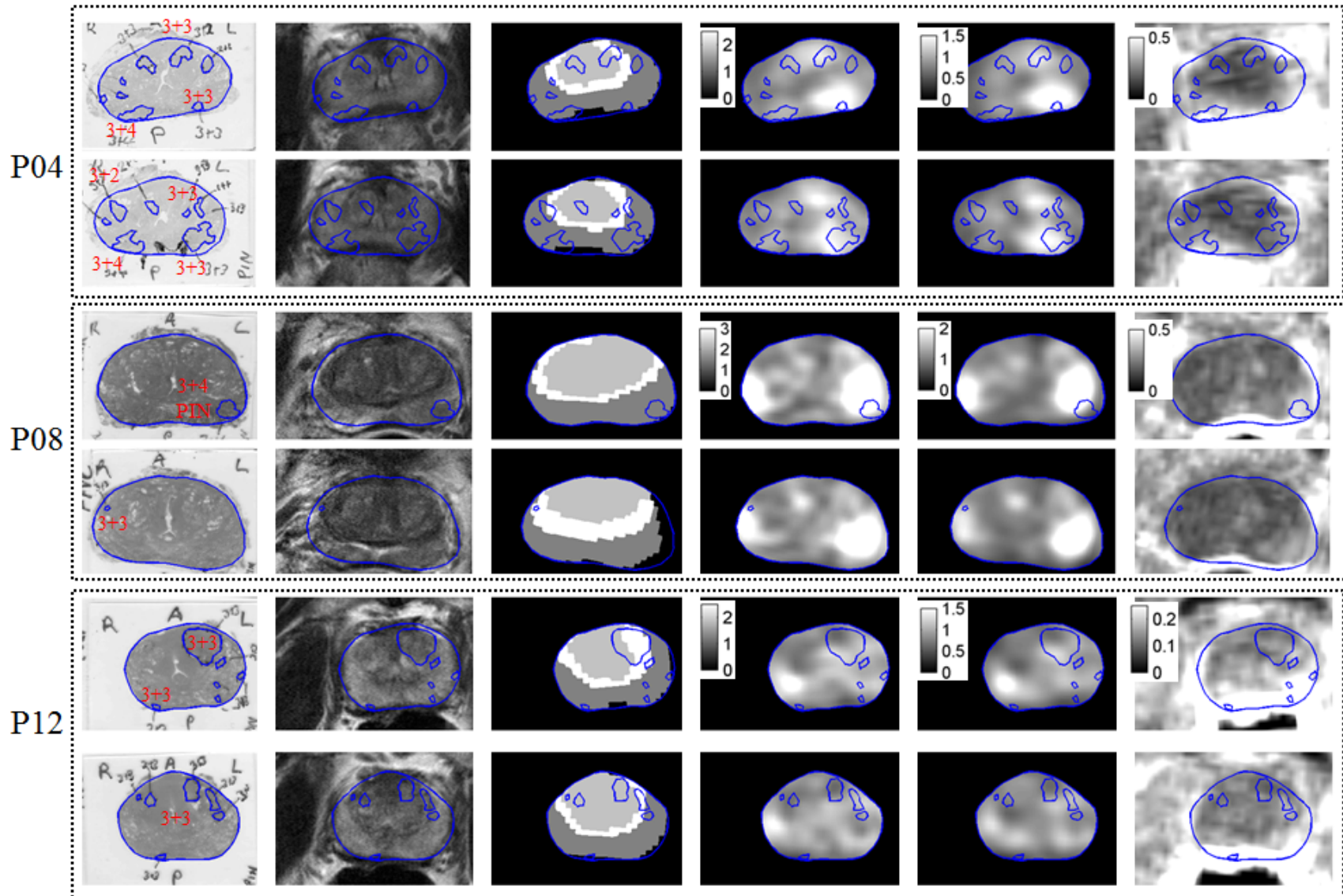


Figure 4-5. Sample results of shear moduli ( $|G|$  and  $G$ ) and maximum shear strain ( $\tau_{\max}$ ) as registered to histopathology slides.

Figure 4-6 shows average value of shear modulus in two regions of the prostate gland for normal and cancer tissue. Cancerous tissue with Gleason score at least 3+3 was significantly ( $p < 0.05$ ) different from normal tissue in ten out of eleven cases (91%) with tumors in PZ, and 5 out of nine cases (56%) with tumors in CG.

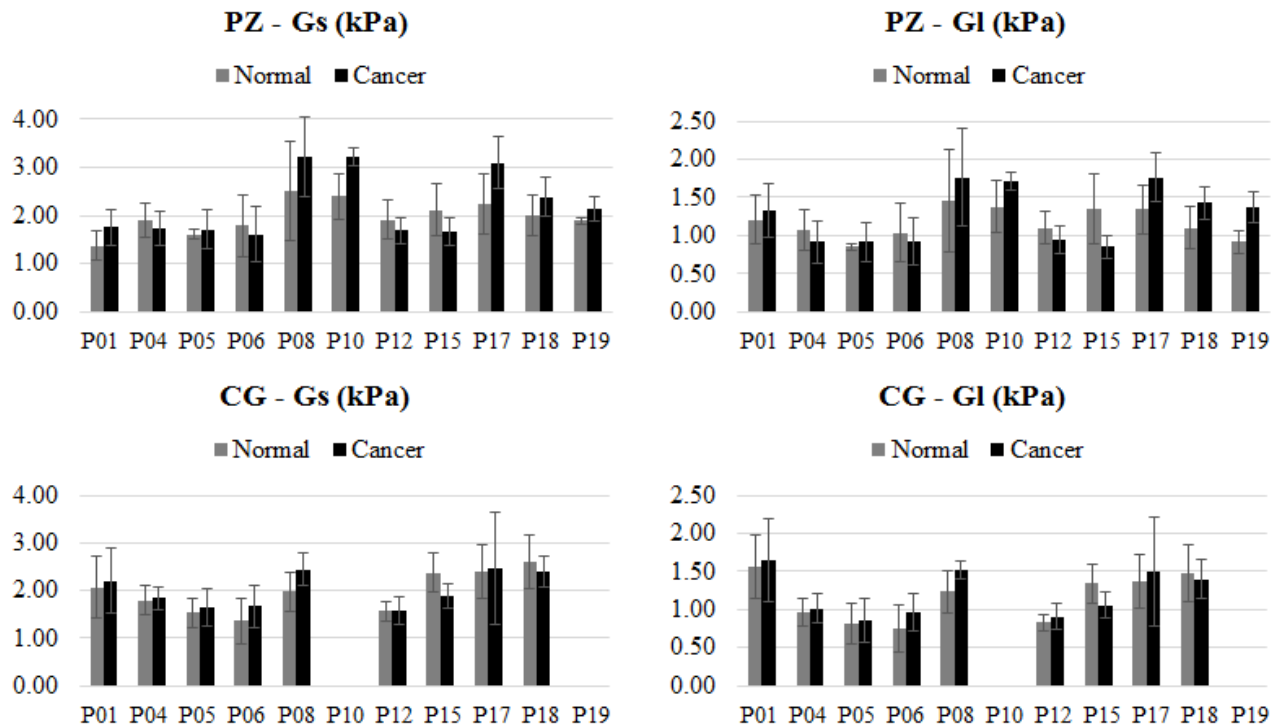


Figure 4-6. Normal versus cancer stiffness for each case in PZ and CG.

Figure 4-7 shows the receiver-operator-characteristic curve for each case in the two dominant zones of the prostate PZ and CG. The overall case-by-case averaged sensitivity (specificity) was 0.67 (0.68) for |G| and 0.68 (0.70) for G1 in PZ; 0.56 (0.57) for |G| and 0.58 (0.60) for G1 in CG. The corresponding AUC in PZ was 0.73 and 0.72, and in CG was 0.61 (0.62), for |G| and G1 respectively. Figure 4-8 shows the corresponding shear modulus histogram (normal vs tumor) in each case.

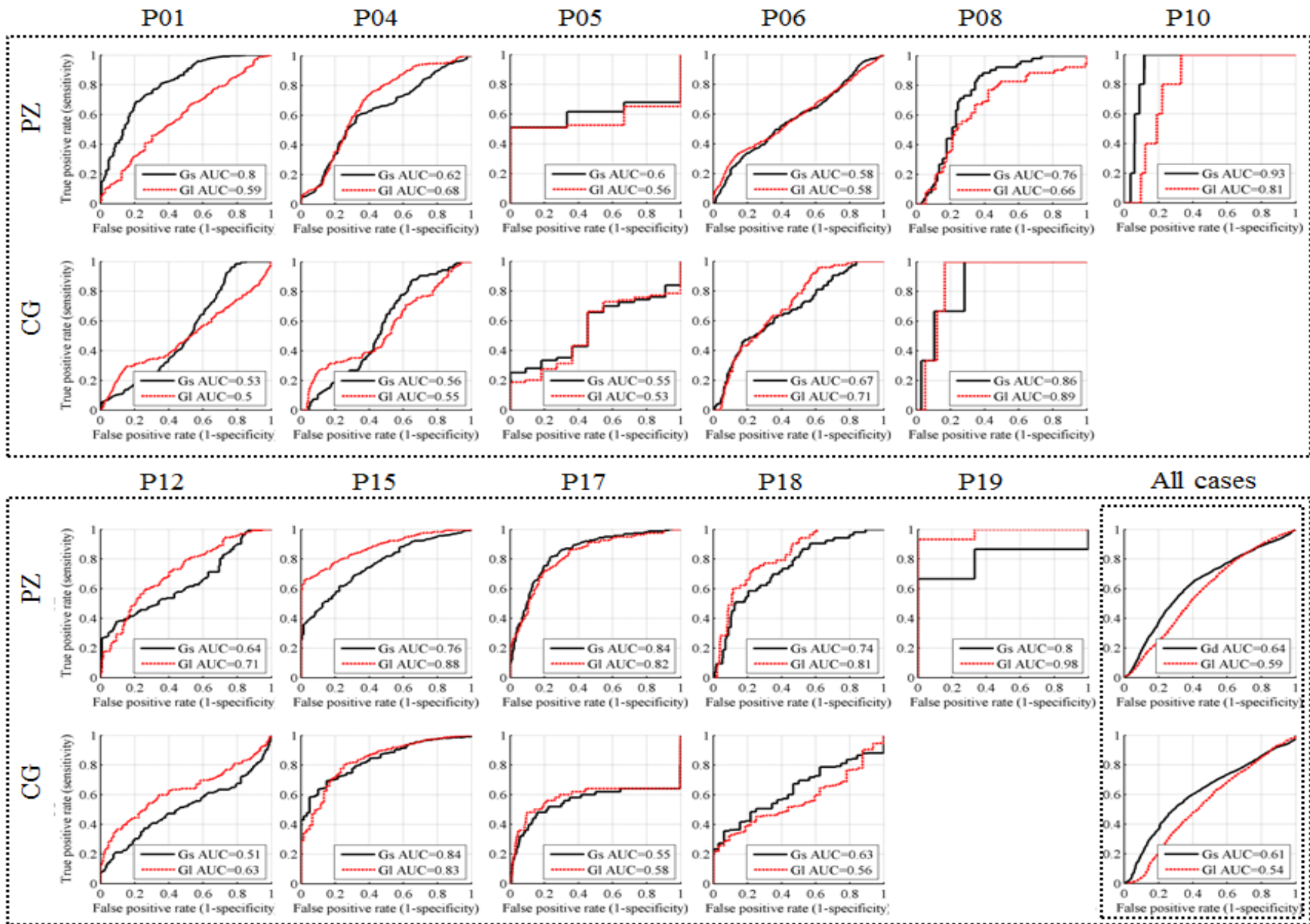


Figure 4-7. The receiver-operator-characteristic curve and the corresponding AUC is shown for each case for parameters Gs=|G| and GI in two dominant zones of the prostate PZ and CG.

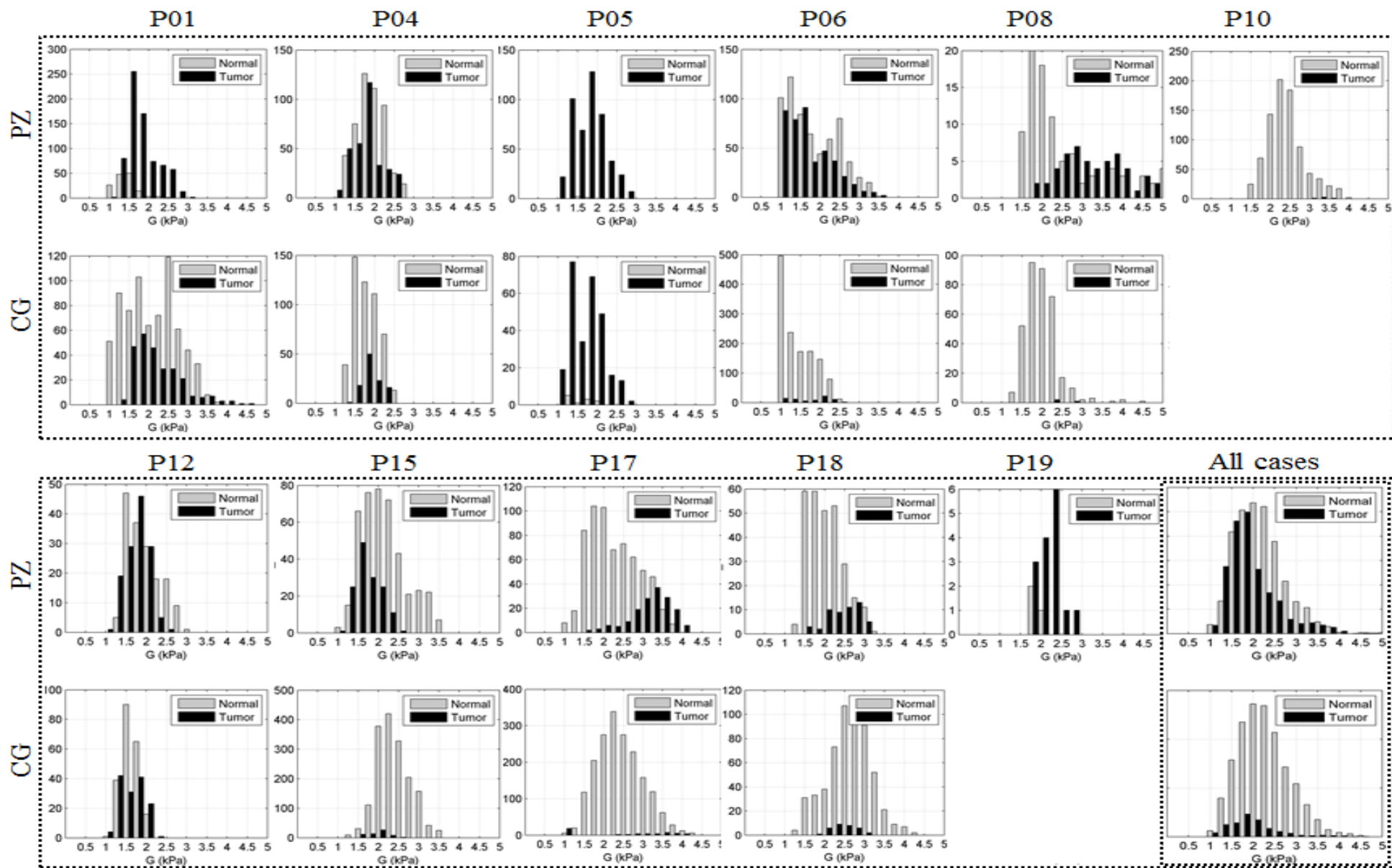


Figure 4-8. The histogram of tumor and normal tissue where the horizontal axis is the shear modulus  $G_d$  (kPa) and vertical axis is the number of bins.

The overall combined (pooled entire data) sensitivity (specificity) was 0.62 (0.62) for |G| and 0.57 (0.57) for GI in PZ; 0.60 (0.60) for |G| and 0.54 (0.54) for GI in CG. The corresponding AUC in PZ was 0.64 and 0.59, and in CG was 0.61 (0.54), for |G| and GI respectively. These lower results are due to the shifting baseline value of the shear modulus as observed in Figure 4-6.

## 4.4 Discussion

The quality metrics of the wave field allowed us to check for meaningful reconstruction of the viscoelastic maps. The quality metrics mainly involved PNR, total wave amplitude, non-linearity effects, and misalignment errors between each component of the displacement field.

The reconstructed  $|G|$  and  $G'$  images were registered to the histology slides with an error comparable to the in-plane resolution of the MRE experiments.

We found that the central gland (CG) was stiffer than the peripheral zone (PZ) in volunteers and patients. Cancerous tissue with Gleason score at least 6 was significantly ( $p < 0.005$ ) different from normal tissue in 91% of the cases with tumors in PZ and 56% with tumors in CG. Stiffer structures within the prostate may be mistaken for tumors, and the effect of other confounders such as benign prostatic hyperplasia (BPH), scarring from previous biopsy tracts, prostatic lithiasis (calcification), or androgen therapy on the mechanical parameters is not known. Even though many false positives existed, the absolute shear modulus was able to diagnose cancer with an averaged AUC of 0.73 in PZ and 0.72 in CG.

The prostate capsule was well delineated in the shear strain images. The shear strain did not appear show the tumors, but these result are preliminary. The shear strain maps are relative strain (as opposed to absolute shear stiffness images) and are shown for comparison only.

Most studies rely on biopsy and sectioned whole mount slides as a gold standard [54], [125]. Unfortunately, in these methods the spatially information is lost and the researcher has to guess the location of the biopsy or the section of the whole mount from the pathology report. In this study the ROC analysis was truly quantitative and objective since the comparison between the images and whole mount slides was applied on a voxel-to-voxel basis. The tumors were delineated not in the resulting images (T2,  $|G|$ ) but rather on the whole mount glass slides by the pathologists who was blinded from the results. Also, normal tissue was objectively defined as tissue surrounding the tumor with defined offsets.

In terms of limitations, though the overall MRE system is repeatable in phantoms (not shown in this study), in patient studies the voxel-to-voxel coefficient of repeatability was only 1.1 kPa. This represents a variation in the stiffness images of more than 25%. The volunteer study showed that the reconstruction maps are sensitive to small changes in the wave patterns in repeat cases. This is due to two effects. The first one is patient motion for this long acquisition process that presently takes at minimum 20 min for two consecutive scans. This is clearly observed in the ICC of the magnitude image alone was approximately 77%. This issue can be addressed by developing motion compensation algorithms and faster MRE sequences. The second reason is the nodes in the standing wave pattern, which are frequency dependent, affect the reconstructed stiffness maps. A  $\pm 2$  Hz shift in the frequency resulted in a coefficient of repeatability between 0.8 and 1.51 kPa. Also, patient motion played a big role in the voxel-to-voxel approach in the repeatability studies because the voxels did not corresponds to each other where patient motion up to 10.2 mm was recorded in some cases. This problem can

be addressed by using multi-frequency MRE to effectively average out the standing wave ripples. The effect of SNR and wave amplitude on biasing the shear stiffness maps have been discussed in [43], [115], but more studies are needed.

Another limitation of this study was the long mechanical wave length (between 15 and 35 mm) due to the 70 Hz excitation frequency. This limited the smallest detectable tumor. Trans-perineal excitation beyond 100 Hz may not be feasible due to the high attenuation of the waves near the perineum. Though lesions smaller than the mechanical wavelength can be detected, this comes at the expense of larger error in stiffness reconstruction. This issue may be addressed either by improving the current trans-perineal method (higher frequencies, using multi-frequency excitation and increasing PNR by improving sequence) or employing a trans-rectal transducer which enable higher excitation frequencies [56]. Another potential solution maybe to use the longer wavelengths for strain reconstruction.

Also, note that this is a preliminary small patient study, and due to patient selection for radical prostatectomy only medium grade cancers are studied here.

## **4.5 Case studies**

Using the exact same patient setup, two repeatability studies were performed to demonstrate that (i) the sensitivity of the reconstruction on small wave pattern changes, and (ii) the repeatability does improved with a faster acquisition sequence.

### **4.5.1 Repeatability in phantom (200±6 Hz frequency shift)**

For the phantom was images at three frequencies 194, 200, 206Hz. This is a percentage change of 3% which is equivalent tests performed at 70±2 Hz in volunteers. The purpose of this test is to get an idea about the sensitivity of the reconstruction to changes in the wave pattern.

The wave images and the reconstructed stiffness image for each experiment is shown in Figure 4-9. The percentage difference images and the Bland-Altman plots comparing the cases is shown in Figure 4-10. This figure shows that comparing 194Hz and 200Hz the coefficient of repeatability (CR) is 1.5 kPa and the intraclass-correlation coefficient (ICC) is 97%. Comparing 200 Hz and 206 Hz CR was 1.4 kPa and ICC was 98%. Comparing 194 Hz and 206 Hz, CR was 1.1 kPa and ICC was 98%. The voxel-by-voxel percentage difference for all cases was 7±10%. The results in this case study show that the methods are very repeatable and not sensitive to small wave pattern effects in phantoms (where no motion is present).

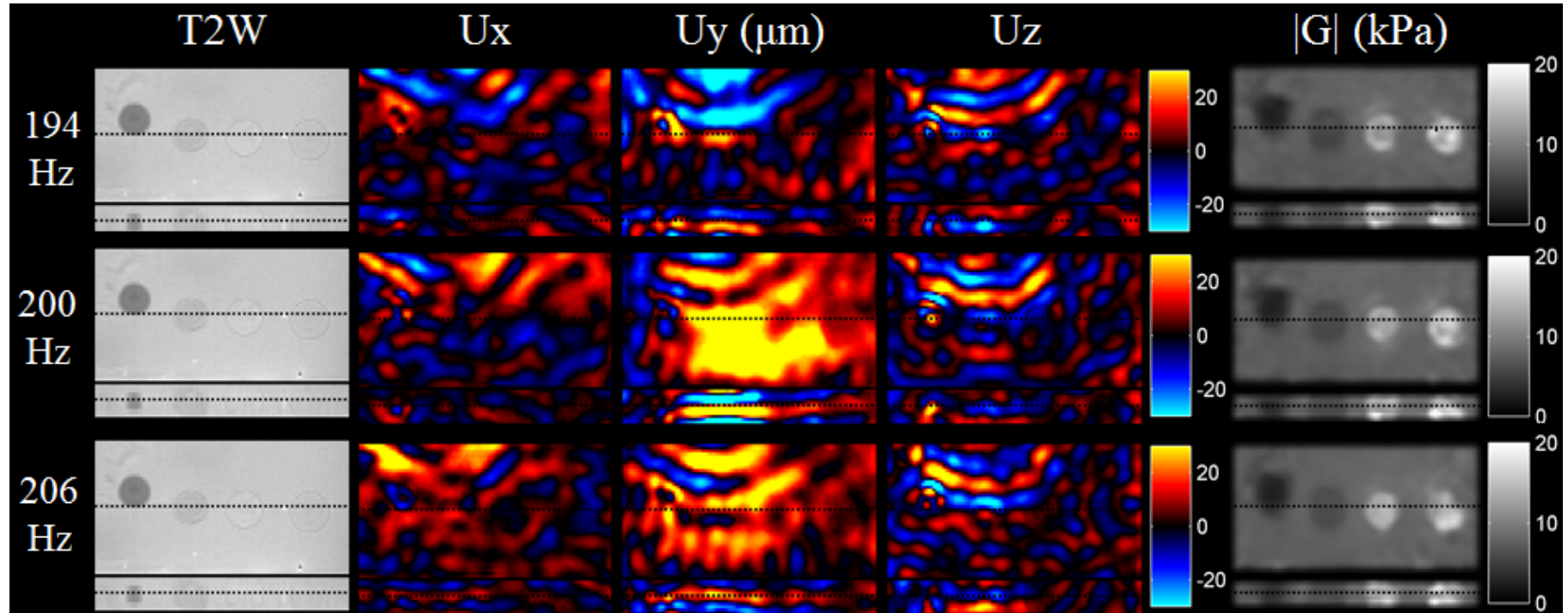


Figure 4-9. Phantom repeat studies at 194 Hz, 200 Hz and 206 Hz. The T2-weighted, 3D waves, reconstructed shear modulus  $|G|$  are shown for each case.

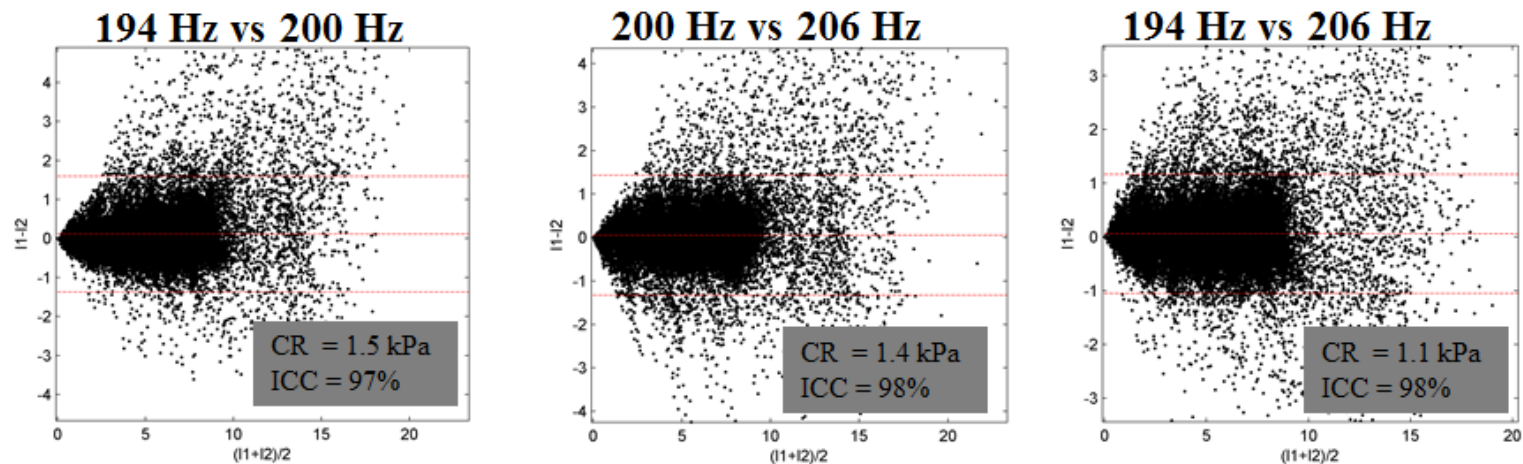
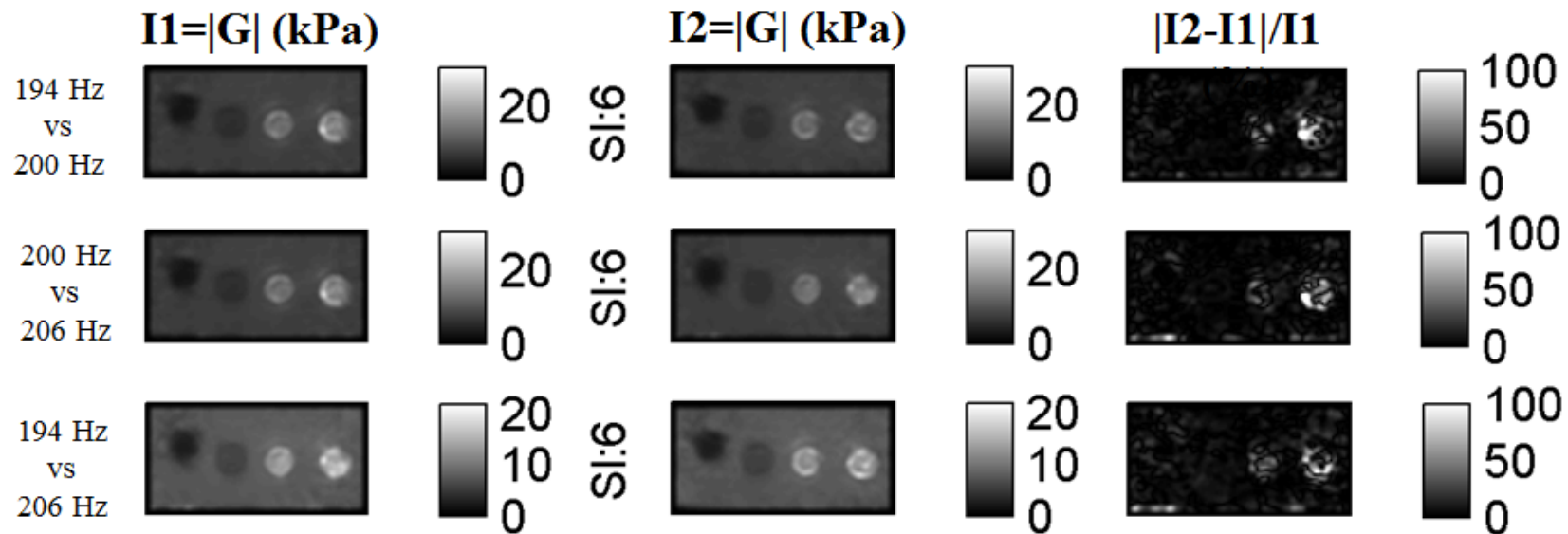


Figure 4-10. The top row shows the pair-wise comparison for the three experiments. In each case the reconstructed shear modulus is shown, and on the right the voxel-by-voxel percentage difference is shown. The percentage difference was an average of 7% for all cases. The bottom row shows the Bland-Altman plots for these experiments where the coefficient of repeatability and Intra-class coefficient are marked on each plot. The results show that the methods are very repeatable for small changes in the mechanical excitation frequency (and wave pattern effects) in phantoms.

## **4.5.2 Repeatability in Volunteers**

To demonstrate that the repeatability of the results can be improved with faster acquisition, several tests were performed on a volunteer using a modified scan. To speed up the sequence the number of slices was reduced from 24 to 9, and the number of mechanical phase shifts was reduced from 8 to 4. This allowed the acquisition time to be reduced from 10 min to just 2 min for the full 3D displacement data (in other words 4X speed up). Another way to speed up the sequence would be to use an EPI readout on top of the eXpresso sequence. After implementing this method, though it increased the acquisition speed by 2-3 times, the images suffered from geometric distortions and poor wave encoding in the subjects, thus this method was not used.

### **4.5.2.1 Repeat 70 Hz with 4X faster acquisition**

In the first experiment with the faster sequence, a volunteer was imaged 3 times at 70 Hz with exactly the same settings for all experiments.

The repeatability results are shown in Figure 4-11. The voxel-by-voxel percentage difference images show an average change of 13% to 21% for successive images at 70 Hz. The coefficient of repeatability ranges from 0.3 kPa to 0.58 kPa, while ICC consistently stays above 97%. This result is in sharp contrast to repeatability results acquired using the original sequence. Sample results for the original repeatability study is shown in Figure 4-12. The percentage difference ranged between 18% to 27%, CR ranged between 0.8 to 1.5 kPa, and ICC ranged between 73% to 88%.

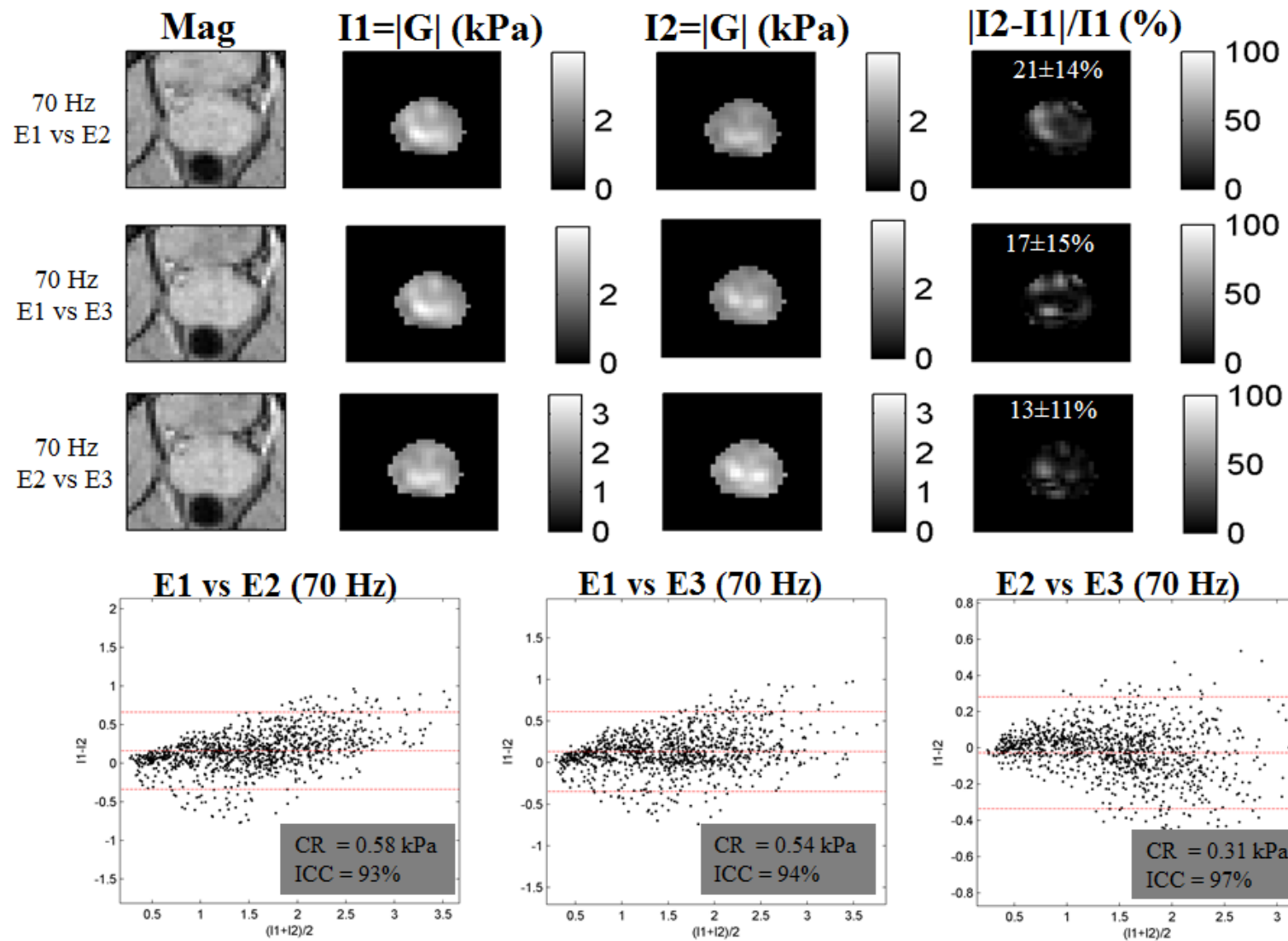


Figure 4-11. The top row shows the pair-wise comparison for the three experiments at 70 Hz in a volunteer using a faster scan. In each case the reconstructed shear modulus is shown, and on the right the voxel-by-voxel percentage difference is shown. The bottom row shows the Bland-Altman plots for these experiments where the coefficient of repeatability and Intra-class coefficient are marked on each plot.

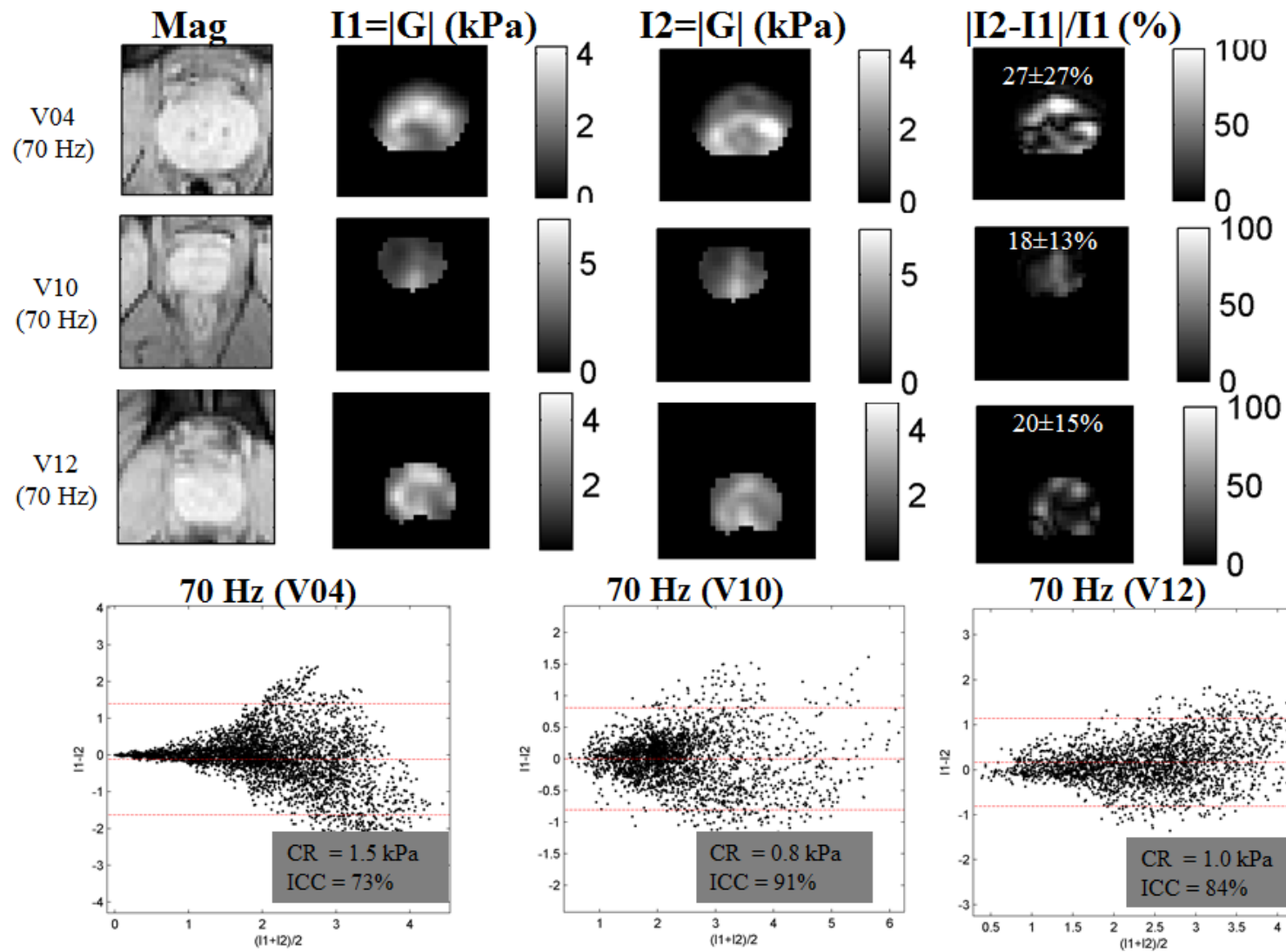


Figure 4-12. The top row shows the pair-wise comparison for the three experiments at 70 Hz in three volunteers using a the original. In each case the reconstructed shear modulus is shown, and on the right the voxel-by-voxel percentage difference is shown. The bottom row shows the Bland-Altman plots for these experiments where the coefficient of repeatability and Intra-class coefficient are marked on each plot.

#### **4.5.2.2 Repeat $70\pm 2$ Hz with 4X faster acquisition**

In the second experiment with the faster sequence, a volunteer was imaged 3 times (once at 68Hz, once at 70 Hz and once at 72 Hz). All other settings were kept the same for all experiments.

The repeatability results are shown in Figure 4-13. The voxel-by-voxel percentage difference images show an average change of 12% to 18% for repeat images with  $\pm 2$  Hz frequency shift. The coefficient of repeatability ranges from 0.3 kPa to 0.47 kPa, while ICC consistently stays above 93%. These results are similar to repeat studies at 70 Hz with the faster acquisition sequence. However, this result is again in sharp contrast to repeatability results acquired using the original sequence at  $70\pm 2$  Hz. Sample results for the original repeatability study is shown in Figure 4-14. The percentage difference ranged between 15% to 22%, CR ranged between 1.0 to 1.1 kPa, and ICC was around 88%.

These results show that the repeatability can be improved by approximately 2 times by reducing the acquisition time by 4 times.

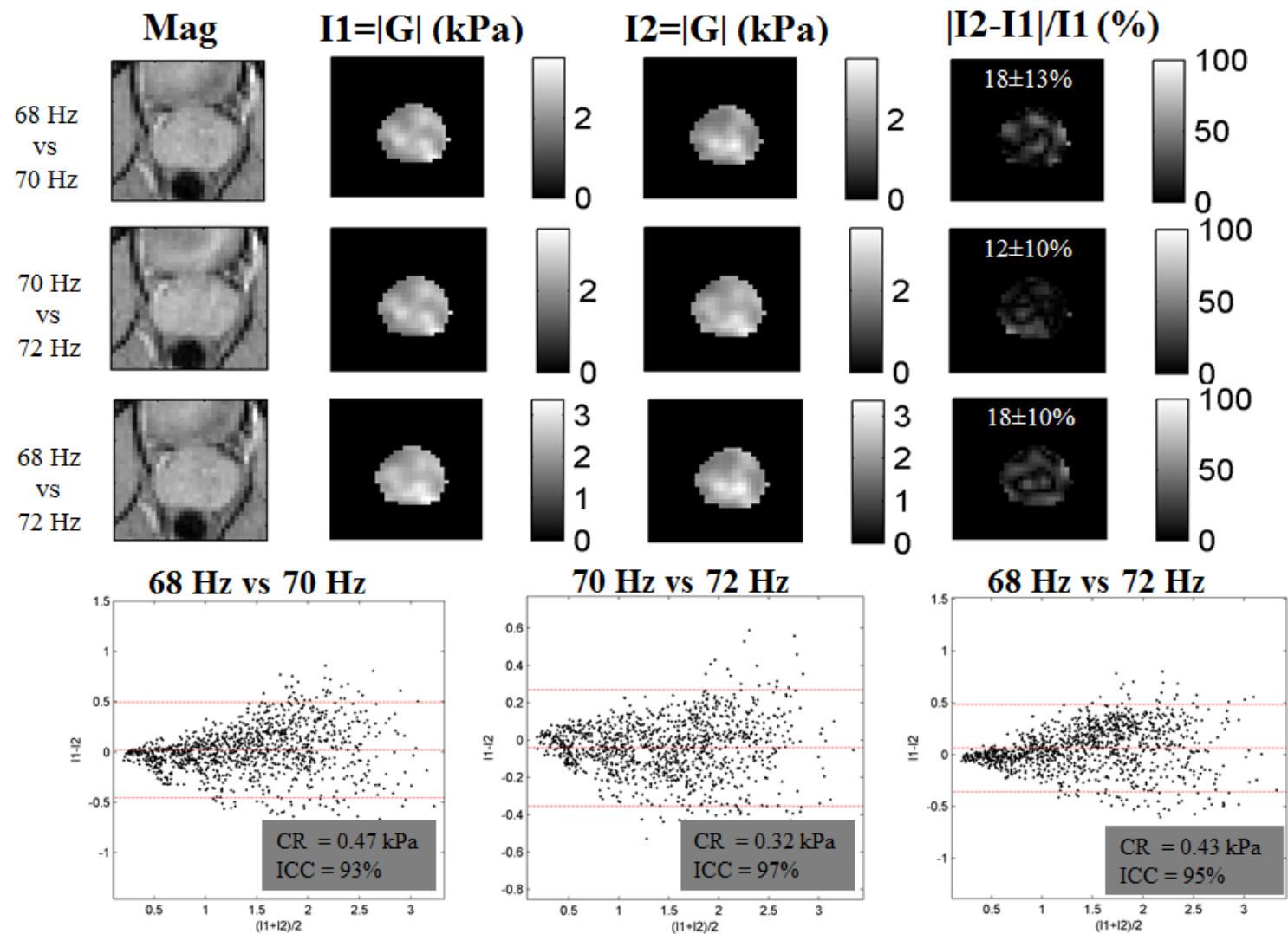


Figure 4-13. The top row shows the pair-wise comparison for the three experiments (68Hz, 70 Hz and 72 Hz) in a volunteer using a faster scan. In each case the reconstructed shear modulus is shown, and on the right the voxel-by-voxel percentage difference is shown. The bottom row shows the Bland-Altman plots for these experiments where the coefficient of repeatability and Intra-class coefficient are marked on each plot

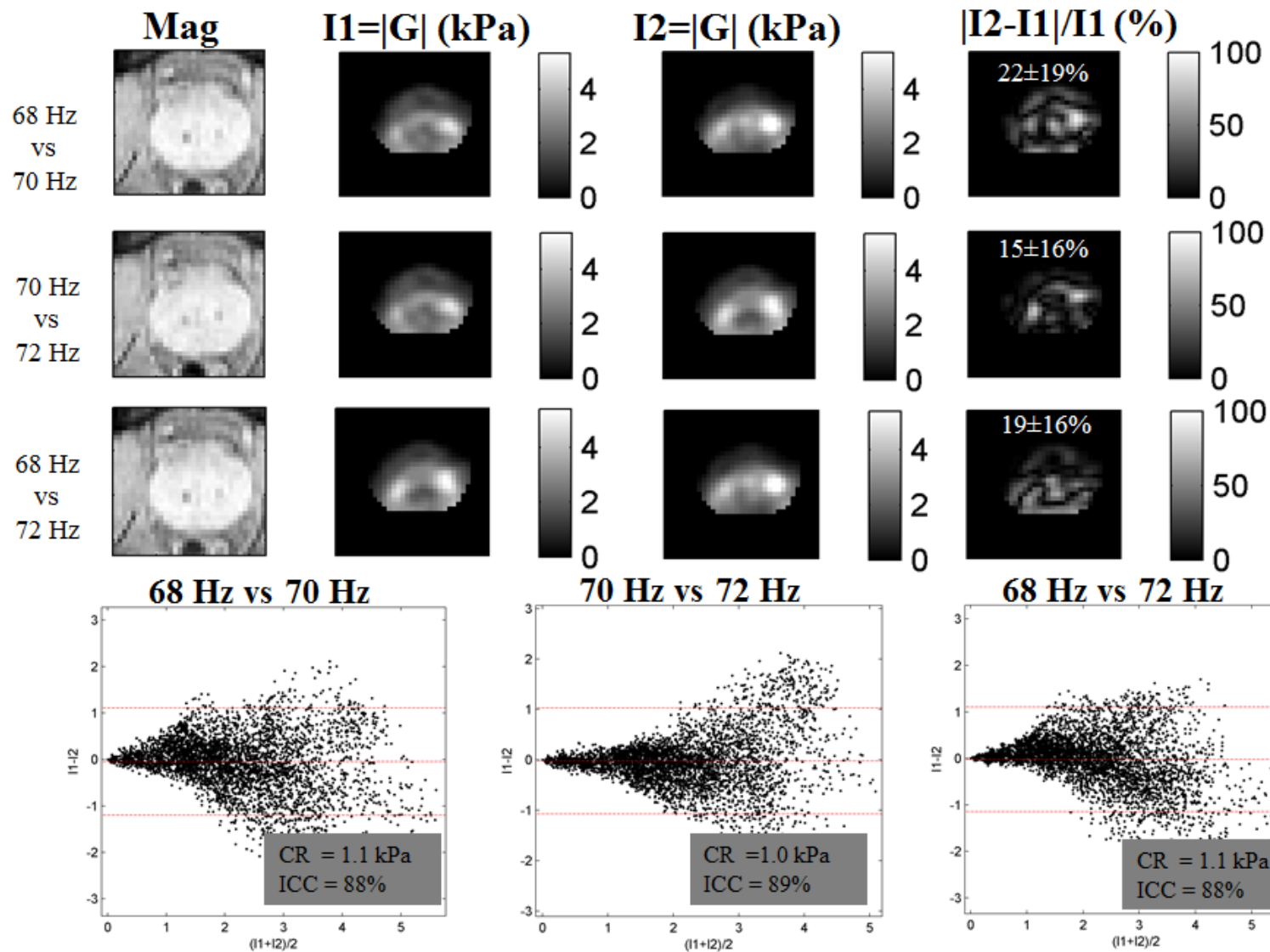


Figure 4-14. The top row shows the pair-wise comparison for the three experiments (68Hz, 70 Hz and 72 Hz) in volunteers using the original scan. In each case the reconstructed shear modulus is shown, and on the right the voxel-by-voxel percentage difference is shown. The bottom row shows the Bland-Altman plots for these experiments where the coefficient of repeatability and Intra-class coefficient are marked on each plot

## 4.6 Conclusion

In conclusion, the work in this chapter presents the first prostate cancer MRE study where the results are compared to histopathology. Even though many false positives existed, the absolute shear modulus was able to diagnose cancer with an average AUC of 0.73 in PZ and 0.72 in CG. Cancerous tissue was not always stiffer than normal tissue. It was observed that the inversion algorithm was sensitive to i) vibration amplitude and displacement nodes, and ii) misalignment of the 3D wave field due to subject movement. This made voxel based analysis of the shear modulus reliable only when the patient movement was at a minimum. The repeatability of the MRE system may be improved by employing multi-frequency excitation to reduce standing wave ripples.

# Chapter 5 - *Ex-vivo* prostate cancer MRE and diffusion-weighted imaging: quantitative comparison to histopathology

## 5.1 Introduction

This chapter is dedicated to *ex-vivo* prostate cancer MRE. First, the setup and transducer mechanism of the 7T MRE system developed for this work are described. The methods were validated in a phantom study. This system was then used in a patient study to assess the diagnostic power of mono- and multi-frequency MRE and diffusion weighted imaging (DWI) alone and combined to diagnose cancer. The results were compared to whole mount histopathology marked by the Gleason score. This study presents the first work in the literature to compare MRE and DWI of *ex-vivo* prostate cancer with whole mount histopathology. Finally, the limitations of this study are presented in the discussion section.

## 5.2 Methods

### 5.2.1 Patient study

Ethics board approval and informed consent were obtained from fourteen patients scheduled for radical prostatectomy recruited between December 2011 and February 2013. Clinical data including fixation time, gland size, prostatectomy Gleason scores, and clinical stage, the number and size of tumors, and notes from Pathology for the sixteen patients who had biopsy confirmed cancer are summarized in Table 5-1. Following surgery, the prostate specimens were immersed in formalin for various times as listed in Table 5-1. The MRI experiments were performed after the fixation process. In two cases, incomplete data was acquired due to technical issues (overheating of gradient coil, damaged mechanical transducer) and were not included in the study. In one patient (P13) the Gleason score was not assigned by the pathologist due to previous androgen therapy, and thus was not included in the analysis. The analysis in this thesis is performed on the remaining twelve patients (mean age of 66 yrs).

**Table 5-1. Clinical data for patients with biopsy confirmed cancer. (NPH=Nodular prostatic hyperplasia, PIN=Prostatic Intraepithelial neoplasia, PNI= Perineural invasion, SV= seminal vesicles, PUE=Prostatic Urethral Ectasia, BPU=Benign prostatic urothelium).**

| Case | Age (yr) | fixation (hrs) | Gland size (gr) | Gleason Score | Clinical Stage | # Tumors (size range mm) | Pathology  |
|------|----------|----------------|-----------------|---------------|----------------|--------------------------|--|
| P01  | 61       | 24             | 48              | 4+3 (PZ)      | pT2c           | 8<br>(4-20)              | NPH, PIN   |
| P04  | 71       | 84             | 61              | 3+4 (PZ)      | pT2c           | 7<br>(2-9)               | PNI, PIN, NPH, irregular nodule 10mm in left PZ  |
| P05  | 59       | 72             | 32 (no SV)      | 3+3 (CG)      | -              | 5<br>(3-8)               | PIN, NPH, cyst (15mm) with calcification in TZ   |
| P06  | 63       | 82             | 65              | 4+3 (PZ)      | pT3b           | 5<br>(2-11)              | PNI, PIN,NPH   |
| P08  | 66       | 96             | 64              | 3+4 (PZ)      | pT2c           | 3<br>(2-7)               | PNI, PIN, NPH, irregular nodule 5mm right PZ base  |
| P09  | 67       | 48             | 86              | 3+3 (CG)      | pT2a           | 2<br>(3)                 | PIN, scars from biopsy, BPH with fibriadenoma-like pattern                                     |
| P10  | 72       | 72             | 34              | 3+4 (PZ)      | pT2c           | 5<br>(2-9)               | prominent PIN, PIN, NPH, irregular nodule anterior, irregular mottling 10m PZ base             |
| P11  | 69       | 24             | 40              | 3+4 (CG)      | pT3a           | 15<br>(2-15)             | PIN, NPH, irregular yellowish nodule left anterior PZ  |
| P13  | 76       | 36             | 74              | NA            | pT2a           | 6<br>(3-7)               | Pre-op androgen therapy, 8-month withdrawal  |
| P16  | 70       | 72             | 72              | 3+4 (PZ)      | -              | 11<br>(2-9)              | PNI, PIN, NPH, scars from biopsy   |
| P17  | 70       | 96             | 53              | 4+3 (PZ)      | pT2a           | 4<br>(4-11)              | PIN, PUE, scars from biopsy, NPH, cystic atrophy, Transurethral Curettage                      |
| P18  | 53       | 96             | 39              | 4+3 (PZ)      | pT2c           | 6<br>(1-6)               | PIN,NPH, BPU, 1 cm cyst  |
| P19  | 53       | 72             | 53              | 4+4 (PZ)      | pT3c           | 13<br>(2-18)             | PNI, PIN, BPU, 1 cm utricular cyst,  |
| P20  | 60       | 48             | 111             | 3+4 (PZ)      | pT2c           | 22<br>(1-8)              | PIN, NPH, BPU, scars from biopsy, benign cyst, compression of PZ by hyperplastic nodules of TZ |

## **5.2.2 Mechanical transducer and experimental setup**

Figure 5-1 shows the electromagnetic transducer designed for this study. The actuation source of the transducer consists of two counter-wound concentric coils with the same geometry as the transducer introduced in Chapter 2 of this thesis. When placed in the magnetic field of the MRI scanner (as shown in Figure 5-1a and b), the inner coil exerts a torque proportional to its current, producing an almost linear mechanical motion in the excitation rod. This driver has several quick release and adjustment mechanisms to facilitate rapid setup of the experiments. The adjustment plate attached directly to the main magnet allows for vertical centering of the transducer. The vibration is coupled to the specimen via an 8 mm diameter rigid carbon-fiber tube. A constant compression of approximately 5 N is applied to the specimen by an adjustable spring on the transducer.

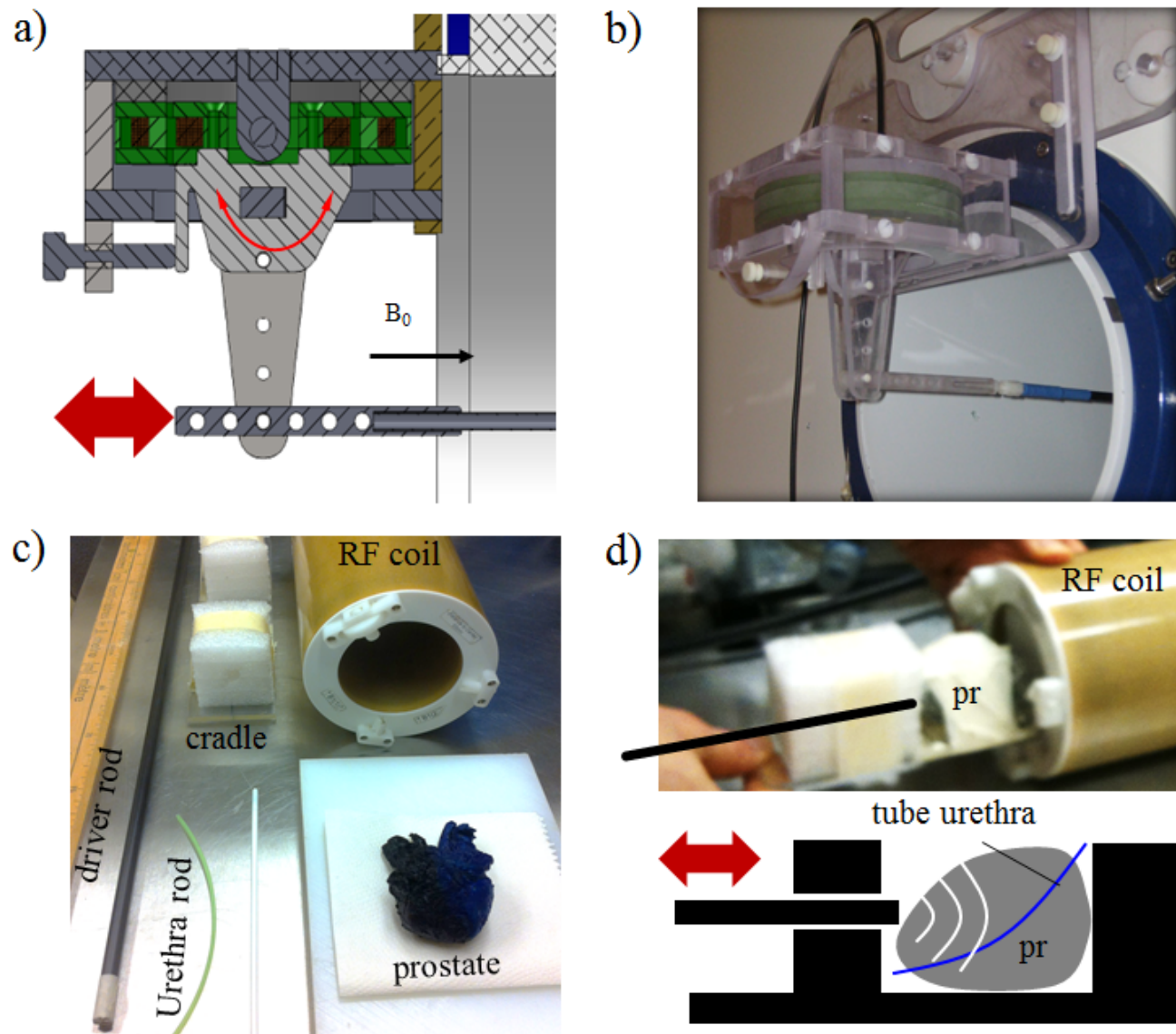


Figure 5-1. a) The custom made mechanical transducer consists of a swiveling current-carrying coil that generates linear vibrations when the transducer is placed in the fringe field of the MR scanner. b) shows a photo of manufactured transducer as attached to the scanner outside the bore. c) The prostate specimen (with a rod inserted in the urethra) is placed on a cradle that is inserted into the RF coil. d) The transducer rod is a carbon-fiber tube that on one side is pressing on the apex of the prostate and on the other side is fastened to the transducer.

The *ex-vivo* prostate specimen is placed in a sealed plastic bag with 2 mm diameter plastic rod inserted in the urethra as shown in Figure 5-1c and d. The anterior of the specimen is placed flush against a plastic cradle with the vibration applied to the apex. The specimen is taped to the cradle to ensure that it remains in place when the mechanical excitation is applied. The cradle is then inserted into the RF coil and secured by tape. Once the RF coil is centered in the iso-center of the scanner, the transducer rod is introduced into the cradle, fastened to the transducer, and the pre-compression is adjusted to ensure proper mechanical coupling.

### 5.2.3 Acquisition

MRI: All MRI experiments were carried out on a 7-Tesla animal scanner (Bruker BioSpin GmbH., Ettlingen, Germany). A standard quadrature RF coil with inner diameter of 60 mm was used. The gradient coils can generate gradient fields up to 400 mT/m with 0.1 ms rise time. A T2-weighted Rapid Acquisition with Refocused Echos (RARE) sequence with an echo time of 70 ms, repetition time of 5 s, and RARE factor 8 was used. The transverse images were planned such that they were perpendicular to the urethra (apparent with the inserted plastic rod) and also perpendicular to the floor of the cradle. This ensured that the histology cuts are parallel to the acquired images. All subsequent images have the same orientation as this T2-weighted image. The total imaging time was 2.5 hours.

MRE: For MRE imaging, a conventional motion-sensitized spin-echo pulse sequence was used ( $G_{\max} = 200$  mT/m) (provided by Dr. Ralph Sinkus [126]). For the first five cases, the 3D wave field was acquired on 9 slices for a  $64 \times 64$  matrix with  $1 \text{ mm}^3$  isotropic voxels. The mechanical displacement was sampled at 8 time points per period. The heat buildup in the gradient coils limited our initial efforts to image the entire gland. For the cases performed after a hardware upgrade (gradient coils and chiller), the 3D wave field was acquired on more than 20 slices (entire prostate gland) for a  $64 \times 64$  matrix with 1 mm in-plane resolution and 2 mm slice thickness. The mechanical displacement was sampled at 4 time points per period. Echo times from 35 ms to 50 ms and repetition times between 0.8-1.2 s were used. For mono frequency experiments, the mechanical excitation was 800 Hz. In six cases (P06, P08, P09, P18, P19, P20) multi-frequency experiments were performed at three acquisition frequencies of 600, 800 and 1000 Hz. The imaging time was 22 min per frequency.

DWI: for the diffusion-weighted imaging, the acquisition field of view was matched to the MRE experiments but the in-plane resolution was doubled to 0.5 mm. Four b-values of 250, 500, 750 and 1000  $\text{s/mm}^2$  with echo time of 21 ms and repetition time of 3.9 s were used. The apparent-diffusion coefficient (ADC) map was calculated based on a mono-exponential fit to the magnitude images of the diffusion-weighted sequence on a per-pixel basis. The imaging time was approximately 21 min. The DWI study was not performed for cases P01, P04 and P10 due to time limitations.

## 5.2.4 Image processing

A voxel was marked invalid if (i) its magnitude in the image was below a threshold of 10% of the average magnitude; or (ii) the total wave amplitude  $U_{tot}$  was less than  $0.5 \mu\text{m}$ .

The dynamic shear modulus  $G_d$  and loss modulus  $G_l$ , and complex modulus  $G_s$  were calculated by local inversion of the linear viscoelastic 3D wave equation [122]. The frequency,  $\omega$ , dependence of each parameter, modeled by a power law ( $G \propto \omega^\gamma$ ), was assessed using the exponent parameter  $\gamma$ .  $\gamma$ - $G$  refers to the power law exponent for  $G_d$ , and  $\gamma$ - $G_l$  refers to the power law exponent of  $G_l$ .

## 5.2.5 Quality metrics for 3D wave field

Similar to the previous chapter, several parameters were calculated from each data set to evaluate the quality of the acquired wave field. The quality metrics are tabulated in Table 5-2 for the patient study. For more images of the raw waves refer to Appendix D.

Table 5-2. Quality metrics for the patient study at 800 Hz.

| Case          | PNR (dB) | Wave Ampl. ( $\mu\text{m}$ ) | Total Harmonic Distortion (%) | Displacement Misalignment error (mm) |      |      |                                 |      |      |                                 |      |      |
|---------------|----------|------------------------------|-------------------------------|--------------------------------------|------|------|---------------------------------|------|------|---------------------------------|------|------|
|               |          |                              |                               | U <sub>x</sub> - U <sub>y</sub>      |      |      | U <sub>x</sub> - U <sub>z</sub> |      |      | U <sub>y</sub> - U <sub>z</sub> |      |      |
|               |          |                              |                               | x                                    | y    | z    | x                               | y    | z    | x                               | y    | z    |
| P01           | 12.9     | 62                           | 52                            | 0                                    | 0    | 0    | 0.04                            | 0    | 0    | 0.04                            | 0    | 0    |
| P04           | 15.9     | 151                          | 21                            | 0.04                                 | 0.04 | 0.04 | 0                               | 0    | 0    | 0.04                            | 0    | 0.04 |
| P05           | 14.8     | 104                          | 30                            | 0                                    | 0.04 | 0.12 | 0                               | 0.04 | 0.08 | 0                               | 0.08 | 0.2  |
| P06           | 11.9     | 63                           | 47                            | 0                                    | 0    | 0.15 | 0                               | 0    | 0    | 0                               | 0    | 0.15 |
| P08           | 13.5     | 76                           | 55                            | 0                                    | 0.04 | 0    | 0                               | 0    | 0    | 0.04                            | 0    | 0.08 |
| P10           | 15.1     | 53                           | 24                            | 0                                    | 0    | 0    | 0                               | 0    | 0    | 0                               | 0.03 | 0    |
| P11           | 17.0     | 51                           | 92                            | 0                                    | 0    | 0    | 0                               | 0    | 0    | 0                               | 0    | 0    |
| P13           | 13.7     | 34                           | 53                            | 0.04                                 | 0    | 0    | 0                               | 0.04 | 0    | 0.04                            | 0.04 | 0    |
| P16           | 24.2     | 219                          | 12                            | 0                                    | 0    | 0    | 0                               | 0    | 0    | 0                               | 0    | 0    |
| P17           | 19.6     | 84                           | 3                             | 0                                    | 0    | 0    | 0                               | 0    | 0    | 0                               | 0    | 0    |
| P18           | 22.1     | 150                          | 2                             | 0                                    | 0    | 0    | 0                               | 0    | 0    | 0                               | 0    | 0    |
| P19           | 17.1     | 62                           | 3                             | 0                                    | 0    | 0    | 0                               | 0    | 0    | 0                               | 0    | 0    |
| P20           | 17.2     | 45                           | 4                             | 0                                    | 0    | 0    | 0                               | 0    | 0    | 0                               | 0    | 0    |
| Mean patients | 17 ± 4   | 89 ± 54                      | 31 ± 28                       | 0.01                                 | 0.01 | 0.02 | 0.00                            | 0.01 | 0.01 | 0.01                            | 0.01 | 0.04 |

## 5.2.6 Histology, registration and data analysis

Histology: Following surgery, the prostate gland is immersed in formalin solution until the day of the MRI imaging study (70 hrs on average). The fixation time ranged between 24 and 96 hours. In cases where the gland was large, the formalin was injected into the gland using a syringe. After imaging, the specimens were sliced at 4 mm intervals similar to methods discussed by [123] using a custom cutting device, in an attempt to align the histology slides with the transverse images. The slices were then sent for whole mount histology, where an experienced pathologist (Dr. Edward Jones) marked the outline of the tumours, along with the Gleason score, on the histology slides.

Registration: The outline of the prostate was segmented on the histology slides and the T2-weighted images. An experienced radiologist verified the segmentations. The 2D segmented contours of the histopathology were then registered to the surface of prostate that was extracted from the segmented T2-weighted volume [124]. The segmentation method [124] uses particle filtering to minimize the Euclidean distance between the contours and the surface with respect to in-plane translation and rotation of each histology slice alone, and out-of-plane translation and rotation of all the slices together.

ROC analysis: The analysis was performed using MATLAB<sup>®</sup> (Mathworks Inc., USA) software. For each case, the tumors marked with the Gleason score were outlined in Stradwin (Medical Imaging Group, Cambridge University, UK) to generate binary masks. The prostate capsule (PC), peripheral zone (PZ), central gland (CG) and transition zone (TZ) were identified in the T2-weighted images by the author (some cases were verified by an experienced radiologist) for zonal analysis. After the registration process, the calculated transformation was applied to the images (T2-weighted, Gd, Gl, ADC) as well as masks to transform them to the histology slide coordinates. For tumors smaller than 4 mm in diameter the mask was dilated by approximately 1.5 mm, and for tumors larger than 8 mm the mask was eroded by approximately 1.5 mm. This was done to account for errors such as registration misalignments, and enable analysis of smaller tumors. Depending on the zonal masks (PC, PZ and CG), the mask for normal tissue was calculated by removing all the tumors marked in the histology slides and eroding the masks by approximately 3.5 mm. The analysis for each case was performed by dividing the data in windows (size between 5-6 mm) with 10% overlap between subsequent windows. A window was labeled as cancer if more than half of the window intersected with a Gleason 3+3=6 tumor, otherwise it was marked as normal. Similarly for the zones, if more than half of the window intersected with, for example PZ, the zone was labeled as PZ. The data was then used to calculate the receiver-operating characteristic curve (ROC), and the sensitivity, specificity and area-under-curve (AUC) values were calculated. A Naive Bayesian statistical classifier was used to construct a model for combined Gd, Gl and ADC. The prediction from this model was used to plot the ROC and calculate the performance parameters. A Wilcoxon rank sum test was performed to test the differentiation between normal and cancerous tissue.

### **5.2.7 Phantom validation**

As described in previous chapters the methods were validated in quantitative quality-assurance phantoms (Model 049, CIRS Inc, USA) with simplified spherical inclusions. In this study a new phantom imaging study was constructed to ensure that the inversion method can reconstruct spatially-heterogeneous inclusions which are common in real tissue. This phantom was designed and constructed by my colleague Mohammad Honarvar. The phantom used in this experiment is an Agar-gelatin phantom with the concentration of 1% for the background and 2% for the hard inclusions. To generate T2-weighted and visual contrast, acrylic color was added to the 2% agar solution before being injected into the background solution. The inclusions were injected by a syringe before the gelatin solution was solidified. Many inclusions of various sizes and shapes were created in this manner. For the phantom MRE study, a sinusoidal mechanical excitation of 350 Hz was applied.

## **5.3 Results**

### **5.3.1 Transducer and phantom study**

The transducer was tested in a frequency range of 20 Hz and 2 kHz, and amplitudes beyond 200  $\mu\text{m}$  peak-to-peak. The transducer did not overheat even during extended examinations (2-3 hours). The T2-weighted image, displacement field in three directions  $U_x$ ,  $U_y$  and  $U_z$ , as well as the real part of the shear modulus  $G_d$  are shown in Figure 5-2 with the three orthogonal projections (axial, sagittal and coronal). The waves uniformly distributed across the phantom and the acquired images were free of artifacts due to the electromagnetic transducer. The total harmonic distortion in the displacement field was less than 10%. In fact, as seen in Table 5-2 the THD decreased considerably when the new electromagnetic transducer was used starting with P17. The elasticity image closely corresponds to the T2-weighted image.

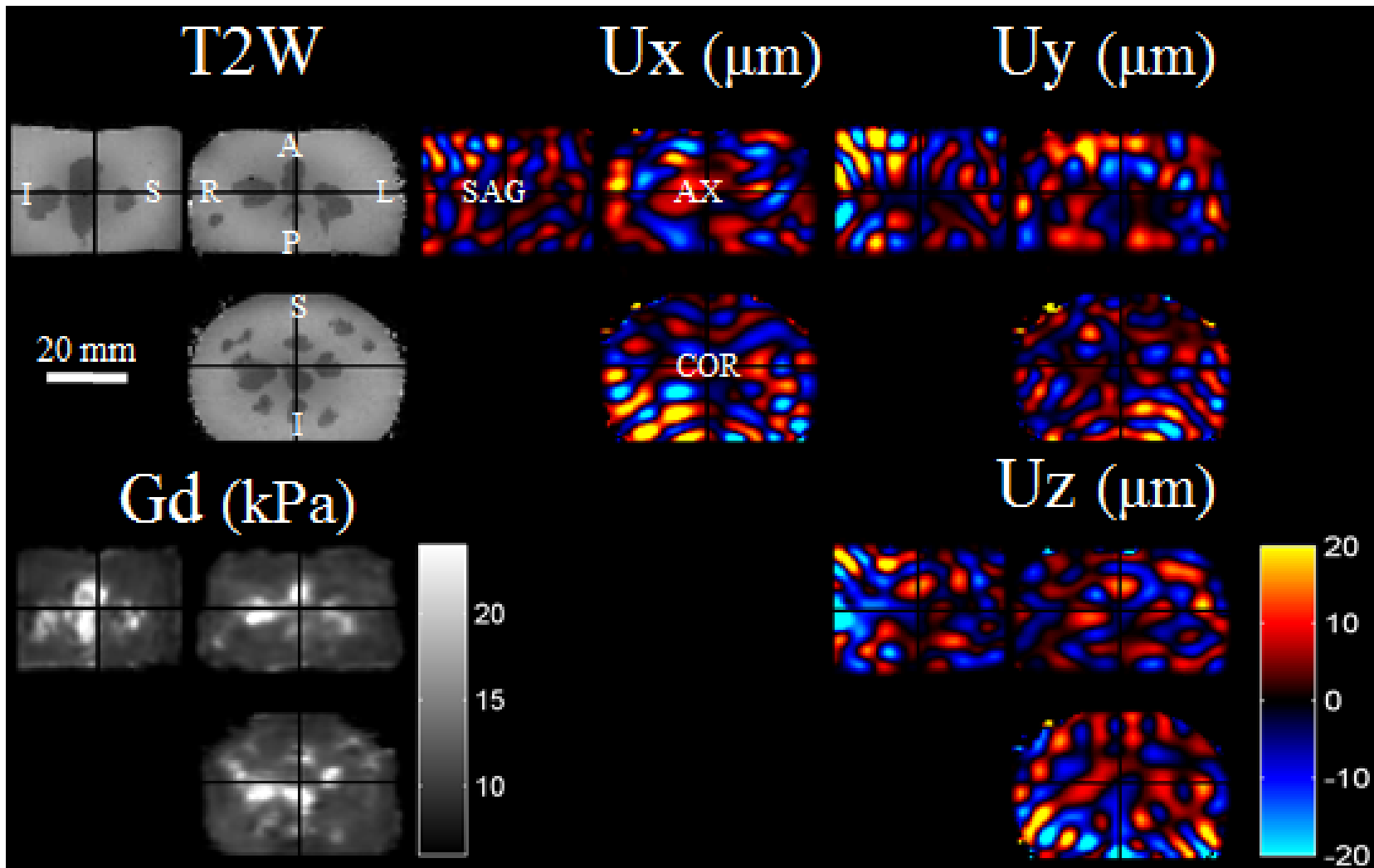


Figure 5-2. A T2-weighted anatomical image of a phantom with spatially heterogeneous inclusions of different elasticity values was tested with the transducer. The resulting mechanical waves (350Hz) and the projection in the three orthogonal planes are as shown. The inclusions can be easily visualized in the reconstruction elastogram

### 5.3.2 Patient study

In Figure 5-3, a typical *ex-vivo* prostate specimen is shown with its corresponding wave images at the three excitation frequencies 600, 800 and 1000 Hz. The figure shows the T2-weighted image, as well as the corresponding magnitude image from the MRE experiment, waves in all three dimensions, the reconstructed elastogram and the map of Gamma. The displacement field revealed that the wave propagation is complex and the waves are present in all spatial components. Also, the elasticity increased with frequency according to the power law with a mean exponent  $Gd-\gamma$  of  $1.1 \pm 1.3$  for this case across the gland. For more images refer to Appendix D.

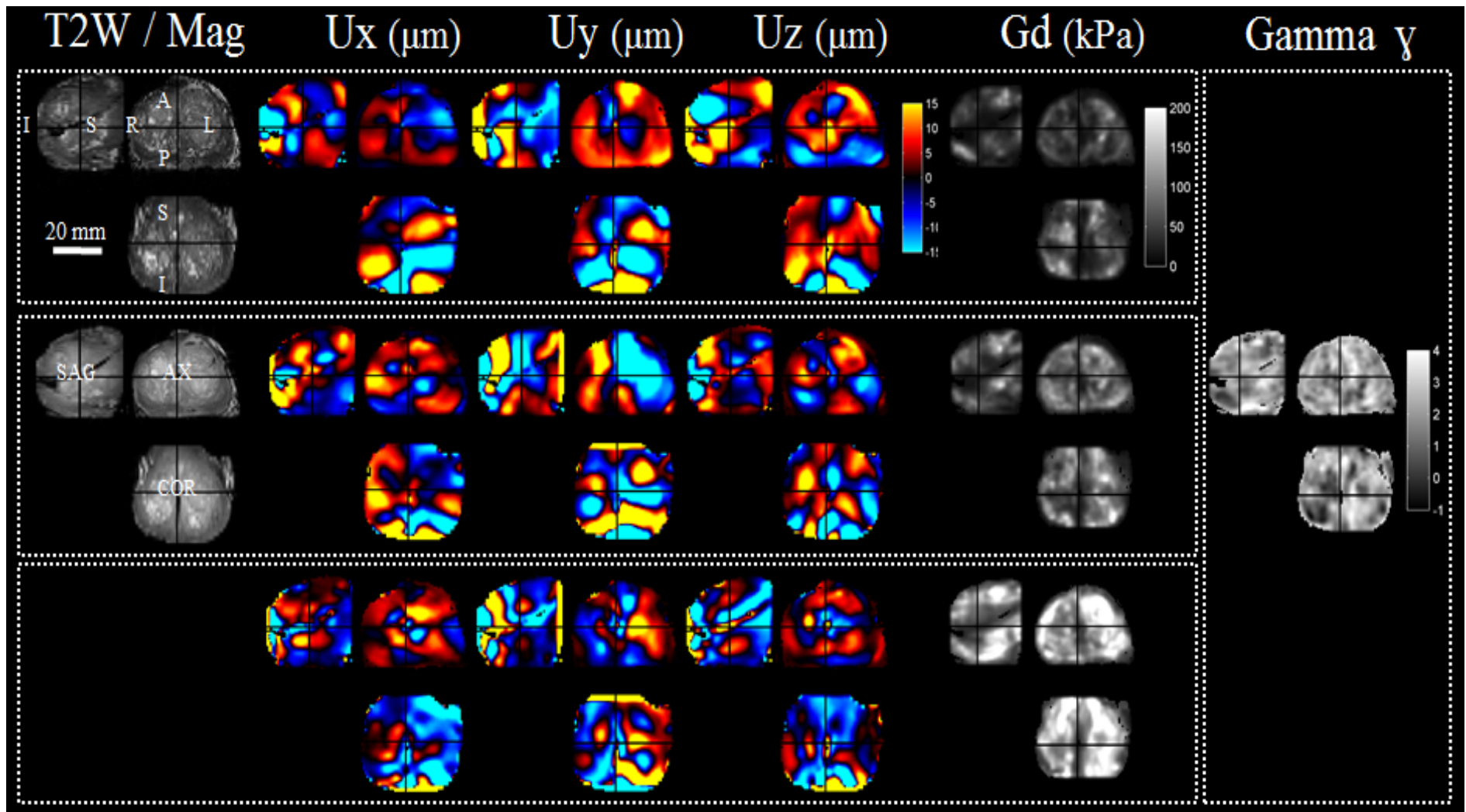


Figure 5-3. Typical images acquired for an *ex-vivo* prostate: T2-weighted, magnitude image of MRE, waves, reconstructed shear modulus  $G_d$  and the power-law exponent  $\gamma$ . The axial, sagittal and coronal projections of the displacement field in the three dimensions are shown. The experiment was repeated for different excitation frequencies (600, 800 and 1000Hz). The wave propagation is complex and present in all three axes.

Sample results as registered to the pathology slides are shown in Figure 5-4. The following images are shown in each case: the histology slides with marked tumors, the registered T2-weighted anatomy, the registered masks of the zones, registered Gd and G1, and ADC. In terms of registration performance, the area overlap between the segmented histology and registered segmented MR slices was  $94.8 \pm 3.5\%$ , and the error between landmarks on histology and the corresponding registered MR was  $1.8 \pm 1.1$  mm. As seen in the figure, the tumors can be visualized in the elasticity images even though in some cases they are not obvious in the ADC maps. For more images refer to Appendix D.

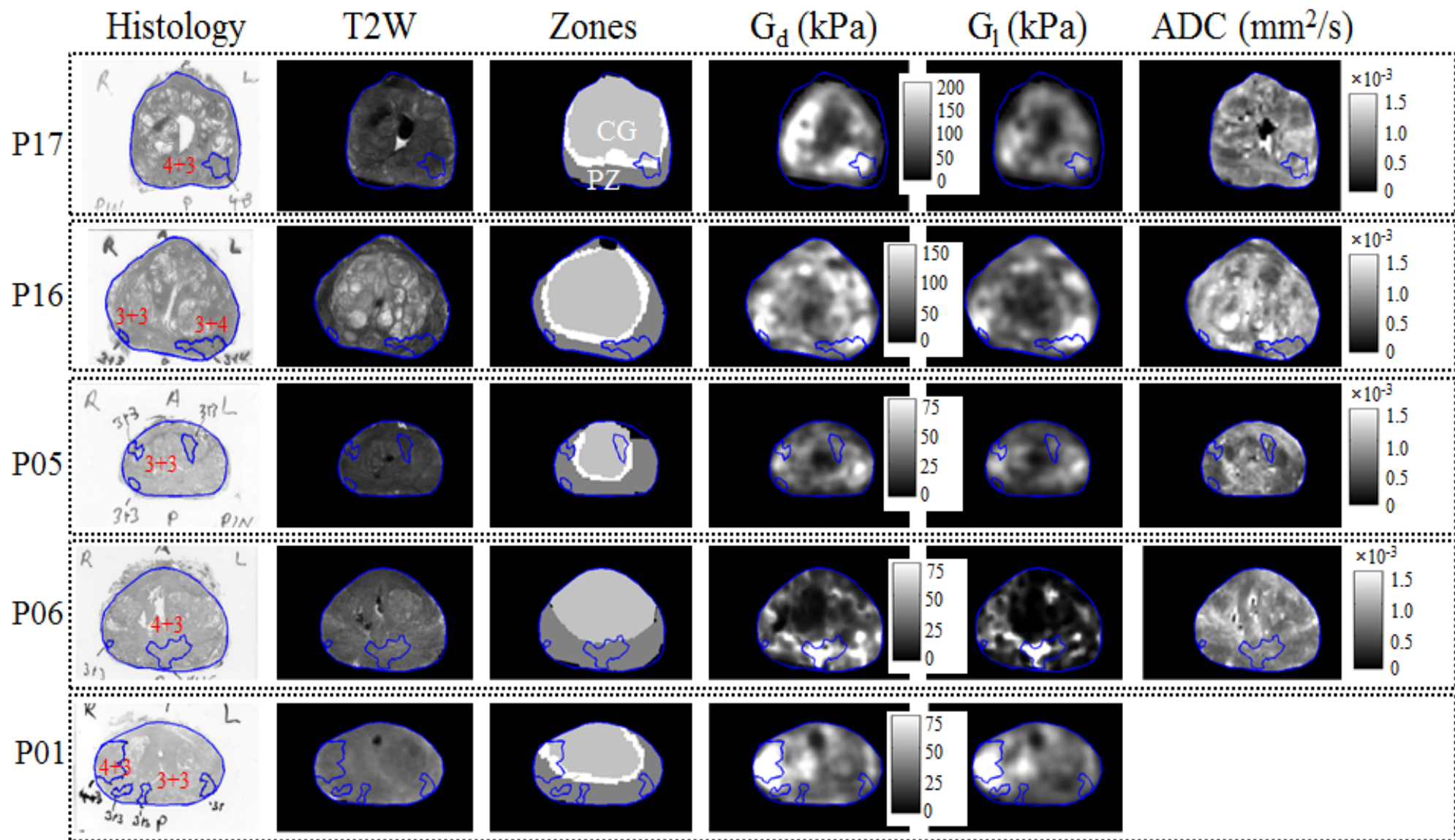


Figure 5-4. Sample results of shear moduli ( $G_d$  and  $G_l$ ) and ADC as registered to histopathology. The tumors are visible in the viscoelastic maps and in some cases in the ADC maps.

In Table 5-3, the average value of the dynamic shear modulus (Gd), loss modulus (G1) and apparent diffusion coefficient (ADC) are recorded for normal and cancerous tissue in PZ and CG. In the cases that the table is empty no tumor was found in the corresponding zone. The differentiation between normal and cancerous tissue (p-value) are also recorded in this table.

A hundred-and-twelve tumors were analyzed with an equivalent diameter between 3 and 30 mm (mean of 6 mm) and Gleason score of at least 3+3=6. The receiver operating characteristic for each is shown in Figure 5-5 and its corresponding histogram (normal vs tumor) is shown in Figure 5-6. The resulting sensitivity, specificity and AUC is recorded in Table 5-4.

The overall sensitivity (specificity) was 0.69 (0.69) for Gd, 0.69 (0.69) for G1, and 0.65 (0.65) for ADC in PZ; 0.65 (0.65) for Gd, 0.69 (0.66) for G1, and 0.59 (0.60) for ADC in CG. The overall AUC was 0.75, 0.75 and 0.68 in PZ; and 0.69, 0.70 and 0.62 in CG, for Gd, G1 and ADC respectively. For the predictor model of the combined Gd, G1 and ADC case the overall sensitivity (specificity) was 0.75 (0.75) in PZ and 0.71 (0.71) in CG. The overall AUC for the combined case was 0.82 in PZ and 0.78 in CG.

Table 5-3. Average values for Gd, GI and ADC in the PZ and CG zone for normal tissue and cancer. (p-value: <0.005 \*\*\*; <0.05 \*\*; <0.1 \*)

| Case | Zone | t-test<br>(p-value) | Gd (kPa) |        | GI (kPa) |        | ADC $\times 10^{-3}$ (mm <sup>2</sup> /s) |           |
|------|------|---------------------|----------|--------|----------|--------|---|-----------|
|      |      |                     | Normal   | Cancer | Normal   | Cancer | Normal                                    | Cancer    |
| P01  | PZ   | ***, ***, 0.88      | 30±5     | 102±17 | 24±5     | 84±9   | -   | -         |
|      | CG   | ***, ***, **        | 41±14    | 75±7   | 37±12    | 65±7   | -   | -         |
| P04  | PZ   | ***, ***, **        | 74±13    | 56±12  | 67±9     | 51±10  | -   | -         |
|      | CG   | **, **, 0.77        | 55±21    | 89±6   | 54±20    | 84±4   | -   | -         |
| P05  | PZ   | ***, ***, ***       | 54±12    | 38±11  | 57±11    | 38±12  | 0.55±0.10                                 | 0.71±0.18 |
|      | CG   | 0.35, 0.53, **      | 32±12    | 33±10  | 29±10    | 30±11  | 0.75±0.16                                 | 0.78±0.15 |
| P06  | PZ   | ***, ***, 0.37      | 22±7     | 28±10  | 21±7     | 26±9   | 0.85±0.14                                 | 0.83±0.11 |
|      | CG   | **, **, 0.65        | 16±8     | 22±3   | 14±7     | 20±3   | 0.93±0.16                                 | 0.91±0.08 |
| P08  | PZ   | ***, ***, ***       | 32±15    | 19±8   | 30±13    | 17±6   | 0.94±0.22                                 | 0.83±0.26 |
|      | CG   | -                   | -        | -      | -        | -      | -   | -         |
| P10  | PZ   | ***, ***, ***       | 94±59    | 80±42  | 79±48    | 62±29  | -   | -         |
|      | CG   | -                   | -        | -      | -        | -      | -   | -         |
| P11  | PZ   | ***, ***, ***       | 58±24    | 74±22  | 45±16    | 62±20  | 1.00±0.15                                 | 0.75±0.15 |
|      | CG   | ***, ***, ***       | 39±14    | 53±15  | 26±14    | 40±17  | 0.79±0.19                                 | 0.63±0.10 |
| P16  | PZ   | ***, ***, **        | 98±44    | 86±38  | 90±46    | 78±38  | 0.86±0.21                                 | 0.84±0.17 |
|      | CG   | *, ***, ***         | 75±30    | 78±27  | 62±28    | 72±22  | 1.00±0.24                                 | 0.87±0.20 |
| P17  | PZ   | ***, ***, ***       | 68±24    | 75±18  | 54±18    | 63±17  | 0.83±0.19                                 | 0.95±0.15 |
|      | CG   | 0.28, 0.22, ***     | 84±48    | 79±20  | 72±42    | 66±14  | 0.83±0.26                                 | 1.05±0.18 |
| P18  | PZ   | ***, ***, *         | 74±32    | 100±30 | 62±27    | 77±26  | 0.82±0.18                                 | 0.79±0.09 |
|      | CG   | 0.11, *, 0.71       | 73±31    | 83±15  | 57±24    | 66±7   | 0.77±0.17                                 | 0.78±0.07 |
| P19  | PZ   | ***, ***, ***       | 122±50   | 90±29  | 98±44    | 73±23  | 0.78±0.14                                 | 0.51±0.11 |
|      | CG   | *, 0.25, *          | 67±24    | 61±27  | 54±23    | 50±27  | 0.63±0.11                                 | 0.60±0.13 |
| P20  | PZ   | **, **, 0.62        | 57±21    | 77±11  | 47±14    | 62±11  | 0.89±0.18                                 | 0.93±0.07 |
|      | CG   | *, **, 0.17         | 64±21    | 56±15  | 52±18    | 43±15  | 0.78±0.20                                 | 0.73±0.16 |
| Mean | PZ   | -                   | 65±25    | 69±21  | 56±21    | 58±17  | 0.84±0.17                                 | 0.79±0.14 |
|      | CG   | -                   | 55±22    | 63±14  | 46±20    | 54±13  | 0.81±0.19                                 | 0.79±0.13 |

Table 5-4. The results from the receiver-operator-characteristic analysis are summarized (Sens=Sensitivity, Spec=Specificity, AUC= area under curve).

| Case | Zone | Gd   |      |      | GI   |      |      | ADC  |      |      | Combined (Gd+GI+ADC) |      |      |
|------|------|------|------|------|------|------|------|------|------|------|----------------------|------|------|
|      |      | Sens | Spec | AUC  | Sens | Spec | AUC  | Sens | Spec | AUC  | Sens                 | Spec | AUC  |
| P01  | PZ   | 1.00 | 1.00 | 1.00 | 1.00 | 1.00 | 1.00 | -    | -    | -    | -                    | -    | -    |
|      | CG   | 0.89 | 0.92 | 0.98 | 0.89 | 0.89 | 0.96 | -    | -    | -    | -                    | -    | -    |
| P04  | PZ   | 0.71 | 0.71 | 0.84 | 0.76 | 0.77 | 0.88 | -    | -    | -    | -                    | -    | -    |
|      | CG   | 1.00 | 0.94 | 0.97 | 1.00 | 0.94 | 0.97 | -    | -    | -    | -                    | -    | -    |
| P05  | PZ   | 0.72 | 0.72 | 0.84 | 0.74 | 0.74 | 0.87 | 0.71 | 0.71 | 0.79 | 0.77                 | 0.77 | 0.88 |
|      | CG   | 0.48 | 0.48 | 0.51 | 0.47 | 0.47 | 0.49 | 0.52 | 0.52 | 0.56 | 0.55                 | 0.55 | 0.60 |
| P06  | PZ   | 0.60 | 0.60 | 0.67 | 0.58 | 0.58 | 0.66 | 0.50 | 0.50 | 0.52 | 0.62                 | 0.62 | 0.69 |
|      | CG   | 0.67 | 0.68 | 0.74 | 0.67 | 0.67 | 0.75 | 0.55 | 0.58 | 0.53 | 0.79                 | 0.75 | 0.88 |
| P08  | PZ   | 0.71 | 0.71 | 0.78 | 0.77 | 0.78 | 0.83 | 0.66 | 0.66 | 0.69 | 0.77                 | 0.77 | 0.83 |
|      | CG   | -    | -    | -    | -    | -    | -    | -    | -    | -    | -                    | -    | -    |
| P10  | PZ   | 0.57 | 0.57 | 0.64 | 0.58 | 0.58 | 0.64 | -    | -    | -    | -                    | -    | -    |
|      | CG   | -    | -    | -    | -    | -    | -    | -    | -    | -    | -                    | -    | -    |
| P11  | PZ   | 0.63 | 0.63 | 0.69 | 0.71 | 0.71 | 0.75 | 0.82 | 0.81 | 0.89 | 0.81                 | 0.81 | 0.91 |
|      | CG   | 0.67 | 0.67 | 0.75 | 0.63 | 0.63 | 0.74 | 0.71 | 0.71 | 0.76 | 0.81                 | 0.81 | 0.88 |
| P16  | PZ   | 0.59 | 0.59 | 0.59 | 0.57 | 0.57 | 0.59 | 0.53 | 0.53 | 0.54 | 0.62                 | 0.62 | 0.64 |
|      | CG   | 0.55 | 0.55 | 0.54 | 0.63 | 0.63 | 0.66 | 0.62 | 0.62 | 0.66 | 0.62                 | 0.62 | 0.70 |
| P17  | PZ   | 0.57 | 0.57 | 0.61 | 0.60 | 0.60 | 0.65 | 0.67 | 0.67 | 0.71 | 0.69                 | 0.69 | 0.77 |
|      | CG   | 0.51 | 0.50 | 0.52 | 0.53 | 0.53 | 0.52 | 0.75 | 0.75 | 0.78 | 0.77                 | 0.78 | 0.86 |
| P18  | PZ   | 0.68 | 0.68 | 0.75 | 0.64 | 0.64 | 0.69 | 0.56 | 0.56 | 0.54 | 0.68                 | 0.68 | 0.75 |
|      | CG   | 0.56 | 0.56 | 0.65 | 0.60 | 0.61 | 0.64 | 0.48 | 0.48 | 0.52 | 0.84                 | 0.84 | 0.90 |
| P19  | PZ   | 0.65 | 0.65 | 0.70 | 0.64 | 0.63 | 0.67 | 0.86 | 0.86 | 0.94 | 0.92                 | 0.92 | 0.97 |
|      | CG   | 0.54 | 0.54 | 0.58 | 0.54 | 0.54 | 0.57 | 0.56 | 0.56 | 0.57 | 0.66                 | 0.66 | 0.70 |
| P20  | PZ   | 0.86 | 0.82 | 0.85 | 0.71 | 0.71 | 0.81 | 0.57 | 0.57 | 0.53 | 0.86                 | 0.86 | 0.93 |
|      | CG   | 0.67 | 0.67 | 0.63 | 0.67 | 0.67 | 0.66 | 0.56 | 0.58 | 0.59 | 0.64                 | 0.63 | 0.75 |
| Mean | PZ   | 0.69 | 0.69 | 0.75 | 0.69 | 0.69 | 0.75 | 0.65 | 0.65 | 0.68 | 0.75                 | 0.75 | 0.82 |
|      | CG   | 0.65 | 0.65 | 0.69 | 0.66 | 0.66 | 0.70 | 0.59 | 0.60 | 0.62 | 0.71                 | 0.71 | 0.78 |

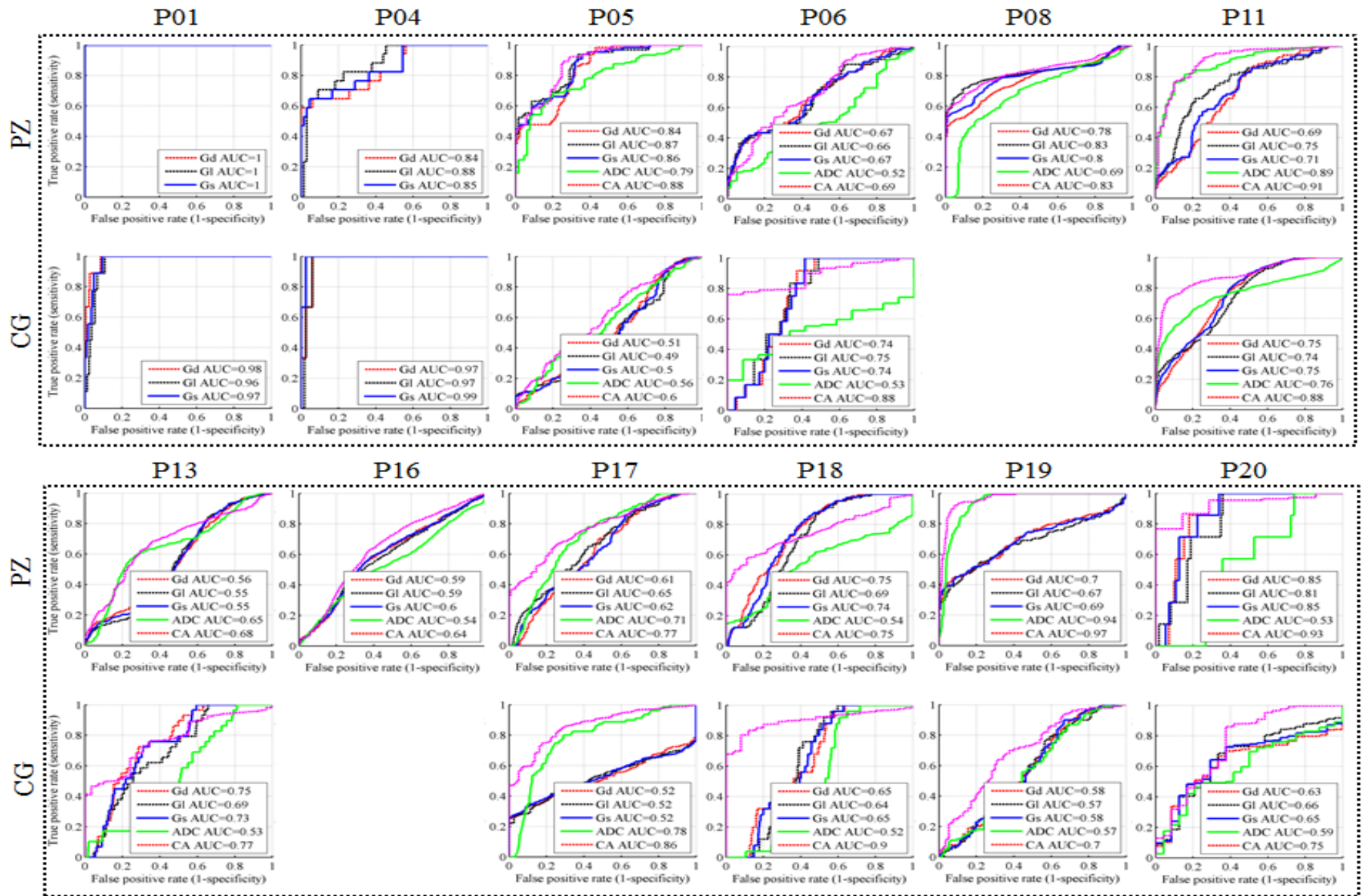


Figure 5-5. The receiver-operator-characteristic curve and the corresponding AUC is shown for each case for parameters Gd, GI, ADC and combined (CA).

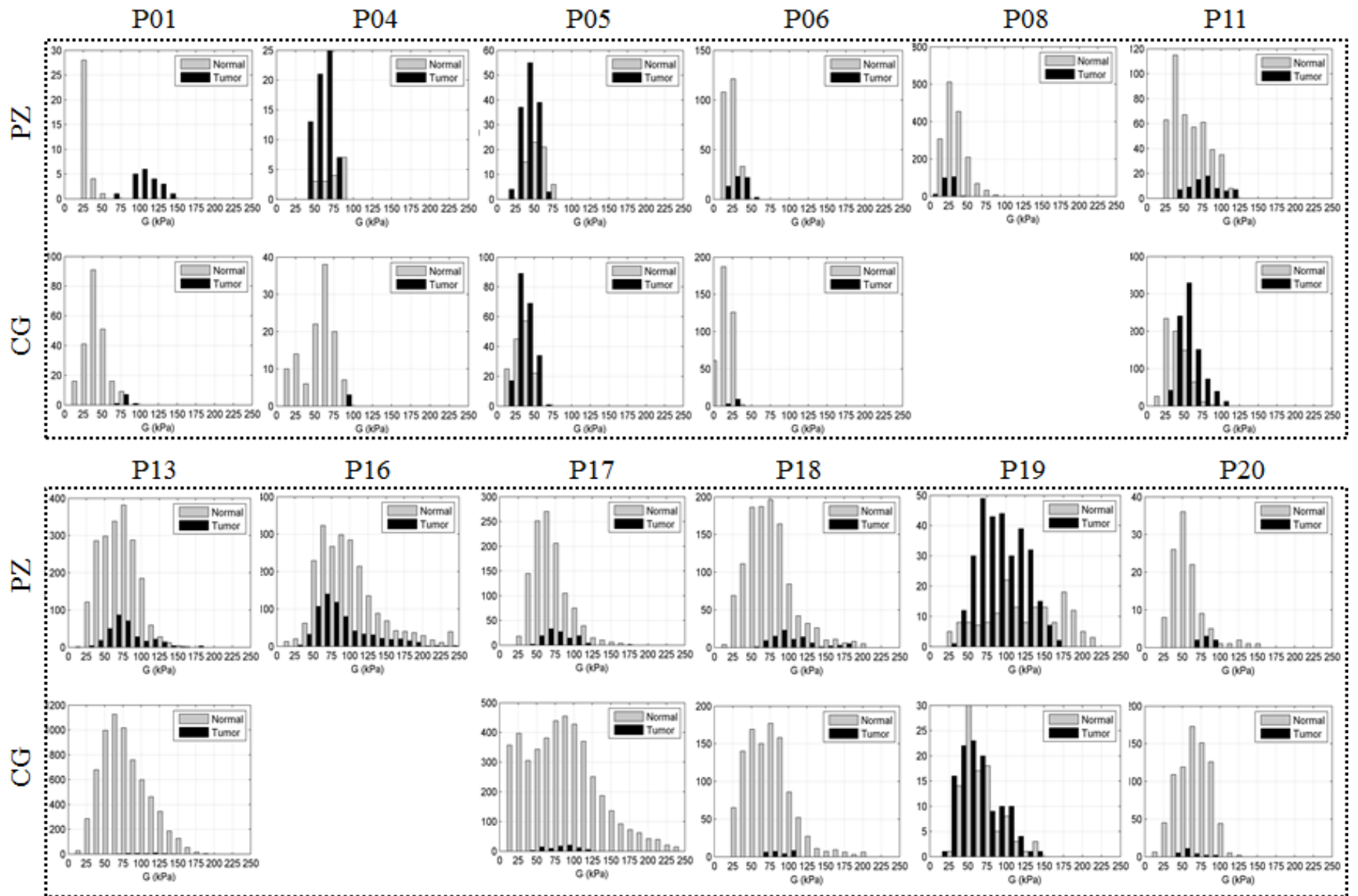


Figure 5-6. The histogram of tumor and normal tissue where the horizontal axis is the shear modulus  $G_d$  (kPa) and vertical axis is the number of bins.

A sample image of the six cases that had multi-frequency data is shown in Figure 5-7 and Figure 5-8. The following images are shown: the histology slides with marked tumors, the registered T2-weighted anatomy, the registered masks of the zones, registered Gd and G1, Gamma as well as ADC. Even though the tumors are not particularly visible in the viscoelastic maps (or the ADC image), the Gamma map seemed to highlight the small tumor.

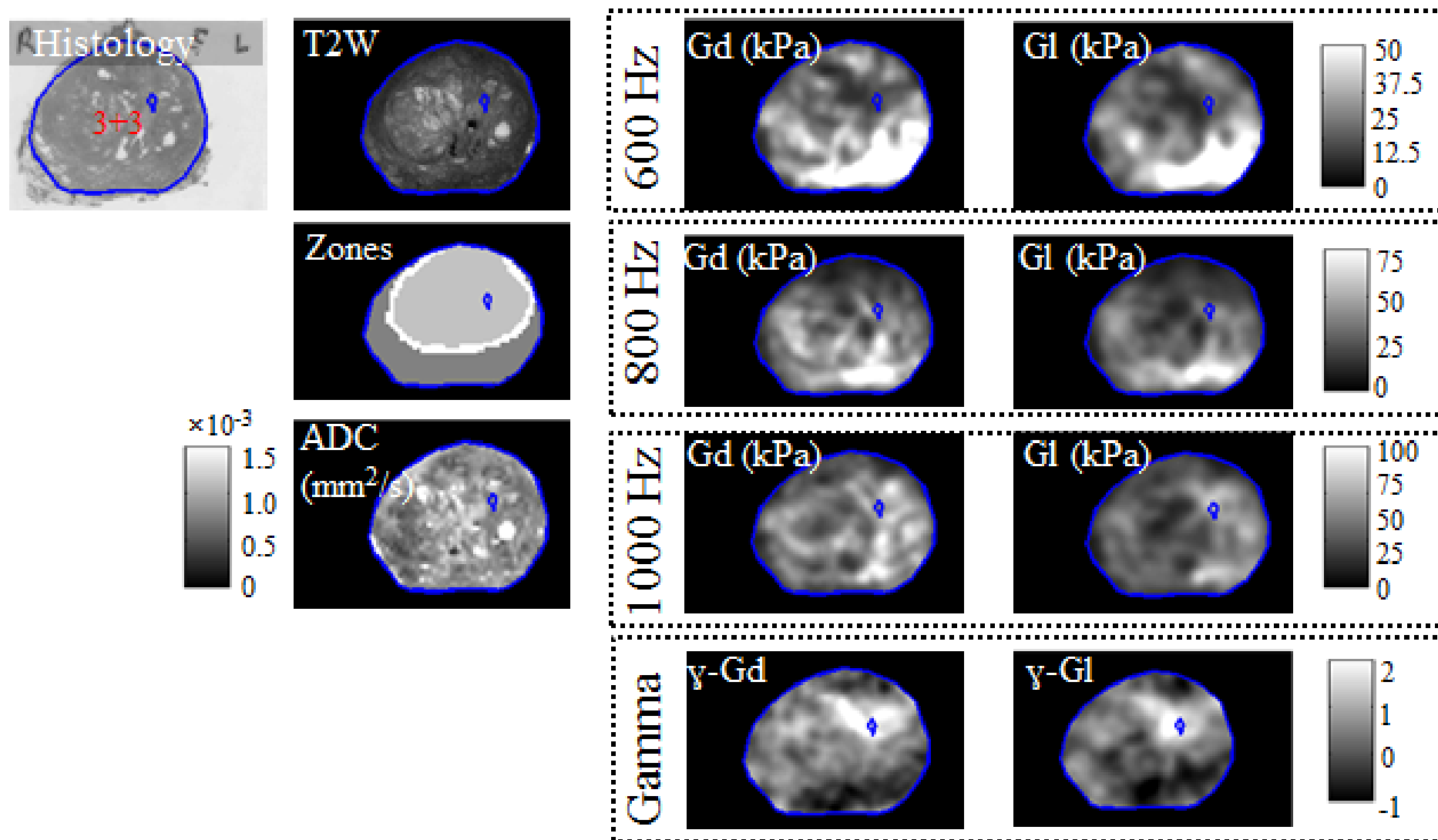


Figure 5-7. Sample results of multi-frequency shear moduli ( $G_d$  and  $G_1$ ) and power-law exponent Gamma as registered to histopathology. Even though the tumors are not particularly visible in the viscoelastic maps or the ADC image, the Gamma map seems to highlight the small Gleason 3+3 tumor.

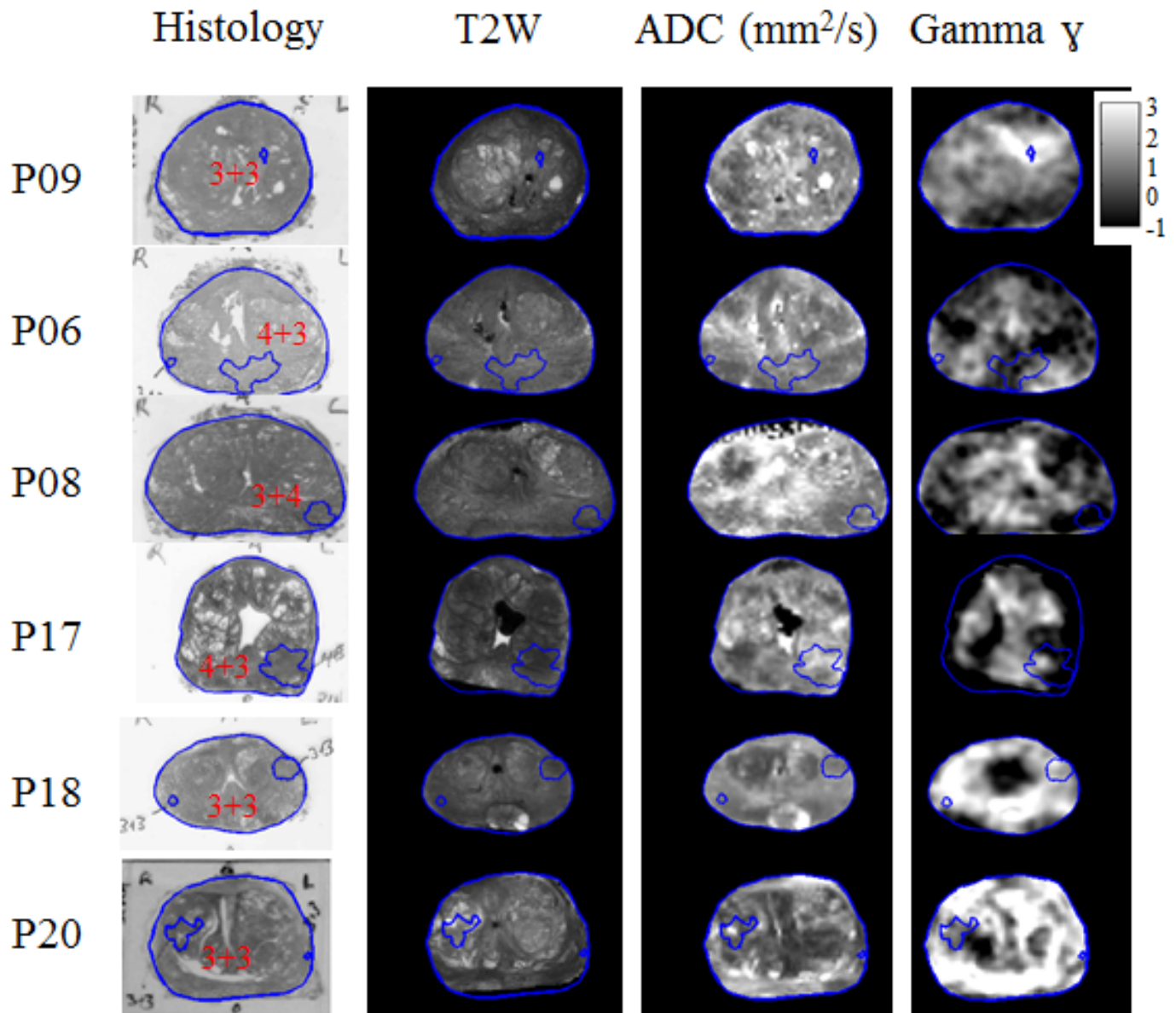


Figure 5-8. Result for Gamma for all six patients with multi-frequency MRE data.

The mean Gamma in normal (cancer) was  $1.6 \pm 0.8$  ( $1.1 \pm 0.7$ ) for Gd and  $1.2 \pm 0.9$  ( $0.7 \pm 0.7$ ) for Gl in PZ; and  $1.1 \pm 0.9$  ( $1.3 \pm 0.8$ ) for Gd and  $0.8 \pm 1.0$  ( $1.2 \pm 0.8$ ) for Gl in CG.

The differentiation of PZ from CG was not significant ( $p < 0.2$ ) for Gamma.

The overall sensitivity (specificity) was 0.66 (0.69) for  $\gamma$ -Gd, and 0.68 (0.68) for  $\gamma$ -Gl in PZ; 0.65 (0.65) for  $\gamma$ -Gd and 0.66 (0.66) for  $\gamma$ -Gl in CG. The overall AUC was 0.69 and 0.70 in PZ; and 0.67 and 0.69 in CG, for  $\gamma$ -Gd and  $\gamma$ -Gl, respectively.

A correlation between the elasticity modulus and the fixation time was observed (especially in PZ) as shown in Figure 5-9. Both Gd and Gl were increased in normal tissue the longer the specimens were immersed in the fixation solution (approximately  $+0.20$  kPa/h). This effect is more prominent for fixation time less than 80 hours

(tumors size dependent). The shear moduli decreased in tumorous tissue as a function of fixation time at approximately 0.4 kPa/h. This effect resulted in reduced differentiation between normal and cancer. Similarly the ADC values for normal PZ tissue decreased at an approximate rate of  $-1.5 \times 10^{-6} \text{ mm}^2/\text{s}/\text{hr}$  while cancer tissue increased at an approximate rate of  $0.8 \times 10^{-6} \text{ mm}^2/\text{s}/\text{hr}$ .

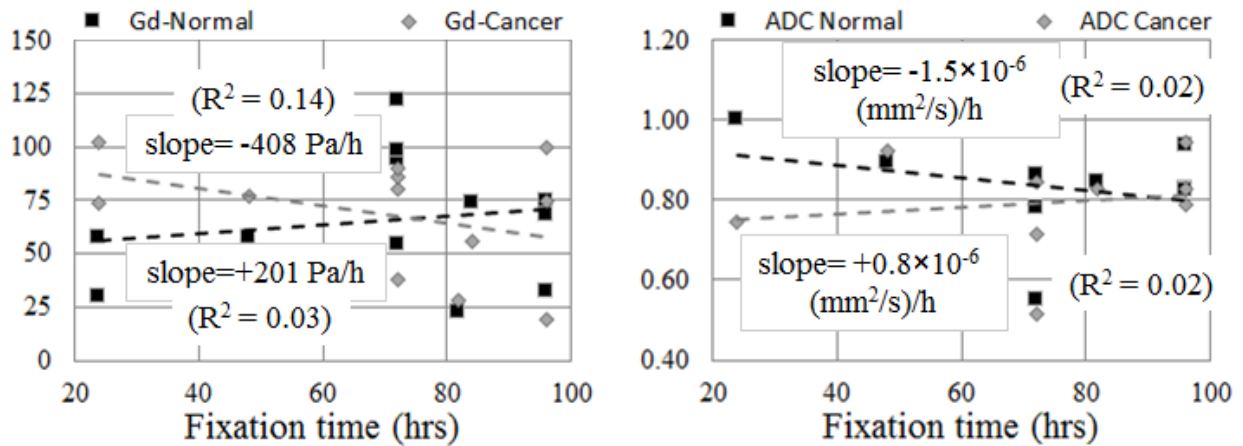


Figure 5-9. A plot of shear moduli Gd and ADC in the normal and cancer tissue in the peripheral zone as a function of the time the *ex-vivo* prostate gland was immersed in fixation solution.

Figure 5-10 shows average value of shear modulus in two regions of the prostate gland for normal and cancer tissue. A modest differentiation was observed in the shear moduli values between the peripheral zone (PZ) and central gland (CG) but the differentiation was not significant ( $p < 0.065$  for Gd and  $< 0.058$  for GI).

Figure 5-11 shows for each case, the percentage differentiation between cancer and normal in Gd versus the percentage differentiation between cancer and normal in ADC.

## 5.4 Discussion

The phantom study verified that the transducer did not interfere with the MRE experiments and did not overheat. The setup of the transducer alone took between 2 and 10 minutes. The transducer was capable of inducing waves with amplitudes beyond 200  $\mu\text{m}$  peak-to-peak at 350 Hz and less than 10% distortion.

For the patient study, waves were clearly visible in all directions at multiple frequencies in *ex-vivo* prostate glands with an amplitude of between 1-100  $\mu\text{m}$  for frequencies 600-1000 Hz.

The reconstructed Gd and GI images were registered to the histology slides with an error comparable to the in-plane resolution of the MRE experiments.

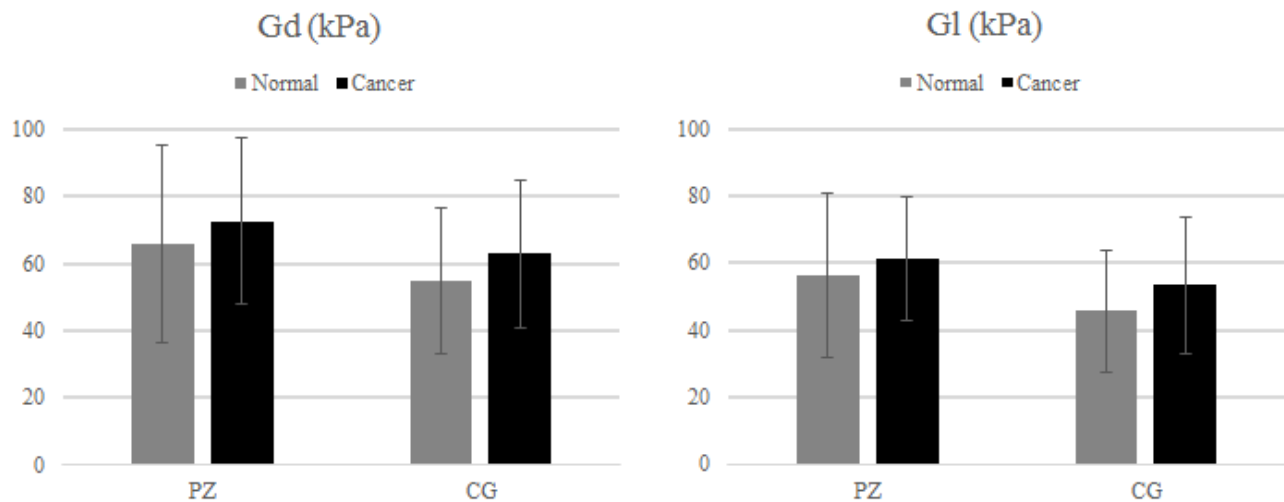


**Figure 5-10. A modest differentiation was observed in the shear moduli values between the peripheral zone (PZ) and central gland (CG) but the differentiation was not significant ( $p < 0.065$  for Gd and  $< 0.058$  for Gl).**

No significant delineation between PZ and CG was observed in the elastograms or the power law exponent, although a modest differentiation was observed.

The cancer detection rate based on Gd and Gl was modest and with many false positives but comparable to that of ADC with an approximate AUC of 0.62-0.75. The combined MRE+DWI method improved the AUC to 0.78-0.82, suggesting that complementary information from MRE and DWI can improve results for the *in-vivo* case, which remains to be proven.

Cancer tumors were observed in MRE and DWI images. We can make the following observations. Not all cancer tumors are stiffer than normal tissue surrounding it (e.g., P05, P08, P10, P16, and P19). Some cancer could not be detected in any of the MR images T2, Gd, Gl, or ADC (e.g., P08 upper left tumor). In some cases, the tumors were observed in the shear modulus images but not in the ADC images (e.g., P17 and P06). Also not all tumors had lower ADC compared to the surrounding normal tissue (e.g., P17 and P05). Figure 5-11 shows how the patient data is distributed in a Gd versus ADC plot. The values are expressed as the differentiation between cancer and normal tissue expressed in percentage value. From the current consensus, one would expect that all cancer to have a higher shear modulus and lower ADC value. This corresponds the second quadrant of this plot. However, as seen in Figure 5-11, only for a sub set of tumors (the large and more aggressive ones) fall in this quadrant. In fact, it appears that many tumors have lower shear modulus compared to the background. Also, three out of eight cases here show that ADC is in fact higher for tumors than normal tissue.

Stiffer structures within the prostate were mistaken for tumors. The effect of other confounders such as Benign prostatic hyperplasia (BPH), scarring from previous biopsy tracts, calcifications, or androgen therapy on the mechanical parameters is not known.

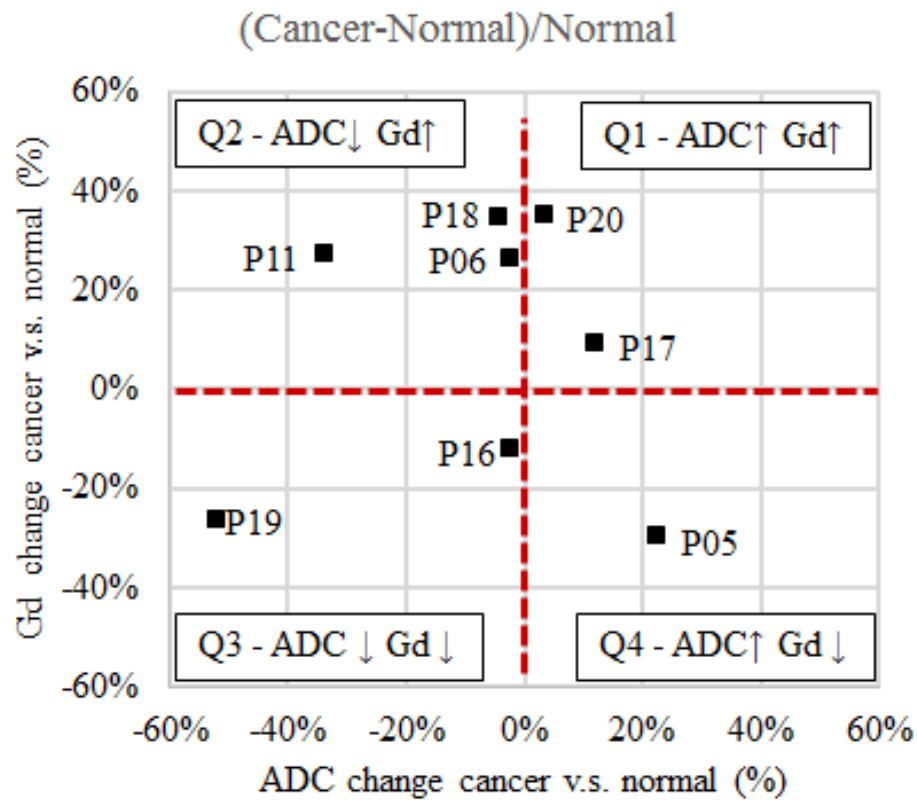


Figure 5-11. The differentiation (expressed as percentage) between cancer and normal tissue for Gd versus ADC.

The narrow frequency span limited the applicability of the power law which may be widened for future experiments and is typically several orders of magnitude in materials science studies.

Effect of Fixation: One of the key limitations of this study, other than the small patient sample size, was the significant effect of the fixation process on the prostate. The fixation alters the cells and tissue on a molecular level to increase their mechanical strength and stability. This increased strength and rigidity is desired to preserve the morphology of the sample for further analysis and grading the Gleason score. Unfortunately, when the gland is soaked in the formalin fixation solution, the chemical solution does not infuse uniformly across the specimen. Usually the tissue interface closer to the solution will be stiffer than the tissue farther away from the solution. Also, the stiffening is time dependent which was not controlled in this work. The higher stiffness of the gland required higher excitation frequencies to be used in MRE. The ADC value was also affected by the fixation process in a spatially non-uniform manner as observed by McGrath *et al.* [127]. Therefore, there are limitations on how these results can be translated for *in-vivo* applications. The fixation process may explain why the PZ appears stiffer (because the periphery of the prostate is closer to the chemical solution) than the CG in this work and others [127], while the opposite in *in-vivo* tissue in this work and others [57]. Another consequence of the fixation process, changed the baseline stiffness for each case dependent on the time the gland was left in the formaldehyde solution (see Figure 5-9). This prevented meaningful ROC analysis of pooling all data sets since each data set is different, thus only average values of sensitivity, specificity and AUC were reported.

In comparison to the literature, Dresner *et al.* [48] applied dynamic MR elastography to seventeen post-mortem *ex-vivo* human prostate cancer specimens at 1.5 T at several excitation frequencies (100-600 Hz). The displacement field was encoded on a single direction. The study showed that the central gland is significantly stiffer compared to the peripheral zone, and that the elasticity increased as a function of mechanical excitation frequency. In addition, preliminary results suggested that prostate cancer may be delineated in the images. These findings are consistent with the results found in our work. In another study by Dresner *et al.* [49], seventeen fresh specimens resected for adenocarcinoma were assessed with MRE and compared to histology (manually matched with corresponding anatomy image). The specimens were immersed in polysaccharide gel with the transducer rod inserted in the urethra. The excitation frequency was 350 Hz. The displacement field was encoded in all three spatial directions in a volume with a resolution of  $0.31 \times 1.25 \times 3$  mm. For analysis, the specimens were split in 12 segments (A/P, R/L, Base/Mid/Apex) and only tumors larger than 4 mm were considered. Shear modulus values for cancer were calculated based on a manual ROI taken from the elasticity image. Shear modulus values for normal tissue were calculated based on the shear modulus of the whole segment. The elasticity value for normal tissue was  $11.89 \pm 3.72$  kPa and  $24.23 \pm 7.62$  kPa with sensitivity of 89% and specificity of 90%. In our study, we found a much lower differentiation between cancer and normal (approximately between 3% and 240%) compared to Dresner *et al.* (approximately between 100% and 400%). We associate this discrepancy with the issue of the fixation process. Also, some of the discrepancies are related to (i) the voxel-to-voxel analysis approach used in this work and the 12-segment analysis approach reported by [49], and (ii) the differences in excitation frequency (ours 600-1000 Hz vs. Dresner *et al.* 350 Hz). Most recently, McGrath *et al.* [51], [127] used quasi-static MRE (1-5 Hz) methods at 7T to study effects of pathology before and after fixation on *ex-vivo* human and canine prostate specimens. The prostate was immersed in a gel prior to imaging. The displacement was encoded in a single direction over a volume with a resolution of  $0.5 \times 0.5 \times 3$  mm. They showed that fixation significantly increases the elasticity value ( $4 \pm 1$  times) in a non-uniform manner. The increases correlated to fixation time (approximately 2.3 kPa/h) and the distance from the tissue edge formalin had diffused. This is consistent with the results we observed in our work. The stiffness dramatically increases in the first 24 hours. We had access to the specimen only after 24 which explains why we have a different values for the slope of stiffness increase as a function of fixation time. Also, we found that the stiffness of the fixed *ex-vivo* specimen (at 800 Hz) had increased by  $40 \pm 30$  times compared to the *in-vivo* gland (at 70 Hz). This value is much larger than reported by McGrath *et al.* We associated this difference to (i) experimental methods (ours is a 3D direct inversion of dynamic MRE while McGrath *et al.* used a 1D quasi-static MRE) and (ii) experimental conditions (ours compared *in-vivo* to *ex-vivo* after fixation while McGrath *et al.* compared *ex-vivo* before and after fixation). McGrath *et al.* also observed similar effects in ADC value where it decreased as a function of fixation time. The changes were hypothesized to occur by the fixation-induced cross-linking, or methylene bridges, between neighbouring proteins [128]. They found that the overall volume shrinkage of the prostate gland was 4% compared to the initial fresh specimen.

## 5.5 Comparison between in-vivo and ex-vivo MRE

A number of patients are shared among the two studies. Sample images comparing the in-vivo and ex-vivo results are shown in Figure 5-12. For complete comparison between these two studies refer to the images in Appendix C and D. Probably the best agreement was seen in P17, while the rest of the cases large differences were observed. The differences arise due to: (i) experimental conditions where the *ex-vivo* tissue was fixed in formalin prior to MRE, (ii) experimental settings such as the excitation frequency *in-vivo* (70 Hz) and *ex-vivo* (600-1000 Hz), (iii) errors due to patient motion and reconstruction issues at low amplitude voxels.

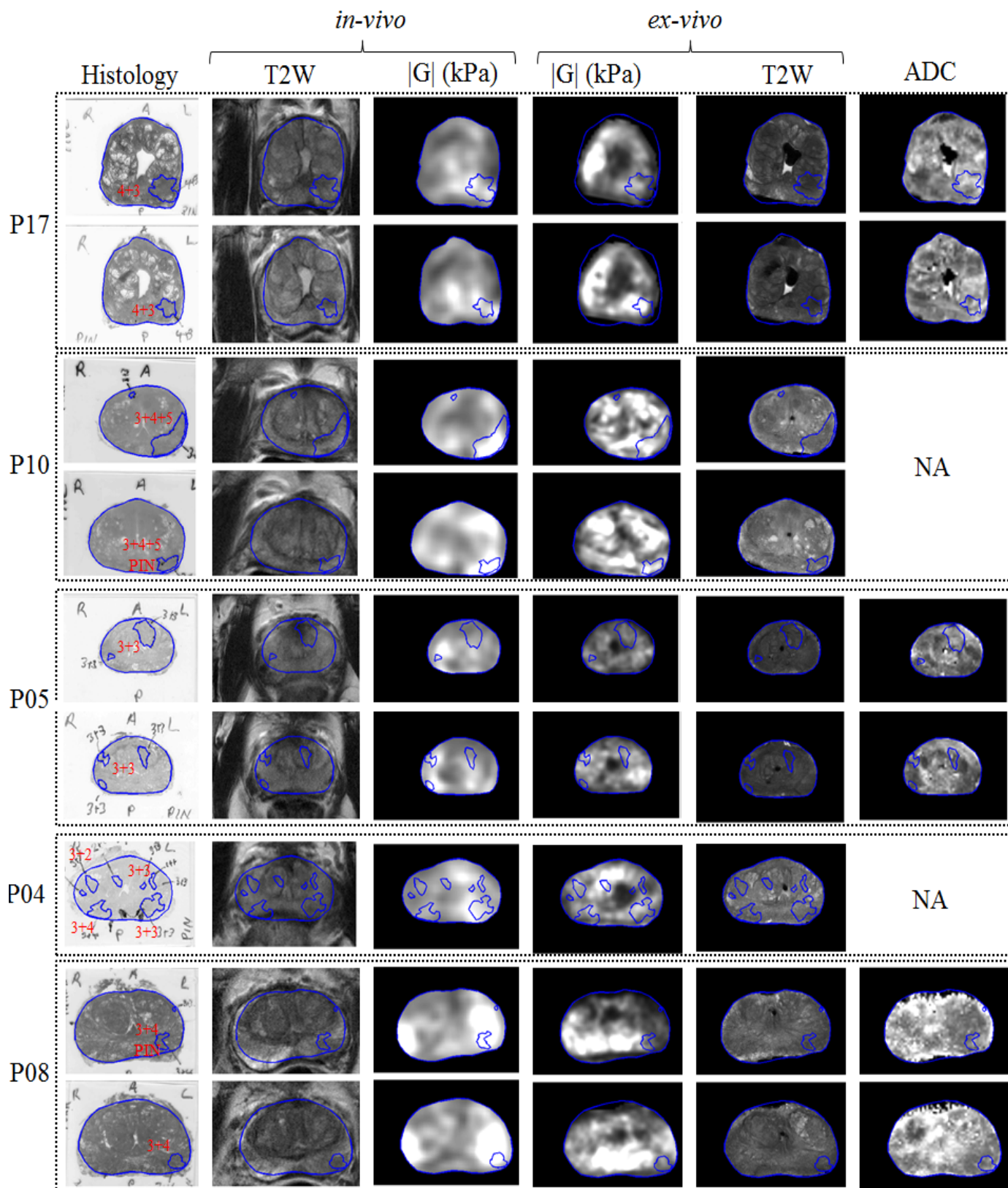


Figure 5-12. Sample images comparison *in-vivo* and *ex-vivo* MRE of the same patients.

## 5.6 Conclusion

In conclusion, an electromagnetic transducer was developed for *ex-vivo* MRE studies and validated in a phantom study. The elasticity reconstruction of the spatially heterogeneous inclusions matched well with T2 images proving that the inversion algorithm is capable of reconstructing shear modulus values in tumor-mimicking material. The MRE system was used in an *ex-vivo* prostate cancer study where the results are compared to whole mount histopathology. The absolute shear modulus was able to diagnose cancer with an average AUC of 0.75 in PZ and 0.75 in CG. ADC and shear moduli may provide complementary information (combined AUC of 0.82 in PZ); in fact MRE performed better than ADC to distinguish normal from cancerous tissue in some cases. Multi-frequency did not appear to greatly improve the results, but again these results are preliminary. A correlation was found between fixation-time of the prostate specimen to the stiffness of the tissue which may affect the diagnostic power results. It is thus recommended to continue the study with the examination performed before the fixation process.

# Chapter 6 - Conclusion

## 6.1 Summary

Tissue mechanical properties such as shear stiffness can be non-invasively imaged using MR elastography methods. In this work, the potential for MRE to diagnosis prostate cancer was investigated.

In Chapter 2, the combination of hydraulic trans-perineal excitation and harmonic imaging allowed for acquisition of the 3D displacement field of *in-vivo* human prostate. The hydraulic transducer did not interfere with the acquisition process. The phantom validation study proved that the methods are in fact repeatable and that the average stiffness values match with the values provided by the manufacturer. The system was repeatable and well-tolerated by the volunteers. The shortcoming of the transducer were: (i) the long setup time which made the system impractical in a clinical setting, and (ii) limited excitation amplitude at higher excitation frequencies. In terms of the acquisition method, reducing the voxel size was also a limitation that would have made the imaging time clinically impractical.

In Chapter 3, the combination of the newly developed fractionally-encoded gradient echo pulse sequence and rapidly set up trans-perineal electromagnetic transducer allowed for imaging of the prostate in just 10 min – making this system suitable for multi-parametric imaging. The phantom validation study showed that the 3D displacement field could be acquired using this system and that the shielding was effective for minimizing the effects of the electromagnetic transducer on the resulting images. The initial volunteer and patients studies using this system proved that the 3D displacement could be acquired using this system, and that the excitation was well tolerated by patients.

Chapter 4 present the results from the patient study using the developed MRE system in Chapter 3. We observed that even though many false positives existed, the absolute shear modulus was able to diagnose cancer with an average AUC of 0.73 in PZ and 0.72 in CG. The prostate gland stand out in the stiffness and shear strain images and that the central gland and in particular the transition zone was stiffer than the peripheral zone. Cancerous tissue was not always stiffer than normal tissue. The volunteer study showed that subject motion and peak-and-valley ripples in the standing wave degraded the repeatability of the reconstructed stiffness maps.

In Chapter 5, an electromagnetic transducer similar to the one developed in Chapter 3 was developed for *ex-vivo* prostate imaging for a patient study. The transducer did not overheat during extended studies and did not interfere with the image acquisition process. The phantom study showed that reconstruction of spatially heterogeneous works and matches closely with T2 weighted images. In the patient study, we observed that the absolute shear modulus was able to diagnose cancer with an average AUC of 0.75 in PZ and 0.75 in CG. ADC and shear moduli may provide complementary information (combined AUC of 0.82 in PZ); in fact MRE

performed better than ADC to distinguish normal from cancerous tissue in some cases. Multi-frequency did not appear to greatly improve the results, but these results are preliminary. A correlation was found between fixation-time of the prostate specimen to the stiffness of the tissue which degraded the stiffness contrast.

## 6.2 Contributions

The contributions of this thesis are summarized as follows.

- New method for prostate MRE
  - The trans-perineal prostate MR elastography method allows for non-invasive and non-instrusive elasticity imaging of the prostate that is well tolerated by the subjects. This method is well suited for integration in multi-parametric MRI studies of the prostate.
- New transducers for MR elastography
  - Designed and developed two new MR compatible transducers: (i) hydraulic transducer and (ii) shielded electromagnetic transducer (for both *in-vivo* and *ex-vivo* studies) for MRE. Also, the mounting base allows for rapid setup and positioning of the transducers while patient lies in the scanner.
- New acquisition method for MR elastography
  - Co-developed the eXpresso pulse sequence with Dr. Philippe Garteiser. The author assisted with the idea, and subsequently designed, implemented, and ran several repeatability studies with this pulse sequence. This method was applied for liver and prostate imaging.
- Validation and repeatability studies
  - Performed validation studies in phantoms (quality assurance and spatially heterogeneous), and repeatability studies in volunteers using methods developed in this thesis.
- Clinical evaluation of prostate MRE
  - Developed a clinically acceptable patient protocol for *in-vivo* and *ex-vivo* studies. Performed preliminary clinical assessment of MRE for prostate cancer diagnosis for both *in-vivo* and *ex-vivo* (including multi-frequency MRE and DWI) cases.
- MRE datasets for development of reconstruction algorithms
  - Developed a database of MRE acquisitions of phantoms (including harmonic and band-limited multi-frequency experiments), volunteer, patient for development of advanced reconstruction algorithms. The algorithms developed based on these datasets: (i) TWE reconstruction method developed by Dr. Ali Baghani, (ii) sparsity regularized mixed FEM method by Mohammad Honarvar, (iii) the curl-based FEM algorithm developed by Mohammad Honarvar, (iv) and maximum shear strain imaging method developed by the author with assistance from Mohammad Honarvar.

## 6.3 Future Work

Looking to the future, the MRE system may be incorporated in mpMRI studies to assess whether MRE in combination with DTI and DCE can indeed improve the sensitivity and specificity. To further improve the prostate MRE system the following research directions are proposed.

Multi-frequency MRE is the next logical step in this research. In order to average out the ripples of the standing mechanical wave for uniform wave illumination, it is desirable to have the frequencies relatively close together (as opposed to multiples of each other). However, to study frequency dependent parameters, the frequency needs to be varied in a large range (ideally several orders of magnitude). Also, it is desirable to have the mechanical excitation with multiple excitation frequencies applied simultaneously to reduce examination time.

Several opportunities exist to develop advanced pulse sequences for this purpose. For example, development of a sequence that can simultaneously acquire multi-frequency signals that are not multiples of each other. Also, sequences that could minimize the effects due to patient motion are also attractive. The sequences used in this work acquire each displacement direction in a separate experiment. The time delay between the first and last acquisition increase the chances of misalignment errors between the displacement components due to patient motion. For example, if all directions of the displacement component are acquired in a sector by sector approach, the sequence may become more immune to such errors.

A limitation of the current system is that the excitation frequency may be too low for dynamic MRE studies of prostate cancer. The wavelength is longer than the size of the tumors typically encountered in prostate cancer. Attempts with trans-perineal excitation at 90 Hz were successful, however frequencies beyond 100 Hz may not be feasible. Higher excitation frequencies can be achieved by using endo-cavity transducer approaches which allow the transducer to come much closer to the prostate gland. Indeed, excitation up to 300 Hz have been successfully demonstrated in *in-vivo* human prostate by Arani *et al.* [57].

On a different note, it is clear that the fixation process greatly changes the stiffness contrast in a spatially non-uniform manner. For further *ex-vivo* MRE studies it is recommended to perform the experiment on the fresh specimen, if possible.

# Bibliography

- [1] R. Siegel, D. Naishadham, and A. Jemal, “Cancer statistics, 2013,” *CA. Cancer J. Clin.*, vol. 63, no. 1, pp. 11–30, 2013.
- [2] S. Nag, D. Beyer, J. Friedland, P. Grimm, and R. Nath, “American Brachytherapy Society (ABS) recommendations for transperineal permanent brachytherapy of prostate cancer,” *Int. J. Radiat. Oncol. Biol. Phys.*, vol. 44, no. 4, pp. 789–799, 1999.
- [3] T. J. Wilt, R. MacDonald, I. Rutks, T. A. Shamliyan, B. C. Taylor, and R. L. Kane, “Systematic Review: Comparative Effectiveness and Harms of Treatments for Clinically Localized Prostate Cancer,” *Ann. Intern. Med.*, vol. 148, no. 6, pp. 435–448, Mar. 2008.
- [4] K. M. Partin AW, “Combination of prostate-specific antigen, clinical stage, and gleason score to predict pathological stage of localized prostate cancer: A multi-institutional update,” *JAMA*, vol. 277, no. 18, pp. 1445–1451, May 1997.
- [5] U. Patel, “TRUS and prostate biopsy: current status,” *Prostate Cancer Prostatic Dis.*, vol. 7, no. 3, pp. 208–210, 2004.
- [6] M. Zhang, P. Nigwekar, B. Castaneda, K. Hoyt, J. V. Joseph, A. di Sant’Agnese, E. M. Messing, J. G. Strang, D. J. Rubens, and K. J. Parker, “Quantitative characterization of viscoelastic properties of human prostate correlated with histology,” *Ultrasound Med. Biol.*, vol. 34, no. 7, pp. 1033–1042, 2008.
- [7] C. R. King and J. P. Long, “Prostate biopsy grading errors: a sampling problem?,” *Int. J. Cancer J. Int. Cancer*, vol. 90, no. 6, pp. 326–330, Dec. 2000.
- [8] K. G. Fink, G. Hutarew, W. Lumper, A. Jungwirth, O. Dietze, and N. T. Schmeller, “Prostate cancer detection with two sets of ten-core compared with two sets of sextant biopsies,” *Urology*, vol. 58, no. 5, pp. 735–739, Nov. 2001.
- [9] P. Emiliozzi, S. Maymone, A. Paterno, P. Scarpone, M. Amini, G. Proietti, M. Cordahi, and V. Pansadoro, “Increased accuracy of biopsy Gleason score obtained by extended needle biopsy,” *J. Urol.*, vol. 172, no. 6 Pt 1, pp. 2224–2226, Dec. 2004.
- [10] G. J. Jager, E. T. Ruijter, C. A. van de Kaa, J. J. de la Rosette, G. O. Oosterhof, J. R. Thornbury, and J. O. Barentsz, “Local staging of prostate cancer with endorectal MR imaging: correlation with histopathology,” *AJR Am. J. Roentgenol.*, vol. 166, no. 4, pp. 845–852, Apr. 1996.
- [11] M. R. Engelbrecht, G. J. Jager, R. J. Laheij, A. L. M. Verbeek, H. J. van Lier, and J. O. Barentsz, “Local staging of prostate cancer using magnetic resonance imaging: a meta-analysis,” *Eur. Radiol.*, vol. 12, no. 9, pp. 2294–2302, Sep. 2002.
- [12] B. N. Bloch, E. Furman-Haran, T. H. Helbich, R. E. Lenkinski, H. Degani, C. Kratzik, M. Susani, A. Haitel, S. Jaromi, L. Ngo, and N. M. Rofsky, “Prostate cancer: accurate determination of extracapsular extension with high-spatial-resolution dynamic contrast-enhanced and T2-weighted MR imaging--initial results,” *Radiology*, vol. 245, no. 1, pp. 176–185, Oct. 2007.
- [13] S. Ikonen, P. Kärkkäinen, L. Kivisaari, J. O. Salo, K. Taari, T. Vehmas, P. Tervahartiala, and S. Rannikko, “Magnetic resonance imaging of clinically localized prostatic cancer,” *J. Urol.*, vol. 159, no. 3, pp. 915–919, Mar. 1998.
- [14] M. Sanchez-Chapado, J. C. Angulo, C. Ibarburen, F. Aguado, A. Ruiz, J. Viano, A. M. Garcia-Segura, J. Gonzalez-Esteban, and J. M. Rodriguez-Vallejo, “Comparison of digital rectal examination,

- transrectal ultrasonography, and Multicoil magnetic resonance imaging for preoperative evaluation of prostate cancer,” *Eur. Urol.*, vol. 32, no. 2, pp. 140–149.
- [15] P. Kozłowski, S. D. Chang, R. Meng, B. Mädler, R. Bell, E. C. Jones, and S. L. Goldenberg, “Combined prostate diffusion tensor imaging and dynamic contrast enhanced MRI at 3T--quantitative correlation with biopsy,” *Magn. Reson. Imaging*, vol. 28, no. 5, pp. 621–628, Jun. 2010.
- [16] J. Kurhanewicz, D. Vigneron, P. Carroll, and F. Coakley, “Multiparametric magnetic resonance imaging in prostate cancer: present and future,” *Curr. Opin. Urol.*, vol. 18, no. 1, pp. 71–77, Jan. 2008.
- [17] F. Pinto, A. Totaro, A. Calarco, E. Sacco, A. Volpe, M. Racioppi, A. D’Addessi, G. Gulino, and P. Bassi, “Imaging in Prostate Cancer Diagnosis: Present Role and Future Perspectives,” *Urol. Int.*, vol. 86, no. 4, pp. 373–382, Mar. 2011.
- [18] J. J. Fütterer, S. W. T. P. J. Heijmink, T. W. J. Scheenen, J. Veltman, H. J. Huisman, P. Vos, C. A. Hulsbergen-Van de Kaa, J. A. Witjes, P. F. M. Krabbe, A. Heerschap, and J. O. Barentsz, “Prostate cancer localization with dynamic contrast-enhanced MR imaging and proton MR spectroscopic imaging,” *Radiology*, vol. 241, no. 2, pp. 449–458, Nov. 2006.
- [19] S. W. T. P. J. Heijmink, J. J. Fütterer, T. Hambroek, S. Takahashi, T. W. J. Scheenen, H. J. Huisman, C. A. Hulsbergen-Van de Kaa, B. C. Knipscheer, L. A. L. M. Kiemeney, J. A. Witjes, and J. O. Barentsz, “Prostate cancer: body-array versus endorectal coil MR imaging at 3 T--comparison of image quality, localization, and staging performance,” *Radiology*, vol. 244, no. 1, pp. 184–195, Jul. 2007.
- [20] J. J. Fütterer, S. W. T. P. J. Heijmink, T. W. J. Scheenen, G. J. Jager, C. A. Hulsbergen-Van de Kaa, J. A. Witjes, and J. O. Barentsz, “Prostate cancer: local staging at 3-T endorectal MR imaging--early experience,” *Radiology*, vol. 238, no. 1, pp. 184–191, Jan. 2006.
- [21] C. K. Kim, B. K. Park, H. M. Lee, and G. Y. Kwon, “Value of diffusion-weighted imaging for the prediction of prostate cancer location at 3T using a phased-array coil: preliminary results,” *Invest. Radiol.*, vol. 42, no. 12, pp. 842–847, Dec. 2007.
- [22] H. K. Lim, J. K. Kim, K. A. Kim, and K.-S. Cho, “Prostate cancer: apparent diffusion coefficient map with T2-weighted images for detection--a multireader study,” *Radiology*, vol. 250, no. 1, pp. 145–151, Jan. 2009.
- [23] K. Ogura, S. Maekawa, K. Okubo, Y. Aoki, T. Okada, K. Oda, Y. Watanabe, C. Tsukayama, and Y. Arai, “Dynamic endorectal magnetic resonance imaging for local staging and detection of neurovascular bundle involvement of prostate cancer: correlation with histopathologic results,” *Urology*, vol. 57, no. 4, pp. 721–726, Apr. 2001.
- [24] C. K. Kim, B. K. Park, and B. Kim, “Localization of prostate cancer using 3T MRI: comparison of T2-weighted and dynamic contrast-enhanced imaging,” *J. Comput. Assist. Tomogr.*, vol. 30, no. 1, pp. 7–11, Feb. 2006.
- [25] M. A. Haider, T. H. van der Kwast, J. Tanguay, A. J. Evans, A.-T. Hashmi, G. Lockwood, and J. Trachtenberg, “Combined T2-weighted and diffusion-weighted MRI for localization of prostate cancer,” *AJR Am. J. Roentgenol.*, vol. 189, no. 2, pp. 323–328, Aug. 2007.
- [26] H. A. Vargas, O. Akin, T. Franiel, Y. Mazaheri, J. Zheng, C. Moskowitz, K. Udo, J. Eastham, and H. Hricak, “Diffusion-weighted endorectal MR imaging at 3 T for prostate cancer: tumor detection and assessment of aggressiveness,” *Radiology*, vol. 259, no. 3, pp. 775–784, Jun. 2011.
- [27] R. Sinkus, J. Lorenzen, D. Schrader, M. Lorenzen, M. Dargatz, and D. Holz, “High-resolution tensor MR elastography for breast tumour detection,” *Phys. Med. Biol.*, vol. 45, p. 1649, 2000.
- [28] R. Muthupillai, D. J. Lomas, P. J. Rossman, J. F. Greenleaf, A. Manduca, and R. L. Ehman, “Magnetic resonance elastography by direct visualization of propagating acoustic strain waves,” *Science*, vol. 269, no. 5232, p. 1854, 1995.

- [29] R. Muthupillai, P. J. Rossman, D. J. Lomas, J. F. Greenleaf, S. J. Riederer, and R. L. Ehman, "Magnetic resonance imaging of transverse acoustic strain waves," *Magn. Reson. Med.*, vol. 36, no. 2, pp. 266–274, 1996.
- [30] K. J. Glaser and R. L. Ehman, "Elastography," *Encycl. Magn. Reson.*, 2010.
- [31] J. Ophir, I. Cespedes, H. Ponnekanti, Y. Yazdi, and X. Li, "Elastography: a quantitative method for imaging the elasticity of biological tissues," *Ultrason. Imaging*, vol. 13, no. 2, pp. 111–134, 1991.
- [32] S. E. Salcudean, D. French, S. Bachmann, R. Zahiri-Azar, X. Wen, and W. J. Morris, "Viscoelasticity modeling of the prostate region using vibro-elastography," *Med. Image Comput. Comput.-Assist. Interv. MICCAI Int. Conf. Med. Image Comput. Comput.-Assist. Interv.*, vol. 9, no. Pt 1, pp. 389–396, 2006.
- [33] L. Pallwein, M. Mitterberger, P. Struve, G. Pinggera, W. Horninger, G. Bartsch, F. Aigner, A. Lorenz, F. Pedross, and F. Frauscher, "Real-time elastography for detecting prostate cancer: preliminary experience," *BJU Int.*, vol. 100, no. 1, pp. 42–46, Jul. 2007.
- [34] L. Huwart, F. Peeters, R. Sinkus, L. Annet, N. Salameh, L. C. ter Beek, Y. Horsmans, and B. E. Van Beers, "Liver fibrosis: non-invasive assessment with MR elastography," *NMR Biomed.*, vol. 19, no. 2, pp. 173–179, 2006.
- [35] L. Huwart, N. Salameh, L. ter Beek, E. Vicaut, F. Peeters, R. Sinkus, and B. E. Van Beers, "MR elastography of liver fibrosis: preliminary results comparing spin-echo and echo-planar imaging," *Eur. Radiol.*, vol. 18, no. 11, pp. 2535–2541, 2008.
- [36] M. Yin, J. A. Talwalkar, K. J. Glaser, A. Manduca, R. C. Grimm, P. J. Rossman, J. L. Fidler, and R. L. Ehman, "A preliminary assessment of hepatic fibrosis with magnetic resonance elastography," *Clin. Gastroenterol. Hepatol. Off. Clin. Pr. J. Am. Gastroenterol. Assoc.*, vol. 5, no. 10, p. 1207, 2007.
- [37] A. L. McKnight, J. L. Kugel, P. J. Rossman, A. Manduca, L. C. Hartmann, and R. L. Ehman, "MR elastography of breast cancer: preliminary results," *Am. J. Roentgenol.*, vol. 178, no. 6, p. 1411, 2002.
- [38] R. Sinkus, M. Tanter, T. Xydeas, S. Catheline, J. Bercoff, and M. Fink, "Viscoelastic shear properties of in vivo breast lesions measured by MR elastography," *Magn. Reson. Imaging*, vol. 23, no. 2, pp. 159–165, 2005.
- [39] D. Klatt, U. Hamhaber, P. Asbach, J. Braun, and I. Sack, "Noninvasive assessment of the rheological behavior of human organs using multifrequency MR elastography: a study of brain and liver viscoelasticity," *Phys. Med. Biol.*, vol. 52, p. 7281, 2007.
- [40] S. A. Kruse, G. H. Rose, K. J. Glaser, A. Manduca, J. P. Felmlee, C. R. Jack Jr, and R. L. Ehman, "Magnetic resonance elastography of the brain," *Neuroimage*, vol. 39, no. 1, pp. 231–237, 2008.
- [41] I. Sack, B. Beierbach, J. Wuerfel, D. Klatt, U. Hamhaber, S. Papazoglou, P. Martus, and J. Braun, "The impact of aging and gender on brain viscoelasticity," *Neuroimage*, vol. 46, no. 3, pp. 652–657, 2009.
- [42] U. Hamhaber, I. Sack, S. Papazoglou, J. Rump, D. Klatt, and J. Braun, "Three-dimensional analysis of shear wave propagation observed by in vivo magnetic resonance elastography of the brain," *Acta Biomater.*, vol. 3, no. 1, pp. 127–138, 2007.
- [43] K. P. McGee, R. D. Hubmayr, and R. L. Ehman, "MR elastography of the lung with hyperpolarized  $^3\text{He}$ ," *Magn. Reson. Med.*, vol. 59, no. 1, pp. 14–18, 2008.
- [44] B. C. Goss, K. P. McGee, E. C. Ehman, A. Manduca, and R. L. Ehman, "Magnetic resonance elastography of the lung: technical feasibility," *Magn. Reson. Med.*, vol. 56, no. 5, pp. 1060–1066, 2006.
- [45] I. Sack, J. Rump, T. Elgeti, A. Samani, and J. Braun, "MR elastography of the human heart: noninvasive assessment of myocardial elasticity changes by shear wave amplitude variations," *Magn. Reson. Med.*, vol. 61, no. 3, pp. 668–677, 2009.

- [46] B. Robert, R. Sinkus, J. L. Gennisson, and M. Fink, "Application of DENSE-MR-elastography to the human heart," *Magn. Reson. Med.*, vol. 62, no. 5, pp. 1155–1163, 2009.
- [47] R. Sinkus, K. Siegmann, T. Xydeas, M. Tanter, C. Claussen, and M. Fink, "MR elastography of breast lesions: understanding the solid/liquid duality can improve the specificity of contrast-enhanced MR mammography," *Magn. Reson. Med.*, vol. 58, no. 6, pp. 1135–1144, 2007.
- [48] M. A. Dresner, P. J. Rossman, S. A. Kruse, and R. L. Ehman, "MR elastography of the prostate," in *Proceedings of the 10th Annual Meeting of ISMRM, Philadelphia*, 1999, p. 526.
- [49] M. A. Dresner, J. C. Cheville, R. P. Myers, and R. L. Ehman, "MR elastography of prostate cancer," in *Proceedings of the 11th Annual Meeting of ISMRM, Toronto, Ontario, Canada*, 2003, p. 578.
- [50] D. M. McGrath, W. D. Foltz, N. Samavati, J. Lee, M. A. Jewett, T. H. van der Kwast, C. Ménard, and K. K. Brock, "Biomechanical Property Quantification of Prostate Cancer by Quasi-static MR Elastography at 7 Telsa of Radical Prostatectomy, and Correlation with Whole Mount Histology," in *Proceedings of the 19th Annual Meeting of ISMRM, Montreal, Canada*, 2011, vol. 19, p. 1483.
- [51] D. M. McGrath, W. D. Foltz, and K. K. Brock, "Progressive Change in Biomechanical Properties of Ex vivo Prostate with Pathology Fixation as Measured by MR Elastography at 7 Tesla, and Correlation with Changes in T1, T2 and ADC," in *Proceedings of the 19th Annual Meeting of ISMRM, Montreal, Canada*, 2011, vol. 19, p. 1478.
- [52] A. Arani, D. Plewes, and R. Chopra, "Transurethral prostate magnetic resonance elastography: Prospective imaging requirements," *Magn. Reson. Med.*, vol. 65, no. 2, pp. 340–349, Feb. 2011.
- [53] J. Kemper, R. Sinkus, J. Lorenzen, C. Nolte-Ernsting, A. Stork, and G. Adam, "MR elastography of the prostate: Initial in-vivo application= MR-Elastographie der Prostata: Erste In-vivo-Anwendung," in *Rofo. Fortschritte auf dem Gebiet der Rontgenstrahlen und der bildgebenden Verfahren*, 2004, vol. 176, pp. 1094–1099.
- [54] S. Li, M. Chen, W. Wang, W. Zhao, J. Wang, X. Zhao, and C. Zhou, "A feasibility study of MR elastography in the diagnosis of prostate cancer at 3.0T," *Acta Radiol. Stockh. Swed.* 1987, vol. 52, no. 3, pp. 354–358, Apr. 2011.
- [55] R. Chopra, A. Arani, Y. Huang, M. Musquera, J. Wachsmuth, M. Bronskill, and D. Plewes, "In vivo MR elastography of the prostate gland using a transurethral actuator," *Magn. Reson. Med.*, vol. 62, no. 3, pp. 665–671, 2009.
- [56] A. Arani, D. Plewes, A. Krieger, and R. Chopra, "The feasibility of endorectal MR elastography for prostate cancer localization," *Magn. Reson. Med.*, vol. 66, no. 6, pp. 1649–1657, 2011.
- [57] A. Arani, M. Da Rosa, E. Ramsay, D. B. Plewes, M. A. Haider, and R. Chopra, "Incorporating endorectal MR elastography into multi-parametric MRI for prostate cancer imaging: Initial feasibility in volunteers," *J. Magn. Reson. Imaging*, p. n/a–n/a, 2013.
- [58] Z. T. H. Tse, H. Janssen, A. Hamed, M. Ristic, I. Young, and M. Lamperth, "Magnetic resonance elastography hardware design: a survey," *Proc. Inst. Mech. Eng. [H]*, vol. 223, no. 4, pp. 497–514, 2009.
- [59] D. Klatt, P. Asbach, J. Rump, S. Papazoglou, R. Somasundaram, J. Modrow, J. Braun, and I. Sack, "In vivo determination of hepatic stiffness using steady-state free precession magnetic resonance elastography," *Invest. Radiol.*, vol. 41, no. 12, p. 841, 2006.
- [60] U. Hamhaber, I. Sack, S. Papazoglou, J. Rump, D. Klatt, and J. Braun, "Three-dimensional analysis of shear wave propagation observed by in vivo magnetic resonance elastography of the brain," *Acta Biomater.*, vol. 3, no. 1, pp. 127–138, 2007.
- [61] P. J. Rossman, R. Muthupillai, and R. L. Ehman, "Driver device for MR elastography," 5,952,828/1999.
- [62] J. Bishop, A. Samani, J. Sciarretta, and D. B. Plewes, "Two-dimensional MR elastography with linear inversion reconstruction: methodology and noise analysis," *Phys. Med. Biol.*, vol. 45, p. 2081, 2000.

- [63] Q. C. C. Chan, G. Li, R. L. Ehman, R. C. Grimm, R. Li, and E. S. Yang, "Needle shear wave driver for magnetic resonance elastography," *Magn. Reson. Med.*, vol. 55, no. 5, pp. 1175–1179, 2006.
- [64] K. Uffmann, C. Abicht, W. Grote, H. H. Quick, and M. E. Ladd, "Design of an MR-compatible piezoelectric actuator for MR elastography," *Concepts Magn. Reson.*, vol. 15, no. 4, pp. 239–254, 2002.
- [65] G. S. Fischer, I. Iordachita, C. Csoma, J. Tokuda, S. P. DiMaio, C. M. Tempany, N. Hata, and G. Fichtinger, "MRI-compatible pneumatic robot for transperineal prostate needle placement," *Mechatronics IEEEASME Trans.*, vol. 13, no. 3, pp. 295–305, 2008.
- [66] R. S. Sahebjavaheer, R. Sinkus, and S. E. Salcudean, "Rapid 3D MR Elastography of the Prostate with a Shielded Electromagnetic Driver and Multi-slice Steady-state Gradient Echo Sequence: design and characterization results (submitted to JMRI)," *Magn. Reson. Med.*, 2013.
- [67] D. B. Plewes, J. Bishop, A. Samani, and J. Sciarretta, "Visualization and quantification of breast cancer biomechanical properties with magnetic resonance elastography," *Phys. Med. Biol.*, vol. 45, p. 1591, 2000.
- [68] J. Braun, K. Braun, and I. Sack, "Electromagnetic actuator for generating variably oriented shear waves in MR elastography," *Magn. Reson. Med.*, vol. 50, no. 1, pp. 220–222, 2003.
- [69] R. S. Sahebjavaheer, A. Baghani, M. Honarvar, R. Sinkus, and S. E. Salcudean, "Transperineal prostate MR elastography: Initial in vivo results," *Magn. Reson. Med.*, vol. 69, no. 2, pp. 411–20, 2013.
- [70] M. Dresner, J. Fidler, and R. Ehman, "MR elastography of in vivo human liver," in *Proceedings of ISMRM 2004*, 2004, vol. 11, p. 502.
- [71] J. A. Talwalkar, M. Yin, J. L. Fidler, S. O. Sanderson, P. S. Kamath, and R. L. Ehman, "Magnetic resonance imaging of hepatic fibrosis: emerging clinical applications," *Hepatology*, vol. 47, no. 1, pp. 332–342, 2008.
- [72] P. Latta, M. L. H. Gruwel, P. Debergue, B. Matwiy, U. N. Sbotto-Frankensteen, and B. Tomanek, "Convertible pneumatic actuator for magnetic resonance elastography of the brain," *Magn. Reson. Imaging*, vol. 29, no. 1, pp. 147–152, Jan. 2011.
- [73] R. L. Ehman, P. J. Rossman, and J. Chen, "Passive Acoustic Driver For Magnetic Resonance Elastography," 20,090/299,168Apr-2009.
- [74] Y. K. Mariappan, P. J. Rossman, K. J. Glaser, A. Manduca, and R. L. Ehman, "Magnetic resonance elastography with a phased-array acoustic driver system," *Magn. Reson. Med.*, vol. 61, no. 3, pp. 678–685, 2009.
- [75] X. G. Zhao, Y. Zheng, Q. C. C. Chan, X. F. Yang, G. Li, and E. S. Yang, "Biopsy needle as MRE driver for tumor detection," in *Engineering in Medicine and Biology Society, 2007. EMBS 2007. 29th Annual International Conference of the IEEE*, 2007, pp. 2050–2052.
- [76] G. Thörmer, M. Reiss-Zimmermann, J. Otto, K.-T. Hoffmann, M. Moche, N. Garnov, T. Kahn, and H. Busse, "Novel technique for MR elastography of the prostate using a modified standard endorectal coil as actuator," *J. Magn. Reson. Imaging*, p. in press, 2012.
- [77] E. C. Ehman, P. J. Rossman, S. A. Kruse, A. V. Sahakian, and K. J. Glaser, "Vibration safety limits for magnetic resonance elastography," *Phys. Med. Biol.*, vol. 53, no. 4, pp. 925–935, Feb. 2008.
- [78] J. Bishop, G. Poole, M. Leitch, and D. B. Plewes, "Magnetic resonance imaging of shear wave propagation in excised tissue," *J. Magn. Reson. Imaging JMRI*, vol. 8, no. 6, pp. 1257–1265, Dec. 1998.
- [79] A. Manduca, V. Dutt, D. T. Borup, R. Muthupillai, R. L. Ehman, and J. F. Greenleaf, "Reconstruction of elasticity and attenuation maps in shear wave imaging: An inverse approach," in *Medical Image Computing and Computer-Assisted Intervention — MICCAI'98*, vol. 1496, W. M. Wells, A. Colchester, and S. Delp, Eds. Berlin/Heidelberg: Springer-Verlag, pp. 606–613.

- [80] D. B. Plewes and W. Kucharczyk, "Physics of MRI: a primer," *J. Magn. Reson. Imaging JMRI*, vol. 35, no. 5, pp. 1038–1054, May 2012.
- [81] P. R. Moran, "A flow velocity zeugmatographic interlace for NMR imaging in humans," *Magn. Reson. Imaging*, vol. 1, no. 4, pp. 197–203, 1982.
- [82] R. Muthupillai, D. J. Lomas, P. J. Rossman, J. F. Greenleaf, A. Manduca, and R. L. Ehman, "Magnetic resonance elastography by direct visualization of propagating acoustic strain waves," *Science*, vol. 269, no. 5232, p. 1854, 1995.
- [83] P. Garteiser, R. S. Sahebjavaher, L. ter Beek, S. E. Salcudean, V. Vilgrain, and R. Sinkus, "Rapid acquisition of multifrequency, multislice and multidirectional magnetic resonance elastography data with a fractionally encoded gradient echo sequence," *NMR Biomed. Press*, Nov. 2012.
- [84] D. A. Herzka, M. S. Kotys, R. Sinkus, R. I. Pettigrew, and A. M. Gharib, "Magnetic resonance elastography in the liver at 3 Tesla using a second harmonic approach," *Magn. Reson. Med.*, vol. 62, no. 2, pp. 284–291, 2009.
- [85] K. J. Glaser, A. Manduca, and R. L. Ehman, "Review of MR elastography applications and recent developments," *J. Magn. Reson. Imaging JMRI*, vol. 36, no. 4, p. spcone, Oct. 2012.
- [86] C. D. G. Hines, T. A. Bley, M. J. Lindstrom, and S. B. Reeder, "Repeatability of magnetic resonance elastography for quantification of hepatic stiffness," *J. Magn. Reson. Imaging JMRI*, vol. 31, no. 3, pp. 725–731, Mar. 2010.
- [87] O. Rouvière, M. Yin, M. A. Dresner, P. J. Rossman, L. J. Burgart, J. L. Fidler, and R. L. Ehman, "MR elastography of the liver: preliminary results," *Radiology*, vol. 240, no. 2, pp. 440–448, Aug. 2006.
- [88] S. Maderwald, K. Uffmann, C. J. Galbán, A. de Greiff, and M. E. Ladd, "Accelerating MR elastography: a multiecho phase-contrast gradient-echo sequence," *J. Magn. Reson. Imaging JMRI*, vol. 23, no. 5, pp. 774–780, May 2006.
- [89] P. Asbach, D. Klatt, U. Hamhaber, J. Braun, R. Somasundaram, B. Hamm, and I. Sack, "Assessment of liver viscoelasticity using multifrequency MR elastography," *Magn. Reson. Med. Off. J. Soc. Magn. Reson. Med. Soc. Magn. Reson. Med.*, vol. 60, no. 2, pp. 373–379, Aug. 2008.
- [90] P. Asbach, D. Klatt, B. Schlosser, M. Biermer, M. Muche, A. Rieger, C. Loddenkemper, R. Somasundaram, T. Berg, B. Hamm, J. Braun, and I. Sack, "Viscoelasticity-based staging of hepatic fibrosis with multifrequency MR elastography," *Radiology*, vol. 257, no. 1, pp. 80–86, Oct. 2010.
- [91] L. Huwart, C. Sempoux, E. Vicaud, N. Salameh, L. Annet, E. Danse, F. Peeters, L. C. ter Beek, J. Rahier, R. Sinkus, Y. Horsmans, and B. E. Van Beers, "Magnetic Resonance Elastography for the Noninvasive Staging of Liver Fibrosis," *Gastroenterology*, vol. 135, no. 1, pp. 32–40, Jul. 2008.
- [92] G. I. Nedredal, M. Yin, T. McKenzie, J. Lillegard, J. Luebke-Wheeler, J. Talwalkar, R. Ehman, and S. L. Nyberg, "Portal hypertension correlates with splenic stiffness as measured with MR elastography," *J. Magn. Reson. Imaging JMRI*, vol. 34, no. 1, pp. 79–87, Jul. 2011.
- [93] J. Rump, D. Klatt, J. Braun, C. Warmuth, and I. Sack, "Fractional encoding of harmonic motions in MR elastography," *Magn. Reson. Med. Off. J. Soc. Magn. Reson. Med. Soc. Magn. Reson. Med.*, vol. 57, no. 2, pp. 388–395, Feb. 2007.
- [94] A. Kolipaka, K. P. McGee, P. A. Araoz, K. J. Glaser, A. Manduca, and R. L. Ehman, "Evaluation of a rapid, multiphase MRE sequence in a heart-simulating phantom," *Magn. Reson. Med. Off. J. Soc. Magn. Reson. Med. Soc. Magn. Reson. Med.*, vol. 62, no. 3, pp. 691–698, Sep. 2009.
- [95] A. Kolipaka, K. P. McGee, P. A. Araoz, K. J. Glaser, A. Manduca, A. J. Romano, and R. L. Ehman, "MR elastography as a method for the assessment of myocardial stiffness: comparison with an established pressure-volume model in a left ventricular model of the heart," *Magn. Reson. Med. Off. J. Soc. Magn. Reson. Med. Soc. Magn. Reson. Med.*, vol. 62, no. 1, pp. 135–140, Jul. 2009.

- [96] T. Elgeti, H. Tzschätzsch, S. Hirsch, D. Krefting, D. Klatt, T. Niendorf, J. Braun, and I. Sack, "Vibration-synchronized magnetic resonance imaging for the detection of myocardial elasticity changes," *Magn. Reson. Med. Off. J. Soc. Magn. Reson. Med. Soc. Magn. Reson. Med.*, vol. 67, no. 4, pp. 919–924, Apr. 2012.
- [97] A. Manduca, T. E. Oliphant, M. A. Dresner, J. L. Mahowald, S. A. Kruse, E. Amromin, J. P. Felmlee, J. F. Greenleaf, and R. L. Ehman, "Magnetic resonance elastography: non-invasive mapping of tissue elasticity," *Med. Image Anal.*, vol. 5, no. 4, p. 237, 2001.
- [98] T. A. Krouskop, T. M. Wheeler, F. Kallel, B. S. Garra, and T. Hall, "Elastic moduli of breast and prostate tissues under compression," *Ultrason. Imaging*, vol. 20, no. 4, pp. 260–274, 1998.
- [99] K. J. Parker, S. R. Huang, R. M. Lerner, F. Lee Jr, D. Rubens, and D. Roach, "Elastic and ultrasonic properties of the prostate," in *Ultrasonics Symposium, 1993. Proceedings., IEEE 1993*, 2002, pp. 1035–1038.
- [100] T. H. J. Yang, S. K. W. Leung, S. Phipps, R. L. Reuben, S. A. McNeill, F. K. Habib, A. Schnieder, and R. Stevens, "In-vitro dynamic micro-probing and the mechanical properties of human prostate tissues," *Technol. Health Care*, vol. 14, no. 4, pp. 281–296, 2006.
- [101] S. Phipps, T. H. J. Yang, F. K. Habib, R. L. Reuben, and S. A. McNeill, "Measurement of tissue mechanical characteristics to distinguish between benign and malignant prostatic disease," *Urology*, vol. 66, no. 2, pp. 447–450, 2005.
- [102] K. Hoyt, B. Castaneda, M. Zhang, P. Nigwekar, P. A. di Sant'Agnes, J. V. Joseph, J. Strang, D. J. Rubens, and K. J. Parker, "Tissue elasticity properties as biomarkers for prostate cancer," *Cancer Biomark.*, vol. 4, no. 4, pp. 213–225, 2008.
- [103] Y. Murayama, S. Omata, T. Yajima, Q. Peng, K. Shishido, D. M. Peehl, and C. E. Constantinou, "High resolution regional elasticity mapping of the human prostate," in *Engineering in Medicine and Biology Society, 2007. EMBS 2007. 29th Annual International Conference of the IEEE*, 2007, pp. 5802–5805.
- [104] B.-M. Ahn, J. Kim, L. Ian, K.-H. Rha, and H.-J. Kim, "Mechanical Property Characterization of Prostate Cancer Using a Minimally Motorized Indenter in an Ex Vivo Indentation Experiment," *Urology*, vol. 76, no. 4, pp. 1007–1011, Oct. 2010.
- [105] T. Sarvazyan, V. Stolarsky, V. Fishman, and A. Sarvazyan, "Development of mechanical models of breast and prostate with palpable nodules," in *Engineering in Medicine and Biology Society, 1998. Proceedings of the 20th Annual International Conference of the IEEE*, 2002, vol. 2, pp. 736–739.
- [106] A. R. Skovorda, A. N. Klishko, D. A. Gusakian, E. I. Maevskii, V. D. Ermilova, G. A. Oranskaia, and A. P. Sarvazian, "Quantitative analysis of mechanical characteristics of pathologically altered soft biological tissues," *Biofizika*, vol. 40, no. 6, p. 1335, 1995.
- [107] R. Sinkus, T. Nisius, J. Lorenzen, J. Kemper, and M. Dargatz, "In-vivo prostate MR-elastography," in *Proceedings of the 11th Annual Meeting of ISMRM, Toronto, Canada*, 2003, p. 586.
- [108] R. Souchon, V. Hervieu, A. Gelet, J. Ophir, and J.-Y. Chapelon, "Human prostate elastography: in vitro study," in *2003 IEEE Symposium on Ultrasonics*, 2003, vol. 2, pp. 1251–1253 Vol.2.
- [109] A. Baghani, S. Salcudean, M. Honarvar, R. Sahebjavaher, R. Rohling, and R. Sinkus, "Travelling Wave Expansion: A Model Fitting Approach to the Inverse Problem of Elasticity Reconstruction," *IEEE Trans. Med. Imaging*, vol. 30, no. 8, pp. 1555 – 1565, 2011.
- [110] M. Honarvar, R. S. Sahebjavaher, S. E. Salcudean, and R. Rohling, "Sparsity regularization in dynamic elastography," *Phys. Med. Biol.*, vol. 57, no. 19, pp. 5909–5927, Oct. 2012.
- [111] M. Honarvar, R. S. Sahebjavaher, R. Sinkus, R. Rohling, and S. E. Salcudean, "Curl-based Finite Element Reconstruction of the Shear Modulus Without Assuming Local Homogeneity: Time Harmonic Case," *Trans. Med. Imaging Submitt.*, 2013.

- [112] Ramin S. Sahebjavaher, A. Baghani, R. Sinkus, and S. E. Salcudean, "Prostate MRE at 3T: Transperineal wave propagation," in *International Society for Magnetic Resonance in Medicine*, 2011, vol. 19, p. 1477.
- [113] R. Hausmann, J. S. Lewin, and G. Laub, "Phase-contrast MR angiography with reduced acquisition time: new concepts in sequence design," *J. Magn. Reson. Imaging JMRI*, vol. 1, no. 4, pp. 415–422, Aug. 1991.
- [114] J. M. Bland and D. G. Altman, "Applying the right statistics: analyses of measurement studies," *Ultrasound Obstet. Gynecol. Off. J. Int. Soc. Ultrasound Obstet. Gynecol.*, vol. 22, no. 1, pp. 85–93, Jul. 2003.
- [115] Garteiser, Philippe, Doblaz, Sabrina, VanBeers, Bernard E., Vilgrain, Valerie, and Sinkus, Ralph, "Physical Boundary Conditions Reconstruction: a Novel Method to Determine Viscoelastic Parameters from Magnetic Resonance Elastography Data," in *Proceedings of the 19th Annual Meeting of ISMRM, Montreal*, 2011, vol. 19, p. 3382.
- [116] J. Rump, D. Klatt, J. Braun, C. Warmuth, and I. Sack, "Fractional encoding of harmonic motions in MR elastography," *Magn. Reson. Med.*, vol. 57, no. 2, pp. 388–395, 2007.
- [117] Ramin S. Sahebjavaher, P. Garteiser, B. Van Beers, S. E. Salcudean, and R. Sinkus, "Rapid 3D motion-encoding using spoiled FFE: application towards multi-frequency MR rheology in liver," in *European Society for Magnetic Resonance in Medicine and Biology*, Leipzig, Germany, 2011, p. 124.
- [118] Ramin S. Sahebjavaher, P. Garteiser, R. Sinkus, L. O. Gagnon, A. Baghani, S. Chang, S. Chatelin, E. C. Jones, C. Nguan, L. Goldenberg, M. Moradi, P. Kozlowski, and S. E. Salcudean, "3D MR Elastography of in-vivo Prostate Cancer and Correlation with Histology: Preliminary results.," in *International Society for Magnetic Resonance in Medicine*, Melbourne, Australia, 2012, p. 2521.
- [119] O. Bieri, S. Maderwald, M. E. Ladd, and K. Scheffler, "Balanced alternating steady-state elastography," *Magn. Reson. Med. Off. J. Soc. Magn. Reson. Med. Soc. Magn. Reson. Med.*, vol. 55, no. 2, pp. 233–241, Feb. 2006.
- [120] M. Honarvar, R. S. Sahebjavaher, S. E. Salcudean, and R. Rohling, "Sparsity regularization in dynamic elastography," *Phys. Med. Biol.*, vol. 57, no. 19, pp. 5909–5927, Oct. 2012.
- [121] E. Park and A. M. Maniatty, "Shear modulus reconstruction in dynamic elastography: time harmonic case," *Phys. Med. Biol.*, vol. 51, no. 15, pp. 3697–3721, Aug. 2006.
- [122] R. S. Garteiser, S. Doblaz, B. E. VanBeers, V. Vilgrain, and R. Sinkus, "Physical Boundary Conditions Reconstruction: a Novel Method to Determine Viscoelastic Parameters from Magnetic Resonance Elastography Data," in *International Society for Magnetic Resonance in Medicine*, Montreal, Canada, 2011, p. 3382.
- [123] B. Drew, E. C. Jones, S. Reinsberg, A. C. Yung, S. L. Goldenberg, and P. Kozlowski, "Device for sectioning prostatectomy specimens to facilitate comparison between histology and in vivo MRI," *J. Magn. Reson. Imaging JMRI*, vol. 32, no. 4, pp. 992–996, Oct. 2010.
- [124] G. Nir and S. E. Salcudean, "Registration of whole-mount histology and tomography of the prostate using particle filtering," in *Proceedings of SPIE Medical Imaging*, 2013.
- [125] D. L. Cochlin, R. H. Ganatra, and D. F. R. Griffiths, "Elastography in the detection of prostatic cancer," *Clin. Radiol.*, vol. 57, no. 11, pp. 1014–1020, 2002.
- [126] L. Jugé, B.-T. Doan, J. Seguin, M. Albuquerque, B. Larrat, N. Mignet, G. G. Chabot, D. Scherman, V. Paradis, V. Vilgrain, B. E. Van Beers, and R. Sinkus, "Colon tumor growth and antivascular treatment in mice: complementary assessment with MR elastography and diffusion-weighted MR imaging," *Radiology*, vol. 264, no. 2, pp. 436–444, Aug. 2012.

- [127] D. M. McGrath, W. D. Foltz, A. Al-Mayah, C. J. Niu, and K. K. Brock, “Quasi-static magnetic resonance elastography at 7 T to measure the effect of pathology before and after fixation on tissue biomechanical properties,” *Magn. Reson. Med. Off. J. Soc. Magn. Reson. Med. Soc. Magn. Reson. Med.*, vol. 68, no. 1, pp. 152–165, Jul. 2012.
- [128] A. Porea and A. G. Webb, “Reversible and irreversible effects of chemical fixation on the NMR properties of single cells,” *Magn. Reson. Med. Off. J. Soc. Magn. Reson. Med. Soc. Magn. Reson. Med.*, vol. 56, no. 4, pp. 927–931, Oct. 2006.
- [129] A. Akers, M. Gassman, and R. Smith, *Hydraulic Power System Analysis*. CRC Press, 2006.
- [130] Y. Cengel and J. Cimbala, *Fluid Mechanics with Student Resources DVD*, 2nd ed. McGraw-Hill Science/Engineering/Math, 2009.
- [131] J. Mazumdar, *Biofluid mechanics*. World Scientific, 1992.
- [132] T. Nakamura, *Flow-induced vibrations: classifications and lessons from practical experiences*. Elsevier, 2008.

# Appendix A – Modeling of the Hydraulic Transducer

For the modeling the mechanical response of the hydraulic transducer the following cases have been considered: static, steady-state, and dynamic responses.

**STATIC:** In the static case, the stiffness of the system are of interest which includes the stiffness of the conduit (or container) and stiffness of the springs at both ends of the transducer. The stiffness of the conduit is defined by the bulk modulus  $\beta_e$ , or its equivalent spring constant  $K_{Container}$ ,

$$\beta_e = \frac{dp}{dV/V} = \frac{\delta E}{d_c} = \frac{(1.7mm)(1GPa)}{(12.4mm)} = 137MPa \quad (A-1)$$

$$K_{Container} = \beta_e \frac{A_c}{L_c} = \frac{\pi}{4} \delta E \frac{d_c}{L_c} = \frac{\pi}{4} (1.7mm)(1GPa) \left( \frac{12.4mm}{2.2m} \right) = 7.5 \frac{N}{mm} \quad (A-2)$$

where the parameters are pressure change  $\Delta p$  and volume change  $\Delta V$ , total volume  $V$ , wall thickness of hose/pipe  $\delta$ , cross-sectional area  $A_c$ , total length  $L_c$ , and Young's modulus  $E$  and diameter  $d_c$  (=12.4 mm). The stiffness of the springs is given by,

$$K_{Spring} = \frac{A_s E}{L_s} \left[ \frac{N}{m} \right] \quad (A-3)$$

where the parameters are defined as before. These equations are later used in the dynamic model. It was not possible to remove all traces of air bubbles; therefore, this effect of air bubble on the stiffness of the system must be considered. The effective bulk modulus of a hydraulic system with entrapped air is found as [129]

$$\beta_{effective} = \left( \beta_{water}^{-1} + \frac{V_{air}}{V_{total}} \beta_{air}^{-1} \right)^{-1} \quad (A-4)$$

where

$$\frac{V_{air}}{V_{total}} = \frac{P_{atm}}{P + P_{atm}}, \quad \beta_{air} = \gamma_{air} P \quad (A-5), (A-6)$$

The isentropic expansion factor  $\gamma_{air}$  is about 1.4 for air at room temperature. The normalized effective bulk modulus in of the hydraulic system is shown in Figure A-1 as a function of system pressure  $P$  from equation (A-4).

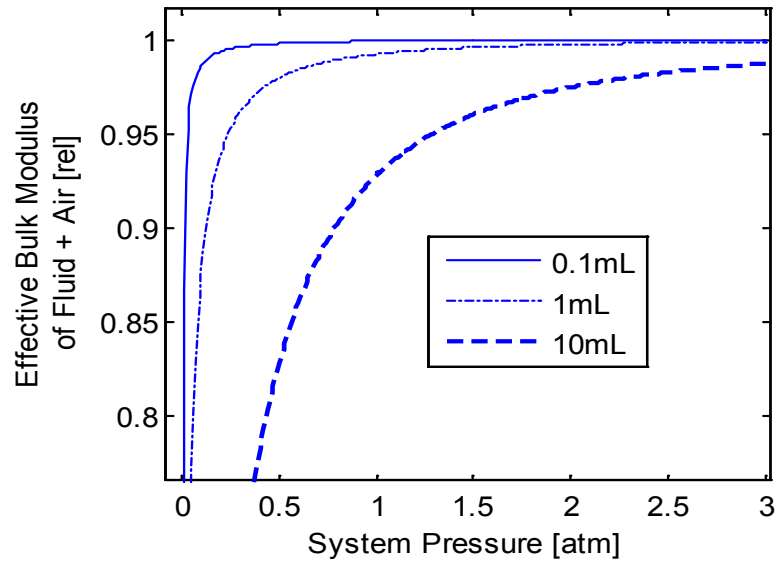


Figure A-1. Effective bulk modulus of the hydraulic system as a function of volume of entrapped air bubbles in 1L of fluid. Any air bubbles less than 1mL are difficult to remove in practice. The working pressure is between 0.5 and 2 atm.

From this plot it becomes apparent that only a small amount of entrapped air bubble can significantly reduce the overall stiffness of the hydraulic system. However, increasing the pressure of the hydraulic system mitigates this problem. The hydraulic transducer is de-aired by first directing all the air bubbles to one end of the system and reducing the pressure to as low as possible and then extracting the air bubbles using a transdermal syringe. The bulk modulus of the hydraulic transducer were measured in terms of volume and linear displacement as a function of system pressure. The pressure change was induced by regulating the added fluid via a syringe. The results are shown in Figure A-2. In the latest version of the hydraulic transducer (HS v2.1) compared to the old system (HSv2.0), for example, the bulk modulus of the conduit increased from 26 MPa (1.6 N/mm) to 110 MPa (5.9 N/mm). The spring stiffness of the input (active-end) was determined to be 3 N/mm (in the non-saturated region) and the stiffness of the output (subject-end) spring was 38 N/mm. The stiffness values are reasonably close to the analytic solutions found in (A-1) and (A-2) considering that the Young's modulus was assumed, which is typically 1 GPa for polyethylene tubes. The effect of entrapped air bubbles was not immediately visible in these graphs since the pressure gauge used in this experiment could only measure pressures above 40 kPa (0.4 atm). Above this pressure, no increase in the bulk modulus of the container was present, so most likely the air bubbles are less than 1 mL in 1 L (= 0.1%) of water.

If the two ends of the hydraulic system are at different heights, a static pressure drop develops that can be calculated from the Bernoulli equation,

$$\frac{1}{2} \rho v_1^2 + \rho g z_1 + p_1 = \frac{1}{2} \rho v_2^2 + \rho g z_2 + p_2 \quad (\text{A-7})$$

with density of hydraulic fluid  $\rho$ , fluid velocity  $v$ , fluid pressure  $p$  and vertical position  $z$  at point 1 (active-end) and point 2 (subject-end). For example, typically  $v_1 = v_2$  and if there is a change in height between the two

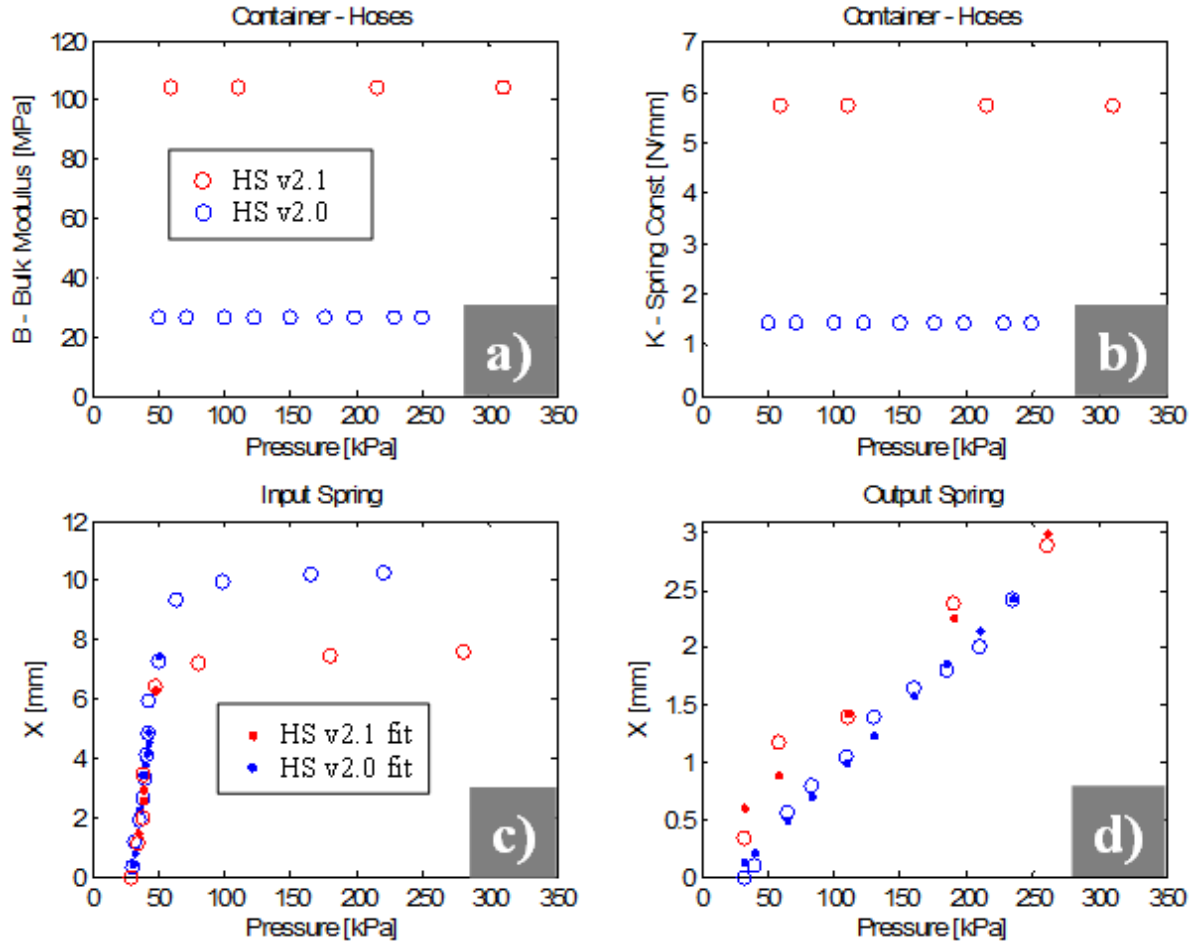


Figure A-2. Static characterization of hydraulic transducer (HSv2.0 and HSv2.1): bulk modulus (a) and spring constant (b) of pipe. The spring constants of input(c) and output (d) springs as determined from  $V$  vs.  $P$  and position vs.  $P$  measurements.

points is 0.2 m, then  $\Delta p$  is 2 kPa. This pressure difference is negligible when compared to system pressure of  $>50$  kPa. This pressure difference results in a smaller than 0.1 mm offset from the center position of the output spring. The offset in position due to the change in height is negligible and can be reduced if the height difference is reduced.

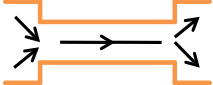
**STEADY-STATE:** In analysing the system in steady-state, the power requirements and the amount of pressure drop were considered. The relevant equation are derived from [62-65] and are summarized in Table A-1. All equations are based on root mean square (r.m.s.) values and are in terms of the diameter of the conduit  $d_f$ , amplitude at patient-end  $x_o$ , amplitude of hydraulic fluid in the conduit  $x_f$ , frequency of excitation  $f$ , length of conduit  $L_f$ , bend diameter of the bent pipe  $D$ , dynamic  $\mu$  and density  $\rho$ . If at the patient an amplitude of  $x_o = 1$  mm<sub>pk-pk</sub> (0.71 mm<sub>r.m.s.</sub>) is assumed, the amplitude of the moving fluid can be found from the geometry of the diaphragms ( $d_o = 22.9$  mm and  $d_i = 37.2$  mm) as

$$x_{patient} = x_o = 1mm_{pk-pk}$$

$$x_{f,rms} = \frac{x_o}{\sqrt{2}} \left( \frac{d_o}{d_f} \right)^2 \quad (A-8)$$

where the displacement of fluid  $x_f$  is 2.4 mm in the pipe, velocity  $v_f$  is 0.69 m/s and acceleration  $a_f$  is 194 m/s<sup>2</sup>. The flow rate  $Q_f$  becomes 82 mL/s which results in a Reynolds number of RE = 8600 (turbulent flow) for a 12.4 mm equivalent inner diameter conduit. First, the necessary pressure and power required to move the fluid mass itself where calculated (first row in Table A-1). The losses of the pipe stem from the frictional loss in the straight parts of the conduit, the bends, geometrical changes, such as sudden expansion and contraction, and the height difference between the two ends of the system.

**Table A-1. Required power (or loss of power) and pressure drop for various cases in the hydraulic transmission pipe.**

| Case  | Basic Eqn.               | Power [W]  | Pressure [kPa], Force [N]   |
|---|--------------------------|--|---|
|    | $P_{fluid} = F \cdot V$  | $\pi^4 \rho L_f x_o^2 d_o^4 d_f^{-2} f^3 = 132W$   | $+\frac{\pi^2}{4\sqrt{2}} \rho L_f x_o^2 d_o^2 d_f^{-2} f^2 = +102kPa$<br>$F_{input} = \Delta p_{fluid} A_i = \frac{\pi^3}{16\sqrt{2}} \cdot \rho L_f x_o^2 d_o^2 d_f^2 f^2 = 111N$ |
|    | $P = Q_f \cdot \Delta p$ | $2.37 \mu^{0.25} \rho^{0.75} L_f x_o^{2.75} d_o^{5.5} d_f^{-4.75} f^{2.75} = 0.1W$       | $-0.68 \rho^{0.75} \mu^{0.25} L_f x_o^{1.75} d_o^{3.5} d_f^{-4.75} f^{1.75} = -1.7kPa$  |
|    | $P = Q_f \cdot \Delta p$ | $0.80 \cdot D^{0.9} \mu^{0.2} \rho^{0.8} x_o^{2.8} d_o^{5.6} d_f^{-4.7} f^{2.8} = 1.5mW$ | $-0.23 \cdot D^{0.9} \mu^{0.2} \rho^{0.8} x_o^{1.8} d_o^{3.6} d_f^{-4.7} f^{1.8} = -58Pa$   |
|    | $P = Q_f \cdot \Delta p$ | $\approx \frac{\pi^4}{4\sqrt{2}} \rho x_o^3 d_o^6 d_f^{-4} f^2 = 10mW$                   | $S.C. = -\frac{\pi^2}{2} \rho x_o^2 d_o^4 d_f^{-4} f^2 \beta^4 (1 - \beta^2) = -8Pa$<br>$S.E. = -\frac{\pi^2}{2} \rho x_o^2 d_o^4 d_f^{-4} f^2 \beta^4 (1 - \beta^2)^2 = -7Pa$      |
|  | $P = Q_f \cdot \Delta p$ | $\frac{\pi^2}{2\sqrt{2}} \rho g \Delta z \cdot x_o d_o^2 f = 0.1W$                       | $-\rho g \Delta z = -1.9kPa$  |

As seen in Table A-1, most of the power (calculated at 45 Hz) goes towards moving the fluid mass, and the frictional losses are negligible for pipe diameters larger than 5 mm in diameter. The required power (in logarithmic scale) as a function of frequency, pipe diameter and amplitude is shown in Figure A-3. The pressure drop along the hydraulic system is shown in Figure A-3d. The most important results from these graphs and Table A-1 are that the required power depends on the (i) frequency of excitation to the power of three, (ii) inverse of the diameter of the pipe to the power of two, and (iii) the amplitude of excitation to the power of two. The dominant pressure drop is related to the turbulent frictional losses and the height difference (if present) between the two ends of the hydraulic exciter. The pressure drop affects the phase (i.e., delay) of the system.

At this time the only steady-state measurement performed, involved the measurement of the amplitude (0.6 mm pk-pk) and the input power 30 W. The limiting factor in the input power was that above 30 W either the amplifier would automatically shut down as a result of overheating or the commercial electromagnetic exciter would overheat.

**DYNAMIC:** The model shown in Figure A-4 was used to approximate the dynamic response of the Hydraulic transducer. The mass of the moving table of the commercial exciter and half the mass of the moving fluid constitutes  $m_1$ . The mass  $m_2$  constitutes the other half of the moving fluid. The spring  $k_1$  is the internal spring

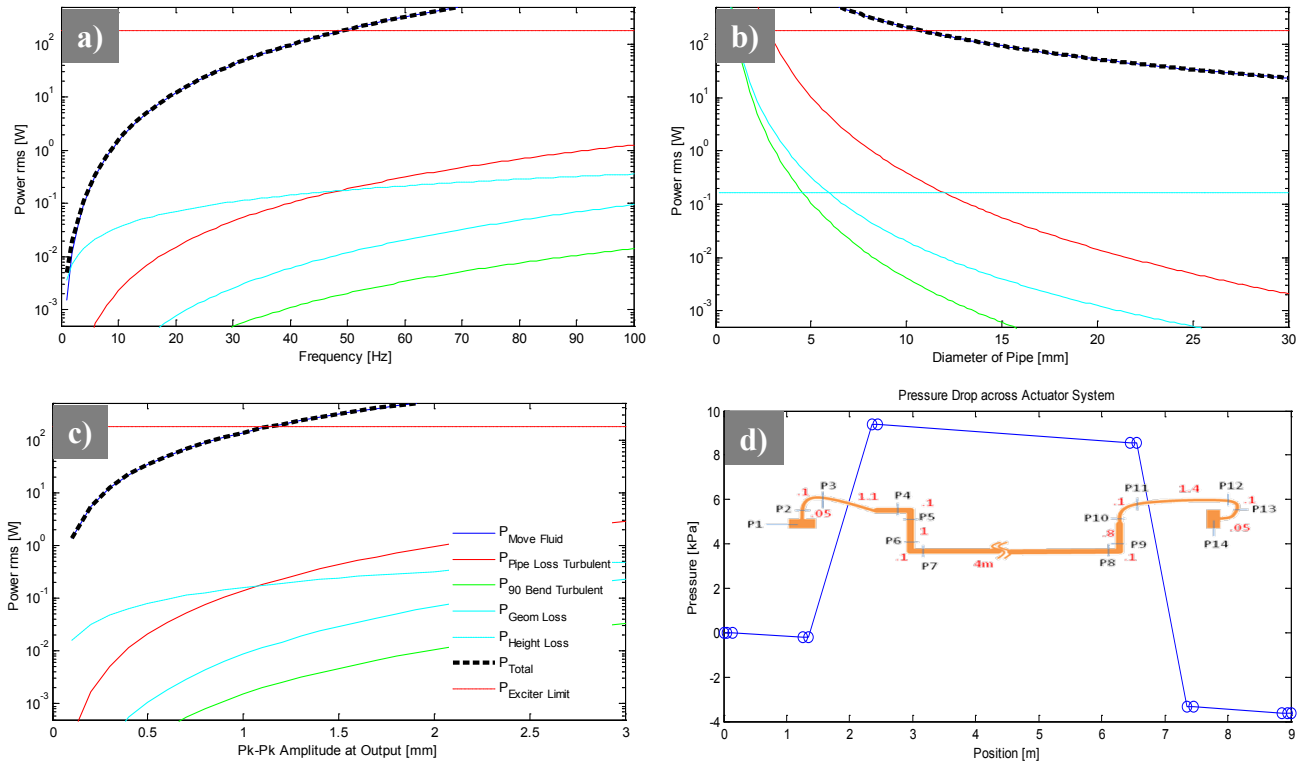


**Figure A-3.** Required power for each case is shown in as a function on excitation frequency (a), pipe diameter (b) and amplitude of output (c). The red dotted line represents the theoretical power limit of the commercial exciter (180W). The calculated pressure drop along the hydraulic exciter is shown in (d).

stiffness of the commercial exciter,  $k_2$  represents the stiffness of the conduit. The mass of the load is  $m_3$  that represents tissue such as perineum and prostate where the stiffness and damping of the load is modelled by  $k_4$  and  $b_4$ . The springs  $k_5$  and  $k_6$  represent the input (active-end) spring and output (subject-end) spring, respectively. The damping values for the load (tissue) were estimated from measured MRE values.

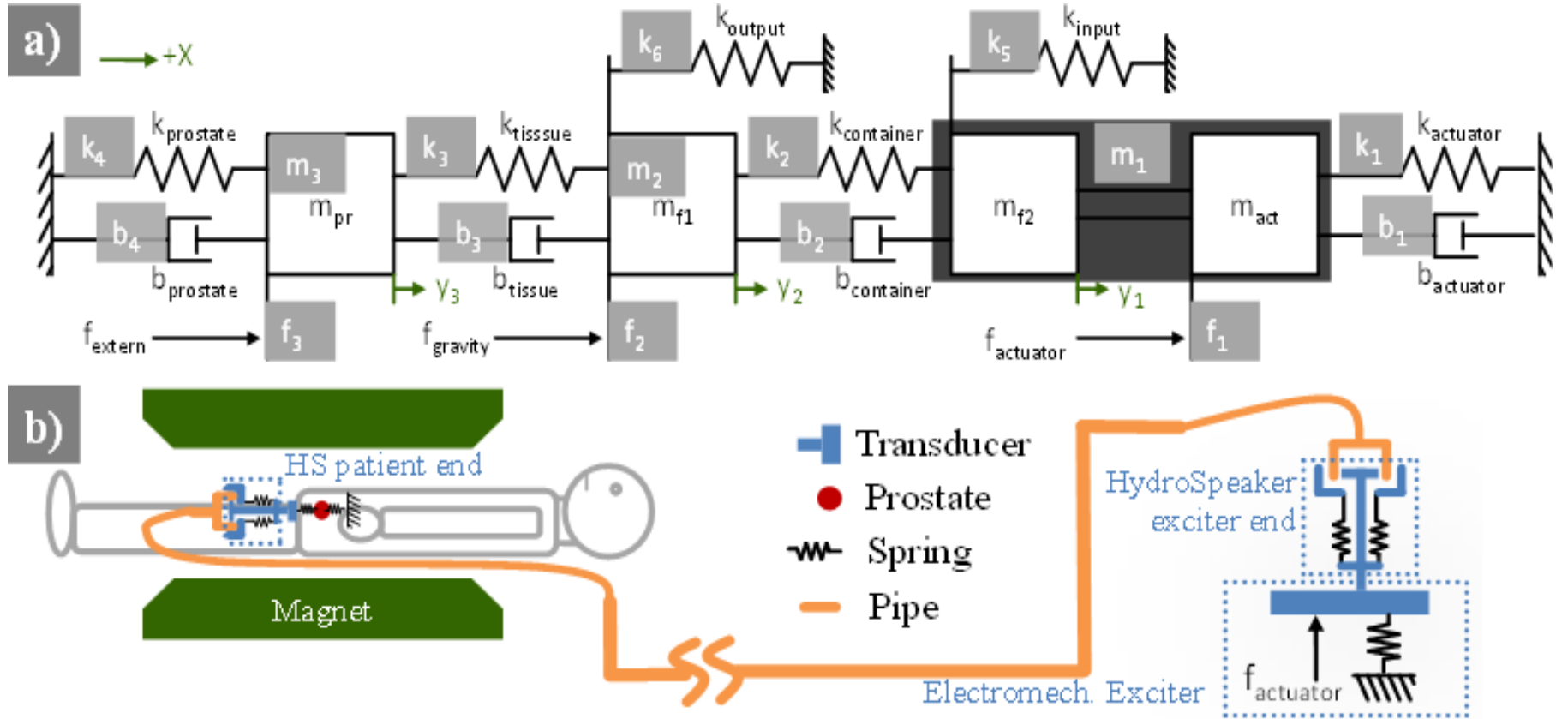


Figure A-4. The multi-degrees of freedom model (a) and its schematic (b) used in approximating the dynamic response of the hydraulic transducer.

The damping for the mechanics was estimated using the pressure drop and power calculations mentioned in the steady-state analysis:

$$P_{turbulant} = \Delta p Q = P_{Mech.loss} = b.V \quad (A-9)$$

$$b = \frac{\Delta p Q}{V} = \frac{\Delta p V A_f}{V} = \Delta p A_f = \frac{1.25\pi}{4} \rho^{0.75} \mu^{0.25} L_f x_f^{1.75} d_f^{0.75} f^{1.75} \left[ \frac{N.s}{m} \right] \quad (A-10)$$

The analytical solution becomes a standard multi-degree-of-freedom system, where the response of the system is given by the equation of motion

$$M\ddot{y} + B\dot{y} + Ky = F \quad (A-11)$$

where the matrices of mass  $M$ , damping  $B$  and spring constants  $K$  are found as,

$$M = \begin{pmatrix} m_1 & 0 & 0 \\ 0 & m_2 & 0 \\ 0 & 0 & m_3 \end{pmatrix},$$

$$B = \begin{pmatrix} b_1 + b_2 & -b_2 & 0 \\ -b_2 & b_2 + b_3 & -b_3 \\ 0 & -b_3 & b_3 + b_4 \end{pmatrix}, \quad (A-12)$$

$$K = \begin{pmatrix} k_1 + k_2 + k_5 & -k_2 & 0 \\ -k_2 & k_2 + k_3 + k_6 & -k_3 \\ 0 & -k_3 & k_3 + k_4 \end{pmatrix}$$

The transfer function of the system  $H(w)$  can be found by applying the Laplace transform to equation (A-11). Assuming force  $F$  as the input and displacements  $Y$  as the output the transfer function becomes,

$$H(s) = \frac{Y}{F} = (Ms^2 + Bs + K)^{-1} \quad (A-13)$$

where the transfer function matrix is

$$H(s) = \begin{pmatrix} h_{11} & h_{21} & h_{31} \\ h_{12} & h_{22} & h_{32} \\ h_{13} & h_{23} & h_{33} \end{pmatrix} \quad (A-14)$$

Since we are interested in the dynamic response we can assume that  $f_2$  and  $f_3$  are zero and  $f_1$  is a sinusoidal excitation from the electromechanical vibration source. We are interested in the amplitude of motion at the patient end  $y_3$ . Therefore, the parameter of interest in Equation (A-14) becomes  $z_{31}$  (i.e.,  $y_3 = h_{31} \times f_1$ ). The normalized response of the output amplitude  $y_3$  for frequencies between 1-500 Hz is shown in (A-14) as a function of (a) diameter of pipe/hose, (b) stiffness of input spring, and (c) stiffness of output spring. The dynamics of the Hydraulic transducer were measured using ICP accelerometers (PCB-Piezotronics model 352C33) mounted on both ends of the system. The signal was analyzed with a dynamic signal analyzer (HP3562A) that would generate a bode plot as show in Figure A-5d. The measured data could not be accessed directly, so a photograph of the display was taken and post-processed using image processing techniques to extract the bode plot. The model was later fit to the measured using least squares approach that was minimized using Matlab's *fminsearch* function. This result is shown in Figure A-5d. Since the model is very simplistic, the fitted parameters do not exactly match with the estimated parameters but they are the same order of magnitude. That being said, a reasonable fit was achieved using the model from which useful prediction can be made for the next design. In general, one can see three resonances as it is a three mass-spring system. In case of Figure A-5a, an increasing pipe diameter results in higher amplitudes at the subject-end but lowers the resonance frequencies and increases system delays (phase-lags). In terms of the spring stiffness in case b and c, higher spring stiffness results in higher resonance frequency but lower amplitude. The effect of the output spring has a larger impact on the amplitude.

From these graphs one can conclude that a larger pipe diameter and less stiff springs at the ends of the Hydraulic transducer would result in larger amplitudes at the patient end at the cost of lower resonant frequencies and increased phase-lags. Note that since this exciter is operated in steady state, the phase-lag issues become less important. That being said, if the phase-lag becomes dependent on the external effects such as temperature changes, this could result in phase instabilities which results in low-quality wave images. In addition, it was seen in the steady-state section, that a larger pipe diameter would result in a lower power requirements and lower pipe losses which translates into higher amplitudes at the patient end. A larger pipe means that the displacement in the fluid become smaller which results in lower vibrations levels of the conduit.

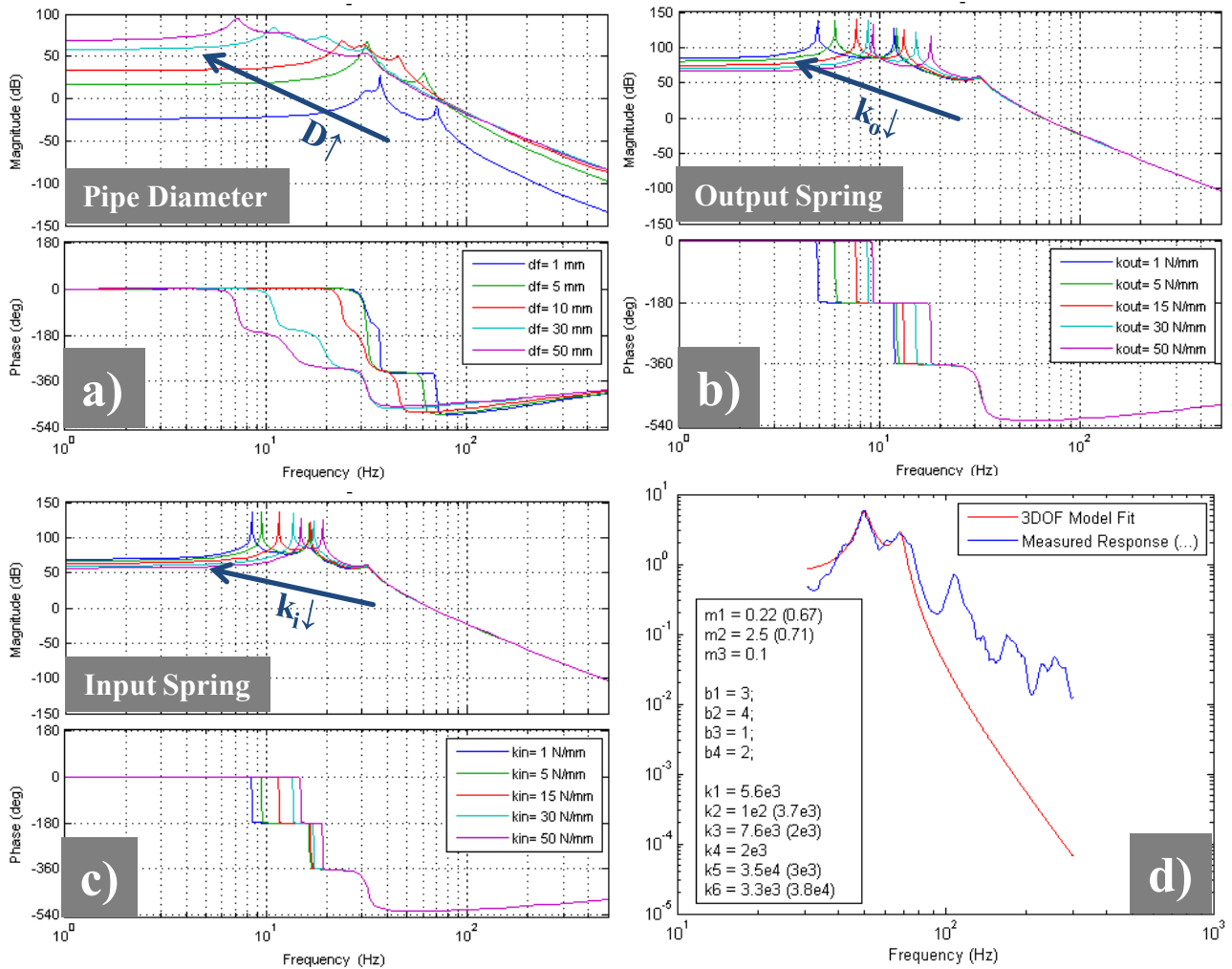


Figure A-5. The results from dynamic response simulation as a function of pipe diameter (a), input spring (b) and output spring (c). The model was fitted to the measured dynamic response to identify the parameters (d).

# Appendix B – Consent form



UNIVERSITY OF BRITISH COLUMBIA

Department of Electrical and Computer Engineering

2332 Main Mall, Vancouver, B.C., V6T 1Z4

**SUBJECT INFORMATION AND CONSENT FORM**

## Optimization of MR Elastography Imaging of the Prostate

Principal Investigator:

**Dr. Tim Salcudean**

Department of Electrical and Computer Engineering, UBC

Tel: (xxx) xxx-xxxx

Co-Investigators:

**Dr. Piotr Kozlowski**

Department of Urologic Sciences, UBC

The Prostate Centre at VGH

Tel: (xxx) xxx-xxxx

**Dr. Larry S. Goldenberg**

Department of Urologic Sciences, UBC

Tel: (xxx) xxx-xxxx

**Dr. Silvia Chang**

Department of Radiology, UBC

Tel: (xxx) xxx-xxxx

**Dr. Mehdi Moradi**

Department of Electrical and Computer Engineering, UBC

Tel: (xxx) xxx-xxxx

**Ramin S. Sahebjavaheer**

Department of Electrical and Computer Engineering, UBC

Tel: (xxx) xxx-xxxx

**Dr. Christopher Nguan**

Department of Urologic Sciences, UBC

Tel: (xxx) xxx-xxxx

**Dr. Steven Tang**

Department of Urologic Sciences, UBC

Sponsor:

Natural Sciences and Engineering Research Council of Canada;

Canadian Institutes of Health Research;

British Columbia Innovation Council

Emergency telephone number (24 hours a day, 7 days a week):

**Dr. Christopher Nguan: (xxx) xxx-xxxx**

## **1. INTRODUCTION – ‘The invitation to participate’**

You are being invited to participate in this study because you will be undergoing a prostatectomy surgery.

## **2. YOUR PARTICIPATION IS VOLUNTARY**

Your participation is entirely voluntary, so it is up to you to decide whether or not to take part in this study. Before you decide, it is important for you to understand what the research involves. This consent form will tell you about the study, why the research is being done, what will happen to you during the study and the possible benefits, risks and discomforts.

If you wish to participate, you will be asked to sign this form. If you do decide to take part in this study, you are still free to withdraw at any time and without giving any reasons for your decision.

If you do not wish to participate, you do not have to provide any reason for your decision not to participate nor will you lose the benefit of any medical care to which you are entitled or are presently receiving.

Please take time to read the following information carefully and to discuss it with your family, friends, and doctor before you decide.

## **3. WHO IS CONDUCTING THE STUDY?**

The study is being conducted by the Department of Electrical and Computer Engineering at the University of British Columbia (UBC), Vancouver, Canada. The research has been funded by the Natural Sciences and Engineering Research Council of Canada, by the Canadian Institutes of Health Research, and by the British Columbia Innovation Council (BCIC).

**The investigators conducting this study will not receive any personal payments for conducting this study. In addition, neither the clinic nor any of the investigators or staff conducting this study will receive any direct financial benefit from conducting this study.**

**The investigators conducting this study** invented some aspects of the technology and may eventually financially gain from it. Note that the subject will not be reimbursed should this occur.

## **4. BACKGROUND**

Magnetic Resonance Imaging (MRI) technology uses coils (loops of wire) to record electrical signals from which the images are then reconstructed. Current standard imaging methods, such as conventional MRI, cannot distinguish between soft and hard abnormalities in the prostate. A new imaging method called “MR elastography”, which is being investigated in this study, classifies various types of tissue based on their “elasticity” and “viscosity”, basically based on how stiff they are. One subjective method of finding hard masses in the prostate is through touching as done by your physician. It is known that most cancers have higher elasticity (they feel “stiff”) and higher viscosity (they feel “thick”) than their background tissue. You can think of “MR elastography” as an objective method of palpation or touching, performed using an MRI imaging system. By performing “MR elastography”, the radiologist will be able to see images of the elasticity and viscosity of the underlying prostate tissue non-invasively. We are trying to determine whether a better decision can be made on whether an abnormality is cancer or not, in order to reduce the number of unnecessary biopsies.

A “MR elastography” procedure is very similar to a standard MRI procedure. For example, both of them are performed with the same machine and the positioning of the subjects will be similar. MR elastography is non-invasive and does not cause any pain.

## **5. WHAT IS THE PURPOSE OF THE STUDY?**

The overall objective of this study is to acquire elasticity, viscosity and MRI pictures of the prostate. Subsequently, the accuracy of these images in finding possible prostate abnormalities will be tested. For this study up to 20 patients may be enrolled. The long-term goal of this study is to improve the outcome of MRI examinations for diagnosing prostate cancer.

## **6. WHO CAN PARTICIPATE IN THE STUDY?**

You may participate in this study if:

You fully understand the study and give your informed consent to participate as demonstrated by signing this consent form.

You are scheduled for a prostatectomy procedure.

## **7. WHAT DOES THE STUDY INVOLVE?**

You will be positioned on the subject table of an MRI scanner, lying on your back, and a pelvic phased-array coil (specially designed loops of insulated wire) will be wrapped around your pelvis. An external shaker will be positioned between your legs and is adjusted until it comfortably applies a mild vibration to the perineal region over your clothing. The amplitude of the vibration will be less than 1 mm. The frequency of the vibration motion will be less than 200 Hz, meaning that as many as 200 complete movements towards and away from the perineum will be applied at every second. For a quick comparison, the frequency of the vibrations in the MR elastography system will be comparable to the vibration of a typical cell-phone when it is set on “vibrate” mode. The table on which you are lying is then moved into the centre of the magnet, which has a cylindrical bore of 60 cm (= 2 ft). A series of MR images of your prostate will be acquired. During the scan you will hear acoustic noises of varying intensity from the magnet. After about 15 minutes the MR elastography image will be taken, for which the vibration will be enabled. This procedure by itself will take approximately 20 min. You will then be removed from the magnet. The entire procedure will take approximately 60 min.

You will be given a remote control which you may press at anytime during the procedure to call the operators and stop the experiment at anytime you may feel uncomfortable.

We will answer any questions about the tests to ensure that you are fully informed.

### **Exclusions:**

#### **To be able to participate in this study, you must not have:**

- cardiac pacemaker, wires, or defibrillator
- artificial heart valve
- brain aneurysm clip
- electrical stimulator for nerves or bones
- ear or eye implant
- implanted drug infusion pump
- coil, catheter, or filter in any blood vessel
- orthopaedic hardware (artificial joint, plate, screws)
- Harrington rod for scoliosis
- other metallic prostheses
- shrapnel, bullets, or other metal fragments
- dentures, braces, or retainer

However, if you have metal or non-metal implants that are safe and compatible with the MRI scanner, as determined by the radiological staff, you will be able to participate in the study.

Also, the following are required to be able to participate in this study:

You have not had surgery in the last 6 weeks.

You have never been a metal worker or a machinist.

You have never had an injury where a piece of metal lodged in your eyes.

You do not have any pierced body parts (other than earrings) or recent tattoos, including tattooed eye-liner.

You have not had an injection into any joint in the last 4 weeks.

## **8. WHAT ARE THE POSSIBLE HARMS AND SIDE EFFECTS OF PARTICIPATING?**

There is very little risk with undergoing an MRI scan in general. A small number of people may encounter claustrophobia (i.e. an abnormal fear of being in narrow or enclosed spaces) when placed in the MR scanner. If this occurs then the study will then be terminated.

In MR elastography the only change to the subjects relative to the standard MRI experiments is the application of a mild vibration to the skin close to the prostate - i.e., the perineum. Given the mild vibration, there is no potential risk to the patient. However, this small buzzing stimulus may introduce a sensation which will be similar to that of placing a vibrating cell-phone on the perineum.

## **9. WHAT ARE THE BENEFITS OF PARTICIPATING IN THIS STUDY?**

Participation in this study does not alter in any way your treatment as a patient. MRI examination proposed in this study will be performed in addition to, not instead of, the standard diagnostic tests and procedures routinely applied in such cases. As part of the standard treatment you will undergo prostatectomy. The results of the pathology examination that follows the prostatectomy will be correlated with the MRI examination in order to determine whether MR elastography can correctly determine prostate abnormalities. Should new information arise during this study that may affect your willingness to participate in the study, you will be advised of this information immediately.

## **10. WHAT ARE THE ALTERNATIVES TO THE STUDY TREATMENT?**

You understand that if you decide not to participate or to withdraw at some later date there will be no consequences to your treatment.

## **11. WHAT IF NEW INFORMATION BECOMES AVAILABLE THAT MAY AFFECT MY DECISION TO PARTICIPATE?**

If new information arises during the research study that may materially affect your willingness to remain in the study, you will be advised of this information.

## **12. WHAT HAPPENS IF I DECIDE TO WITHDRAW MY CONSENT TO PARTICIPATE?**

Your participation in this research is entirely voluntary. You may withdraw from this study at any time. If you decide to enter the study and to withdraw at any time in the future, there will be no penalty or loss of benefits to which you are otherwise entitled, and your future medical care will not be affected.

The study doctor(s)/investigators may decide to discontinue the study at any time, or withdraw you from the study at any time, if they feel that it is in your best interests.

If you choose to enter the study and then decide to withdraw at a later time, all data collected about you during your enrolment in the study will be retained for analysis. By law, this data cannot be destroyed.

## **13. WHAT HAPPENS IF SOMETHING GOES WRONG?**

If you are injured as a consequence of participation in the study due to the administration of the study procedures, your medical condition will be evaluated and medical care will be provided by one of the investigators or you will be referred for appropriate treatment. If you are injured as a result of participating in this study, the costs of your medical treatment will be paid for by your provincial medical plan to the extent that such coverage is available.

**You do not waive any of your legal rights for compensation by signing this form.**

#### **14. WHAT WILL THE STUDY COST ME?**

You will not be paid for participating in this study. Also, participation in this study is free of charge.

#### **15. WILL MY TAKING PART IN THIS STUDY BE KEPT CONFIDENTIAL?**

Your confidentiality will be respected. No information that discloses your identity will be released or published without your specific consent to the disclosure. However, research records and medical records identifying you may be inspected in the presence of the Investigators or their representative, Health Canada, and the UBC Research Ethics Board for the purpose of monitoring the research. However, no records which identify you by name or initials will be allowed to leave the Investigators' offices.

The information gathered from this study, with information identifying you removed, will be used to determine whether MR elastography is accurate in detecting and analyzing prostate abnormalities. The information will be shared with the sponsors of the trial, the governmental regulatory agencies that oversee such research, the investigators who have conducted this trial and other doctors and researchers through publication of the results of this study.

#### **16. WHO DO I CONTACT IF I HAVE QUESTIONS ABOUT THE STUDY DURING MY PARTICIPATION?**

If you have any questions or desire further information about this study before or during participation, you can contact the principal investigator or one of the co-investigators (telephone numbers provided on the first page of this form.)

#### **17. WHO DO I CONTACT IF I HAVE ANY QUESTIONS OR CONCERNS ABOUT MY RIGHTS AS A SUBJECT DURING THE STUDY?**

If you have any concerns about your rights as a research subject and/or your experiences while participating in this study, contact the Research Subject Information Line in the University of British Columbia Office of Research Services by e-mail at [RSIL@ors.ubc.ca](mailto:RSIL@ors.ubc.ca) or by phone at 604-822-8598.

#### **18. SUBJECT CONSENT TO PARTICIPATE**

I understand that participation in this study is entirely voluntary. I authorize access to my medical record as described in this consent form. I may choose not to participate or I may withdraw from the study at any time and I will continue to be offered the best available medical care. I understand that I may ask questions about this study in the future. I will receive a signed copy of this consent form including all attachments, for my own records.

By signing this consent form, I understand that:

- *I have read and understood the subject information and consent form.*

- *I have had sufficient time to consider the information provided and to ask for advice if necessary.*
- *I have had the opportunity to ask questions and have had satisfactory responses to my questions.*
- *I understand that all of the information collected will be kept confidential and that the result will only be used for scientific objectives.*
- *I understand that my participation in this study is voluntary and that I am completely free to refuse to participate or to withdraw from this study at any time without changing in any way the quality of care that I receive.*
- *I understand that I am not waiving any of my legal rights as a result of signing this consent form.*
- *I understand that there is no guarantee that this study will provide any benefits to me.*
- *I have read this form and I freely consent to participate in this study.*
- *I have been told that I will receive a dated and signed copy of this form.*

|                          |              |      |
|--------------------------|--------------|------|
|                          |              |      |
| Signature of the Subject | Printed name | Date |

|  |              |      |
|--|--------------|------|
|  |              |      |
| Signature of the Principal<br>Investigator or Designated<br>Representative | Printed name | Date |

# Appendix C – Additional images from *in-vivo* patient studies

P01 Mag P01 AX

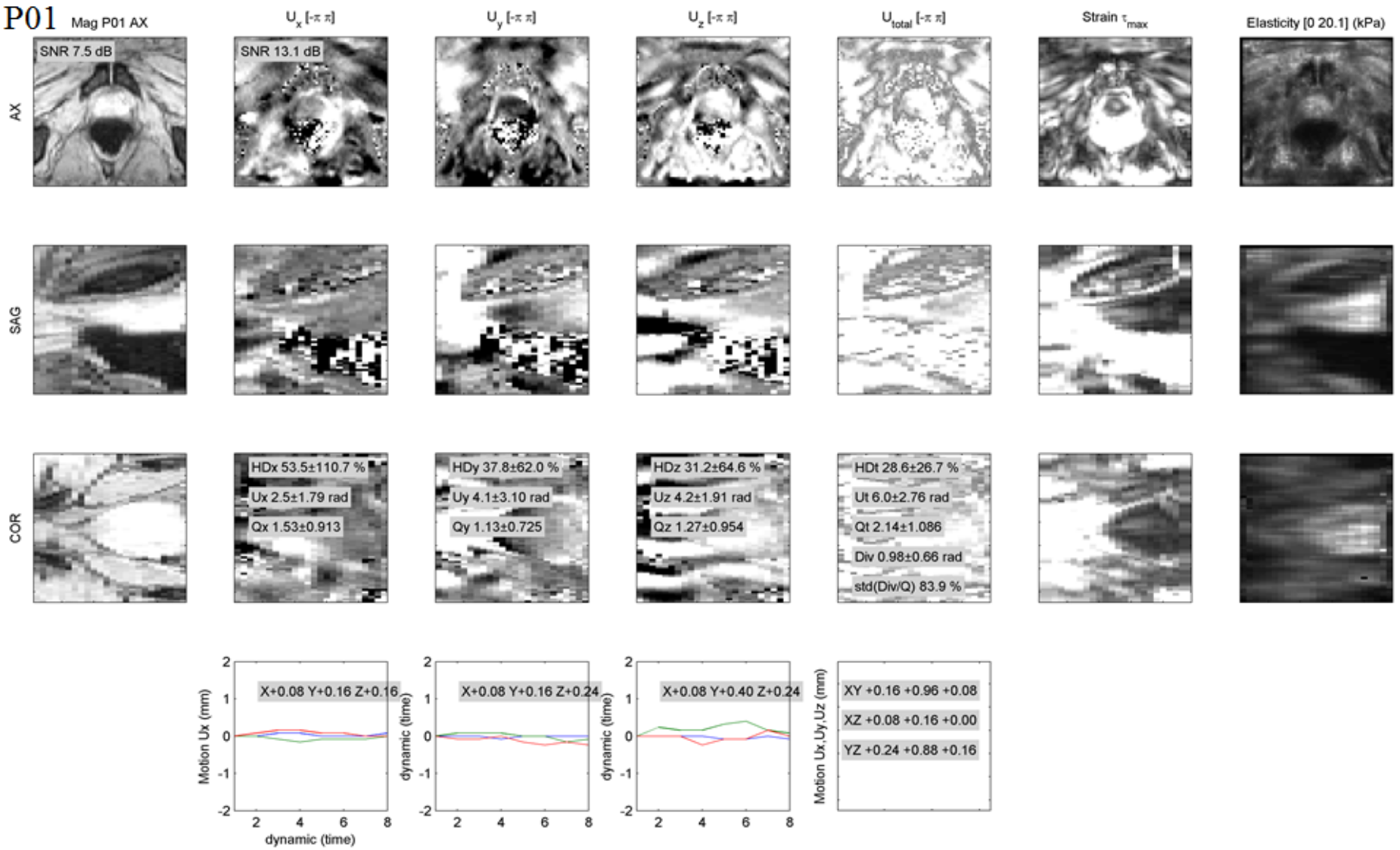


Figure C-1. Raw data for patient P01.

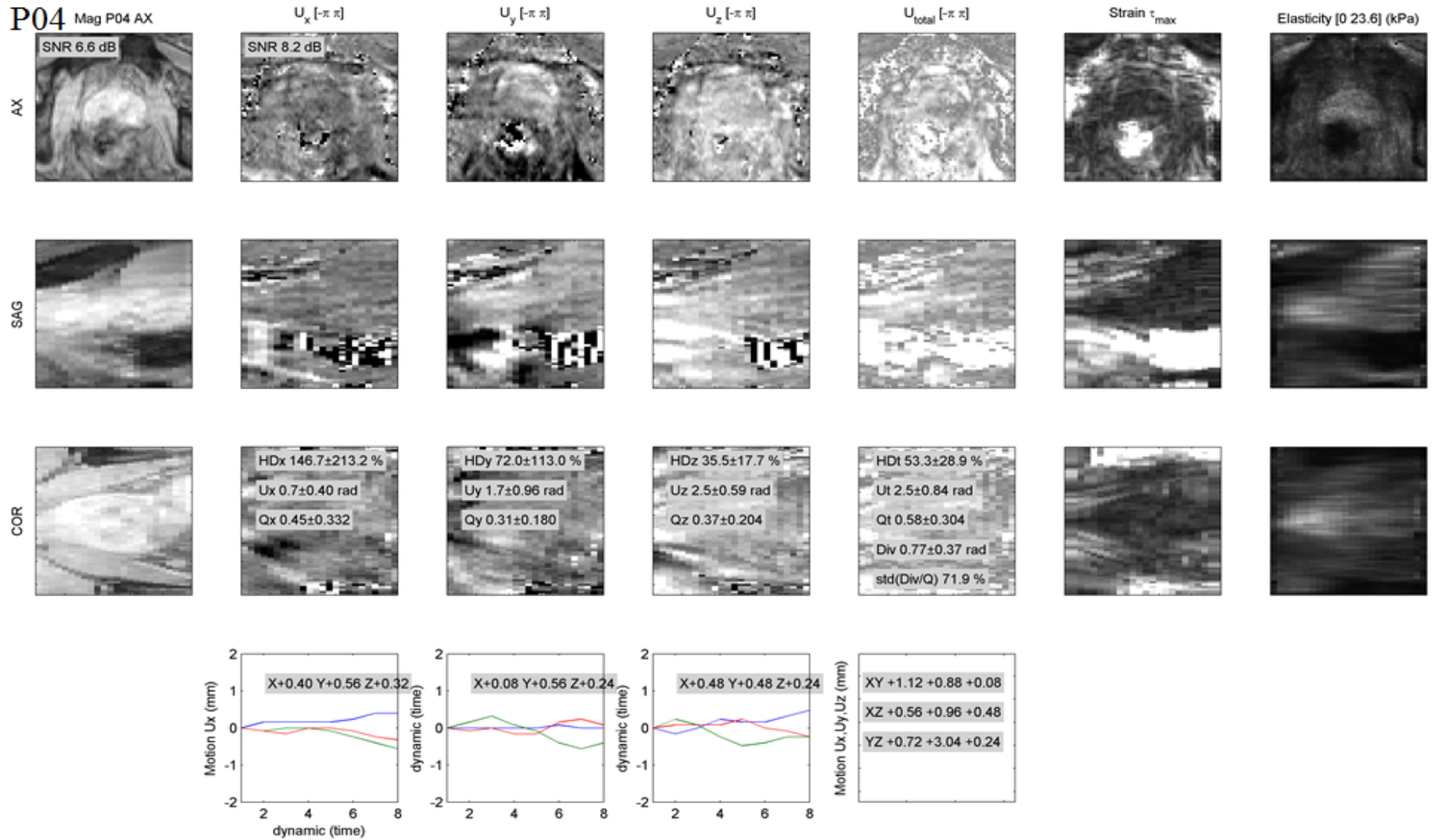


Figure C-2. Raw data for patient P04.

P05

Mag P05 AX

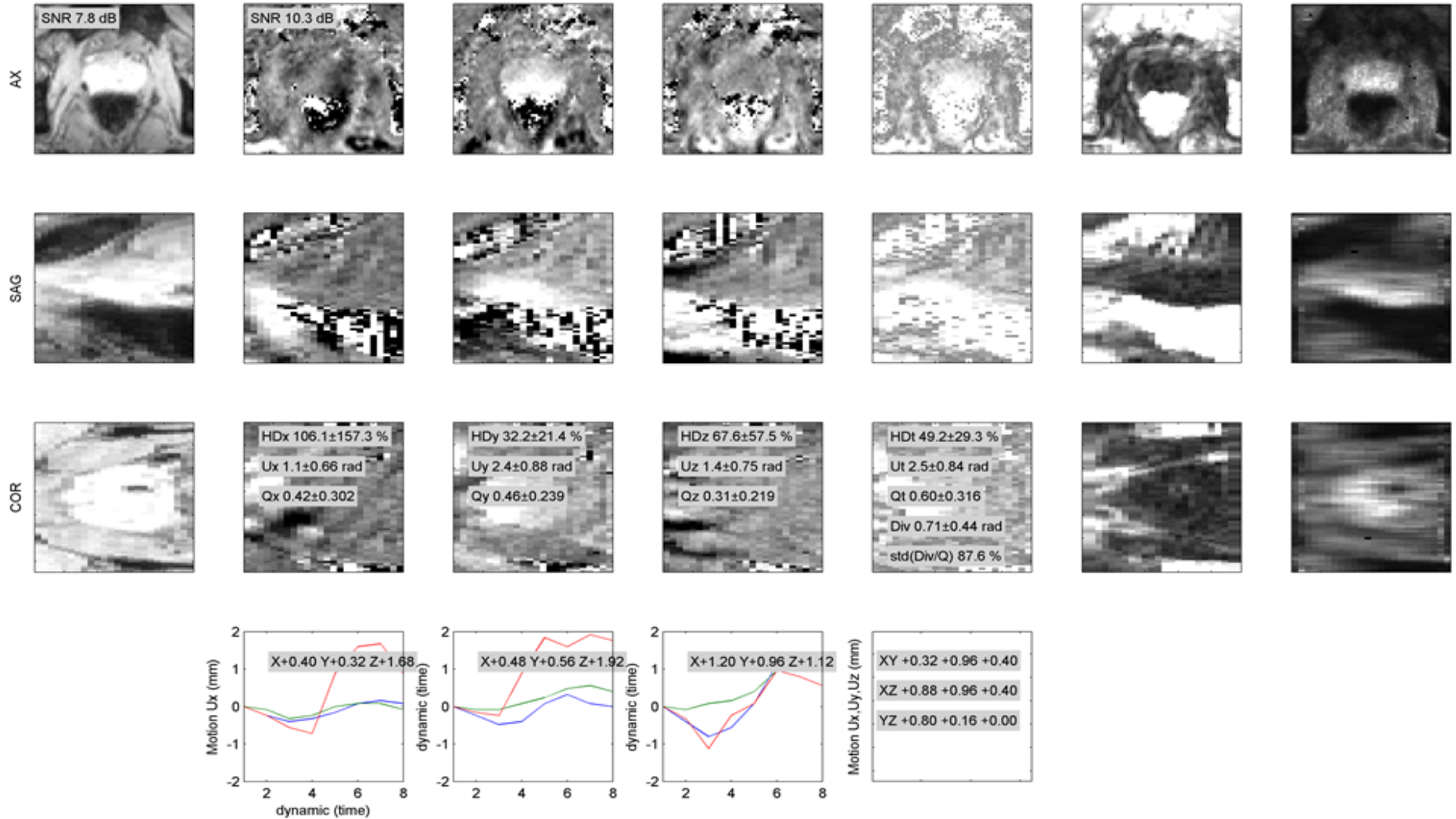


Figure C-3. Raw data for patient P05.

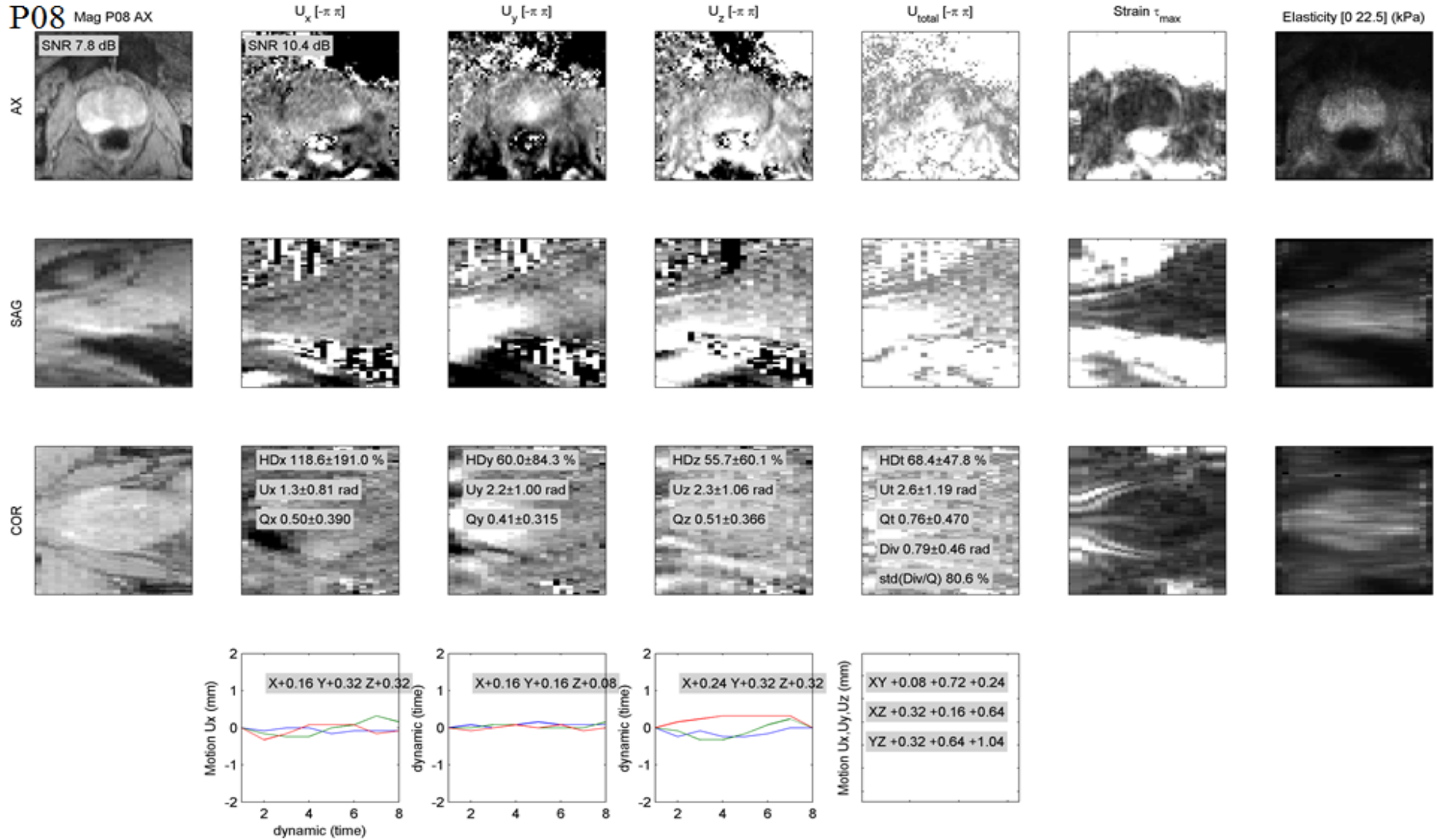


Figure C-4. Raw data for patient P08.

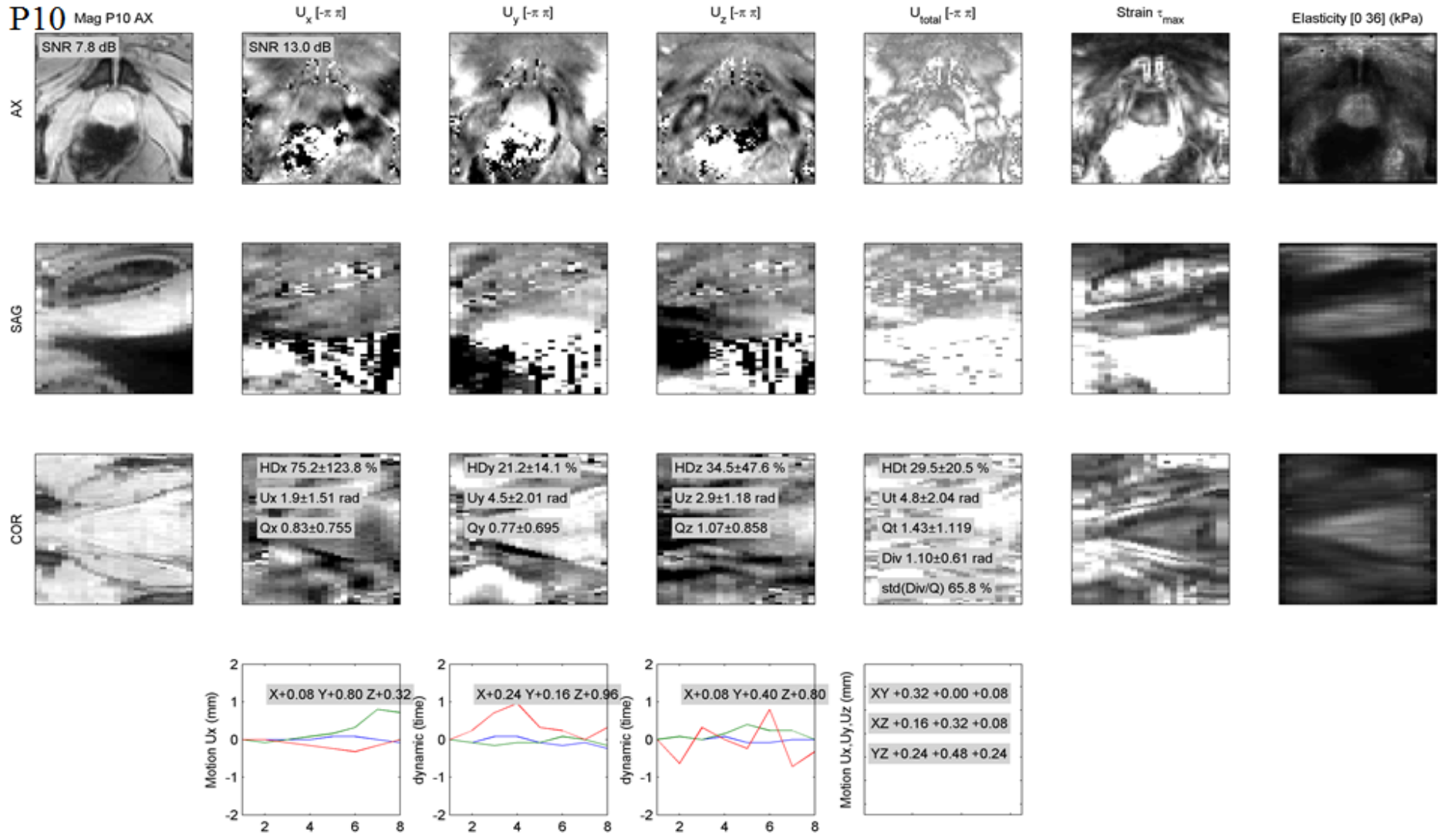


Figure C-5. Raw data for patient P10.

P12 Mag P12 AX

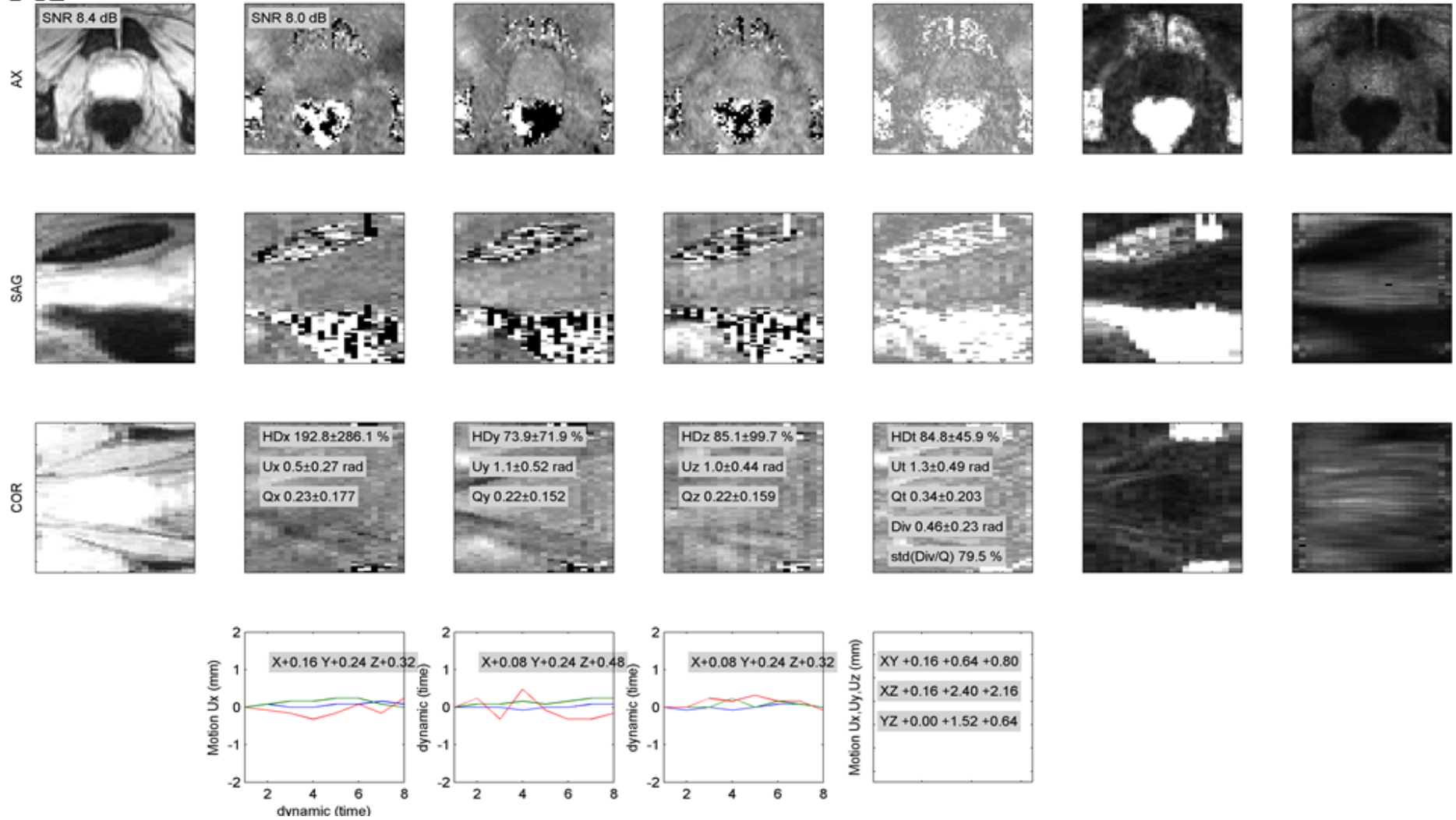


Figure C-6. Raw data for patient P12.

**P13** Mag P13 AX

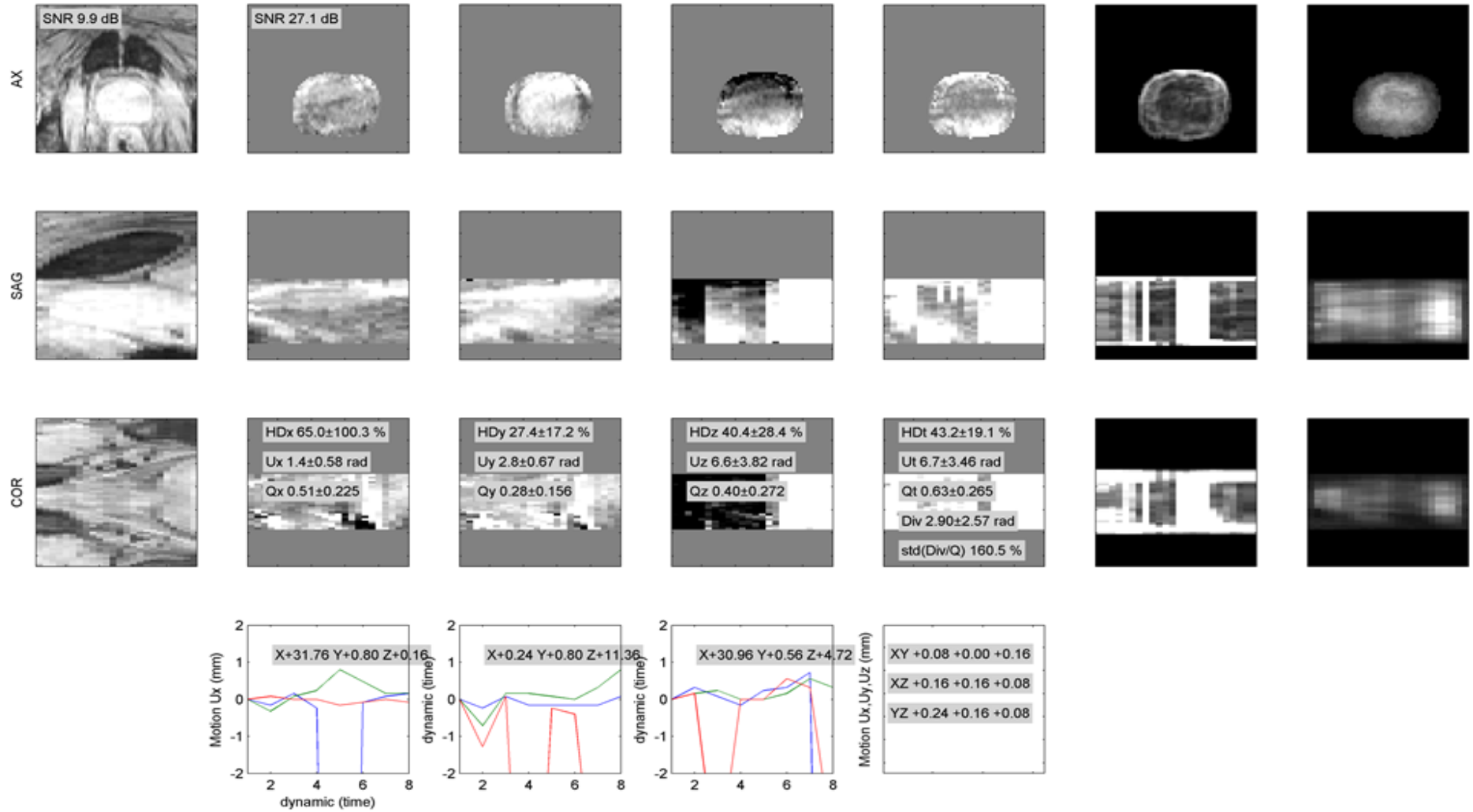


Figure C-7. Raw data for patient P13.

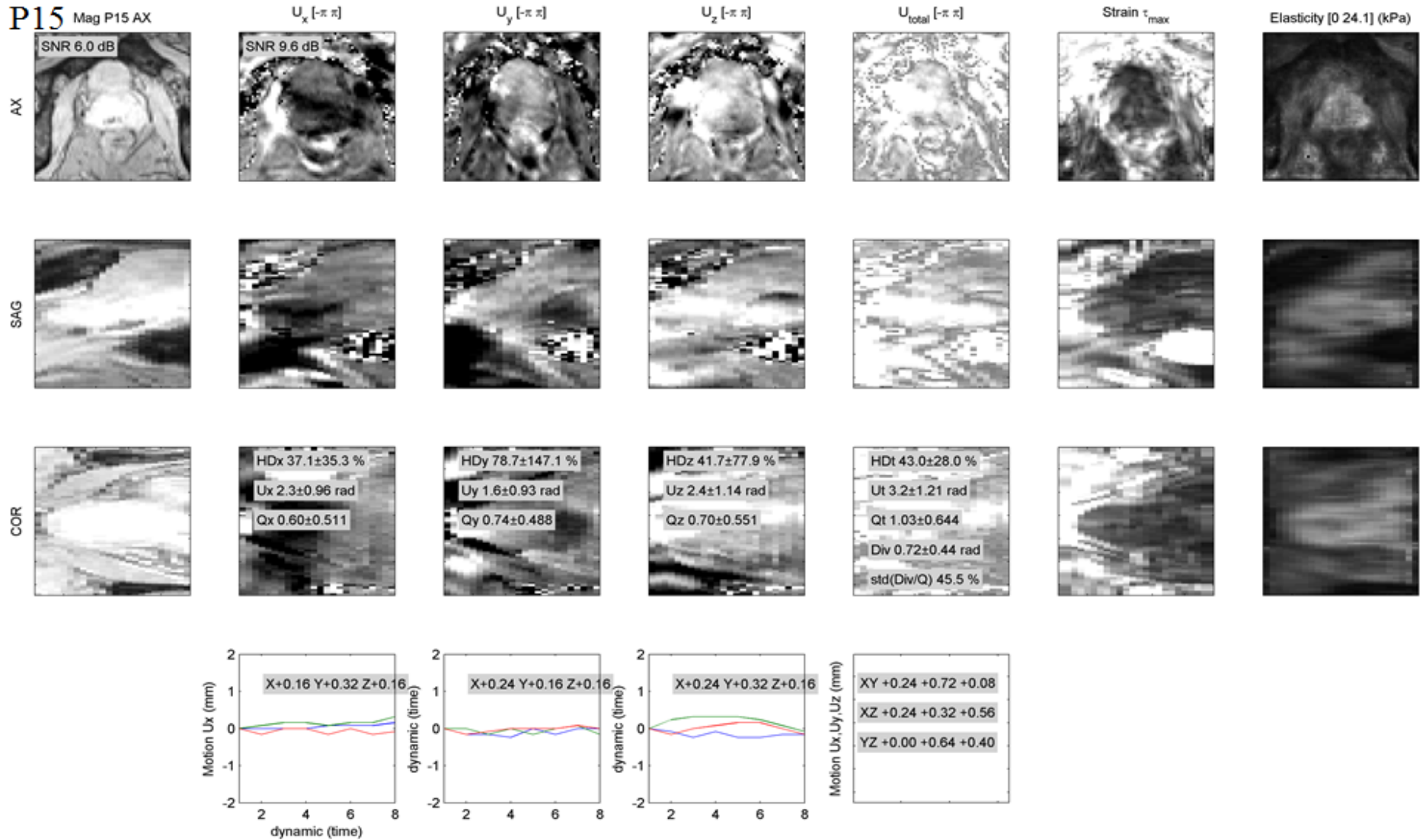


Figure C-8. Raw data for patient P15.

P17 Mag P17 AX

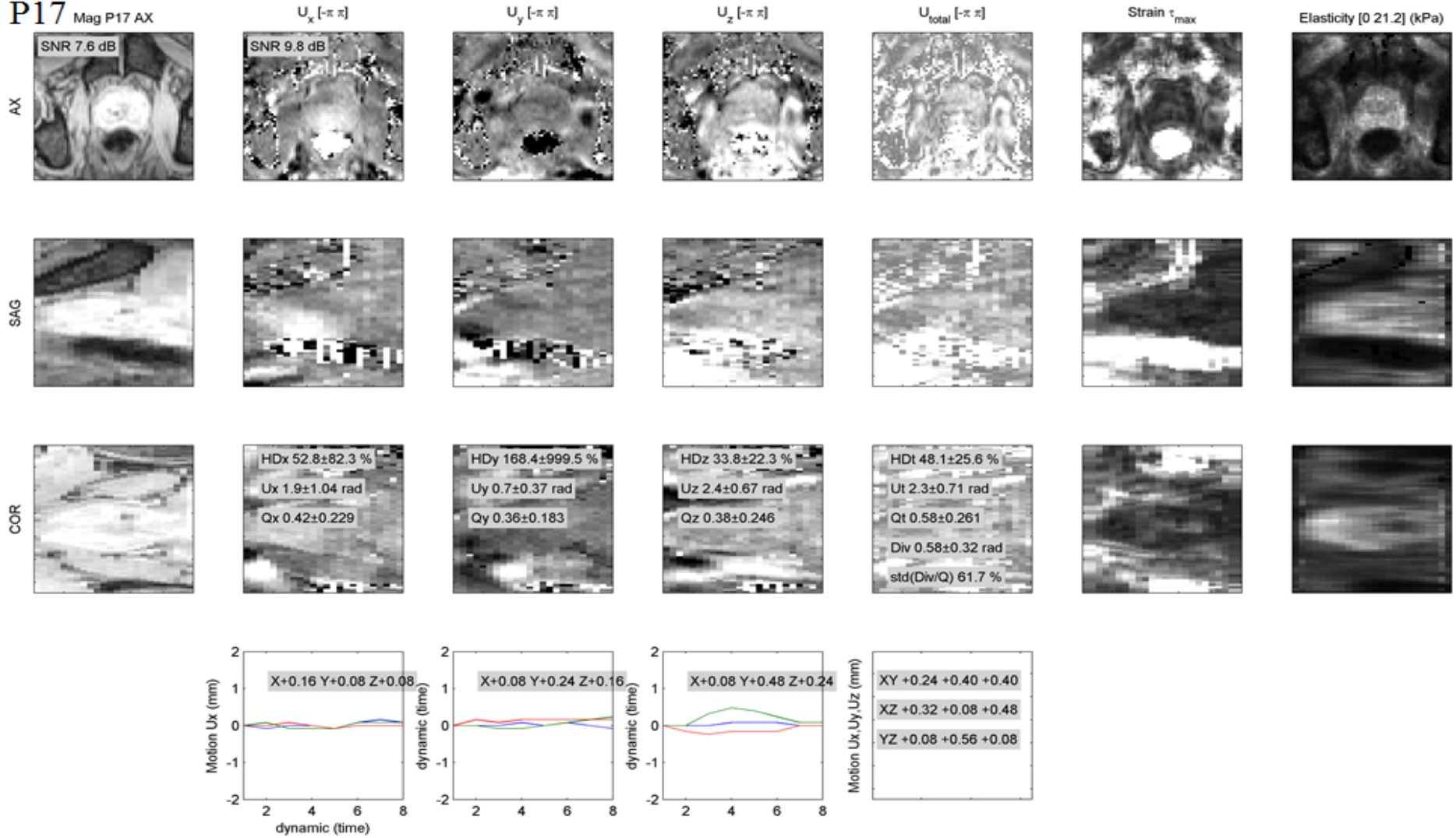


Figure C-9. Raw data for patient P17.

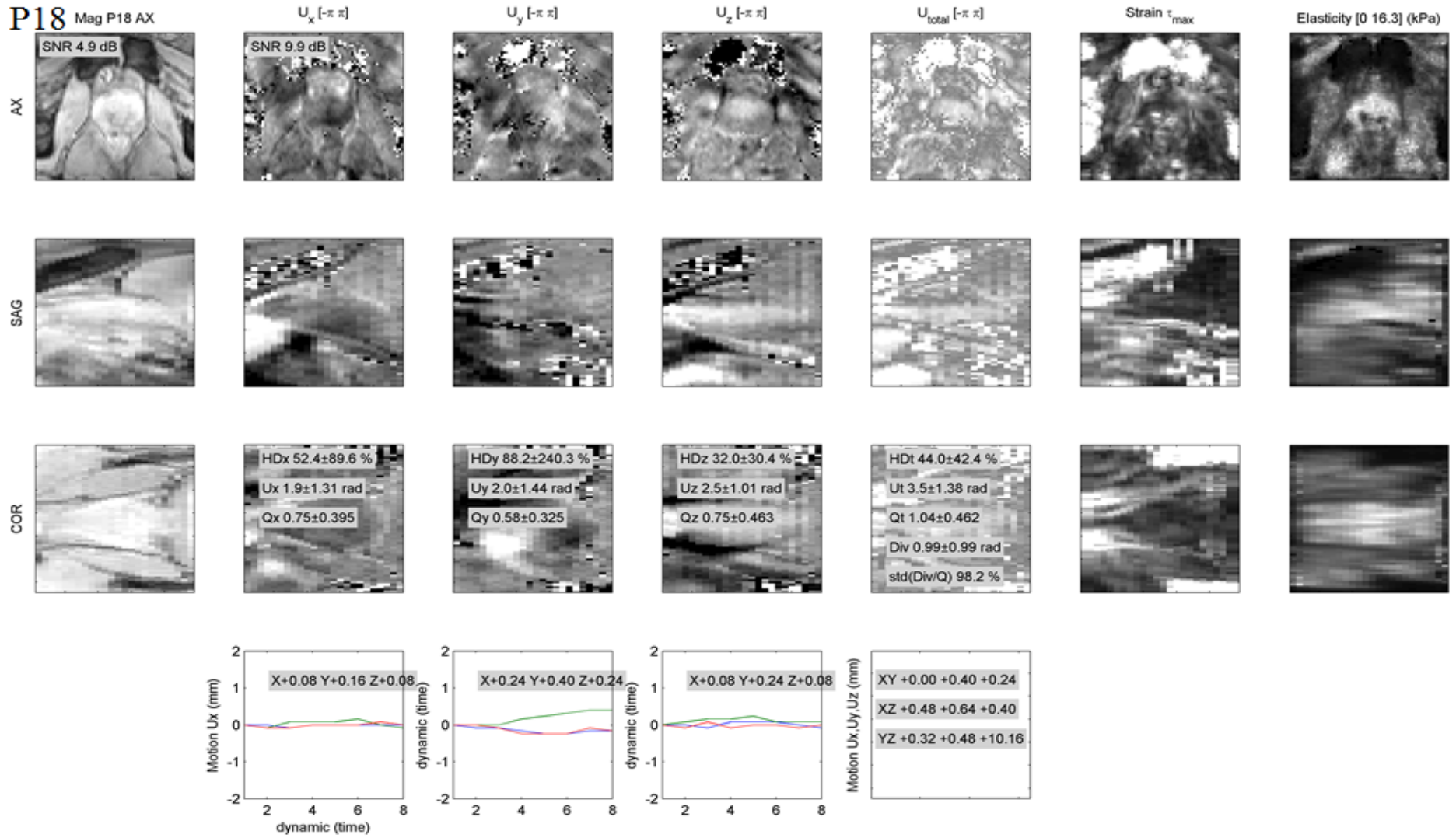


Figure C-10. Raw data for patient P18.

P19

Mag P19 AX

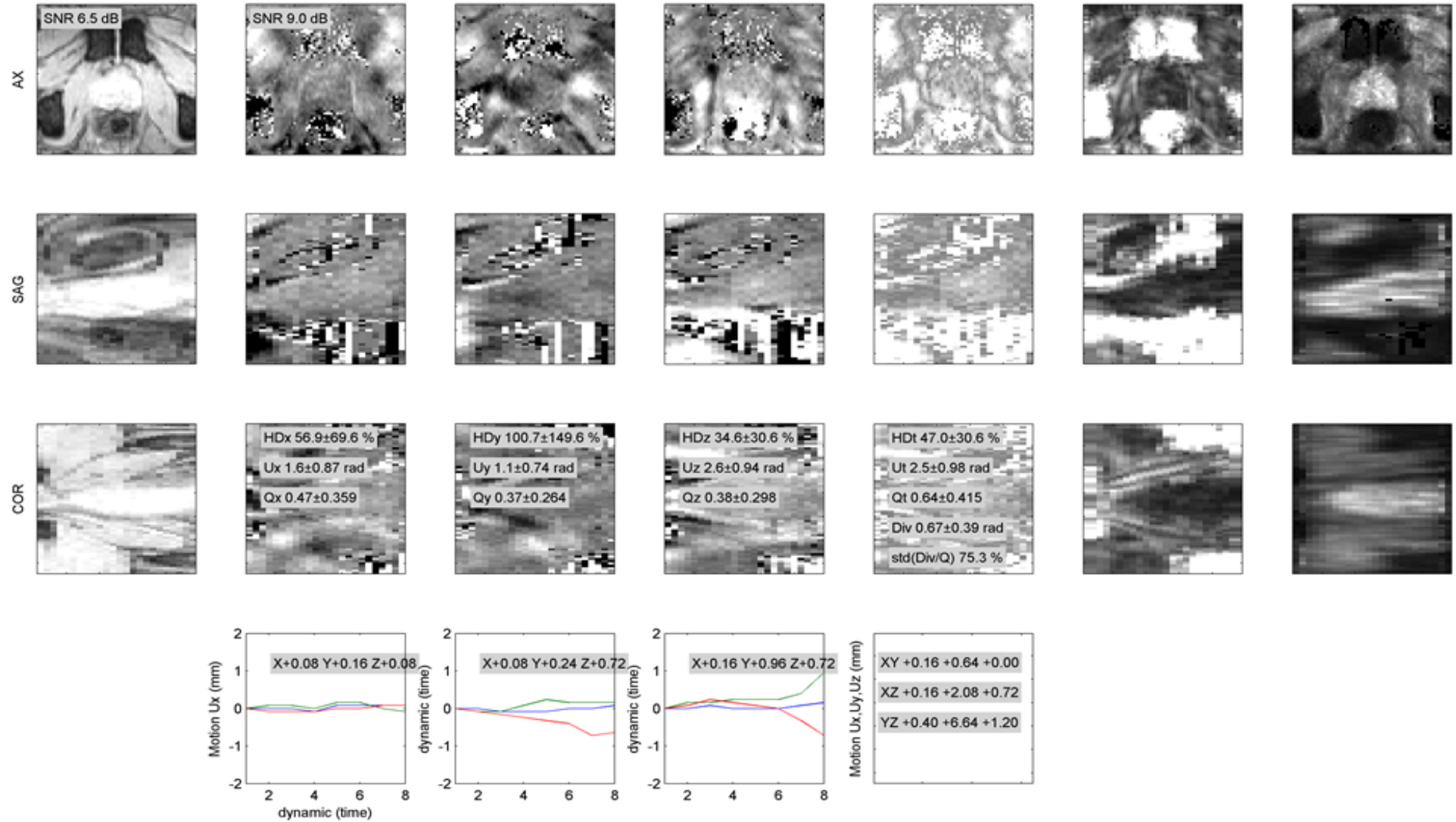


Figure C-11. Raw data for patient P19.

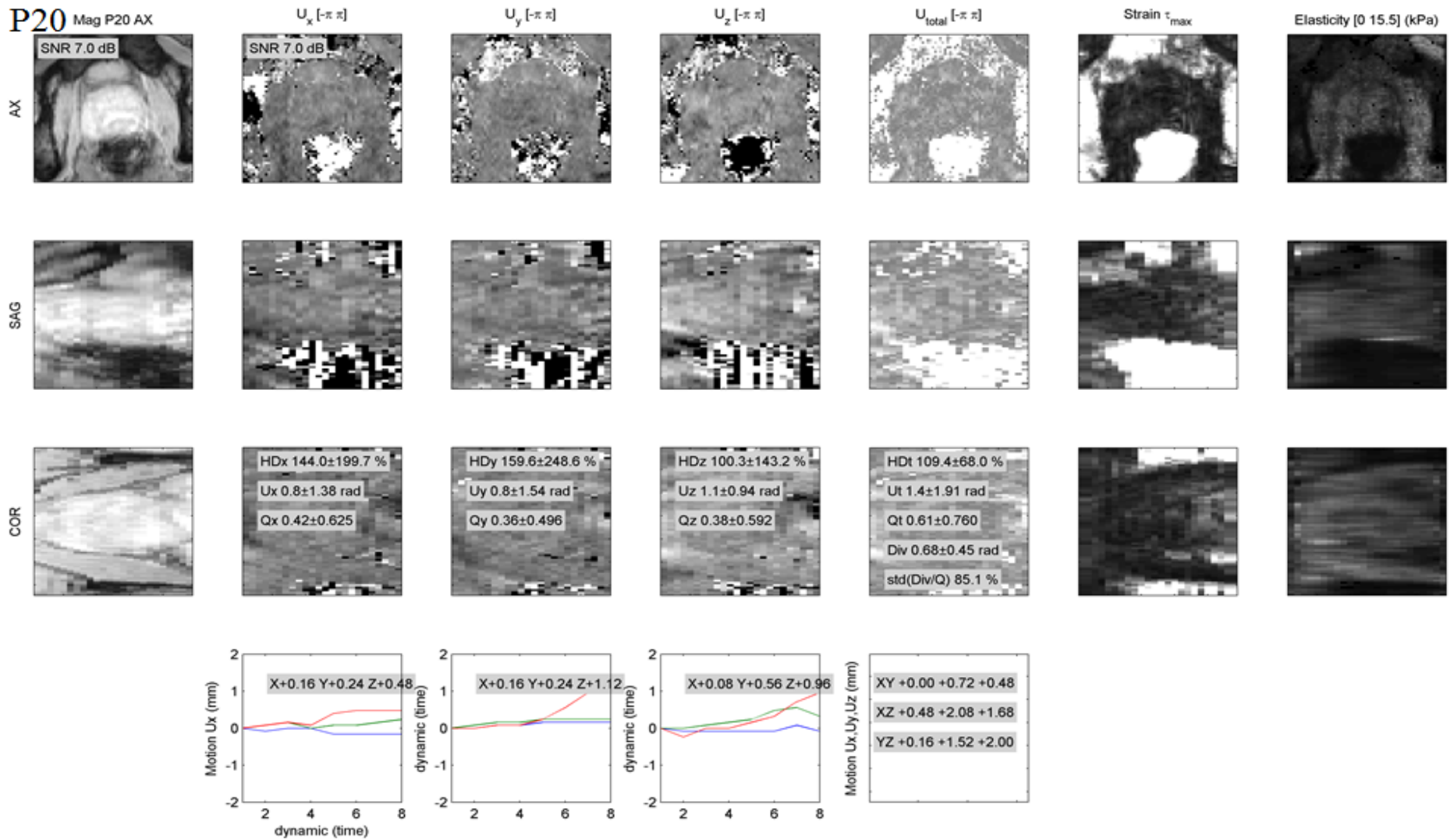


Figure C-12. Raw data for patient P20.

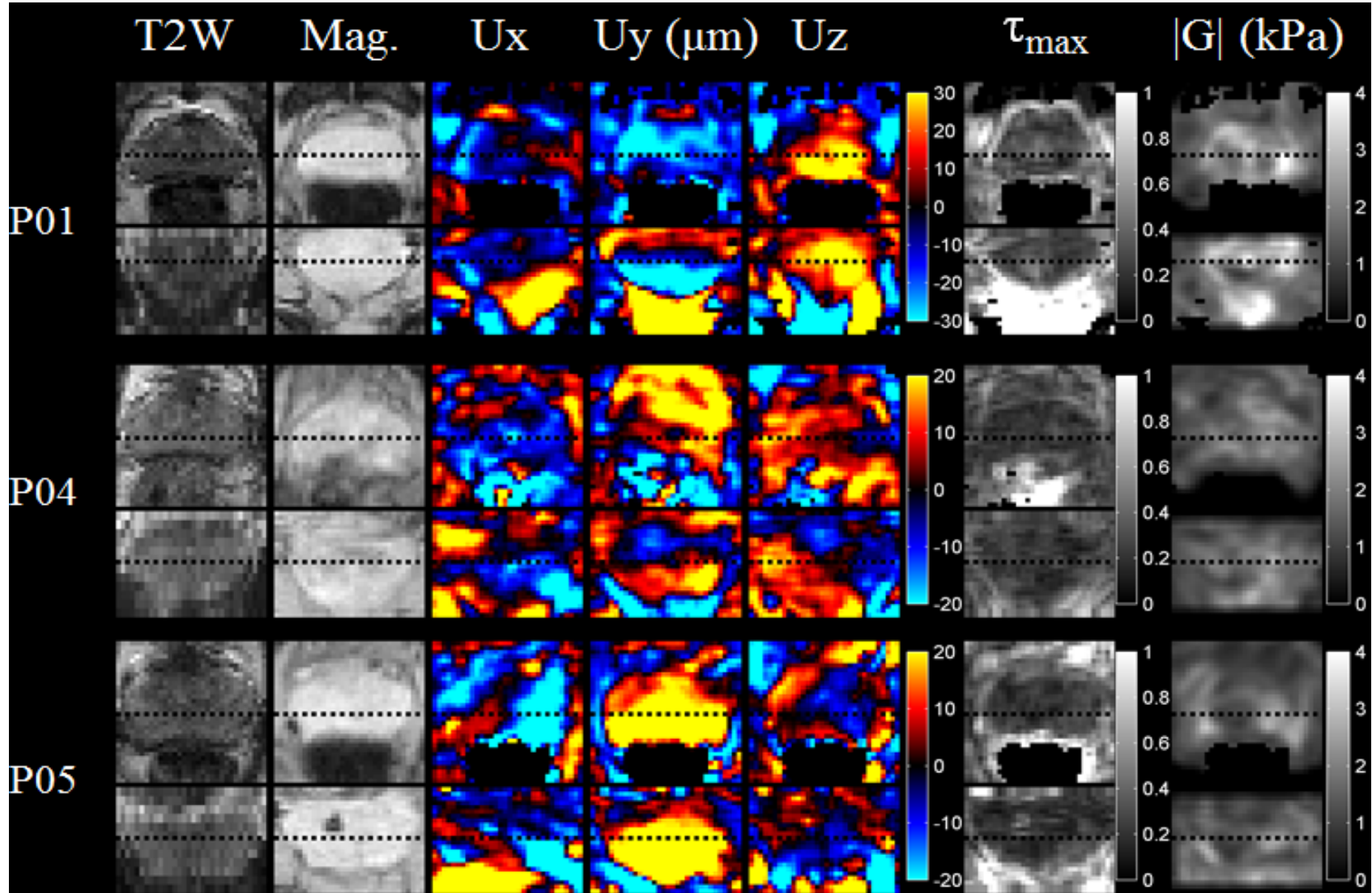


Figure C-13. Waves, maximum shear strain and absolute value of shear modulus for patients P01, P04 and P05.

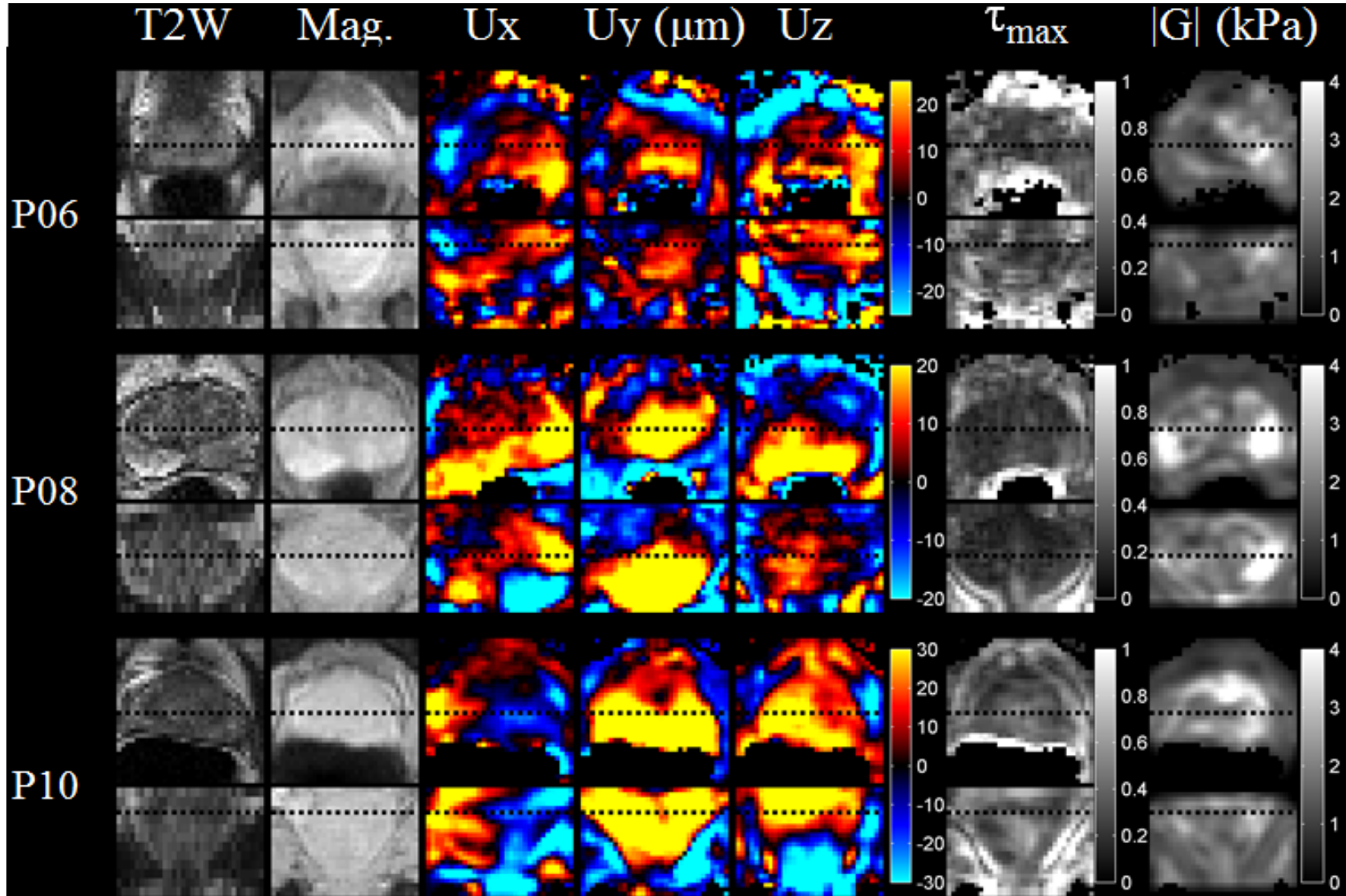


Figure C-14. Waves, maximum shear strain and absolute value of shear modulus for patients P06, P08 and P10.

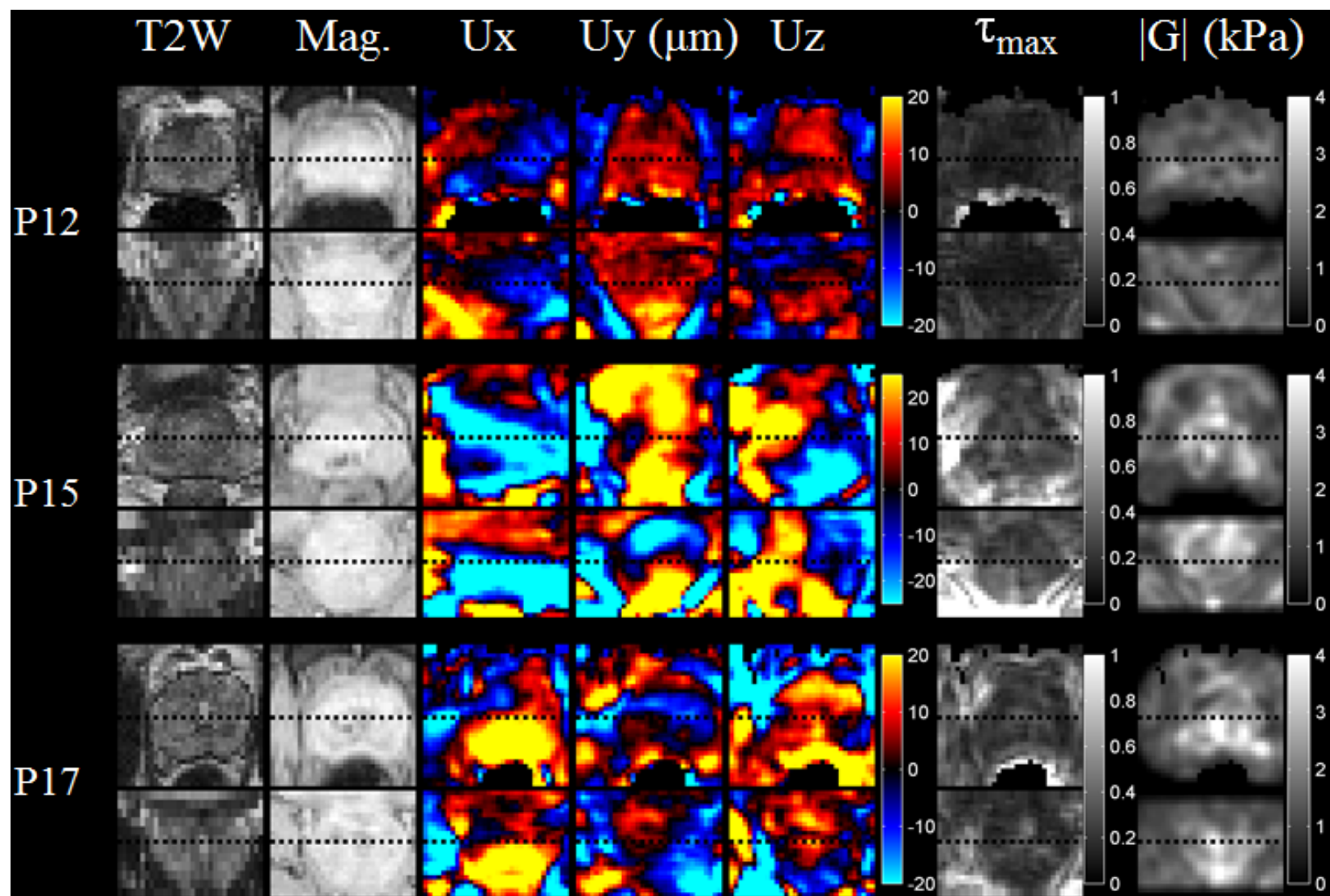


Figure C-15. Waves, maximum shear strain and absolute value of shear modulus for patients P12, P15 and P17.

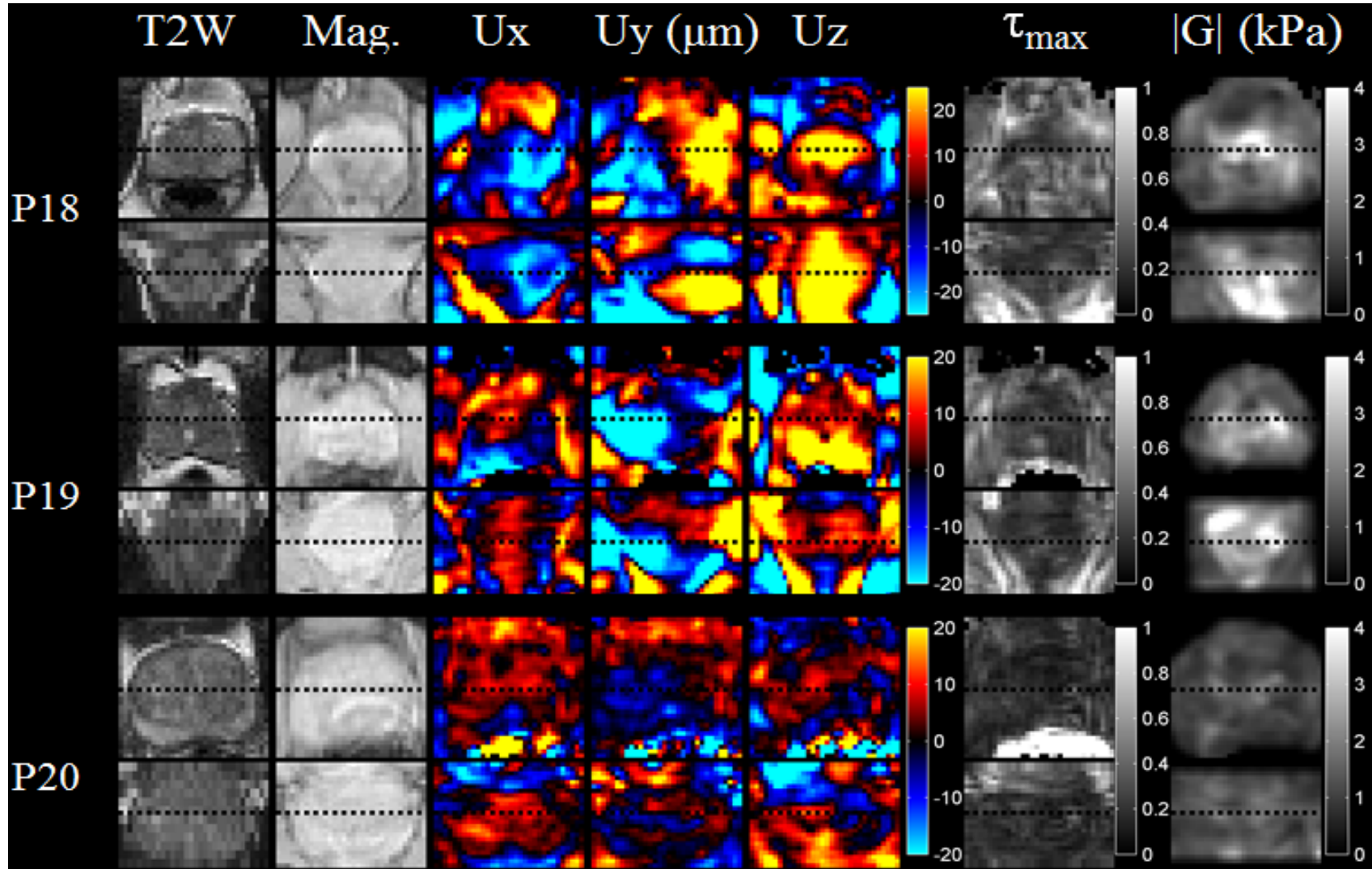


Figure C-16. Waves, maximum shear strain and absolute value of shear modulus for patients P18, P19 and P20.

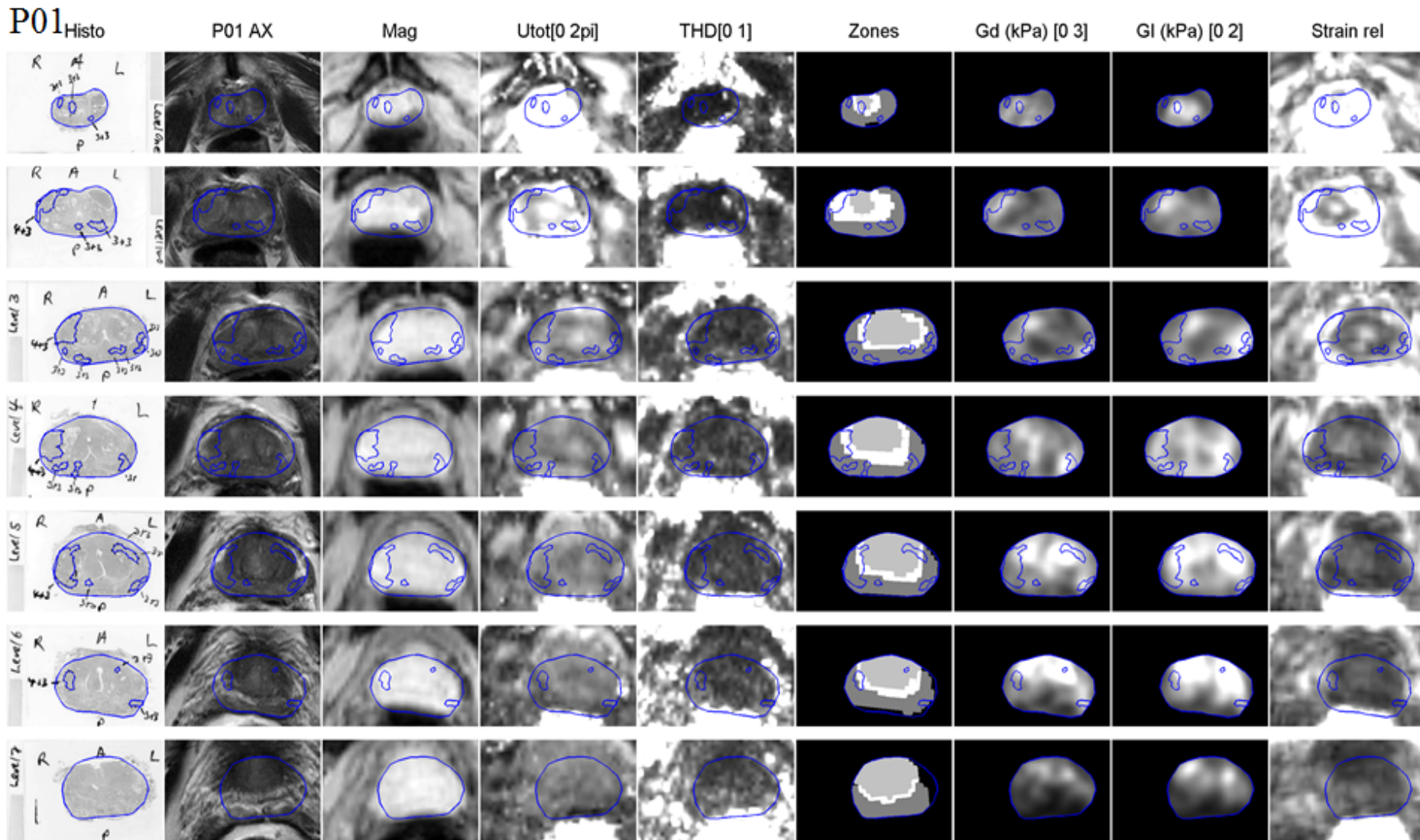


Figure C-17. Results for P01. Shear moduli ( $G_d$  and  $G_l$ ) and maximum shear strain ( $\tau_{max}$ ) as registered to histopathology slides. The total wave amplitude and THD are also shown.

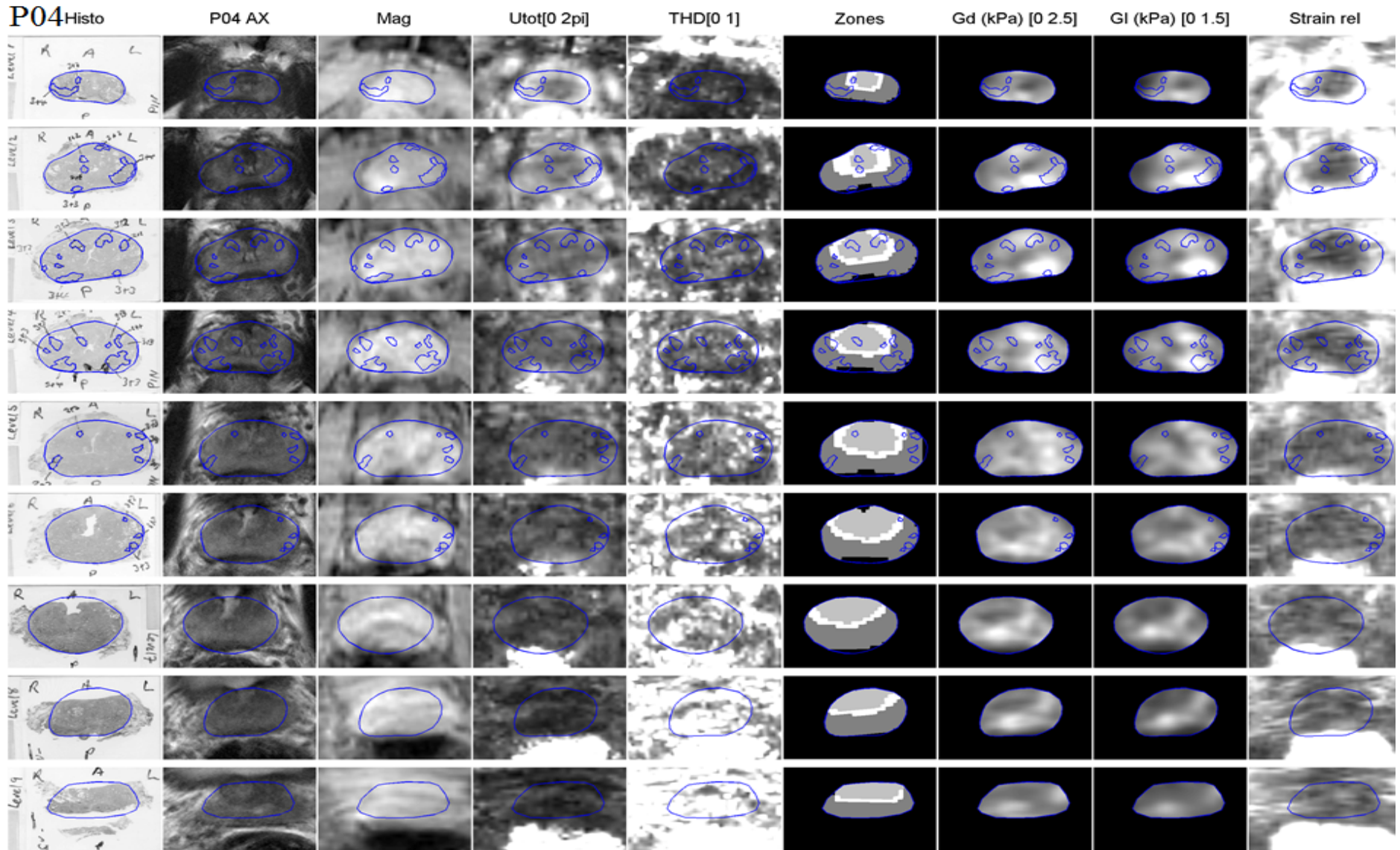


Figure C-18. Results for P04. Shear moduli ( $G$  and  $G_I$ ) and maximum shear strain ( $\tau_{max}$ ) as registered to histopathology slides. The total wave amplitude and THD are also shown.

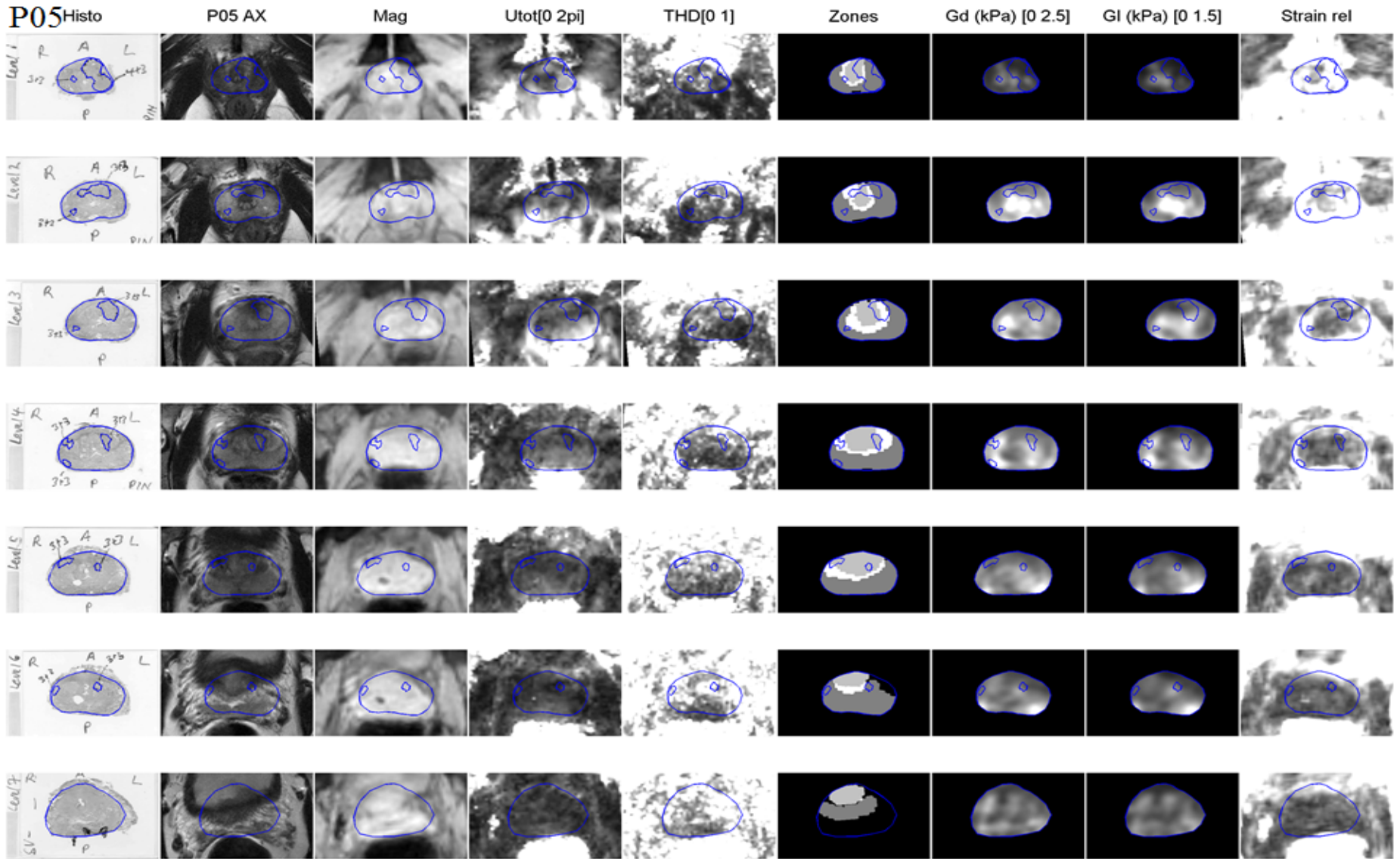


Figure C-19. Results for P05. Shear moduli ( $G$  and  $G_I$ ) and maximum shear strain ( $\tau_{max}$ ) as registered to histopathology slides. The total wave amplitude and THD are also shown.

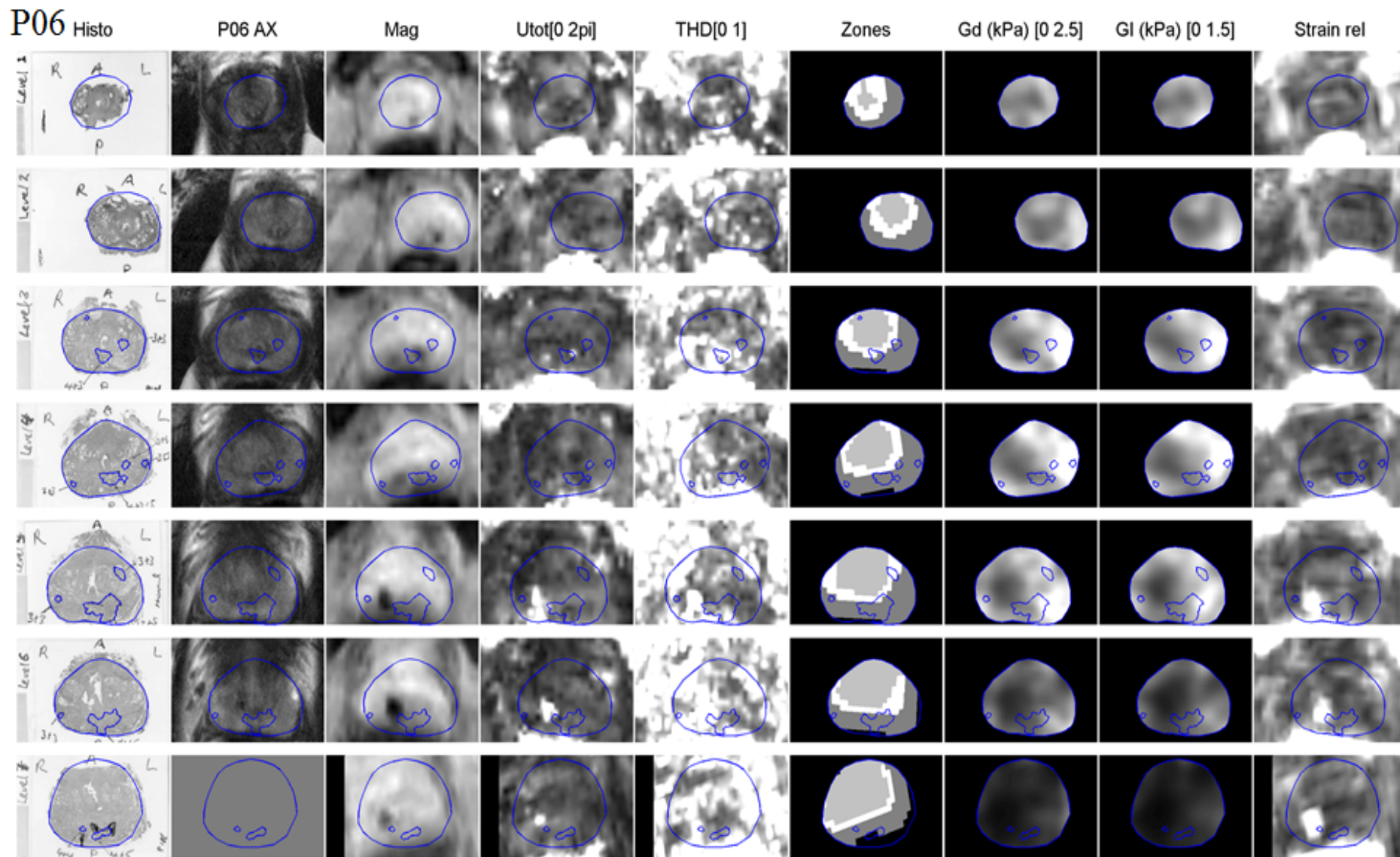


Figure C-20. Results for P06. Shear moduli ( $G$  and  $G_I$ ) and maximum shear strain ( $\tau_{max}$ ) as registered to histopathology slides. The total wave amplitude and THD are also shown.

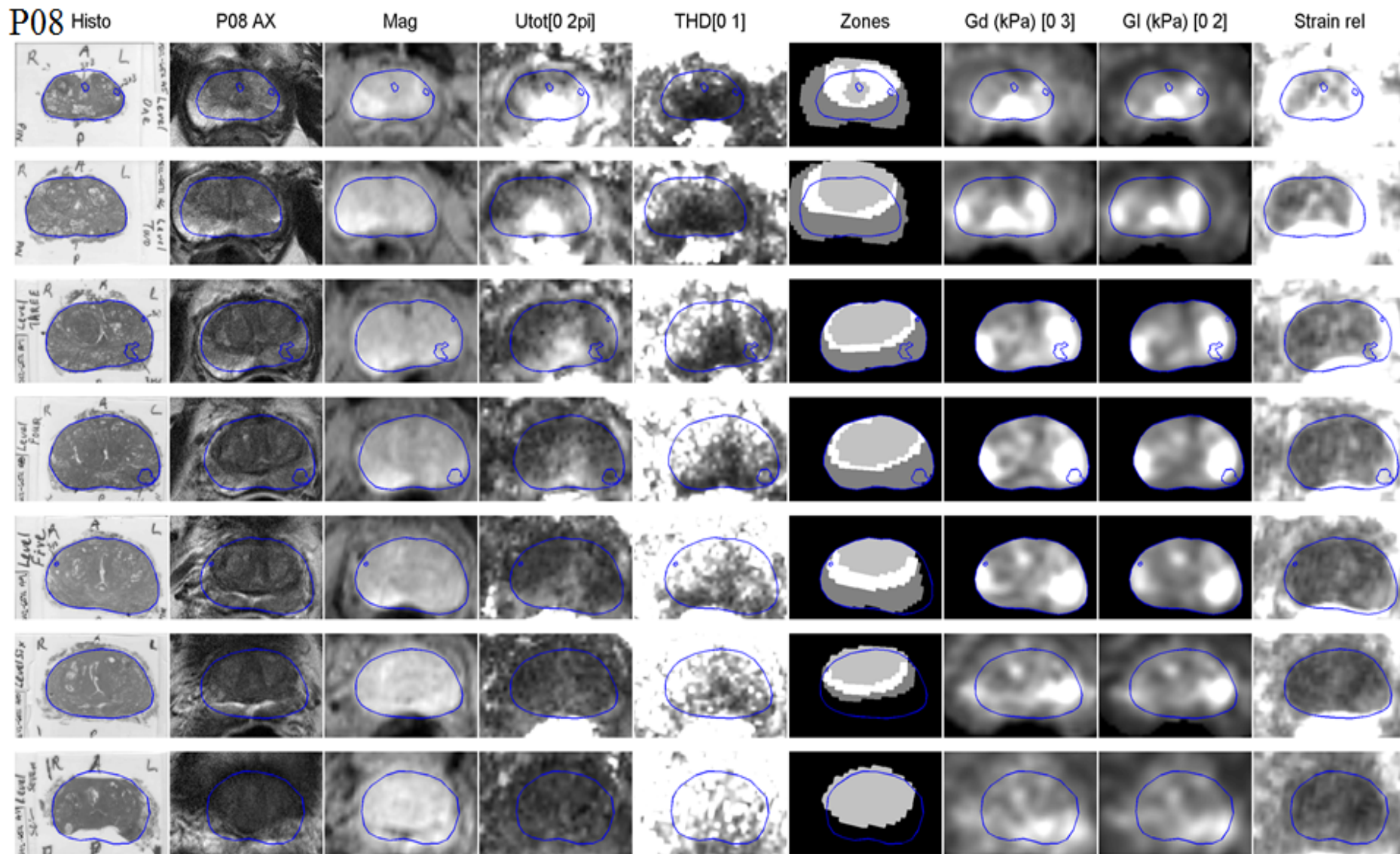


Figure C-21. Results for P08. Shear moduli ( $G$  and  $G_I$ ) and maximum shear strain ( $\tau_{max}$ ) as registered to histopathology slides. The total wave amplitude and THD are also shown.

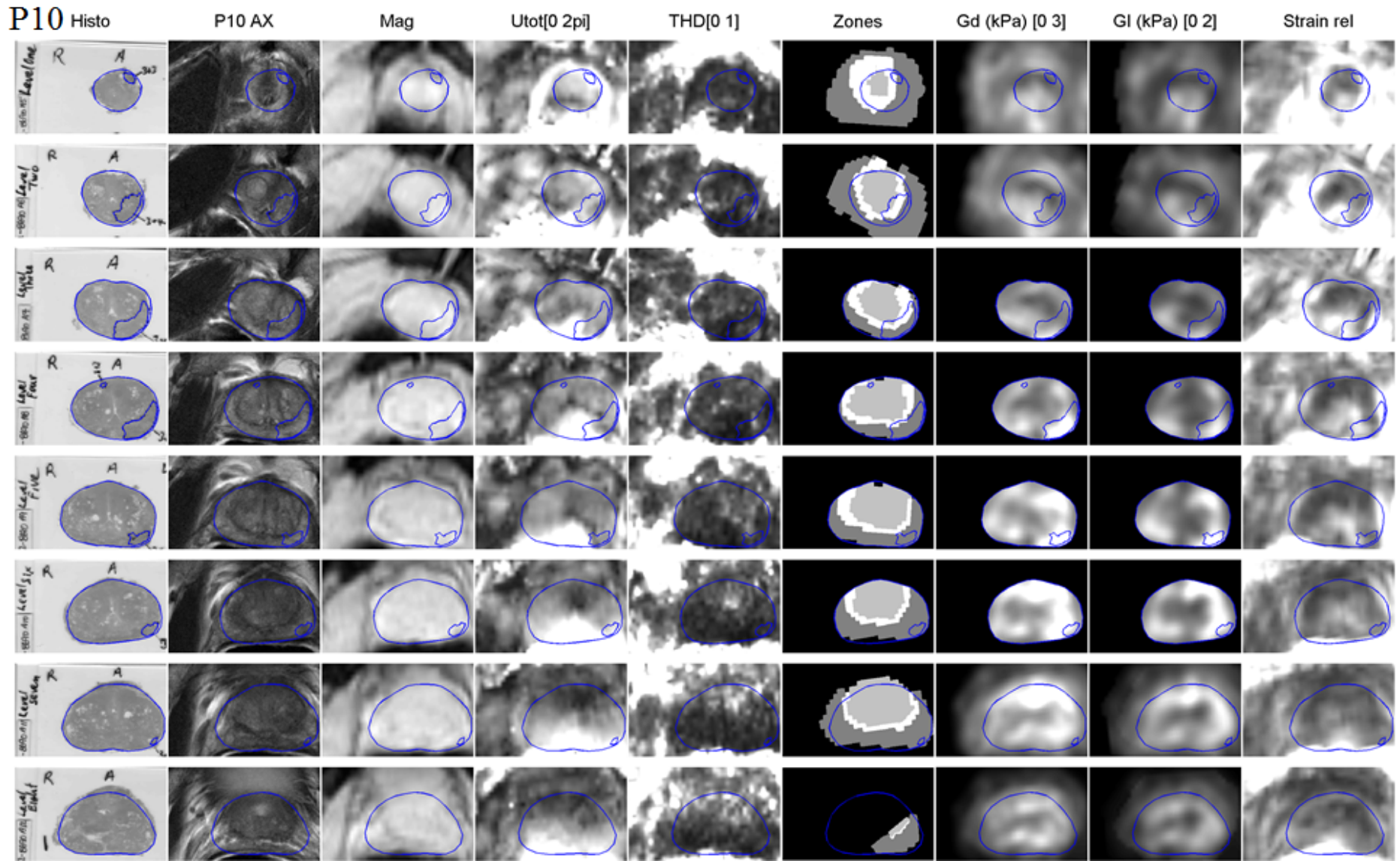


Figure C-22. Results for P10. Shear moduli ( $G$  and  $G_I$ ) and maximum shear strain ( $\tau_{max}$ ) as registered to histopathology slides. The total wave amplitude and THD are also shown.

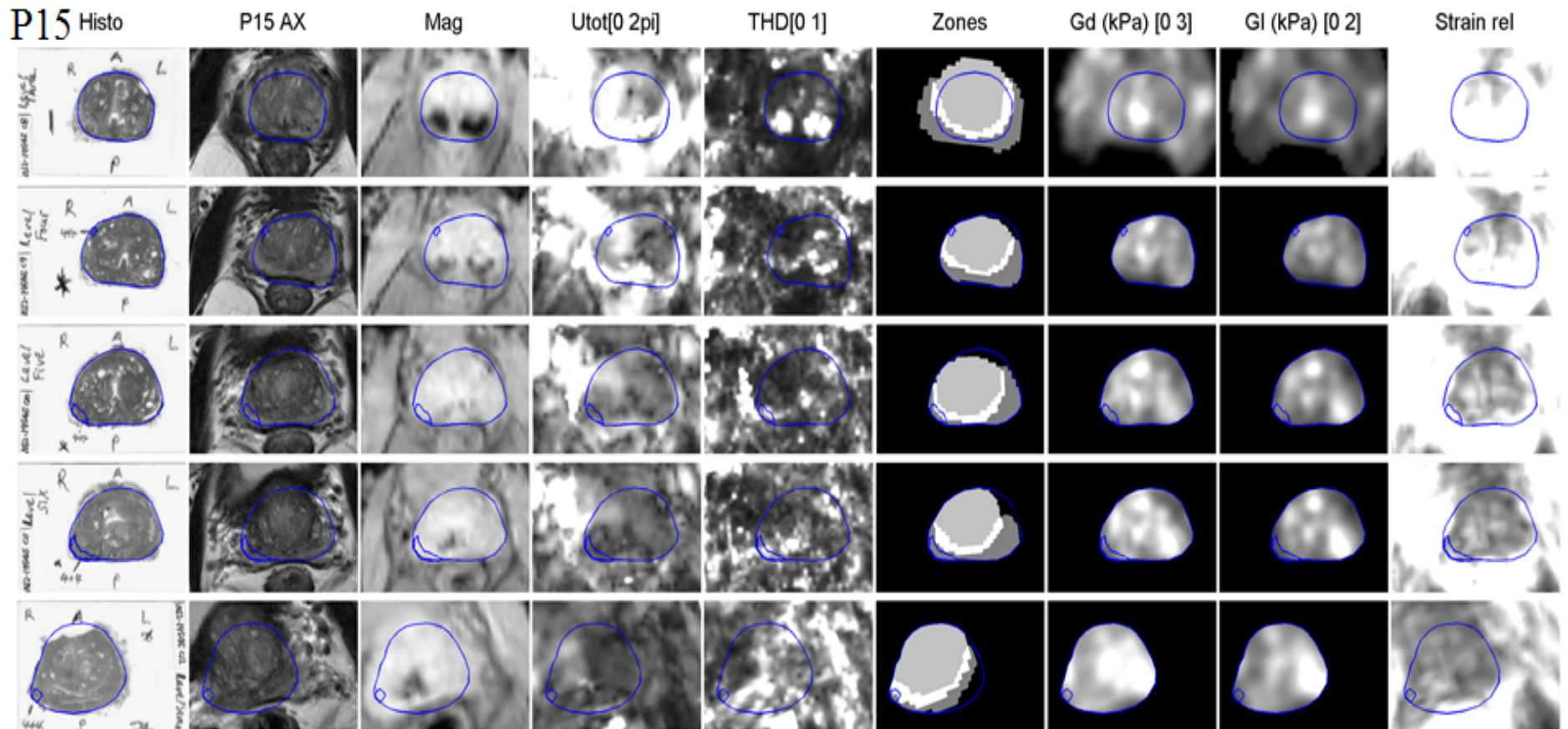


Figure C-23. Results for P15. Shear moduli ( $G$  and  $G_I$ ) and maximum shear strain ( $\tau_{max}$ ) as registered to histopathology slides. The total wave amplitude and THD are also shown.

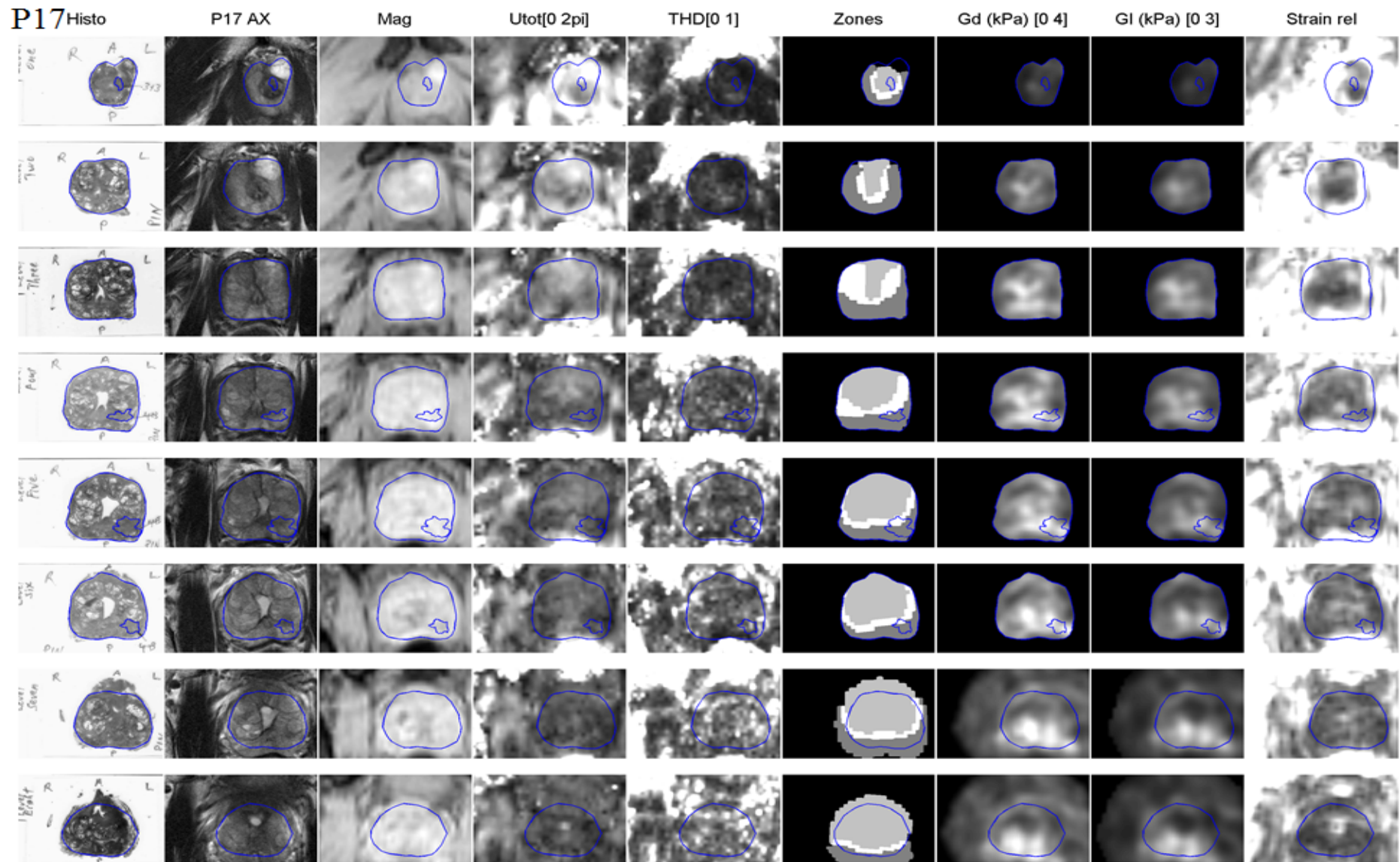


Figure C-24. Results for P17. Shear moduli ( $G$  and  $G_I$ ) and maximum shear strain ( $\tau_{\max}$ ) as registered to histopathology slides. The total wave amplitude and THD are also shown.

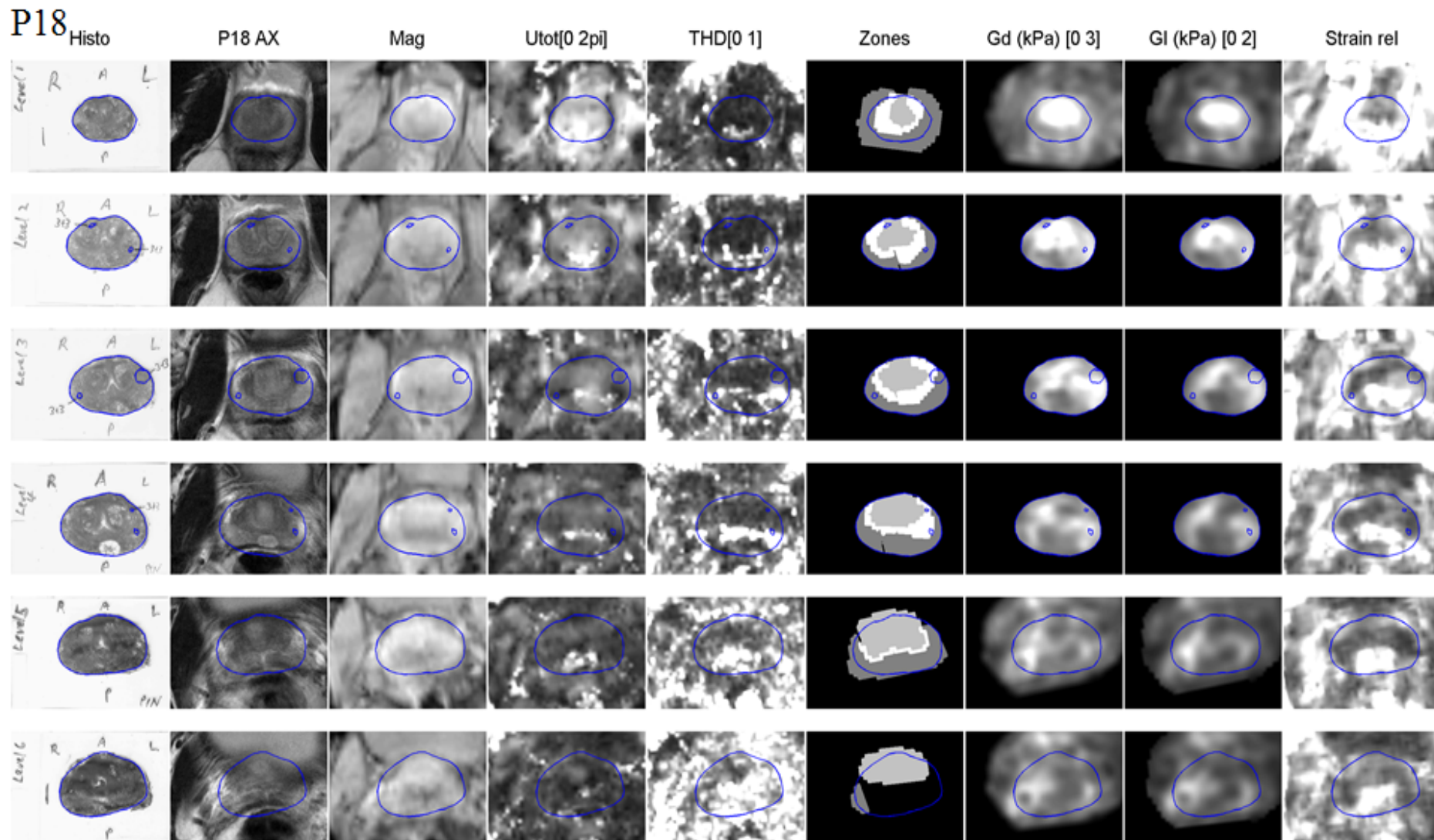


Figure C-25. Results for P18. Shear moduli ( $G$  and  $G_I$ ) and maximum shear strain ( $\tau_{max}$ ) as registered to histopathology slides. The total wave amplitude and THD are also shown.

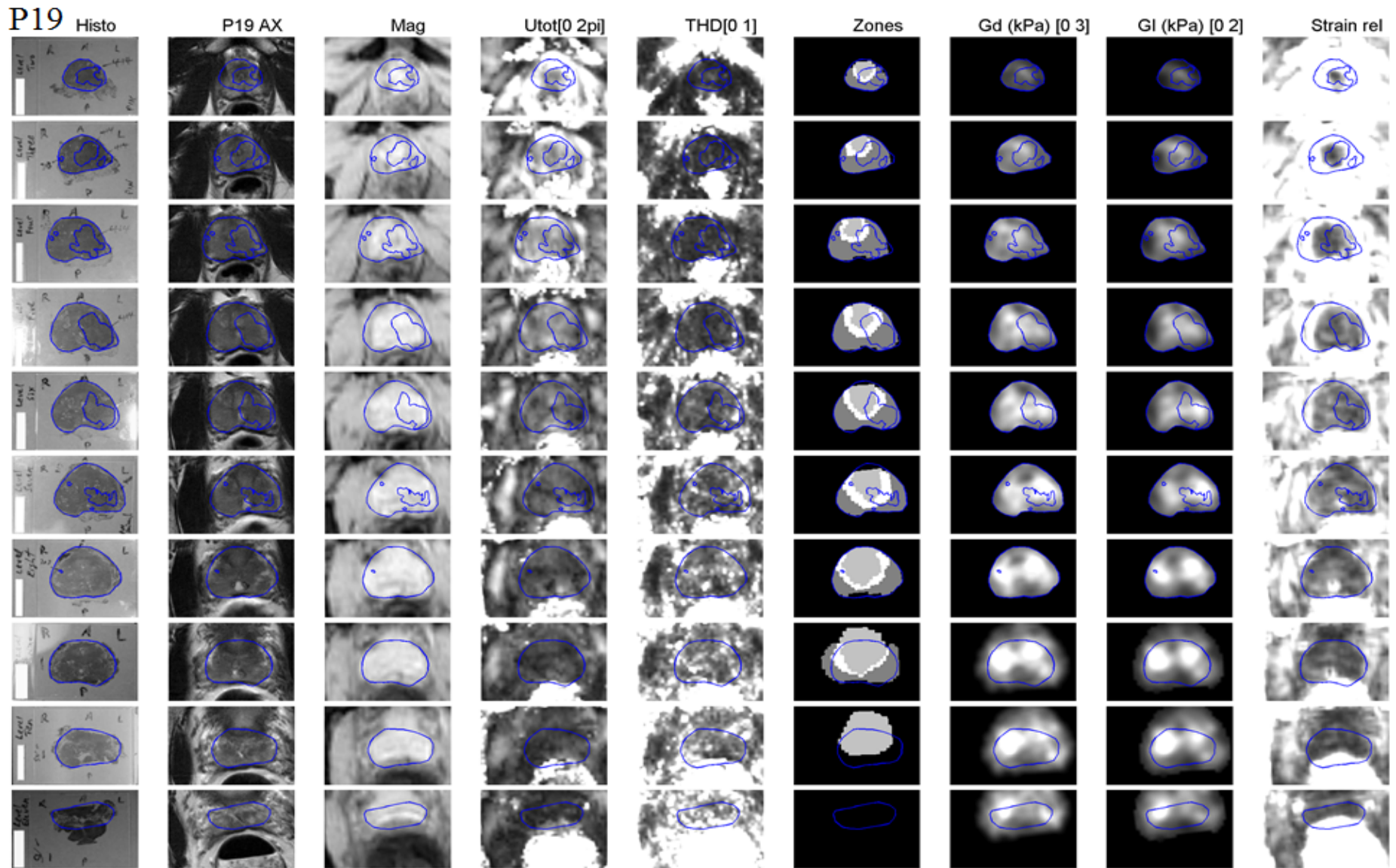


Figure C-26. Results for P19. Shear moduli ( $G$  and  $G_I$ ) and maximum shear strain ( $\tau_{\max}$ ) as registered to histopathology slides. The total wave amplitude and THD are also shown.

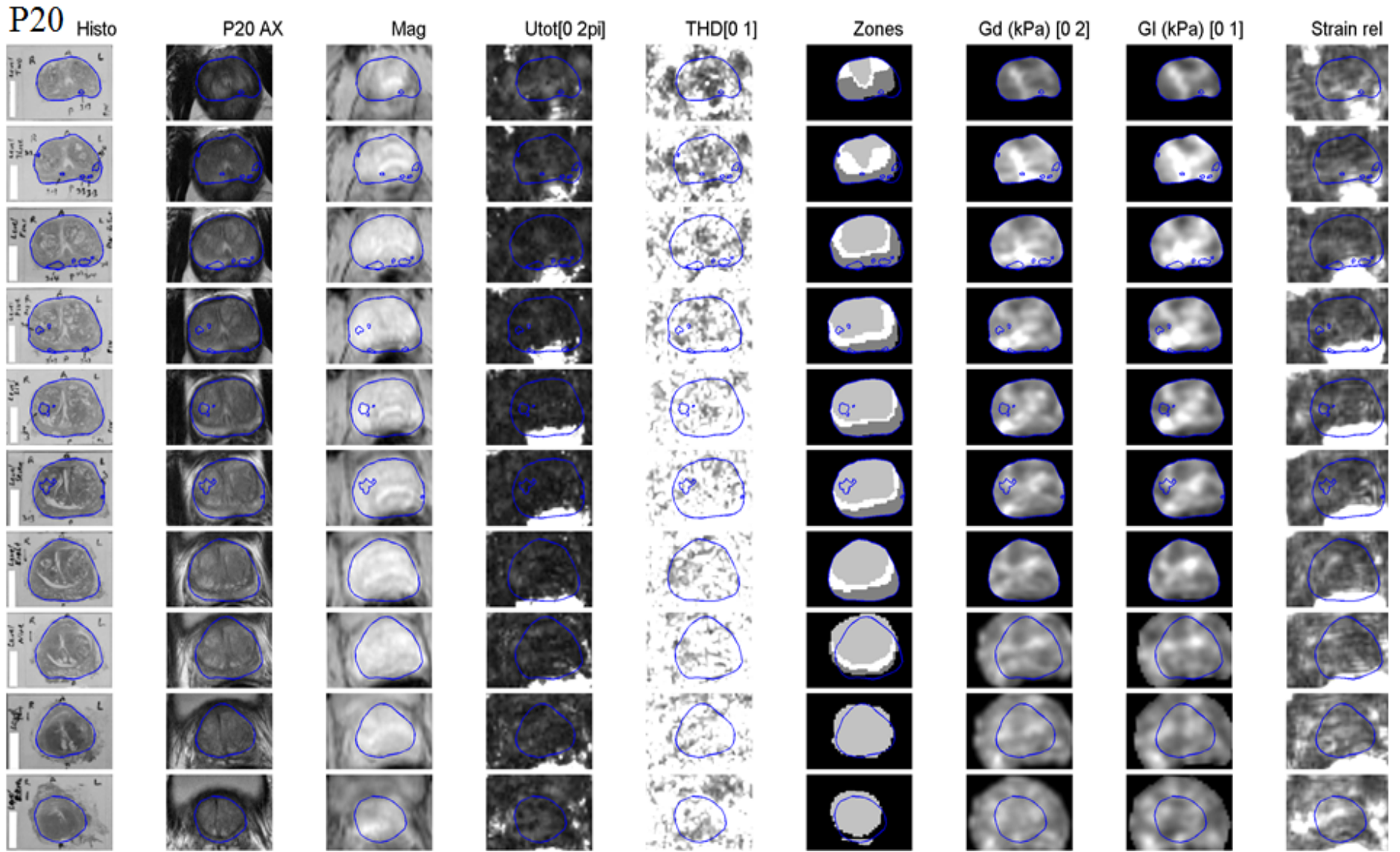


Figure C-27. Results for P20. Shear moduli ( $G$  and  $G_I$ ) and maximum shear strain ( $\tau_{max}$ ) as registered to histopathology slides. The total wave amplitude and THD are also shown.

# Appendix D – Additional images from *ex-vivo* patient studies

P01 600

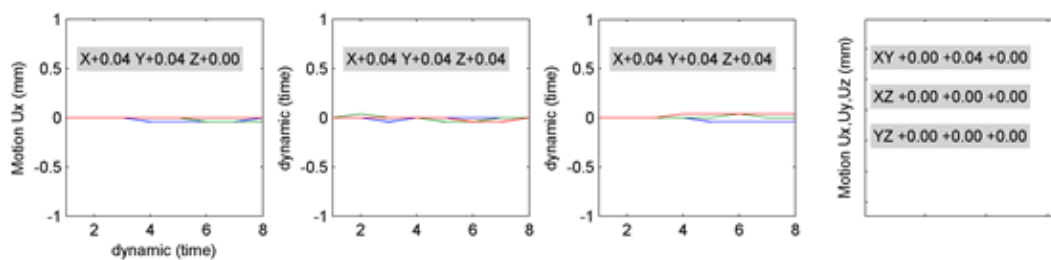
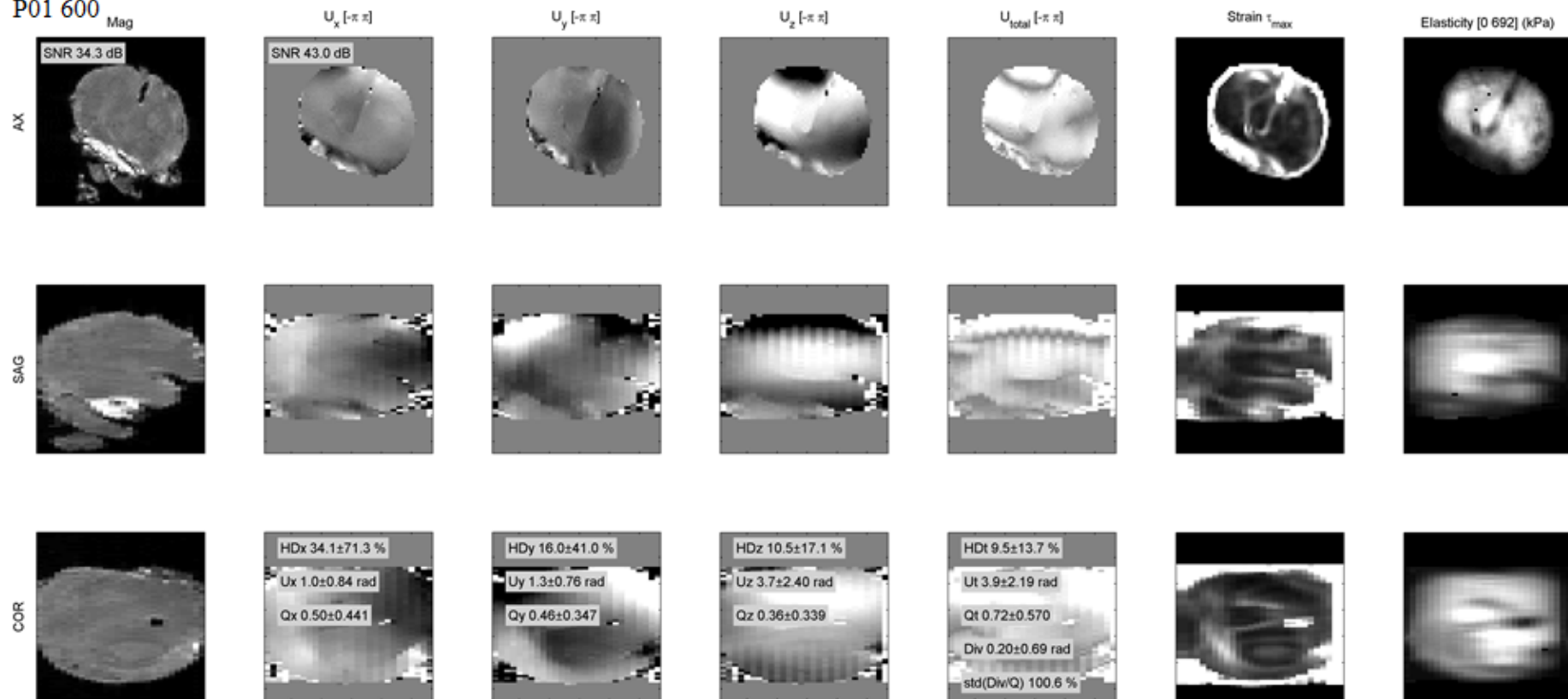


Figure D-1. Raw data for patient P01 600 Hz.

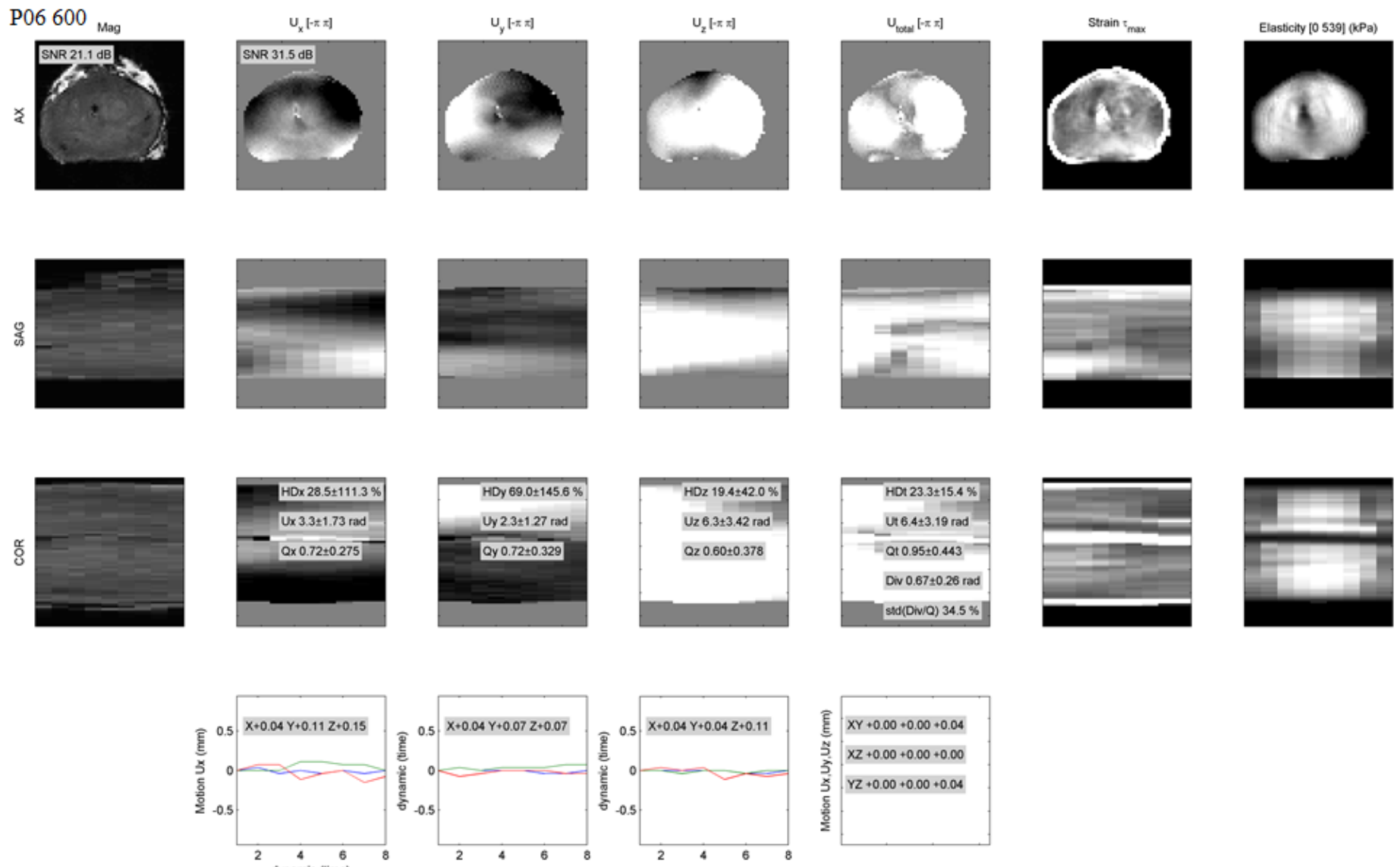


Figure D-2. Raw data for patient P04 600 Hz.

P08 600

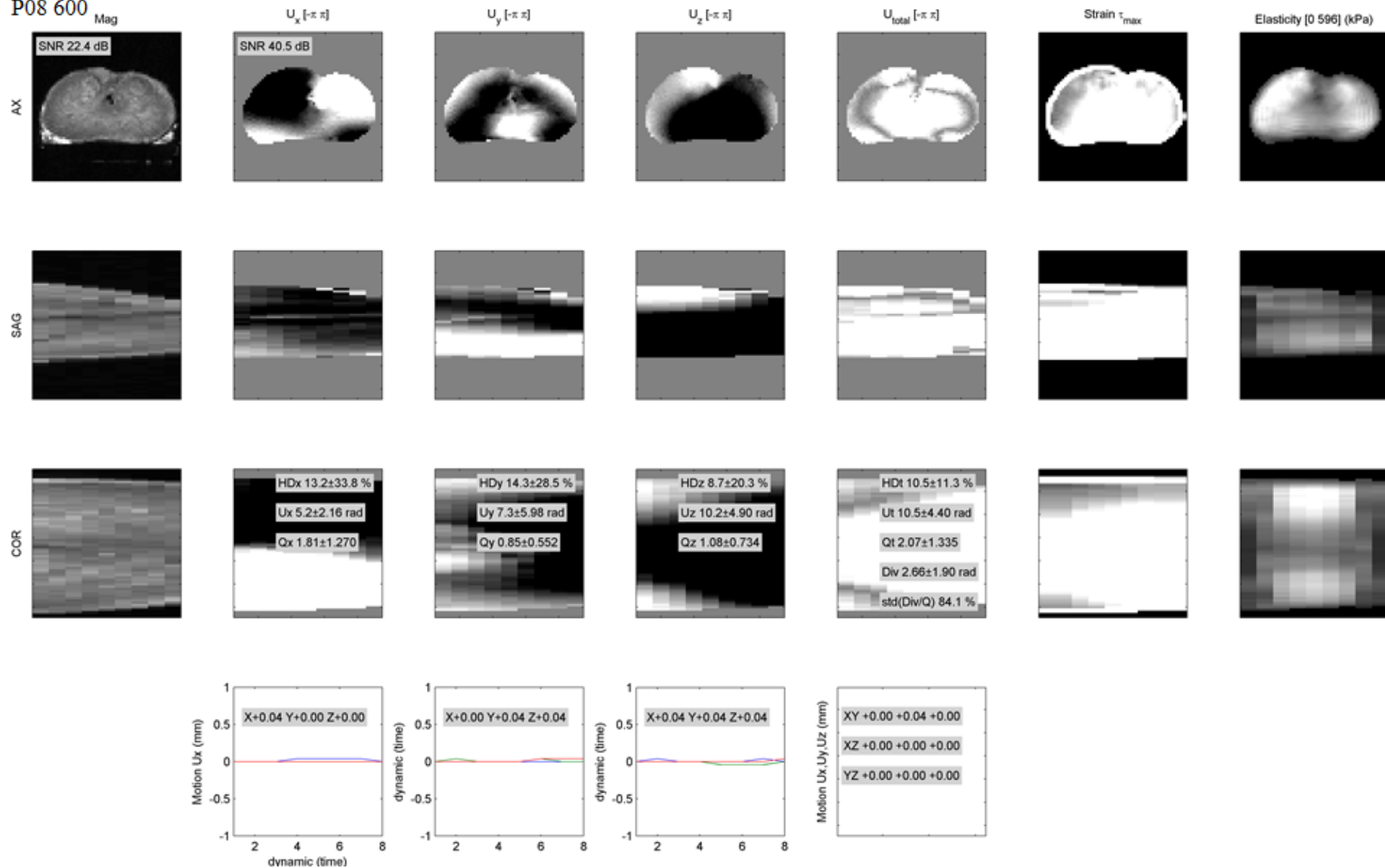


Figure D-3. Raw data for patient P08 600 Hz.

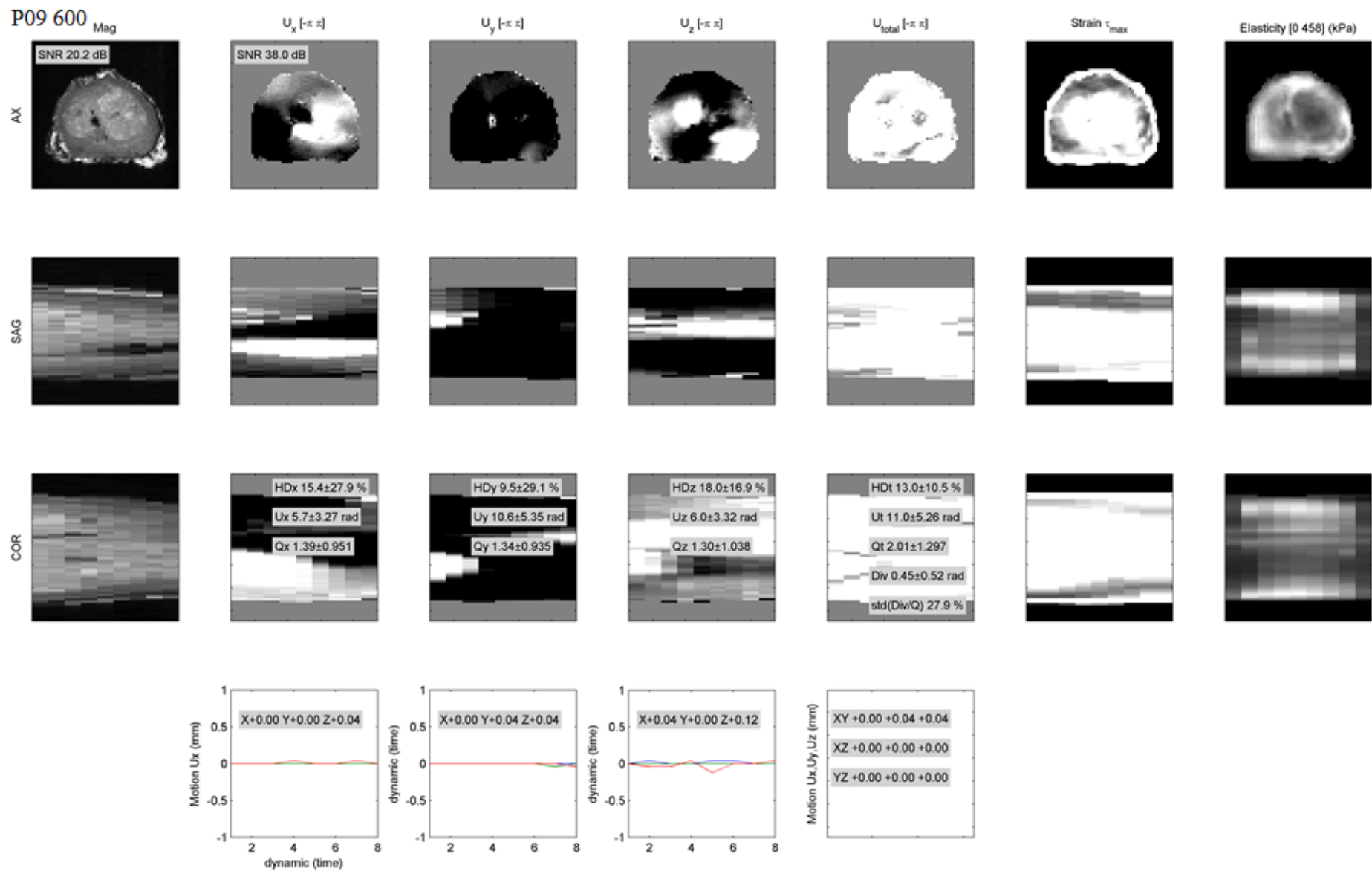


Figure D-4. Raw data for patient P09 600 Hz.

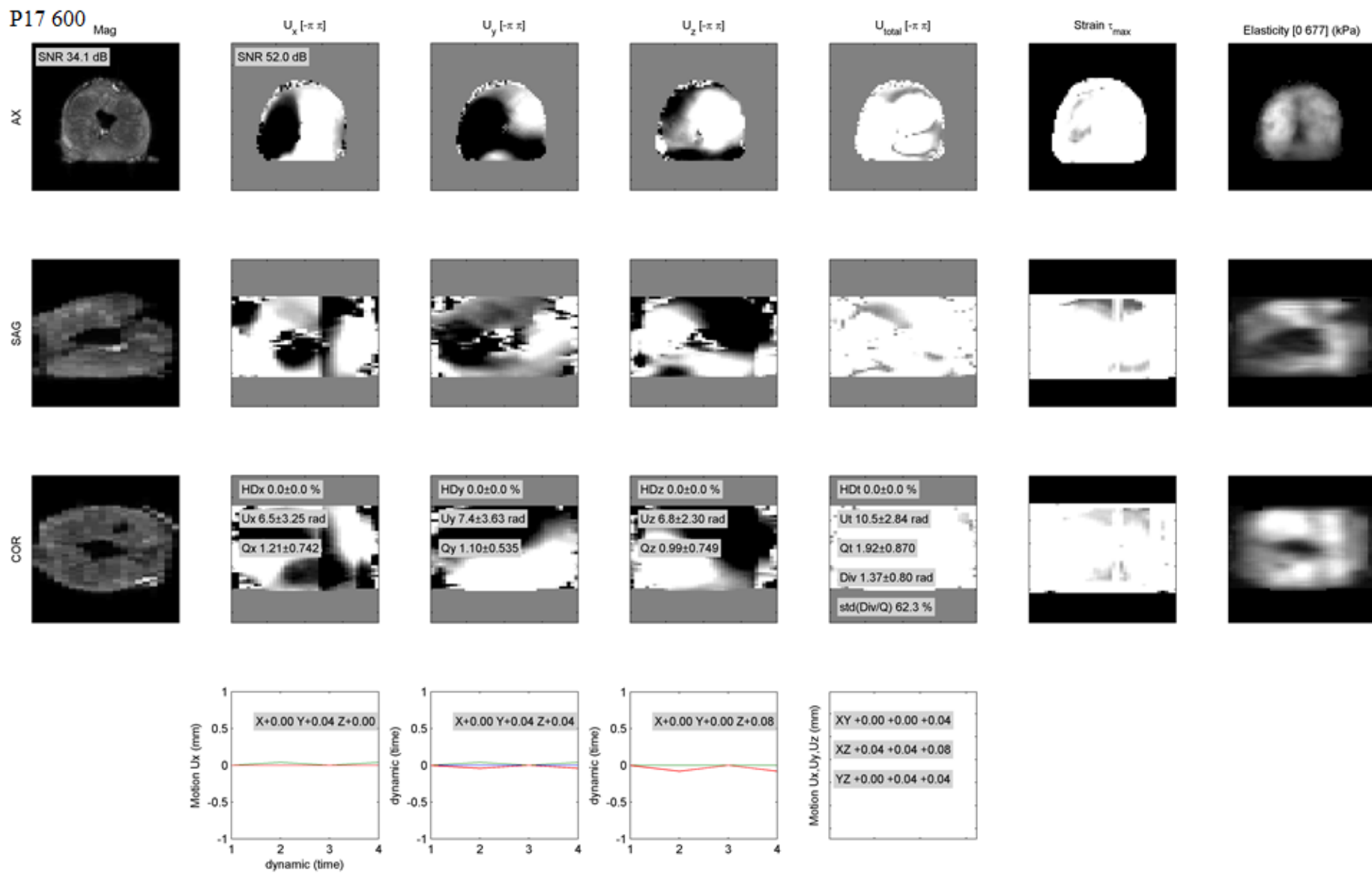


Figure D-5. Raw data for patient P17 600 Hz.

P18 600

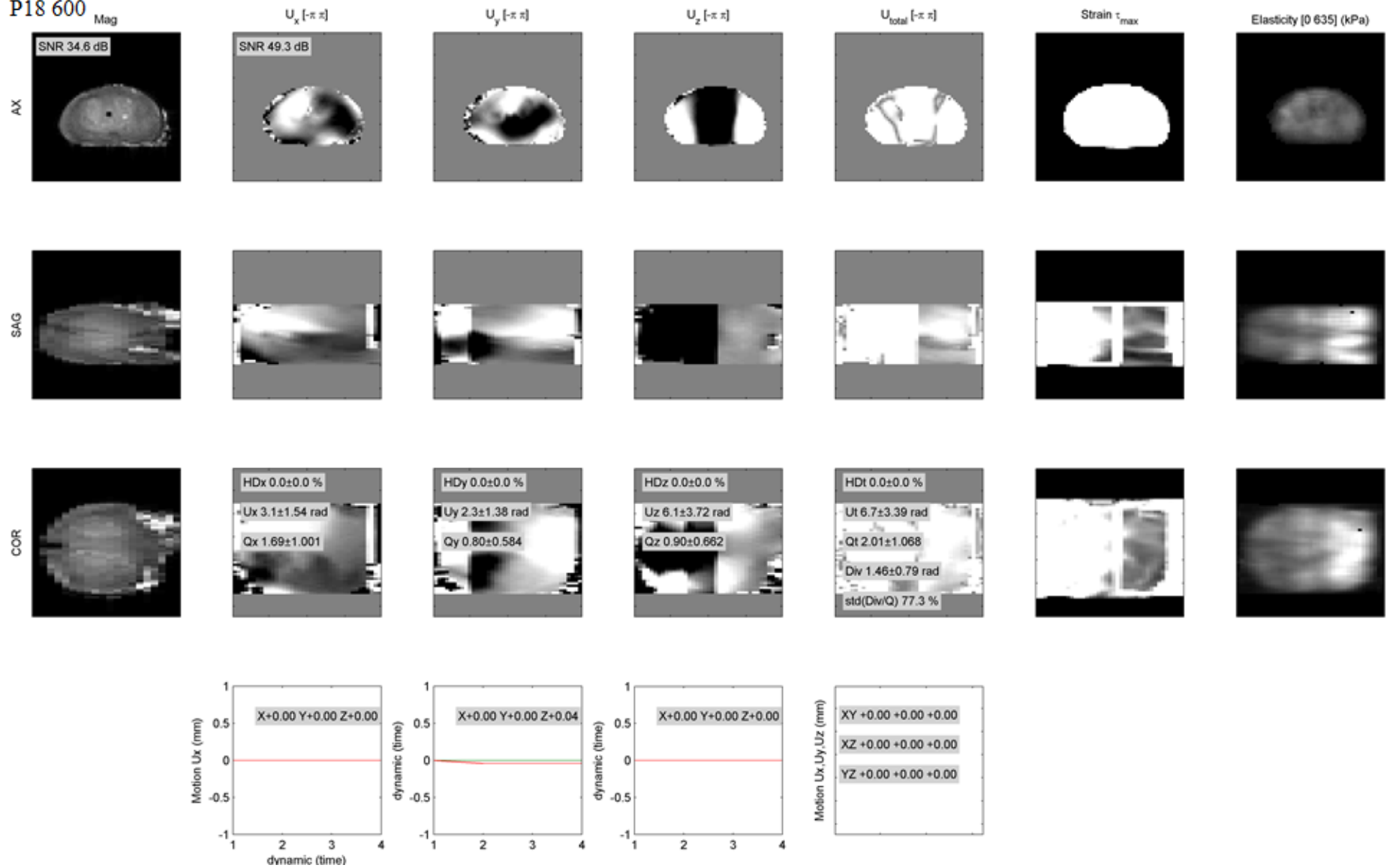


Figure D-6. Raw data for patient P18 600 Hz.

P19 600

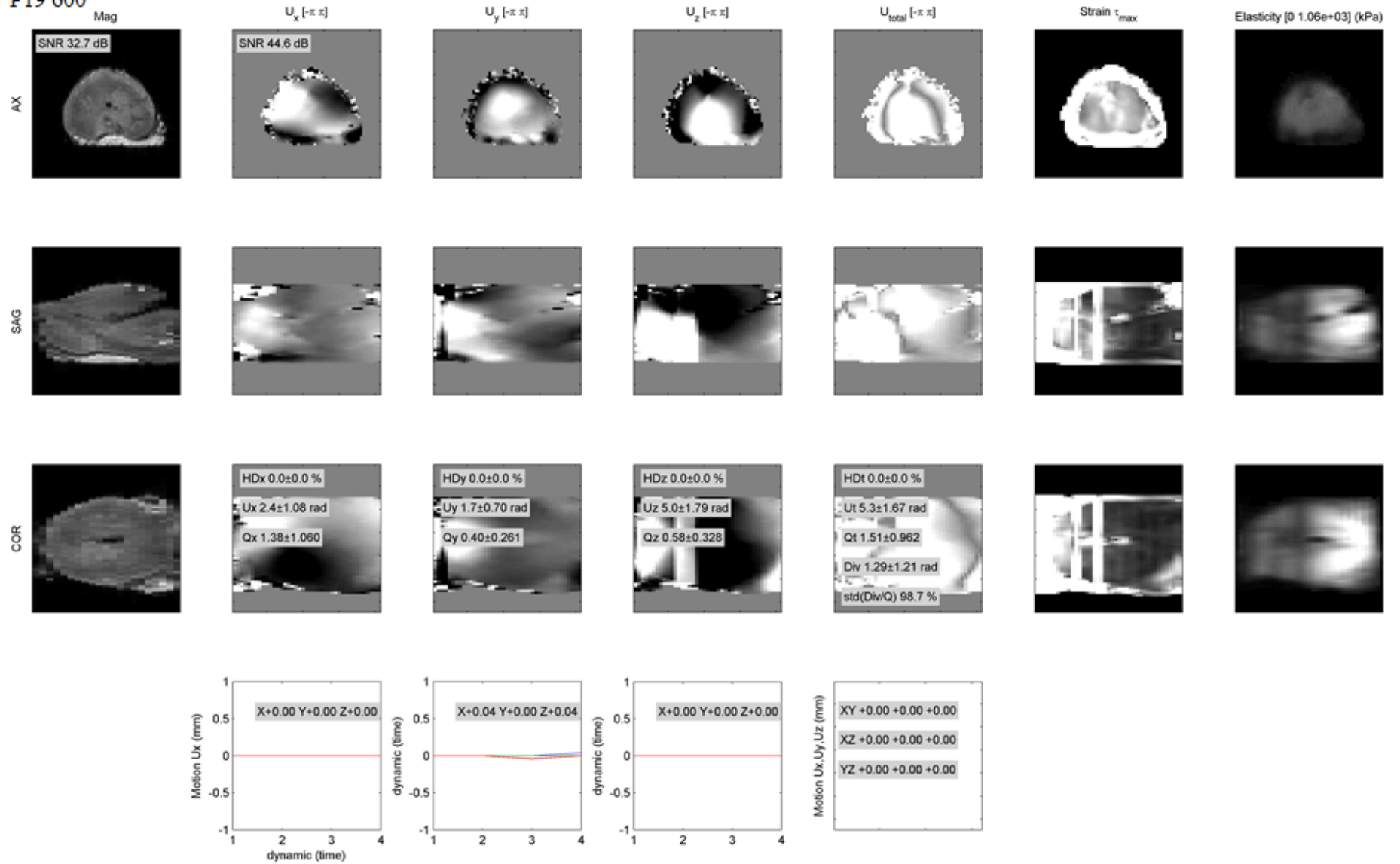


Figure D-7. Raw data for patient P19 600 Hz.

P20 600

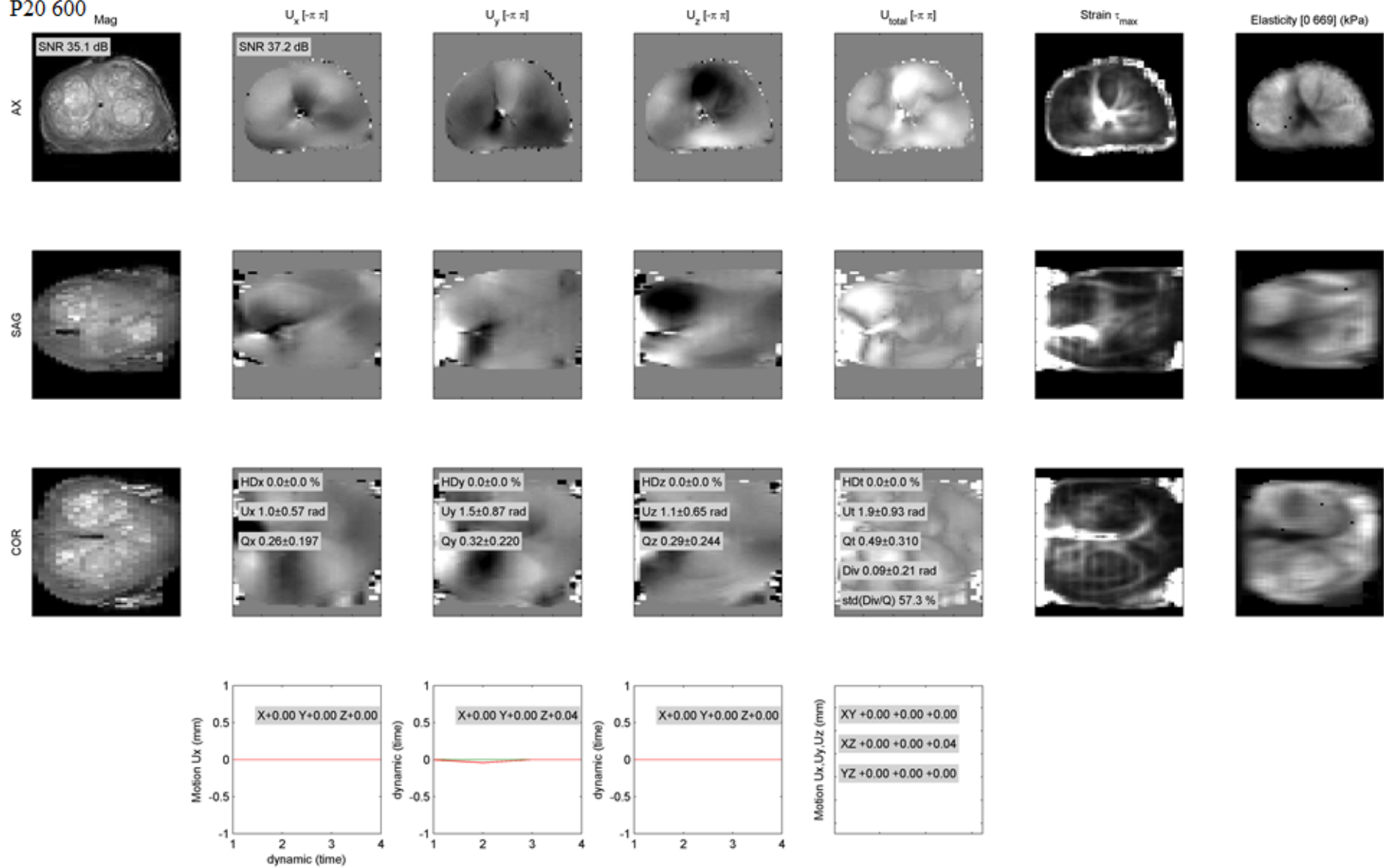


Figure D-8. Raw data for patient P20 600 Hz.

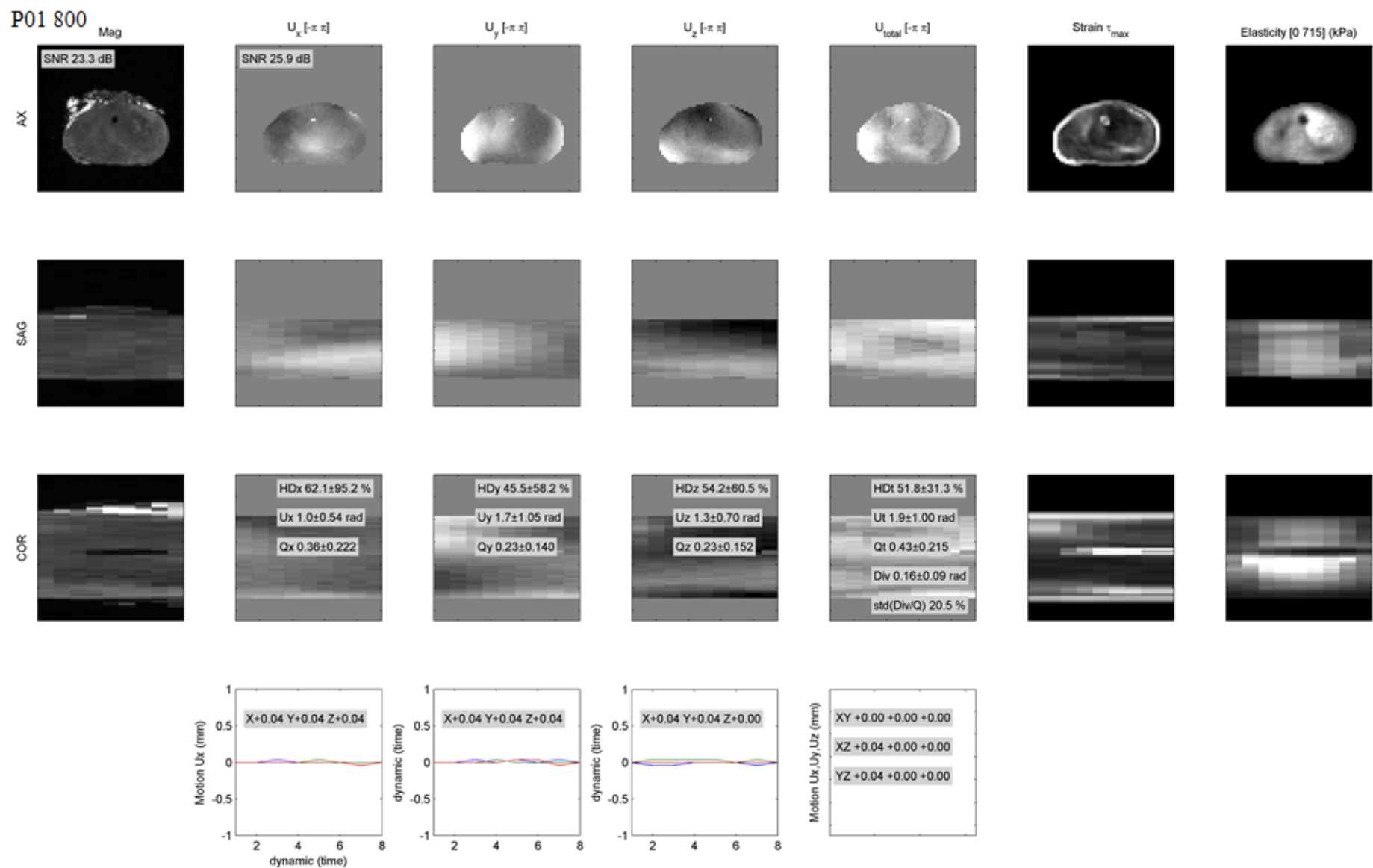


Figure D-9. Raw data for patient P01 800 Hz.

P04 800

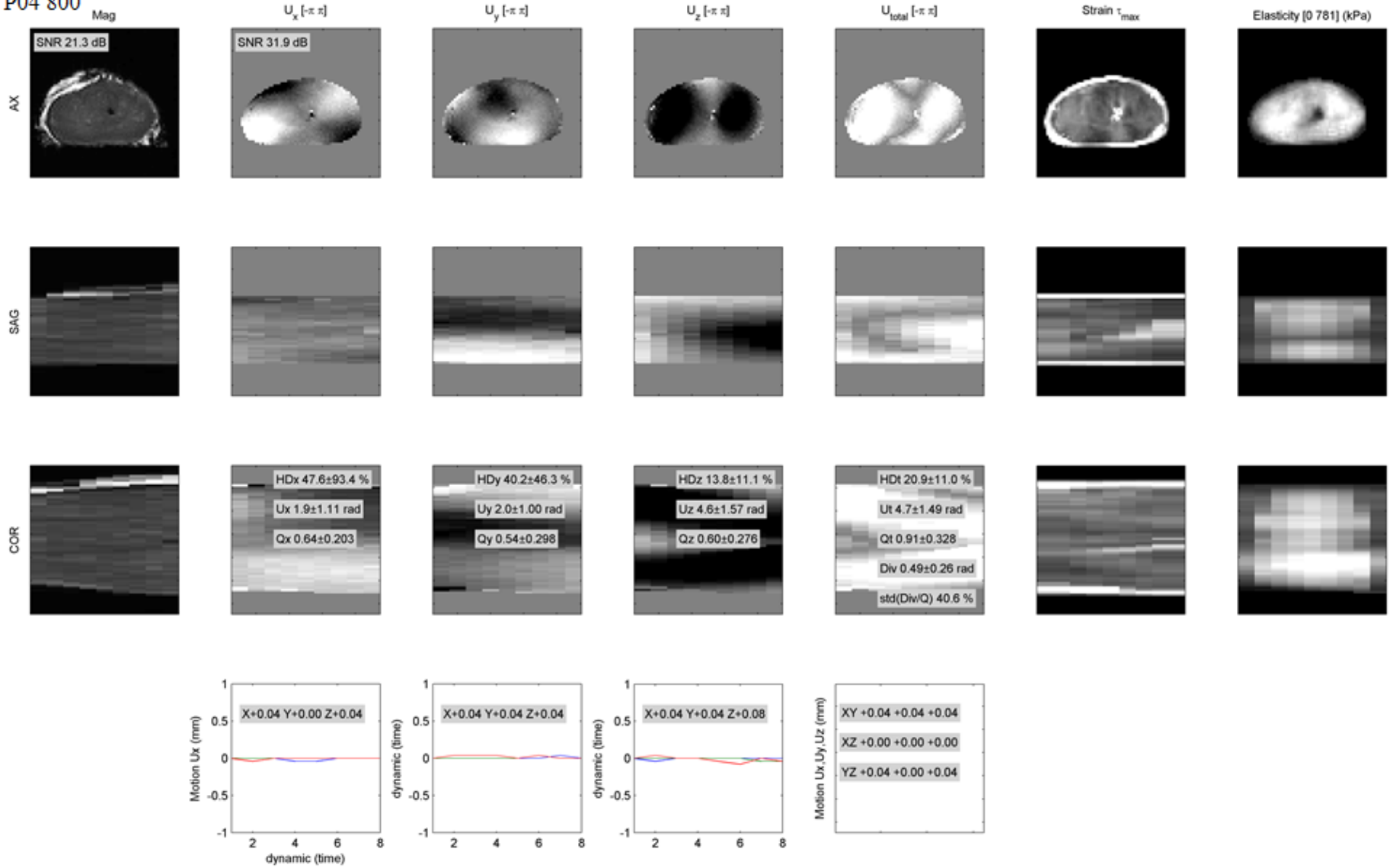


Figure D-10. Raw data for patient P04 800 Hz.

P05 800

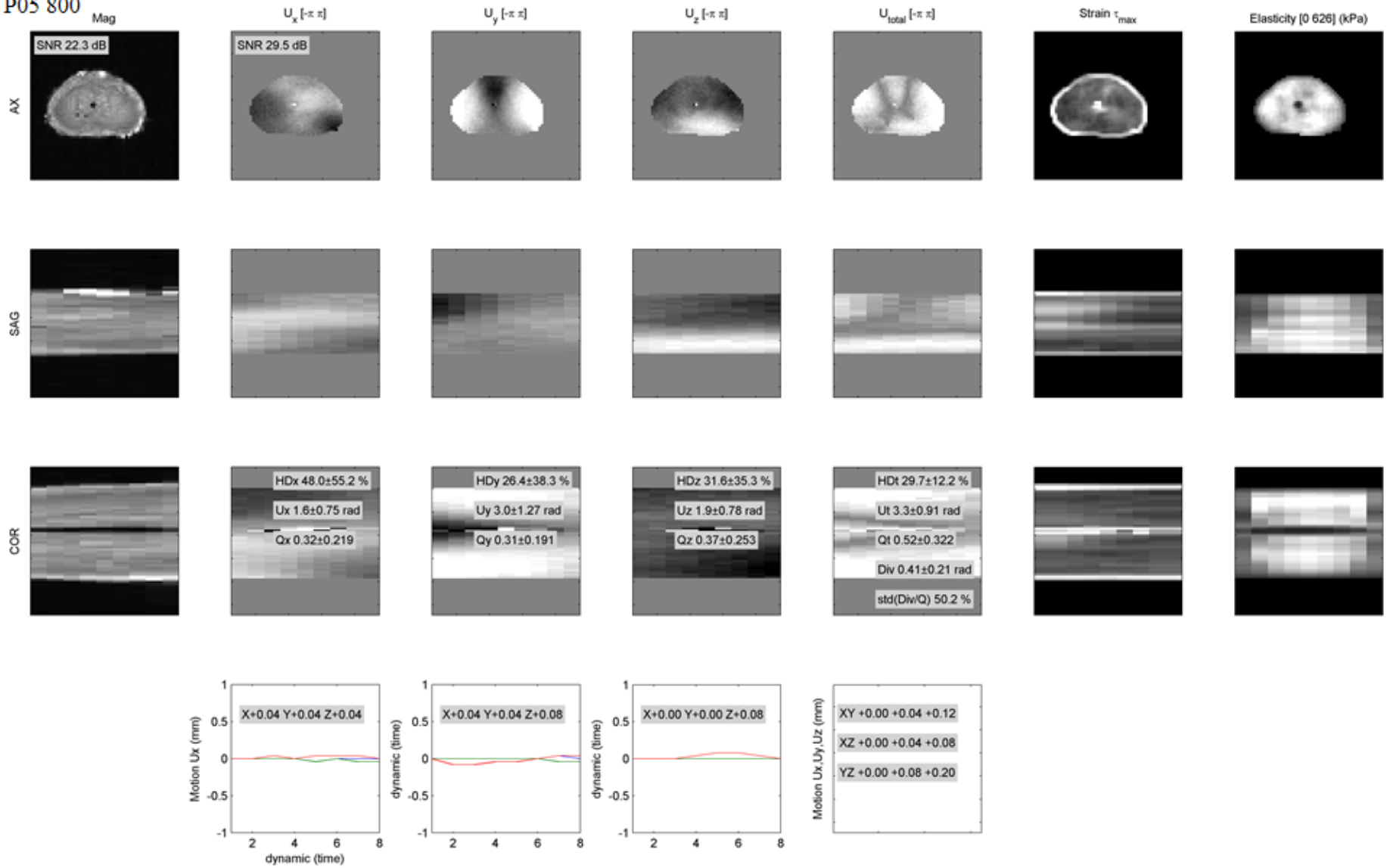


Figure D-11. Raw data for patient P05 800 Hz.

P06 800

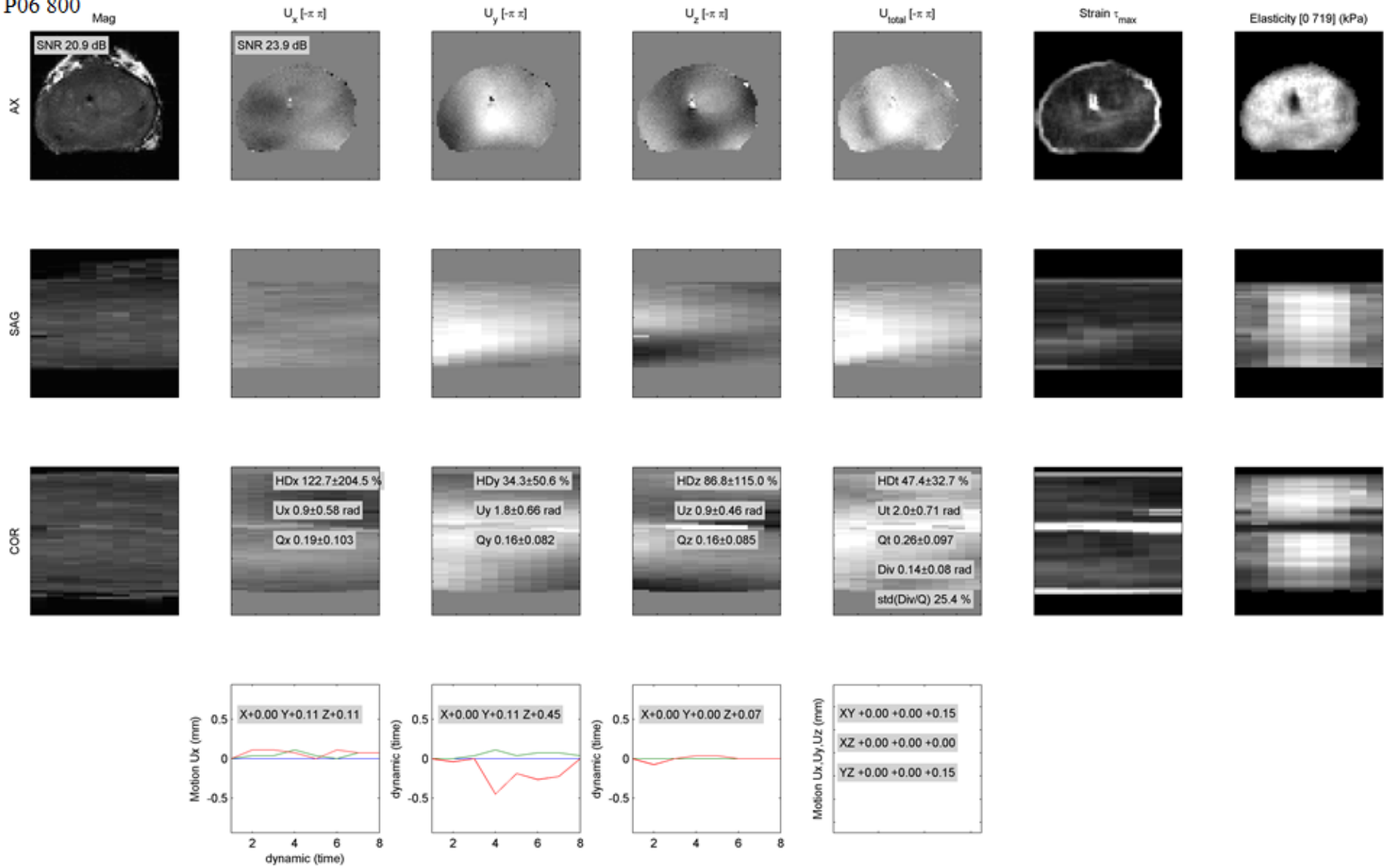


Figure D-12. Raw data for patient P06 800 Hz.

P08 800

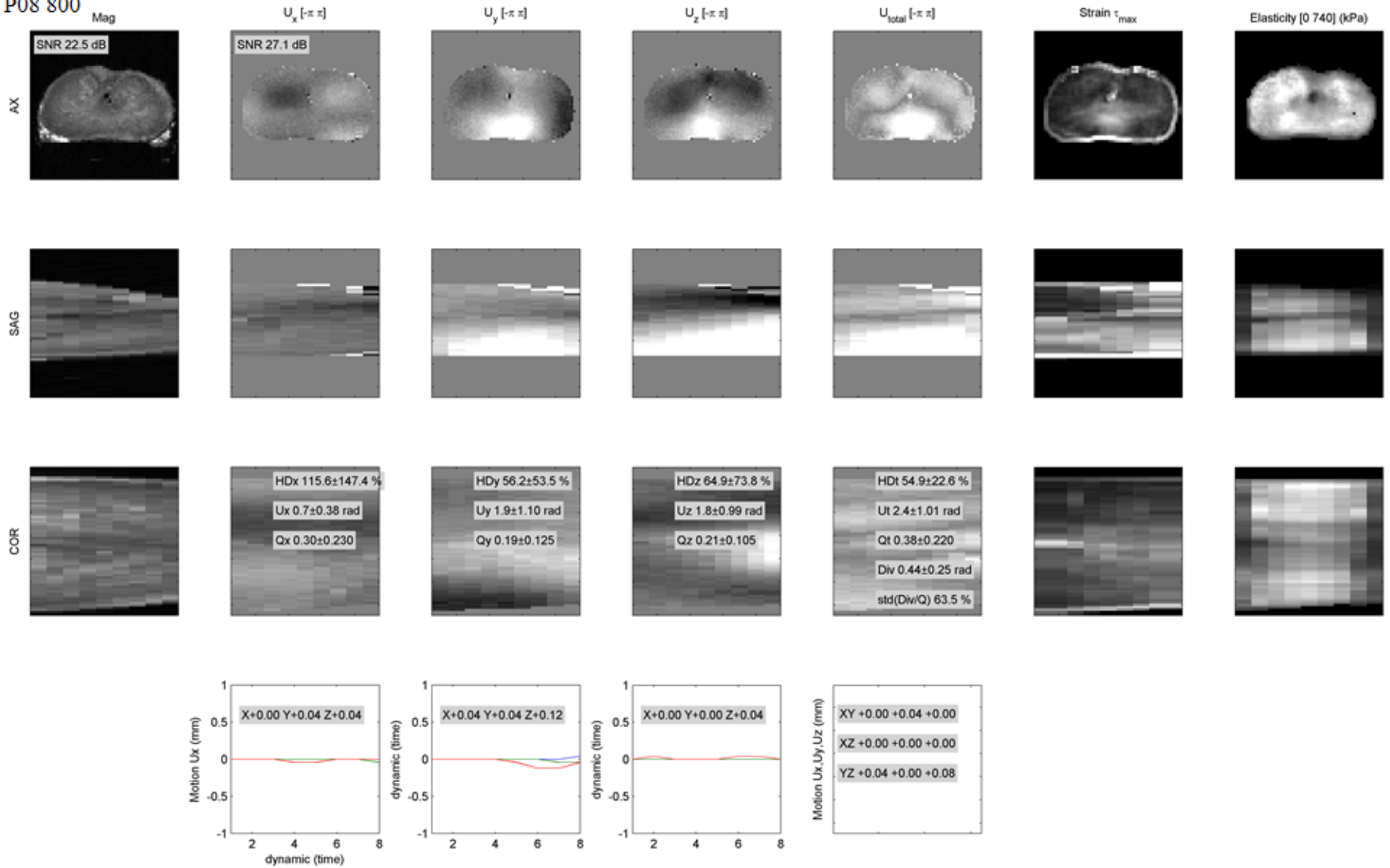


Figure D-13. Raw data for patient P08 800 Hz.

P09 800

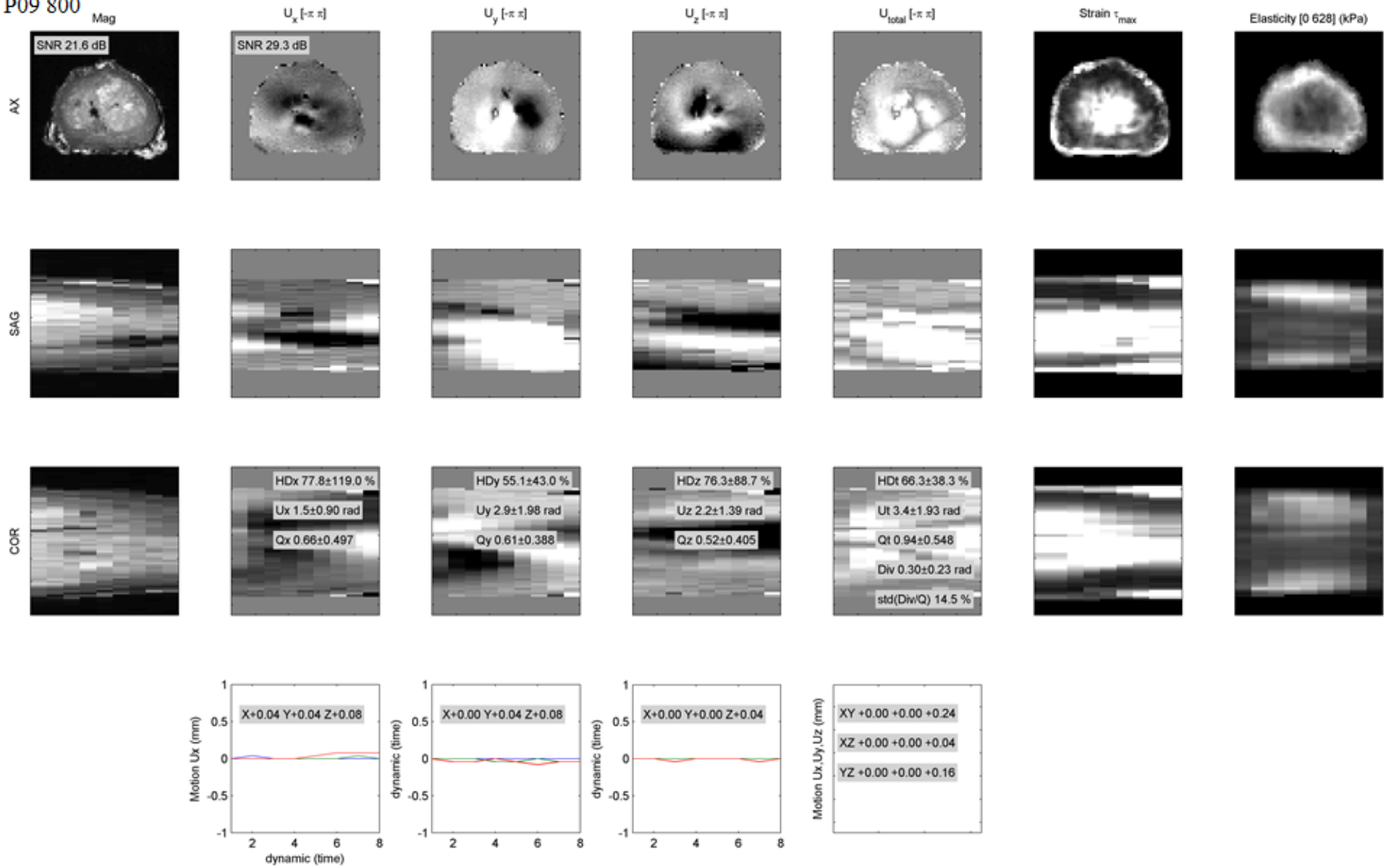


Figure D-14. Raw data for patient P09 800 Hz.

P10 800

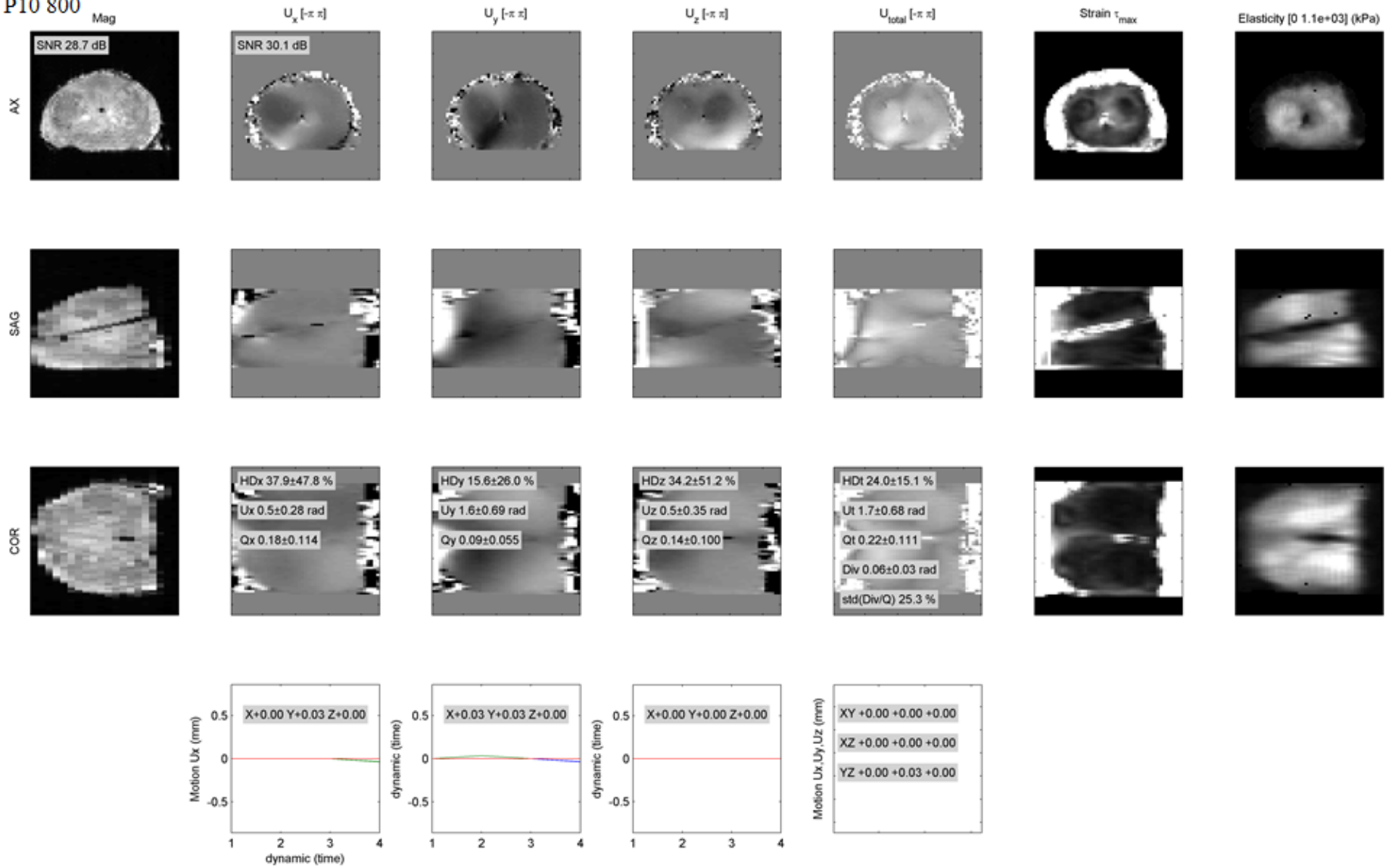


Figure D-15. Raw data for patient P10 800 Hz.

P11 800

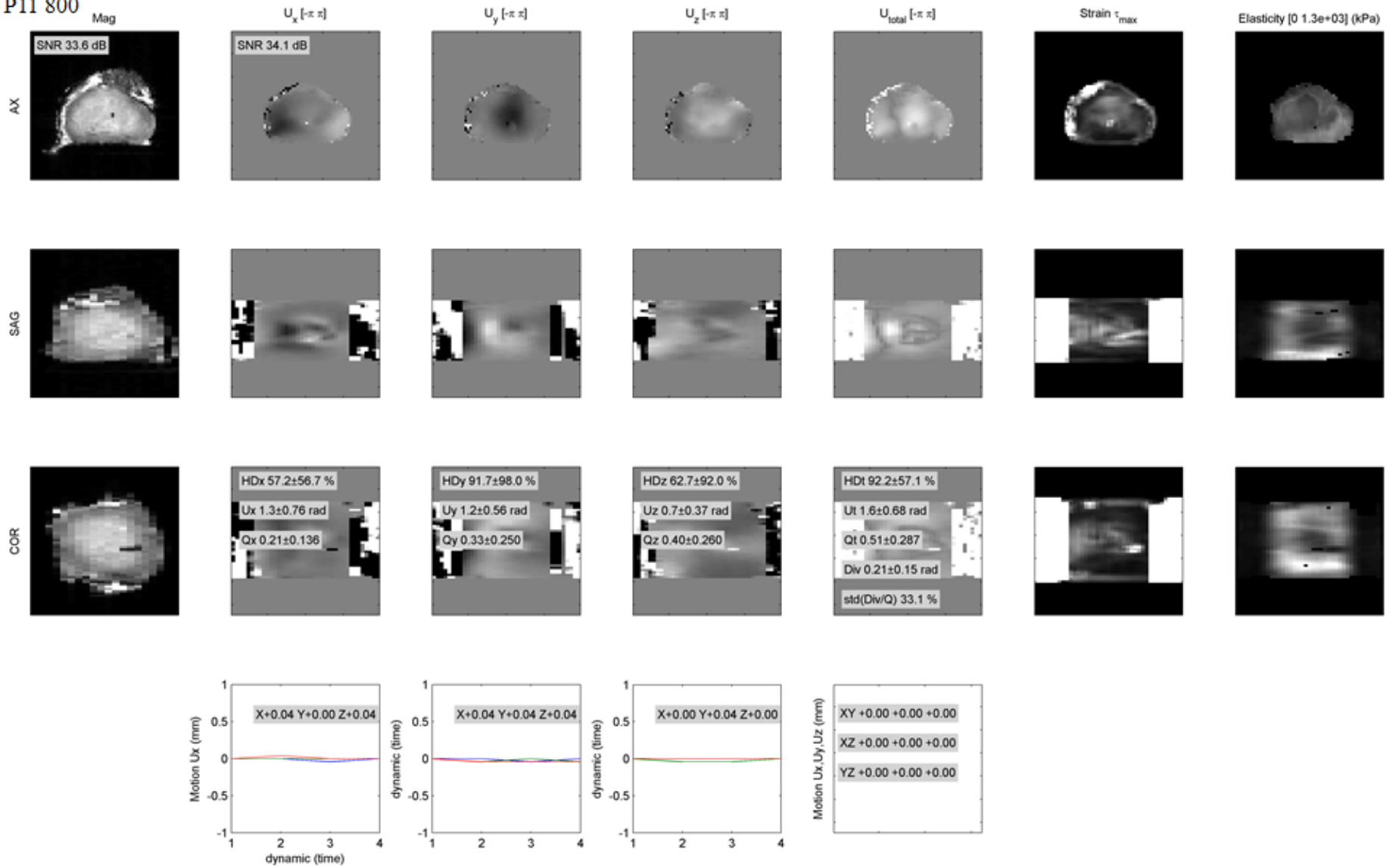


Figure D-16. Raw data for patient P11 800 Hz.

P13 800

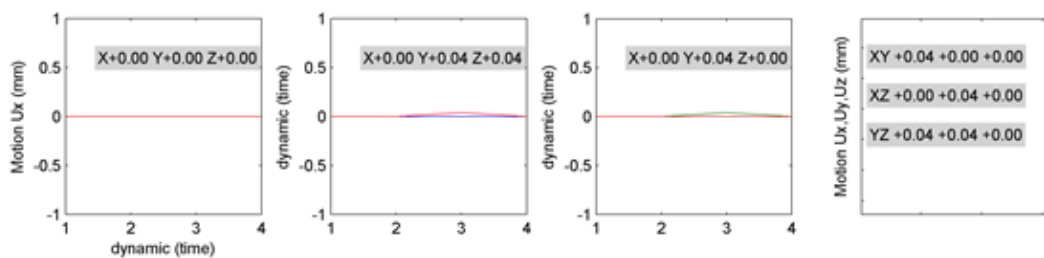
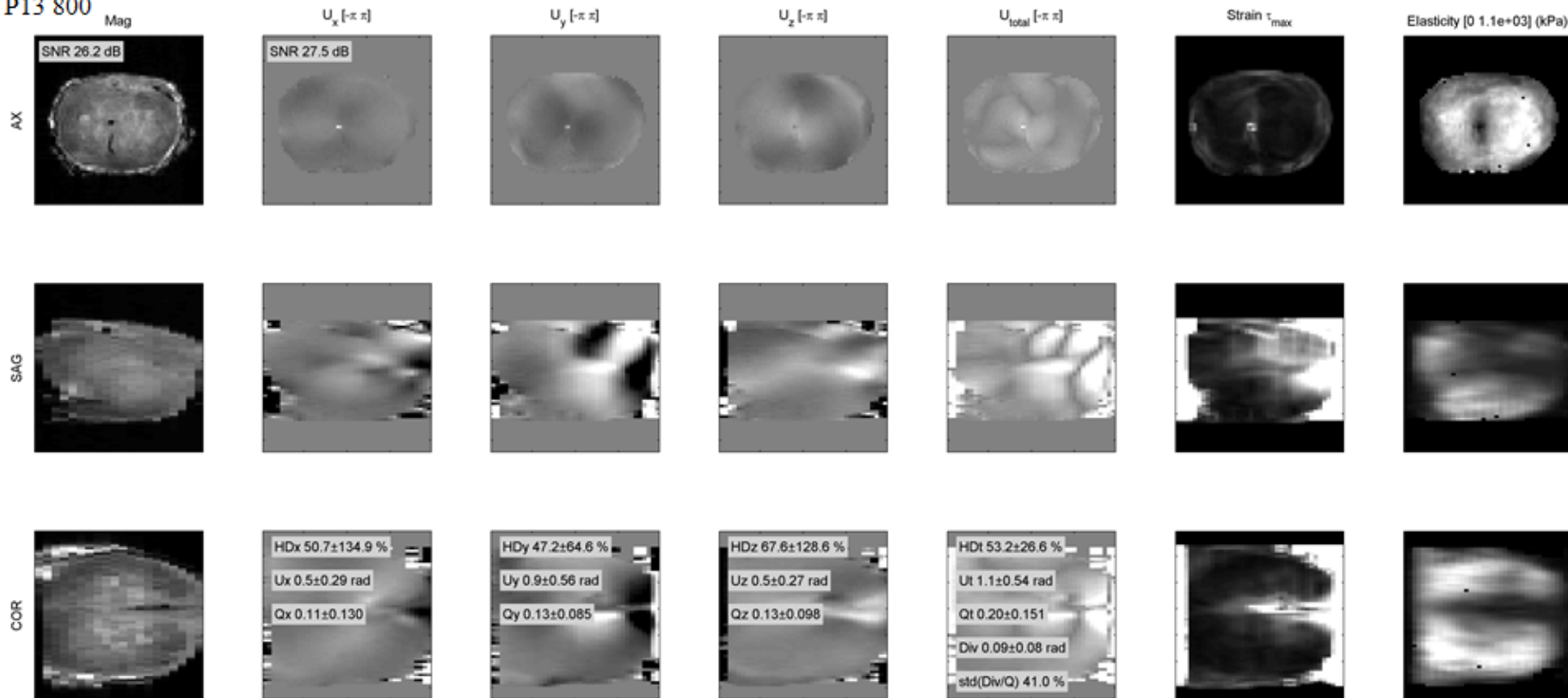


Figure D-17. Raw data for patient P13 800 Hz.

P16 800

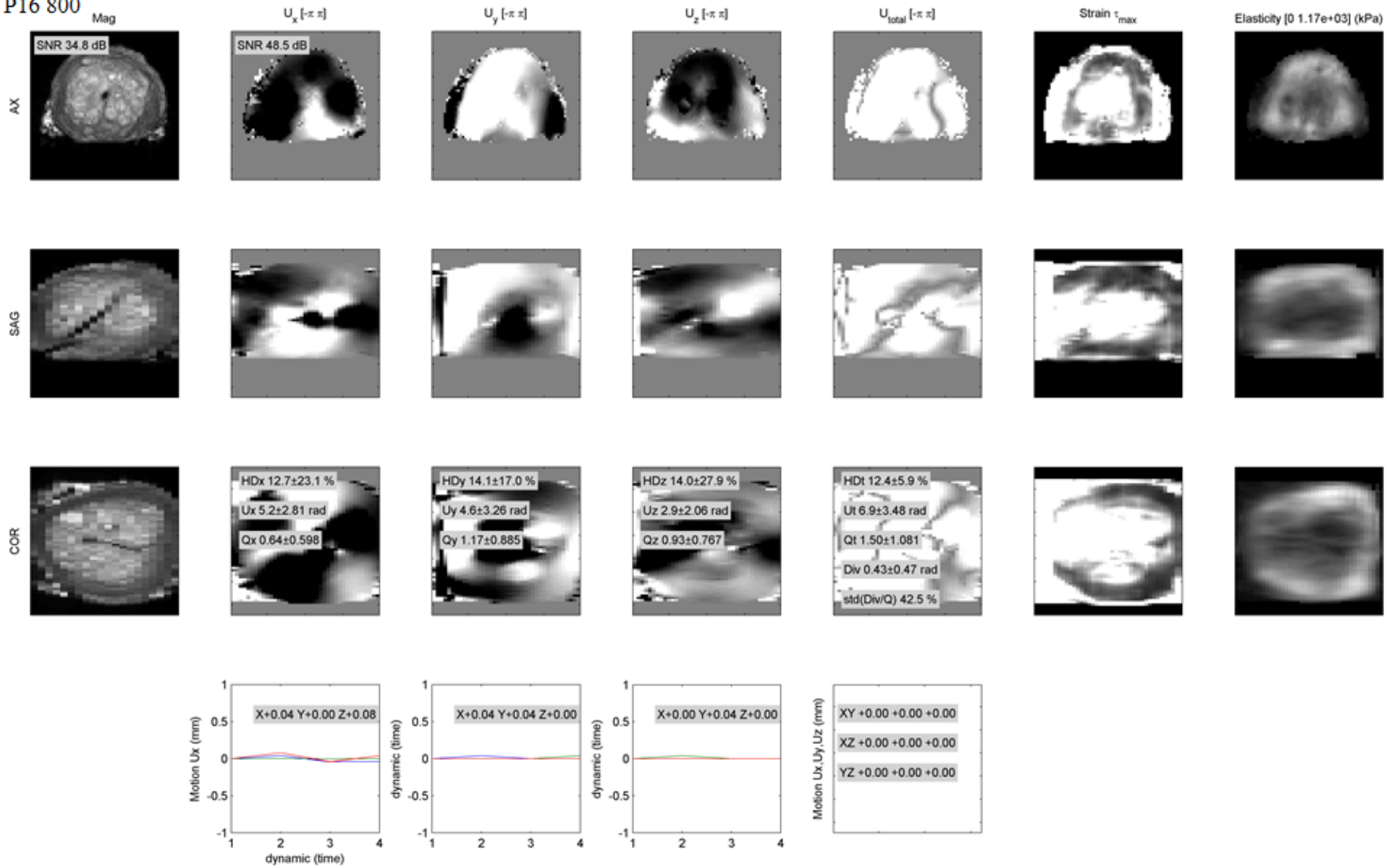


Figure D-18. Raw data for patient P16 800 Hz.

P17 800

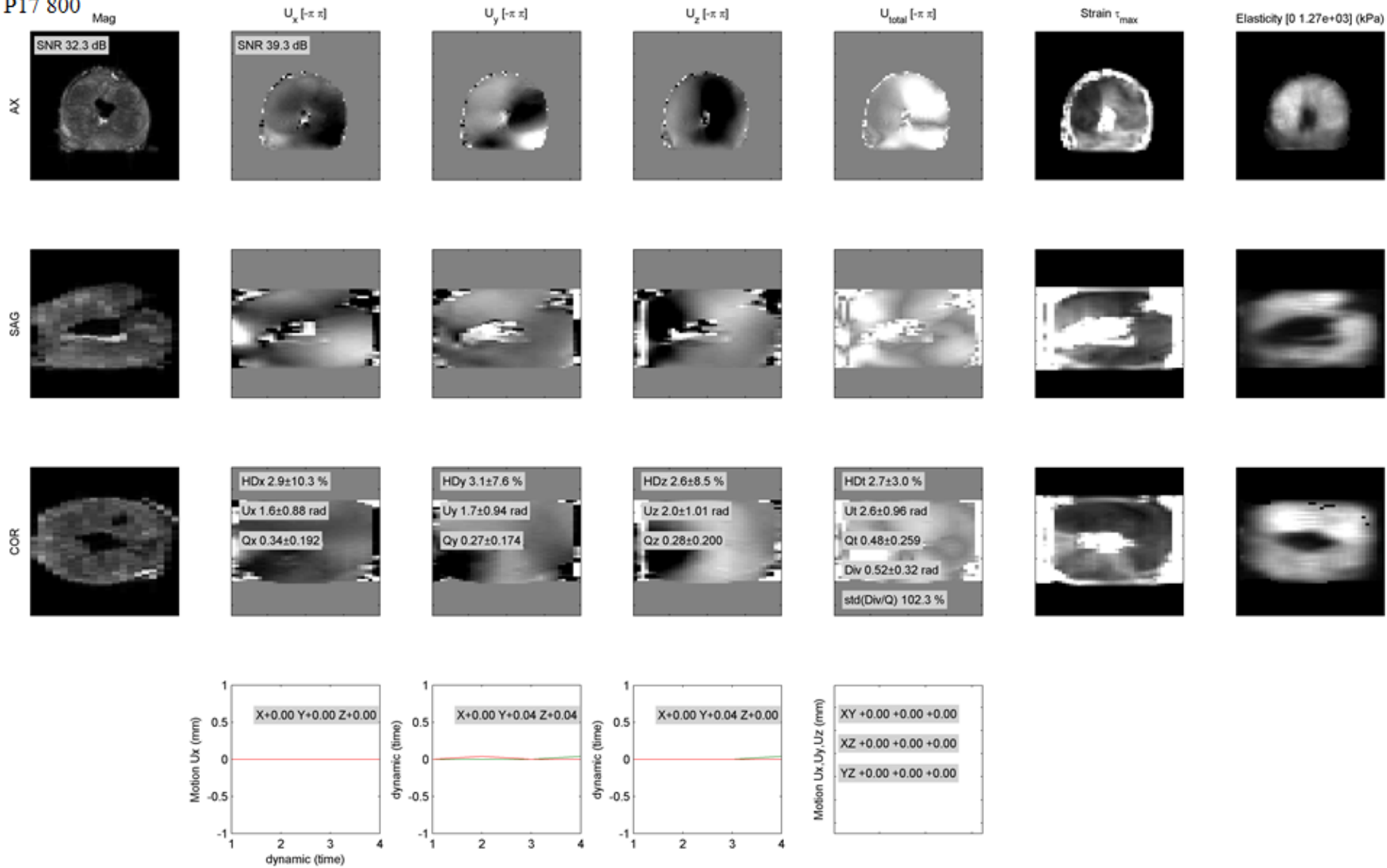


Figure D-19. Raw data for patient P17 800 Hz.

P18 800

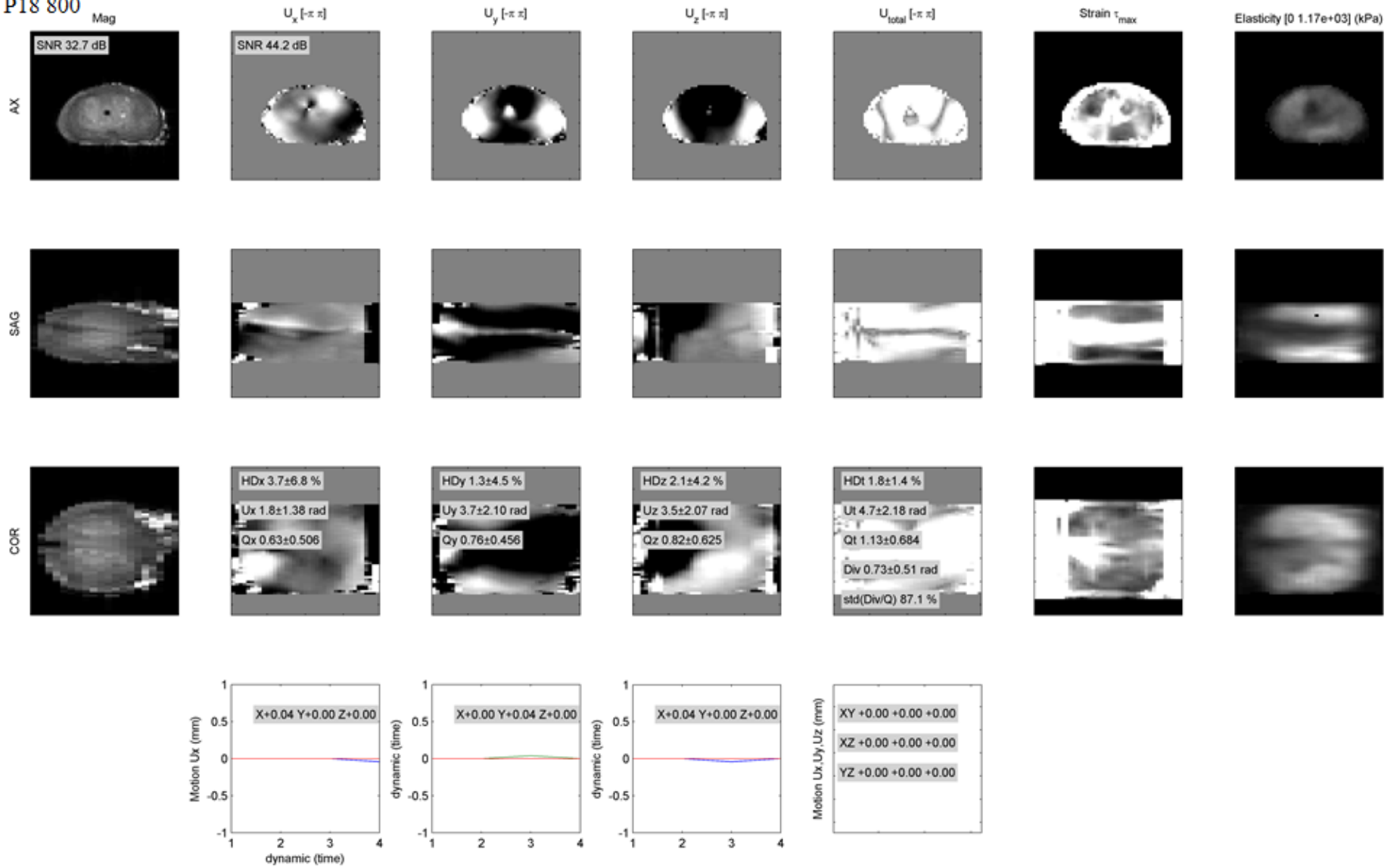


Figure D-20. Raw data for patient P18 800 Hz.

P19 800

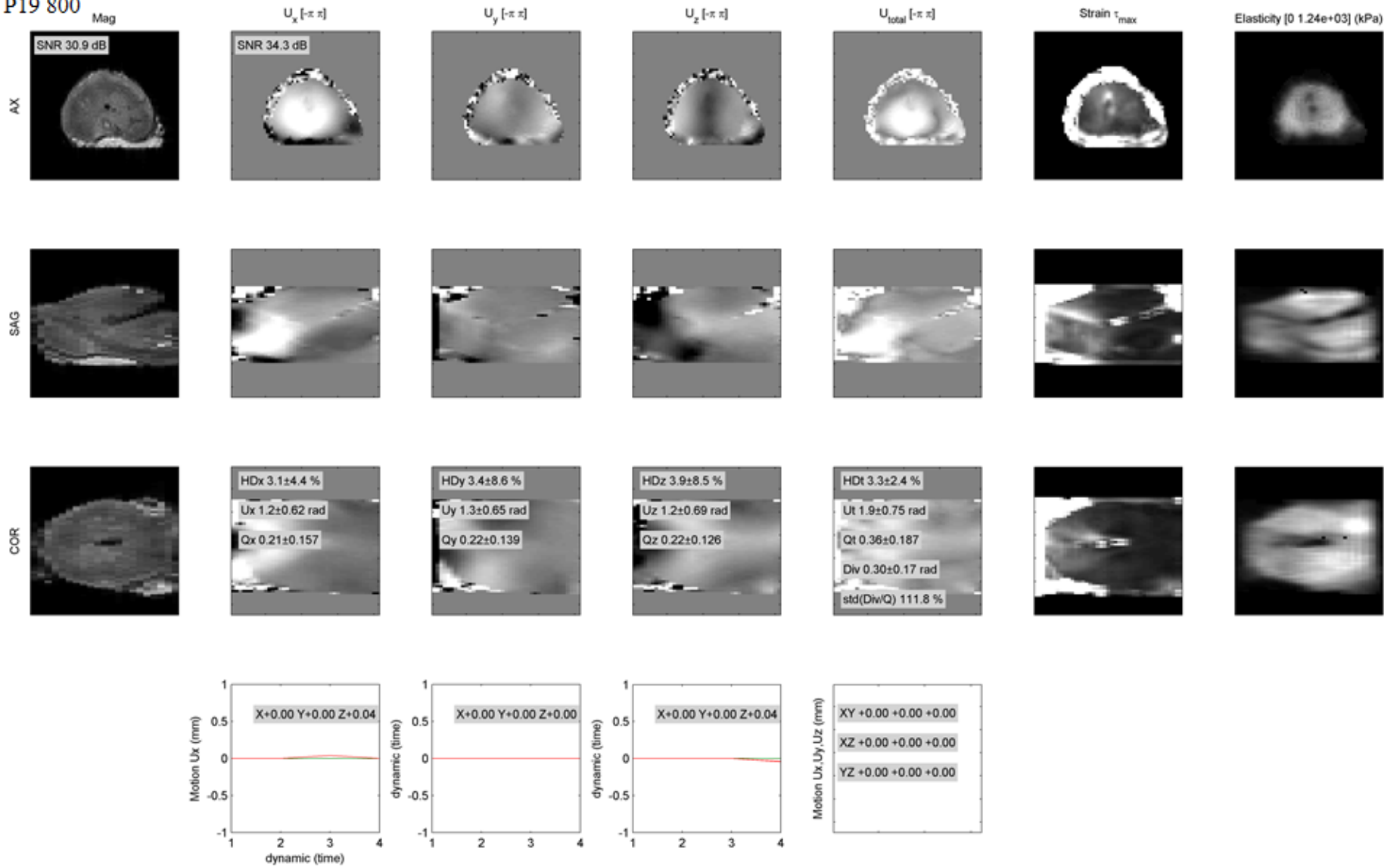


Figure D-21. Raw data for patient P19 800 Hz.

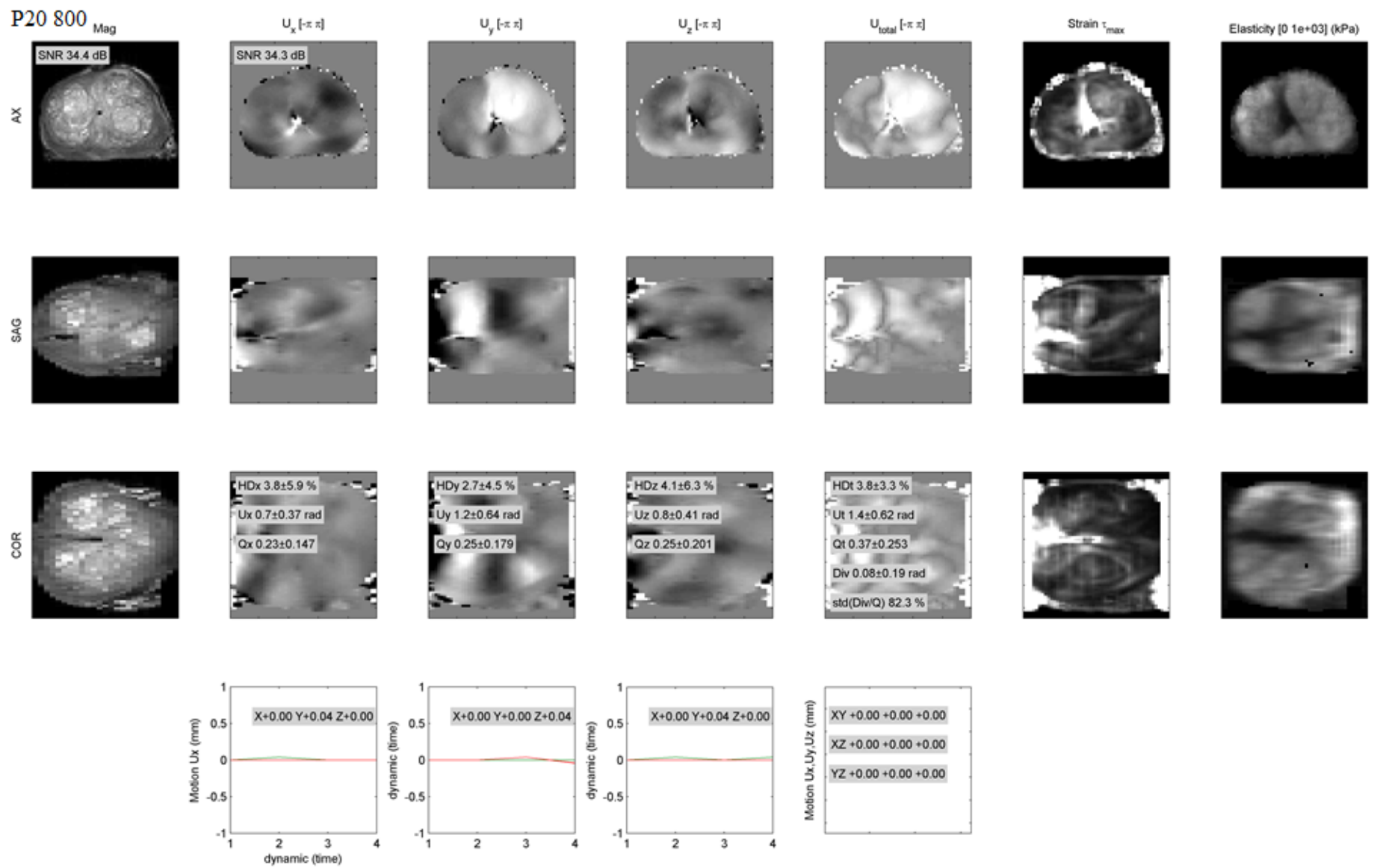


Figure D-22. Raw data for patient P20 800 Hz.

P01 1000  
Mag

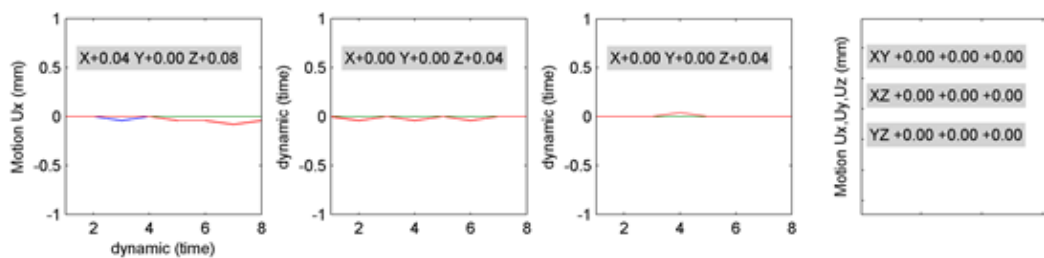
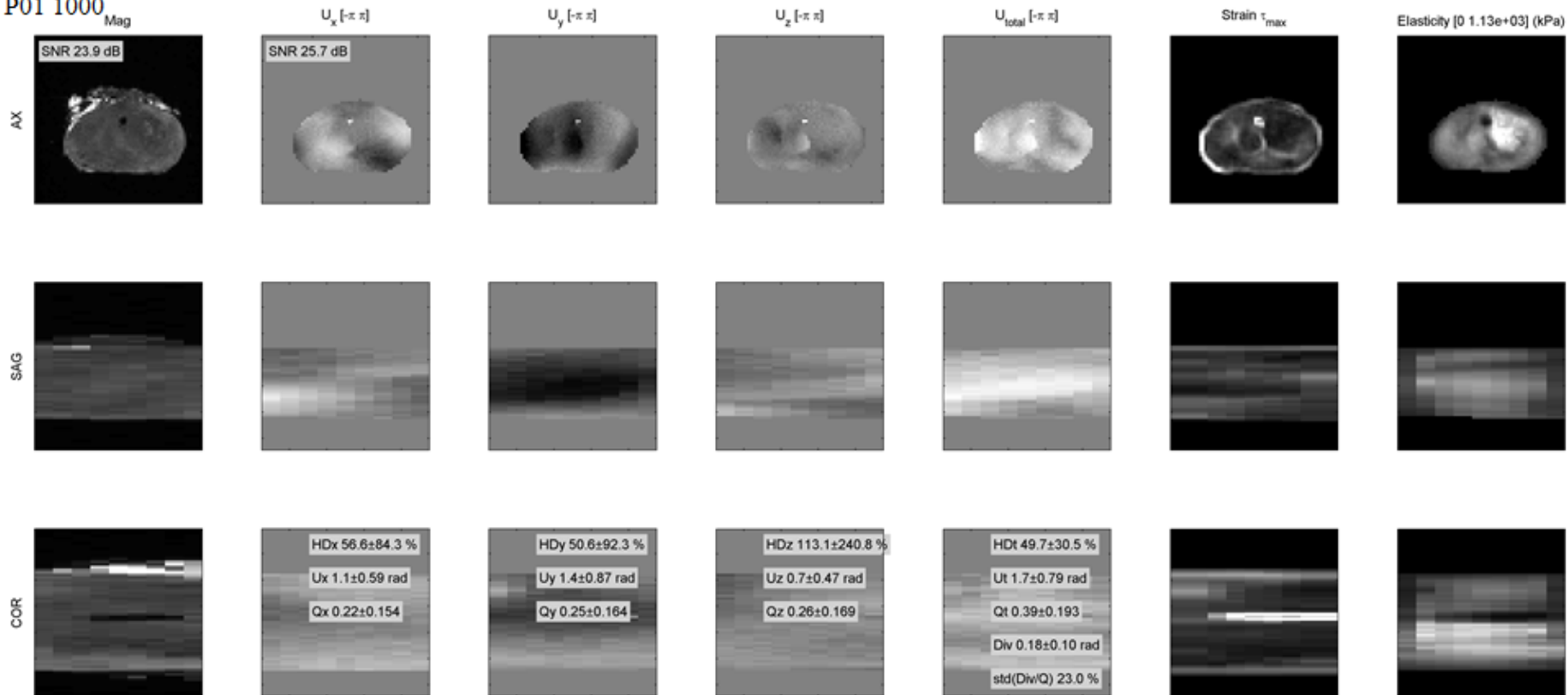


Figure D-23. Raw data for patient P01 1000 Hz.

P06 1000  
Mag

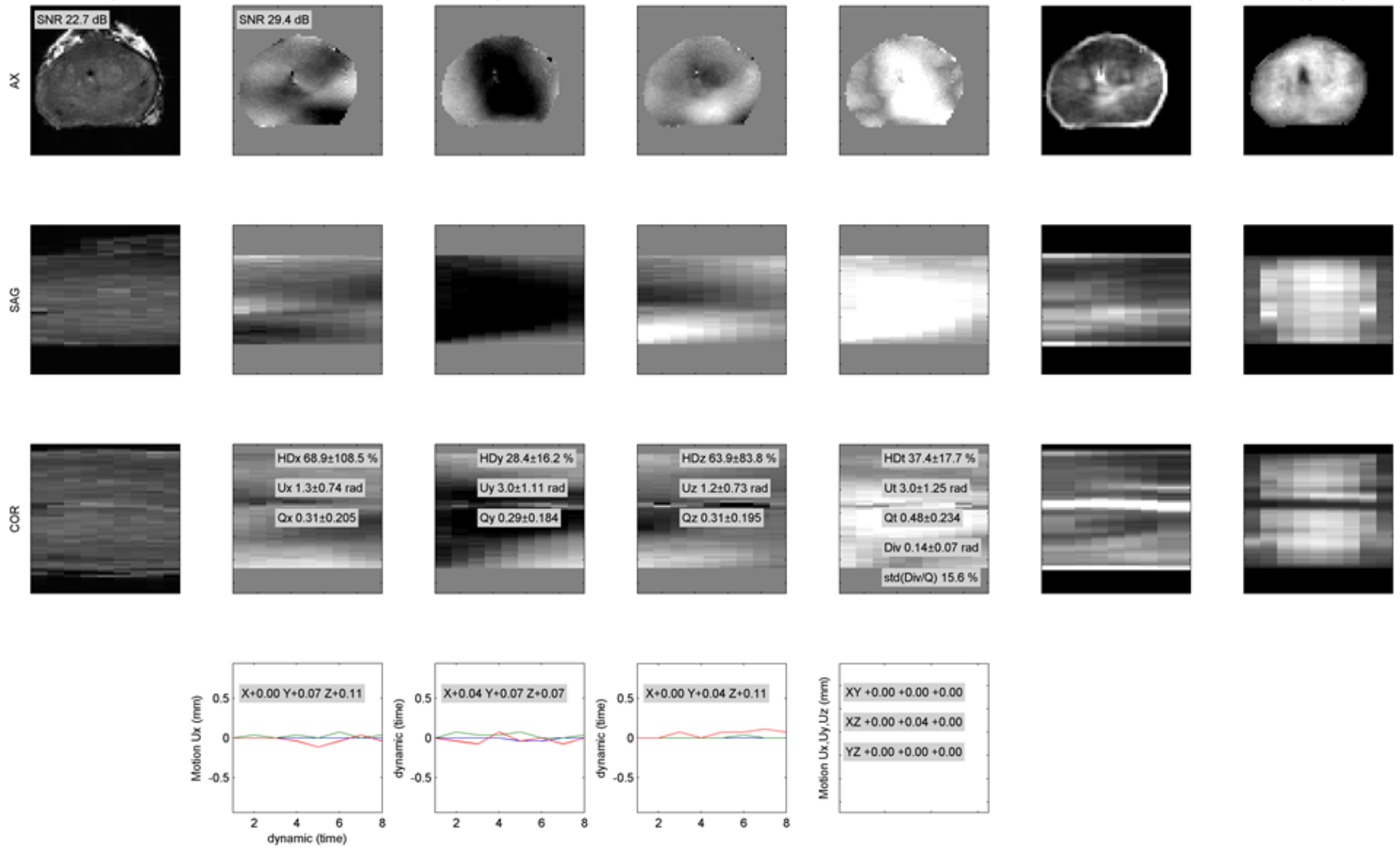


Figure D-24. Raw data for patient P06 1000 Hz.

P08 1000

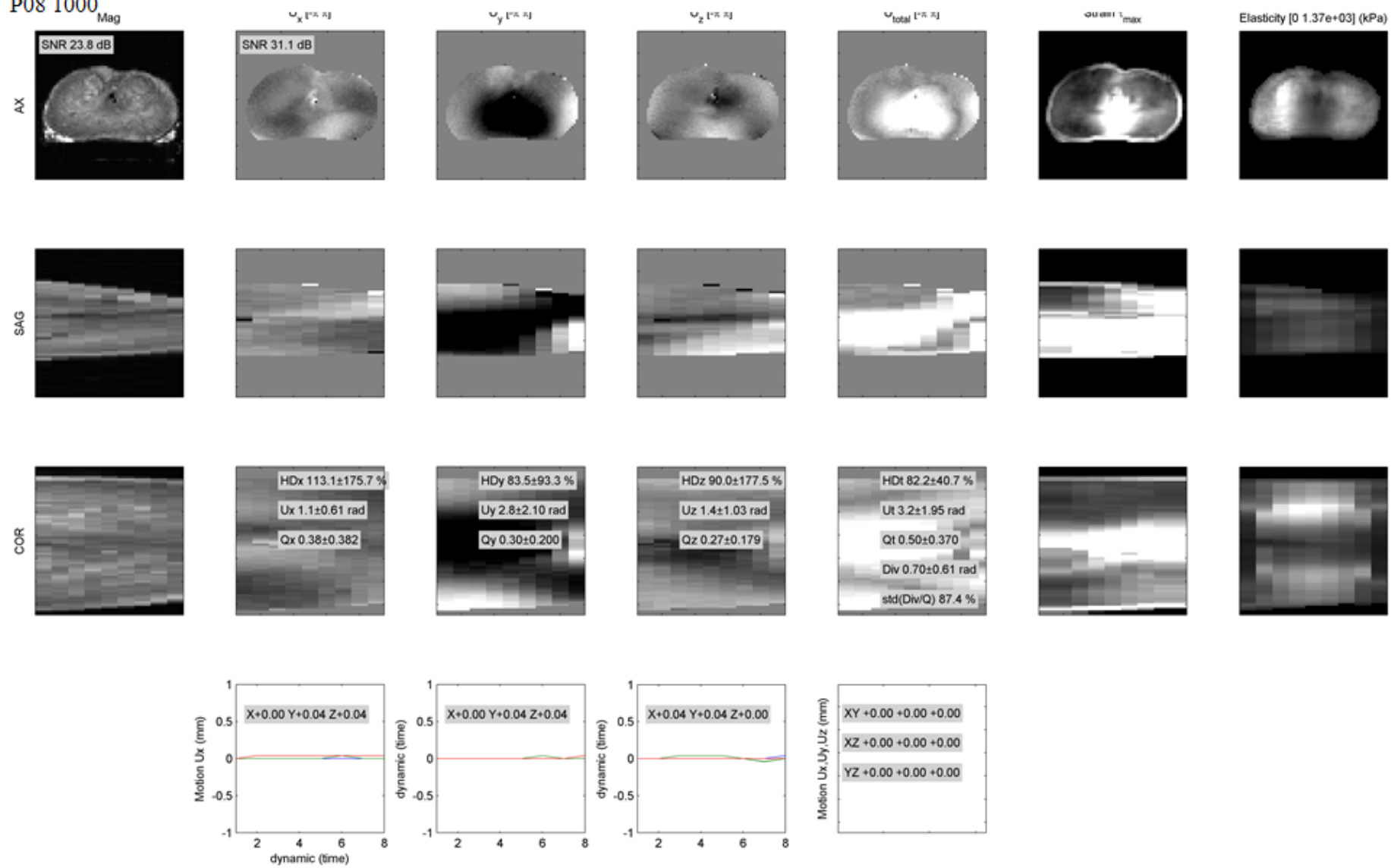


Figure D-25. Raw data for patient P08 1000 Hz.

P09 1000  
Mag

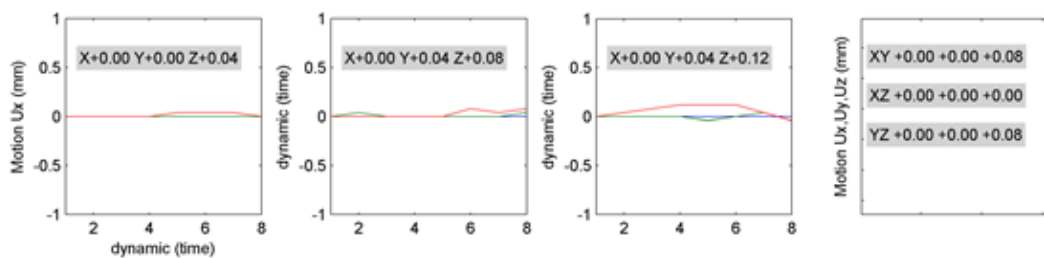
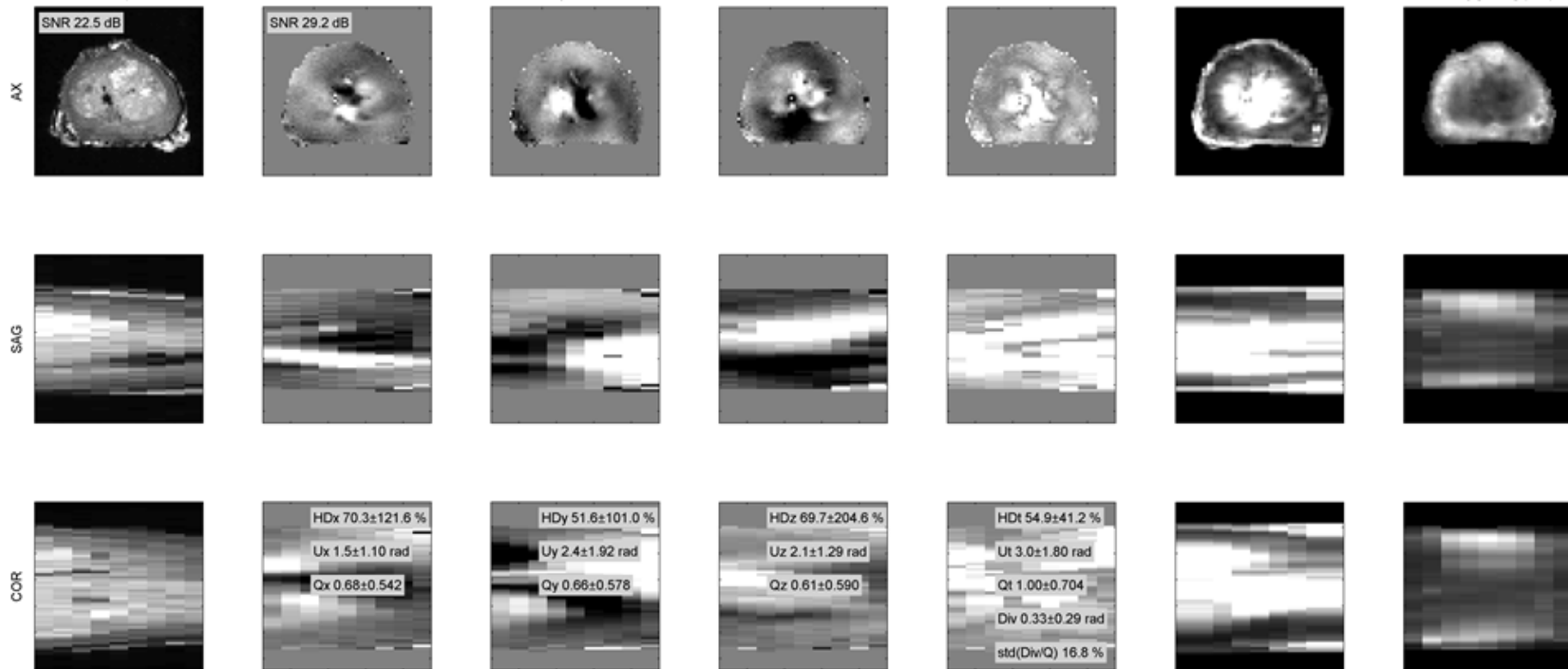


Figure D-26. Raw data for patient P09 1000 Hz.

P11 1000

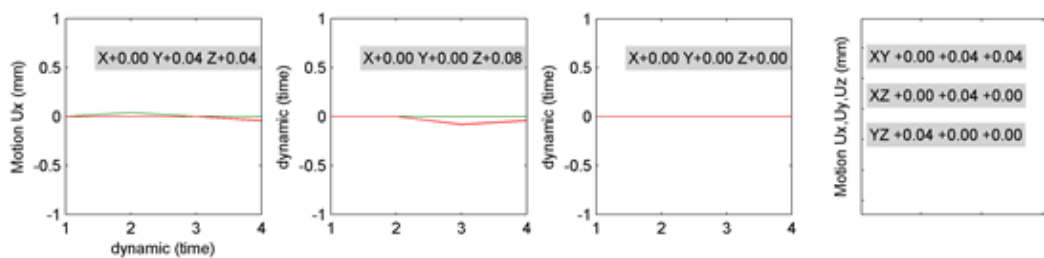
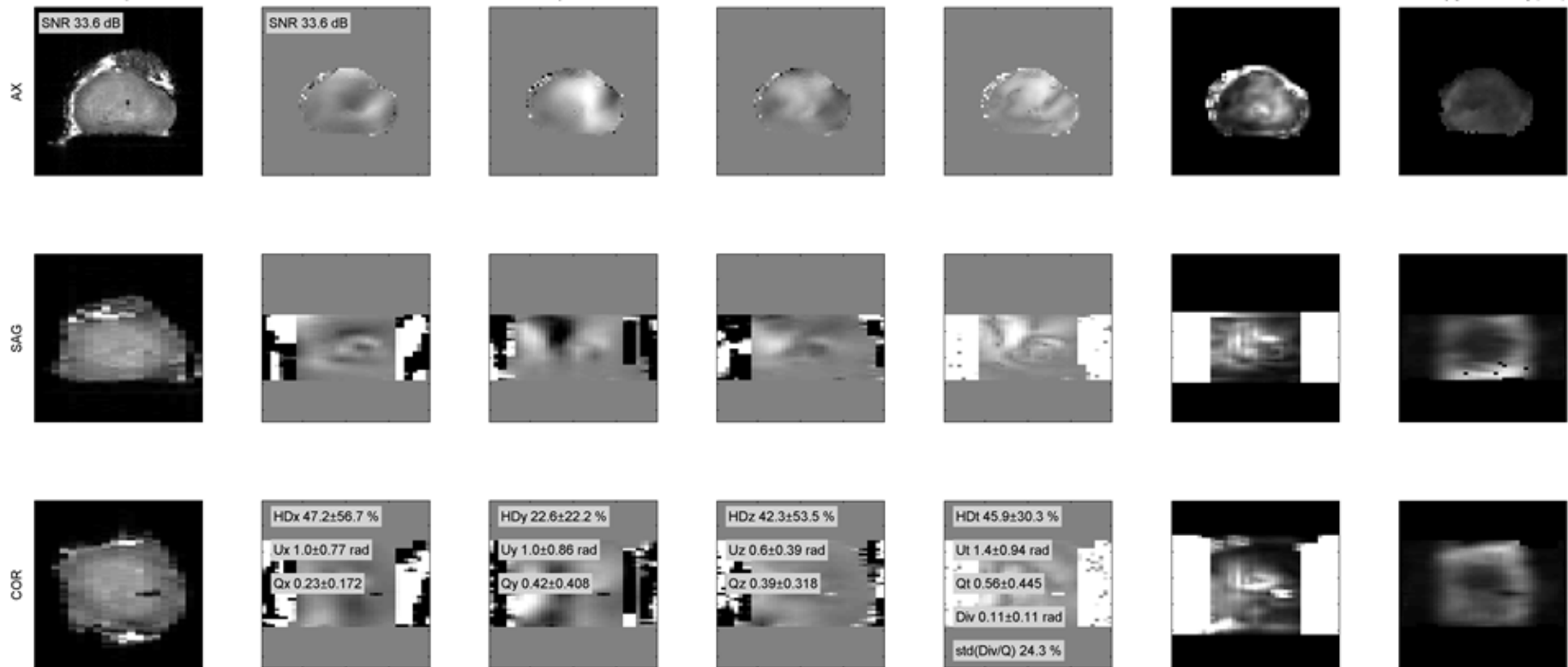


Figure D-27. Raw data for patient P11 1000 Hz.

P13 1000

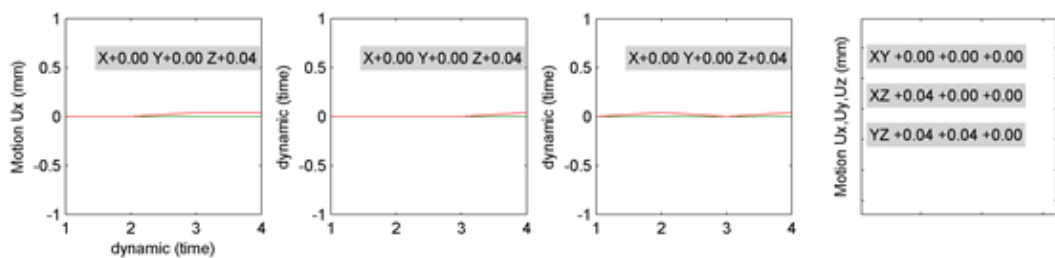
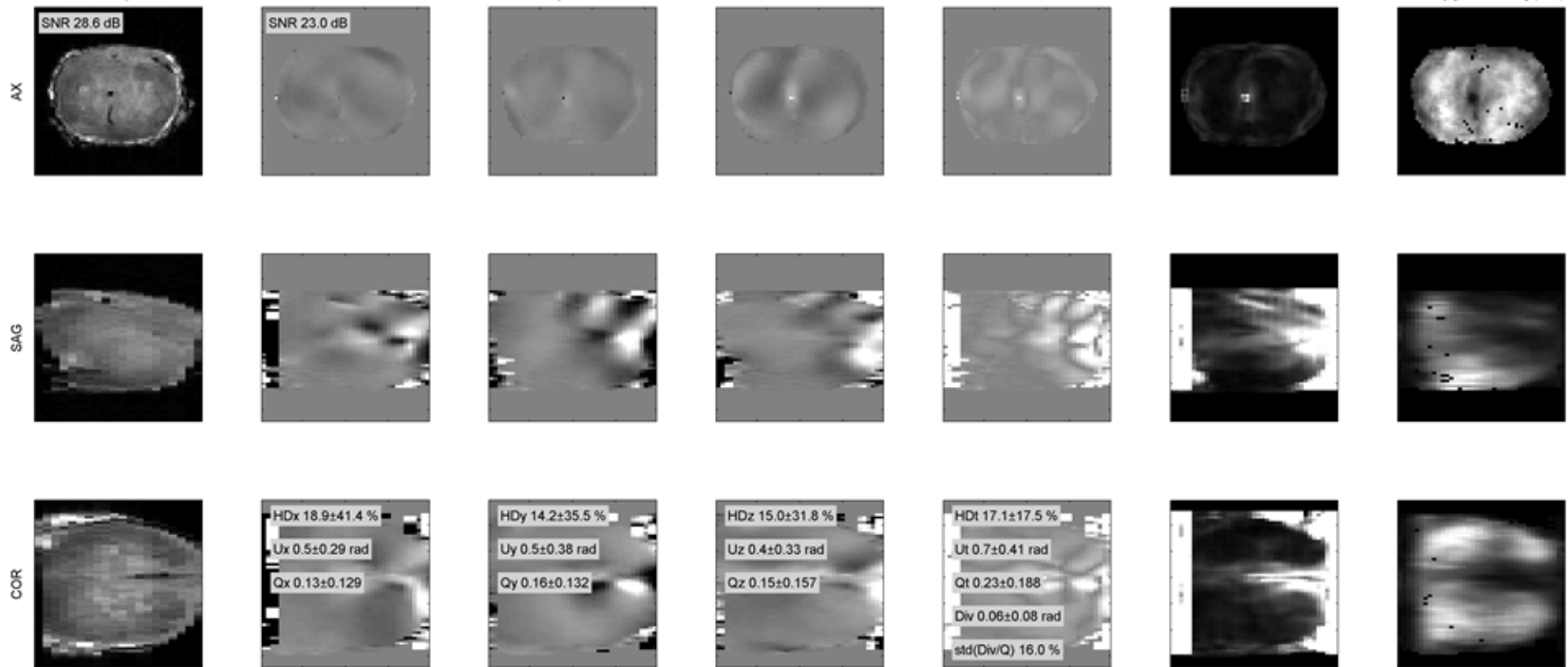


Figure D-28. Raw data for patient P13 1000 Hz.

P16 1000

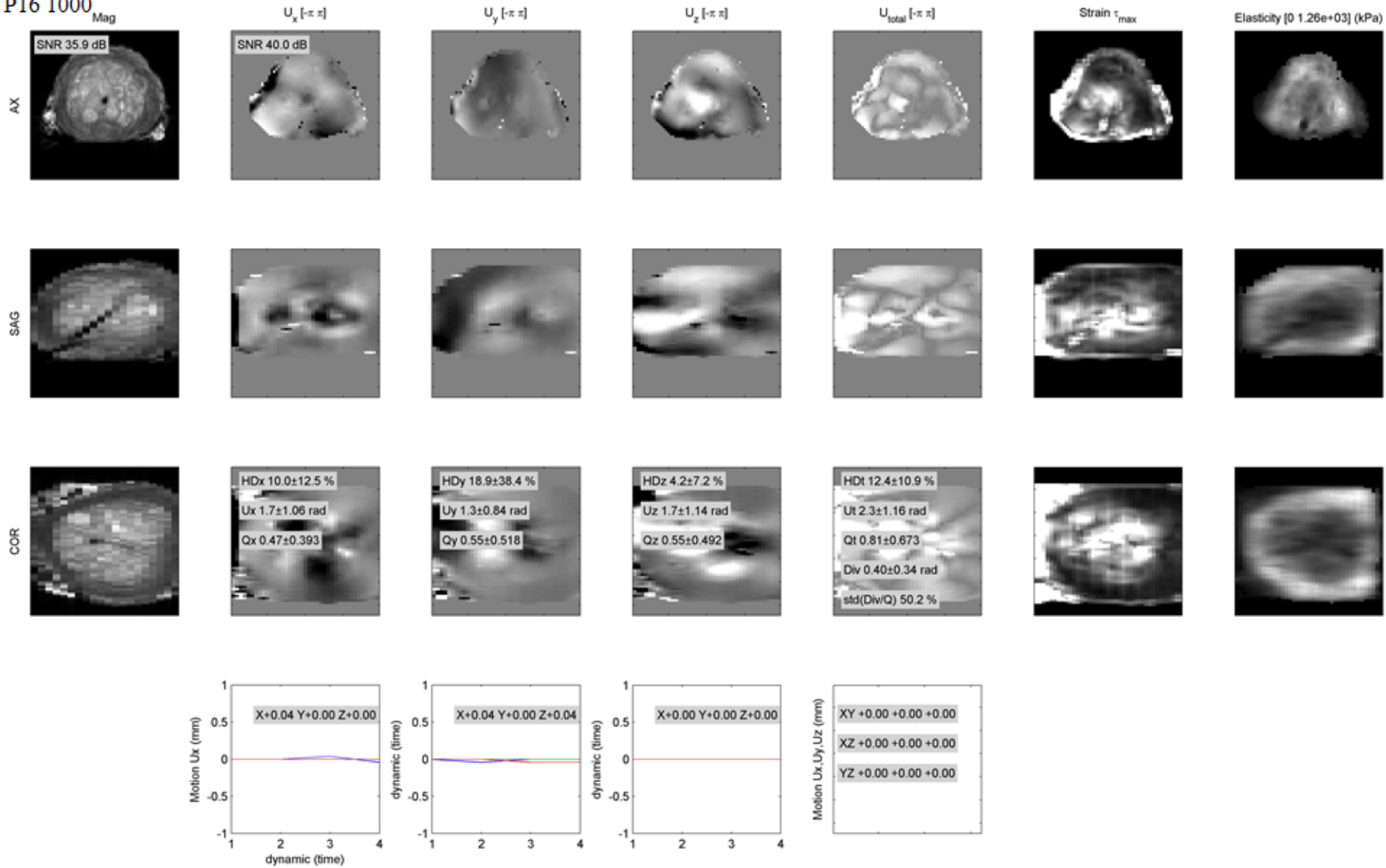


Figure D-29. Raw data for patient P16 1000 Hz.

P17 1000  
Mag

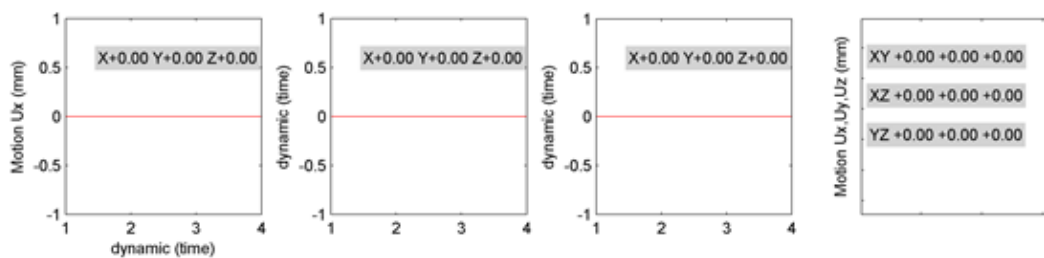
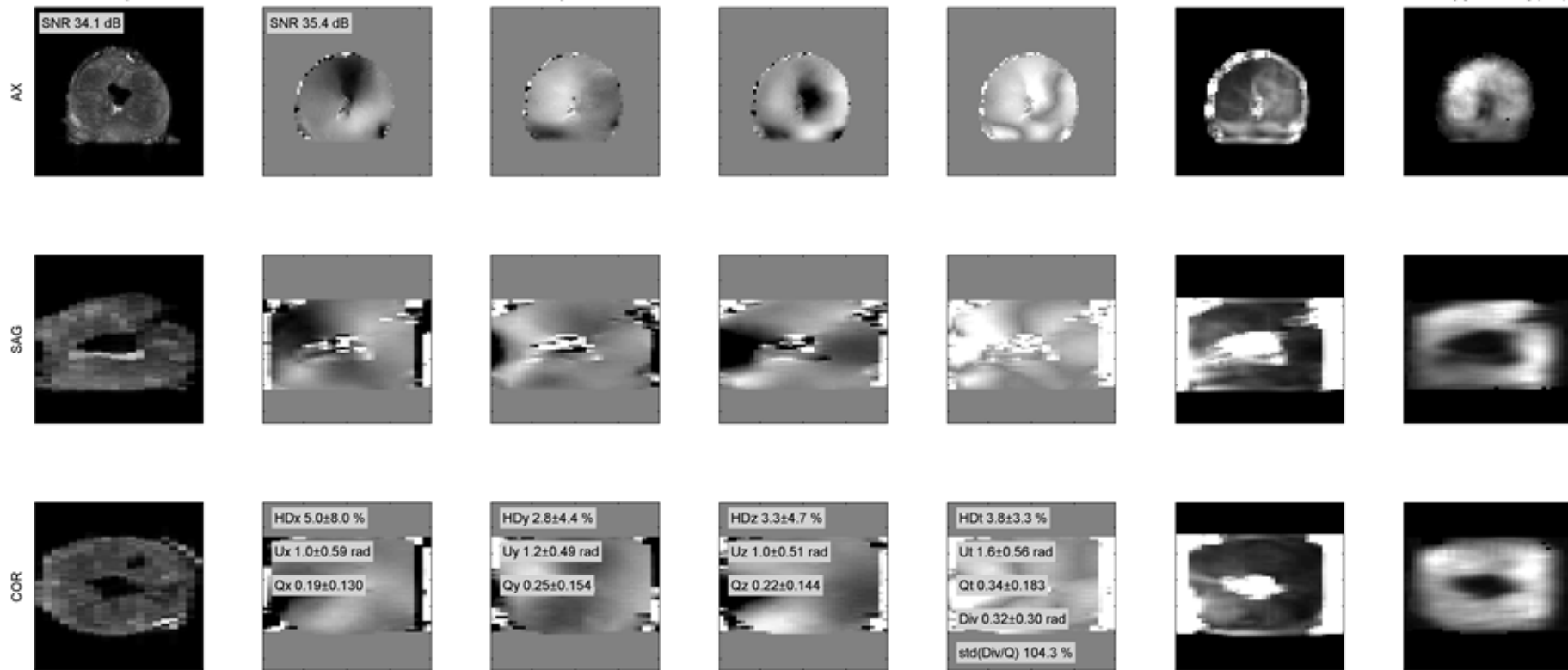


Figure D-30. Raw data for patient P17 1000 Hz.

P18 1000

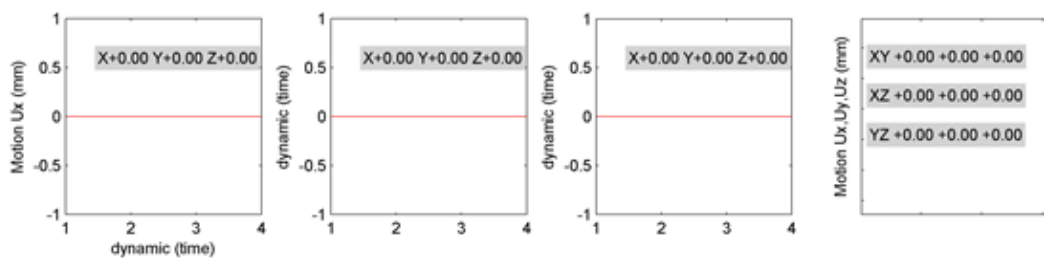
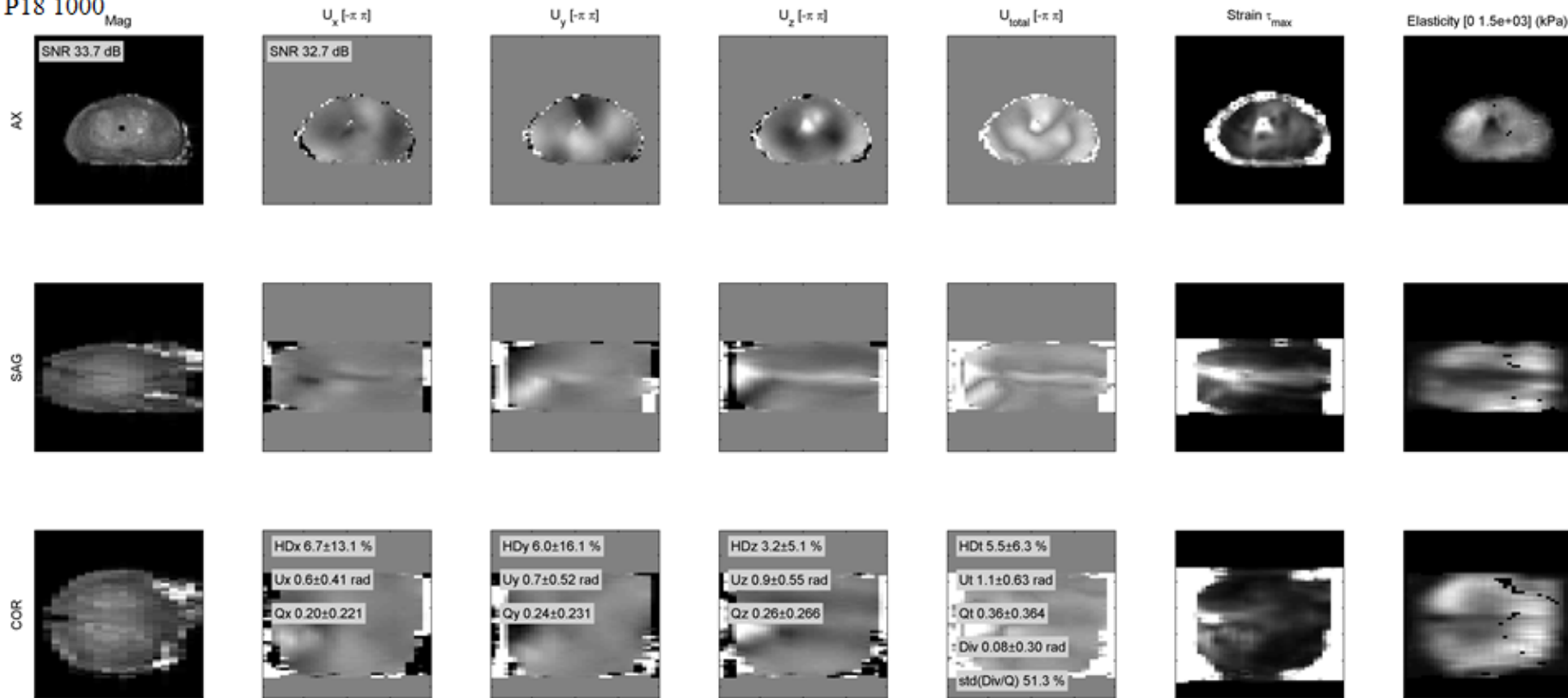


Figure D-31. Raw data for patient P18 1000 Hz.

P19 1000

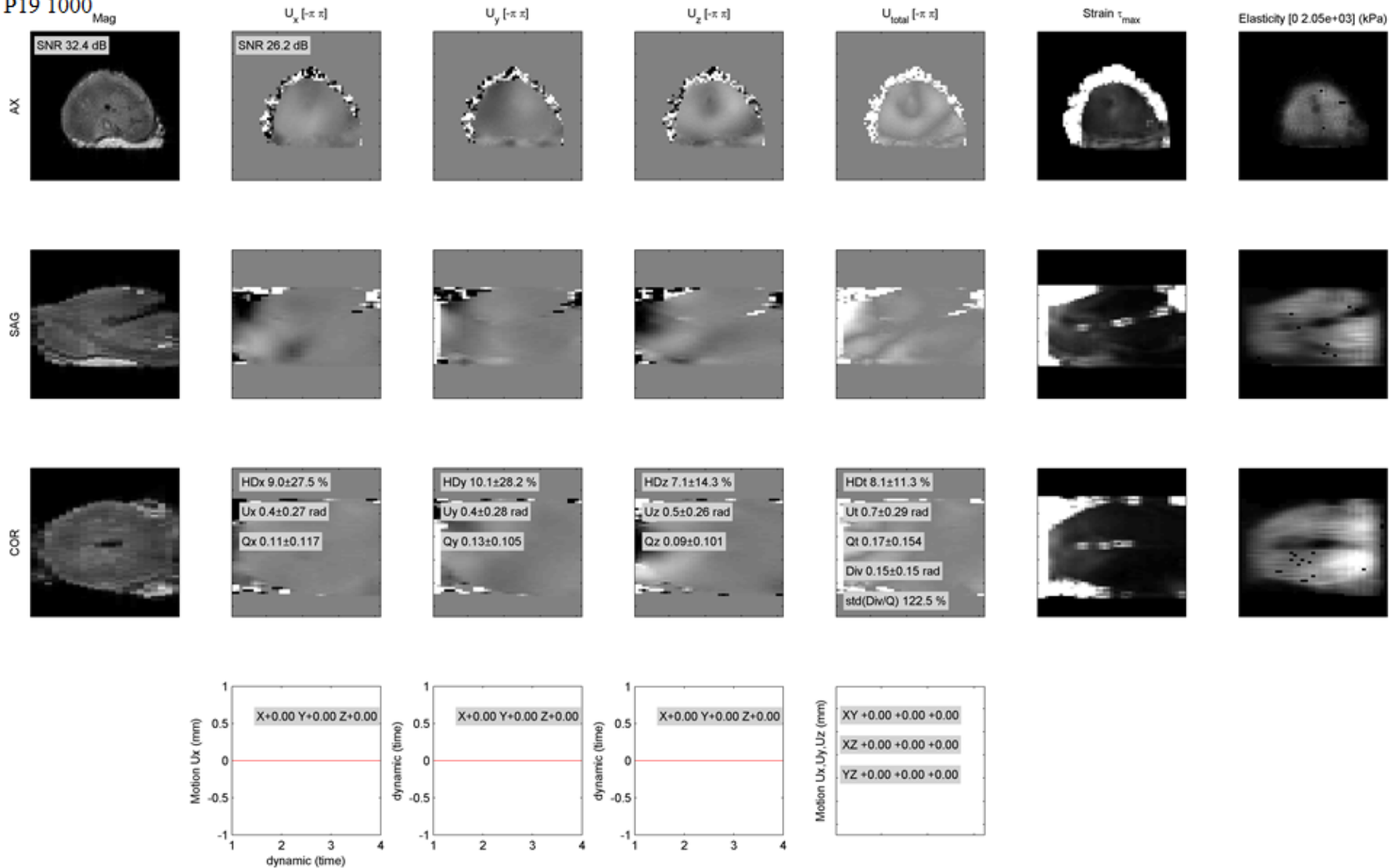


Figure D-32. Raw data for patient P19 1000 Hz.

P20 1000

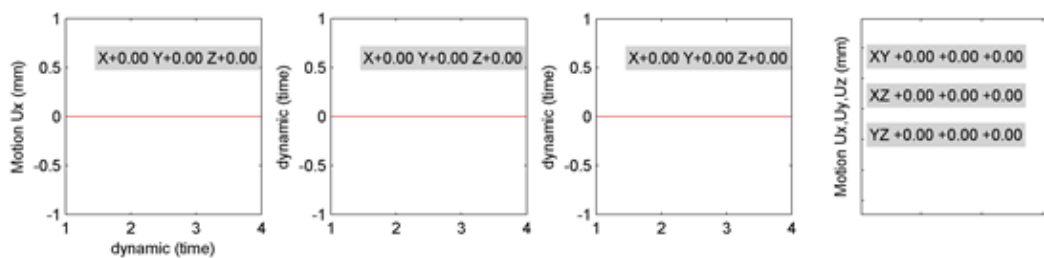
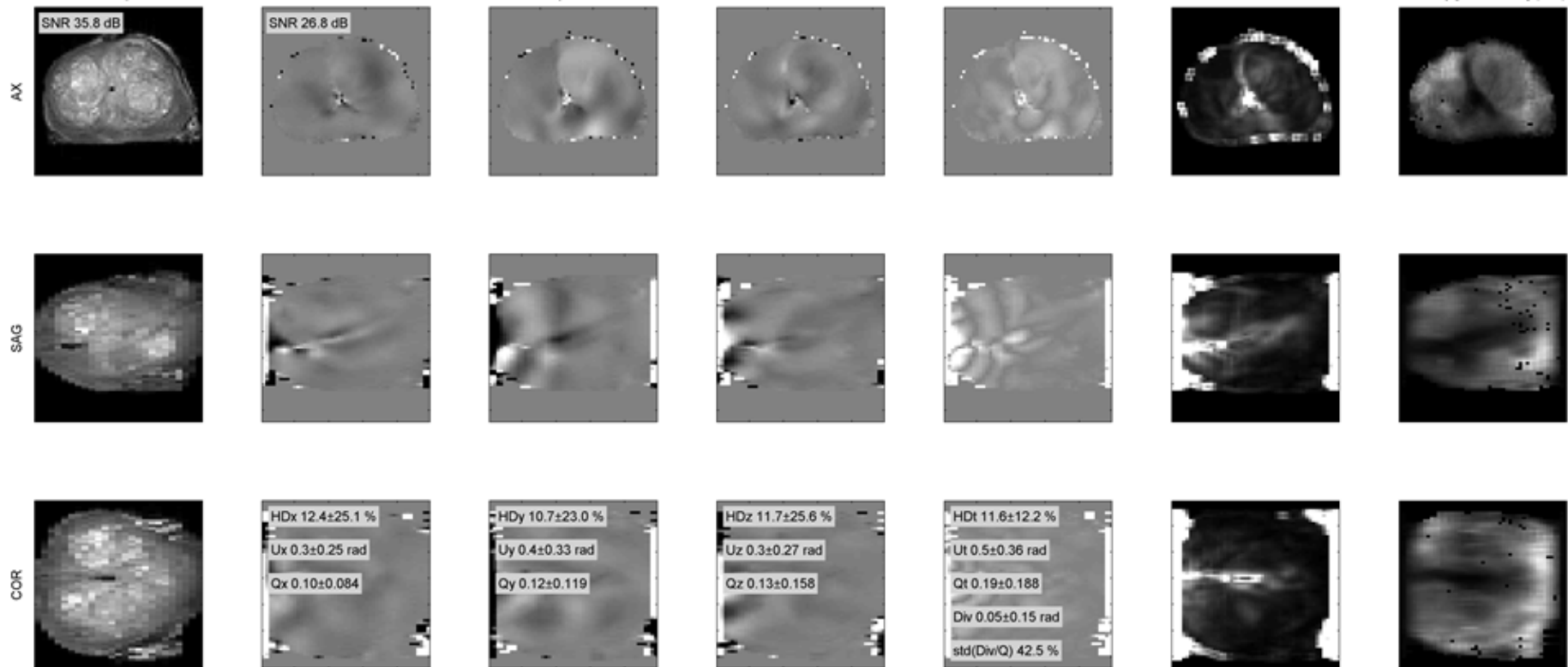


Figure D-33. Raw data for patient P20 1000 Hz.

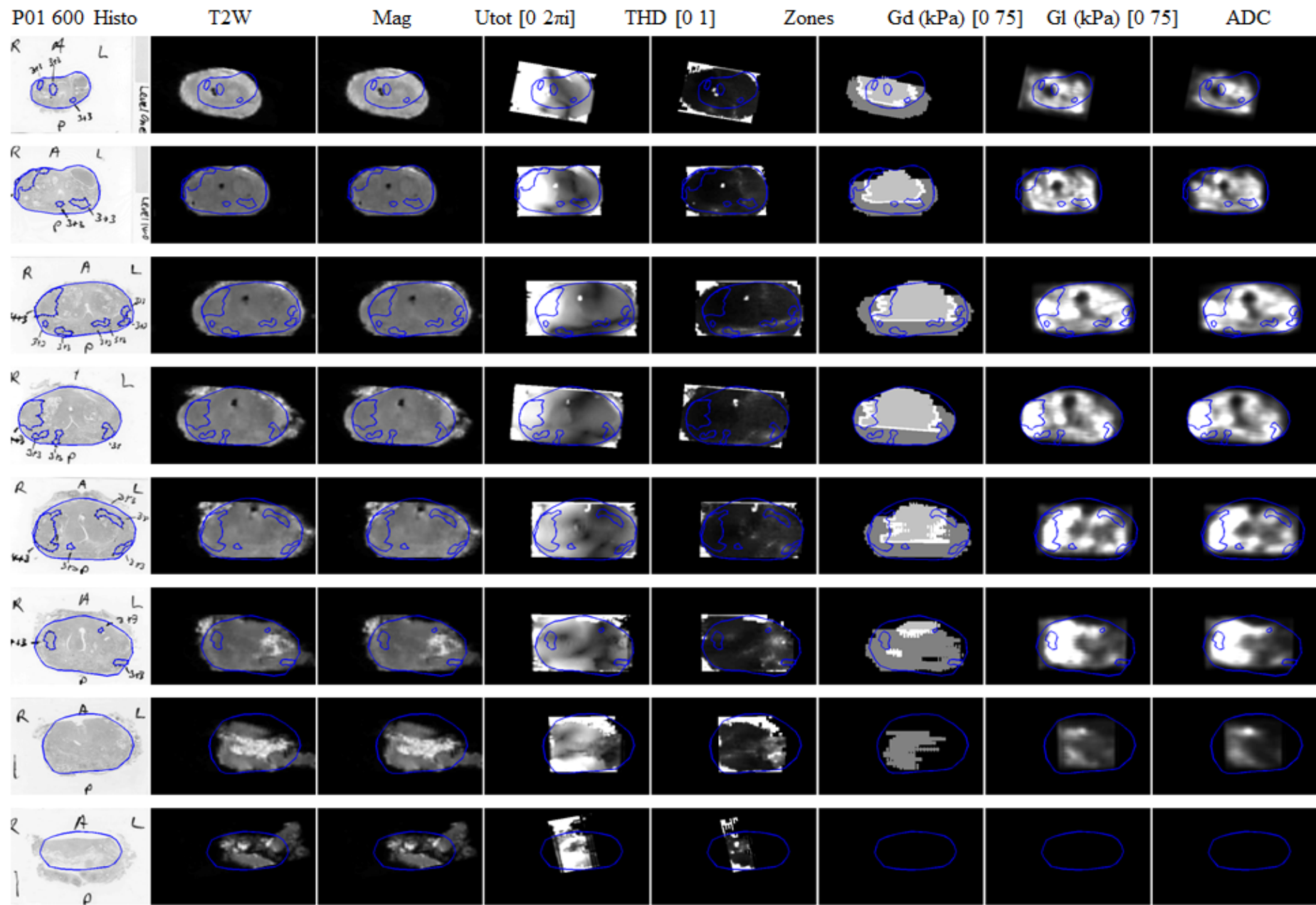


Figure D-34. Results for P01 600 Hz. Shear moduli ( $|G|$  and  $G_I$ ) as registered to histopathology slides. The total wave amplitude and THD are also shown.

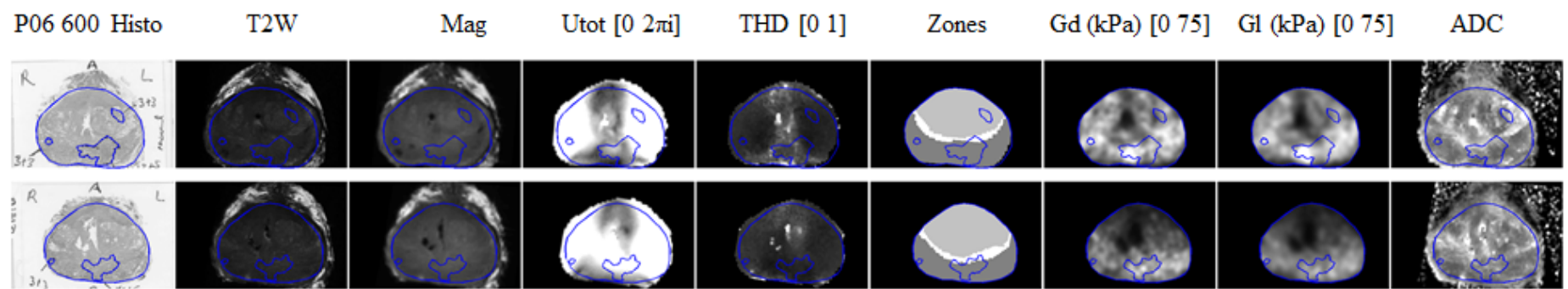


Figure D-35. Results for P06 600 Hz. Shear moduli ( $|G|$  and  $G_I$ ) as registered to histopathology slides. The total wave amplitude and THD are also shown.

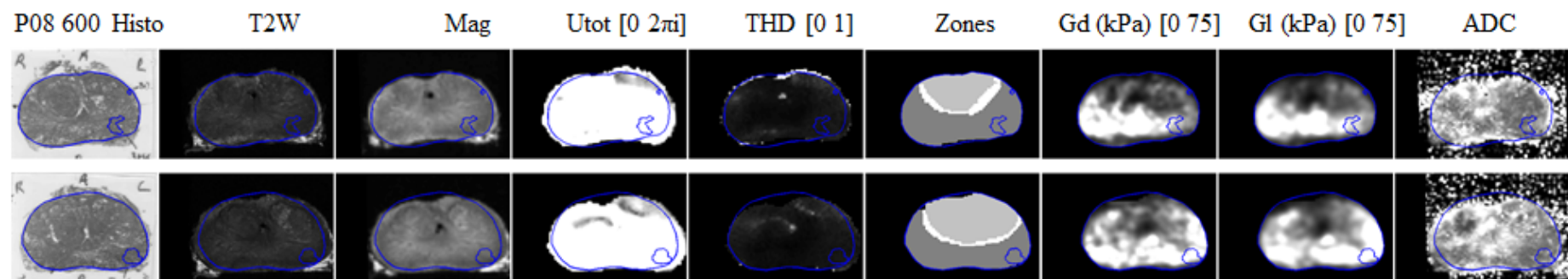


Figure D-36. Results for P08 600 Hz. Shear moduli ( $|G|$  and  $G_I$ ) as registered to histopathology slides. The total wave amplitude and THD are also shown.

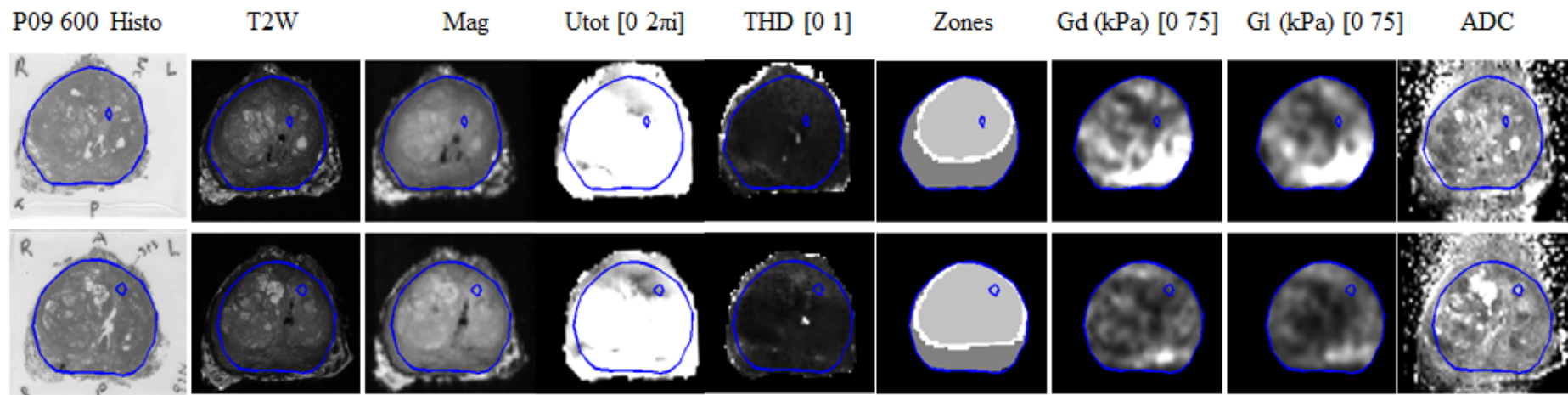


Figure D-37. Results for P09 600 Hz. Shear moduli ( $|G|$  and  $G_I$ ) as registered to histopathology slides. The total wave amplitude and THD are also shown.

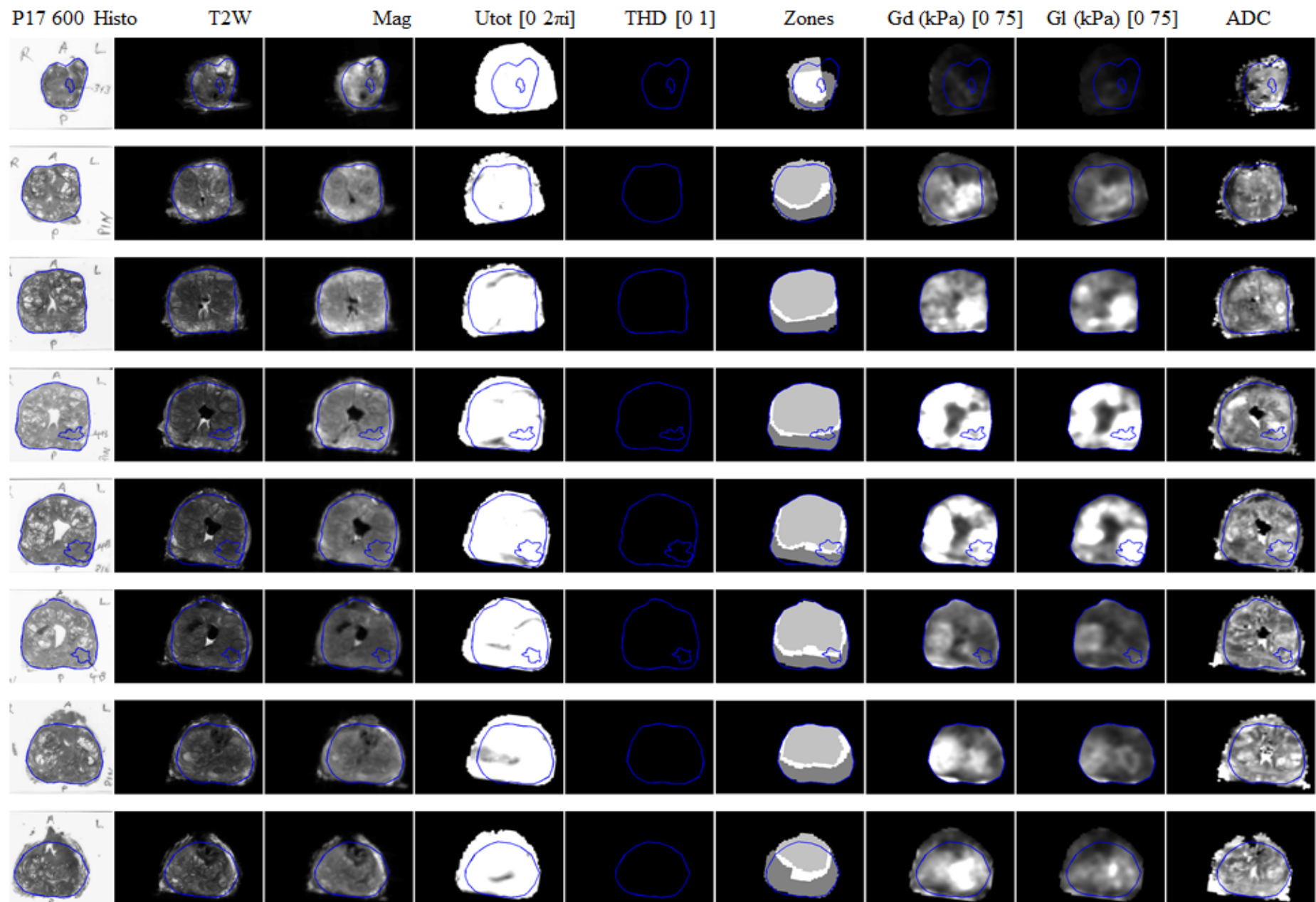


Figure D-38. Results for P17 600 Hz. Shear moduli ( $|G|$  and  $G_I$ ) as registered to histopathology slides. The total wave amplitude and THD are also shown.

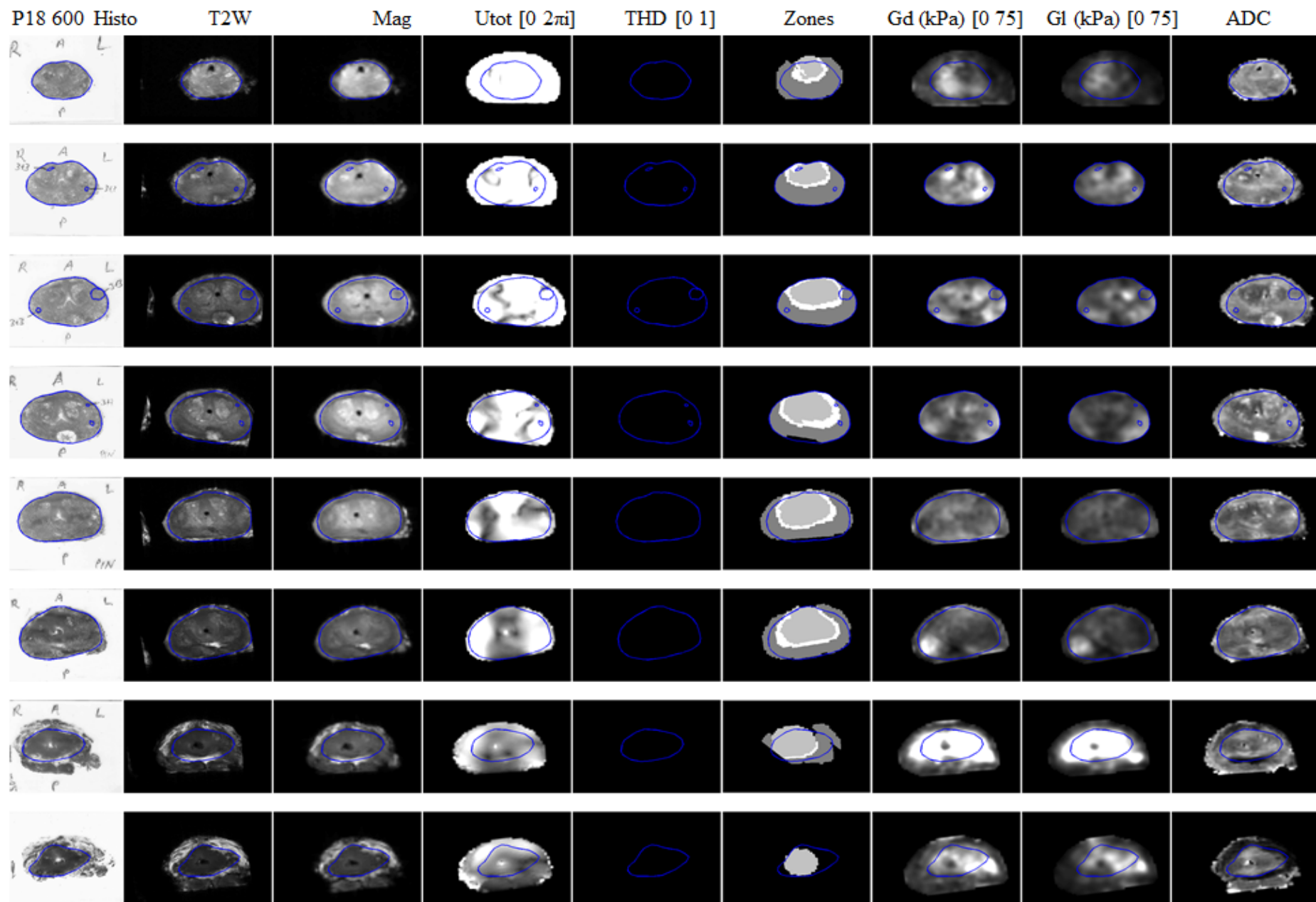


Figure D-39. Results for P18 600 Hz. Shear moduli ( $|G|$  and  $G_I$ ) as registered to histopathology slides. The total wave amplitude and THD are also shown.

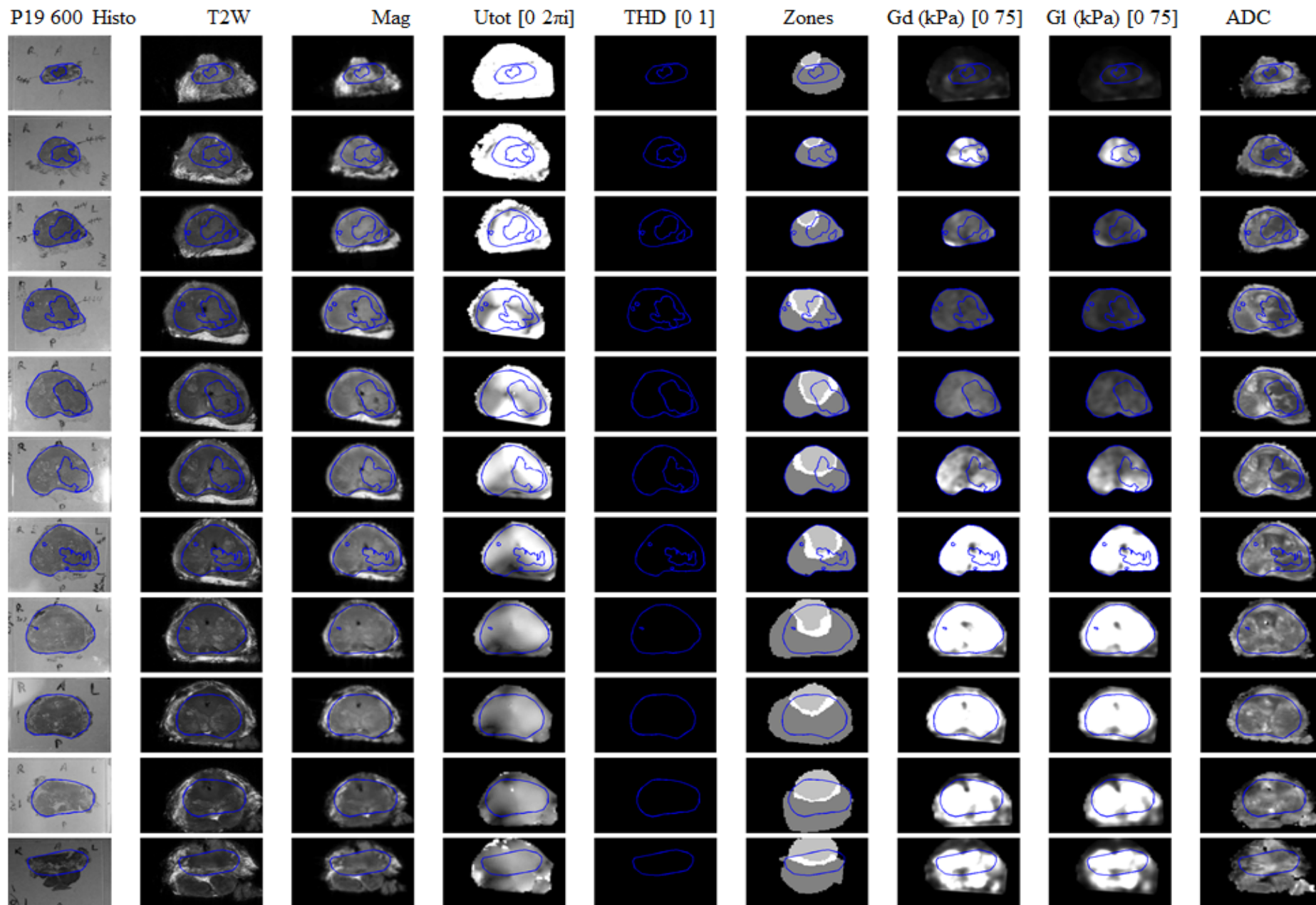


Figure D-40. Results for P19 600 Hz. Shear moduli ( $|G|$  and  $G_1$ ) as registered to histopathology slides. The total wave amplitude and THD are also shown.

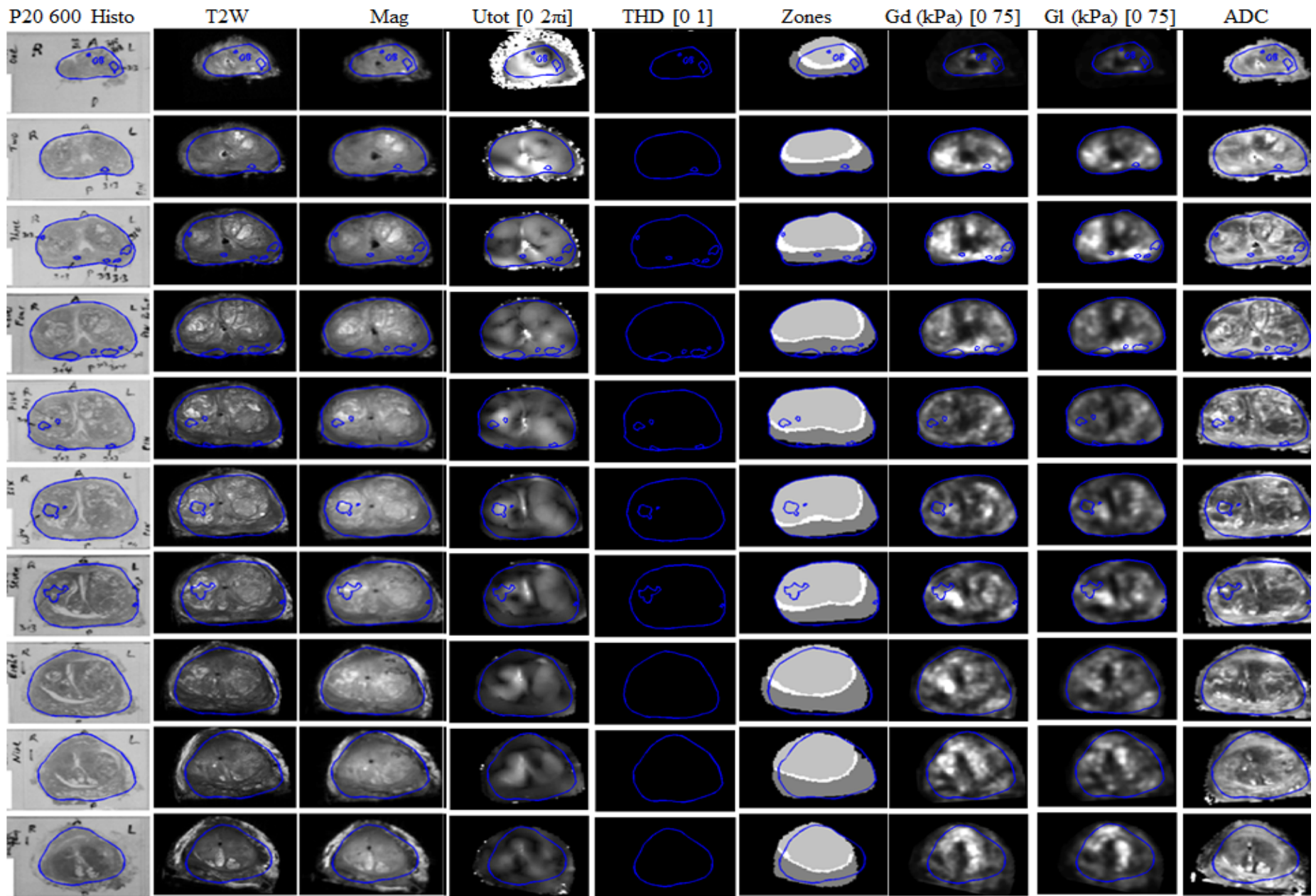


Figure D-41. Results for P20 600 Hz. Shear moduli ( $|G|$  and  $G_I$ ) as registered to histopathology slides. The total wave amplitude and THD are also shown.

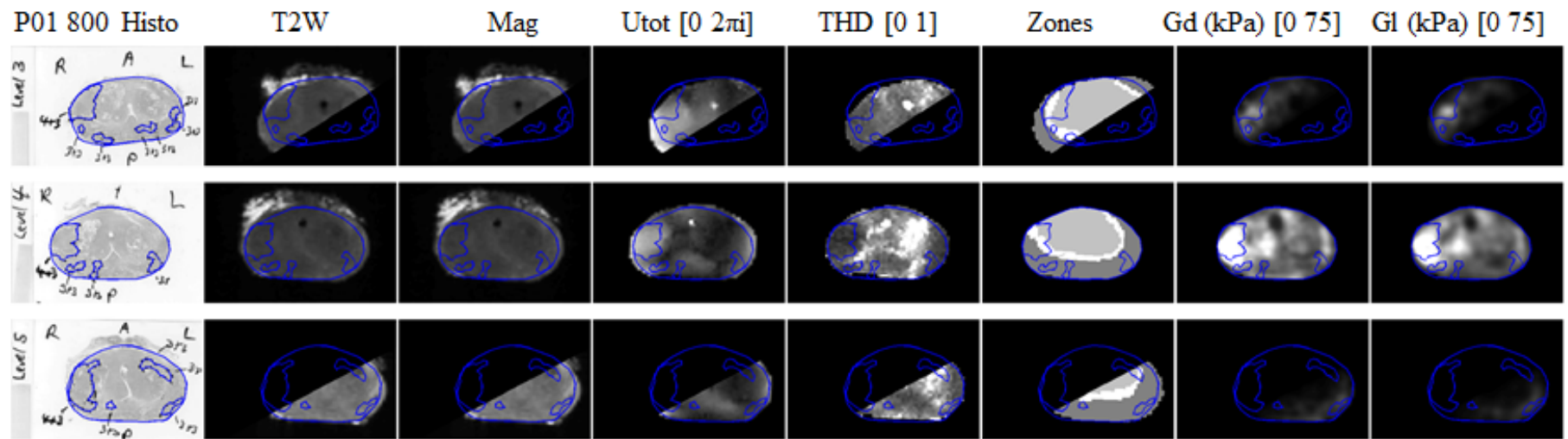


Figure D-42. Results for P01 800 Hz. Shear moduli ( $|G|$  and  $G_l$ ) as registered to histopathology slides. The total wave amplitude and THD are also shown.

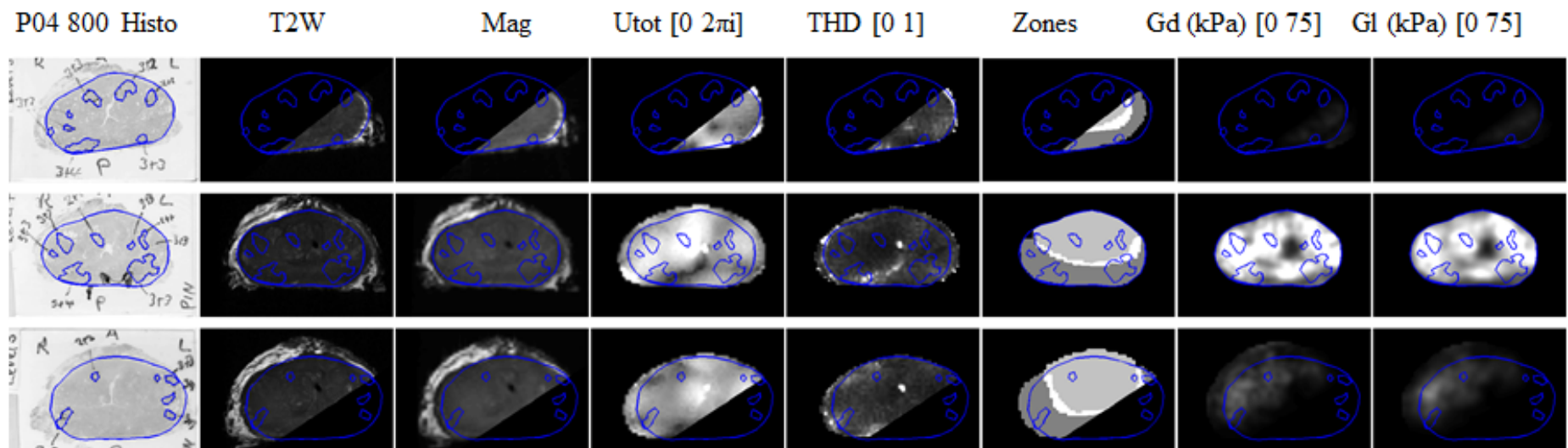


Figure D-43. Results for P04 800 Hz. Shear moduli ( $|G|$  and  $G_I$ ) as registered to histopathology slides. The total wave amplitude and THD are also shown.

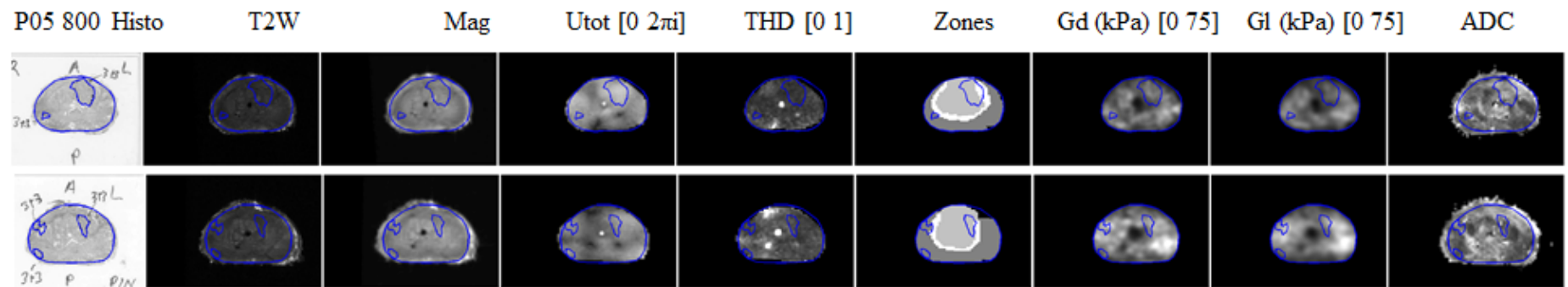


Figure D-44. Results for P05 800 Hz. Shear moduli ( $|G|$  and  $G_I$ ) as registered to histopathology slides. The total wave amplitude and THD are also shown.

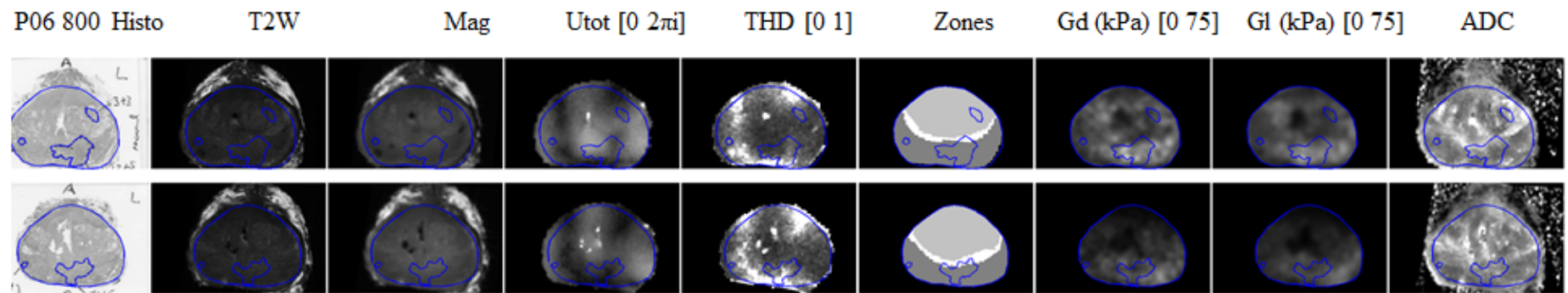


Figure D-45. Results for P06 800 Hz. Shear moduli ( $|G|$  and  $G_l$ ) as registered to histopathology slides. The total wave amplitude and THD are also shown.

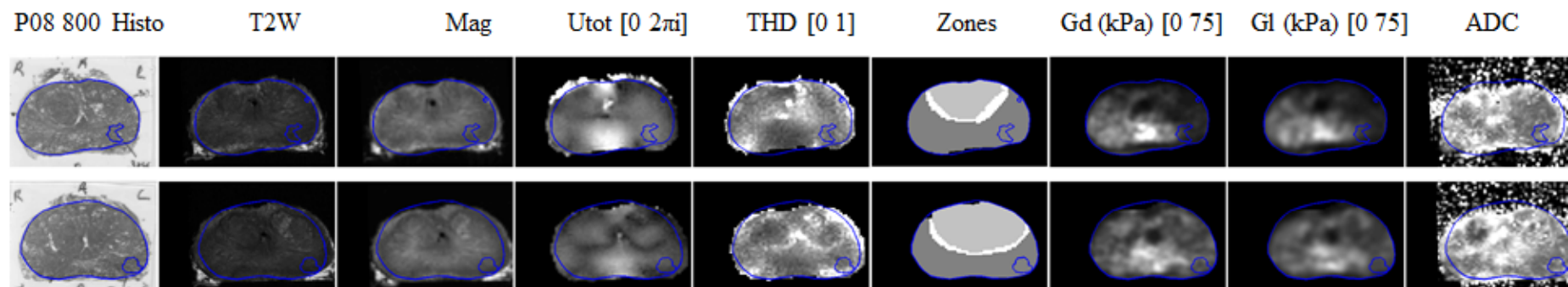


Figure D-46. Results for P08 800 Hz. Shear moduli ( $|G|$  and  $G_I$ ) as registered to histopathology slides. The total wave amplitude and THD are also shown.

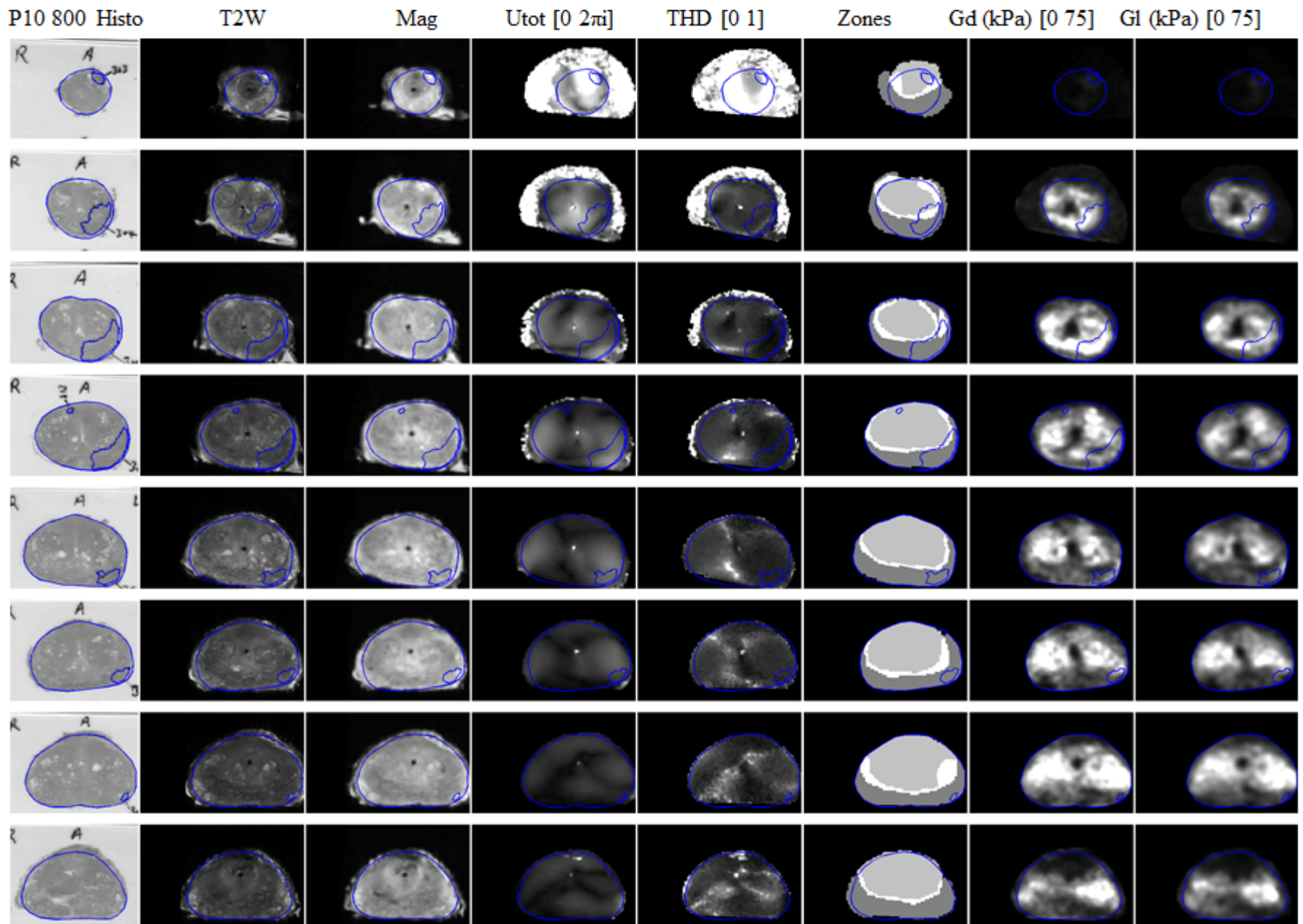


Figure D-47. Results for P10 800 Hz. Shear moduli ( $|G|$  and  $G_I$ ) as registered to histopathology slides. The total wave amplitude and THD are also shown.

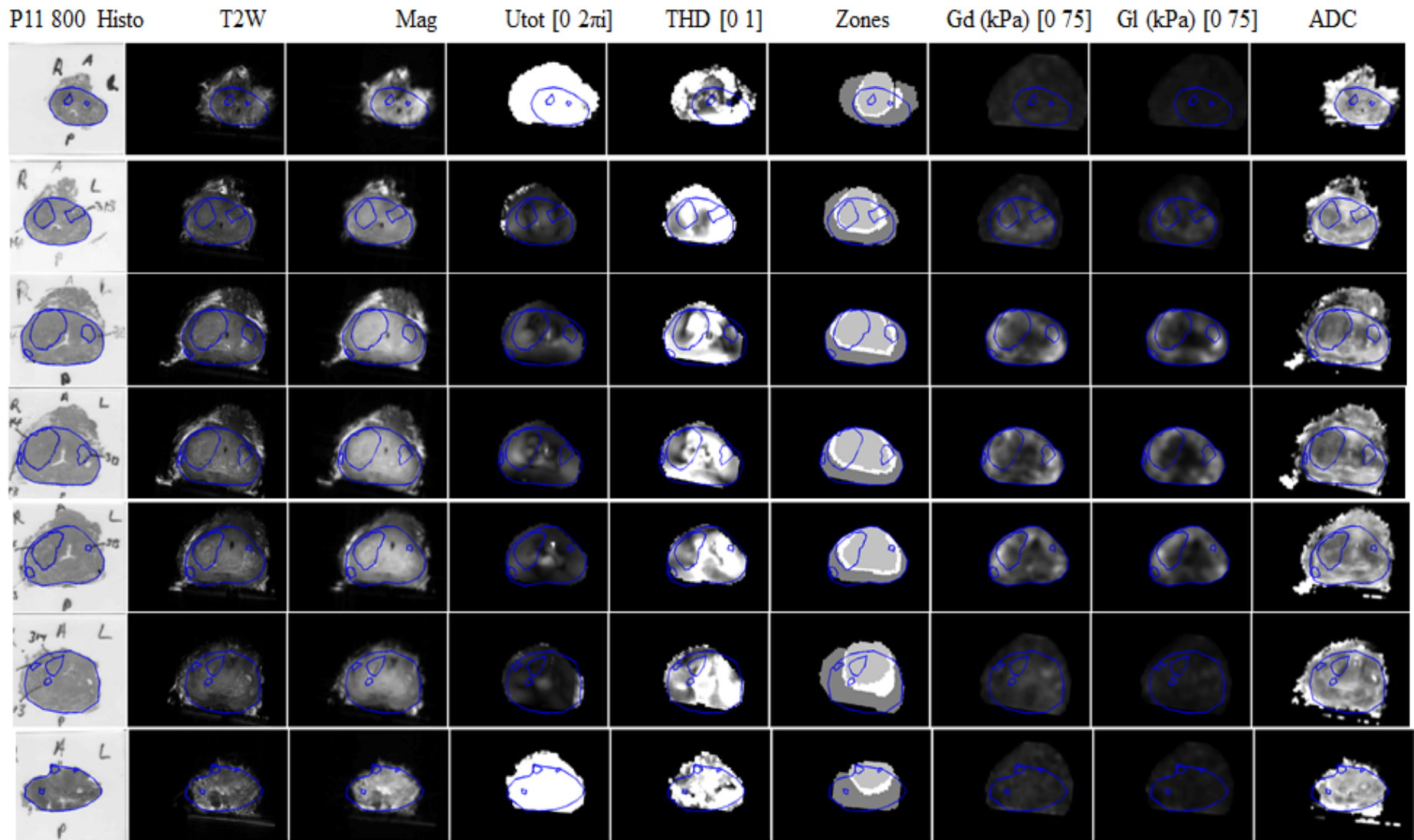


Figure D-48. Results for P11 800 Hz. Shear moduli ( $|G|$  and  $G_I$ ) as registered to histopathology slides. The total wave amplitude and THD are also shown.

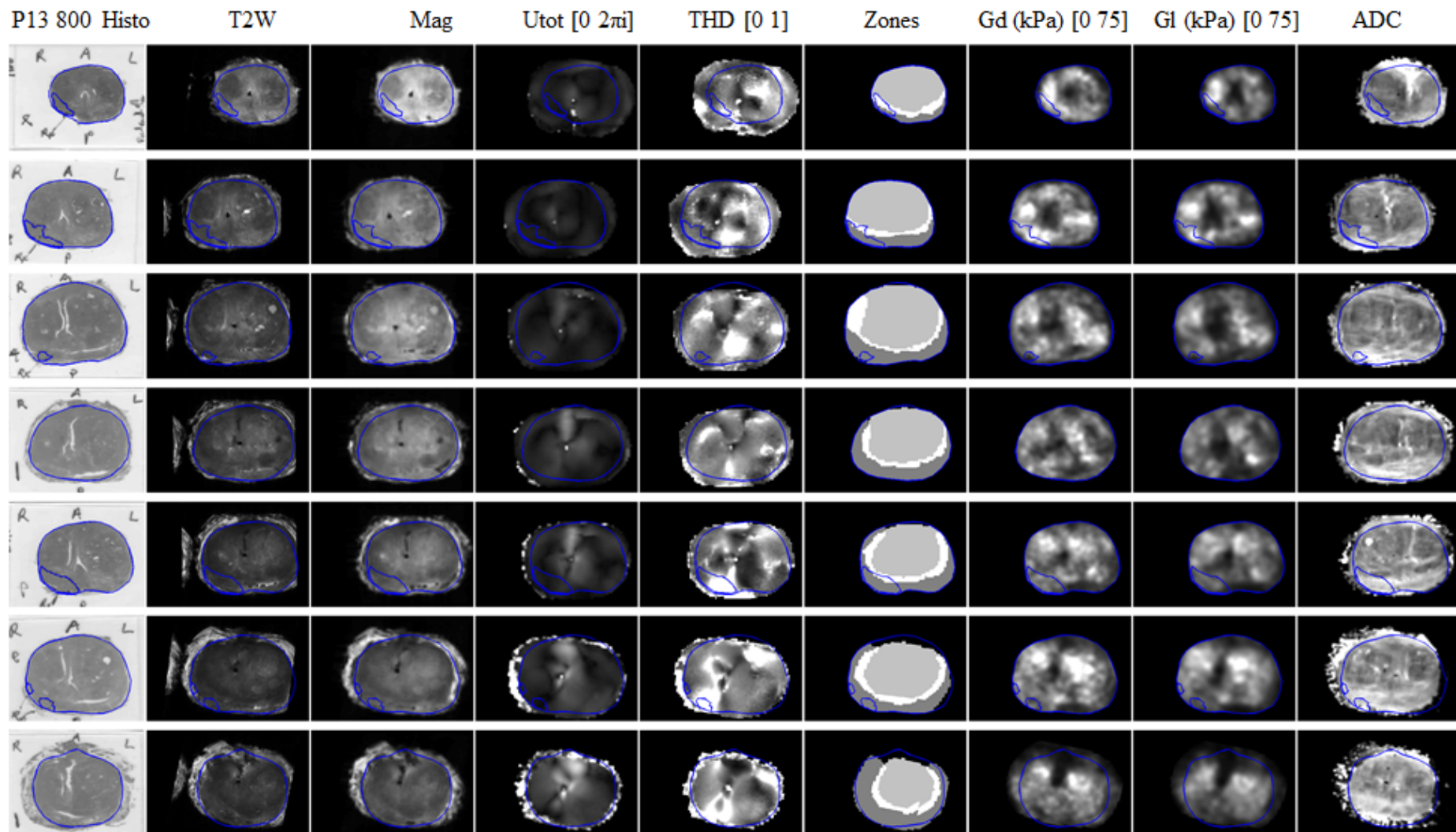


Figure D-49. Results for P13 800 Hz. Shear moduli ( $|G|$  and  $G_l$ ) as registered to histopathology slides. The total wave amplitude and THD are also shown.

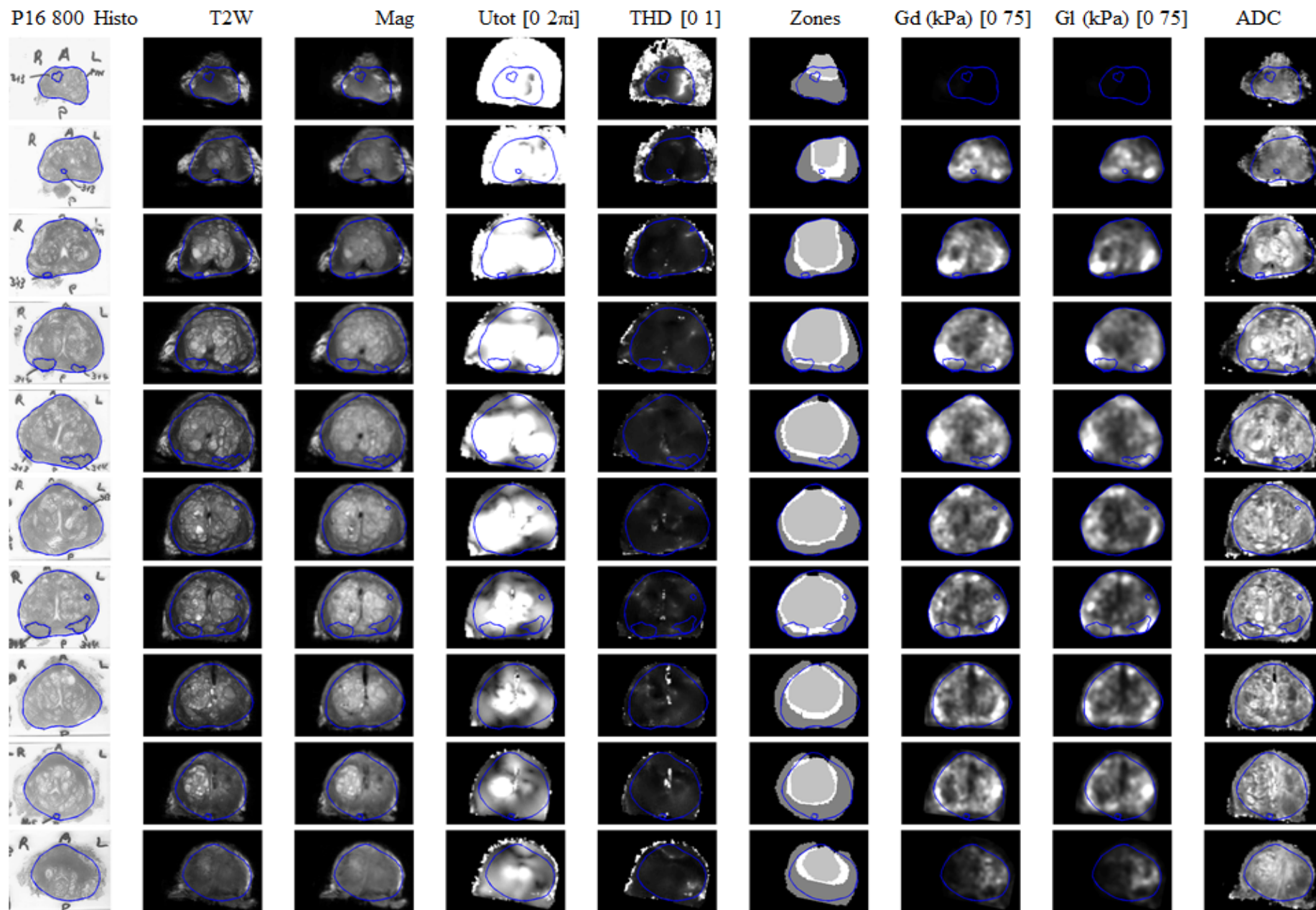


Figure D-50. Results for P16 800 Hz. Shear moduli ( $|G|$  and  $G_I$ ) as registered to histopathology slides. The total wave amplitude and THD are also shown.

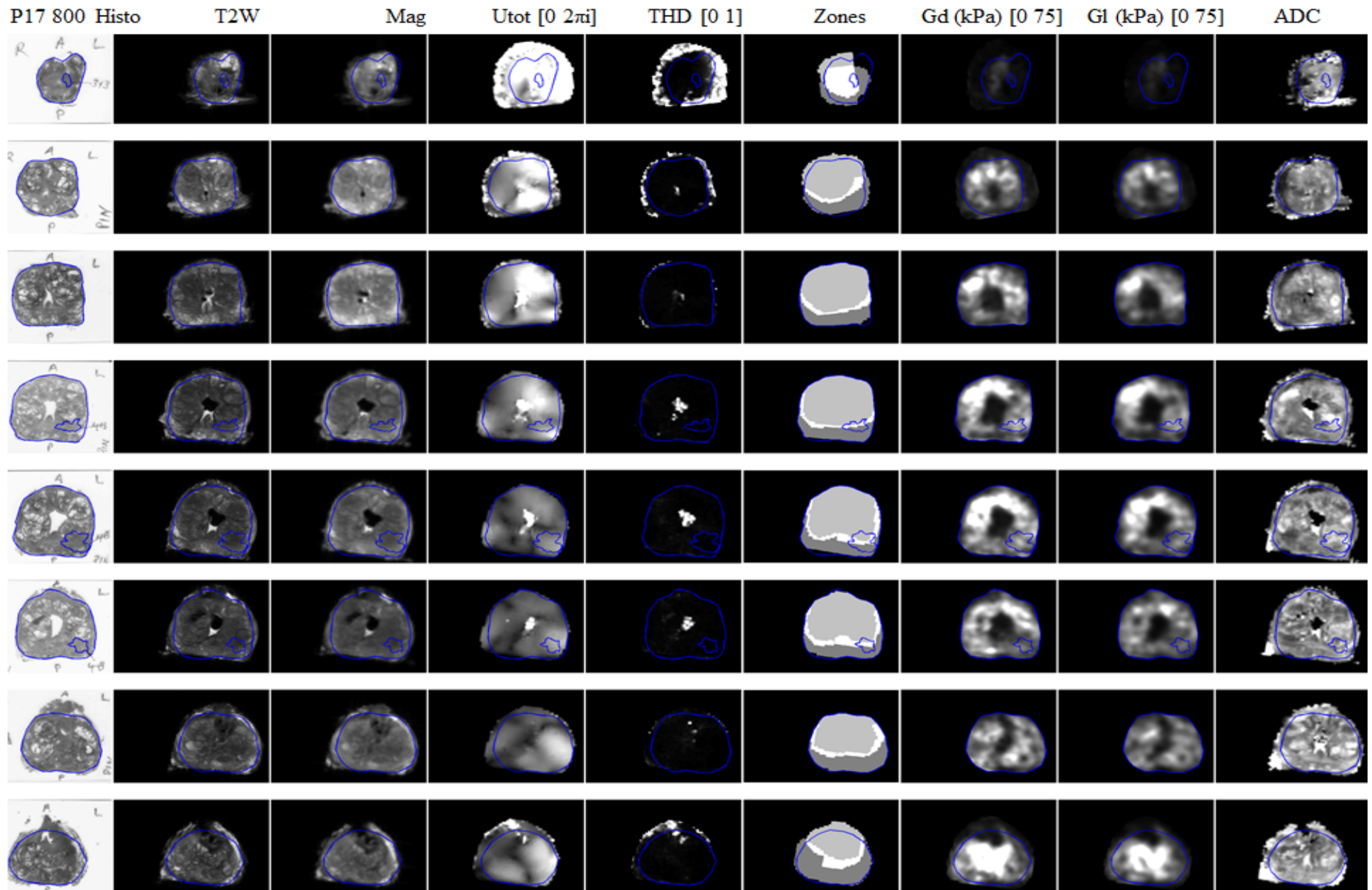


Figure D-51. Results for P17 800 Hz. Shear moduli ( $|G|$  and  $G_I$ ) as registered to histopathology slides. The total wave amplitude and THD are also shown.

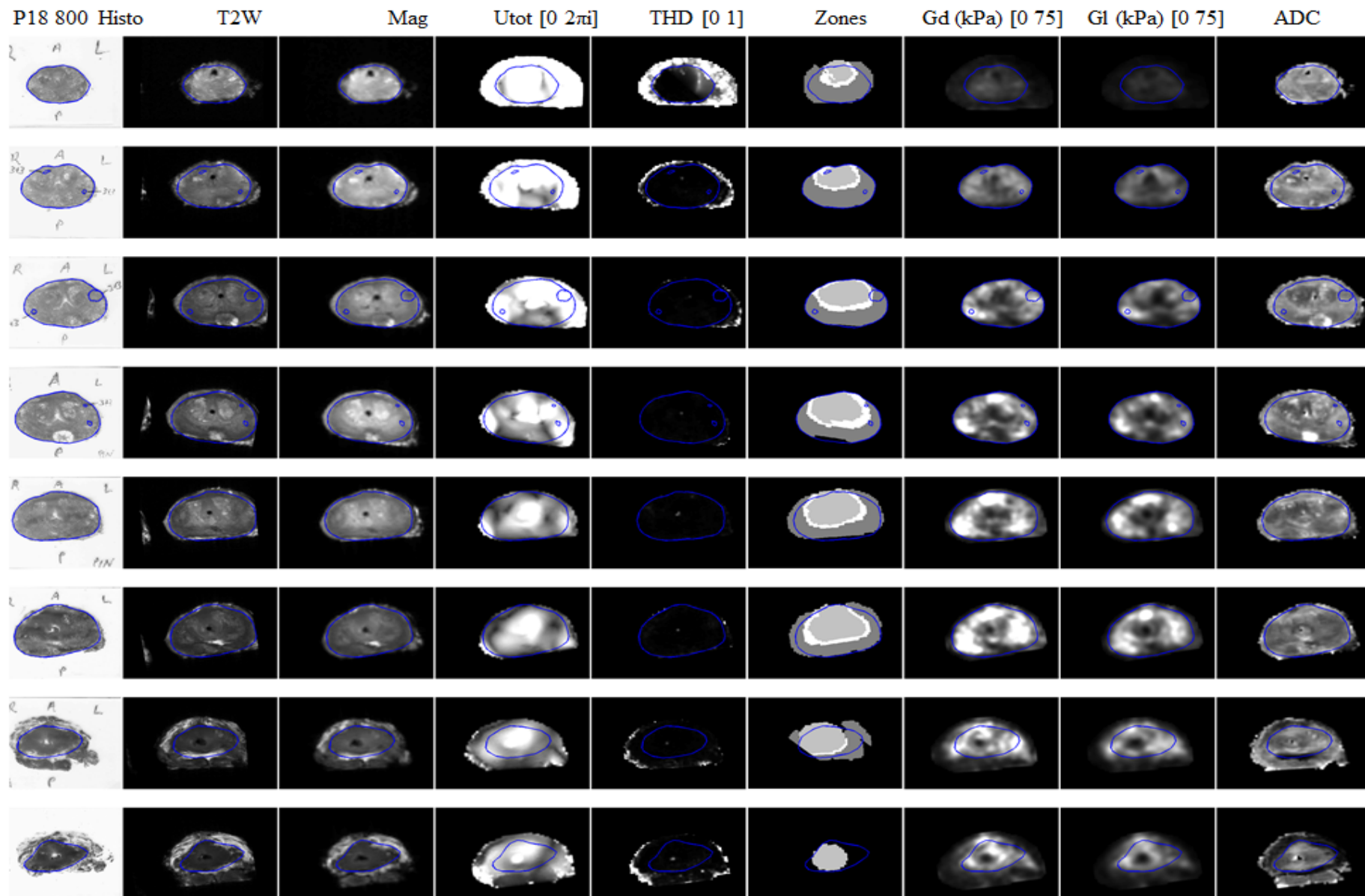


Figure D-52. Results for P18 800 Hz. Shear moduli ( $|G|$  and  $G_I$ ) as registered to histopathology slides. The total wave amplitude and THD are also shown.

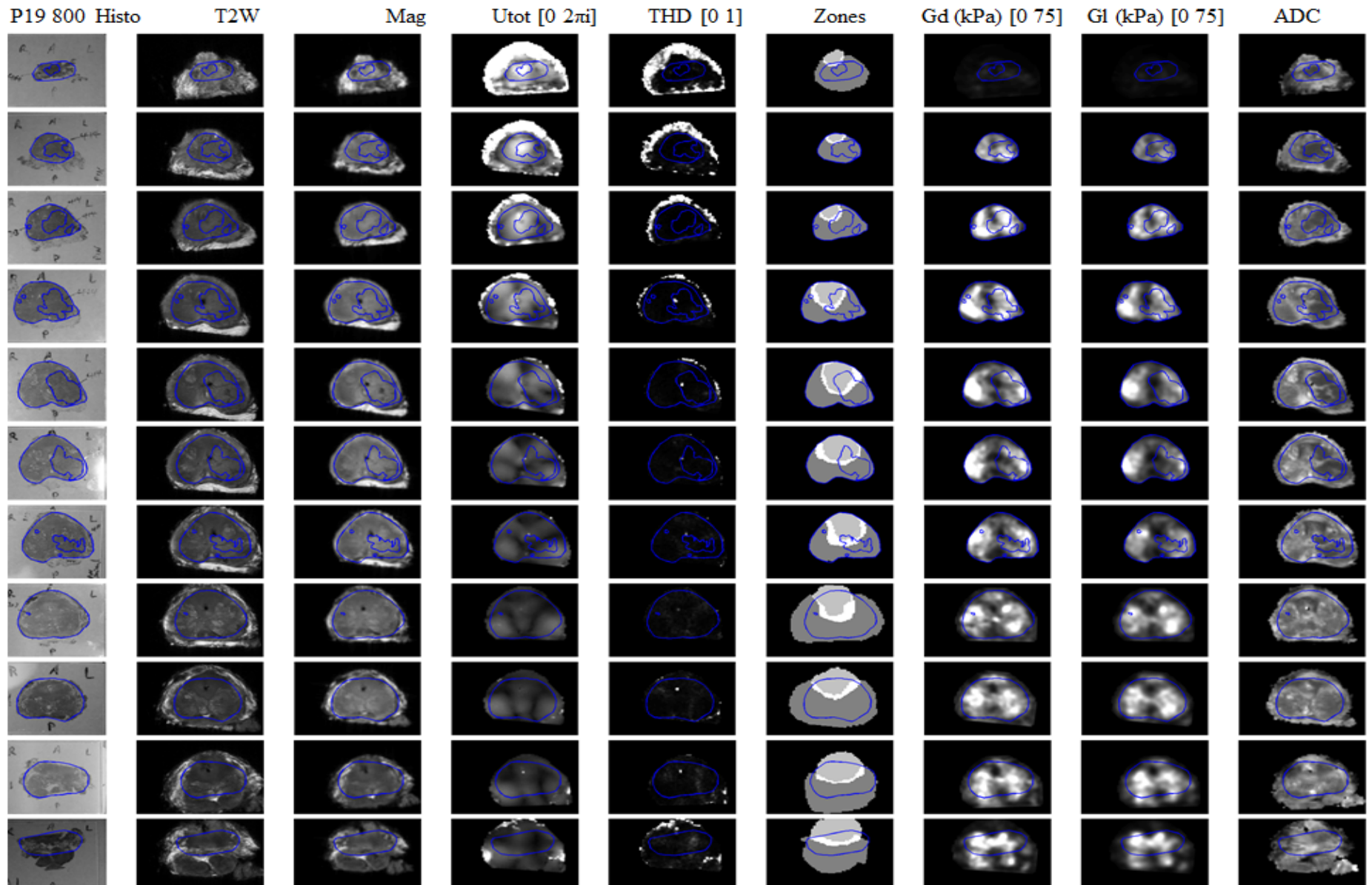


Figure D-53. Results for P19 800 Hz. Shear moduli ( $|G|$  and  $G_I$ ) as registered to histopathology slides. The total wave amplitude and THD are also shown.

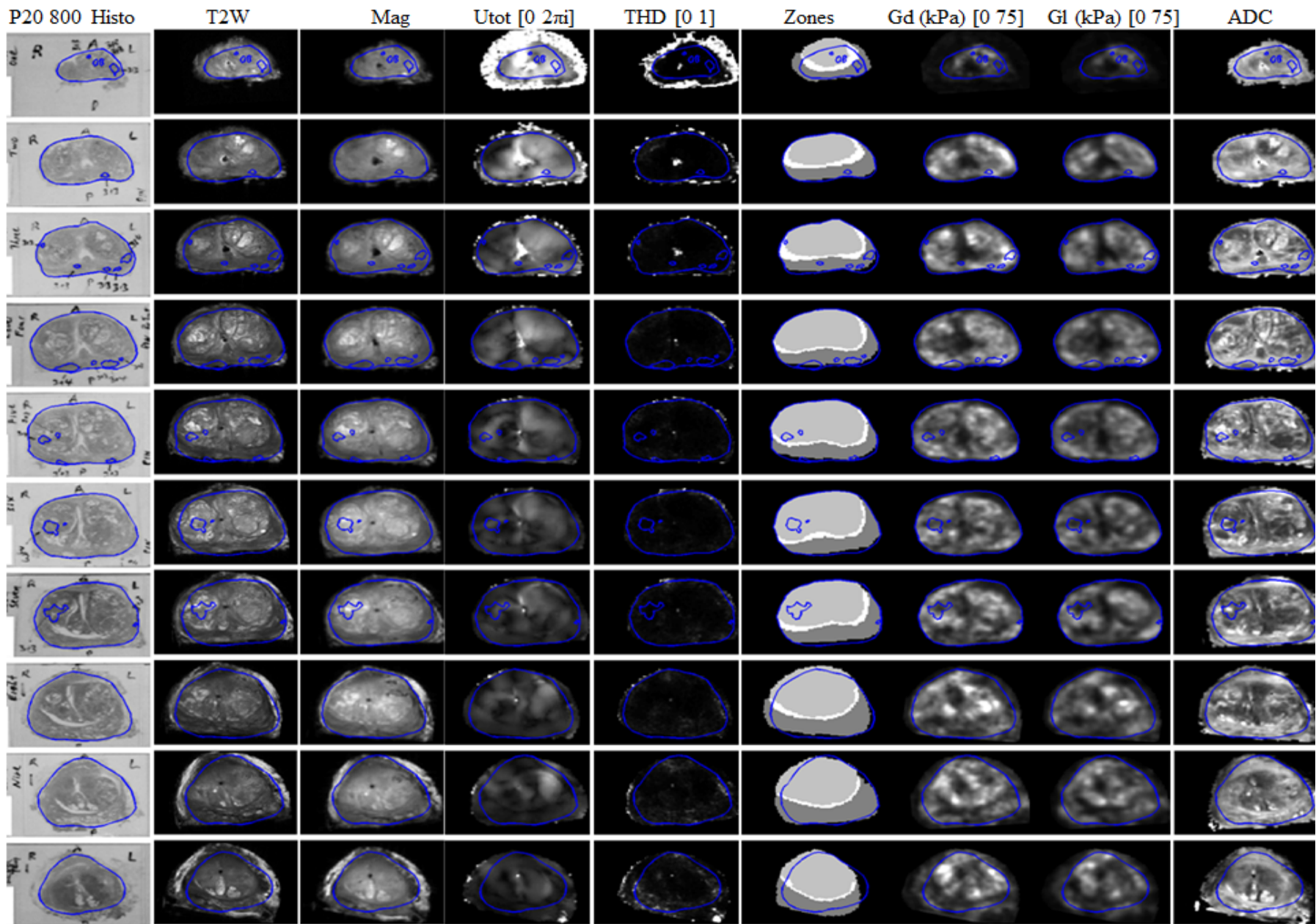


Figure D-54. Results for P20 800 Hz. Shear moduli ( $|G|$  and  $G_I$ ) as registered to histopathology slides. The total wave amplitude and THD are also shown.

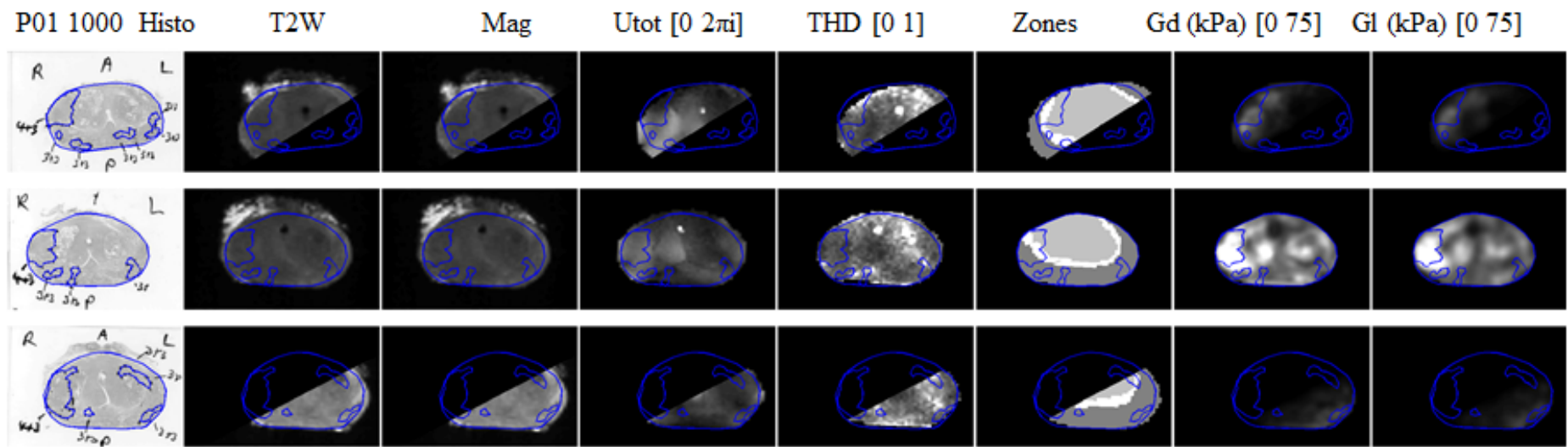


Figure D-55. Results for P01 1000 Hz. Shear moduli ( $G_d$  and  $G_l$ ) as registered to histopathology slides. The total wave amplitude and THD are also shown.

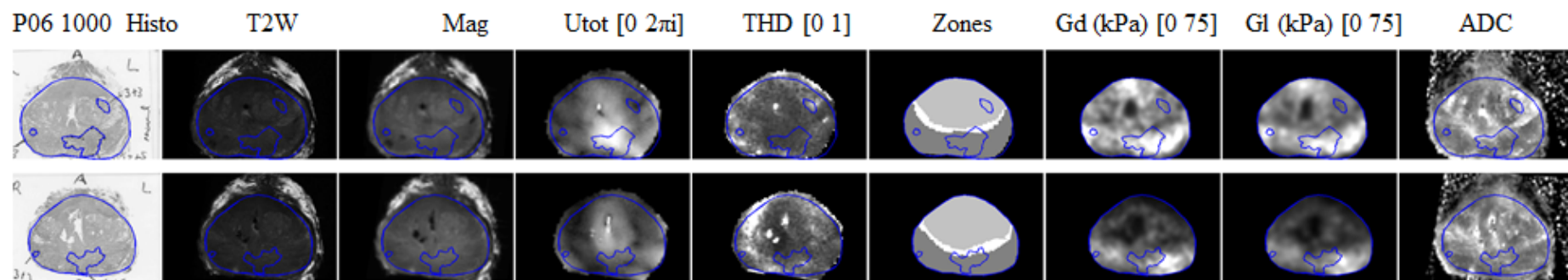


Figure D-56. Results for P06 1000 Hz. Shear moduli ( $G_d$  and  $G_l$ ) as registered to histopathology slides. The total wave amplitude and THD are also shown.

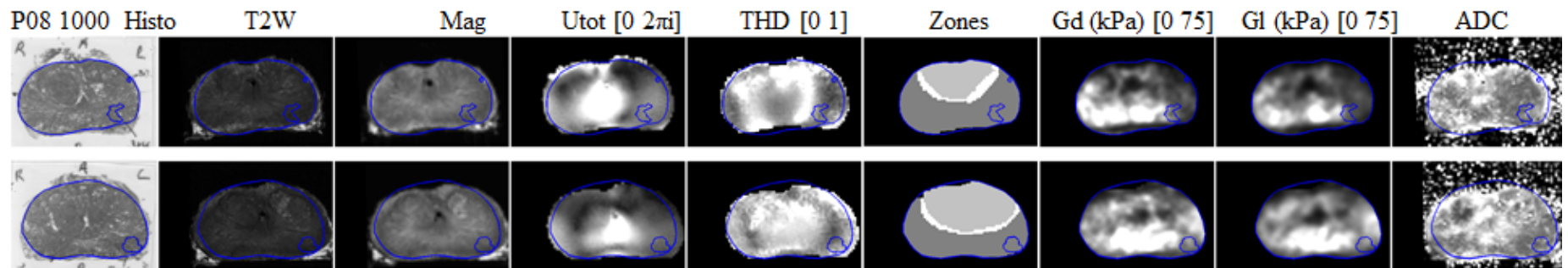


Figure D-57. Results for P08 1000 Hz. Shear moduli ( $G$  and  $G_I$ ) as registered to histopathology slides. The total wave amplitude and THD are also shown.

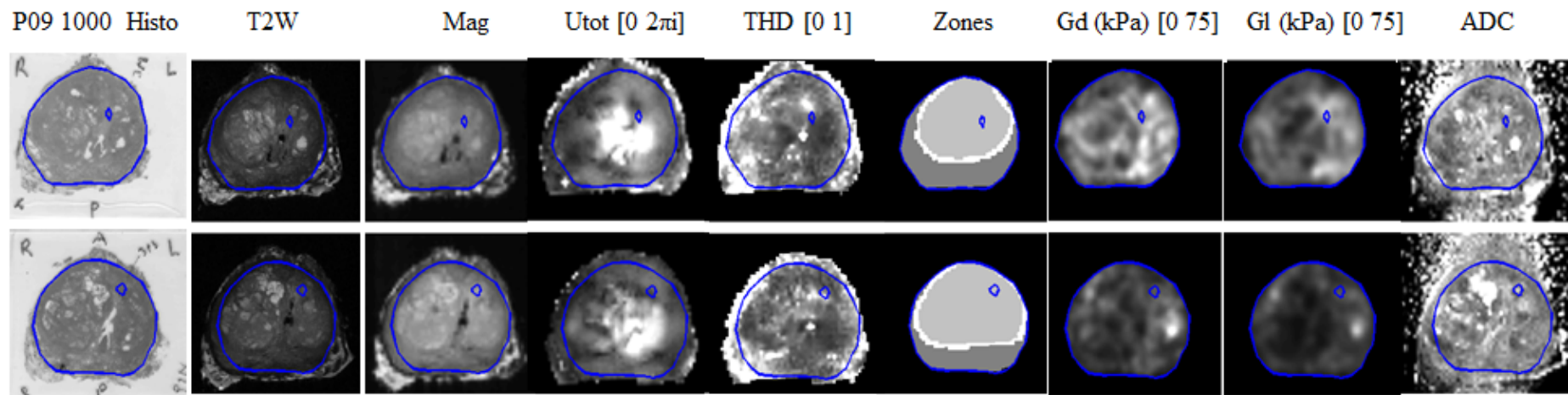


Figure D-58. Results for P09 1000 Hz. Shear moduli ( $G$  and  $G_I$ ) as registered to histopathology slides. The total wave amplitude and THD are also shown.

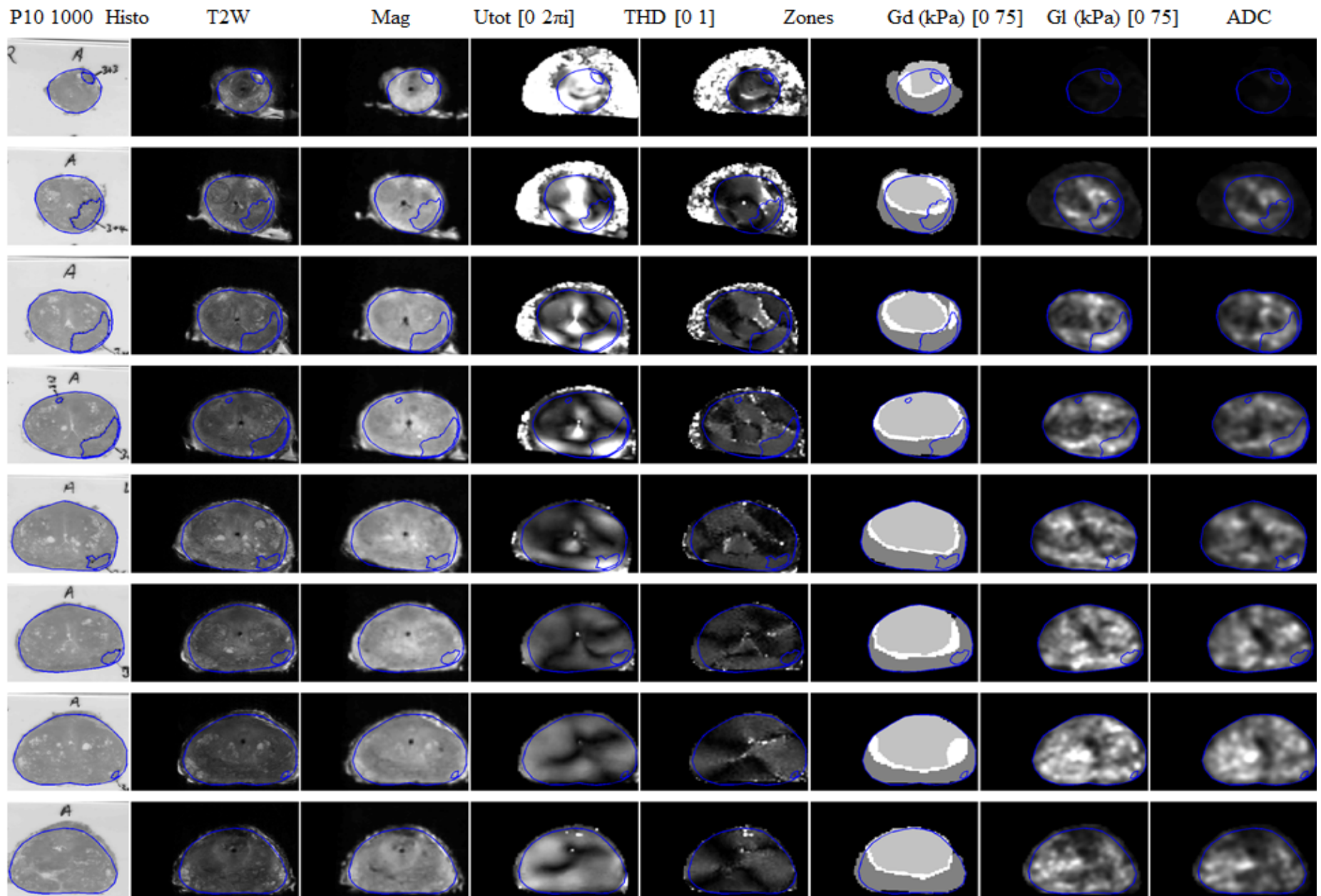


Figure D-59. Results for P10 1000 Hz. Shear moduli ( $G_d$  and  $G_l$ ) as registered to histopathology slides. The total wave amplitude and THD are also shown.

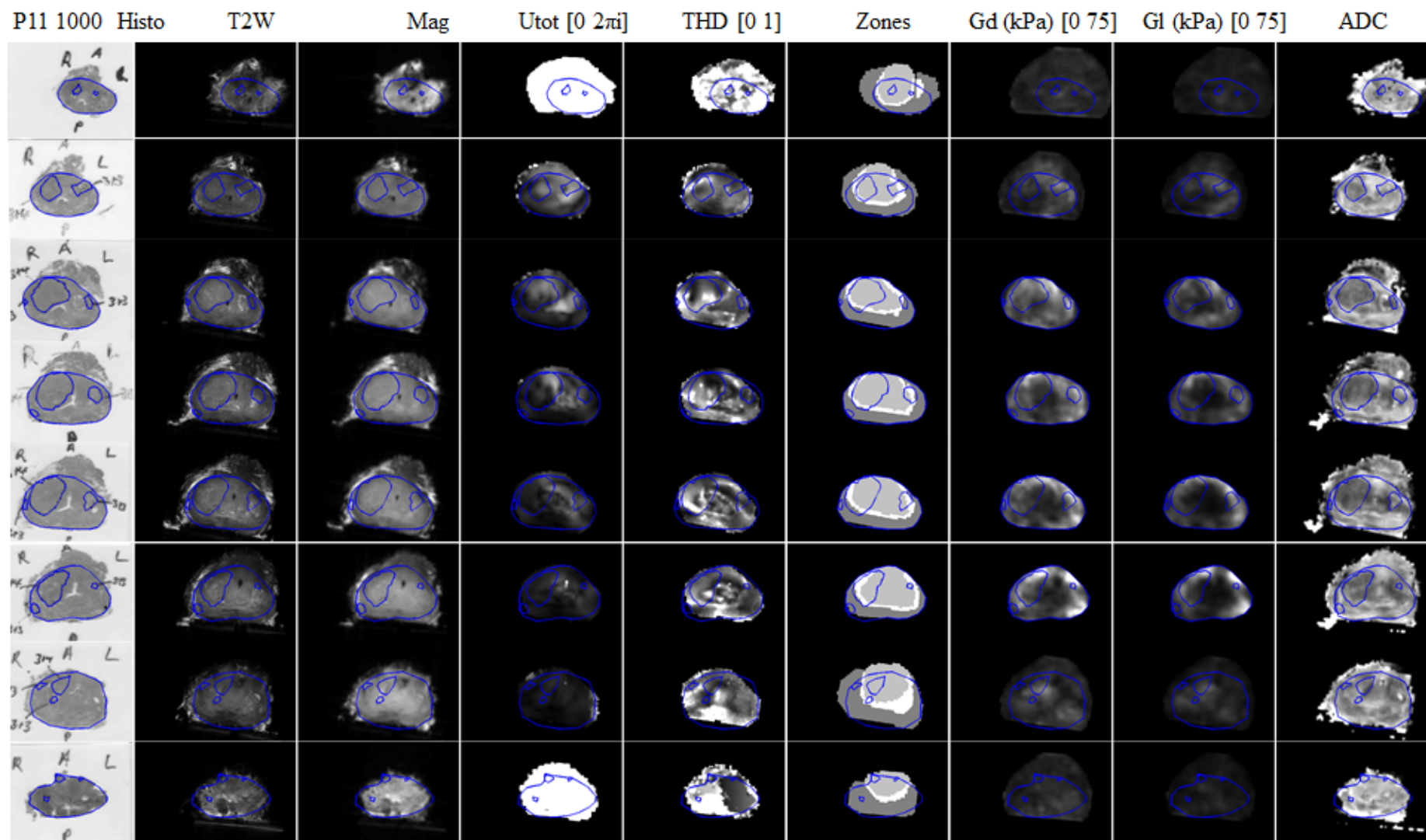


Figure D-60. Results for P11 1000 Hz. Shear moduli ( $G$  and  $G_I$ ) as registered to histopathology slides. The total wave amplitude and THD are also shown.

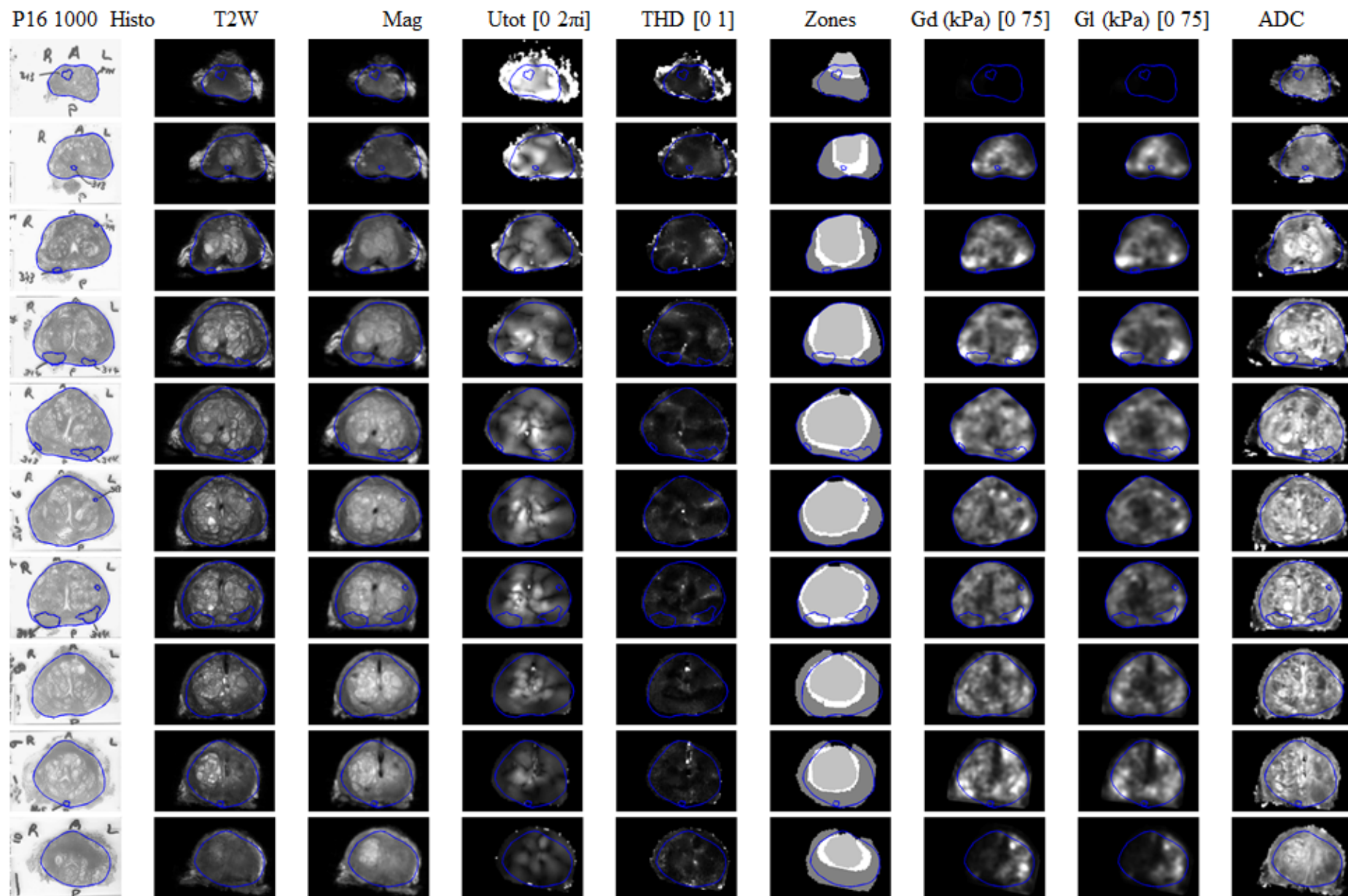


Figure D-61. Results for P16 1000 Hz. Shear moduli ( $G$  and  $G_1$ ) as registered to histopathology slides. The total wave amplitude and THD are also shown.

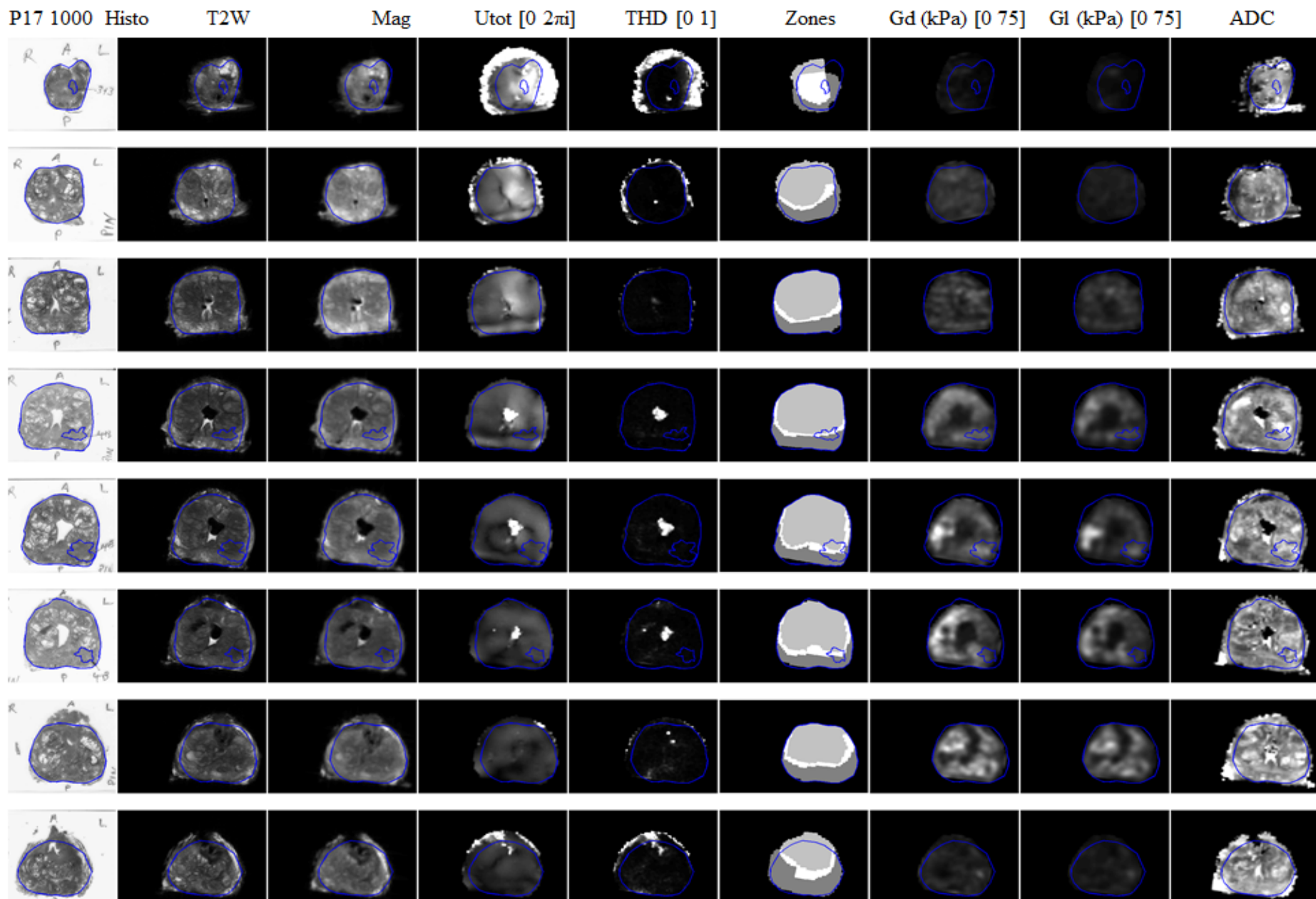


Figure D-62. Results for P17 1000 Hz. Shear moduli ( $G_d$  and  $G_l$ ) as registered to histopathology slides. The total wave amplitude and THD are also shown.

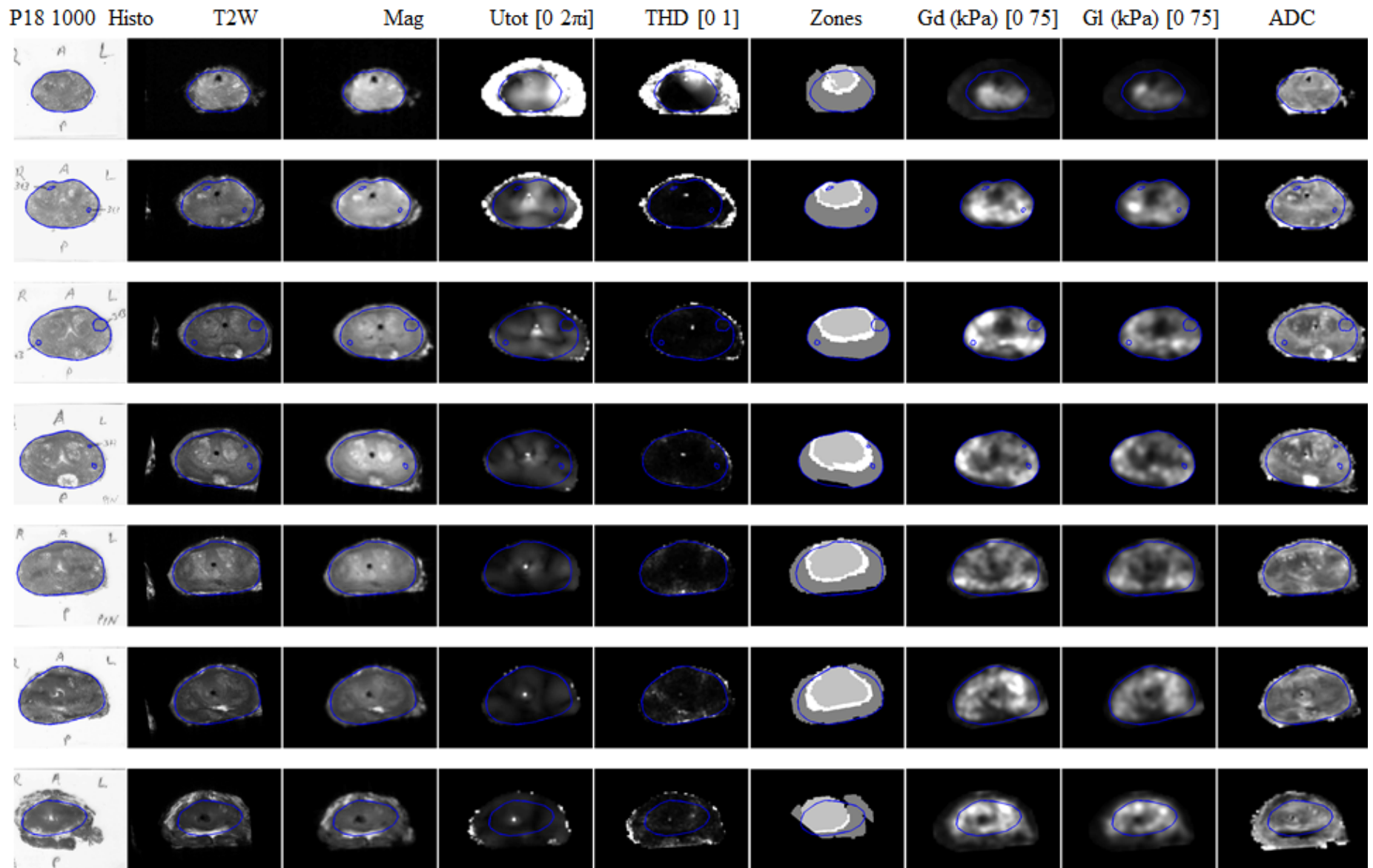


Figure D-63. Results for P18 1000 Hz. Shear moduli ( $G$  and  $G_I$ ) as registered to histopathology slides. The total wave amplitude and THD are also shown.

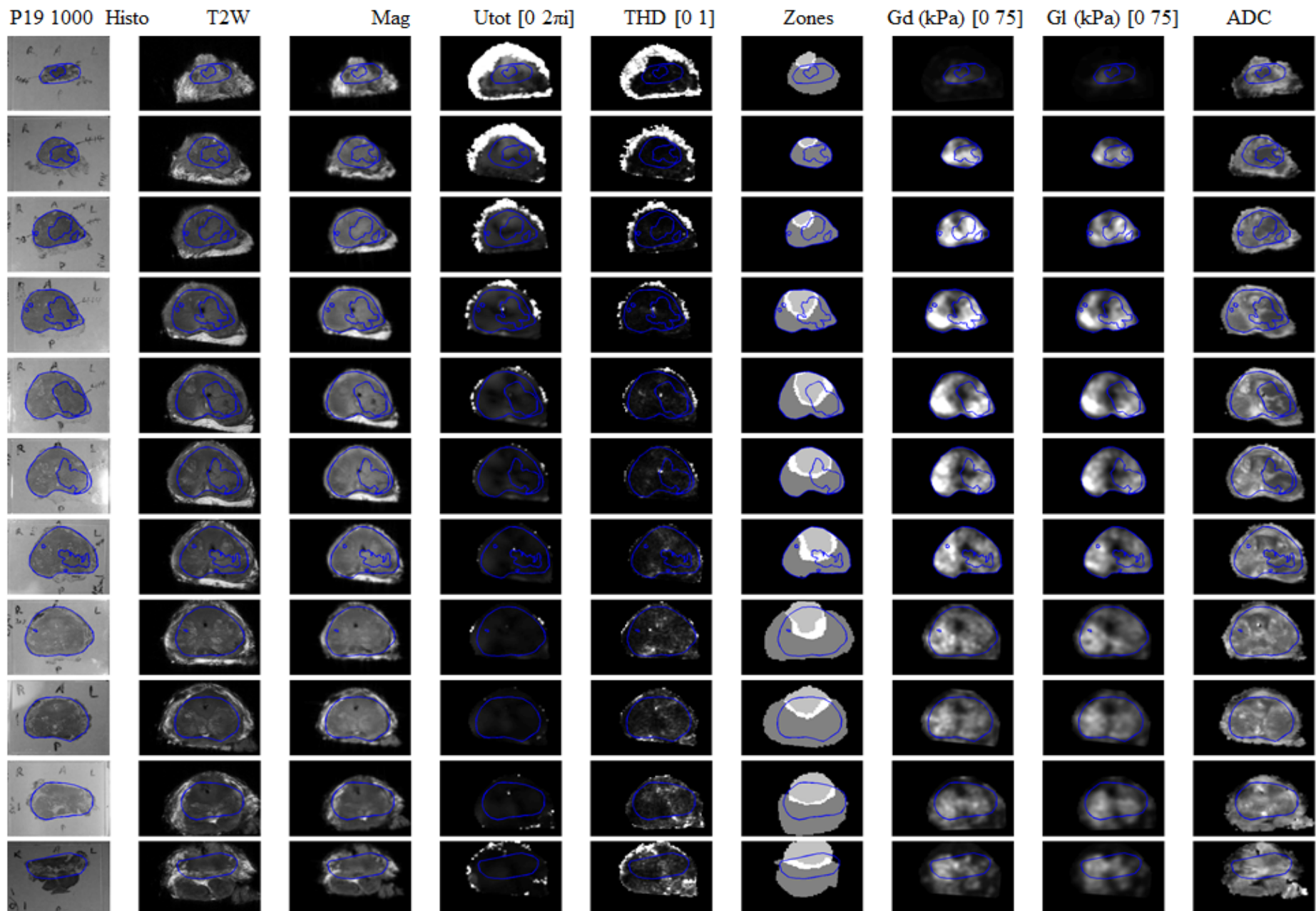


Figure D-64. Results for P19 1000 Hz. Shear moduli ( $G$  and  $G_I$ ) as registered to histopathology slides. The total wave amplitude and THD are also shown.

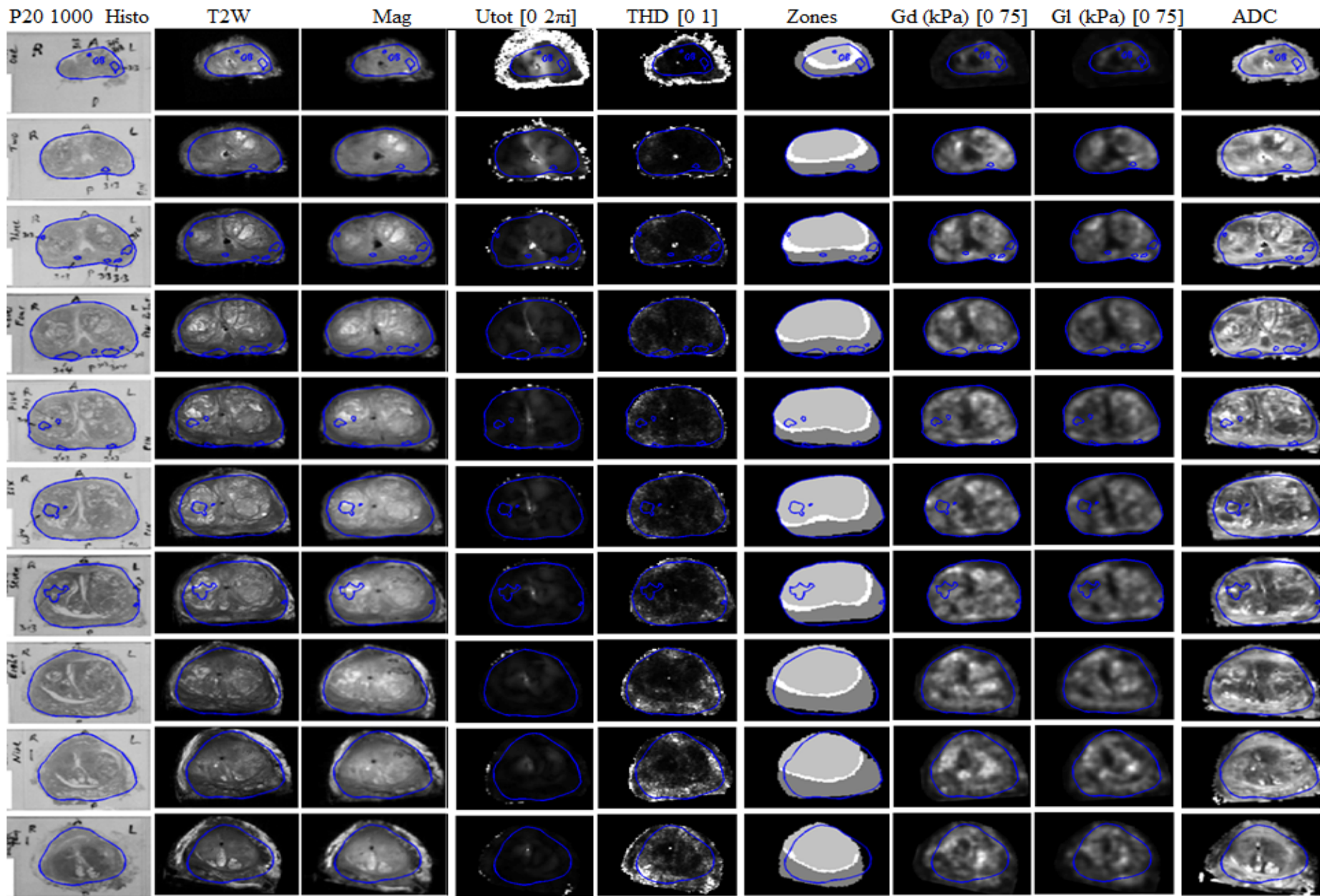


Figure D-65. Results for P20 1000 Hz. Shear moduli ( $|G|$  and  $G_I$ ) as registered to histopathology slides. The total wave amplitude and THD are also shown.



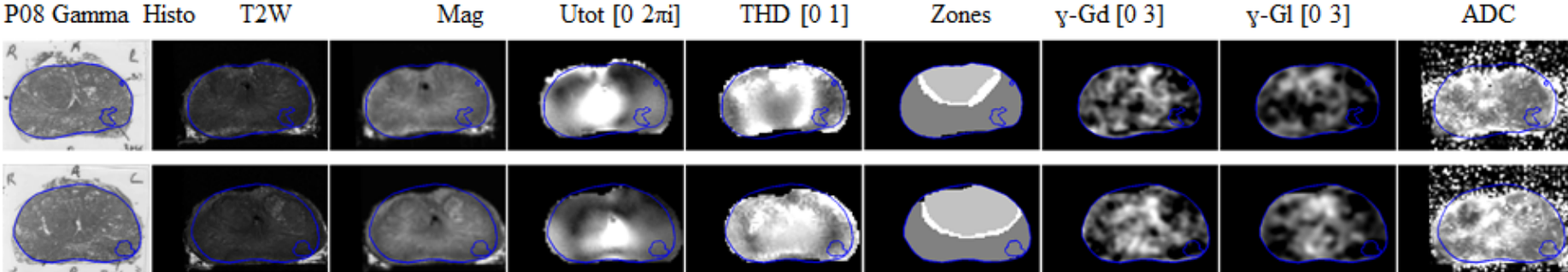


Figure D-67. Results for P08 gamma. The power law for Gd and Gl as registered to histopathology slides. The total wave amplitude and THD are also shown.

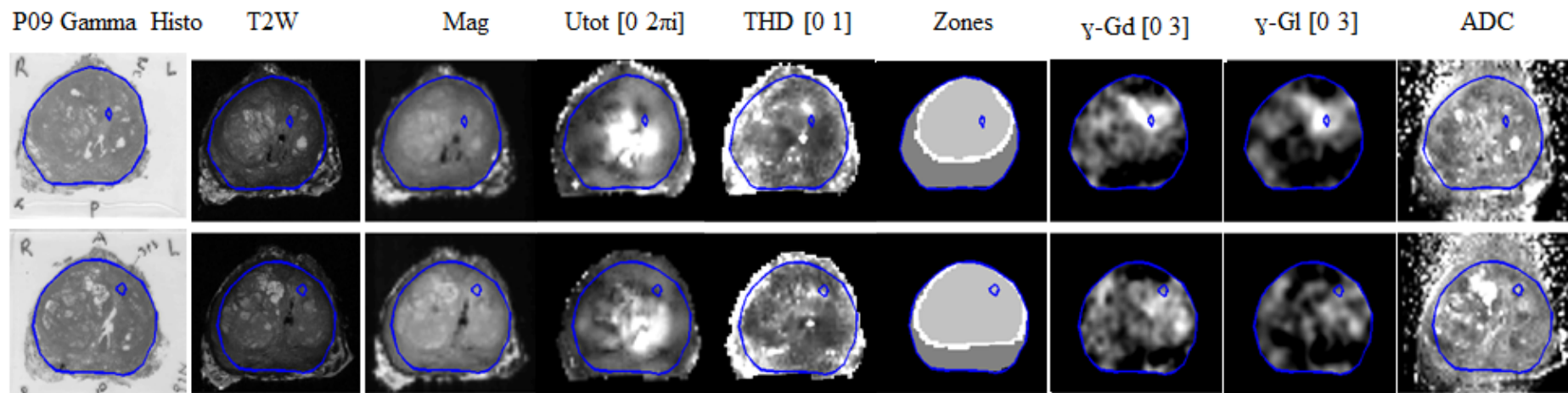


Figure D-68. Results for P09 gamma. The power law for Gd and Gl as registered to histopathology slides. The total wave amplitude and THD are also shown.

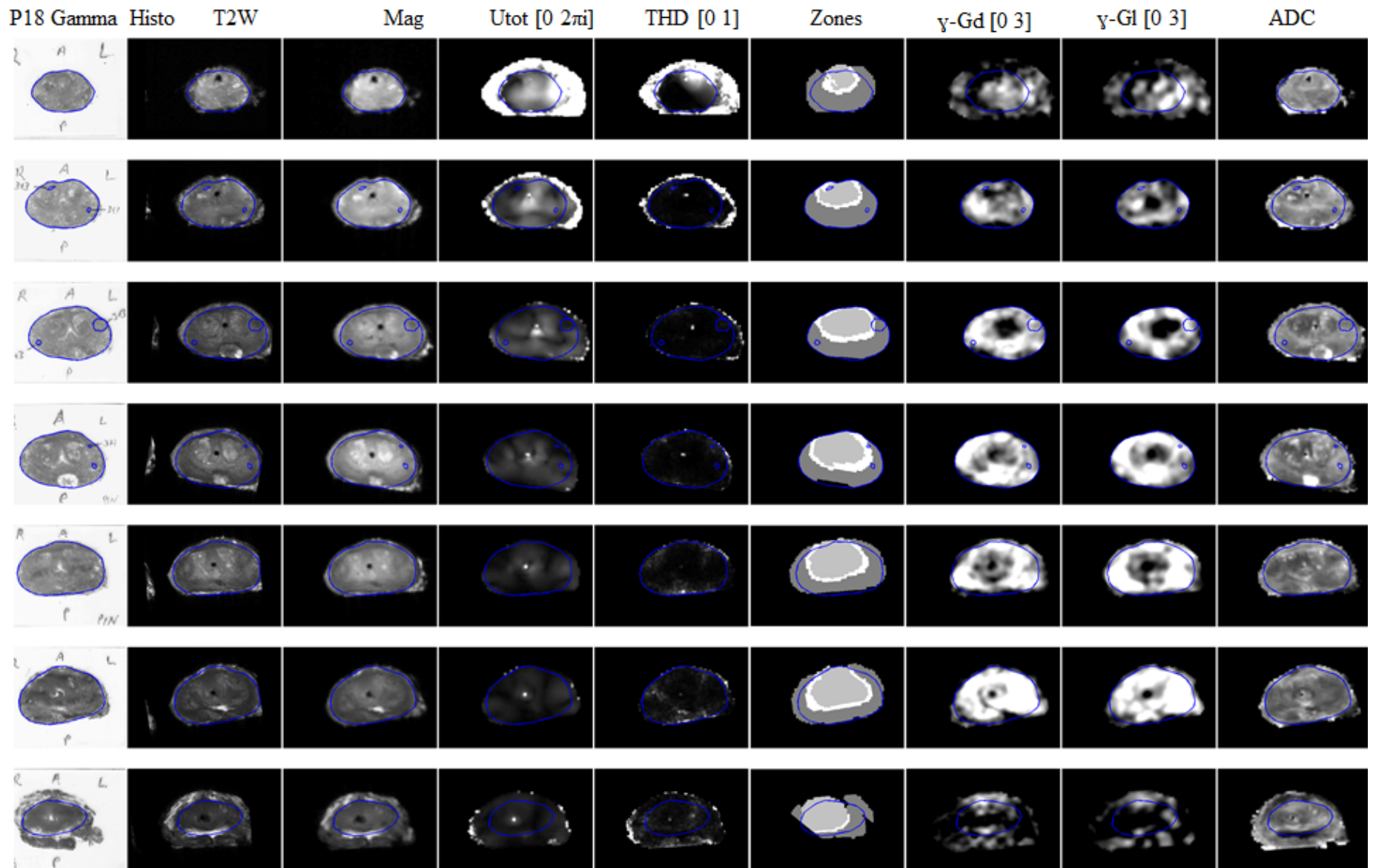


Figure D-69. Results for P18 gamma. The power law for Gd and Gl as registered to histopathology slides. The total wave amplitude and THD are also shown.

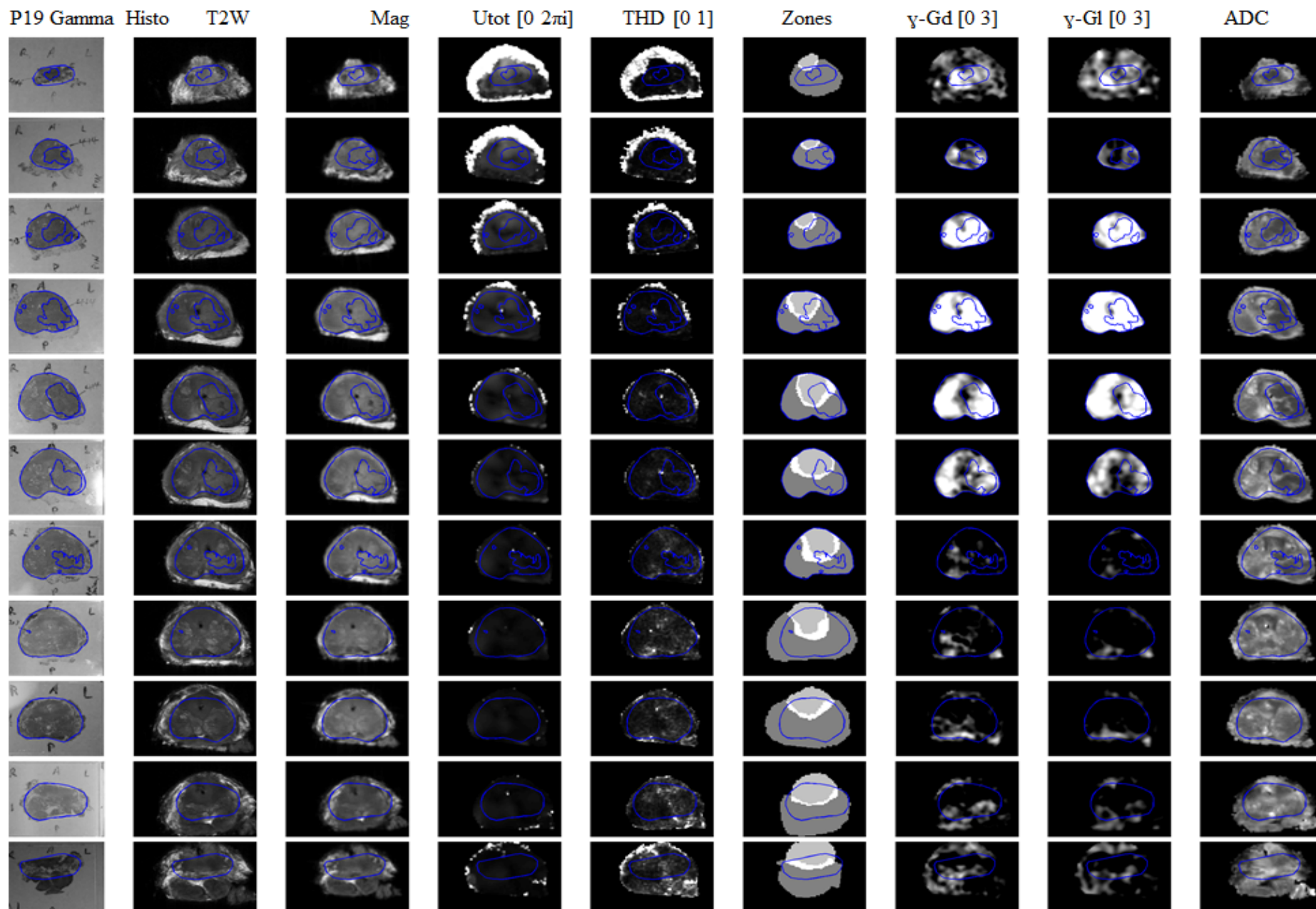


Figure D-70. Results for P19 gamma. The power law for Gd and GI as registered to histopathology slides. The total wave amplitude and THD are also shown.

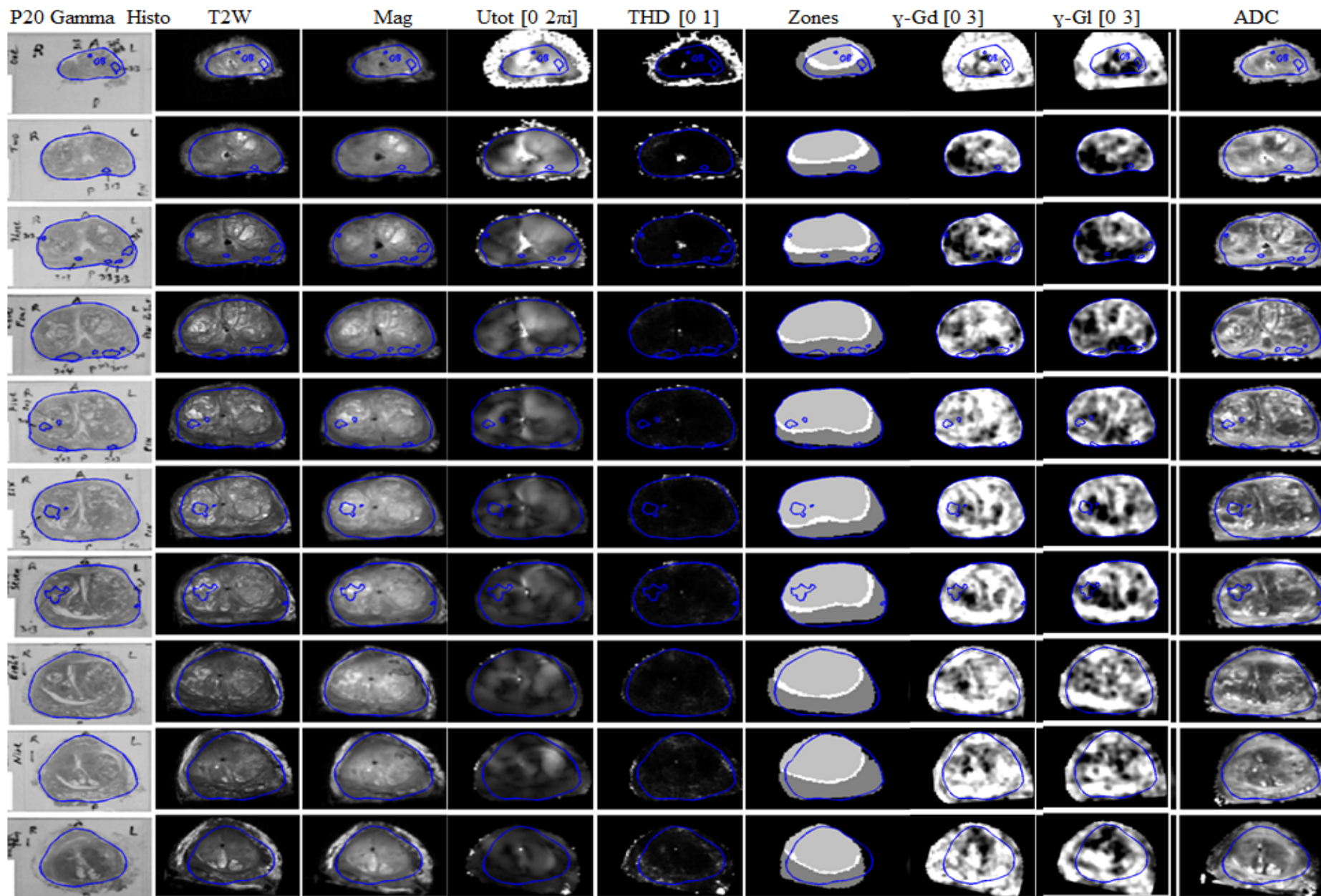


Figure D-71. Results for P20 gamma. The power law for Gd and Gl as registered to histopathology slides. The total wave amplitude and THD are also shown.

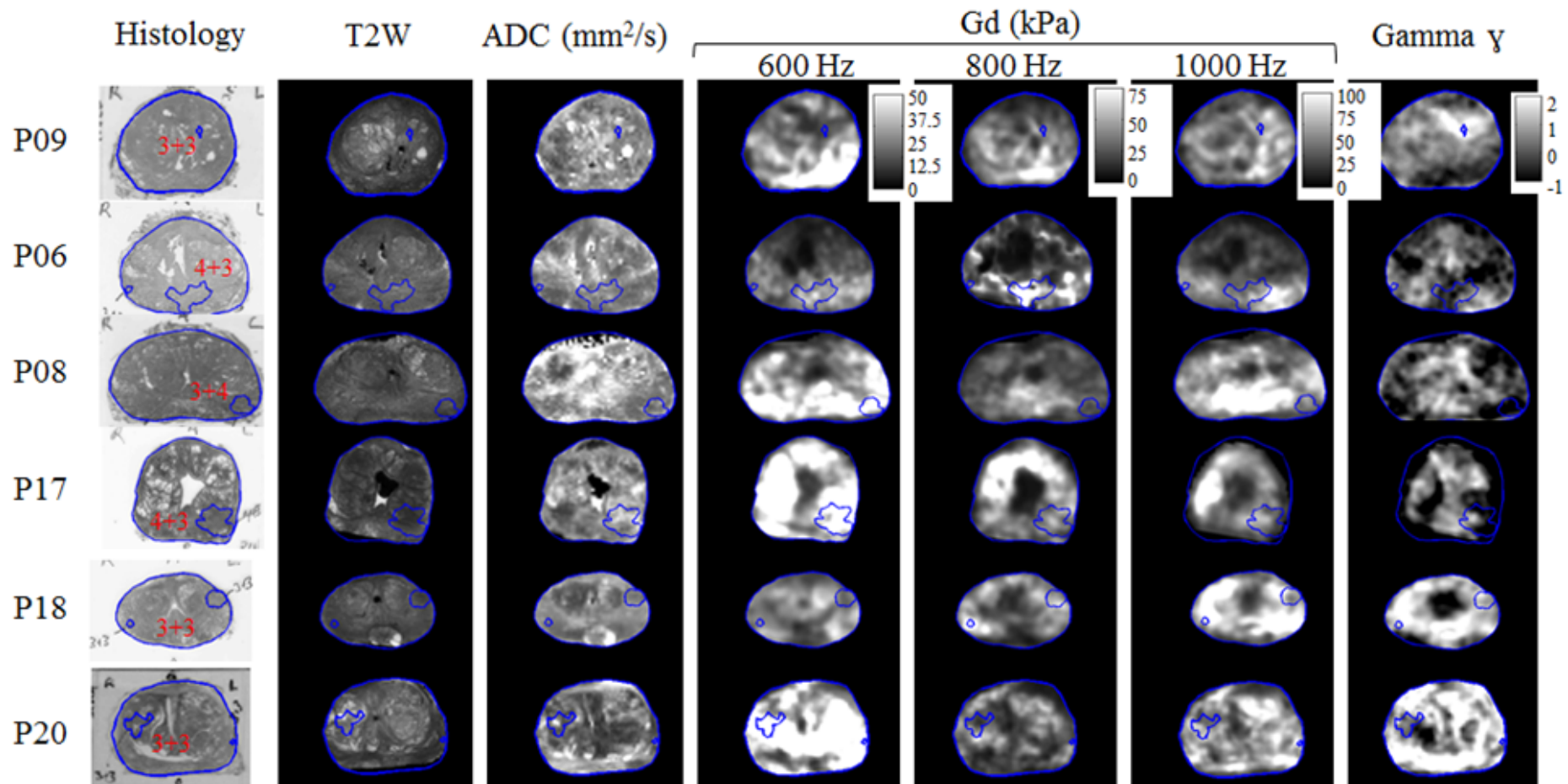


Figure D-72. Summary of multi-frequency results.